Springer Proceedings in Physics 247

Olena Fesenko
Leonid Yatsenko *Editors*

Nanooptics and Photonics, Nanochemistry and Nanobiotechnology, and Their Applications

Selected Proceedings of the 7th International Conference Nanotechnology and Nanomaterials (NANO2019), 27–30 August 2019, Lviv, Ukraine

Springer

Springer Proceedings in Physics

Volume 247

Indexed by Scopus

The series Springer Proceedings in Physics, founded in 1984, is devoted to timely reports of state-of-the-art developments in physics and related sciences. Typically based on material presented at conferences, workshops and similar scientific meetings, volumes published in this series will constitute a comprehensive up-to-date source of reference on a field or subfield of relevance in contemporary physics. Proposals must include the following:

- name, place and date of the scientific meeting
- a link to the committees (local organization, international advisors etc.)
- scientific description of the meeting
- list of invited/plenary speakers
- an estimate of the planned proceedings book parameters (number of pages/articles, requested number of bulk copies, submission deadline).

More information about this series at http://www.springer.com/series/361

Olena Fesenko · Leonid Yatsenko
Editors

Nanooptics and Photonics, Nanochemistry and Nanobiotechnology, and Their Applications

Selected Proceedings of the 7th International Conference Nanotechnology and Nanomaterials (NANO2019), 27–30 August 2019, Lviv, Ukraine

Springer

Editors
Olena Fesenko
Institute of Physics
National Academy of Sciences of Ukraine
Kyiv, Ukraine

Leonid Yatsenko
Institute of Physics
National Academy of Sciences of Ukraine
Kyiv, Ukraine

ISSN 0930-8989 ISSN 1867-4941 (electronic)
Springer Proceedings in Physics
ISBN 978-3-030-52267-4 ISBN 978-3-030-52268-1 (eBook)
https://doi.org/10.1007/978-3-030-52268-1

This Springer imprint is published by the registered company Springer Nature Switzerland AG
The registered company address is: Gewerbestrasse 11, 6330 Cham, Switzerland

Preface

This book highlights the most recent advances in nanoscience from leading researchers in Ukraine, Europe, and beyond. It features contributions from participants of the 7th International Research and Practice Conference "Nanotechnology and Nanomaterials" (NANO-2019), held in Lviv, Ukraine, on August 27 to 30, 2019. This event was organized jointly by the Institute of Physics of the National Academy of Sciences of Ukraine, Lviv Polytechnic National University (Ukraine), University of Tartu (Estonia), University of Turin (Italy), and Pierre and Marie Curie University (France). Internationally recognized experts from a wide range of universities and research institutes shared their knowledge and key results in the areas of nanooptics and nanophotonics, nanoplasmonics, surface-enhanced spectroscopy, nanocomposites and nanomaterials, nanostructured surfaces, microscopy of nano-objects, nanochemistry, nanobiotechnology, and nanobiotechnology for health care.

Today, nanotechnology is becoming one of the most actively developing and promising fields of science. Numerous nanotechnology investigations are already producing practical results that can be applied in various areas of human life from science and technology to medicine and pharmacology. The aim of these books is to highlight the latest investigations from different areas of nanoscience and to stimulate new interest in this field. Volume I of this two-volume work covers important topics such as nanostructured interfaces and surfaces, nanochemistry and biotechnology, nanooptics and photonics, nanoplasmonics, and its applications.

This book is divided into two parts: first part—*Nanochemistry and Biotechnology*, and second part—*Nanooptics and Photonics*. Parts covering nanoscale physics, nanostructured interfaces and surfaces, and nanocomposites and nanomaterials can be found in Volume II: *Nanomaterials and Nanocomposites, Nanostructure Surfaces, and Their Applications*.

The papers published in these five parts fall under the broad categories of nanomaterial preparation and characterization, nanobiotechnology, nanodevices and quantum structures, and spectroscopy and nanooptics. The book will help readers to familiarize with current research and practical applications in nanoscience and thus

to promote further implementation of nanotechnologies into innovations according to public needs. We hope that both volumes will be equally useful and interesting for young scientists or Ph.D. students and mature scientists alike.

Kyiv, Ukraine

Olena Fesenko
Leonid Yatsenko

Contents

Contributors

Yevgen Aftandiliants National University of Life and Environmental Sciences of Ukraine, Kyiv, Ukraine

M. A. Alieksandrov Taras Shevchenko National University of Kyiv, Kyiv, Ukraine

S. B. Artemkina Nikolaev Institute of Inorganic Chemistry SB RAS, Novosibirsk, Russia

A. E. Artyukhov Processes and Equipment of Chemical and Petroleum-Refineries Department, Sumy State University, Sumy, Ukraine

Artem Artyukhov Sumy State University, Sumy, Ukraine

N. O. Artyukhova Processes and Equipment of Chemical and Petroleum-Refineries Department, Sumy State University, Sumy, Ukraine

I. Asterlin National Technical University of Ukraine "Igor Sikorsky Kyiv Polytechnic Institute, Kiev, Ukraine

Natalya Babenko Department of Cryopathophysiology and Immunology, Institute for Problems of Cryobiology & Cryomedicine of the National Academy of Sciences of Ukraine, Kharkiv, Ukraine

Y. Bobitski Department of Photonics, Lviv Polytechnic National University, Lviv, Ukraine;
Faculty of Mathematics and Natural Sciences, University of Rzeszow, Rzeszow, Poland

Jozef Bocko Technical University of Košice, Košice, Slovak Republic

Mykola Bondarovych Department of Cryopathophysiology and Immunology, Institute for Problems of Cryobiology & Cryomedicine of the National Academy of Sciences of Ukraine, Kharkiv, Ukraine

Viacheslav Boretskij Taras Shevchenko National University of Kyiv, Kyiv, Ukraine

E. Broda Department of Radiochemistry and Environmental Chemistry, Institute of Chemical Sciences, Faculty of Chemistry, Maria Curie-Sklodowska University, Lublin, Poland

T. Bulavinets Department of Photonics, Lviv Polytechnic National University, Lviv, Ukraine

T. O. Busko Taras Shevchenko National University of Kyiv, Kyiv, Ukraine

J. Cebulski University of Rzeszow, Rzeszow, Poland

Oleksandr I. Datsenko Physics Department, Taras Shevchenko National University of Kyiv, Kiev, Ukraine

L. V. Denis Taras Shevchenko National University of Kyiv, Kyiv, Ukraine

O. A. Diyuk Institute for Sorption and Problems of Endoecology, National Academy of Sciences of Ukraine, Kiev, Ukraine

O. P. Dmytrenko Taras Shevchenko National University of Kyiv, Kyiv, Ukraine

Tatiana Dubrava Department of Cryopathophysiology and Immunology, Institute for Problems of Cryobiology & Cryomedicine of the National Academy of Sciences of Ukraine, Kharkiv, Ukraine

P. Dulian Faculty of Chemical Engineering and Technology, Cracow University of Technology, Cracow, Poland

Alina V. Dvornichenko Sumy State University, Sumy, Ukraine

Ganna Dzhyga Odessa I.I. Mechnikov National University, Odesa, Ukraine

V. E. Fedorov Nikolaev Institute of Inorganic Chemistry SB RAS, Novosibirsk, Russia

V. Fitio Department of Photonics, Lviv Polytechnic National University, Lviv, Ukraine

Paola Frigeri Institute of Materials for Electronics and Magnetism, IMEM-CNR, Parma, Italy

L. Frolova Ukrainian State University of Chemical Technology, Dnipro, Ukraine

Angelina Gab University “Ukraine”, Kiev, Ukraine;
Ecole Polytechnique, CNRS, UMR 6595, Technopôle deChateau Gombert, Marseille Cedex 13, France

Yuliya Gaevska Department of Cryopathophysiology and Immunology, Institute for Problems of Cryobiology & Cryomedicine of the National Academy of Sciences of Ukraine, Kharkiv, Ukraine

Marcelle Gaune-Escard Ecole Polytechnique, CNRS, UMR 6595, Technopôle de Chateau Gombert, Marseille, France

Sergii Golovynskyi Key Laboratory of Optoelectronic Devices and Systems of Ministry of Education and Guangdong Province, College of Physics and Optoelectronic Engineering, Shenzhen University, Shenzhen, People's Republic of China

Anatoliy Goltsev Department of Cryopathophysiology and Immunology, Institute for Problems of Cryobiology & Cryomedicine of the National Academy of Sciences of Ukraine, Kharkiv, Ukraine

N. A. Goncharenko Taras Shevchenko National University of Kyiv, Kyiv, Ukraine

P. P. Gorbyk Chuiko Institute of Surface Chemistry of NAS of Ukraine, Kyiv, Ukraine

Yu. E. Grabovskiy Taras Shevchenko National University of Kyiv, Kyiv, Ukraine

A. Grebenyuk Chuiko Institute of Surface Chemistry, NAS of Ukraine, Kiev, Ukraine

V. O. Gubanov Taras Shevchenko National University of Kyiv, Kiev, Ukraine

O. O. Honcharova Taras Shevchenko National University of Kyiv, Kyiv, Ukraine

L. I. Ieremenko Frantsevych Institute for Problems of Materials Science of NAS of Ukraine, Kiev, Ukraine

H. A. Ilchuk Department of General Physics, Lviv Polytechnic National University, Lviv, Ukraine

A. Ingram Opole University of Technology, Opole, Poland

I. Ivanenko National Technical University of Ukraine "Igor Sikorsky Kyiv Polytechnic Institute, Kiev, Ukraine

A. I. Kashuba Department of General Physics, Lviv Polytechnic National University, Lviv, Ukraine

Vasyl O. Kharchenko Institute of Applied Physics, National Academy of Sciences of Ukraine, Sumy, Ukraine

O. Khmelenko Oles Honchar Dnipro National University, Dnipro, Ukraine

Tatyana Kiose Odessa I.I. Mechnikov National University, Odesa, Ukraine

Vladimir Klochkov Department of Nanocrystal Materials, Institute for Scintillation Materials of the National Academy of Sciences of Ukraine, Kharkiv, Ukraine

O. F. Kolomys V.E. Lashkaryov Institute of Semiconductor Physics, Kyiv, Ukraine

N. E. Kornienko Taras Shevchenko National University of Kyiv, Kiev, Ukraine

Igor Kovalenko Department for Low Temperature preservation, Institute for Problems of Cryobiology & Cryomedicine of the National Academy of Sciences of Ukraine, Kharkiv, Ukraine

O. Kravets Ivan Franko National University of Lviv, Lviv, Ukraine

J. Krmela Department of Numerical Methods and Computational Modeling, Alexander Dubcek University of Trencin, Puchov, Slovak Republic

L. A. Krushynska Frantsevych Institute for Problems of Materials Science of NAS of Ukraine, Kiev, Ukraine

I. Kud Frantsevych Institute for Problems of Materials Science of NAS of Ukraine, Kiev, Ukraine

A. Kukh National Technical University of Ukraine "Igor Sikorsky Kyiv Polytechnic Institute, Kiev, Ukraine

L. M. Kulikov Frantsevich Institute for Problems of Materials Science, National Academy of Science of Ukraine, Kyiv-142, Ukraine

M. P. Kulish Taras Shevchenko National University of Kyiv, Kyiv, Ukraine

M. M. Kurmach L. V. Pisarzhevskii Institute of Physical Chemistry, National Academy of Sciences of Ukraine, Kiev, Ukraine

O. Kushnerov Oles Honchar Dnipro National University, Dnipro, Ukraine

N. Kutsevol Taras Shevchenko National University of Kyiv, Kiev, Ukraine

Nataliya Kutsevol Taras Shevchenko National University of Kyiv, Kiev, Ukraine

O. Kychkyruk Ivan Franko Zhytomyr State University, Zhytomyr, Ukraine

A. I. Lesiuk Taras Shevchenko National University of Kyiv, Kyiv, Ukraine

Baikui Li Key Laboratory of Optoelectronic Devices and Systems of Ministry of Education and Guangdong Province, College of Physics and Optoelectronic Engineering, Shenzhen University, Shenzhen, People's Republic of China

Kostyantin Lopatko National University of Life and Environmental Sciences of Ukraine, Kyiv, Ukraine

Serafim Lopatko National University of Life and Environmental Sciences of Ukraine, Kyiv, Ukraine

M. Losytskyi Taras Shevchenko National University of Kyiv, Kiev, Ukraine

A. Luchechko Ivan Franko National University of Lviv, Lviv, Ukraine

Tetiana Lukashenko Open International University of Human Development "Ukraine", Kiev, Ukraine

A. Maizelis Department of Technical Electrochemistry, National Technical University «Kharkiv Polytechnic Institute», Kharkiv, Ukraine

Viktor Malyshev Open International University of Human Development "Ukraine", Kiev, Ukraine

Yurii Malyukin Department of Nanocrystal Materials, Institute for Scintillation Materials of the National Academy of Sciences of Ukraine, Kharkiv, Ukraine

Iu. Mukha Chuiko Institute of Surface Chemistry, NAS of Ukraine, Kiev, Ukraine

O. Nadtoka Taras Shevchenko National University of Kyiv, Kiev, Ukraine

A. P. Naumenko Taras Shevchenko National University of Kyiv, Kiev, Ukraine

Antonina Naumenko Taras Shevchenko National University of Kyiv, Kiev, Ukraine

L. Ol'khovik National Taras Shevchenko University of Kyiv, Kiev, Ukraine

A. P. Onanko Taras Shevchenko National University of Kyiv, Kyiv, Ukraine

V. Orel National Cancer Institute, Kiev, Ukraine;
Biomedical Engineering Department, NTUU Igor Sikorsky KPI, Kiev, Ukraine

V. B. Orel Medical Faculty, Bogomolets National Medical University, Kiev, Ukraine

Ruslan Ostroha Sumy State University, Sumy, Ukraine

O. L. Pavlenko Taras Shevchenko National University of Kyiv, Kyiv, Ukraine

A. L. Petranovska Chuiko Institute of Surface Chemistry of NAS of Ukraine, Kyiv, Ukraine

R. Y. Petrus Department of General Physics, Lviv Polytechnic National University, Lviv, Ukraine

T. M. Pinchuk-Rugal Taras Shevchenko National University of Kyiv, Kyiv, Ukraine

Y. Polonska National Taras Shevchenko University of Kyiv, Kiev, Ukraine

I. P. Pundyk Taras Shevchenko National University of Kyiv, Kyiv, Ukraine

Junle Qu Key Laboratory of Optoelectronic Devices and Systems of Ministry of Education and Guangdong Province, College of Physics and Optoelectronic Engineering, Shenzhen University, Shenzhen, People's Republic of China

Tatyana Rakitskaya Odessa I.I. Mechnikov National University, Odesa, Ukraine

Ivan Rogovskiy National University of Life and Environmental Sciences of Ukraine, Kyiv, Ukraine

O. Rykhalskyi National Cancer Institute, Kiev, Ukraine

O. V. Sachuk Institute for Sorption and Problems of Endoecology, National Academy of Sciences of Ukraine, Kiev, Ukraine

Oleg Sapsay Open International University of Human Development "Ukraine", Kiev, Ukraine

I. A. Savchenko National Taras Shevchenko University of Kyiv, Kiev, Ukraine

E. V. Semenko Institute of Veterinary Medicine, Quality and Safety of Animal Products, National University of Life and Environmental Sciences of Ukraine, Kiev, Ukraine

I. V. Semkiv Department of General Physics, Lviv Polytechnic National University, Lviv, Ukraine

Luca Seravalli Institute of Materials for Electronics and Magnetism, IMEM-CNR, Parma, Italy

Dmytro Shakhnin Open International University of Human Development "Ukraine", Kiev, Ukraine

O. V. Shcherbak Institute of Animals Breeding and Genetics nd.a. M.V. Zubets, National Academy of Agrarian Sciences of Ukraine, Boryspil District, Kyiv Region, Ukraine

A. Shevchenko G.V. Kurdyumov Institute for Metal Physics, Kiev, Ukraine

O. Shpotyuk Jan Dlugosz University in Częstochowa, Czestochowa, Poland; Vlokh Institute of Physical Optics, Lviv, Ukraine

Y. Shpotyuk Ivan Franko National University of Lviv, Lviv, Ukraine; University of Rzeszow, Rzeszow, Poland

O. V. Shyrokov Frantsevych Institute for Problems of Materials Science of NAS of Ukraine, Kiev, Ukraine

Yuriy Skorenkyy Ternopil Ivan Puluj National Technical University, Ternopil, Ukraine

E. Skwarek Department of Radiochemistry and Environmental Chemistry, Institute of Chemical Sciences, Faculty of Chemistry, Maria Curie-Sklodowska University, Lublin, Poland

O. Smirnova Chuiko Institute of Surface Chemistry, NAS of Ukraine, Kiev, Ukraine

V. L. Starchevskyy National University Lviv Polytechnic, Lviv, Ukraine

D. Sternik Maria Curie-Skłodowska University, Lublin, Poland

V. V. Strelchuk V.E. Lashkaryov Institute of Semiconductor Physics, NAS of Ukraine of Kyiv, Kyiv, Ukraine

K. Szmuc University of Rzeszow, Rzeszow, Poland

Luiudmyla Titova National University of Life and Environmental Sciences of Ukraine, Kyiv, Ukraine

Tetiana Tmenova Taras Shevchenko National University of Kyiv, Kyiv, Ukraine

Valentyna Trach Institute of Physiology of Plants and Genetic of National Academy of Science of Ukraine, Kyiv, Ukraine

Arkadii Tretiakov University "Ukraine", Kiev, Ukraine;
Ecole Polytechnique, CNRS, UMR 6595, Technopôle deChateau Gombert, Marseille Cedex 13, France

Giovanna Trevisi Institute of Materials for Electronics and Magnetism, IMEM-CNR, Parma, Italy

Anatoly Veklich Taras Shevchenko National University of Kyiv, Kyiv, Ukraine

O. Vernyhor Department of Photonics, Lviv Polytechnic National University, Lviv, Ukraine

P. Virych Taras Shevchenko National University of Kyiv, Kiev, Ukraine

N. Vityuk Chuiko Institute of Surface Chemistry, NAS of Ukraine, Kiev, Ukraine

Vitaliya Volkova Odessa I.I. Mechnikov National University, Odesa, Ukraine

E. Yanovska National Taras Shevchenko University of Kyiv, Kiev, Ukraine

I. Yaremchuk Department of Photonics, Lviv Polytechnic National University, Lviv, Ukraine

V. Yashchuck Taras Shevchenko National University of Kyiv, Kiev, Ukraine

Mykola Yukhymenko Sumy State University, Sumy, Ukraine

M. Zabolotny Taras Shevchenko National University of Kyiv, Kiev, Ukraine

O. Zaremba Ivan Franko National University of Lviv, Lviv, Ukraine

V. A. Zazhigalov Institute for Sorption and Problems of Endoecology, National Academy of Sciences of Ukraine, Kiev, Ukraine

Oksana Zazimko National University of Life and Environmental Sciences of Ukraine, Kyiv, Ukraine

O. B. Zgalat-Lozynskyi Frantsevych Institute for Problems of Materials Science of NAS of Ukraine, Kiev, Ukraine

D. P. Zyatkevych Frantsevych Institute for Problems of Materials Science of NAS of Ukraine, Kiev, Ukraine

Nanochemistry and Biotechnology

Mechanisms of Antitumor Effect of Nanomaterials Based on Rare Earth Orthovanadates

Anatoliy Goltsev, Yurii Malyukin, Natalya Babenko, Yuliya Gaevska, Mykola Bondarovych, Igor Kovalenko, Tatiana Dubrava, and Vladimir Klochkov

1 Introduction

According to the World Health Organization's data in 2018, cancer has caused 9 million deaths worldwide within the reporting period and is expected to increase

A. Goltsev (✉) · N. Babenko · Y. Gaevska · M. Bondarovych · T. Dubrava
Department of Cryopathophysiology and Immunology, Institute for Problems of Cryobiology & Cryomedicine of the National Academy of Sciences of Ukraine, Pereyaslavska Street 23, 61016 Kharkiv, Ukraine
e-mail: cryopato@gmail.com

N. Babenko
e-mail: natybabenko@gmail.com

Y. Gaevska
e-mail: yugaevska@gmail.com

M. Bondarovych
e-mail: nikolay.bondarovicg@gmail.com

T. Dubrava
e-mail: tgdubrava@gmail.com

Y. Malyukin · V. Klochkov
Department of Nanocrystal Materials, Institute for Scintillation Materials of the National Academy of Sciences of Ukraine, 60 Nauki Avenue, 61001 Kharkiv, Ukraine
e-mail: maljukin@nas.gov.ua

V. Klochkov
e-mail: klochkov@isma.kharkov.ua

I. Kovalenko
Department for Low Temperature preservation, Institute for Problems of Cryobiology & Cryomedicine of the National Academy of Sciences of Ukraine, Pereyaslavska Street 23, 61016 Kharkiv, Ukraine
e-mail: i.kovalenko.ipcic@gmail.com

O. Fesenko and L. Yatsenko (eds.), *Nanooptics and Photonics, Nanochemistry and Nanobiotechnology, and Their Applications*, Springer Proceedings in Physics 247, https://doi.org/10.1007/978-3-030-52268-1_1

up to 22 million by 2035 [1]. Modern cancer treatments include surgery, radiation and chemotherapy, the main drawback of those is their non-specificity. Conventional chemotherapeutic agents have no deliberate action and affect both cancer and normal cells, thereby leading to non-optimal treatment as a result of excessive toxicity.

Targeted therapy using a variety of nanomaterials has become one of the means of overcoming the lack of specificity to tumor cells of conventional chemotherapy drugs. Due to the tremendous efforts that have been made in nanomedicine over the past decades, several therapeutic strategies have been proposed to treat oncopathology, including photothermal ablation therapy using silicon nanoshells [2], carbon nanotubes [3], gold nanorods [4]. In addition, nanoparticles (NPs) are used for targeted delivery of antitumor agents [5].

Successful use of NPs in the clinic requires their specific design with adapted properties for safer and more effective cancer treatment. A significant advantage of inorganic gadolinium and yttrium orthovanadate nanoparticles is their high biocompatibility and ability to simultaneously target tumor cells and inhibit their function. When studying the toxicity, the dynamics of accumulation and excretion of NPs based on orthovanadates, it has been found that their oral and intraperitoneal administration to rats did not lead to the death of animals and a change in the mass coefficients of internal organs, which made it possible to attribute the synthesized samples of nanovanadates to practically nontoxic compounds (toxicity class V). Complete excretion of NPs from the body occurred 30 days after administration [6]. Low IC50 (half maximal inhibitory concentration) of vanadium compounds [7] supports the evidence of the absence of toxic effects of vanadium (IV) on normal non-cancerous cells [8].

Owing to its atomic mass (Mr = 64), gadolinium is a good electron emitter, which greatly enhances radiation-induced destruction of cells previously sensitized by nanoparticles [9]. In addition, the NPs based on rare-earth metals have photophysical properties, including a high photostability for a long time, a significant Stokes shift of luminescence, the absence of flicker, the stability of characteristic narrow luminescence bands, that opens up the prospect of their use as luminescent labels and probes [10].

As reported [11] the antitumor effect of some organic derivatives of vanadium [V (IV)] (bis (maltolato) oxovanadium (IV), bis (coyato) oxovanadium (IV) and bis 2,2′-bipyridine) oxovanadium (IV) sulfate was shown, the addition of which to the culture of H-35 tumor cells at a concentration of 0.5–5.0 mM led to significant inhibition of its growth and proliferation. Vanadyl sulfate [V (IV)] or vanadate [V (V)] had a similar effect on tumor cells [12].

Vanadium compounds can cause selective oxidation of pyrimidine bases, which prevents a complementary DNA folding [13]. The tumor cells, characterized by the disorders of the DNA repair system, are especially subjected to it. Another proposed mechanism for the antitumor effect of vanadium compounds is their impaired permeability of the tumor cell mitochondrial membrane as a result of generation of reactive oxygen species [14], that leads to a release of cytochrome C and induction of apoptosis [15].

However, elucidation of the conditions and mechanisms for implementation of the ability of NPs based on rare-earth orthovanadates to change the proliferative and metabolic activity of tumor cells has remained an urgent task.

Targeted accumulation of nanoparticles in tumor cells can be achieved by modifying them and creating on their base of nanoemulsions, namely combining them with cholesterol [16]. It is known that cancer cells, with high metabolic activity, are able to selectively capture cholesterol from a biological environment [17]. Therefore, cholesterol supplementation is a prerequisite for successful targeted delivery to tumor sites. They are kinetically stable dispersion systems, resistant to stratification for several months. In addition, the nanoemulsion of cholesterol is relatively resistant to reactive oxygen species, which allows a long-term circulation of cholesterol in the bloodstream [16].

The purpose of this study was to investigate the possibility of using $GdYEuVO_4$ nanoparticles and hybrid nanocomplexes synthesized on their basis to visualize and use in the treatment of malignant tumors.

2 Physico-Chemical Characteristics of Nanomaterials Based on Rare-Earth Orthovanadates

2.1 Synthesis of Aqueous Solutions of $GdYEuVO_4$ Nanoparticles

Aqueous solutions of nanoparticles based on $Gd_{0.7}Y_{0.2}Eu_{0.1}VO_4$ rare-earth orthovanadates were obtained by colloidal synthesis [18]. In brief: in a 50 ml flask, 1 M aqueous solutions of rare-earth chlorides (Sigma Aldrich) were mixed: gadolinium chloride 0.35 ml, 0.1 ml yttrium chloride and 0.05 ml europium chloride, then the solution was added with bidistilled water to the mark. After this, the resulting solution was mixed with the one of sodium citrate (37.5 ml, 0.01 mol/l). Then, an aqueous solution of sodium orthovanadate (37.5 ml, 0.01 mol/l) was added dropwise to the resulting mixture using a magnetic stirrer. The pH of the resulting solution was adjusted with hydrochloric acid to 10.5. Then the reaction mixture was heated in a thermostat at 60 °C for 90 min.

After finishing heat treatment and cooling, the solution was dialyzed through a 12 kDa membrane (pore size made 2.5 nm). The dialysis lasted for 3 days, however, every 6 h the distilled water was replaced in a glass. The cleaning of the dialyzed solution from electrolyte impurities was monitored by determining the dialysate electrical conductivity. Concentrated solutions were obtained by evaporation with a rotary evaporator at 60 °C.

The applied colloidal synthesis technique allows the obtaining of aggregatively stable hydrosols of nanoparticles (NPs) with controlled geometric parameters of a solid phase. The absence in the aqueous solutions of nanoparticles of toxic impurities,

surfactants and polymers that are able to interact with biological objects makes them suitable for biological testing.

2.2 Characterization of Aqueous Solutions of $GdYEuVO_4$ Nanoparticles

Like typical colloidal systems, the studied aqueous solutions of NPs are transparent in transmitted light and opalescent under lateral illumination (Tyndall cone is observed).

Under UV irradiation, aqueous solutions of NPs exhibit bright red luminescence. Their pH value is within the range of 7.4–7.8. The ζ potential of NPs in colloidal solutions was measured using a ZetaPALS analyzer (Brookhaven Instruments Corp., USA) at a 15° scattering angle. In calculating the ζ potential, the Doppler shift of the beam of light scattered by the particles was measured, followed by recalculation according to the Smoluchowski equations. The value of ζ potential may be -36 ± 4 mV, depending on the type of NPs and storage time.

Colloidal solutions of NPs easily pass through nitrocellulose ultrafilters with a pore diameter of 100 nm. The solid phase concentration of aqueous solutions of NPs is 1.3 g/L. The resulting solutions can be stored for more than 6 months under standard conditions without changing their properties. Sterilization of NPs solutions at 120 °C for 1–2 h in the sealed ampoules does not cause sedimentation and coagulation of colloids.

The size and morphology of the NPs were evaluated using transmission electron microscopy (TEM) with a 125K TEM electron microscope (Selmi, Ukraine) at an accelerating voltage of 100 kV (magnification up to $\times$100,000). For studies in a transmission mode, the samples were prepared according to the standard method by applying a colloidal solution to copper grids coated with a thin layer of carbon, followed by drying at room temperature.

The method of TEM showed that the NPs had a spherical shape with an average diameter of 3 nm (Fig. 1). Size dispersion did not exceed 15%.

To obtain the absorption spectra, a SPECORD 200 spectrophotometer (Analytik-Jena, Germany) was used by means of both single-beam and double-beam schemes. The absorption spectra of aqueous solutions of NPs exhibit a broadband with a maximum of 271 nm, which corresponds to optical transitions with charge transfer from oxygen ligands to the central vanadium ion in VO_4^3 (Fig. 2). It is worthy of noting that for ionic solutions of salts containing $VO_4{}^{3-}$ ions, the absorption maximum is in the region of $\lambda_{max} = 266$ nm, a shift of this band to the long-wavelength region indicates that $VO_4{}^{3-}$ is in the crystalline field.

The dependence of an optical density on the concentration of NPs is linear in the studied concentration range of 5×10^{-5}–1×10^{-3} mol/l (0.01–0.25 g/l), which indicates the compliance with the Bouguer–Lambert–Beer absorption law for these systems. The values of the absorption maximum are used to determine the concentration of NPs in solutions [19].

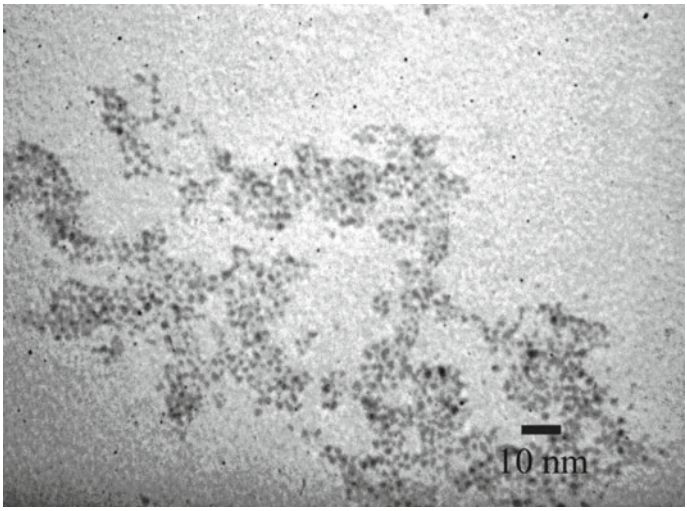

Fig. 1 TEM image of solid phase of aqueous solution of $GdYEuVO_4$ nanoparticles

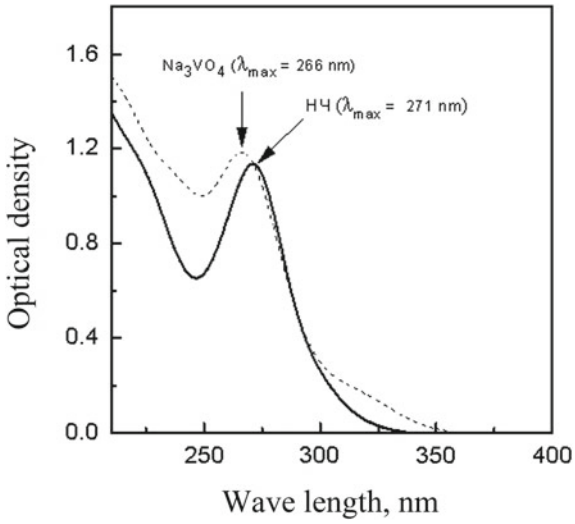

Fig. 2 Absorption spectra of Na_3VO_4 solution and aqueous solution of $GdYEuVO_4$ nanoparticles

Luminescence spectra were measured with a Lumina spectrophotometer (ThermoScientific, USA). An intense band was observed in the luminescence excitation spectrum of an aqueous solution of $GdYEuVO_4$ nanoparticles, which coincided with the absorption band, as well as several low-intensity narrow lines in the longer wavelength region (395, 465, 536 nm) corresponding to optical f–f transitions of europium in the orthovanadate matrix (Fig. 3). The absorption intensity of f–f transitions of Eu^{3+} is very weak when compared with the absorption if the VO_4^3 group, indicating

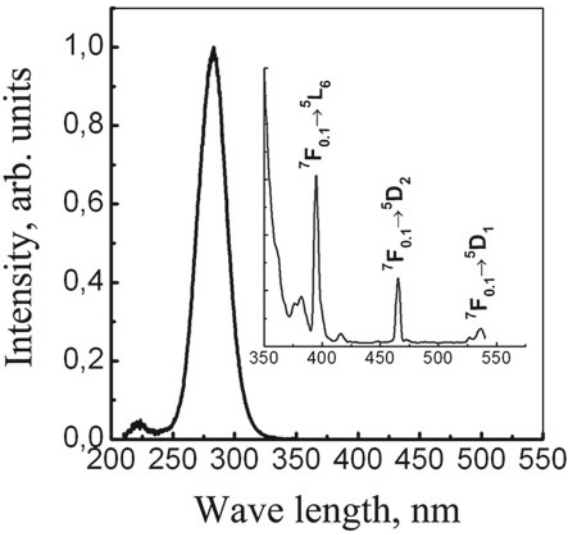

Fig. 3 Luminescence excitation spectrum ($\lambda = 270$ nm) of an aqueous solution of $GdYEuVO_4$ nanoparticles. Insert An enlarged image of bands in visible region of spectrum

that excitation of Eu^{3+} ions, mainly through VO_4^3 groups, that is, by transferring energy from the VO_4^3 group to Eu^{3+} ions. It should be noted that during the matrix excitation (270 nm), the Stokes shift exceeds 300 nm, which provides visual contrast and separation of the luminescence of NPs from the autoluminescence of cells during testing.

The luminescence spectrum (Fig. 4) of the studied aqueous solution of $GdYEuVO_4$ nanoparticles is represented by narrow bands of the $^5D_0 \rightarrow {}^7F_J$ transitions ($J = 0, 1, 2, 3, 4$), characteristic of the europium ion in the composition of orthovanadate matrix. The most intense peaks are observed at the $^5D_0$–$^7F_2$ electric dipole transition at 615 and 618 nm. The band corresponding to the $^5D_0$–$^7F_4$ electric dipole transition contains narrow lines with maxima of 698 and 704 nm. At 650 nm, weak lines are observed corresponding to the $^5D_0$–$^7F_3$ magnetic dipole transition. Narrow lines and their fine structure confirm the crystalline nature of NPs. The presence of these bands within a visible range allows the identification and registration of NPs using luminescence microscopy in experiments in vitro and in vivo.

It has been established that in biological environments of the NPs, based on orthovanadates of the rare-earth elements are not inert. They are often subjected to aggregates and/or agglomeration, especially in salines, that may lead to formation of new molecular complexes [20]. To stabilize the NPs, the isotonic solution of 5% glucose was used as a solvent, since previous studies have demonstrated no changes in the NPs diameter occur under these conditions, that is a strong advantage for further investigations in biosystems.

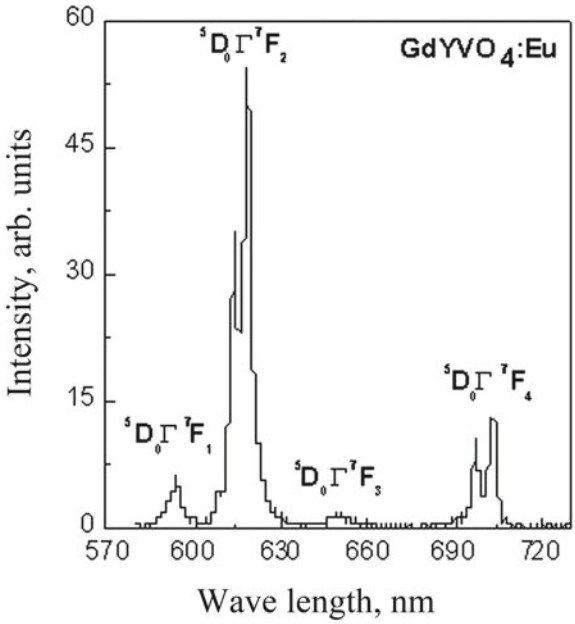

Fig. 4 Luminescence spectrum ($\lambda = 618$ nm) of aqueous solution of $GdYEuVO_4$ nanoparticles

2.3 Synthesis and Physicochemical Properties of Hybrid Nanocomplexes

A hybrid nanocomplexes (NCs) is an aqueous dispersion of sheep cholesterol in concentration of 0.55 g/l (Acros organics, Belgium) using $GdYEuVO_4$ nanoparticles (of 2–3 nm diameter) at a concentration of 1.30 g/l. Hybrid nanocomplexes were first synthesized at the Institute for Scintillation Materials of the National Academy of Sciences of Ukraine (Kharkiv) as reported [16]. A method of eliminating the NCs involves dissolving the cholesterol in ethyl alcohol and adding to the mixture a stabilizer substance, stirring the mixture with subsequent evaporation with a rotary evaporator. The use of NPs above 5 nm reduces the probability of their localization on the surface of the dispersed cholesterol particles and does not provide sufficient electrokinetic potential (charge) on the surface of the dispersed cholesterol particles for their electrostatic repulsion in solution, and therefore does not contribute to their aggregation.

In hybrid NCs the negatively charged NPs are localized along the periphery of cholesterol particles owing to van der Waals and hydrophobic interactions. The NPs stabilize the hybrid NCs via electrostatic interactions. The sizes of the synthesized NCs do not exceed 100 nm. Negatively charged hybrid NPs of orthovanadates interfere an adhesion and aggregation of cholesterol particles. Structure of hybrid NCs is shown in Fig. 5.

The ideology of using such hybrid NCs in cancer therapy is based on the assumption that the antitumor effect of each of its components is mutually reinforced

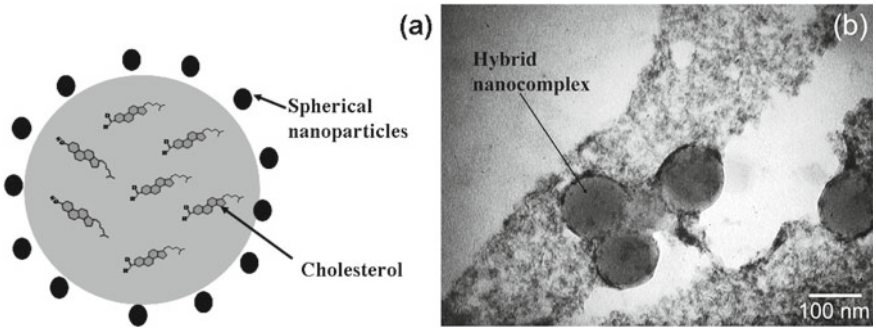

Fig. 5 Hybrid nanocomplex: **a** schematic representation, **b** transmission electron microscopy photomicrography of hybrid nanocomplexes, procured from cholesterol aqueous solution placed on carbon network

due to the presence of cholesterol in them, which has an affinity for the tumor cell membranes with a simultaneous possibility of their identification due to the luminescent properties of orthovanadates NPs [16].

It is known that cholesterol is actively "eliminated" from the bloodstream by proliferating cancer cells to build biomembranes. This is facilitated by the presence on the surface of tumor cells of a large number of SR-B1 (scavenger receptor, class B type I) and caveolin-1 (Cav-1) receptors that can bind to free cholesterol from the bloodstream [17]. Thus, the incorporation of cholesterol into the membranes of tumor cells can serve as a prerequisite for targeted delivery of hybrid NCs directly into a cell.

3 The Ways to Inhibit the Tumor Growth by Using Nanomaterials Based on Rare-Earth Orthovanadates

The possibility of nanomaterials based on $GdYEuVO_4$ rare-earth orthovanadates to identify and specifically inhibited the tumor-inducing cells should, first of all, be assessed under adequate experimental conditions. A convenient model for performing such experimental research is the inoculated tumor cell line of Ehrlich carcinoma (EC), which was obtained from spontaneous breast cancer in mice [21]. The EC tumor cell inoculation is 100%.

According to the histological structure, the EC is an undifferentiated tumor that has lost its epithelial character. Ehrlich carcinoma exists in the form of two strains, i.e., subcutaneous and ascites. The average life span of animals with the ascites EC induced by intraperitoneal injection of 3×10^6 cells/mouse is 10–16 days, and with subcutaneous inoculation, it makes 16–20 days [21]. Such properties of EC as growth rate, good reproducibility, and the relative constancy of morphological and biological properties make it possible to use it in experimental oncology.

Previous assessment of phenotypic characteristics and functional potential of the ascites EC has shown that this tumor is a heterogeneous population of tumor cells of various degrees of differentiation, related to highly and less potent tumor-inducing precursors [22]. In general, the differentiation row of subpopulations of breast cancer cells can be represented as follows:

$$CD44^{high} \rightarrow CD44^{+}CD24^{-} \rightarrow CD44^{+}CD24^{+} \rightarrow CD44^{-}CD24^{+}$$

At the same time, a higher (10-fold) tumorigenic activity of $CD44^{+}$ cells of EC in comparison with $CD44^{-}$ cells has been proven. In the compared pair, $CD44^{+}$ cells had a higher potential to form subpopulations of $CD44^{high}$, $CD44^{+}CD24^{-}$ and $CD44^{+}CD24^{+}$ cells in peritoneal cavity (PC) of mice, emphasizing the presence of stem cancer cells in the $CD44^{+}$ population [22].

Thus, an excellent inoculation, easy reproducibility, and analysis of the EC subpopulation composition suggest its successful use in testing new drugs, including nanomaterials. It has been previously shown that the NPs of rare-earth orthovanades of various shapes and sizes (spherical, spindle-like, and rod-like) had different binding potentials for the EC tumor cells in vitro. Spectral analysis demonstrated that NPs of only spherical and spindle-shaped forms can identify the tumor cells in the total pool of EC [23].

The question on the duration of interaction of tumor cells with nanomaterials remains unclear since, in these studies, the incubation time was selected according to the data obtained from healthy liver cells [24]. The most informative way to find out the dynamics of the accumulation of nanomaterials inside a cell is to use a multispectral analysis using a laser scanning microscope. The capabilities of a conventional fluorescence microscope are limited and it is safe to say that NPs are on or inside the cell surface. On the contrary, using the optical slicing method and subsequent 3D reconstruction of the object, it is possible to reproduce the volume distribution of nanomaterials in a cell and to evaluate the results of studies in four dimensions: length, width, depth and time.

Therefore, the number of cells that bind to NPs and hybrid NCs was counted using an LSM 510 META confocal laser scanning microscope (Carl Zeiss, Germany) after different incubation periods (1, 2, 3, and 4 h). The results of the study showed that the EC cells without the addition of nanomaterials (Control) throughout the observation period had an average fluorescence intensity of 15.33 ± 3.28 arb. units corresponding to an electronic noise level of the detector (Fig. 6).

Confocal microscopy showed a gradual penetration and accumulation of NPs in the EC cells during the study time period (1–4 h) (Figs. 6a, 7). After 1 h of incubation, an increase in mean fluorescence intensity (97.73 ± 10.13 arb. units) was found in all the EC cells compared to the control (15.33 ± 3.28 arb. units), which indicates the penetration of NPs inside cells. After 2 h of incubation, average fluorescence intensity of total pool of the EC cells continued to increase (125.33 ± 20.28 arb. units) and reached a maximum by 3 h (177.27 ± 24.50 arb. units). At this time single cells with hyperhigh ($2.220.50 \pm 119.50$ arb. units), which did not exceed 5% appeared. After 4 h of incubation, the mean fluorescence intensity of the total cell

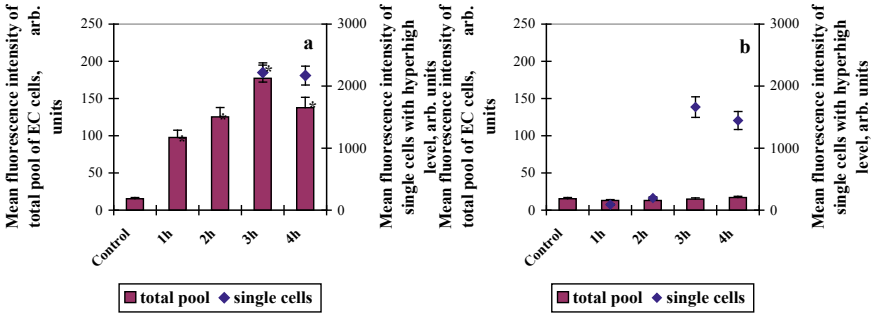

Fig. 6 Mean fluorescence intensity of total EC cell population (rectangular columns) and fluorescence of individual cells (blue marker) after incubation with spherical NPs (**a**) and hybrid NCs (**b**) for 1, 2, 3 and 4 h. *Note* Asterisk—difference is statistically significant compared with similar indices of EC cells without incubation with NPs or NCs (control) ($p < 0.05$)

population decreased slightly (137.75 ± 14.84 arb. units), with the number of single cells with a hyperhigh degree of luminescence remaining at the same level (2172 ± 110.70 arb. units) as after 3 h incubation.

Thus, NPs have been shown to be able to penetrate and accumulate in virtually all cells in total EC pool. The maximum accumulation of NPs in tumor cells is established after their 3-hour incubation. In the same period, the single cells with hyperhigh level of fluorescence appeared, the number of which did not exceed 5%. This indicates that NPs have the ability to identify all the tumor cells. The intensity of intracellular accumulation of NPs was different. Only a small population of tumor cells was capable of increased accumulation of the NPs under study.

Unlike NPs, the incubation of EC cells with hybrid NCs within the whole observation period practically did not change the mean fluorescence intensity of the total pool of cells compared to the control (Figs. 6b, 7). However, starting from the first hour of incubation, the appearance of individual cells with an extremely high level of fluorescence intensity (89 ± 5.72 arb. units), which reached maximum values after 3 h of incubation (1662 ± 33.89 arb. units), was noted (Fig. 6b). At the 4th hour of incubation, the fluorescence intensity of single cells with hyperhigh levels did not change significantly, remaining at a fairly high level (1445 ± 11.70 arb. units). The number of cells with hyperhigh fluorescence intensity gradually increased during the observation time, from 0.2% in the first hour to 1% of the total number of cells in a vision field at 3 h of incubation, remaining at this level until the end of the observation period.

Thus, the hybrid NCs have been established to be able of selective binding only to individual tumor cells, the number of which did not exceed 1% in the absence of their accumulation in total population of EC cells.

To determine to which EC population on phenotypic signs the cells with high levels of fluorescence belong were simultaneously treated with the cells with nanomaterials and monoclonal antibodies to CD44 (Fig. 8). The incubation period of cells with hybrid NCs and NPs with double staining was 3 h according to the above data on the

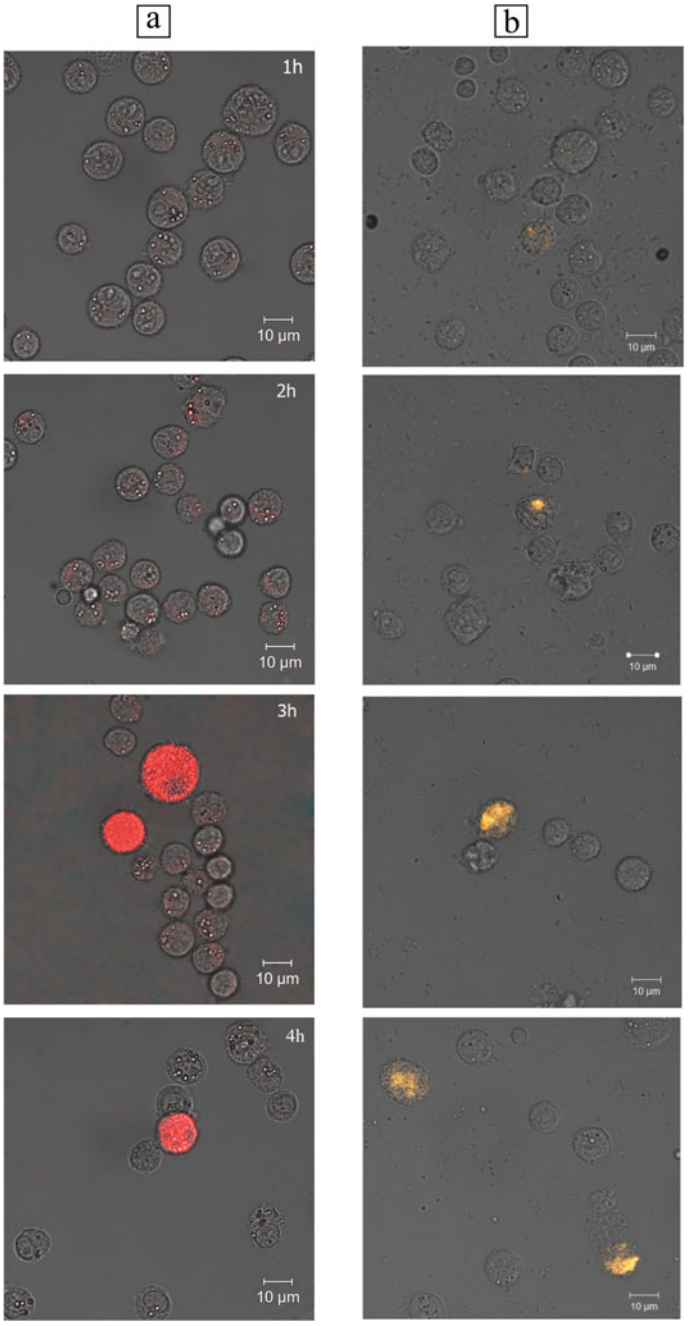

Fig. 7 Confocal microscopy of EC cells after incubation with spherical NPs (**a**) and hybrid NCs (**b**) for 1, 2, 3, and 4 h

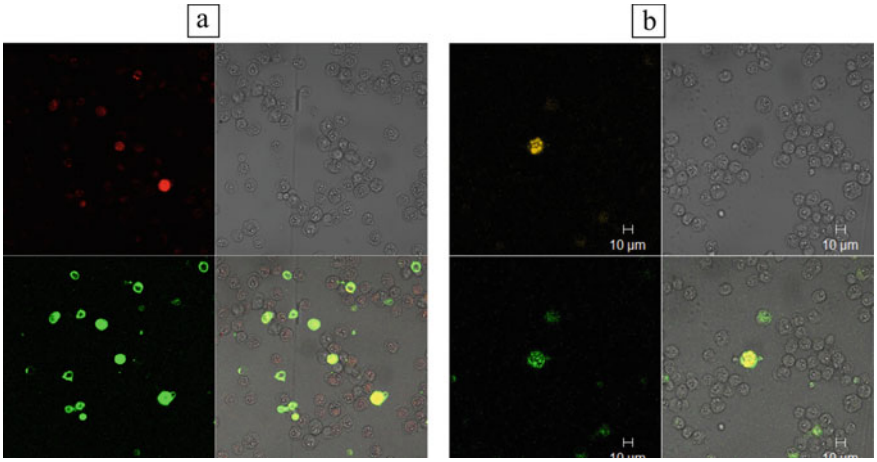

Fig. 8 Double staining of EC cells with nanomaterials—red and yellow fluorescence and monoclonal antibodies to CD44—green fluorescence (**a** treatment with spherical nanoparticles, **b** treatment with hybrid nanocomplexes). Confocal microscopy of EC cells after 3 h incubation with nanomaterials

maximum accumulation of nanomaterials during exactly this period. The rationale for this approach was the previously established fact that it is $CD44^+$ cells that have a proliferative potential, estimated by the tumor growth rate in vivo, and play a critical role in tumorigenesis [22].

Confocal microscopy data confirmed (Table 1) that the number of $CD44^+$ cells with green fluorescence was $7.00 \pm 0.58\%$ of the total EC pool. However, these cells were found to have different levels of fluorescence intensity. Thus, $5.83 \pm 0.63\%$ of $CD44^+$ cells had a fluorescence intensity of 300.25 ± 96 arb. units. At that time, only $1.17 \pm 0.10\%$ of $CD44^+$ cells had ultra-high fluorescence (1297.29 ± 46 arb. units) and can be attributed to $CD44^{high}$ cells. It is well known that they are stem cancer cells and have the highest tumor-inducing potential [22].

Table 1 Fluorescence intensities of EC cells after their double staining with monoclonal antibodies to CD44 and nanomaterials

	Number of cells with fluorescence versus total EC pool (%)		
	Staining type		
	CD44	CD44 + NPs	CD44 + NCs
Fluorescence intensity (arb. units)	7.00 ± 0.58	6.74 ± 0.41	1.20 ± 0.13
With the highest fluorescence (%)	$1.17 \pm 0{,}10$	5.16 ± 0.41	1.20 ± 0.13
Fluorescence intensity (arb. units)	1297.29 ± 46	2220.50 ± 119.50	1662.49 ± 33.89
With mean fluorescence (%)	5.83 ± 0.63	2.04 ± 0.17	–
Fluorescence intensity (arb. units)	300.25 ± 96	177.27 ± 24.50	–

The double staining of EC cells by nanoparticles and monoclonal antibodies to CD44 was found to be characteristic of 6.74 ± 0.41% of total EC pool cells. This indicates that NPs are capable of accumulating in almost all the cells expressing the CD44 marker (Fig. 8a, Table 1). The vast majority of $CD44^+$ cells (76.56%) were capable of intense NPs accumulation, as evidenced by their ultra-high fluorescence level of this marker (2220.50 ± 119.50 arb. units). The number of cells with mean NPs fluorescence was about one-third of the entire $CD44^+$ population. It was noted that this level had no statistically significant differences from the fluorescence level of cells in total EC pool capable of accumulating NPs. Thus, the NPs were found to have some affinity to $CD44^+$ cells, but not absolute, due to their presence in the vast majority of cells lacking the CD44 marker.

Figure 8 demonstrated the difference in a selective accumulation of NPs and hybrid NCs in CD44 population. It is quite illustrative. Thus, unlike NPs, the accumulation of hybrid NCs was observed only in 1.20 ± 0.13% of cells in a total pool of EC (Table 1). At the same time, all $CD44^+$ cells, which were characterized with their ability to accumulate NCs, had extremely high levels of their fluorescence, i.e., at the level of 1662 ± 33.89 arb. units. The data obtained indicate that only 17.14 ± 2.13% of EC cells, expressing the CD44, are capable of accumulating NCs. This subpopulation may certainly be CD44 cells, suggesting that tumor cells with stem potential (CD44 cells) may be the preferred target for the anti-proliferative properties of hybrid NCs.

One of the possible pathways of antitumor action of nanomaterials based on orthovanadate is to generate reactive oxygen species with subsequent mitochondrial function damage or induction of cell death by apoptosis/necrosis [15]. Therefore, at the end of each incubation period of cells with NPs and hybrid NCs (1–4 h), the activity indices of mitochondrial cell respiration were determined using the Cell Growth Determination Kit MTT based (Sigma, USA) according to the manufacturer's instructions, as well as the number of apoptotic and necrotic cells using annexin-V—An (BD, USA) and Propidium iodide—PI (Sigma, USA) on a FACS Calibur Becton–Dickinson flow cytometer.

According to the research results after the first hour of incubation of the EC cells with NPs and hybrid NCs, there was a tendency to a decrease in the level of mitochondrial respiration (Fig. 9); functions of NADP-H-dependent oxide reductase enzymes of mitochondria. After 2 h of incubation with NPs and hybrid NCs, the difference in control was statistically significant (by 20.5 and 27%, respectively). At the third hour of observation, the optical density of formazan solution in both types of treatment reached the minimum values, remaining at this level and at the fourth hour of incubation (optical density for NPs was 35.8 and hybrid NCs it made 46% if compared with control). That is, treatment of both by NPs and hybrid NCs for 3 h contributed to the maximum inhibition of mitochondrial respiration of EC cells.

The results suggest that inhibition of mitochondrial respiration through damage to the mitochondrial enzymatic system is an early sign of the toxic effect of nanomaterials used in the work in respect of EC cells, and this may subsequently lead to their death.

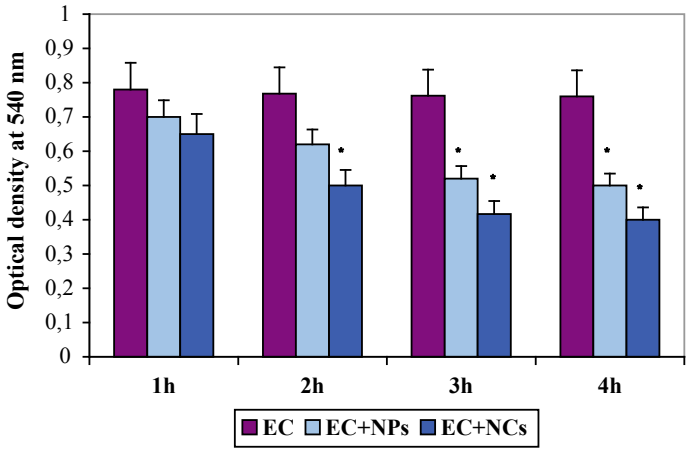

Fig. 9 Metabolic activity of EC cells before and after incubation with spherical NPs (**a**) and hybrid NCs (**b**) for 1, 2, 3 and 4 h. *Note* Asterisk—difference is statistically significant compared with similar indices of EC cells without incubation with NPs or hybrid NCs (control) ($p < 0.05$)

Mitochondria are considered the main link that integrates the various signals involved into implementation of apoptosis, the programmed cell death [15]. Simultaneous staining with annexin-V and PI allows the determination of the type of cell death. Annexin-V in the presence of Ca^{2+} and Mg^{2+} ions interact with phosphatidylserine, which at the early stages of apoptosis moves from the inner membrane of the cell to the outer. The living cell membrane is impermeable to PI. However, with irreversible damage to the cell (necrosis), the PI passes through the cell membrane and is capable of intercalation with defragmented DNA. Double staining with annexin-V and propidium iodide indicates late stages of apoptosis.

It has been found that in the control samples, regardless of incubation time, the number of living cells (An^-/PI^-) was $90 \pm 2.3\%$, those of early apoptosis (An^+/PI^-) made $1.34 \pm 0.67\%$, the ones of late apoptosis (An^+/PI^+) was $1.26 \pm 0.13\%$ and necrosis (An^-/PI^+) was $3.16 \pm 0.42\%$ (Fig. 10). Addition of both types of nanomaterials (NPs or hybrid NCs) to the EC cells resulted in a gradual decrease in the proportion of living cells (An^-/PI^-) throughout the observation period.

At the same time, from the first days of incubation, the difference in the effect of NPs or hybrid NC_S on the type of cell death was noted. It has been shown that the addition of NPs to the EC cells after 1 h caused an increase in the amount of An^+/PI^- from 1.34% up to 6.11% ($p < 0.05$), which indicates the restructuring of the composition of membranes under the action of NPs and the beginning of the implementation of the mechanism of apoptotic cell death. In contrast, hybrid NCs were able to induce a statistically significant rise in the number of late-onset apoptosis (An^+/PI^+) and necrosis (An^-/PI^+) cells after 1 h of incubation (Fig. 10).

Further incubation of the cells with NPs (2–4 h) led to a gradual decrease in the proportion of cells in early apoptosis (An^+/PI^-) on the background of a rise in the

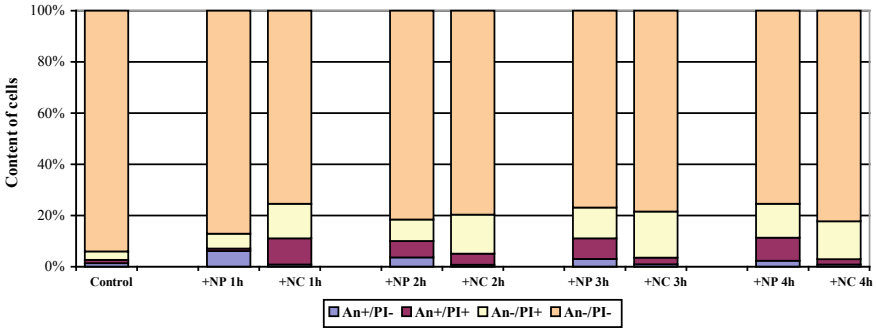

Fig. 10 The ratio of apoptotic/necrotic cells revealed with annexin-V/PI staining before and after incubation with spherical NPs (**a**) and hybrid NCs (**b**) for 1, 2, 3 and 4 h

percentage of cells in late apoptosis (An^+/PI^+) and necrosis (An^-/PI^+). It has been shown that 3 h after the start of incubation under the influence of NPs, the maximum redistribution of the number of cells in the apoptosis/necrosis occurs: the number of early apoptotic cells decreased by 2 times compared to 1 h of incubation, and the number of necrotic and late apoptotic cells increased by 2 and 7 times, respectively, compared to 1 h of treatment with NPs. Prolongation of the time of exposure of NPs to tumor cells up to 4 h did not lead to statistically significant differences in the ratio of the proportion of living, apoptotic and necrotic cells (Fig. 10). Thus, at the third hour of exposure to the NPs, the maximum cell death was observed by both necrosis and apoptosis with some advantage of the latter.

Thus, the data obtained suggest that NPs belong to those unique compounds that can simultaneously cause several types of cell death. Compounds which act in a similar manner are known [25]. The authors attribute this to simultaneous damage to both the inner and outer mitochondrial membranes. When the inner membrane is disrupted, the mitochondrial membrane potential changes, that is a prerequisite for cell death by necrosis. On the other hand, when the outer mitochondrial membrane is damaged, the cytochrome C is released, causing apoptosis. The above experimental data on mitochondrial dysfunction throughout the observation period indicate that hybrid NPs can act in the same way.

Regarding the effect of hybrid NCs on the EC cells, it has been established even starting from the first time of incubation and later throughout the observation period that the predominant tumor cell death was by necrosis. Moreover, within 1–4 h, a gradual increase in the percentage of necrotic cells (An^-/PI^+) was found compared to the control with maximum values reached after 3 h of incubation ($19.29 \pm 2.43\%$) (Fig. 10). In this case, the number of cells being in early apoptosis (An^+/PI^-) remained virtually unchanged within 1–4 h and did not differ significantly from the control values. Under the influence of hybrid NCs, the proportion of cells in late apoptosis (An^+/PI^+) was significantly increased by 1 h of incubation ($9.58 \pm 7.54\%$ compared

with 1.26 ± 0.13% in control). This index decreased rapidly throughout the observation period down to 2.79 ± 0.32% at the third hour, remaining at this level up to 4 h (2.06 ± 0.11%).

Thus, it draws attention to the fact that, in contrast to the effects of NPs, incubation of tumor cells with hybrid NCs for 3 h caused the highest cell death by necrosis and this was accompanied by a maximal decrease in metabolic activity of mitochondria. The established features of NPs or hybrid NCs on a cell death type are important for further development/inactivation of tumor in vivo.

It is believed that one of the reasons for ineffectiveness of the body's antitumor immune response and formation of immunological tolerance in malignant tumors is activation of cell death by apoptosis [26]. It is known that the apoptotic pathway of cell death leads to an activation of phagocytosis without consequences for the body in the form of alteration and inflammation [27]. In case of tumor cell death by necrosis, the release of DNA, RNA and tumor-specific proteins, which are DAMPs (damage-associated molecular patterns) and are recognized by the immune system, triggering a tumor-specific immune response. [28]. The release of DAMPs and cell death by necrosis leads to an activation of the TLR4 signaling pathway, which enhances the production of the transcription factor NF-kB, that resulted in an increased production of proinflammatory cytokines and development of immune-inflammatory process [29].

Therefore, depending on the method of cell death in the body of the tumor carrier can develop as an immune inflammative and immune-suppressive state. This demonstrates the need to review therapeutic strategies and target them to "switch" the mechanism of tumor cell death from apoptotic to necrotic. The above data indicate that hybrid NCs are capable of this task solving.

This assumption was experimentally confirmed in vivo by estimating the intensity of EC development from cells that had been pre-incubated with NPs and hybrid NCs for different times (1–4 h) (Table 2).

After 7 days of in vivo culturing of the EC cells of all the groups, inhibitory action of NPs and hybrid NCs was observed on an absolute number of EC cells in PC. However, only after 3-h incubation of both types of nanomaterials with EC cells, a statistically significant decrease in an absolute number of EC cells in PC (23.03 ± 4.87% in the NPs and 18.27 ± 1.23 in the hybrid NCs) compared to the control (55.09 ± 7.56%). The advantageous effect of nanocomplexes in minimizing the accumulation of tumor cells was noted, but first of all, in the group with the induction of EC cells, which had been pre-incubated with hybrid NCs for at least 3 h.

The decrease in an absolute number of the EC cells in PC (Table 2) under the action of nanomaterials in all the experimental groups indicates suppression of EC intensity growth. Judging by this index the hybrid NCs had a maximum antitumor effect. After 3-h of incubation, it was 33.16 ± 4.67%.

Thus, the data obtained indicate that only after 3 h of incubation of nanomaterials with the EC cells their significant antitumor effect was marked. With the same time of previous exposure to tumor cells (3 h), the hybrid NCs had some advantage over the use of just NPs.

Table 2 Intensity of growth of EC cells pretreated with spherical NPs and hybrid NCs for 1, 2, 3 and 4 h

Group	Volume of ascitic fluid (ml)	Number of EC cells in PC ($\times 10^7$)	Absolute number of EC cells in PC ($\times 10^7$)	Intensity growth of EC (%)
Control (EC cells)	5.84 ± 0.77	9.54 ± 1.55	55.09 ± 7.56	100
EC + NPs 1 h	4.4 ± 0.56	12.00 ± 2.03	51.14 ± 9.87	92.82 ± 5.65
EC + NPs 2 h	4.26 ± 0.85	10.23 ± 1.38	43.57 ± 6.71	79.10 ± 4.38
EC + NPs 3 h	3.08 ± 1.02	7.48 ± 2.09	23.03 ± 4.87*	41.80 ± 3.54
EC + NPs 4 h	2.62 ± 0.71	10.89 ± 1.90	27.58 ± 7.87*	49.06 ± 2.78
EC + NCs 1 h	4.5 ± 0.64	11.10 ± 0.84	49.5 ± 3.74	89.85 ± 4,87
EC + NCs 2 h	3.8 ± 0.72	10.75 ± 0.94	40.66 ± 5.41	73.81 ± 3,23
EC + NCs 3 h	2.9 ± 0.43	6.37 ± 0.72	18.27 ± 1.23*	33.16 ± 4,67
EC + NCs 4 h	3.1 ± 0.27	5.68 ± 0.64	17.6 ± 1.58*	31.95 ± 3,89

Notes An absolute number of EC cells in PC was found by the formula: ANC = Vol * Conc, where Vol is the volume of ascites fluid in PC of animals (ml), Conc is the concentration of tumor cells counted in Goryaev's chamber ($\times 10^7$ cells/ml)
Intensity growth of EC (I) was calculated by the formula: I = [(ANC (experiment)/ANC (Control)] * 100%, where ANC (experiment) is the absolute number of tumor cells in PC of animals with EC, which was initiated by treated nanomaterial cells; ANC (Control) is the absolute number of cells in PC of animals with EC, which was initiated by untreated nanomaterial cells

Thus, successful implementation of antitumor ability of hybrid NCs involves the implementation of a multi-stage cascade, namely, their penetration, accumulation inside cells, impaired mitochondrial function with subsequent induction of apoptotic and necrotic changes. There is absolutely no possibility of existence of "alternative" mechanisms for the implementation of the antitumor action of hybrid NCs. As we established in our previous studies, the treatment of EC cells with hybrid NCs led to the formation of a pool of tumor cells with reduced expression of pluripotency genes, primarily *nanog*, which is key in determining the self-support of cancer stem cells [30]. In general, the obtained results complement the understanding of the mechanisms of implementation of anticancer therapy of nanomaterials based on rare-earth orthovanadates.

4 Conclusions

1. In experimental conditions in vivo the possibility of using $GdYEuVO_4$ nanoparticles and hybrid nanocomplexes synthesized on their basis for the identification of cancer cells and inhibition of tumor growth is substantiated, that allows attributing these nanomaterials to promising drugs for the diagnosis and treatment of malignancies.

2. The dependence of an antitumor effect of nanomaterials on the time of their pre-incubation with tumor cells was established. Treatment of EC cells in vitro with hybrid nanocomplexes within 3 h resulted in a minimal EC intensity growth in vivo (33.16 ± 4.67%).
3. Implementation of an antitumor effect of nanomaterials involves their penetration, accumulation inside tumor cells, damage to mitochondrial function with subsequent induction of apoptotic and necrotic changes. The established fact of the death of EC cells mainly by necrosis under the action of hybrid NCs is one of the conditions for further inactivation of a tumor.
4. Double staining of EC cells with monoclonal antibodies to CD44, together with hybrid NCs, allowed them to establish their selective accumulation capacity in $CD44^+$ EC cells with ultra-high fluorescence intensity of this marker (CD44 cells). This confirms that a successful implementation of anti-proliferative properties of hybrid NCs is accomplished by inhibiting the function of tumor cells with a stem potential.

References

1. World Health Organization (2018) Global status report on noncommunicable diseases 2018. WHO Press, Geneva
2. Hirsch LR, Stafford RJ, Bankson JA et al (2003) Nanoshell-mediated near-infrared thermal therapy of tumors under magnetic resonance guidance. PNAS 100:13549–13554
3. Liu X, Tao H, Yang K et al (2011) Optimization of surface chemistry on single-walled carbon nanotubes for in vivo photothermal ablation of tumors. Biomaterials 32:144–151. https://doi.org/10.1016/j.biomaterials.2010.08.096
4. Du X, Lin WC, Su HH (2019) Highly efficient polyethylene glycol-functionalised gold nanorods for photothermal ablation of hepatocellular carcinoma cells. IET Nanobiotechnol 13(8):842–849. https://doi.org/10.1049/iet-nbt.2018.5417. PMID: 31625525
5. Xu L, Wang SB, Xu C et al (2019) Multifunctional albumin-based delivery system generated by programmed assembly for tumor-targeted multimodal therapy and imaging. ACS Appl Mater Interfaces 11(42):38385–38394. https://doi.org/10.1021/acsami.9b11263
6. Karpenko NA, Malukin YV, Koreneva EM et al (2013) The effects of chronic intake of nanoparticles of cerium dioxide or gadolinium ortovanadate into aging male rats. In: Proceedings of the 3rd international conference «Nanomaterials: applications and properties '2013». Alushta, Ukraine, 2(4):04NAMB28-1–04NAMB28-4
7. Rozzo C, Sanna D, Garribba E et al (2017) Antitumoral effect of vanadium compounds in malignant melanoma cell lines. J Inorg Biochem 174:14–24. https://doi.org/10.1016/j.jinorgbio.2017.05.010
8. Leon IE, Cadavid-Vargas JF, Di Virgilio AL, Etcheverry SB (2017) Vanadium, ruthenium and copper compounds: a new class of nonplatinum metallodrugs with anticancer activity. Curr Med Chem 24:112–148. https://doi.org/10.2174/0929867323666160824162546
9. Štefančíková L, Lacombe S, Salado D et al (2016) Effect of gadolinium-based nanoparticles on nuclear DNA damage and repair in glioblastoma tumor cells. J Nanobiotechnol 14(1):63. https://doi.org/10.1186/s12951-016-0215-8
10. Klochkov VK, Kavok NS, Maljukin JV, Seminozhenko VP (2010) Jeffekt specificheskogo vzaimodejstvija nanokristallov GdYVO4:Eu3 + s jadrami kletok. Dopovidi Nacional'noï akademiï nauk Ukraïni 10:81–86 [Ukrainian]

11. Dabros W, Nikiforuk A, Kordowiak AM (2004) The influence of bis(kojato)-oxovanadium (IV) on viability and proliferation of rat hepatoma cell line H 35-19. In: ELSO proceedings NICE, France Abstract no. 653, p 299
12. Kordowiak AM, Klein A, Goc A, Dabroś W (2007) Comparison of the effect of $VOSO_4$, Na_3VO_4 and $NaVO_3$ on proliferation, viability and morphology of H35-19 rat hepatoma cell line. Pol J Pathol 58(1):51–57
13. Rodrguez-Mercado JJ, Mateos-Nava RA, Altamirano-Lozano MA (2011) DNA damage induction in human cells exposed to vanadium oxides in vitro. Toxicol In Vitro 25:1996–2002. https://doi.org/10.1016/j.tiv.2011.07.009
14. Molinuevo MS, Barrio DA, Cortizo AM, Etcheverry SB (2004) Antitumoral properties of two new vanadyl (IV) complexes in osteoblasts in culture: role of apoptosis and oxidative stress. Cancer Chemother Pharmacol 53(2):163–172
15. Korbecki J, Baranowska-Bosiacka I, Gutowska I, Chlubek D (2012) Biochemical and medical importance of vanadium compounds. Acta Biochim Pol 59(2):195–200
16. Klochkov VK (2015) Method for producing water dispersion of cholesterol. Patent of Ukraine 108011 [Ukrainian]
17. Al – Jarallah A, Trigatti BL (2010) A role for the scavenger receptor, class B type I in high density lipoprotein dependent activation of cellular signaling pathways. Biochim Biophys Acta 1801(12):1239–1248. https://doi.org/10.1016/j.bbalip.2010.08.006
18. Klochkov VK (2009) Aqueous colloid solutions of nanoluminophores nReVO4:Eu3+ (Re = Y, Gd, La). Mater Sci Nanostruct 2:3–8 [Ukrainian]
19. Klochkov VK, Grigorova AV, Sedyh OO, [i dr.] (2012) Harakteristiki zolej nReVO4:Eu3+ (Re = La, Gd, Y, Sm) s nanochasticami raznoj formy i razmerov. ZhPS 79(5):738–742 [Ukrainian]
20. Malyukina M Yu, Piliai LV, Sedih OO, [i dr.] (2018) Aggregation stability of nanoparticles based on rare-earth elements in different microenvironment and biological media. Biophys Bull 40:5–16 [Ukrainian]
21. Ozaslan M, Karagoz ID, Kilic IH, Guldur ME (2011) Ehrlich ascites carcinoma. Afr J Biotechnol 10(13):2375–2378
22. Goltsev AN, Babenko NN, Gaevskaya YA et al (2017) Nanotechniques inactivate cancer stem cells. Nanoscale Res Lett 12(1):415. https://doi.org/10.1186/s11671-017-2175-9
23. Goltsev AN, Babenko NN, Gaevskaya YA et al (2013) Capability of orthovanadate-based nanoparticles to in vitro identification and in vivo inhibition of cancer stem cells. Nanosystems Nanomaterials Nanotechnol 11(4):729–739 [Ukrainian]
24. Klochkov V, Kavok N, Grygorova G et al (2013) Size and shape influence of luminescent orthovanadate nanoparticles on their accumulation in nuclear compartments of rat hepatocytes. Mater Sci Eng C Biol Appl 33(5):2708–2712. https://doi.org/10.1016/j.msec.2013.02.046
25. Arakawa S, Nakanomyo I, Kudo-Sakamoto Y et al (2015) Identification of a novel compound that inhibits both mitochondria-mediated necrosis and apoptosis. Biochem Biophys Res Commun 467(4):1006. https://doi.org/10.1016/j.bbrc.2015.10.022
26. Fulda S (2013) Regulation of cell death in cancer - possible implications for immunotherapy. Front Oncol 3:29. https://doi.org/10.3389/fonc.2013.00029
27. Nagata S, Tanaka M (2017) Programmed cell death and the immune system. Nat Rev Immunol 17(5):333–340. https://doi.org/10.1038/nri.2016.153
28. Sathianathen NJ, Krishna S, Anderson JK et al (2017) The current status of immunobased therapies for metastatic renal-cell carcinoma. Immunotargets Ther 6:83. https://doi.org/10.2147/ITT.S134850
29. Luo J-L, Kamata H, Karin M (2005) IKK/NF-κB signaling: balancing life and death – a new approach to cancer therapy. J Clin Invest 115(10):2625. https://doi.org/10.1172/JCI26322
30. Goltsev AN, Babenko NN, Gayevskaya YuA et al (2015) Antitumor effect of hybrid nanocomplexes containing nanoparticles of orthovanadates rare earth elements and cholesterol. Genes Cells 10(2):54–60 [Russian]

Synthesis and Consolidation of Powders Based on Si_3N_4–Zr

I. Kud, L. I. Ieremenko, L. A. Krushynska, D. P. Zyatkevych, O. B. Zgalat-Lozynskyi, and O. V. Shyrokov

1 Introduction

The complex of the physicomechanical and chemical properties of porousless nanocomposites with a ceramic matrix based on Si_3N_4 and reinforced by nanosized particles of carbides and nitrides of transition metals makes them promising candidates for the development of next-generation ceramic bearings and seals intended for operation under conditions of severe friction. For instance, the introduction of zirconium nitride into the silicon nitride matrix makes it possible to enhance the corrosion resistance due to the formation of insoluble oxide layers, which provides the self-healing effect of the material. During contact in an aqueous medium, a gel that has a larger volume and protects grains boundaries against subsequent corrosion forms [1].

The low chemical activity of these ceramic materials, high oxidation resistance, and extremely low porosity of products manufactured from them by the spark plasma sintering (SPS) method guarantee increased operating characteristics of rolling and plain bearings intended for operation under severe conditions in corrosive-erosive media without lubrication.

In the development of new silicon nitride composite powder materials with a uniform distribution of components and a homogeneous character of development of structural transformation, it is reasonable to use precursors containing all elements required for the synthesis of the final composition. In this case, the main requirements for precursors are as follows:

I. Kud (✉) · L. I. Ieremenko · L. A. Krushynska · D. P. Zyatkevych · O. B. Zgalat-Lozynskyi · O. V. Shyrokov
Frantsevych Institute for Problems of Materials Science of NAS of Ukraine, Krzhyzhanovsky St., 3, Kiev 03142, Ukraine
e-mail: eli123@ukr.net

O. Fesenko and L. Yatsenko (eds.), *Nanooptics and Photonics, Nanochemistry and Nanobiotechnology, and Their Applications*, Springer Proceedings in Physics 247, https://doi.org/10.1007/978-3-030-52268-1_2

– the thermodynamic instability at relatively low temperatures as compared with the thermodynamic stability of interaction products;
– the completeness of the reaction.

Our previous investigations in the development of methods for preparing nanopowders of nitride composite materials [2] and the literature data [3, 4] indicate the prospects of using silicides of transition metals containing all components of their nitriding products as initial components (precursors). However, the use of disilicides as precursors restricts the possibility of preparing nitride composite materials in a wide concentration range [3].

The aim of the present work is to investigate the synthesis of nanodisperse composite powders of the Si_3N_4–ZrN system in a wide concentration range and their consolidation.

2 Experimental Technique

During phase transformations in the process of decomposition of complex substances, high-activity ingredients, which are initial components in the synthesis of new compounds, form [4]. The interaction of a transition metal with silicon nitride in vacuum is an example of such a process. The metal accelerates the dissociation process of silicon nitride at temperatures much lower than the decomposition temperature of pure Si_3N_4 in vacuum. Due to the decomposition of Si_3N_4 into high-activity silicon and nitrogen, in the process of their interaction with the metal in vacuum, the possibility of obtaining a disperse product, namely, metal nitride or silicide, arises [5].

Zirconium and β-Si_3N_4 powders were used as initial materials. The commercial zirconium powder (PTsE grade) had a mean particle size of 20 μm. The β-Si_3N_4 powder synthesized under laboratory conditions had a specific surface of 3.8 m^2/g and nitrogen content of 38.0 mass%. Reaction mixtures were calculated according to the following reaction:

$$Si_3N_4 + 4Zr = 4ZrN + 3Si. \quad (1)$$

To provide a uniform distribution of elements, the components were mixed in a Pulverizette–6 planetary mill (FRITSCH GmbH, Germany) in ethanol in a drum with silicon nitride grinding balls. During mixing, the particle size did not change. Homogenized reaction mixtures were heat-treated in an SNV–1.3,1/20–I1 electric vacuum furnace in a vacuum of ~1×10^{-3} Pa in the temperature range 750–1450 °C and in a nitrogen atmosphere at temperatures of 1000–1200 °C.

The products of the solid-state interaction in a vacuum and a nitrogen atmosphere were investigated by the XRD method on a DRON-3 diffractometer in filtered Cu-$K\alpha$ radiation. The nitrogen and zirconium contents in the final product were determined

by the chemical analysis method according to standard techniques (GOST 27417-87). The evaluation of the particle size of the synthesized powder was performed in a CILAS 990 laser particle size analyzer. Microstructural studies were carried out with a Superprobe-733 scanning electron microscope.

The consolidation of the obtained Si_3N_4–ZrN composite powders was performed by the spark plasma sintering method using an HD25 unit (FCT Systeme GmbH, Germany) (maximal temperature of 2400 °C, maximal pressing pressure of 250 kN, maximal current of 8000 A, maximal voltage of 10 V, media are a vacuum of 5×10^{-2} mbar and nitrogen). Powder mixtures in amounts of about 8 g were loaded into a graphite die with two graphite punches. The temperature on the internal surface of the upper graphite punch was measured with a digital pyrometer.

3 Results and Discussion

The investigation of the behavior of the β-Si_3N_4 + 4Zr reaction mixture in a vacuum under the action of the temperature factor (Table 1) showed that already at a temperature of 750 °C, solid-state interaction occurs. Along with the β-Si_3N_4 phase, in the products of heat treatment at a temperature of 750 °C, the α-$ZrN_{0.28}$ solid solution and ZrN phase, formed by the mechanism of contact diffusion, were recorded. This is connected with the self-diffusion rate of nitrogen in β-Si_3N_4 ($D_i = 6.8 \times 10^2 \exp(-777.5/RT)$ m^2/s). The solubility of nitrogen at this temperature in α-Zr is equal to 4.8 mass% [6].

An increase in the treatment temperature up to 1000 °C leads to the formation of nitride (α-Zr_2N and ZrN) and silicide (Zr_5Si_3, Zr_2Si, and ZrSi) phases of zirconium. Moreover, free silicon and the α-Si_3N_4 phase are present. The product of solid-state interaction at a temperature of 1450 °C is a mixture of ZrN, $ZrSi_2$, and a small amount of β-Si_3N_4. At a temperature of 1450 °C, the complete dissociation of silicon nitride occurs, and the main phases are ZrN and lower zirconium silicides. According to the chemical analysis data, the nitrogen content in the interaction products remains practically unchanged and is nearly equal to its calculated content in the (Si_3N_4 + 4Zr) initial reaction mixture (9.8 mass%). This indicates that practically the whole amount of nitrogen took part in the solid-state interaction.

Table 1 Results of solid-state interaction in vacuum for 1 h

Reaction mixture (mass%)	Temperature (°C)	Phase composition	Nitrogen content (mass%)
28β-Si_3N_4 + 78Zr	750	β-Si_3N_4, α-$ZrN_{0.28}$, ZrN	9.9
	1000	β-Si_3N_4, ZrN, α-Zr_2N, Zr_5Si_3, Zr_2Si, ZrSi, Si, α-$Si_3N_{4(traces)}$	9.6
	1450	ZrN, $ZrSi_2$, β-Si_3N_4	9.3

Thus, as a result of the dissociation of Si_3N_4, the solid-state interaction in vacuum occurs by the mechanism of reaction diffusion on interfaces of zirconium and silicon nitride particles. This suggests that the formation of the composite material occurs on particles of initial zirconium. The diffusion of nitrogen into zirconium at 750 °C is accompanied by the formation of zirconium nitrides, and the diffusion of silicon at 1000 °C is accompanied by the formation of the lower silicide phases Zr_2Si, ZrSi, and Zr_5Si_3. This testifies the reasonability of using the high-activity product of vacuum solid-state interaction at 1000 °C as a precursor for subsequent nitriding. The realization of these operations in a single technological process is economically sound.

The process of subsequent nitriding in a single cycle of the product of preliminary vacuum heat treatment of the β-Si_3N_4 + 4Zr mixture was investigated in the temperature range 1000–1200 °C for 1 h. Characteristics of the final product according to the XRD and chemical analysis data are presented in Table 2.

The analysis of the presented data indicates that, at a nitriding temperature of 1200 °C, the phase composition of the product is ZrN and β-Si_3N_4.

Thus, the optimal synthesis regime of the Si_3N_4–ZrN composite material in a single cycle is vacuum treatment at 1000 °C (stage 1) and nitriding at 1200 °C for 1 h (stage 2). The final product contains only nitride phases of zirconium and silicon. The nitrogen content in the product is equal to its content calculated by reaction (1).

The possibility of obtaining a Si_3N_4–ZrN composite material in a wide concentration range in the established optimal synthesis regime was investigated.

In Fig. 1, X-ray diffraction patterns of the products of the two-stage synthesis of reaction mixtures of different composition are shown. The XRD data analysis indicates that, for all investigated compositions, a two-phase product, in which the ZrN content ranged from 11 up to 33 vol.%, was obtained. It should be noted that in the X-ray diffraction patterns of the mixtures with a ZrN content of 11 and 22 vol.%, traces of $ZrSi_2$ are also present.

The chemical analysis data of the synthesis products (Table 3) in the established regime show that the combination of heat treatment at 1000 °C in vacuum with subsequent nitriding at 1200 °C in a single technological process makes it possible to obtain powders of the composite materials, the nitrogen contents in which are maximally close to the theoretical ones.

Table 2 Characteristics of the product of the two-stage heat treatment of the 22 mass% β-Si_3N_4 + 78 mass% Zr mixture for 1 h

Synthesis regime		Phase composition	Nitrogen content (mass%)
Stage 1 (vacuum)	Stage 2 (nitrogen)		
Temperature (°C)	Temperature (°C)		
1000	1000	ZrN, β-Si_3N_4, $ZrSi_2$	11.7
1000	1100	ZrN, β-Si_3N_4, $ZrSi_2$	12.7
1000	1200	ZrN, β-Si_3N_4	13.1

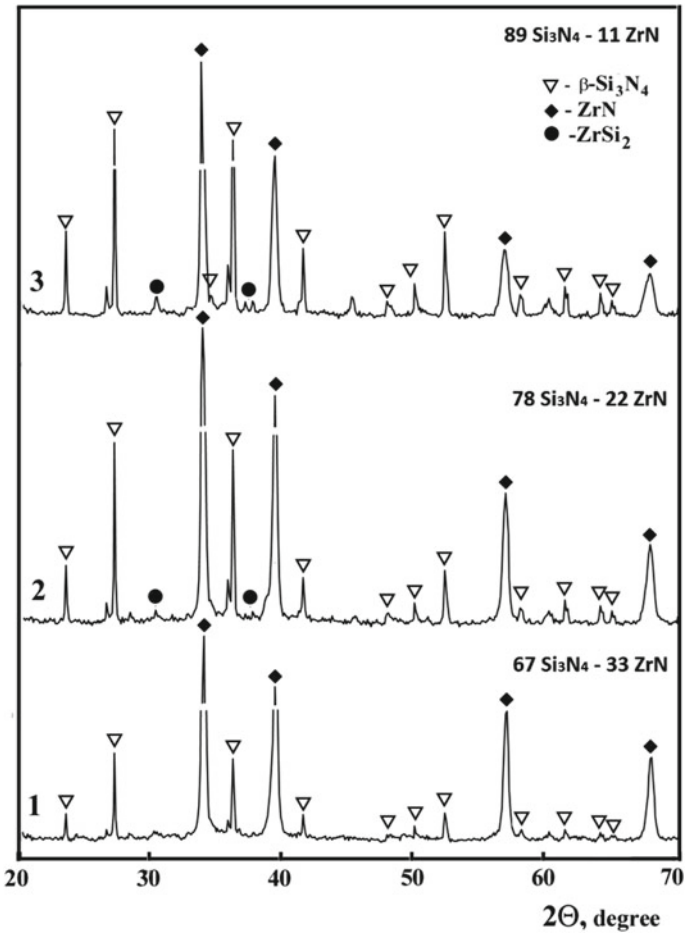

Fig. 1 X-ray diffraction patterns of the products of the two-stage synthesis from reaction mixtures of different composition: (**1**) 67 vol.% Si_3N_4–33 vol.% ZrN, (**2**) 78 vol.% Si_3N_4–22 vol.% ZrN, (**3**) 89 vol.% Si_3N_4–11 vol.% ZrN

Table 3 Certification of composite materials

Composition of the reaction mixture (mass%)	Chemical analysis data (mass%)				Specific surface (m^2/g)	Final composition of the synthesized product (vol.%)	Resistivity ($\mu\acute{\Omega}$ cm)
	N		Zr	Fe			
	Theor.	Exp.					
50Si_3N_4–50Zr	23.8	20.8	48.7	1.9	3.46	67Si_3N_4 + 33ZrN	104×10^5
64Si_3N_4–36Zr	25.4	26.5	31.8	1.2	5.14	78Si_3N_4 + 22ZrN	147×10^5
80Si_3N_4–20Zr	29.7	28.9	22.8	0.5	5.87	89Si_3N_4 + 11ZrN	309×10^{16}

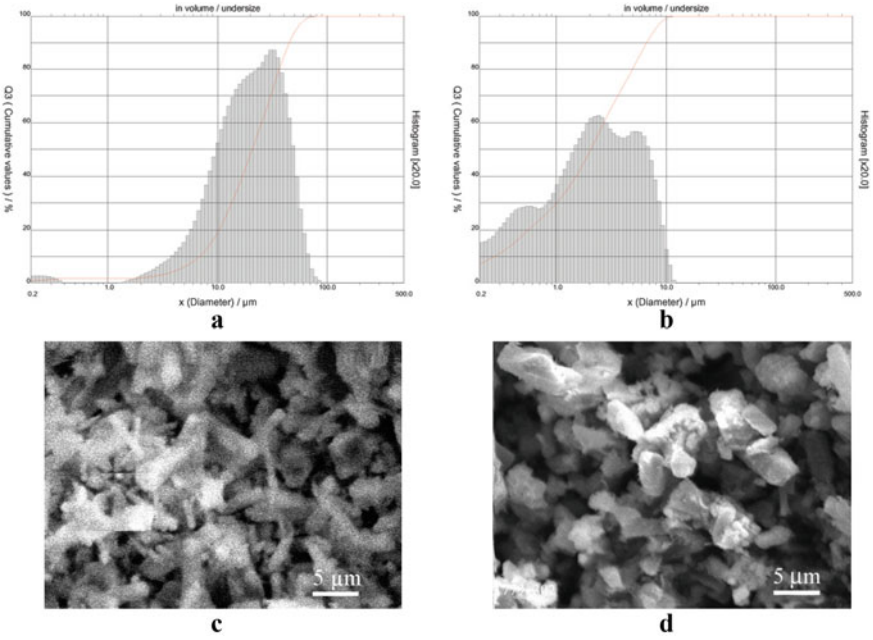

Fig. 2 Particle-size distribution of the 78 vol.% Si_3N_4–22 vol.% ZrN composite powder after synthesis (**a**) and dispersion (**b**) and the morphology of the initial mixture (**c**) and synthesized powder (**d**)

According to the data of evaluation of the particle size of the synthesized 78 vol.% Si_3N_4–22 vol.% ZrN composite powder, the mean size of agglomerates is 23.71 μm (Fig. 2a). After dispersion in isopropyl alcohol, the mean particle size decreased by an order of magnitude down to 2.81 μm (Fig. 2b), and, moreover, the number of submicron and nanosized particles increased.

The analysis of the morphology testifies (Fig. 2d) that the obtained product consists of agglomerates of the Si_3N_4–ZrN composite powder. A comparison of the morphology of the initial mixture based on β-Si_3N_4 (Fig. 2c) with the morphology of the synthesized powder indicates that the shape of particles radically changes from the elongated to the rounded one.

Thus, it is established that the process of vacuum treatment of the Si_3N_4 + Zr reaction mixtures at a temperature of 1000 °C makes it possible to obtain precursors containing the necessary initial components of the nitride ceramics. The combination of the vacuum heat treatment and nitriding (at 1200 °C) processes in a single cycle leads to obtaining disperse powders of the Si_3N_4–ZrN composite materials in a wide concentration range (11–33 vol.% ZrN).

Zirconium nitride, which exhibits high electrical conductivity, strength, and melting point, meets the main requirements to the conductive hardening phase in silicon nitride [1]. Since the difference between the electrical resistivity of silicon nitride (~10^{13}–10^{14} μΏ × cm) and electrical resistivity of zirconium nitride (29 μΏ ×

cm) is extremely large, the electrical conductivity of the composite ceramics depends primarily on the continuity of the conductive 3D network of ZrN particles, the content of ZrN, and the homogeneity of its distribution in the composite ceramics [7, 8].

The conductivity of composite ceramics of the Si_3N_4–ZrN system, as ceramics of a typical insulator–conductor system, must show the percolation behavior, which is characterized by an abrupt decrease in the electrical resistivity at a certain content of the conductive phase [9]. The content of the conductive phase at which a conductive network form is called the percolation concentration or percolation threshold. Since this parameter depends to a great extent on technological regimes of preparation of the material, dispersity, and shape of particles, it is most reasonable to determine it experimentally from concentration dependences of conductivity [7]. For the obtained Si_3N_4–ZrN composite powders, the values of the electrical resistivity were determined (Table 2).

4 Spark Plasma Sintering of Si_3N_4–ZrN Composites

Data on the linear shrinkage of the Si_3N_4–ZrN composite powders in the process of SPS consolidation were monitored as the travel distance of the upper punch (the bottom punch is fixed) and converted into the shrinkage rate of specimens. After loading of about 8 g of the composite powder into the graphite die 20 mm in diameter with a punch unit, a pressure of 50 MPa was applied to establish good contacts between the graphite tools and powder particles. Sintering experiments were performed in the nonlinear consolidation regime developed earlier [10–12]. The Si_3N_4–ZrN composites were consolidated in few-stage regimes, in which pressure was sequentially increased from 50 up to 80 MPa and the heating rate was decreased from 100 °C/min down to 20 °C/min. The temperature was measured by a pyrometer on the inner surface of the upper graphite punch. Isothermal holding for 1.5 min at high temperatures was used to fully densify the Si_3N_4–ZrN composites.

All investigated Si_3N_4–ZrN composites were densified at a temperature of 1750 °C withholding for 5 min. The analysis of the sintering curves shows that the densification process proceeds in two stages (Figs. 3 and 4). The first stage of densification takes place in the temperature range of 400–800 °C. This can be connected with the increase in the pressure, destruction of strong agglomerates in the powder mixture, and rearrangement of particles.

As expected, the composite with 33 vol.% ZrN demonstrates the highest sinterability (Fig. 3, curve 1). This is connected with the large content of the highly conductive phase in the mixture, which forms a branched continuous network of ZrN particles. The densification of the 67 vol.% Si_3N_4–33 vol.% ZrN composite starts at a temperature of 1200 °C and proceeds quite intensively at a shrinkage rate of 1 mm/min up to a temperature of 1600 °C (Fig. 4, curve 1). This agrees well with the character of SPS densification curves of ZrN nanogranular powder (Fig. 5) synthesized by the method of carbothermal reduction-nitriding of a precursor obtained by the sol–gel method (the size of the coherent scattering region is 48 ± 2 nm). The

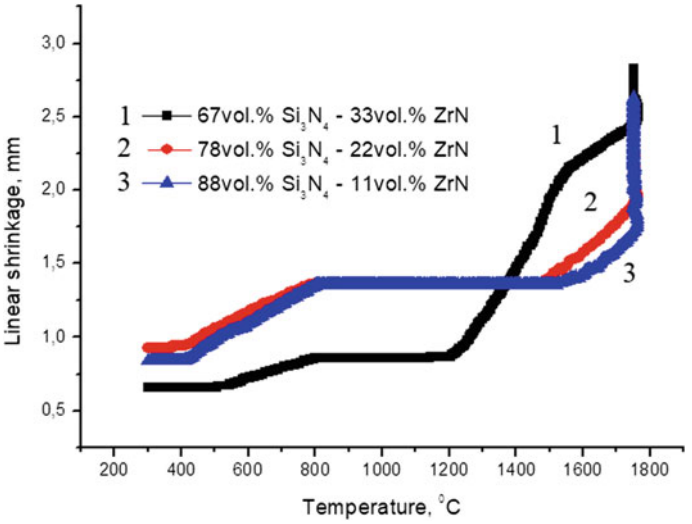

Fig. 3 Linear shrinkage versus temperature for SPS consolidated Si_3N_4–ZrN composites

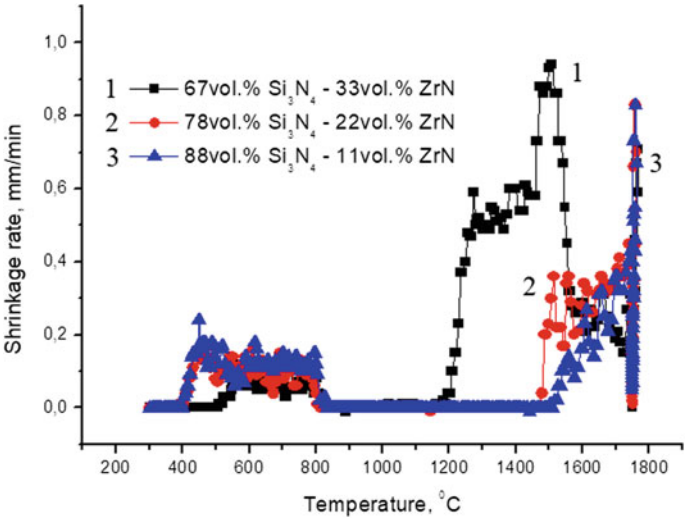

Fig. 4 Shrinkage rate versus temperature for SPS consolidated Si_3N_4–ZrN composites

comparison of the values of the electrical resistivity of ZrN (29 $\mu\acute{\Omega} \times$ cm) and the composite material with 33 vol.% ZrN (104×10^5 $\mu\acute{\Omega}$ cm) enables us to argue that, in the process of consolidation by the SPS method, due to the formation of the continuous 3D network of ZrN particles, the run of the densification curve of the composite is analogous to that for zirconium nitride. In holding at a temperature of

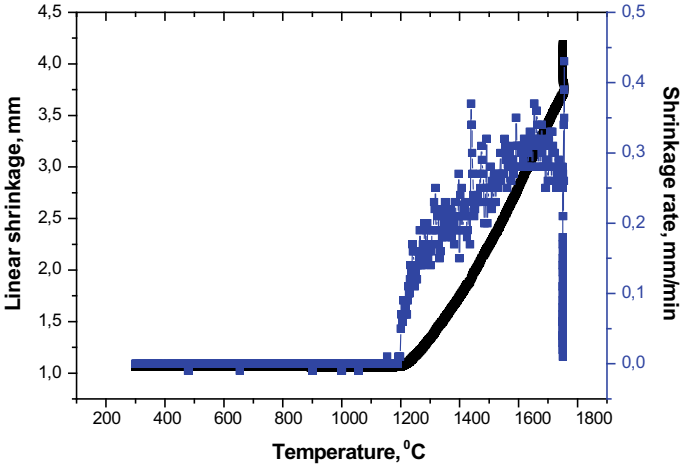

Fig. 5 Linear shrinkage and shrinkage rate versus temperature for SPS consolidated ZrN

1750 °C, minor densification occurs, and the density attains 97% of the theoretical one.

The composites with 22 and 11 vol.% ZrN demonstrate similar conditions of densification during SPS (Fig. 3, curves 2 and 3). For the composites, densification begins at a temperature about 1400 °C and the most intensive phase of shrinkage with a shrinkage rate of 0.9 mm/min is observed during holding at 1750 °C. This can be explained by the low content of the conductive phase (ZrN), which is below the percolation threshold. In contrast to the composite with 33 vol.% ZrN, where densification process is controlled by the ZrN phase, for the composites with 22 and 11 vol.% ZrN, where traces of zirconium disilicide are present (Fig. 1, curves 2 and 3), the sintering process is activated by its phase transformation into zirconium nitride.

The microstructure of the sintered 78 vol.% Si_3N_4–22 vol.% ZrN specimen shown in Fig. 6, indicates the size inhomogeneity of both the ZrN phase (light grains) and Si_3N_4 phase (dark grains). The ZrN phase has the relatively narrow grain size range 200–400 nm, whereas the Si_3N_4 phase, whose fraction is about 80 vol.%, is characterized by bimodality. The wide particle size range 0.2–2 μm is connected with the strong agglomeration of nanograins in the process of consolidation.

In Fig. 6, the microstructure of the sintered 78 vol.% Si_3N_4–22 vol.% ZrN specimen is shown. The structure of this composite is characterized by a bimodal grain size distribution. Zirconium nitride grains (light) have a relatively narrow size range of the order of 100–300 nm. At the same time, the Si_3N_4 phase (dark), whose content is about 80 vol.%, is characterized by a bimodal grain size distribution. Grains with a size of 100–300 nm and needle-like grains with a length up to several microns are present.

The mechanical characteristics of these materials are the following: the hardness is 22.5 ± 1.8 GPa, and the fracture toughness is 6.2 MPa. The high mechanical

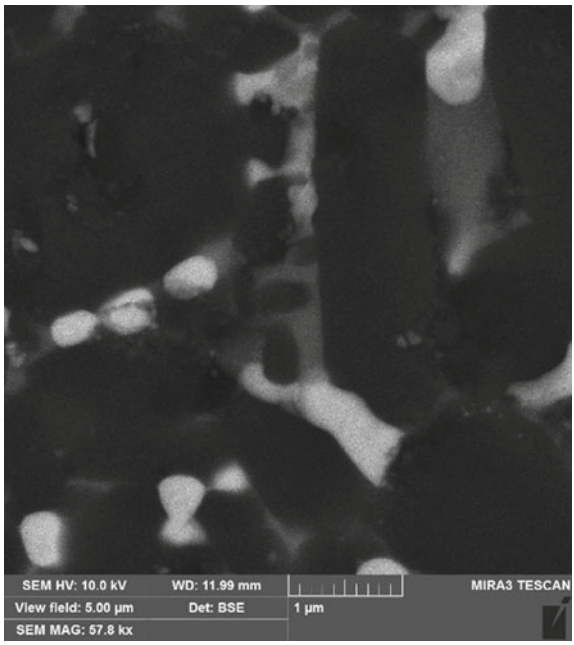

Fig. 6 Microstructure of a sintered 78 vol.% Si_3N_4–22 vol.% ZrN specimen

properties of the obtained material can be explained by the structural features of the composite. The high hardness is achieved due to the decrease in the grain size down to the nanolevel, and the presence of needle-like Si_3N_4 grains enhances the fracture toughness of the composite.

5 Conclusions

The two-stage synthesis process of composite nanopowders in the Si_3N_4–ZrN system is proposed. It has been established that the vacuum treatment process of the Si_3N_4 + Zr reaction mixtures makes it possible to obtain a precursor containing all necessary initial components of the nitride ceramics in the first stage of synthesis at a temperature of 1000 °C. The performance of synthesis in a single cycle that combines the processes of vacuum treatment (1000 °C) and nitriding (1200 °C) leads to obtaining disperse powders of Si_3N_4–ZrN composite materials in the wide concentration range 11–33 vol.% ZrN. The obtained powder mixtures are characterized by the presence of agglomerates up to several microns and nanosized particles.

The consolidation of the synthesized powders of the Si_3N_4–ZrN system has been performed by spark plasma sintering at a temperature of 1750 °C under a pressure of 60 MPa. The composition with 33 vol.% ZrN has shown the best sinterability, which is connected with the formation of a continuous conductive 3D network of ZrN particles. Compact specimens made of the 67 vol.% Si_3N_4–33 vol.% ZrN composite

is characterized by a relative density above 97% and a bimodal structure, where grains with a size of ~200 nm and needle-like silicon nitride grains with a size up to several microns are present. The mechanical properties of this material are as follows: the hardness is 22.5 ± 1.8 GPa, and fracture toughness is 6.2 MPa.

Acknowledgements The authors express their heartfelt thanks and deep gratitude to the Material Lab Ltd. for fruitful cooperation.

References

1. Harrison RW, Lee WE (2016) Processing and properties of ZrC, ZrN and ZrCN ceramics: a review. Adv Appl Ceram 115:294–307
2. Krushinskaya LA, Makarenko GN, Oleynik GS, Uvarova IV, Fedorus VB (2007) Preparation of highly disperse composite powders of the Si_3N_4–TiN system. II. Structural-phase transformations during nitriding of titanium silicide powder. Nanostrukturnoe Materialovedenie (Nanostruct Mater Sci) 1:84–90 (in Russian)
3. Ade M, Haußelt J (2003) Electroconductive ceramic composites with low–to–zero shrinkage during sintering. J Eur Ceram Soc 23:1979–1986
4. Kurnetsov NT (1999) Precursors for carbide, nitride and boride synthesis. In: Gogotsi YG, Andrievski RA (eds) Materials science of carbides, nitrides and borides. NATO science series. Kluwer Academic Publishers, Dordrecht (Netherlands), pp 223–247
5. Kharlamov AI, Bondarenko ME, Rafal AN (1990) Kinetics of the interaction of transition metals with silicon nitride. In Collection of scientific works: silicides and their application in engineering. Institute for Problems of Materials Science of the Academy of Sciences of the Ukrainian SSR, Kiev (Ukrainian SSR), pp 35–40 (in Russian)
6. Polishchuk VS (2003) Intensification of the manufacturing processes of carbides, nitrides, and composite materials based on them. Veber, Sevastopol (Ukraine) (Polishchuk 2003) 7 (in Russian)
7. Zivkovic Lj, Nikolic Z, Boskovic S, Miljkovic M (2004) Microstructural characterization and computer simulation of conductivity in Si_3N_4–TiN composites. J Alloy Compd 373:231–236
8. Zivkovic LjM, Nikolic ZS, Boskovic SM (2002) Electrical properties and percolation concentration in Si_3N_4–TiN based composites. Key Eng Mater 206–213:1489–1492
9. Lux F (1993) Models proposed to explain the electrical conductivity of mixtures made of conductive and insulating materials. J Mater Sci 28:285–301
10. Zgalat-Lozynskyy OB, Herrmann M, Ragulya AV (2011) Spark plasma sintering of TiCN nanopowders in non-linear heating and loading regimes. J Eur Ceram Soc 31:809–813
11. Zgalat-Lozynskyy OB, Ragulya AV, Herrmann M, Andrzejczuk M, Polotai A (2012) Structure and mechanical properties of spark plasma sintered TiN-based nanocomposites. Arch Metall Mater 57:853–858
12. Zgalat-Lozinskii OB (2014) Nanocomposites based on refractory compounds, consolidated by rate-controlled and spark-plasma sintering. Powder Metall Met Ceram 53:19–30

Nickel–Copper Hydroxide Multilayer Coating as Anode Material for Methanol Electro-oxidation

A. Maizelis

1 Introduction

Direct methanol fuel cells (DMFCs) belong to the ideal energy converters [1] due to methanol availability, wide range of sources, low-cost, convenient storage, and high energy density [2]. Methanol oxidation reaction (MOR) is a critical reaction in DMFCs [3].

For the methanol oxidation, mainly sulfuric acid electrolytes and electrodes with a catalytic coating containing precious metals are used. Electrocatalysts based on Pt and Pt alloys have good activity in methanol oxidation, but the high cost of these materials, sluggish kinetics, and loss of activity due to the formation of strongly adsorbed intermediates are very high [4, 5]. The use of alkaline solutions in the fuel cell has many advantages, e.g., wider choice of possible electrode materials, higher efficiency of both anodic and cathodic processes, almost no sensitivity to the surface structure, and little poisoning effects of the catalytically active surface of the electrode [6]. Therefore, considerable efforts are directed to the study of methanol electro-oxidation at high pH [7].

Promising Pt-free non-noble electrode materials intended for the anodic methanol oxidation in an alkaline medium include nickel and nickel-based materials due to its good surface oxidation properties, low price, and abundant content in the earth [8]. Ni catalyst shows excellent electrochemical stability and resistance to poisoning [9]. Many researches on different morphologies and structures Ni-based catalysts have been reported [10–19].

First of all, the study of alloy electrodes is motivated by the expectation of a synergistic electrocatalytic effect when combining the properties of the metals that

A. Maizelis (✉)
Department of Technical Electrochemistry, National Technical University «Kharkiv Polytechnic Institute», Kyrpychova Street 2, Kharkiv 61002, Ukraine
e-mail: a.maizelis@gmail.com

O. Fesenko and L. Yatsenko (eds.), *Nanooptics and Photonics, Nanochemistry and Nanobiotechnology, and Their Applications*, Springer Proceedings in Physics 247, https://doi.org/10.1007/978-3-030-52268-1_3

make up the alloy [6]. Ni–Cu nanoalloy is considered particularly to be a potential alternative to Ni due to their synergistic effects [20, 21].

The doping and underpotential deposition of modifiers on the catalytic surface have been tested [22] to reduce the apparent high overvoltage associated with the process and to overcome the possible effects of adsorption of intermediates. Both copper and nickel are effective catalysts of alcohol electro-oxidation in general, and particularly methanol, along with some other organic substances. They are electrocatalysts of both anode and cathode reactions. The presence of small amount of both nickel and copper on the surface of carbon increases the current density of methanol oxidation compared to pure nickel [9]. The catalytic activity in methanol oxidation reaction on Ni–Cu nanoparticles is higher as compared to pure Ni [7]. It has been shown that the oxygen evolution overvoltage increases in the case of an electrode modified with a Ni–Cu alloy [6].

The increase in the catalytic activity of the nickel–copper alloy in comparison with pure nickel may be due to the filling of the vacancies of the d-orbital of the nickel with electrons from copper. It is shown that the catalytic activity of nickel alloy with 40% copper increases by more than 10 times as compared to nickel at the same potentials [22]. Gupta et al. [23] selected a 70:30 copper–nickel alloy as a potential basis for the manufacture of the anode of a direct methanol fuel cell. Danaee et al. [7] investigated an alloy of 79% nickel and 21% copper, which catalyzes the methanol oxidation reaction. The catalytic activity of the anode increases with decrease of copper content in the coating. The best catalytic activity of the anode is noted at a copper content of 10% [24]. Hameed et al. [25] show that the corrosion resistance of electroless alloys 90% Ni—7% Cu—3% P in a solution of 50% NaOH is higher than the Ni–P alloy.

The change in catalytic activity with the alloy composition may be possible both due to the change of the surface area and the microstructure of the coating [24], e.g., the addition of copper ions into the solution for electroless nickel deposition led to the formation of more dispersed films [25]. Nanoporous amorphous Ni–Cu–P electrode demonstrates higher anodic current density, better stability, and lower onset oxidation potential as compared to a smooth Ni–Cu–P amorphous alloy film [26].

Additional to the effect of alloying, the shape and architecture of catalysts have significant influence on their catalytic properties, e.g., nanowires are promising components in elecrocatalysis process due to their high electrical conductivity and structural stability [27, 28]. Ding et al. [29] proposed highly ordered Ni-Cu alloy hierarchical porous nanowire arrays for this purpose [29]. Unique Cu/Ni–Cu nanowires integrating alloy, core–shell, and one-dimensional structures are prepared by a facile one-pot strategy [30]. Successful synthesis of porous Ni–Cu nanowires increases the contact area between material and electrolyte, the adsorption capacity; it increases the diffusion of ions, which is critical for the efficiency of electrocatalysis [29].

Previous studies have shown the promising use of protective and catalytically active multilayer coatings [31–33], including for the oxidation of ethanol [34] and glucose [35, 36]. Electrode with the nickel–copper oxide multilayer coating has lower activation energy of the methanol oxidation reaction (9.88 ± 0.07 kJ mol^{-1}) as compared to the known nickel–copper containing electrodes [37]. In this work,

we study the catalytic properties of the multilayer nickel–copper oxohydroxide as a mediator in the methanol oxidation reaction.

2 Experimental

Pyrophosphate–ammonium polyligand electrolyte for the multilayer coating deposition contained 0.05 mol L^{-1} Cu^{2+}, 0.25 mol L^{-1} Ni^{2+}, 0.35 mol L^{-1} $P_2O_7^{4-}$, 1.0 mol L^{-1} NH_3 (NH_4^+), 0.1 mol L^{-1} Cl^-, pH 9. It was prepared from analytical grade chemicals and distilled water without further treatment.

Electrochemical measurements were carried out in the three-electrode cell using a potentiostat PI-50.1. The results were transferred from analog form to digital by means of the two-channel voltmeter and « TeleMax » program for PC (5–100 signals per second).

A copper wire with a diameter of 1 mm (immersed in electrolyte for 1 cm) with an electrodeposited dendritic structure on it was used as working electrode. The catalytically active nickel–copper hydroxide multilayer coating was formed on a sublayer of a nickel–copper alloy using a two-pulse potentiostatic mode followed by treatment of multilayer coating in 1 mol L^{-1} KOH solution as described in [37].

The Pt electrode was used as a counter electrode. The saturated Ag/AgCl reference electrode was used in the measurements; all the potentials are given *vs.* this electrode. Cyclic voltammograms were obtained at a potential scan rate of 1–1000 mV s^{-1}. The stabilized cycles are presented. The amount of electricity passing through the electrolyte was determined by integrating the *i–t* dependencies.

3 Experimental Results and Discussion

The CVA of electrode with the nickel–copper hydroxide multilayer coating (NCHME) obtained in 1 M KOH in a wide range of potential scan rate is shown in Fig. 1a. CVAs have the anode peak of the reversible oxidation of nickel hydroxide to oxohydroxide and the cathode peak of the reverse reaction. This electrode is characterized by the wider potential window as compared to the known nickel contained electrodes [9, 22, 38]. Up to scan rate of 50 mV/s nickel hydroxide oxidation is almost over before the oxygen evolution potential is reached. Increase in the potential scan rate leads to increase in the height of anode and cathode peaks and the potential difference of these peaks. This is associated with the presence of diffusion difficulties and an increase in the degree of irreversibility of the oxo-hydroxo transition. The anode branch of the backward part of the CVA corresponds to the oxygen evolution. The cathodic branch of the backward part of CVA begins with the oxygen reduction, and then the peak of nickel oxohydroxide reduction increases.

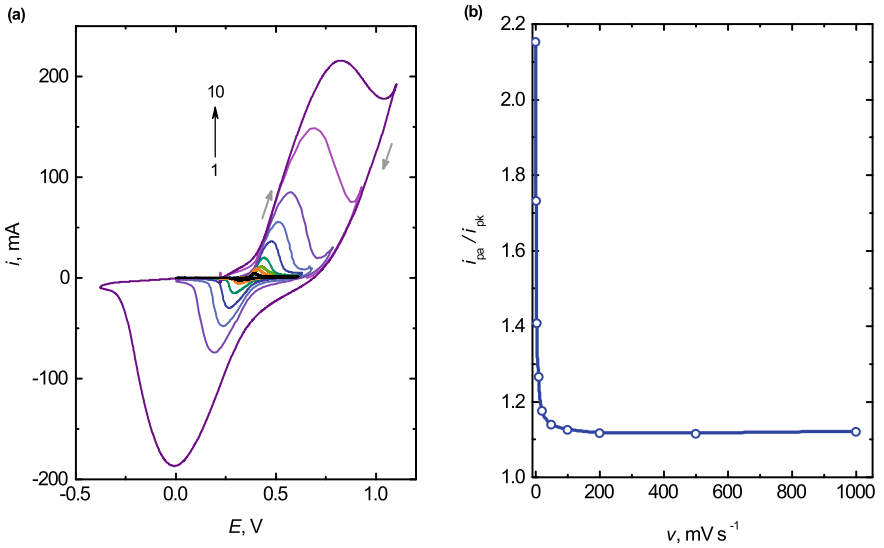

Fig. 1 **a** CVA on NCHME in a solution of 1 mol L^{-1} KOH, and **b** the i_{pa}/i_{pk} ratio. Potential scan rate, mV s^{-1}: 1–1; 2–2; 3–5; 4–10; 5–20; 6–50; 7–100; 8–200; 9–500; 10–1000

The ratio of the currents of anode and cathode peaks (Fig. 1b) decreases with the increase in the potential scan rate from 1 to 1000 mV s^{-1}. The decrease is significant at 1–50 mV s^{-1} and it slightly decrease at 100–1000 mV s^{-1}.

In the presence of 1 mol L^{-1} methanol in alkaline solution (Fig. 2a), the height of the cathode peak at the corresponding potential scan rate is almost unchanged, but in the region of the anode peak of nickel hydroxide oxidation, a peak of methanol oxidation appears, the height of which is much higher than the height of the hydroxide nickel oxidation at an appropriate potential scan rate. The shape of the anode branches of the backward parts of CVAs also changes; in addition to the oxygen evolution, the process of methanol oxidation continues. Apparently, at the potential range of 0.95–1.0 V, the desorption of methanol oxidation products is carried out and new methanol molecules are oxidized at the vacated centers. At low potentials, the limiting stage is the methanol oxidation, while the oxidation and removal of adsorbed intermediates occur at high potentials [7].

The nature of the dependence of the ratio of anode-to-cathode peak currents on the potential scan rate in a wider range of scan rate values (Fig. 2b) is the same as in the absence of methanol in solution (Fig. 1b), but this ratio at low values of potential scan rate is two orders of magnitude higher. It indicates the irreversibility of the methanol oxidation reaction on this electrode.

The irreversibility of the methanol oxidation process is confirmed by the absence of a corresponding increase in the height of the cathode peak with methanol concentration increase (Fig. 3). Additionally, the decrease in the cathode peak area, even when compared to the cathode peak in a KOH solution without methanol at an

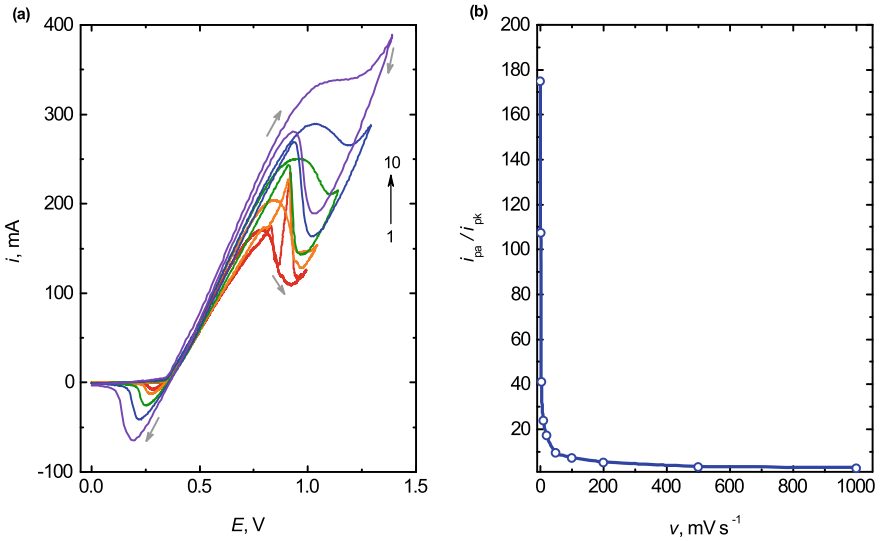

Fig. 2 **a** CVA on NCHME in a solution of 1 mol L^{-1} KOH, 1 mol L^{-1} CH_3OH and **b** the i_{pa}/i_{pk} ratio. Potential scan rate, mV s^{-1}: 1–10; 2–20; 3–50; 4–100; 5–200

Fig. 3 CVA on NCHME in a solution of 1 mol L^{-1} KOH at different concentrations of methanol, mol L^{-1}: 1—0; 2—0.1; 3—0.2; 4—0.3; 5—0.4; 6—1.0. Potential scan rate is 10 mV s^{-1}

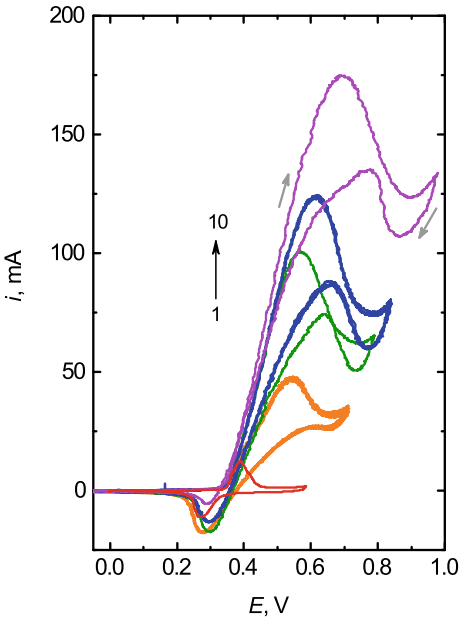

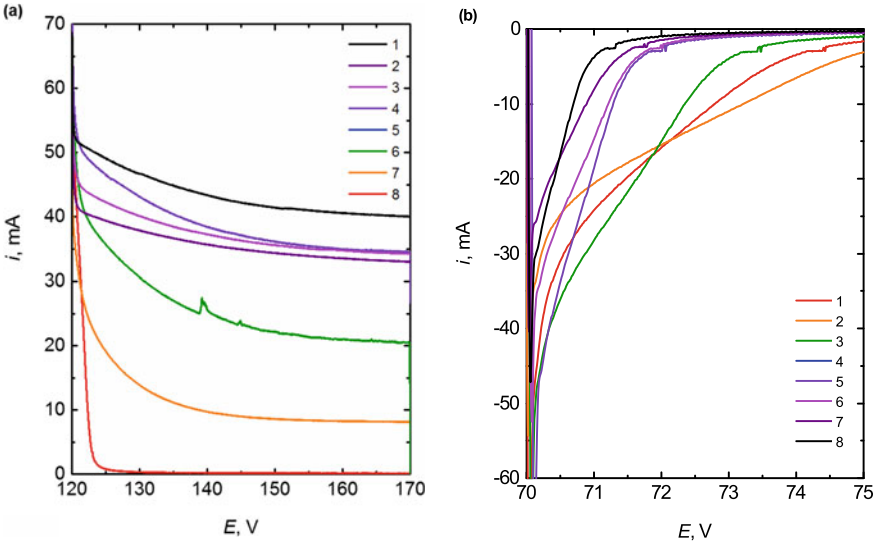

Fig. 4 Start of (**a**) anode and (**b**) cathode parts of *i–t* curves with periodic change of potential from 0.55 V (50 s) to 0.3 V (50 s) in the electrolytes containing 1.0 mol L^{-1} KOH and 1.0 mol L^{-1} (1), 0.6 mol L^{-1} (2), 0.5 mol L^{-1} (3), 0.4 mol L^{-1} (4), 0.3 mol L^{-1} (5), 0.2 mol L^{-1} (6), 0.1 mol L^{-1} (7), and 0 mol L^{-1} (8) of methanol

appropriate potential scan rate, combined with an increase in the anode peak area with increasing methanol concentration, indicates the catalytic nature of process of methanol oxidation on NCHME. Comparison of the ratio of the height of the peaks of methanol oxidation to the height of nickel hydroxide oxidation peak at appropriate concentrations and the potential scan rate with other materials containing copper and nickel [26, 30] shows the advantage of NCHME.

In Fig. 4 presents the parts of chronoamperograms obtained in solutions of 1 mol L^{-1} KOH with different methanol content, under conditions of periodic two-step potential change from 0.55 V (50 s) corresponding to methanol oxidation in the absence of oxygen evolution, to 0.3 V (50 s) corresponding to the peak of nickel oxohydroxide reduction.

The amount of electricity for nickel oxyhydroxide reduction is much less as compared to the amount of electricity for methanol oxidation. In the absence of methanol (Fig. 4a, curve 8), the nickel hydroxide oxidation in alkaline solution stops in just 2 s when it reaches its maximum saturation. Nickel oxidation process are inhibited in the first second at low concentration of methanol in the alkaline solution (curves 7 and 8). Then, the methanol oxidation current approaches its limit value. The methanol oxidation current increases with an increase in methanol concentration.

The cathode branches of the chronoamperograms (Fig. 4b) indicate the rapid reduce of oxohydroxide within 5 s. According to the catalytic mechanism of methanol oxidation, the increasing methanol concentration on the electrode leads to decrease in the number of the remained non-renewable oxohydroxide particles and the current at

the cathode branches of *i–t* curves decreases. The mediator mechanism of methanol oxidation by nickel oxohydroxide is referred in different variants by many authors, e.g., [22]:

$$CH_3OH + Ni(OH)_2 \rightarrow Ni(OH)_2(CH_3OH)_{ad}$$

$$Ni(OH)_2 + OH^- \leftrightarrow NiOOH + H_2O + e$$

$$Ni(OH)_2(CH_3OH)_{ad} + OH^- \rightarrow NiOOH(CH_3OH)_{ad} + H_2O + e$$

$$NiOOH(CH_3OH)_{ad} + NiOOH + 2\ OH^- \rightarrow Ni(OH)_2 + NiOOH(COH)_{ad} + 2\ H_2O + 2\ e$$

$$NiOOH(COH)_{ad} + OH^- \rightarrow Ni(OH)_2 + HCOO^-$$

The amount of electricity for nickel oxohydroxide molecules reduction Q_{cat} remaining after interaction with methanol molecules decreases with increase in methanol concentration (Fig. 5a), while the amount of electricity for catalytic methanol oxidation Q_{an} increases (Fig. 5b). The ratio Q_{an}/Q_{cat} increases with increase in methanol concentration in a straight line (Fig. 5c).

The values of limiting currents i_{lim} determined from the *i–t* curves (Fig. 4a) increase in a linear manner with methanol concentration increase up to 0.4 mol L^{-1}, then their values practically do not change (Fig. 6a). This means a change of mechanism and rate of the limiting stage with methanol concentration increase from methanol oxidation to removing of adsorbed intermediates. The methanol oxidation reaction order *p* is determined using Fig. 6b is 1.

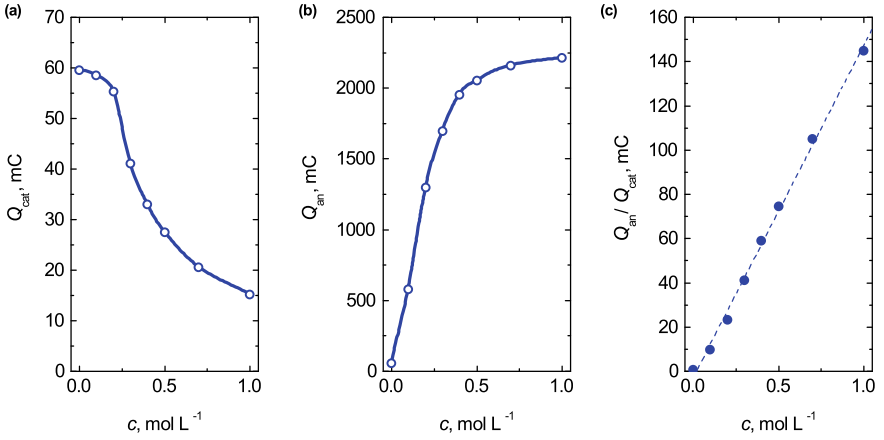

Fig. 5 Changing in the amount of electricity **a** Q_{cat} and **b** Q_{an} and **c** their ratio Q_{an}/Q_{cat} with methanol concentration

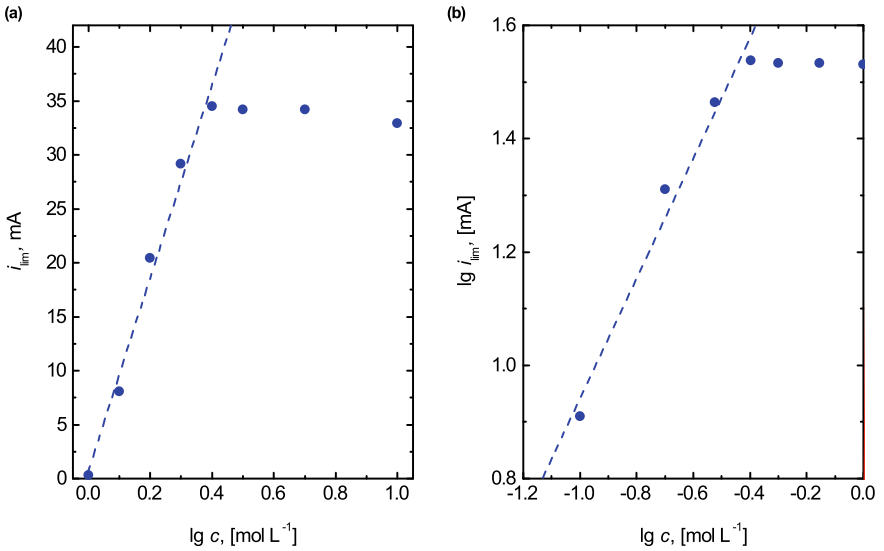

Fig. 6 i_{lim}–c and lg(i_{lim})–lg(c) dependencies

4 Conclusions

A nickel–copper hydroxide multilayer electrode is catalytically active in a methanol oxidation reaction in which nickel oxohydroxide acts as mediator. The ratio of the height of the peak of methanol oxidation to the height of the peak of nickel hydroxide oxidation in the absence of methanol is higher than for other nickel–copper materials. The reaction order p for methanol oxidation is 1. The ratio of the heights of the anodic to cathodic peaks at a potential scan rate of 1–50 mV s^{-1} in an alkaline medium in the presence of 1 mol L^{-1} of methanol is 2 orders of magnitude higher than in its absence. This fact, as well as the absence of a corresponding increase in the height of the cathode peak with methanol concentrations increase, indicates the irreversibility of the methanol oxidation reaction at this electrode. In accordance with the catalytic mechanism of methanol oxidation, the increase in methanol concentration on the electrode leads to increase in the ratio of the amount of electricity for methanol catalytic oxidation to the amount of electricity for reduction of nickel oxohydroxide molecules remaining after interaction with the methanol molecules that increase in a straight line.

References

1. Li X, Faghri A (2013) Review and advances of direct methanol fuel cells (DMFCs) part I: design, fabrication, and testing with high concentration methanol solutions. J Power Sources 226:223–240. https://doi.org/10.1016/j.jpowsour.2012.10.061

2. Joghee P, Malik J, Pylypenko S, O'Hayre R (2015) A review on direct methanol fuel cells. In the perspective of energy and sustainability. MRS Energy Sustain 2:E3. https://doi.org/10.1557/mre.2015.4
3. Tiwari JN, Tiwari RN, Singh G, Kim KS (2013) Recent progress in the development of anode and cathode catalysts for direct methanol fuel cells. Nano Energy 2(5):553–578. https://doi.org/10.1016/j.nanoen.2013.06.009
4. Zhao X, Yin M, Ma L, Liang L et al (2011) Recent advances in catalysts for direct methanol fuel cells. Energy Environ Sci 4(8):2736–2753. https://doi.org/10.1039/c1ee01307f
5. Serov A, Kwak C (2009) Review of non-platinum anode catalysts for DMFC and PEMFC application. Appl Catal B 90(3–4):313–320. https://doi.org/10.1016/j.apcatb.2009.03.030
6. Danaee I, Jafarian M, Forouzandeh F, Gobal F, Mahjani MG (2008) Electrocatalytic oxidation of methanol on Ni and NiCu alloy modified glassy carbon electrode. Int J Hydrog Energy 33(16):4367–4376. https://doi.org/10.1016/j.ijhydene.2008.05.075
7. Danaee I, Jafarian M, Forouzandeh F, Gobal F, Mahjani MG (2009) Electrochemical impedance studies of methanol oxidation on GC/Ni and GC/NiCu electrode. Int J Hydrog Energy 34(2):859–869. https://doi.org/10.1016/j.ijhydene.2008.10.067
8. Rahim MA, Hameed RA, Khalil MW (2004) The role of a bimetallic catalyst in enhancing the electro-catalytic activity towards methanol oxidation. J Power Sources 135(1–2):42–51. https://doi.org/10.1016/j.jpowsour.2004.04.009
9. Hameed RA, El-Khatib KM (2010) Ni–P and Ni–Cu–P modified carbon catalysts for methanol electro-oxidation in KOH solution. J Hydrog Energy 35(6):2517–2529. https://doi.org/10.1016/j.ijhydene.2009.12.145
10. Wang Y, Chen W, Pan D, Xu Q, Ma J, Zheng J, Li R (2017) Methanol electrooxidation reaction in alkaline medium on glassy carbon electrode modified with ordered mesoporous Ni/Al_2O_3. Int J Electrochem Sci 12(3):2194–2206. https://doi.org/10.20964/2017.03.47
11. Sharel PE, Liu D, Lazenby RA, Sloan J, Vidotti M, Unwin PR, Macpherson JV (2016) Electrodeposition of nickel hydroxide nanoparticles on carbon nanotube electrodes: correlation of particle crystallography with electrocatalytic properties. J Phys Chem C 120(29):16059–16068. https://doi.org/10.1021/acs.jpcc.5b12741
12. Hassaninejad-Darzi SK, Rahimnejad M, Mokhtari SE (2016) Ni (II) decorated nano silicoaluminophosphate molecular sieves-modified carbon paste electrode as an electrocatalyst for electrooxidation of methanol. Bull Mater Sci 39(3):901–912. https://doi.org/10.1007/s12034-016-1194-y
13. Luo Q, Peng M, Sun X, Asiri AM (2016) Hierarchical nickel oxide nanosheet@ nanowire arrays on nickel foam: an efficient 3D electrode for methanol electro-oxidation. Catal Sci Technol 6(4):1157–1161. https://doi.org/10.1039/C5CY01427A
14. Jothi PR, Kannan S, Velayutham G (2015) Enhanced methanol electro-oxidation over in-situ carbon and graphene supported one dimensional $NiMoO_4$ nanorods. J Power Sources 277:350–359. https://doi.org/10.1016/j.jpowsour.2014.11.137
15. Rahimnejad M, Hassaninejad-Darzi SK (2015) Organic template-free synthesis of Ni-ZSM-5 nanozeolite: a novel catalyst for formaldehyde electrooxidation onto modified Ni-ZSM-5/CPE. Int J Bio-Inorg Hybr Nanomater 4(3):141–153
16. Chen D, Minteer SD (2015) Mechanistic study of nickel based catalysts for oxygen evolution and methanol oxidation in alkaline medium. J Power Sources 284:27–37. https://doi.org/10.1016/j.jpowsour.2015.02.143
17. Liao Y, Pan S, Bian C, Meng X, Xiao FS (2015) Improved catalytic activity in methanol electro-oxidation over the nickel form of aluminum-rich beta-SDS zeolite modified electrode. J Mater Chem A 3(11):5811–5814. https://doi.org/10.1039/C4TA06699E
18. Hameed RA, El-Sherif RM (2015) Microwave irradiated nickel nanoparticles on Vulcan XC-72R carbon black for methanol oxidation reaction in KOH solution. Appl Catal B Environ 162:217–226. https://doi.org/10.1016/j.apcatb.2014.06.057

19. Fetohi AE, Hameed RA, El-Khatib KM (2015) Development of electroless Ni–P modified aluminum substrates in a simulated fuel cell environment. J Ind Eng Chem 30:239–248. https://dx.doi.org/doi:10.1016/j.jiec.2015.05.028
20. Zhao B, Zhao W, Shao G, Fan B, Zhang R (2015) Morphology-control synthesis of a core–shell structured NiCu alloy with tunable electromagnetic-wave absorption capabilities. ACS Appl Mater Interfaces 7(23):12951–12960. https://doi.org/10.1021/acsami.5b02716
21. Wang K, Xia M, Xiao T, Lei T, Yan W (2017) Metallurgically prepared NiCu alloys as cathode materials for hydrogen evolution reaction. Mater Chem Phys 186:61–66. https://doi.org/10.1016/j.matchemphys.2016.10.029
22. Jafarian M, Moghaddam RB, Mahjani MG, Gobal F (2006) Electro-catalytic oxidation of methanol on a Ni-Cu alloy in alkaline medium. J Appl Electrochem 36(8):913–918. https://doi.org/10.1007/s10800-006-9155-6
23. Gupta SS, Mahapatra SS, Datta J (2004) A potential anode material for the direct alcohol fuel cell. J Power Sources 131(1–2):169–174. https://doi.org/10.1016/j.jpowsour.2004.01.009
24. Shobha T, Aravinda CL, Devi LG, Mayanna SM (2003) Preparation and characterization of oxides of Ni-Cu: anode material for methanol oxidative fuel cells. J Solid State Electr 7(8):451–455. https://doi.org/10.1007/s10008-002-0327-y
25. Hameed RA, Fekry AM (2010) Electrochemical impedance studies of modified Ni-P and Ni–Cu–P deposits in alkaline medium. Electrochim Acta 55(20):5922–5929. https://doi.org/10.1016/j.electacta.2010.05.046
26. Yuan LS, Zheng YX, Jia ML, Zhang SJ, Wang XL, Peng C (2015) Nanoporous nickel-copper-phosphorus amorphous alloy film for methanol electro-oxidation in alkaline medium. Electrochim Acta 154:54–62. https://doi.org/10.1016/j.electacta.2014.12.055
27. Xia Y, Xiong Y, Lim B, Skrabalak SE (2009) Shap-controlled synthesis of metal nanocrystals: simple chemistry meets complex physics? Angew Chem Int Ed 48(1):60–103. https://doi.org/10.1002/anie.200802248
28. Liu X, Wang D, Li Y (2012) Synthesis and catalytic properties of bimetallic nanomaterials with various architectures. Nano Today 7(5):448–466. https://doi.org/10.1016/j.nantod.2012.08.003
29. Ding R, Liu J, Jiang J, Wu F, Zhu J, Huang X (2011) Tailored Ni–Cu alloy hierarchical porous nanowire as a potential efficient catalyst for DMFCs. Catal Sci Technol 1(8):1406–1411. https://doi.org/10.1039/C1CY00164G
30. Wu D, Zhang W, Cheng D (2017) Facile synthesis of Cu/NiCu electrocatalysts integrating alloy, core-shell, and one-dimensional structures for efficient methanol oxidation reaction. ACS Appl Mater Interfaces 9(23):19843–19851. https://doi.org/10.1021/acsami.7b03876
31. Maizelis A, Bairachniy B (2019) Protection of NdFeB magnets by multilayer coating. In 2019 IEEE 39th international conference on electronics and nanotechnology (ELNANO), pp 596–599. https://doi.org/10.1109/ELNANO.2019.8783526
32. Maizelis A, Bairachniy B (2019) Formation of multilayer metal-hydroxide electrode with developed surface for alkaline water electrolysis. Mater Today Proc 6:226–230
33. Maizelis A, Bairachniy B (2017) Electrochemical formation of multilayer SnO_2 – Sb_xO_y coating in complex electrolyte. Nanoscale Res Lett 12(1):119. https://doi.org/10.1186/s11671-017-1902-6
34. Maizelis AA (2019) Electrooxidation of ethanol on nickel-copper multilayer metal hydroxide electrode. Springer Proc Phys 221:59–68. https://doi.org/10.1007/978-3-030-17759-1_4
35. Maizelis A (2019) Multilayer nickel-copper anode for direct glucose fuel cell. J Electrochem Energy Convers Storage 16(4):041003. https://doi.org/10.1115/1.4042986
36. Maizelis A (2019) Electrochemical non-enzymatic detection of glucose at nanostructured multilayer electrode. In 2019 IEEE 39th international conference on electronics and nanotechnology (ELNANO), pp 404–408. https://doi.org/10.1007/978-3-030-17759-1_4

37. Maizelis A, Bairachniy B (2017) Electrochemical formation of multilayer metal and metal oxide coatings in complex electrolytes. Springer Proc Phys 195:557–572. https://doi.org/10.1007/978-3-319-56422-7_41
38. Norouzi B, Norouzi M (2012) Methanol electrooxidation on novel modified carbon paste electrodes with supported poly(isonicotinic acid) (sodium dodecyl sulfate)/Ni–Co electrocatalysts. J Solid State Electrochem 16:3003–3010. https://doi.org/10.1007/s10008-012-1736-1

Investigation of Swelling Behavior of PAA and D-PAA Hydrogels

O. Nadtoka, P. Virych, and N. Kutsevol

1 Introduction

Hydrogels are three-dimensional cross-linked hydrophilic polymers that are able to swell in an aqueous environment or biological fluids. Their capacity to absorb and retain water is caused by the presence of hydrophilic groups such as –OH, –COOH, $–CONH_2$, and $–SO_3H$ in polymer structure forming hydrogel [1]. Because of their high water-absorbing ability (sometimes more than 90 wt%) hydrogels show a unique swelling behavior in an aqueous environment and high permeability due to the presence of chemical cross-links in the hydrogels structure. Besides of covalent chemical bonds the three-dimensional network of a hydrogel can be stabilized by physical (ionic bonds, entanglements, crystallites, charge complexes, hydrogen bonding, van der Waals or hydrophobic interactions) cross-links [2, 3]. The presence of numerous functional groups along the polymer chains leads to strong depending on hydrogels properties on external environmental conditions like temperature, pH, ionic strength, etc. Due to this peculiarity, hydrogels are named as "intelligent" materials which are suitable for the design of regulated systems. Hydrogels are especially promising for bioanalytical applications because of their high water content and elastic nature similar to natural tissue [4, 5].

O. Nadtoka (✉) · P. Virych · N. Kutsevol
Taras Shevchenko National University of Kyiv, Volodymyrska Str., 64, Kiev 01033, Ukraine
e-mail: oksananadtoka@ukr.net

P. Virych
e-mail: sphaenodon@ukr.net

N. Kutsevol
e-mail: kutsevol@ukr.net

O. Fesenko and L. Yatsenko (eds.), *Nanooptics and Photonics, Nanochemistry and Nanobiotechnology, and Their Applications*, Springer Proceedings in Physics 247, https://doi.org/10.1007/978-3-030-52268-1_4

In hydrogel synthesis, different methods of cross-linking have been used. Stable chemically cross-linked gels can be produced by radical polymerization, chemical interaction between functional groups, high-energy irradiation and by using biological active molecules [6].

In the last few years, a lot of studies have been carried out on biomaterials based on proteins and polysaccharides. Many polymeric networks based on dextran, konjac glucomannan, guar gum with acrylic acid have been prepared [1, 7, 8]. Our previous researches [9] have shown that star-like dextran-graft-polyacrylamide copolymers (D-g-PAA) have advantages in comparison with linear polyacrylamide (PAA) because of the possibility to regulate their internal structure during the synthesis process. In water solution, dextran has the coil conformation of various sizes, which depends on dextran molecular weight. Grafting of PAA chains onto dextran coils allows realizing the certain hydrogel structures. In the current study, covalently cross-linked hydrogels PAA and D-PAA were prepared by varying the amount of cross-linking agent and dextran molecular weight.

In the present work, we focused on the study of swelling behavior of prepared hydrogels as a potential material for biomedical application. The absorption and desorption of methylene blue in hydrogels was studied as a model of drug delivery systems.

2 Experimental

2.1 Materials

Acrylamide (AA) obtained from Aldrich was twice recrystallized from chloroform and dried under vacuum at room temperature for 24 h. Cerium (IV) ammonium nitrate (CAN), *N*,*N*′-methylene-bis-acrylamide (MBA), methylene blue and potassium hydroxide were purchased from Aldrich, without additional purification. Dextran (D) and dextran sulfate sodium salt (DSNa) were purchased from Fluka, the characteristics given by the manufacturer are $Mw = 2 \times 10^4$, 1×10^5, 5×10^5 g/mol (designated as D20, D100, D500 and DSNa500 throughout). Distilled water was used throughout the experiments and as polymerization medium during hydrogel synthesis.

2.2 Hydrogel Preparation

Hydrogels base on cross-linked dextran-graft-polyacrylamides (D-PAA-x) were prepared by free radical polymerization according to the procedure reported earlier [10] (Fig. 1a). The required amount of dextran (0.0005 mM) was dissolved in 25 mL of distilled water at ambient temperature (25 °C). This solution was purged

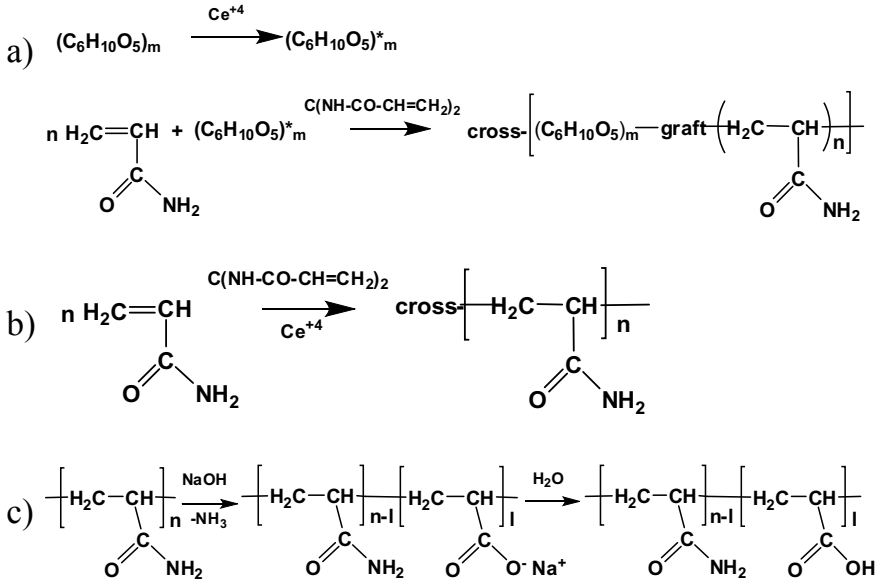

Fig. 1 Synthesis of cross-linked hydrogels: **a** Dextran-*graft*-polyacrylamides (D-PAA-x); **b** polyacrylamides (PAA-x); **c** dextran-*graft*-(polyacrylamide-co-polyacrylic acid) (D-PAA-x-y), where D = D20, D100, D500 and DSNa500; x = 0.2, 0.4 or 0.6 corresponding to MBA concentration; y = 0, 3, 6 or 10, corresponding to hydrolysis time

by argon bubbling for 25 min and ammonium-cerium (IV) nitrate (0.01644 g, 0.03 mmol mL^{-1}) was added as an initiator of reaction. In 2 min acrylamide (0.05 mol) and *N*,*N*′-methylene-bis-acrylamide (0.2–0.6%, w/monomer) were added. Thereafter, argon was passed for 2 min and the reaction mixture was left overnight. The formed hydrogel samples were taken out from the beaker, washed with distilled water and placed in a 400 mL beaker containing 200 mL distilled water (refilled fresh water for every 12 h for two days) to remove unreacted monomer from the hydrogel. Finally, the gels were dried at ambient temperature.

Hydrogels base on cross-linked polyacrylamides (PAA-x) were prepared by the same method but without the addition of dextran (Fig. 1b).

Alkaline hydrolysis of synthesized cross-linked hydrogels samples was carried out as follows: 3.6 g of samples of cross-linked hydrogels were dissolved in 200 ml of distilled water. Swollen samples were placed into 20 ml 5M KOH at 58 °C. In 3; 6 and 10 min the hydrolyzed samples were obtained in the salt form. They were immersed in distilled water at room temperature for 48 h and the water was renewed several times in order to remove NaOH. As a result, the polyelectrolytes dextran-*graft*-(polyacrylamide-co-polyacrylic acid) hydrogels were obtained (Fig. 1c). All samples were dried and kept under vacuum.

Hydrolyzed samples with various cross-linking density and various dextran components were marked as D-PAA-x-y, were D = D20, D100, D500 and DSNa500;

$x = 0.2$, 0.4 or 0.6 corresponding to MBA concentration; $y = 0$, 3, 6 or 10 corresponding to hydrolysis time.

2.3 Swelling Studies

The water absorption of initially dried hydrogels was measured gravimetrically. Dry sample of hydrogel, previously washed and weighed, was placed in distilled water at 25 °C. The sample was removed from solution at certain time intervals and was superficially dried with tissue paper, weighed on an analytic balance and placed back into the bath. The measurements were repeated until a constant weight was achieved. The absorbed water content was calculated in term of the swelling ratio ($S\%$) using (1):

$$S_t\% = \frac{m_t - m_0}{m_0} \times 100 \quad (1)$$

where m_t—the mass of hydrogel in swollen state at time t and m_0—the mass of the dry hydrogel. The dependences of swelling ratio $S\%$ versus time were analyzed. Swelling ratio in equilibrium state ($S_{eq}\%$) represents the maximum capacity of the hydrogel to absorb solution and corresponds to plateau of kinetic curve.

Three solutions of NaCl (pH = 7.4) with different ionic strength (10^{-2}, 10^{-1}, 1 M) were used to estimate the salt effect on the swelling of hydrogel.

2.4 Characterization of Hydrogel Composites

The Fourier transform infrared (FTIR) spectra of non-hydrolyzed and hydrolyzed D-PAA samples were recorded with an FTIR-Spectrophotometer (MAGNA 550, Nicolet Instruments Corporation, USA) using KBr pellet.

The morphology of hydrogel membrane was observed by SEM mod. Stereoscan 440 (LEO), Cambridge, UK instrument. The cryogenically fractured film in liquid nitrogen was mounted vertically on the SEM stub by silver adhesive paste. The specimens were sputter-coated with gold to avoid electrostatic charges and to improve image resolution before being examined by the electron microscopy.

UV–visible spectra of hydrogels were recorded by using a Lambda 35 UV-Vis spectrophotometer (Perkin-Elmer, CA) in the absorbance mode (range 200–1000 nm).

2.5 Absorption and Desorption of Low Molecular Weight Compound Studies

Absorption and desorption of methylene blue were studied using non-hydrolyzed hydrogels based on PAA and D20-PAA. Dried samples of PAA-x-0 and D20-PAA-x-0 (where $x = 0.2; 0.4; 0.6$) were placed in 7.8×10^{-6} M dye solution up to reaching an equilibrium state. The optical density of saturated hydrogels at wavelength 670 nm was measured. Desorption of methylene blue from the hydrogels was investigated by keeping off the dye-saturated samples in distilled water until equilibrium state. For determination of methylene blue concentration in hydrogel or solutions, the calibration curve within the concentration range of 10^{-5}–10^{-6} M was used. The dye concentration changes in hydrogels at absorption and desorption were comprised regard to 1.56×10^{-6} M methylene blue solution.

To calculate the rate of the dye release, the first derivative curve of the concentration versus time was calculated. The curves are described by (2):

$$y = y_0 + A \times e^{-x/t_1} \tag{2}$$

where $y =$ optical absorbance, D; x—time.

An obtained curve was linearized in logarithmic time ($\ln t$) and optical absorption ($\ln D$) coordinates with subsequent adjustment according to linear law ($r > 0.98$). The curve slope corresponds to the rate of function increase or its first derivative. Desorption curves of methylene blue from hydrogels linearized at coordinates ($-\ln t$) and ($-\ln D$). The mathematical data processing was performed using OriginLab 8.0.

3 Results and Discussion

3.1 Hydrogels Synthesis and Characterization

Hydrogels as inert matrices with three-dimensional structure were synthesized. Varying the concentration of the cross-linking agent the polymeric networks with different free space between polymer chains were obtained. The porosity affords an opportunity for the rapid diffusion of water molecules into and out of the polymers and this property may be important for antibacterial applications. Therefore, the mesh size of hydrogels appears to be a key factor for transporting of bioactive molecules such as antibiotics or other pharmaceuticals to the destination.

For modification of hydrogel network, polyacrylamide chains were grafted on dextran macromolecules of different molecular weight. It leads to a more compact structure polymer network than in the case of linear polyacrylamide. As was shown in our previous studies [11] depending on the size of dextran coils in solution the branched copolymers with different macromolecular architecture may be formed.

The conformation of grafts depends on the distance between grafts and can be varied from worm-like to mushroom. The conformation of grafted PAA chains determined the internal structure of hydrogels.

We have shown [12], that after grafting on dextran with $Mw = 2 \times 10^4$ g/mol mainly the worm-like structure of grafted PAA chains is formed, whereas grafting on dextran with $Mw = 1 \times 10^5$ g/mol predominantly causes the formation a mushroom structure at the same PAA concentration.

The synthesized hydrogel samples are represented in Table 1.

For higher water diffusion in hydrogels, PAA was converted into polyelectrolyte. In the present study, the synthesized hydrogels were subjected to alkaline hydrolysis, and samples with different degrees of hydrolysis were obtained depending on the time of the reaction.

For identification and characterization of the PAA-x-y and D-PAA-x-y hydrogels, FTIR spectroscopy and SEM micrograph were used. In the FTIR spectra of the non-hydrolyzed hydrogels PAA-0.4-0 and D20-PAA-0.4-0 (Fig. 2, black and red curves), the peaks between at 1657 and 1611 cm^{-1} can be attributed to-carbonyl valence stretching in carboxamide functional groups and NH deformation stretching, respectively [13]. In the spectrum of hydrolyzed hydrogel D20-PAA-0.4-10 (Fig. 2, green curve), the intense characteristics and at 1550 cm^{-1} is due to –C=O asymmetric stretching in carboxylate anion that is reconfirmed by another sharp peak at 1420 cm^{-1} which is related to the symmetric stretching mode of the carboxylate anion. This confirmed the conversion of amide groups ($–CONH_2$) to the carboxylate functional groups ($–COO^-$).

The SEM micrographs of hydrogel networks of linear PAA and PAA grafted on dextran macromolecules are shown in Fig. 3. The hydrogels of modified PAA by

Table 1 Equilibrium swelling ratio of D-PAA-x-y hydrogels

x[a]	y[a]	Swelling ratio S_{eq}% for samples				
		PAA	D20-PAA	D100-PAA	D500-PAA	DSNa500-PAA
0.2	0	1530	1980	1576	1833	2008
	3	25,134	27,888	22,426	23,022	18,229
	6	25,147	32,106	28,319	23,831	23,488
	10	25,362	34,610	29,650	26,559	23,914
0.4	0	1397	1576	1528	1664	1695
	3	23,974	26,997	19,392	21,520	17,305
	6	25,010	31,246	23,058	23,039	22,250
	10	26,215	34,000	25,042	23,810	22,760
0.6	0	1344	1533	1374	1663	1672
	3	23,437	26,196	19,262	20,091	16,412
	6	23,710	26,924	20,943	21,737	21,084
	10	23,915	30,225	24,034	22,131	21,623

[a]where x and y correspond to MBA concentration and hydrolysis time, respectively

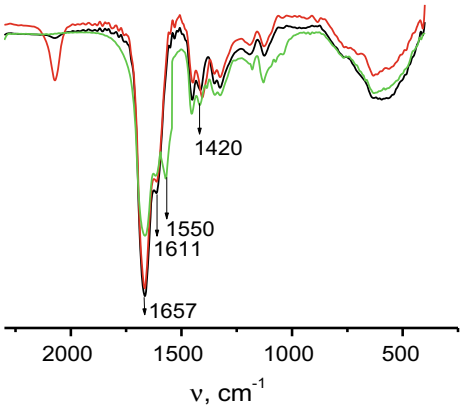

Fig. 2 Infrared spectra of cross-linked non-hydrolyzed PAA-0.4-0 (*black*) and D20-PAA-0.4-0 (*red*) and hydrolyzed D20-PAA-0.4-10 hydrogel (*green*)

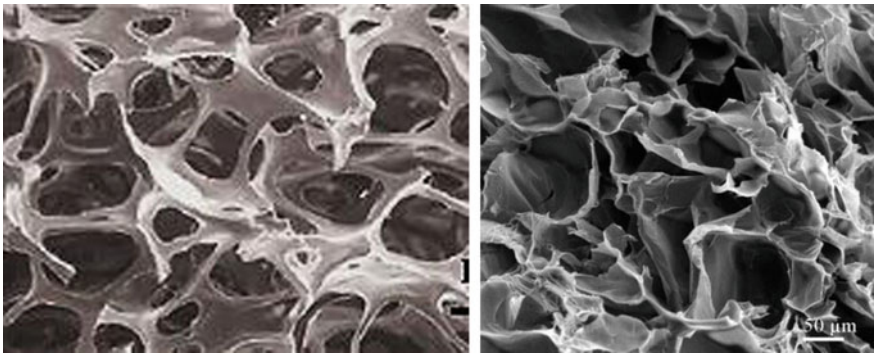

Fig. 3 SEM micrographs of cross-linked linear PAA and branched D-PAA hydrogels

dextran show a more porous surface (Fig. 3). It confirms the possibility to affect the internal structure of hydrogels by means of grafting of PAA on dextran.

3.2 Swelling Studies

3.2.1 Effect of the Cross-Linking Density on the Swelling Capacity

Swelling behaviors of cross-linked hydrogels at different cross-linking density are shown in Fig. 4a (Table 1). As seen in Fig. 4a, the swelling values initially increase rapidly, and then the increase slows down and finally levels off to a constant value. Figure 4b and Table 1 illustrate the effect of concentration of cross-linking agent on the equilibrium swelling percentage (S_{eq}%) while keeping D/PAA composition

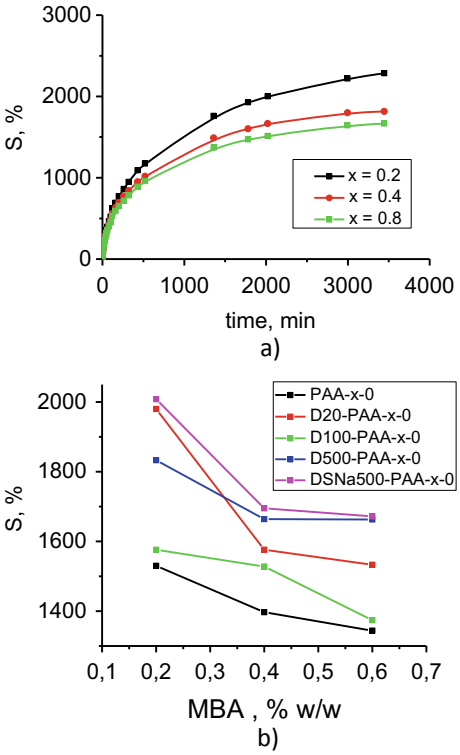

Fig. 4 **a** Swelling kinetics of cross-linked polyacrylamide (PAA-x-0); **b** effect of different concentration of MBA on equilibrium swelling ratio of D-PAA-x-0 hydrogels

constant. It was observed in Fig. 4a,b that the swelling of gels decreased both at linear PAA-x-0 and branched D-PAA-x-0 polymers as the cross-linking agent *N*,*N*′-methylene-bis-acrylamide concentration increases. This decrease in equilibrium swelling percentage with the increasing concentration of MBA in the gel is mainly caused by the growing cross-linked density of polymer chains. So the swelling of hydrogels is decreased with increase in cross-linking ratio due to tighter hydrogel structure.

3.2.2 Effect of the Dextran Component on the Swelling Capacity

The effect of the dextran component on the swelling capacity of hydrogels was studied. Samples of branched polymers based on polysaccharide dextran with different molecular weight were used for swelling investigation in distilled water. In our previous works [14], it was shown, that internal macromolecular structure of grafted polymers strongly depends on the size of polysaccharide and after cross-linking leads to the formation of more compact polymer network. In this case, the obtained networks have higher porosity and ability to swell a larger amount of water. Swelling ratios in equilibrium state (S_{eq}%) of cross-linked polymers based on PAA,

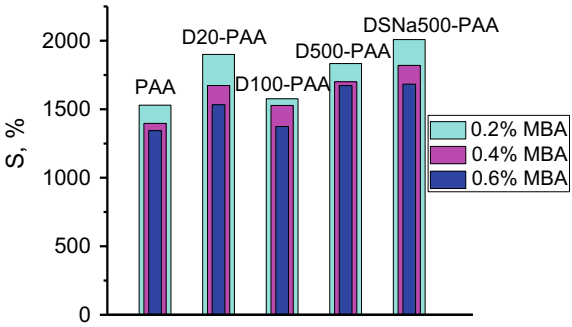

Fig. 5 Effect of the dextran component on the swelling capacity of the synthesized hydrogel

D20-PAA, D100-PAA, D500-PAA, DSNa500-PAA are presented in Fig. 5. As seen in Fig. 5 and general Table 1, an increase of molecular weight of dextran does not directly affect the swelling behavior. Obviously, it can be explained by different internal mesh structure formed at certain size of macromolecular of dextran.

While the data obtained shows that all hydrogels containing dextran have higher swelling parameters caused by their improved porosity than the hydrogel which based only on linear polyacrylamide. In addition, the hydrophilic nature of these gels may be enhanced due to the presence of free –OH groups of dextran. And moreover, the dextran sulfate, of cause, has an excellent absorption property as polyelectrolyte.

The equilibrium swelling percentage (S_{eq}%) of PAA-x-0 and D-PAA-x-0 hydrogels, as expected, decreases with increasing of cross-linking density.

3.2.3 Effect of the Hydrolysis Degrees on the Swelling Capacity

To achieve hydrogels with high swelling capacity, cross-linked PAA-x-0 and D-PAA-x-0 were saponified. During saponification, the amide groups convert to carboxylate groups.

As shown in Fig. 6, swelling of the hydrogels increased by increasing the time of hydrolysis from 3 to 10 min. The increase of water absorbency after hydrolysis is attributed to an increase of carboxyl groups in polymer matrices. Wu et al. have reported a similar conclusion in the hydrolysis of starch-g-PAAm [15]. It was demonstrated that with increasing time of hydrolysis, the concentration of carboxyl groups is increased. In the presence of alkaline, amide groups are attacked by hydroxyl groups of alkali convert them into carboxyl groups. The transformation of polymers polyacrylamide (PAA-x-0) and dextran-*graft*-polyacrylamide (D-PAA-x-0) into polyelectrolytes polyacrylamide-co-polyacrylic acid (PAA-x-y) and dextran-*graft*-(polyacrylamide-co-polyacrylicacid) (D-PAA-x-y) causes the high swelling capacity (Table 1 and Fig. 7). When the time of hydrolysis increases to more than 10 min, the water absorbency almost does not increase.

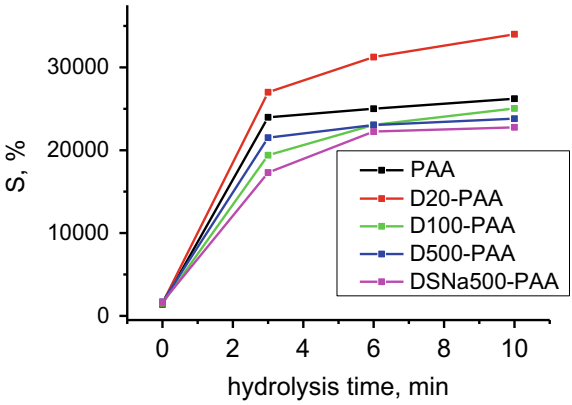

Fig. 6 Effect of hydrolysis time on the swelling capacity of the synthesized hydrogel PAA-x-y and D-PAA-x-y (at cross-linking density $x =$ 0.4)

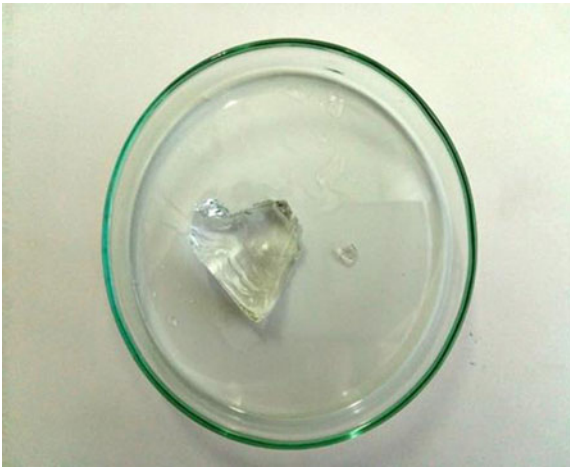

Fig. 7 The swelling capacity of the hydrolyzed hydrogel D-PAA-0.4-10. Swollen hydrogel—*left*; the dried hydrogel—*right*

3.2.4 Effect of the Ionic Strength on the Swelling Capacity

The effect of the ionic strength on the swelling capacity is shown on Fig. 8. It shows that an increase in the ionic strength within the range of 0.01–1 M yields leads to a significant decrease in the swelling ratio of hydrogels. For both non-hydrolyzed (y = 0) cross-linked polymers PAA-0.4-0 and D20-PAA-0.4-0 the effect of the ionic strength on swelling capacity is negligible. At the same time, the high sensitivity of swelling of the anionic PAA-0.4-10 and D20-PAA-0.4-10 towards ionic strength is attributed to the change in the charge distribution on the surface of the gel network. As the concentration of Na^+ ions in the swelling medium increased, a stronger "charge screening effect" of the additional cations is achieved and anion-anion electrostatic repulsion is appeared [16, 17]. Caused by a decreased osmotic pressure difference between the polymer network and the external solution, the swelling of hydrolyzed hydrogels strongly decreased in 1 M NaCl solution.

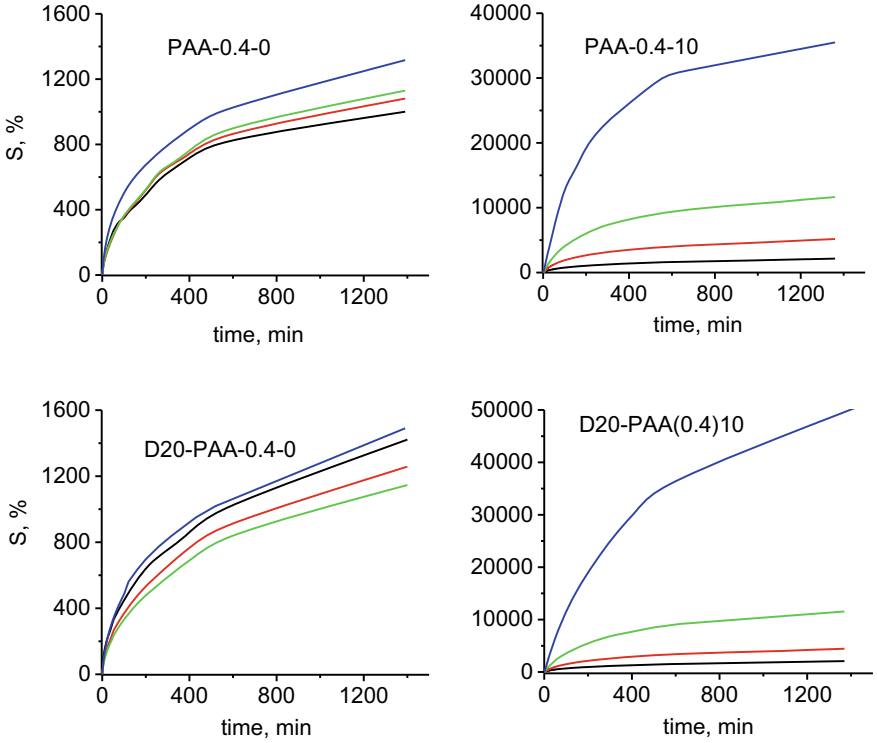

Fig. 8 Effect of the ionic strength of swelling medium on the swelling kinetics of the cross-linked hydrogels: black—1 M, red—0.1 M, green—0.01 M of NaCl and blue—distilled water

Generally, the swelling capacity of hydrogels in the salt solution is decreased compared to the values in distilled water. This peculiarity is important for understanding of swelling behavior of hydrogels in physiological solutions or liquids which imitate the plasma blood.

When the swollen hydrogel is put in the salt solution, the presence of Na^+ ions in the outer medium causes a decrease in osmotic swelling pressure and equilibrium water absorption of the hydrogel sample. Therefore, the swelling is drastically reduced.

3.3 Absorption and Desorption of Methylene Blue

Absorption and desorption of methylene blue by non-hydrolyzed hydrogels was studied. The concentration of methylene blue in hydrogels is inversely proportional to the concentration of the dye in solution. On Fig. 9a optical spectra of the remainder quantity of methylene blue on the solution during its absorption are presented. It was

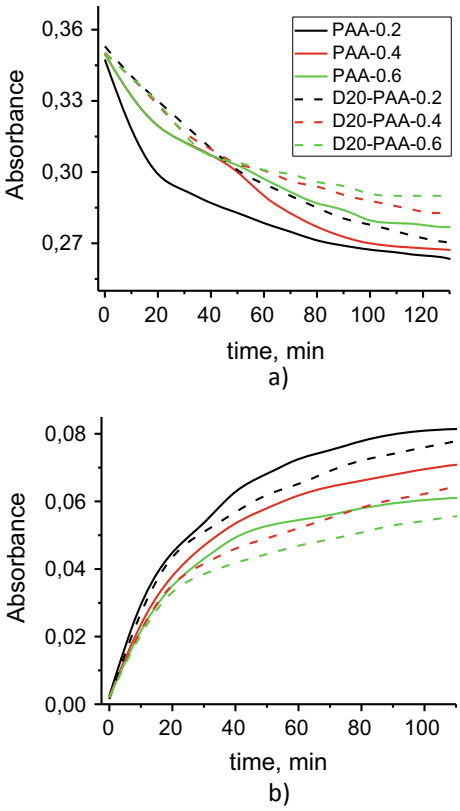

Fig. 9 Kinetics of absorption (**a**) and desorption (**b**) of methylene blue in hydrogels as inversely proportional value to the concentration of the dye in solution

found that dye absorbance values in hydrogels depend on their cross-linking density that correlates with swelling behavior (Fig. 4a). Absorption rate for D20-PAA-x-0 at $x = 0.2$, 0.4 and 0.6 was 0.1012, 0.0762, 0.0693 min^{-1}, correspondingly. For PAA-x-0 hydrogels, the rate is increased: for $x = 0.2$, 0.4 and 0.6 the absorption rates were 0.1232, 0.1054 and 0.0932 min^{-1} correspondingly. These differences may be caused by interactions of the dye with dextran. Due to the positive charge of the methylene blue molecule, dye can form anionic bonds with hydroxyl groups of polysaccharides.

The diffusion rate of methylene blue from the PAA-x-0 and D20-PAA-x-0 with different cross-linking density is presented in Fig. 9b. An equilibrium state after 150 min for all hydrogel samples saturated with 7.8×10^{-6} M dye was observed. The increase of the desorption rate caused by the decrease of hydrogel density. For PAA-x-0 hydrogels for $x = 0.2$, 0.4 and 0.6 desorption rate were 0.4232, 0.3976, 0.3624 min^{-1} correspondingly. For D20-PAA-x-0 hydrogels the calculated desorption rates were lower: for $x = 0.2$, 0.4 and 0.6 desorption rates were 0.3956, 0.3518 and 0.3255 min^{-1} correspondingly. Thus, hydrogels based on branched copolymer provide a more prolonged release and action of the drug.

4 Conclusion

The chemically cross-linked PAA and D-PAA hydrogels were prepared by radical polymerization using dextrans of different molecular weight and various amount of cross-linking agent. For higher water diffusion in hydrogels, PAA chains of hydrogels were converted into polyelectrolyte. It was demonstrated that the internal structure of hydrogels can be regulated by means of grafting of PAA on dextran.

The effect of the cross-linking density, dextran component, hydrolysis degree and ionic strength on the swelling capacity of hydrogels was analyzed. It was found that with increasing cross-linking density of hydrogels the swelling capacity decreases. The dynamic and equilibrium swelling ratio of the hydrogels are directly proportional to hydrolysis degree and are inverse to the ionic strength. All hydrogels containing dextran have higher swelling parameters caused by higher porosity than the hydrogel which based on linear polyacrylamide. It was demonstrated, that hydrogels based on branched copolymers dextran-graft-polyacrylamide can be used due to its potential swelling capacity as a promising candidate for developing materials for medical application. Investigation of absorption and desorption of methylene blue by hydrogels confirms the potential their application as drug delivery system.

References

1. Rodigues IR, Forte MMC, Azambuja DS, Castagno KRL (2007) Synthesis and characterization of hybrid polymeric networks (HPN) based on poly (vinyl alcohol)/chitosan. React Funct Polym 67:708–715
2. Cui J, Campo A (2012) Multivalent H-bonds for self-healing hydrogels. Chem Commun 48:9302–9304
3. Picchioni F, Muljana H (2018) Hydrogels based on dynamic covalent and non covalent bonds: a chemistry perspective. Gels 4:21–31
4. Peppas NA, Hilt ZJ, Khademhosseini A, Langer R (2006) Hydrogels in biology and medicine: from molecular principles to bionanotechnology. Adv Mater 18:1345–1360
5. Allan SH (2002) Hydrogels for biomedical applications. Adv Drug Deliver Rev 43:3–12
6. Mathur AM, Moorjani ShK, Scranton AB (1996) Methods for synthesis of hydrogel networks: a review. J Macromol Sci C 36(2):405–430
7. Cascone MG, Barbani N, Cristallini C, Giusti P, Ciardelli G, Lazzeri L (2001) Bioartificial polymeric materials based on polysaccharides. J Biomater Sci Polym Edn 12(3):267–281
8. Kim IS, Oh IJ (2005) Drug release from the enzyme-degradable and pH-sensitive hydrogel composed of glycidyl methacrylate dextran and poly(acrylic acid). Arch Pharmacal Res 28:983–988
9. Kutsevol N, Chumachenko V, Rawiso M, Shyichuk A (2016) Micro Nano Lett 11(5):256–260
10. Nadtoka O, Kutsevol N, Krysa V, Krysa B (2018) Hybrid polyacryamide hydrogels: synthesis, properties and prospects of application. Mol Cryst Liquid Cryst 672(1):1–10
11. Kutsevol N, Bezugla T, Bezuglyi M, Rawiso M (2012) Branched dextran-graft-polyacrylamide copolymers as perspective materials for nanotechnology. Macromol Symp 317–318:82–90
12. Kutsevol N, Guenet JM, Melnyk N, Sarazin D, Rochas C (2006) Solution properties of dextran-polyacrylamide graft copolymers. Polymer 47:2061–2068
13. Silverstein RM, Webster FX (1998) Spectrometric identification of organic compounds, 6th edn. Wiley, NewYork

14. Kutsevol NV, Chumachenko VA, RawisoM Shkodich VF, Stoyanov OV (2015) Star-like polymers dextran-polyacrylamide: the prospects *of* application for nanotechnology. J Struct Chem 56(5):1016–1023
15. Wu J, Wei Y, Lin J, Lin S (2003) Study on starchg-acrylamide/mineral powder superabsorbent composite. Polymer 44:6513–6520
16. Zhao Y, Su H, Fang L, Tan T (2005) Superabsorbent hydrogels from poly(asparticacid) with salt, temperature and pH-responsiveness properties. Polymer 46:5368–5376
17. Vishal Gupta N, Shivakumar HG (2012) Investigation of swelling behavior and mechanical properties of a pH-sensitive superporous hydrogel composite. Iran J Pharm Res 11(2):481–493

The Sorption Properties of Ukrainian Saponite Clay In Situ Modified of Poly[4-Methacroyloxy-(4′-Carboxy-2′-Nitro)-Azobenzene] to Toxic Metals Ions

I. A. Savchenko, E. Yanovska, Y. Polonska, L. Ol'khovik, D. Sternik, and O. Kychkyruk

1 Introduction

The high level of contamination of Ukraine's natural waters with heavy toxic metal ions due to the long-term discharge of wastewater makes it urgent to search for new low-cost non-toxic materials that can be effectively used as sorbents for the removal of these ions from wastewater or contaminated natural water. For this purpose, it is advisable to use porous natural minerals, whose tonnage deposits are found in our country, including clinoptilolites, bentonites, saponite clays, etc.

Saponite clays (saponites) are unique natural formations of volcanic origin, the industrial occurrences of which were first discovered in the world in Ukraine. Tashkiv and Barbarian occurrences of saponite clays in Khmelnitsky region (Ukraine) were the most promising for solving a number of environmental problems.

Saponite of Tashkiv occurrence is certified in Ukraine as a light porous filler; as a purifier of dairy and other liquid foods from salts of heavy metals and radionuclides; as a complex mineral supplement to animal feed, as a biologically active additive [1, 2].

It is advisable to use composite materials based on natural minerals that are industrially produced in Ukraine to solve specific environmental problems, in particular for sewage treatment of individual industries.

I. A. Savchenko (✉) · E. Yanovska · Y. Polonska · L. Ol'khovik
National Taras Shevchenko University of Kyiv, 60, Volodymyrska Street, Kiev 01601, Ukraine
e-mail: irassavchenko@gmail.com

D. Sternik
Maria Curie-Skłodowska University, 5, Maria Curie-Sklodowska Sq, 20-031 Lublin, Poland

O. Kychkyruk
Ivan Franko Zhytomyr State University, 40, Velyka Berdychivska Street, Zhytomyr 10008, Ukraine

O. Fesenko and L. Yatsenko (eds.), *Nanooptics and Photonics, Nanochemistry and Nanobiotechnology, and Their Applications*, Springer Proceedings in Physics 247, https://doi.org/10.1007/978-3-030-52268-1_5

Modification of the surface of porous inorganic materials with nitrogen-containing polymers allows obtaining sorbents for the removal of toxic metal ions from wastewater due to their complexation with the nitrogen atoms of the immobilized polymer [3–6]. For example, in [7, 8] we have shown that in situ immobilization of the surface of Tashkiv saponite and Sokyrnitsky clinoptilolite with polyaniline leads to an increase in the sorption capacity of these minerals with respect to phosphate and arsenate ions in a neutral aqueous medium, which increases by 2–3 times. And in situ immobilization of the surface of the Tashkiv field saponite [9] and the Tushin field clinoptilolite [10] with complex-forming polymers such as poly [N-(4-carboxyphenyl) methacrylamide] or poly [4-methoxyloxy-(4′-carboxy-2′-nitro) azobenzene] increases their sorption capacity in a neutral aqueous medium with respect to Pb(II), Cd(II), Cu(II) and Fe(III) ions.

One of the promising ways of creating organo-mineral composite materials with valuable sorption properties is polymerization or in situ immobilization, which consists in the direct formation of an immobilized polymer layer in the presence of particles of an inorganic carrier [11]. Azo compounds are the most common dyes, which make up more than half of the total dye production due to the simplicity and cheapness of synthesis. They are used as resistant paints, analytical reagents, luminophores.

Both monomeric and polymeric azo compounds are widely known for their interesting complexing properties [12].

In [13, 14] we showed that in situ immobilization of poly [(4-methacroyloxy-(4′-carboxy-2′-nitro) azobenzene] or poly [4-methacroyloxy-(4′-carboxy-2′-chloro) azobenzene] on the silica gel surface allowed us to obtain a material with a sorption capacity for Cu(II), Pb(II) and Fe(III) ions.

This paper deals with the in situ immobilization of poly [4-methacroyloxy-(4′-carboxy-2′-nitro) azobenzene] on the surface of saponite and investigation of its sorption properties with respect to Cu(II), Pb(II ions), Mn(II) and Fe(III).

2 Experimental

As a mineral porous basis for polymer modification, the saponite of the Tashkiv occurrence of Khmelnitsky region (Ukraine) was used, whose chemical composition and physicochemical properties were described in [2].

The in situ polymerization of 4-methacroyloxy-(4′-carboxy-2′-nitro)azobenzene in the presence of saponite has been carried out under the argon atmosphere. A solution of 11.90 g [(4-methacroyloxy-(4′-carboxy-2′-nitro)azobenzene] and 0.595 g of 2,2′-azobisisobutyronitrile (AIBN) in 250 ml tetrahydrofuran (THF) were poured into a flask containing 23.80 g of saponite. When argon blowing was finished after 15 min, the reaction mixture was heated to 60 °C; polymerization continued for 6 h with stirring. The reaction was stopped by cooling the reaction mixture. The resulting suspension was poured into a porcelain cup and left overnight to evaporate

the solvent; the synthesized composite was washed 3 times with isopropyl alcohol, filtered and air-dried for 24 h at room temperature.

The scheme of the polymerization reaction during the in situ immobilization of 4-methacroyloxy-(4′-carboxy-2′-nitro) azobenzene on the surface of saponite is similar [13].

IR spectra of the original and modified saponite were recorded using an infrared spectrophotometer "Spectrum BX" (Perkin Elmer, Germany) in the range 500–4000 cm^{-1} in tablets KBr.

The amount of immobilized polymer on the saponite surface was evaluated by thermogravimetric analysis results obtained with simultaneous TG/DTA analyzer Shimadzu DTG-60 H (Japan) with computer registration of data in the 15–1000 °C temperature range. The heating rate of samples is 10 °C/min.

Thermal analysis was carried out on a STA 449 Jupiter F1, Netzsch (Germany) with mass spectroscopy console QMS 403C Aeölos (Germany).

The values of the surface area, average volume and average pore diameter were calculated from the data of low-temperature nitrogen adsorption/desorption isotherms using the "ASAP 2420 V1.01" (Micromeritics, USA) sorbetometric software. Before measurements, samples were degassed at 60 °C for 24 h.

The morphology of the surface of saponite before and after modification by polymer was investigated by scanning electron microscopy using the electron microscope "SEM LEO 1430 VP" (Carl Zeiss, Germany).

Sorption characteristics of the synthesized material with respect to Cu(II), Mn(II), Pb(II) and Fe(III) ions were studied in static mode. At the same time, 0.1 g of the composite was contacted with 25–100 ml of working solutions of nitrates of the corresponding metals. The interaction took place for 10, 60, 120 min and day with mechanical shaking. The equilibrium concentration of metal ions was fixed by the atomic absorption method.

The working solutions of the nitrates of the selected metals for the study of the sorption properties of the modified saponite were prepared from the sets of "standard samples of solutions" of these salts (produced by AV Bogatsky, Odessa) on the background of 1 $MHNO_3$ at concentrations of 1 and 10 mg/ml.

The adsorption capacity (A) was calculated using the formula:

$$A = (c_o - [M])V/m \tag{1}$$

where c_o—initial molar metal concentration, $[M]$—balanced molar metal concentration, V—is the volume of the working solution, m—is mass of the adsorbent (g).

The adsorption rate (R) was calculated according to the equation:

$$R = (m_{ads}/m_o) \cdot 100\% = (m_o - [m])/m_o \cdot 100 \tag{2}$$

where m_o—is mass of metal in the starting solution (m kg), m_{ads}—is mass of the metal adsorbed, $[m]$—is mass of the metal at equilibrium after the adsorption, which

was found $[m] = C \bullet V$, where C—is concentration of the metal at equilibrium (mrg/ml) and V—is the volume of the solution at equilibrium (ml).

The balanced metal ions concentration was defined by atom-absorption method. Atom-absorption measuring was made with the help flame atom-absorption spectrophotometer "Saturn" (Ukraine) in flame solution "air- propane-butane". The wavelengths were: for cuprum—324.7 nm, plumbum—283.3 nm, ferum—248.3 nm, and the width of the crack of 0.5 cm. The balanced concentrations calculations in solution were made by comparing the method of their lines intensity in the standard solutions intensity spector. Standard solutions were prepared with metal concentrations of 0.1–1.5 μg/ml.

3 Results and Discussion

The fact of the process of in situ polymerization and fixing of the polymer on the saponite surface was confirmed by a comparative analysis of IR spectra of original mineral (A) and modified saponite (Fig. 1).

– A comparative analysis of the infrared spectra of the synthesized composite and the original saponite (Fig. 1) shows that in the spectrum of the composite, in contrast to the original matrix, there are new absorption bands in the region from 1400 to 1600 and 2800 to 3000 cm^{-1}, which are related to the following vibrations:—at 1405 cm^{-1}, there is a stretching vibrations υ (N=N) bond, characteristic of azo compounds; the absorption band at 1651 cm^{-1} can be attributed to the valence asymmetric vibrations υ_{as} (NO_2). The absorption bands in the region from 2833

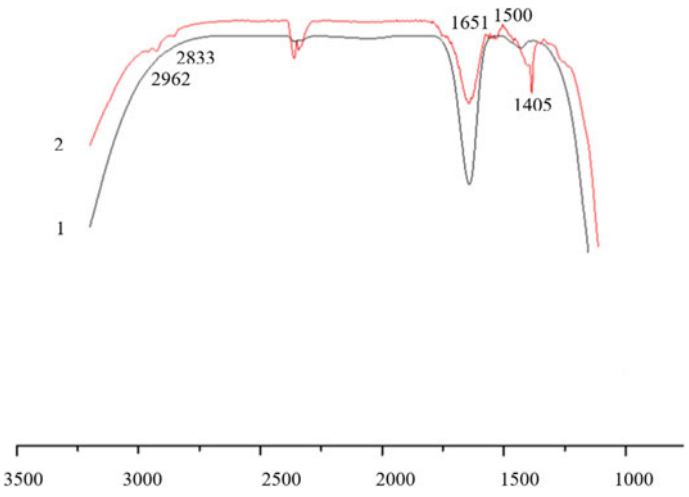

Fig. 1 Infrared spectra of the original (1) and the modified (2) saponite

to 3000 cm^{-1} can be attributed to symmetric valence vibrations in groups of υ (CH) sp^3-hybridized carbon of polymer chains.

– Their presence in the spectrum of the composite testifies to the fact that the polymerization reaction proceeds on the surface of the inorganic matrix [15, 16].

Thus, the results of IR spectroscopy confirm the presence of a polymer on the surface of saponite.

In order to determine the concentration of immobilized polymer, a thermogravimetric analysis of the synthesized composite and the original saponite was performed. The obtained thermograms are shown in Figs. 2 and 3.

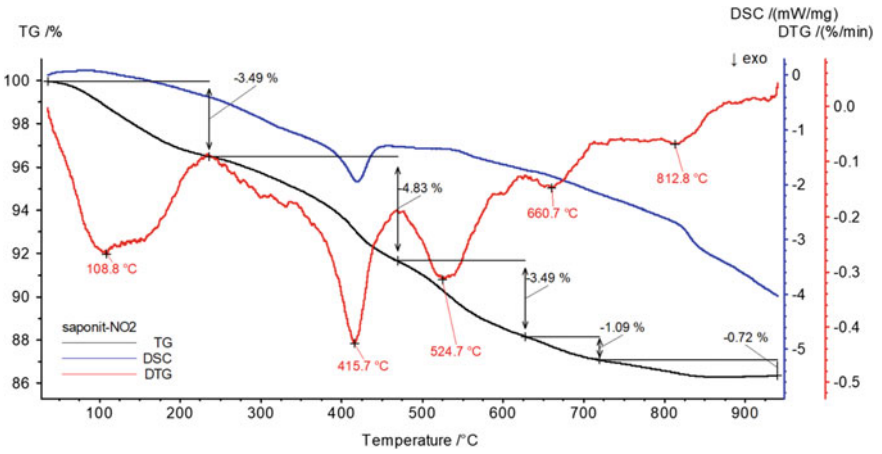

Fig. 2 Thermogram of synthesized composite

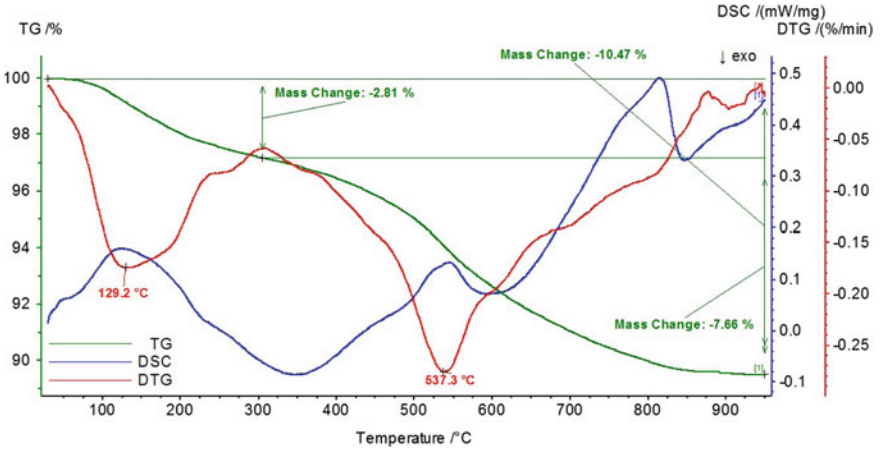

Fig. 3 Thermogram of original saponite

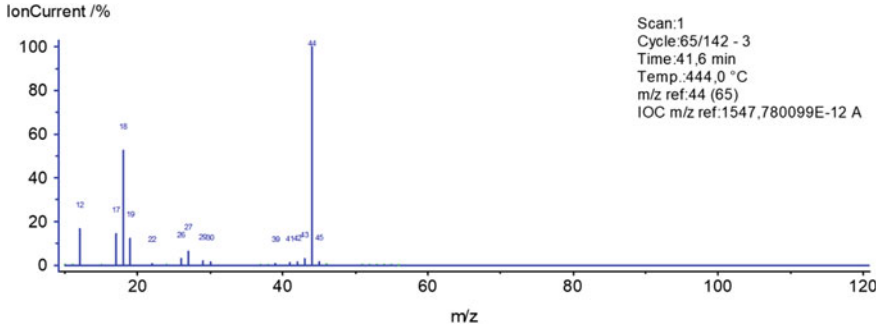

Fig. 4 Mass spectrum of the synthesized composite at 444.0 °C

From Fig. 2, it can be seen that the most intense thermal degradation of the composite occurs in the temperature range from 220 to 480 °C. At the same time, about 13.5% of the weight of the composite is lost. This loss is due to the degradation of the immobilized polymer and the loss of residual water in the mineral, which, according to Fig. 3, is 10.0%. Consequently, the mass of the immobilized polymer is 3.5%.

In order to detail the process of thermodestruction of the composite, a thermogram was obtained at a temperature of 444.0 °C (Fig. 4).

As follows from the analysis of the mass spectrum of the synthesized composite shown in Fig. 4, the complete thermal degradation of the immobilized polymer occurs with the combustion of its fragments to carbon dioxide, water and carbon black, which corresponds to the most intense mass peaks at 44, 18 and 12.

The BET method (low-temperature adsorption-desorption of nitrogen) was used to study the parameters of the saponite surface after immobilization of poly [4-methacryloxy-(4′-carboxy-2′-nitro)-azobenzene]. The adsorption-desorption nitrogen isotherms for the original saponite and the synthesized composite are similar and belong to the IV type isotherm according to the classification of *IUPAC* [17]. Consequently, the structure of the surface of saponite as a result of the fixation of this polymer does not change practically.

The parameters of the surface of the synthesized composite calculated by computer processing of nitrogen adsorption-desorption isotherms are shown in Table 1. The obtained data indicate that after immobilization of the polymer, the porosity of the silica gel surface decreases insignificantly: the surface area decreases from 41 to

Table 1 Characteristics of the surface of saponite and synthesized composite

Sample	Surface area (m^2/g)			Average pore volume (cm^3/g)	Average pore size (nm)
	P/P_0	BET	Langmuir		
Saponite	41.01	41.48	64.85	0.085	8.2
Synthesized composite	8.12	8.39	13.93	0.038	18.2

8 m^2/g, the average pore size decreases from 0.085 to 0.038 cm^3/g, while the average diameter of pores increases from 8.2 to 18.2 nm.

The obtained results (taking into account the small concentration of the immobilized polymer) may indicate a uniform distribution of the polymer over the saponite surface.

Changes in the surface morphology of saponite after modification by an azopolymer were followed by scanning electron microscopy (CEM). The analysis of the obtained photos showed that the polymer on the mineral surface is mostly in the form of a thin film, but there are also loops of macro chains and adsorbed balls (Figs. 5 and 6).

The synthesized composite should detect the sorption ability of ions of transition metals due to the complex activity of the nitrogen atoms of the azo groups and of the nitro group, as well as of the oxygen atoms of the carboxyl groups of the immobilized polymer.

To confirm these considerations, we investigated the sorption of Cu(II) and Fe(III) ions, which have a high affinity for nitrogen-containing ligands [18]. Also, sorption of

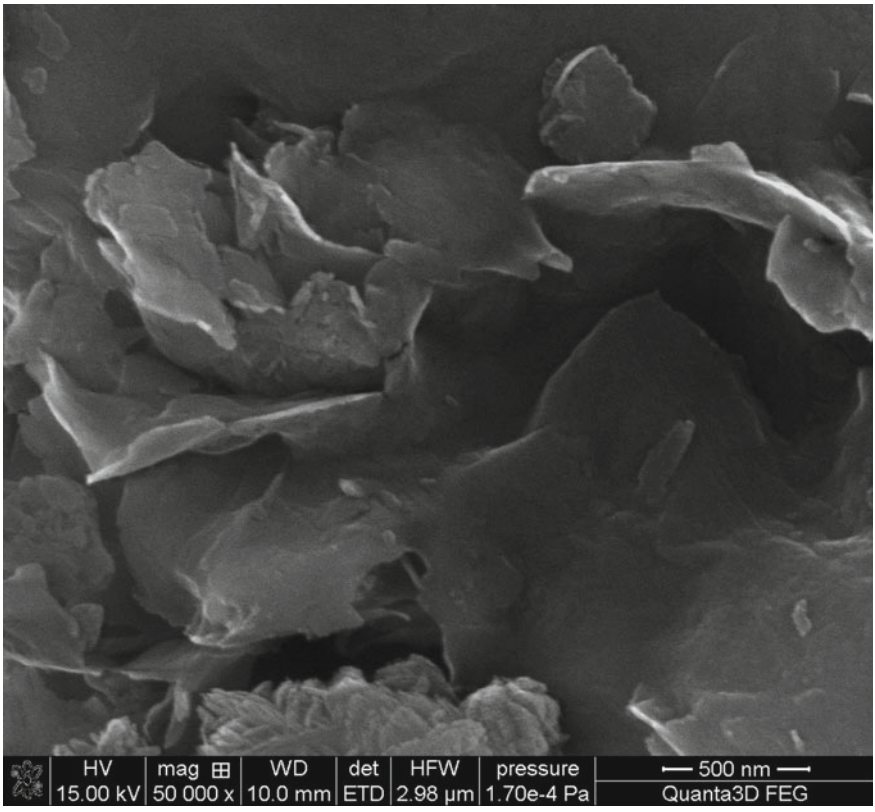

Fig. 5 CEM photo of the surface of the original saponite at an increase of 50,000 times

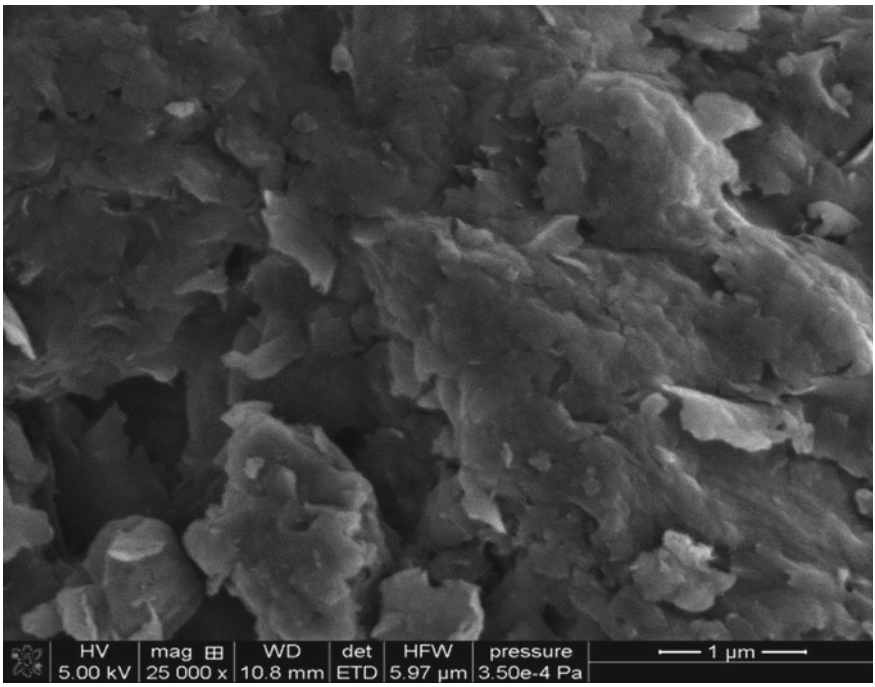

Fig. 6 CEM photo of the surface of the composite at an increase of 25,000 times

ions of toxic metals such as Mn(II) and Pb(II), which form complexes predominantly with oxygen atoms, was studied [18].

Investigation of the sorption capacity of the synthesized composite for these metal ions included:

- determination of the optimal pH range of the sorption medium;
- establishing the required contact time of phases to achieve the sorption equilibrium in the static mode;
- construction of isotherms of sorption of each of the investigated metal ions on the surface of the synthesized composite;
- determination of sorption capacity for each of the investigated metal ions and comparison with the original saponite.

Dependences of the degree of sorption of Cu(II), Mn(II), Pb(II) and Fe(III) ions on the surface of saponite, in situ modified poly [4-methacroyloxy-(4′-carboxy-2′-nitro) azobenzene], from the time of contact in static mode are shown in Table 2.

The obtained data show that Pb(II) ions are maximally adsorbed within the first minutes of contact with the composite surface, Cu(II) ions—during the hour, and Mn(II) and Fe(III) ions—during the contact day.

Table 2 Dependence of the degree of sorption of metals of Cu(II), Mn(II), Pb(II) and Fe(III) ions on the surface of saponite, in situ modified by poly [4-methacroyloxy-(4′-carboxy-2′-nitro)-azobenzene] from the time of contact in a static mode

Time (min)	Degree of adsorption (%)			
	Cu^{2+}	Pb^{2+}	Mn^{2+}	Fe^{3+}
10	88.94	99.99	74.29	87.75
60	99.99	99.99	88.57	90.99
120	99.99	99.99	94.29	91.55
1440	99.99	99.99	99.99	99.99

Experimental conditions: mass of sorbent—0.1 g, volume of solution—25 ml, m_M^0—100 μg, the medium of the initial solutions are neutral

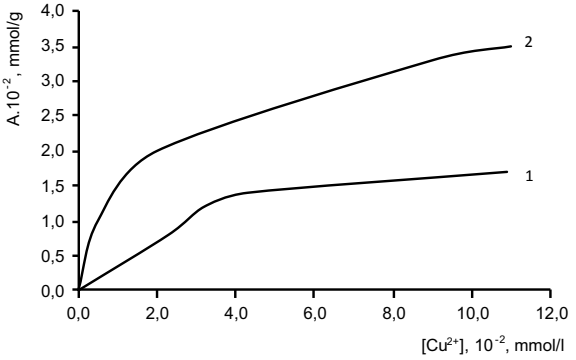

Fig. 7 Isotherms for sorption of Cu(II) ions on the surface of original saponite (1) and in situ modified by poly [4-methacroyloxy-(4′-carboxy-2′-nitro)-azobenzene] saponite (2)

The sorption isotherms of Cu(II) ions on the surface of the original and in situ modified of poly [4-methacroyloxy-(4′-carboxy-2′-nitro) azobenzene] saponite are shown in Fig. 7.

All of the obtained isotherms belong to the 2L-species, which indicates that the sorbed metal ions are distributed evenly on a solid surface of the sorbent. This type of isotherm is typical for porous inorganic matrices, modified by complex-forming substances [9].

The obtained isotherms allow to calculate the sorption capacity of the synthesized composite. The comparison of the sorption capacitance values of the synthesized composite with respect to Cu(II), Pb(II), Fe(III) and Mn(III) ions, and the original saponite is given in Table 3.

The data in the Table 2 suggest that the sorption capacity of saponite after modification of poly [4-methacroyloxy-(4′-carboxy-2′-nitro) azobenzene] with respect to Cu(II) ions increases more than 2 times, with respect to Pb(II) ions 18%, for Fe(III) ions by 14%, and for Mn(II) ions by 6% only. This is the result of immobilization on the mineral surface of the selected polymer, which is capable of complex formation.

The increase in the sorption capacity of the modified saponite compared to the original for Mn(II) ion is within the error of the experiment. Therefore, it can be

Table 3 The comparison of sorption capacities for ions Cu(II), Pb(II), Mn(II) and Fe(III), original saponite and synthesized composites

Cation	Sorption capacity			
	Original saponite		Modified saponite	
	mmol/g	mg/g	mmol/g	mg/g
Fe(III)	0.014	0.78	0.016	0.89
Pb(II)	0.016	3.31	0.019	3.93
Mn(II)	0.016	0.88	0.017	0.94
Cu(II)	0.017	1.09	0.035	2.24

assumed that modification of the surface of the saponite by poly [4-methacroyloxy-(4′-carboxy-2′-nitro)-azobenzene] does not improve its sorption capacity for Mn(II) ions.

4 Conclusions

A new organo-mineral composite material has been synthesized by in situ immobilization of poly [4-methacroyloxy-(4′-carboxy-2′-nitro)-azobenzene] on the saponite surface by polymerization of the [4-methacroyloxy-(4′-carboxy-2′-nitro)-azobenzene] in the presence of 2,2′-azobisisobutyronitrile as the initiator of radical polymerization.

The fact of in situ immobilization of polymer has been confirmed by IR spectroscopy. As a result of thermogravimetric analysis, it has been found that the composition of the synthesized composite includes 3.5 wt% of the polymer.

According to the results of the data processing of sorption isotherms, it was found that the immobilization of the saponite surface of poly [4-methacroyloxy-(4′-carboxy-2′-nitro) azobenzene] leads to an increase of its sorption capacity for Cu(II) ions more than 2 times, relative to ions Pb(II)—by 18%, for Fe(III) ions—by 14% and practically does not improve its sorption capacity for Mn(II) ions.

References

1. Girin VM, Boyko II, Rudichenko VF (1995) The use of natural mineral saponite for water disinfection. Med Bus 5–6:177–179
2. Kulik MF, Zasuha TV, Lutyuk MB (2012) Saponite and aerosil in animal husbandry and medicine. Vinnitsa
3. Savchenko I, Yanovska E, Sternik D, Kychkiruk O, Ol'khovik L, Buriachenko I (2017) In situ immobilization on the silica gel surface and adsorption capacity of poly[N-(4-carboxyphenyl) methacrylamide] on toxic metal ions. Nanoscale Res Lett 12:313

4. Savchenko I, Yanovska E, Polonska Y, Sternik D, Kychkiruk O, Ol'khovik L (2019) In situ immobilization on the silica gel surface and adsorption capacity of polymer-based azobenzene on toxic metal ions. Appl Nanosci 9(5):657–664
5. Yanovska ES, Vretik LO, Nikolaeva OA, Polonska Y, Sternik D, Kichkiruk O (2017) Synthesis and adsorption properties of 4-vinylpyridine and styrene copolymer in situ immobilized on silica surface. Nanoscale Res Lett 12:217–222
6. Yanovska ES, Vretik LO, Nikolaeva OA, Kondratenko OO, Sternik D, Kichkiruk (2018)Synthesis and adsorption properties of 4-vinylpyridine, styrene and maleic anhydride copolymer in situ immobilized on silica surface. Mol Cryst Liq Cryst 672:104–114
7. Budnyak TM, Yanovskaya ES, Tortikh VA, Kichyruk OY (2010) Adsorption properties of natural minerals with in situ immobilized polyaniline with respect to the anionic forms Mo (VI), W (VI), Cr (VI), As (V), V (V) and P (V). Voprosy Khimii i Khimicheskoi Tekhnologii 5:43–47
8. Budnyak TM, Yanovskaya ES, Tortikh VA, Voznyuk VI (2011) The adsorption properties of the composite Sokyrnitsky clinoptilolite-polyaniline with respect to the anions of elements of groups V and VI of the periodic system DI Mendeleyev. Rep NAS Ukraine 3:141–145
9. Yanovska E, Savchenko I, Polonska Y, Ol'khovik L, Sternik D, Kychkiruk O (2017) Sorption properties for ions of toxic metals of Carpathian clinoptilolite (Ukraine), *in situ* modified by poly[N-carboxyphenyl)methacrylamide. New Mater Compd Appl 1:45–53
10. Yanovska E, Savchenko I, Polonska Y, Ol'khovik L, Sternik D, Kychkiruk O (2018) Sorption properties of toxic metal ions of saponite, in situ modified poly [N-(4-carboxyphenyl) methacrylamide]. Ukr Chem J 84:67–72
11. Sapurina I, Stejskal J (2008) The mechanism of the oxidative polymerization of aniline and the formation of supramolecular polyaniline structures. Pol Int 57:295–325
12. Davidenko N, Davidenko I, Savchenko I, Popenaka A (2008) Synthesis and electrooptical properties of metal-containing azopolymers. The influence of steric factors on the electro-optical effect in polycomplexes of azobenzene. Mol Cryst Liq Cryst 485:254–262
13. Savchenko I, Yanovska E, Polonska Y, Ol'khovik L, Sternik D, Kychkiruk O (2018) *In situ* immobilization on the silica gel surface and adsorption capacity of poly[4-methacroyloxy-(4′-carboxy-2′-nitro)-azobenzene] on toxic metals ions. Mol Cryst Liq Cryst 671:164–174
14. Polonska Y, Yanovska E, Savchenko I, Ol'khovik L, Sternik D, Kychkiruk O (2018) Adsorption capacity to toxic metals ions of azocontaining polymers, *in situ* immobilized on the silica gel surface. Mol Cryst Liq Cryst 673:39–47
15. Smith AL (1982) Applied IR spectroscopy. World, Moscow
16. Tarasevich BN (2012) IR spectra of the basic classes of organic compounds. Reference materials. Moscow: MSU them. M.V. Lomonosov
17. Parfitt GD, Rochester CH (1986) Adsorption from solution at the solid liquid interface M. Mir, 488
18. Skopenko VV, Savranskij LI (2004) Coordination chemistry. Kyiv, Lybid

Configurational Model of Quasi-2D Organic Conductor Electron Subsystem

Yuriy Skorenkyy

1 Theoretical Studies of BEDT-TTF Compounds

Now, it is commonly agreed [1–3] that $(BEDT\text{-}TTF)_2X$ organics, where BEDT-TTF stands for bis(ethylenedithio)tetrathiafulvalene molecule, X denotes monovalent anion ($X = Cu[N(CN)_2]Cl$, $Cu[N(CN)_2]Br$, ICl_2, $AuBr_2$, AuI_2, Ibr_2, I_3) are strongly correlated organic conductors. For the theoretical description of their electron subsystems, a generalized Hubbard model with strong intra-site repulsion can be used [4]. Despite intensive studies, the electron-hole asymmetry observed in the carrier concentration-pressure phase diagram was not explained in frameworks of theoretical models developed so far. Suitable approaches have been developed recently for investigation of the conditions for pseudogap opening in the spectrum and anomalies in dispersion of current carriers of quasi-one-dimensional organic conductors [5, 6] in which correlated hopping of electrons has been taken into account.

BEDT-TTF molecule is a basis for large variety of cation-radical salts [8]. In these salts, BEDT-TTF molecules are donors, bound to an acceptor molecule. For electrical conductivity to be realized in cation-radical salts, a partial charge transfer between donor and acceptor is to take place [8] that causes partial filling of the band formed from the highest occupied molecular orbitals (HOMO) of BEDT-TTF molecules. Salts with higher conductance values have oxidation states between $+1/2$ and $+1$. All superconductors, synthesized so far, have donor states with oxidations between $+1/2$ and $+2/3$. Molecular crystals $(BEDT\text{-}TTF)_2X$ are composed of dimerized organic BEDT-TTF molecules and conducting planes of $Cu[N(CN)_2]Cl$ or other anions. Such structure causes spatial anisotropy of conductance. BEDT-TTF is a large planar molecule (see Fig. 1) and different packing types can be realized (Fig. 2). The packing type is denoted with Greek letters, for example, in κ-$(BEDT\text{-}TTF)_2Cu(NCN)_2I$ formula, letter κ means that the lattice unit cell is a dimer formed by BEDT-TTF molecules directly one above the other (Fig. 3).

Y. Skorenkyy (✉)
Ternopil Ivan Puluj National Technical University, Ternopil, Ukraine
e-mail: skorenkyy.tntu@gmail.com

O. Fesenko and L. Yatsenko (eds.), *Nanooptics and Photonics, Nanochemistry and Nanobiotechnology, and Their Applications*, Springer Proceedings in Physics 247, https://doi.org/10.1007/978-3-030-52268-1_6

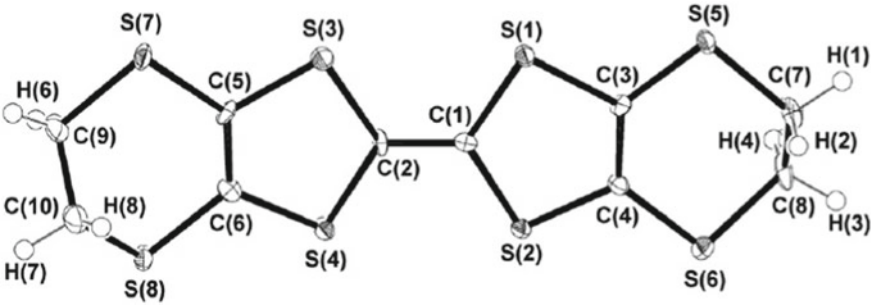

Fig. 1 Bis(ethylenedithio)tetrathiafulvalene (BEDT-TTF) molecule [7]

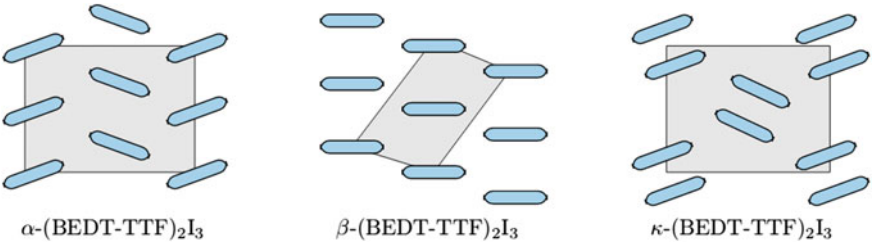

Fig. 2 Packing types of (BEDT-TTF) molecules in a compound [9]

There is exactly one hole per dimer due to electron capture by anion. The dimerization is so strong that the dimer can be modeled as a lattice site. Series of compounds (BEDT-TTF)$_2$Cu$_2$Br$_4$, (BEDT-TTF)$_2$Cu$_6$Br$_{10}$, (BEDT-TTF)$_2$Cu$_6$Br$_7$H$_2$O were synthesized and studied [11] with characteristic lattice parameters $a = 9.401(7)$ Å, $b = 10.841(8)$ Å, $c = 10.035(8)$ Å, $\beta = 98.48(1)°$, V = 1011.7(1) Å^3 and $z = 2$. These systems belong to the same space group that (BEDT-TTF)$_2$(ClO$_4$)$_2$ but have much greater volume of a unit cell due to greater size of anionic cluster $Cu_nBr_m^{-2}$. In (BEDT-TTF)$_2$Cu$_2$Br$_4$, sulfur atoms are bound to copper atoms in Cu$_2$Br$_4$ directly with bond length 2.38 Å forming zig-zag shaped structure along *c*-axis. These salts are special in a sense that valence of BEDT-TTF equals +2 and Cu ions are monovalent. BEDT-TTF molecules are coordinated directly with Cu atom of cation cluster. Direct bonding between BEDT-TTF and Cu gives rise to hybridization of their π- and *d*-electrons. This interaction is enhanced as a result of their direct linkage. Hall coefficient measurements [11] has shown that current carriers are of electron type, carrier concentration is very low (4×10^{19}/mol, which corresponds to one carrier per 10^4 BEDT-TTF molecule) but high mobility of the carriers provides good electric conductance of the material. Carrier concentration rises exponentially with temperature. Magnetic susceptibility follows Curie law with $C = 2/4 \times 10^{-5}$ emu K/mol. Conductance along *c*-axis is greater by one order of magnitude than in transversal direction. Taking into account only the hoppings of

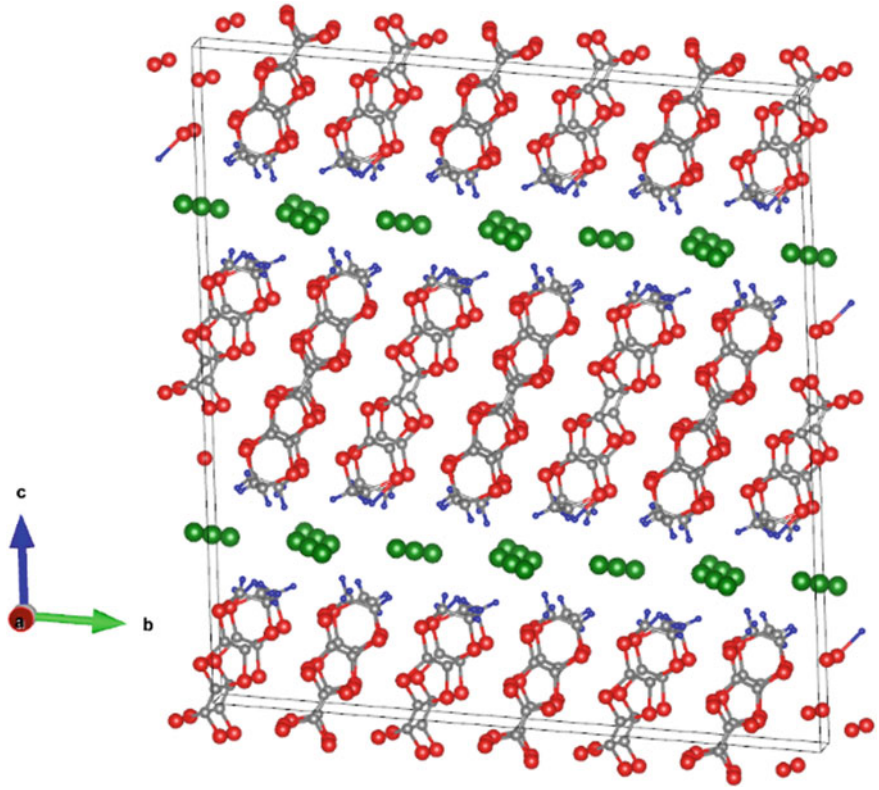

Fig. 3 Layered structure of α-(BEDT-TTF)$_2$I$_3$ [10]

electrons between BEDT-TTF molecules leads to one-dimensional spectrum and *a*-axis conductance whence hoppings through anion Cu_2Br_4 orbitals allows explanation of the higher *c*-axis conductance. Therefore, compounds of (BEDT-TTF)$_2$Cu$_2$Br$_4$ type show the importance of electronic wave functions of organic molecule and anion overlap for electronic properties of the material and its effective dimensionality.

Analyzing the unaxial deformations of α-(BEDT-TTF)$_2$MHg(SCN)$_4$, where M = K, NH_4, under the external pressure [12] one can see that both compounds have common phase diagram and similar properties. Resistance of these compounds decreases considerably with increasing pressure. Spin splitting in de Haas-van Alfven effect for α-(BEDT-TTF)$_2$KHg(SCN)$_4$ compound [13, 14] indicates that the enhancement of interatomic interactions can cause the increase of the effective mass in antiferromagnetic state. From the other side, carrier concentration is low, when the antiferromagnetic gap opens at the Fermi surface, as follows from the Hall effect experiments.

Transition to non-metallic behavior and ethylene molecules ordering in κ-(BEDT-TTF)$_2$Cu(NCN)$_2$I has been studied in work [15]. Under the action of hydrostatic pressure of 1 kbar, this compound undergoes a transition from insulator state to

metallic one and shows superconductivity below 8 K. The maximum of resistance is reached in the metal-to-insulator transition region and the transition point shifts to higher temperatures under external pressure. This salt is situated deep in insulating region of the phase diagram in spite of estimates from the halogene ionic radius.

Two-dimensional metal (BEDT-TTF)$_3$(HSO$_4$)$_2$ undergoes the metal-insulator transition at 126 K. Studies [16] were carried out with use of X-ray diffraction, measurements of conductivity, magnetic susceptibility and electron spin resonance. At the transition point, structural changes were observed, therefore, it can be classified as the Mott transition caused by anisotropic thermal contraction of the lattice. Strain values and angle changes for different directions substantially differ in this family.

Optical reflectance spectra of quasi-2D conductors κ-(BEDT-TTF)$_2$Cu(NCN)$_2$Br and κ-(BEDT-TTF)$_2$Cu(NCN)$_2$Cl in infrared region show [17] the carrier localization on BEDT-TTF dimers below 56–60 K, in Mott insulator regime (antiferromagnetic order stabilizes at 28 K and superconductivity occurs at 11.6 K) and enhancement of their collectivization below 38 K.

The angle-resolved photoemission spectroscopy [18] has been used for investigation of antiferromagnetic insulator κ-(BEDT-TTF)$_2$Cu[N(CN)$_2$]Cl, paramagnetic metal α-(BEDT-TTF)$_2$KHg(SCN)$_4$, semiconductors κ-(BEDT-TTF)$_2$Cu[NSC]$_2$ and κ-(BEDT-TTF)$_2$Cu[NCN]$_2$Br. In all photoemission spectra, the intensity is low in the vicinity of Fermi surface, especially for κ-phase. Band structure calculations using the Hartree–Fock approximation allow qualitative explanation of bands in κ-(BEDT-TTF)$_2$Cu[N(CN)$_2$]Cl, paramagnetic metal α-(BEDT-TTF)$_2$KHg(SCN)$_4$ but give no satisfying description for κ-(BEDT-TTF)$_2$Cu[NSC]$_2$ and κ-(BEDT-TTF)$_2$Cu[NCN]$_2$Br. This means that electron interaction in κ-phase is much stronger than in α-phase.

Insulating state of compounds κ-(BEDT-TTF)$_2$X has been studied by nuclear magnetic resonance with ^{13}C isotope. At low temperatures, lines widening is related to electron localization. It has been noted [19] that temperature decrease gives rise to antiferromagnetic fluctuations. Electron localization effects are crucial for narrow energy bands of these materials.

In paper [20], the magnetic penetration depth λ has been measured for κ-(BEDT-TTF)$_2$Cu[NSC]$_2$ down to 2 K. Ration of Tc to $\frac{1}{\lambda^2}$ in this system was found to decrease with the applied pressure in the same way as it happens in oxides with high-temperature superconductivity (HTSC). Besides, in BEDT-systems, pseudogap phenomena are observed. Unlike HTSC, where Tc is controlled by doping, in BEDT-systems, critical temperature can be changed by the external pressure application. It was shown in paper [20] that the ratio of carrier concentration to effective mass n/m_{eff} decreases at the pressure application, contrary to common view that pressure has no effect on the carrier concentration and lowers the effective mass. Shubnikov-de Haas temperature oscillations allow estimation of the effective masses, renormalized substantially due to correlation effects.

The combined phase diagram of BEDT-TTF family, extending the conceptual phase diagram constructed in [21], is displayed in Fig. 4 with a variety of phases and transitions under the external pressure, temperature changes or anion doping.

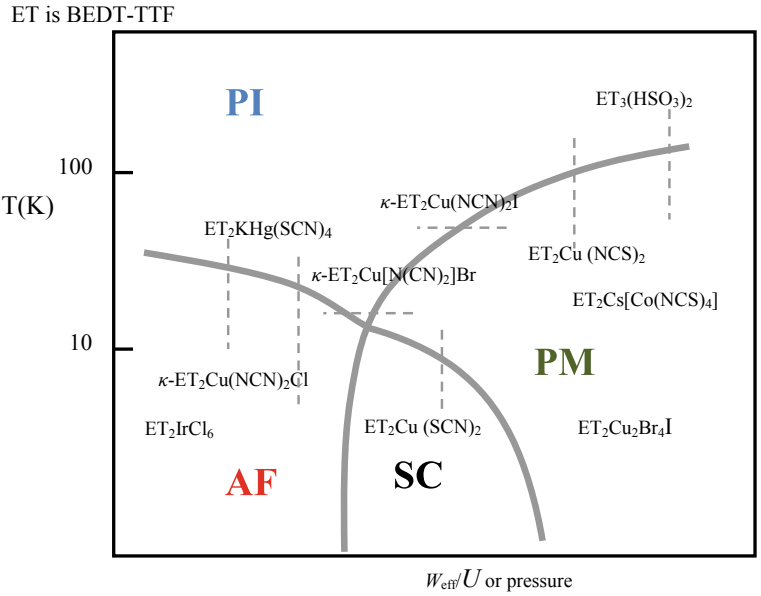

Fig. 4 Combined experimental phase diagram of BEDT-TTF family. Phase transitions between antiferromagnetic insulator (AFI), paramagnetic insulator (PI), paramagnetic metal (PM) and superconducting (SC) states are shown by dashed lines

In particular, at ambient pressures, compound with $X = Cu(CN)_2$ is a paramagnetic insulator and antiferromagnetic phase with magnetic moment $(0.4–1.0)\mu_B$ per dimer is stable for $X = Cu[N(CN)_2]Cl$ below 26 K. Large magnetic moment signifies that there are strong electron correlations in these materials. Antiferromagnetic phase becomes unstable at pressures about 400 bar. Especially interesting is the transition from insulator to metallic phase under the external pressure or decrease of temperature.

Many characteristics of the metallic phase have temperature dependence which strongly differs from that of typical metals. Fermi energy of the organic conductors is about 100 K, which is an order of magnitude lower than predicted by bend structure calculations [22]. In contrast to metals, the resistivity does not rise monotonically with temperature, but has a maximum (for $X = Cu[NSC]_2$ is about 100 K). While subjected to the external pressure, this maximum temperature increases, until the peak disappears at high pressures. In typical metals, their magnetic susceptibility is energy-independent at temperatures well below Fermi energy. For organics, magnetic susceptibility is almost temperature-independent at $T > 50$ K and decreases slightly at lower temperatures. Temperature dependence of Shubnikov–de Haas and de Haas–van Alfven oscillations allows estimations of effective mass of the charge carrier for different Fermi surface orbits. For β-orbital, the obtained values are $m_{eff}/m_e = 5.4 \pm 0.1$ for $X = Cu[N(CN)_2]Br$, $m_{eff}/m_e = 7.1 \pm 0.5$ for $X = Cu(SCN)_2$, and $m_{eff}/m_e = 7.1 \pm 0.5$ for $X = I_3$. For α-orbit in $X = Cu(SCN)_2$, the value $3.3 \pm$

0.1 is obtained (this effective mass further decreases to 1.5 m_e at 20 kbar pressure). These values are twice as big as predicted by band structure calculations neglecting the electron interactions. The fact that effective masses, specific heats and magnetic susceptibilities are much higher than the band structure calculations predictions is a clear indication of substantial bandwidth renormalization and electron interaction importance in real systems.

2 Theoretical Studies of BEDT-TTF Compounds

Theoretical investigations of quasi-2D conductor models are thought to give a clue for resolving a puzzle of the low-temperature superconductive phase mechanisms. In paper [23], the half-filled Hubbard model on triangular lattice has been studied within a mean-field approximation, applied for the energy spectrum calculation. Electron hoppings between the next-nearest-neighbor sites with hopping amplitudes $0.15 < t'_{NNN}/t < 0.5$ destroy antiferromagnetism in this model. Slightly different values $t'_{NNN}/t > 0.6$ are obtained in paper [24] within the mean-field approximation but for more realistic model. In this paper, the stability of antiferromagnetic phase in κ-(BEDT-TTF)$_2$Cu[N(CN)$_2$]Cl below $T_N = 24$ K and the transition into the paramagnetic insulator state at increasing temperature are studied. With the rise of intra-atomic Coulomb repulsion U in the energy spectrum a gap opens, and the transition to antiferromagnetic state is realized. The pressure application was shown to eliminate dimerization, kinetic energy increased and Fermi surface symmetry was broken.

Band structure calculations for κ-(BEDT-TTF)$_2$Cu(SCN)$_2$ using the Hartree–Fock approximation have been carried out for the Hubbard model in paper [25]. Choosing the Coulomb correlation parameter value to be $U/w = 0.6775$, this paper reproduces the half-metallic behavior, but is extremely sensitive to U/w variations.

In paper [26], a dimerized Hubbard model with orientation-dependent hopping parameters has been studied. In the strong correlation limit, the Hamiltonian has been reduced to the effective Heisenberg model, which allows the explanation of the antiferromagnetic insulator phase but not metallic one. This paper criticizes the application of the mean-field theories to organic conductor models and stresses similarities of the metallic phase of organic conductors to that resultant from dynamic mean-field theory (DMFT) in the limit of infinite spatial dimensions. We note that the assumption of infinite coordination number is not applicable to low-dimensional systems or to materials with pronounced correlated hopping of electrons but, instead, there are methods [27–29] developed for strongly correlated systems with correlated hopping with validity domain not restricted by dimensionality of material, which reproduce essential results of DMFT for narrow-band transitional metal compounds. Cluster dynamical mean field [30], being a generalization of DMFT for two-dimensional systems with next-nearest-neighbor hoppings, does not allow studying systems with correlated hopping either.

Numerical Monte Carlo modeling has been applied in paper [31] for investigation of spin correlations and electron pairing of d-type. Calculations for 12×12 cluster corroborate the spin-fluctuation mechanism of superconducting pairing. It has been shown that the concentration of doubly occupied sites increases and long-range order does not stabilize at electron concentration increase up to one electron per site.

Electronic structures differ for various compounds mentioned, in particular, orientations of molecules in unit cell do not coincide, but a value of intra-atomic Coulomb repulsion U for all compounds are in range 0.7–1.3 eV [26]. This allows studying the transition from insulator to metallic phase at the external pressure application or decrease of temperature within the unified model, in which the quasiparticle bandwidths depend on anion type and arrangement of molecules in a unit cell. The band theory successfully explained electrical properties and paramagnetism of the majority of metals within the concept of itinerant electrons but appeared to be incapable to treat properties of these metals, which are manifestation of electron wave function localization, namely ferro- and antiferromagnetism, metal-insulator transition, charge and orbital orderings. The noted localization is caused by strong electron interactions, which lead to substantial conductance band narrowing in metallic solids.

When electrons are confined to one spatial dimension, they cannot evade each other and their interaction plays a more prominent role than in three-dimensional isotropic systems. Mermin–Wagner theorem states that a spontaneous symmetry breaking (e.g., with respect to rotation) cannot occur in low-dimensional system, thus, a long-range order can exist only at zero temperature. In one-dimension, quantum fluctuations have similar destructive effect and even at zero temperature antiferromagnetic or superconducting order is not stable. However, in spite of the absence of the long-range ordering, collective modes exist and propagate at sufficiently long distances below the transition temperature, creating ordered regions of substantial size. At weak or intermediate coupling, the effect of the coupling has pronounced differences. For high dimensionalities, the scattering frequency of quasiparticles at Fermi energy is proportional to $(T/E_F)^2$. As the respective width of Fermi function is of order of (T/E_F), one should expect that quasiparticles will not affect the thermodynamic properties. In one-dimensional case, this argument is not valid that invalidates Fermi-liquid theory starting point. In the resultant Luttinger liquid picture, which substitutes Fermi-liquid picture in limiting case of one dimension, spin and charge of what would be a quasiparticle are separated, become elementary excitations and propagate at different speeds. In two-dimensional case, the quasiparticle picture does not fail completely. From theoretical point of view, in two-dimensional case, there are only weak logarithmic corrections to standard arguments of Fermi liquid. In Mott insulator, many properties do not depend crucially on dimensionality, especially in the high energy region. Mott transition violates no symmetry and can occur at any dimensionality. Such a transition has been observed in two-dimensional organic conductors. From the model point of view, this reflects overlapping of atomic orbitals and, hence, increasing of kinetic energy. Indeed, at low pressure, the system is either a paramagnetic insulator at high temperature or antiferromagnetic insulator at low temperature. At elevated pressures, the first-order transition occurs which leads to metallic states at high temperatures and superconductivity at low temperatures.

3 Model Hamiltonian

The highest occupied molecular orbital forms a conduction band in which there is a hole per each two BEDT-TTF molecules [18]. The lattice is strongly dimerized so every dimer can be modeled as a single lattice site [21], analogously to the approach realized in [6, 32, 33]. Electron hopping integrals for in-plane hoping are quite close in values but differ greatly from that for inter-plane hoppings, so the use of our model for $(BEDT\text{-}TTF)_2X$ in which parameters t and t' describe in-plane and inter-plane hoppings, respectively, is justified. At certain conditions, a transition from metallic state to insulating one (MIT) can occur in such model.

We generalize the approach of works [5, 6, 28, 29] on two-dimensional conductors with strong electron correlations, using the configurational representation of the model Hamiltonian which allows us obtaining of the Green function analytically and calculation of the energy spectrum.

Effective Hamiltonian of the model takes into account the strong intra-site Coulomb, intersite exchange interaction of electrons and correlated hopping of electrons both along the chain and in transversal direction.

$$H_{\text{eff}} = H_0 + H_{\text{tr}} + H'_{\text{tr}} + H_{\text{ex}} + H'_{\text{ex}} + \tilde{H}_{\text{ex}} + \tilde{H}'_{\text{ex}} + H_2, \tag{1}$$

where

$$H_0 = -\mu \sum_i \left(X_i^{\uparrow} + X_i^{\downarrow} + 2X_i^2 \right) + U \sum_i X_i^2 + \frac{1}{2} N V_0 \kappa u^2,$$

$$H_{\text{tr}} = \sum_{\langle ij \rangle \sigma} t_{ij}(n) X_i^{\sigma 0} X_j^{0\sigma} + \sum_{\langle ij \rangle \sigma} \tilde{t}_{ij}(n) X_i^{2\sigma} X_j^{\sigma 2},$$

$$H'_{\text{tr}} = \sum_{\langle\langle il \rangle\rangle \sigma} t'_{il}(n) X_i^{\sigma 0} X_l^{0\sigma} + \sum_{\langle\langle il \rangle\rangle \sigma} \tilde{t}'_{il}(n) X_i^{2\sigma} X_l^{\sigma 2},$$

$$H_{\text{ex}} = -\frac{1}{2} \sum_{\langle ij \rangle \sigma} J(ij) \left(\left(X_i^{\sigma} + X_i^2 \right) \left(X_j^{\sigma} + X_j^2 \right) + X_i^{\sigma\bar{\sigma}} X_j^{\bar{\sigma}\sigma} \right),$$

$$H'_{\text{ex}} = -\frac{1}{2} \sum_{\langle\langle il \rangle\rangle \sigma} J'(il) \left(\left(X_i^{\sigma} + X_j^2 \right) \left(X_l^{\sigma} + X_l^2 \right) + X_i^{\sigma\bar{\sigma}} X_l^{\bar{\sigma}\sigma} \right),$$

$$\tilde{H}_{\text{ex}} = -\frac{1}{2} \sum_{\langle ij \rangle \sigma} \tilde{J}(ij) \left(X_i^{\sigma} X_j^{\sigma} - X_i^{\sigma\bar{\sigma}} X_j^{\bar{\sigma}\sigma} \right),$$

$$\tilde{H}'_{\text{ex}} = -\frac{1}{2} \sum_{\langle\langle il \rangle\rangle \sigma} \tilde{J}'(il) \left(X_i^{\sigma} X_l^{\sigma} - X_i^{\sigma\bar{\sigma}} X_l^{\bar{\sigma}\sigma} \right),$$

$$H_2 = \frac{1}{2} \sum_{ij\sigma\sigma'} V(ij) \left(X_i^{\sigma} + 2X_i^2 \right) \left(X_j^{\sigma'} + 2X_j^2 \right)$$

$$-\frac{1}{2}\sum_{ij\sigma}{}'J(ij)\left(\left(X_i^{\sigma}+X_i^{2}\right)\left(X_j^{\sigma}+X_j^{2}\right)+X_i^{\sigma\bar{\sigma}}X_j^{\bar{\sigma}\sigma}\right).$$

Here, X^{kl} are transition operators of site from state $|l\rangle$ to state $|k\rangle$ (Hubbard operators) in configurational representation. Terms of Hamiltonian (1) have the following meaning. H_0 describes electron subsystem in localization limit (μ is chemical potential, U is Coulomb repulsion of two electrons in the same site), first sum in H_{tr} describes electron hoppings in the plane of molecules between sites occupied with single electron and empty sites with hopping integral $t_{ij}(n)$ (these processes form the lower Hubbard subband), second sum describes hoppings between singly and doubly occupied sites with parameter $\tilde{t}_{ij}(n)$ (these processes form the upper Hubbard subband), H'_{tr} describes the inter-chain electron hoppings with parameters $t'_{il}(n)$ and $\tilde{t}'_{il}(n)$, H_{ex} and H'_{ex} describe direct intersite exchange between nearest neighbors and between next-nearest neighbors, respectively; $\tilde{H}_{\text{ex}}$ describes effective exchange interaction within the plane with effective exchange integral $\tilde{J}(ij)=\frac{\left(\bar{t}_{ij}(n)\right)^2}{U}$, $\tilde{H}'_{\text{ex}}$ describes effective next-nearest-neighbor exchange with integral $\tilde{J}'(il)=\frac{\left(\bar{t}'_{il}(n)\right)^2}{U}$ ($\bar{t}_{il}$ and $\bar{t}'_{il}$ are integrals of hole-doublon pair creation at translation along the molecules plane and between the planes, respectively). H_2 describes intersite Coulomb and exchange interactions (Fig. 5).

In this model, application of the external pressure or chemical doping can be easily modeled by respective renormalization of intersite parameters. Hopping integrals also depend on electron concentration due to correlated hopping of electrons which reduces the hopping probability for occupied sites. $\eta_s = 1$ if $s = \uparrow$ and -1 otherwise. Translation processes are characterized by different hopping integrals,

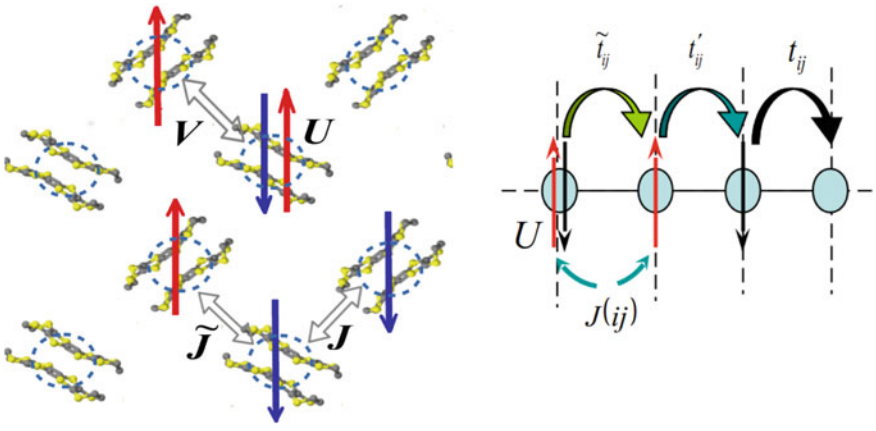

Fig. 5 Interaction parameters of the model Hamiltonian. In the left panel, every dimer is modeled as a lattice site. In the right panel, different hopping integrals between the nearest-neighboring sites are visualized. Only on-site and nearest-neighbors interactions are shown in this figure, though in the model the next-nearest-neighbor interactions are included as well

namely $t_{ij}(n) = (1 + \alpha u)(1 - \tau_1 n)t_{ij}$ and $\tilde{t}_{ij}(n) = (1 + \alpha u)(1 - \tau_1 n - 2\tau_2)t_{ij}$ are hopping parameters for holes and doublons, respectively; $t_{0ij}(n) = (1 + \alpha u)(1 - \tau_1 n - \tau_2)t_{ij}$ is parameter of the hopping of an electron between doublon and hole; correlated hopping parameters τ_2 and τ_1 describe the influence of sites involved into the hopping process and neighbor sites, respectively; parameter $\alpha < 0$ takes into account the renormalization of bandwidth $2w = 2z|t_{ij}|$ at strain u, z is the number of nearest neighbor to a site. Anisotropy of transport characteristics can be described by dimensionless parameter $g = t'_{il}(n)/t_{ij}(n)$ (g may depend on the external pressure or chemical composition).

4 Metal–Insulator Transition in a Model of Organic Conductors

Conducting properties are determined by quasiparticle spectrum of a system. Compound turns to be insulating when an energy gap opens of Fermi level in quasiparticle spectrum. This criterion does not apply for a superconductor: there is a gap in the spectrum but Cooper pairs can move in the external field. Similarly, in semiconductors, the gap in energy spectrum is not equal to the energy needed for creation of electron–hole pair. If there is a disorder (in Anderson insulators), the gap is absent but states close to Fermi energy are localized, therefore, the second of the abovementioned conditions is violated. Below, we study states of the electron subsystem, in which the superconducting pairing, disorder and dopants are absent. Therefore, conductivity tensor is expected to be determined by propagation of individual charge perturbations and their interaction can be neglected.

At finite temperatures, the clear distinction between metals and insulators disappears and both systems have non-zero values of electric conductance. In experiments, sharp change of conductance occurs at small variation of system parameters or the external actions. In this case, the energy gap criterion is used for metal-insulator transition when electron mean energy is much lower than the energy gap width. Energy gap closure at the point of Mott–Hubbard transition is inherent to two-pole approximations [34]. The common idea of these methods is a sequence of equations for Green functions breaking within the projection on a set of basis operators, one of which describes transitions between empty and singly occupied configurations of a site and the other describes transition between singly and doubly occupied configurations. The resulting spectrum consists of two branches, forming the lower and the upper subbands with energy difference between their centers determined by the energy of intra-atomic repulsion of electrons with the opposite spins. At condition of strong Coulomb correlation for site occupancy of exactly one electron per site, all states in the lower subband are occupied and all states in the upper subbands are empty and the system behaves as insulator. With decrease of intra-site repulsion energy or energy bandwidths increase, the gap collapses and MIT occurs. Results of such methods as angle-resolved photoemission spectroscopy corroborate existence

of the Hubbard subbands separated by energy gap in insulating state and their overlap in metallic state. Noted two-pole approximations are criticized for inability of Fermi-liquid behavior of the system, but the question the Fermi-liquid picture validity in the intermediate correlation regime remains open (see [34] for details).

Metal-insulator transition is thoroughly studied in the framework of the Hubbard model (see review [35]) in the limit of large spatial dimensions, when self-energy part becomes diagonal in Wannier representation and the problem can be reduced to a single-site Anderson impurity model [36]. To this end, various methods have been used, depending on studied system peculiarities, namely, the iterative perturbation theory [37, 38], quantum Monte Carlo method [39, 40], exact diagonalization [41], Gutzwiller variation method [42] and numerical renormalization group [43]. Paper [30] summarizes the results obtained for a case of anisotropic hoppings in infinite spatial dimensions. In papers [44–47], the Hubbard model generalized with taking into account the correlated hopping, which is close to ours. Its peculiarity is taking into account different concentration-dependent transfer integrals. The problem of MIT in a model with correlated hopping is still open. The correlated hopping makes direct application of methods like DMFT, Gutzwiller approximation and slave boson technique impossible.

The single-particle Green function is written in Hubbard X_i^{kl}-operators as

$$G_k^{\sigma} = a_{p\sigma} | a_{s\sigma}^{+} = G_k^{l\sigma} - \eta_{\sigma} G_k^{2\sigma} - \eta_{\sigma} G_k^{3\sigma} + G_k^{4\sigma}, \tag{2}$$

where

$$G_k^{1\sigma} = \langle\langle X_p^{0\sigma} \mid X_s^{\sigma 0} \rangle\rangle, \; G_k^{2\sigma} = \langle\langle X_p^{\tilde{\sigma} 2} \mid X_s^{\sigma 0} \rangle\rangle,$$
$$G_k^{3\sigma} = \langle\langle X_p^{0\sigma} \mid X_s^{2\tilde{\sigma}} \rangle\rangle, \; G_k^{4\sigma} = \langle\langle X_p^{\tilde{\sigma} 2} \mid X_s^{2\tilde{\sigma}} \rangle\rangle$$

In the approximation [28, 48], we have

$$G_k^{1\sigma} = \frac{(2 - n + \eta_{\sigma} m)}{4\pi} \left(\frac{A_k^{1\sigma}}{E - E_1^{\sigma}(k)} + \frac{B_k^{1\sigma}}{E - E_2^{\sigma}(k)} \right), \tag{3}$$

$$A_k^{1\sigma} = \frac{1}{2} \left(1 + \frac{U - (\varepsilon^{\sigma} - \tilde{\varepsilon}^{\sigma})(1 + \alpha u) t(k)}{E_2^{\sigma}(k) - E_1^{\sigma}(k)} \right)$$

$$B_k^{1\sigma} = 1 - A_k^{1\sigma},$$

$$G_k^{2\sigma} = -\frac{(2 - n + \eta_{\sigma} m)}{4\pi} \cdot \frac{\varepsilon_2^{\sigma}(1 + \alpha u) t(k)}{E_2^{\sigma}(k) - E_1^{\sigma}(k)} \cdot \left(\frac{1}{E - E_1^{\sigma}(k)} - \frac{1}{E - E_2^{\sigma}(k)} \right) \tag{4}$$

$$G_k^{3\sigma} = -\frac{(n - \eta_{\sigma} m)}{4\pi} \cdot \frac{\varepsilon_1^{\sigma}(1 + \alpha u) t(k)}{E_2^{\sigma}(k) - E_1^{\sigma}(k)} \cdot \left(\frac{1}{E - E_1^{\sigma}(k)} - \frac{1}{E - E_2^{\sigma}(k)} \right), \tag{5}$$

$$G_k^{4\sigma} = \frac{(n - \eta_{\sigma} m)}{4\pi} \left(\frac{A_k^{4\sigma}}{E - E_1^{\sigma}(k)} + \frac{B_k^{4\sigma}}{E - E_2^{\sigma}(k)} \right), \tag{6}$$

$$A_k^{4\sigma} = B_k^{1\sigma}, B_k^{4\sigma} = A_k^{1\sigma},$$

where

$$E_{1,2}^{\sigma}(k) = -\mu - \eta_\sigma h + \frac{U}{2} - \frac{(n+\eta_\sigma m)}{2} zJ + \frac{(\varepsilon^\sigma + \tilde{\varepsilon}^\sigma)}{2}(1+\alpha u)t(k) \mp \frac{1}{2}\sqrt{\left[U - (\varepsilon^\sigma - \tilde{\varepsilon}^\sigma)(1+\alpha u)t(k)\right]^2 + 4\varepsilon_1^\sigma \varepsilon_2^\sigma (1+\alpha u)^2 t(k)^2}, \quad (7)$$

is the quasiparticle energy spectrum for spin σ electrons.

Projection coefficients $\varepsilon^\sigma(pi)$, $\tilde{\varepsilon}^\sigma(pi)$, ε_1^σ and ε_2^σ, which we calculate by the method of papers [28, 49], have the following form

$$\varepsilon^\sigma = \left(1 - \frac{n-\eta_\sigma m}{2}\right) + \frac{1}{2} \cdot \frac{(n+\eta_\sigma m - 2d)(n-\eta_\sigma m - 2d)}{2-n+\eta_\sigma m} - (1-2\tau)\frac{2d(1-n+d)}{2-n+\eta_\sigma m}, \quad (8)$$

$$\tilde{\varepsilon}^\sigma = (1-2\tau)\frac{n-\eta_\sigma m}{2} + \frac{1-2\tau}{2} \cdot \frac{(n+\eta_\sigma m - 2d)(n-\eta_\sigma m - 2d)}{n-\eta_\sigma m} - \frac{2d(1-n+d)}{n-\eta_\sigma m}, \quad (9)$$

$$\varepsilon_1^\sigma = -(1-\tau)\left(1 - \frac{n-\eta_\sigma m}{2}\right), \quad (10)$$

$$\varepsilon_2^\sigma = -(1-\tau)\frac{n-\eta_\sigma m}{2}, \quad (11)$$

where a relation $c - d = 1 - n$ between the doublon concentration d and the empty states concentration c is used.

Concentration of electrons with spin σ is determined by the expression

$$n_\uparrow = \frac{1}{N}\sum_k \int_{-\infty}^{\infty} S_k^{\uparrow}(E)\mathrm{d}E, \quad (12)$$

where $S_k^\sigma(E)$ is a spectral density of Green function (2). In our approach, single-particle Green function (2) and energy spectrum (7) are exact in the band and atomic limits.

At application of the external pressure to narrow-band material, the correlation effects can be described by renormalization of transfer parameters at the crystal lattice deformation. Under the external pressure p, the dependence of bandwidth on the relative strain $u = \frac{\Delta V}{V_0} \sim p$ (here V_0 is the unit volume) so the relation between the half bandwidth and bare (unperturbed) half bandwidth w_0 can be established [50]:

$$w = w_0(1 + \alpha u) \quad \left(\alpha = \frac{V_0}{w_0} \cdot \frac{\partial w}{\partial V} < 0\right). \tag{13}$$

Analogous renormalization is to be applied to the upper subbandwidth. The relative strain u is determined from the minimum condition of the Gibbs thermodynamic potential

$$G = F + NpV_0(1 + u), \tag{14}$$

where F denotes free energy. Using the relation

$$\frac{\partial F}{\partial \overline{u}} = \left\langle \frac{\partial H}{\partial \overline{u}} \right\rangle = \frac{\partial E(\overline{u})}{\partial \overline{u}} \sum_{i\sigma} \langle a^+_{i\sigma} a_{i\sigma} \rangle + \sum_{ij\sigma} \frac{\partial t_{ij}(\overline{u})}{\partial \overline{u}} \left\langle a^+_{j\sigma} a_{i\sigma} \right\rangle + NV_0 C\overline{u}, \tag{14}$$

one can rewrite (14) for parameter u in form

$$\left\langle \frac{\partial H}{\partial u} \right\rangle + NpV_0 = 0, \tag{15}$$

where H is model Hamiltonian. Within the mean-field approximation, one has $\alpha u = \tau p V_0$.

From the minimality condition, for Gibbs potential, one has

$$\overline{u} = -\frac{1}{NV_0 C} \left(S \sum_{i\sigma} \langle c^+_{i\sigma} c_{i\sigma} \rangle + \frac{BV_0}{2w} \sum_{ij\sigma} t_{ij} \langle c^+_{i\sigma} c_{j\sigma} \rangle + NV_0 P \right), \tag{16}$$

After Fourier transformation, the equilibrium strain can be expressed as

$$\overline{u} = -\frac{1}{V_0 C} \left(\frac{S}{N} \sum_{\vec{k}\sigma} \left\langle c^+_{\vec{k}\sigma} c_{\vec{k}\sigma} \right\rangle + \frac{BV_0}{2w} \frac{1}{N} \sum_{\vec{k}\sigma} t_{\vec{k}} \left\langle c^+_{\vec{k}\sigma} c_{\vec{k}\sigma} \right\rangle \right) - \frac{PV_0}{CV_0}, \tag{17}$$

where

$$\left\langle c^+_{\vec{k}\sigma} c_{\vec{k}\sigma} \right\rangle = \int_{-\infty}^{\infty} dE J^s(E) = \sum_{\vec{k}} \int_{-\infty}^{\infty} dE J^s_{\vec{k}}(E).$$

is determined by spectral intensity of the Green function. Calculation of the correlation functions at zero temperature can be done analytically with the model rectangular density of states

$$\frac{1}{N}\sum_{\vec{k}}\left\langle c^{+}_{k\uparrow}c_{k\uparrow}\right\rangle = \frac{1}{N}\sum_{\vec{k}}\frac{1}{\mathrm{e}^{\frac{E_2(\vec{k})}{\theta}}+1} = \frac{1}{2w}\int\limits_{-w}^{w}\frac{\mathrm{d}\varepsilon}{\mathrm{e}^{b+a\varepsilon}+1} = -\frac{1}{2a\Delta}\ln\left|\frac{\mathrm{e}^{-b-aw}+1}{\mathrm{e}^{-`b+aw}+1}\right|, \tag{18}$$

and numerically for the term

$$\frac{1}{N}\sum_{\vec{k}} t_{\vec{k}}\left\langle c^{+}_{k\uparrow}c_{k\uparrow}\right\rangle = \frac{1}{2w}\int\limits_{-w}^{w}\frac{\varepsilon\mathrm{d}\varepsilon}{\mathrm{e}^{b+a\varepsilon}+1}, \tag{19}$$

where $a = \frac{1}{\theta}\left(1+\frac{BV_0}{2w}\overline{u}\right)$; $b = \frac{1}{\theta}(-\mu + E_b(\overline{u}))$.

For the localized electrons,

$$\frac{1}{N}\sum_{k}\left\langle d^{+}_{k\uparrow}d_{k\uparrow}\right\rangle = \frac{\left\langle 1-n_{p\downarrow}\right\rangle}{e^{\frac{E_1}{\theta}}+1} + \frac{\left\langle n_{p\downarrow}\right\rangle}{\mathrm{e}^{\frac{E_3}{\theta}}+1}. \tag{20}$$

In the paramagnetic state $\left\langle n_{p\uparrow}\right\rangle = \left\langle n_{p\downarrow}\right\rangle$, therefore,

$$\left\langle n_{p\uparrow}\right\rangle = \left(\left(\mathrm{e}^{\frac{E_1}{\theta}}+1\right)\left(1+\frac{1}{\mathrm{e}^{\frac{E_1}{\theta}}+1}-\frac{1}{\mathrm{e}^{\frac{E_3}{\theta}}+1}\right)\right)^{-1}. \tag{21}$$

We obtain the system of equations for numerical calculation of the equilibrium value of the lattice strain and the chemical potential

$$\overline{u} = \frac{1}{CV_0}\left(\frac{S}{aw}\ln\left|\frac{\mathrm{e}^{-b-a\Delta}+1}{\mathrm{e}^{-b+a\Delta}+1}\right| - \frac{BV_0}{2w^2}\int\limits_{-w}^{w}\frac{\varepsilon\mathrm{d}\varepsilon}{\mathrm{e}^{b+a\varepsilon}+1} - pV_0\right), \tag{22}$$

$$\langle n\rangle = -\frac{1}{aw}\ln\left|\frac{\mathrm{e}^{-b-a\Delta}+1}{e^{-b+a\Delta}+1}\right| + 2\left[\left(\mathrm{e}^{\frac{-\mu}{\theta}}+1\right)\left(1+\frac{1}{\mathrm{e}^{\frac{-\mu}{\theta}}+1}-\frac{1}{\mathrm{e}^{\frac{-\mu+u}{\theta}}+1}\right)\right]^{-1} \tag{23}$$

which allow us taking into account the external action effect on the system characteristics. With these calculated equilibrium values of lattice strain and chemical potential, we can obtain from (7) the energy gap for paramagnetic phase at integer band filling to interpret the phase diagram in Fig. 4 theoretically and study conditions of metal-to insulator transition (Fig. 6) at temperature or correlated hopping parameters changes, the external pressure application, etc.

In the case, when the Coulomb correlation parameter is much greater than the non-perturbed bandwidth, expressions for $A_1^{\uparrow}(\varepsilon)$ and $B_1^{\uparrow}(\varepsilon)$ can be expanded over parameter $\frac{\varepsilon}{U}$:

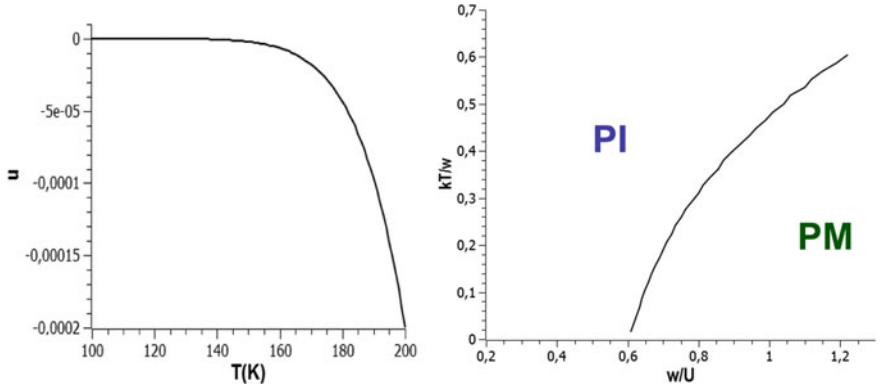

Fig. 6 In the left panel, the dependence of the equilibrium value of lattice strain on temperature is shown. In the right panel, theoretical phase diagram of the metal-to-insulator transition under temperature change or external pressure application is shown

$$A_1^{\uparrow}(\varepsilon) \cong 1 - \varepsilon_1^{\uparrow}\varepsilon_2^{\uparrow}\left(\frac{\varepsilon}{U}\right)^2,$$

$$B_1^{\uparrow}(\varepsilon) \cong \varepsilon_1^{\uparrow}\varepsilon_2^{\uparrow}\left(\frac{\varepsilon}{U}\right)^2$$

The energy spectrum takes the form

$$E_1(k) = -\mu + \varepsilon(1+\alpha u)t_k - \varepsilon_1\varepsilon_2\frac{((1+\alpha u)t_k)^2}{U} - \left(X^{\uparrow} + X^2\right)zJ, \tag{24}$$

$$E_2(k) = -\mu + U + \tilde{\varepsilon}(1+\alpha u)t_k + \varepsilon_1\varepsilon_2\frac{((1+\alpha u)t_k)^2}{U} - \left(X^{\uparrow} + X^2\right)zJ. \tag{25}$$

Neglecting all terms proportional to $\frac{\varepsilon}{U}$ one obtains a criterion for stabilization of ferromagnetic order at external pressure application

$$\frac{zJ}{4(1+\alpha u)w}(2-n) + \frac{1-n}{2-2n+n^2}\cdot\frac{\mu + nzJ}{(1+\alpha u)w} > 1 - \frac{n}{2-n}, \tag{26}$$

as a generalization of similar expressions, obtained in papers [51–55].

From the above expression, one can see that at small electron concentration ($n \to 0$) the criterion of ferromagnetism stabilization in absence of the external field reproduces one for weak Coulomb repulsion:

$$zJ > 2w.$$

And in the case of half-filled band, one reproduces the result of the mean-field method [52, 53]:

$$zJ > 0.$$

When the terms proportional to $\frac{\varepsilon}{U}$ are kept in expansion and relation $d \cong \frac{w^2}{24U}$ is taken into account, one obtains the correction to the mean-field result [54, 55]

$$zJ + \frac{w^2}{12U} > 0,$$

which accounts for short-range antiferromagnetic correlations (see [49] in this respect).

5 Antiferromagnetic Ordering in the Model

To exploit clarity of the two-pole approximation for determining condition of antiferromagnetic ordering stabilization, we restrict ourselves to the case of very low temperatures. In real compounds, there exist a region of superconductivity, which we do not consider here to be one of the competing phase. This restriction limits to some extent the usability of the following theoretical treatment, however, the analytical expression for chemical potential and sublattice magnetization calculation may still be of practical value for estimations at higher temperature. Using the procedure of decoupling for the Green function equations [49], we obtain the quasiparticle Green function as

$$\left\langle\left\langle X_s^{0\uparrow} | X_{s'}^{\uparrow 0}\right\rangle\right\rangle_{\vec{k}} = \frac{\left\langle X_s^0 + X_s^{\uparrow}\right\rangle}{2\pi}\left(\frac{A_{\vec{k}}^{\uparrow}}{E - E_1^{\uparrow}\left(\vec{k}\right)} + \frac{B_{\vec{k}}^{\uparrow}}{E - E_2^{\uparrow}\left(\vec{k}\right)}\right), \tag{27}$$

$$A_{\vec{k}}^{\uparrow} = \frac{1}{2}\left(1 - \frac{K^{\uparrow}}{\sqrt{\left(K^{\uparrow}\right)^2 + 4\alpha_s\alpha_p\left(t_{\vec{k}}'\right)^2}}\right), B_{\vec{k}}^{\uparrow} = 1 - A_{\vec{k}},$$

where (two-pole) energy spectrum is

$$E_{1,2}^{\uparrow}(\vec{k}) = -\mu + \frac{1}{2}\sum_x\left(\alpha_x^{\uparrow}t_{\vec{k}}(n) + \beta_x^{\uparrow}(\vec{k}) - C_x^{\uparrow}\right) \mp \frac{1}{2}\sqrt{\left(K^{\uparrow}\right)^2 + 4\alpha_s\alpha_p\left(t_{\vec{k}}'\right)^2}, \tag{28}$$

x numbers lattice sites p or s which belongs either to spin-up or to spin-down sublattices,

$$K^{\uparrow} = (\alpha_s^{\uparrow} - \alpha_p^{\uparrow})t_{\vec{k}}(n) + \beta_s^{\uparrow} - \beta_p^{\uparrow} - C_s^{\uparrow} + C_p^{\uparrow},$$

$$C_x^{\uparrow} = z_1 J \lambda_x^{\uparrow} + \frac{1}{2} z_2 J' \lambda_x + z_1 \tilde{J} \tilde{\lambda}_x^{\uparrow} + \frac{1}{2} z_2 \tilde{J}' \tilde{\lambda}_x,$$

α_x^{σ} and $\alpha_x^{\prime\sigma}$ are correlation subband narrowing factors and $\beta_x^{\sigma}\left(\vec{k}\right)$ are spin-dependent shifts of subband centers. Magnitudes of the correlation narrowing factors α_x^{σ} та $\alpha_x^{\prime\sigma}$, as well as parameters λ_x^{σ}, $\lambda_x^{\prime\sigma}$, λ_x^{σ}, $\tilde{\lambda}_x^{\prime\sigma}$ can be obtained using the quasiclassical approximation for calculation of averages of $\left\langle X_s^{\downarrow\uparrow} X_j^{\uparrow\downarrow} \right\rangle$-type, if we chose for $\left\langle X_s^{\sigma} \right\rangle$ expressions, characteristic for the studied type of magnetic ordering. In every case, the spin-dependent shifts of the subband centers $\beta_x^{\sigma}(\vec{k})$ are to be calculated self-consistently.

$$\alpha_s^{\uparrow} = \left\langle X_s^0 + X_s^{\uparrow} \right\rangle + \frac{\left\langle X_s^{\downarrow\uparrow} X_j^{\uparrow\downarrow} \right\rangle}{\left\langle X_j^0 + X_j^{\uparrow} \right\rangle},$$

$$\alpha_s = \left\langle X_s^0 + X_s^{\uparrow} \right\rangle + \frac{\left\langle X_s^{\downarrow\uparrow} X_l^{\uparrow\downarrow} \right\rangle}{\left\langle X_l^0 + X_l^{\uparrow} \right\rangle},$$

$$\beta_s^{\uparrow} = -\frac{1}{\left\langle X_s^0 + X_s^{\uparrow} \right\rangle} \sum_j t_{sj}(n) \left\langle X_s^{0\downarrow} X_j^{\downarrow 0} \right\rangle,$$

$$\alpha_p^{\uparrow} = \left\langle X_p^0 + X_p^{\uparrow} \right\rangle + \frac{\left\langle X_p^{\downarrow\uparrow} X_r^{\uparrow\downarrow} \right\rangle}{\left\langle X_r^0 + X_r^{\uparrow} \right\rangle},$$

$$\alpha_p^{\prime\uparrow} = \left\langle X_p^0 + X_p^{\uparrow} \right\rangle + \frac{\left\langle X_p^{\downarrow\uparrow} X_i^{\uparrow\downarrow} \right\rangle}{\left\langle X_i^0 + X_i^{\uparrow} \right\rangle},$$

$$\beta_p^{\uparrow} = -\frac{1}{\left\langle X_p^0 + X_p^{\uparrow} \right\rangle} \sum_r t_{pr}(n) \left\langle X_p^{0\vee} X_r^{\vee 0} \right\rangle,$$

$$\lambda_s^{\uparrow} = \left\langle X_j^{\uparrow} \right\rangle + \frac{\left\langle X_j^{\downarrow\uparrow} X_s^{\uparrow\downarrow} \right\rangle}{\left\langle X_s^0 + X_s^{\uparrow} \right\rangle}, \quad \lambda_s^{\hat{\prime}} = \left\langle X_l^{\uparrow} \right\rangle + \frac{\left\langle X_l^{\downarrow\uparrow} X_s^{\uparrow\downarrow} \right\rangle}{\left\langle X_s^0 + X_s^{\uparrow} \right\rangle},$$

$$\tilde{\lambda}_s^{\uparrow} = \left\langle X_j^{\downarrow} \right\rangle + \frac{\left\langle X_j^{\downarrow\uparrow} X_s^{\uparrow\downarrow} \right\rangle}{\left\langle X_s^0 + X_s^{\uparrow} \right\rangle}, \quad \tilde{\lambda}_s^{\uparrow} = \left\langle X_l^{\downarrow} \right\rangle + \frac{\left\langle X_l^{\downarrow\uparrow} X_s^{\uparrow\downarrow} \right\rangle}{\left\langle X_s^0 + X_s^{\uparrow} \right\rangle},$$

$$\tilde{\lambda}_p^{\uparrow} = \left\langle X_r^{\downarrow} \right\rangle + \frac{\left\langle X_r^{\downarrow\uparrow} X_p^{\uparrow\downarrow} \right\rangle}{\left\langle X_p^0 + X_p^{\uparrow} \right\rangle}, \quad \tilde{\lambda}_p^{\hat{\prime}} = \left\langle X_i^{\downarrow} \right\rangle + \frac{\left\langle X_i^{\downarrow\uparrow} X_p^{\uparrow\downarrow} \right\rangle}{\left\langle X_p^0 + X_p^{\uparrow} \right\rangle}.$$

If in these expressions the averages for a particular phase of interest are substituted, then the energy spectra for different kinds of antiferromagnetic ordering are obtained. In particular, for paramagnetic case

$$\langle X_s^\sigma \rangle = \langle X_i^\sigma \rangle = \langle X_j^\sigma \rangle = \langle X_p^\sigma \rangle = \langle X_l^\sigma \rangle = \langle X_r^\sigma \rangle = \frac{n}{2},$$

for ferromagnetic state

$$\langle X_s^\sigma \rangle = \langle X_i^\sigma \rangle = \langle X_j^\sigma \rangle = \langle X_p^\sigma \rangle = \langle X_l^\sigma \rangle = \langle X_r^\sigma \rangle = \frac{n + \eta_\sigma m}{2},$$

for ferromagnetic ordering within the plane and antiferromagnetically ordered planes one has

$$\langle X_s^\sigma \rangle = \langle X_i^\sigma \rangle = \langle X_j^\sigma \rangle = \frac{n + \eta_\sigma m}{2},$$
$$\langle X_p^\sigma \rangle = \langle X_l^\sigma \rangle = \langle X_r^\sigma \rangle = \frac{n - \eta_\sigma m}{2}.$$

If antiferromagnetic ordering within planes stabilizes simultaneously with ferromagnetically ordered neighbors from the adjacent planes

$$\langle X_s^\sigma \rangle = \langle X_i^\sigma \rangle = \langle X_p^\sigma \rangle = \langle X_l^\sigma \rangle = \frac{n + \eta_\sigma m}{2},$$
$$\langle X_j^\sigma \rangle = \langle X_r^\sigma \rangle = \frac{n - \eta_\sigma m}{2}.$$

For checkerboard antiferromagnetic phase

$$\langle X_s^\sigma \rangle = \langle X_i^\sigma \rangle = \langle X_r^\sigma \rangle = \frac{n + \eta_\sigma m}{2},$$
$$\langle X_p^\sigma \rangle = \langle X_l^\sigma \rangle = \langle X_j^\sigma \rangle = \frac{n - \eta_\sigma m}{2}.$$

If for calculation of averages $\left\langle X_i^{\downarrow\uparrow} X_j^{\uparrow\downarrow} \right\rangle$ a quasiclassical approximation [54] is used, we obtain for antiferromagnetic state under consideration

$$\alpha_i^\sigma = \alpha_i'^\sigma = \frac{(2 - n + \eta_\sigma \eta_i m)^2 + n^2 - m^2}{(2 - n + \eta_\sigma \eta_i m)},$$
$$\beta_i^\sigma = \frac{w(n)(1 - n)(n - \eta_\sigma \eta_i m)}{2 - n + \eta_\sigma \eta_i m},$$
$$\lambda_s^\sigma = \lambda_s^\sigma = \tilde{\lambda}_p^\sigma = \tilde{\lambda}_p^\sigma = \frac{n - \eta_\sigma m}{2} + \frac{1}{2} \cdot \frac{n^2 - m^2}{2 - n + \eta_\sigma m},$$
$$\lambda_p^\sigma = \lambda_p^\sigma = \tilde{\lambda}_s^\sigma = \tilde{\lambda}_s^\sigma = \frac{n + \eta_\sigma m}{2} + \frac{1}{2} \cdot \frac{n^2 - m^2}{2 - n + \eta_\sigma m},$$

with $\eta_s = 1$ and $\eta_p = -1$. In these expressions $w_{||}(n) = z_1|t_{ij}(n)|$, n denotes electron concentration and m stands for the sublattice magnetization.

Transition to the antiferromagnet phase in a system with spectrum (28) is related to the gap opening in the spectrum, where square root depends on the magnetization, thus on temperatures. For concentration of electrons of spin-projection σ, application of model rectangular DOS results in

$$n_{s\sigma} = \frac{\langle X_s^0 + X_s^\sigma \rangle}{2w} \times \int_{-w}^{w} \left(\frac{A_\varepsilon^\sigma}{\exp(E_1^\sigma / kT) + 1} + \frac{B_\varepsilon^\sigma}{\exp(E_2^\sigma / kT) + 1} \right) d\varepsilon. \quad (29)$$

This formula allows us obtaining conditions for chemical potential calculation $n_{s\uparrow} + n_{s\downarrow} = n$, as well as magnetization $n_{s\uparrow} + n_{s\downarrow} = m$. For a uniform ferromagnet, one can represent combinations of parameters by a product in which at least one multiplier does not depend on the magnetization sign:

$$\begin{aligned}
\alpha_s^\sigma - \alpha_p^\sigma &= \eta_\sigma m \left(1 - \frac{n^2 - m^2}{(2-n)^2 - m^2}\right), \\
\alpha_s^\sigma + \alpha_p^\sigma &= (2-n)\left(1 + \frac{n^2 - m^2}{(2-n)^2 - m^2}\right), \\
\beta_s^\sigma - \beta_p^\sigma &= -4\eta_\sigma m \frac{w(1-n)}{(2-n)^2 - m^2}, \\
\beta_s^\sigma + \beta_p^\sigma &= 2w(1-n)\frac{n(2-n) + m^2}{(2-n)^2 - m^2}, \\
C_s^\sigma - C_p^\sigma &= \eta_\sigma m \left(z_1(J - \tilde{J}) + \frac{z_2}{2}(J' - \tilde{J}')\right), \\
C_s^\sigma + C_p^\sigma &= \eta_\sigma m \left(z_1(J + \tilde{J}) + \frac{z_2}{2}(J' + \tilde{J}')\right), \\
\alpha_s \alpha_p &= \frac{((2-n)^2 + n^2)^2 - 4m^2(2-n)^2}{4((2-n)^2 - m^2)}.
\end{aligned}$$

Therefore, we obtain $K^\sigma = \eta_\sigma m L$, where

$$\begin{aligned}
L &= \left(1 - \frac{n^2 - m^2}{(2-n)^2 - m^2}\right) t_{\vec{k}} - \frac{4w(1-n)}{(2-n)^2 - m^2} + zJ_{eff}, \\
zJ_{eff} &= z_1(J - \tilde{J}) + z_2(J' - \tilde{J}')/2 < 0,
\end{aligned}$$

and z_1 is the number of the nearest neighbors in plane, z_2—in adjacent plane.

The system of equations for magnetization and chemical potential may be represented as

$$m = \frac{m}{4w} \int_{-w}^{w} d\varepsilon (f(E_1) + f(E_2)) - \frac{m(2-n)}{4w} \int_{-w}^{w} \mathrm{d}\varepsilon \frac{L(\varepsilon)}{\sqrt{D}} (f(E_1) - f(E_2)),$$

$$n = \frac{2-n}{2wn}\int_{-w}^{w} \mathrm{d}\varepsilon (f(E_1)+f(E_2)) - \frac{m^2(2-n)}{4w}\int_{-w}^{w} \mathrm{d}\varepsilon \frac{L(\varepsilon)}{\sqrt{D}}(f(E_1)-f(E_2)), \tag{30}$$

here $\sqrt{D} = \sqrt{\left(K_\varepsilon^\sigma\right)^2 + 4\alpha_s'^\sigma \alpha_p'^\sigma g^2\varepsilon^2}$, $f(E) = 1/(\exp(E/kT)+1)$. For small anisotropy parameters $g^2 << 1$, one may use expansion

$$\left(1+\frac{4\alpha_s'^\sigma \alpha_p'^\sigma g^2\varepsilon^2}{\left(K_\varepsilon^\sigma\right)^2}\right)^{-\frac{1}{2}} = 1 - \frac{2\alpha_s'^\sigma \alpha_p'^\sigma g^2\varepsilon^2}{\left(K_\varepsilon^\sigma\right)^2},$$

then

$$A_\varepsilon^\sigma = \frac{\alpha_s'^\sigma \alpha_p'^\sigma g^2\varepsilon^2}{\left((\alpha_s^\sigma - \alpha_{ps}^\sigma)\varepsilon + \beta_s^\sigma - \beta_p^\sigma - \left(C_s^\sigma - C_p^\sigma\right)\right)^2}.$$

From expression (30), one can calculate the sublattice magnetization as a function of temperature, external pressure and model parameters, and from the condition $m(T) \to 0$ one can obtain an equation for Neel temperature. This equation is to be supplemented with the equation for chemical potential

$$\frac{2n}{2-n} = 2 - \frac{\Theta_N}{\alpha_1 w}\ln\left(\frac{\exp\left(\frac{\mu}{\Theta_N}\right)+\exp\left(\frac{\alpha_1 w}{\Theta_N}\right)}{\exp\left(\frac{\mu}{\Theta_N}\right)+\exp\left(-\frac{\alpha_1 w}{\Theta_N}\right)}\right) - \frac{\Theta_N}{\alpha_2 w}\ln\left(\frac{\exp\left(\frac{\mu}{\Theta_N}\right)+\exp\left(\frac{\alpha_2 w}{\Theta_N}\right)}{\exp\left(\frac{\mu}{\Theta_N}\right)+\exp\left(-\frac{\alpha_2 w}{\Theta_N}\right)}\right) \tag{31}$$

where $\Theta_N = kT_N$, $\mu^* = \mu - \beta^* + C^*$,

$$\alpha_{1,2} = (1 \mp g)\frac{2-2n+n^2}{2-n},$$
$$\beta^* = \frac{w(1-n)n}{2-n},$$
$$C^* = \frac{n}{2}\left(z_1\left(J+\tilde{J}\right) + z_2\left(J'+\tilde{J}'\right)\Big/2\right).$$

Though there is no estimations for correlated hopping parameters from electron wave functions overlap for BEDT-TTF molecules available in literature, one may take reasonable set of parameters to characterize general tendencies. From Fig. 7, we conclude that the present model has a potential to describe onset of antiferromagnetic ordering at decrease of temperature and its destabilization by the applied pressure,

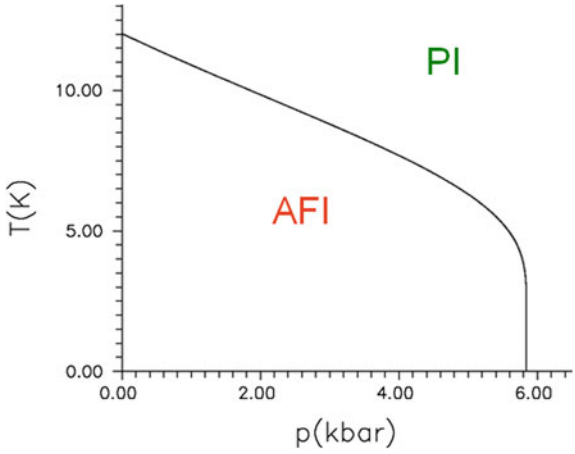

Fig. 7 Theoretical phase diagram of antiferromagnetic insulator–paramagnetic insulator transition at model parameters $zJ_{\text{eff}}/w = 0.25$, $g = 0.1$, $\alpha = 0.02$

which also induces metallization. The present model also has the additional degree of freedom, namely the correlated hopping parameter, to account for peculiarities of particular type of anion in BEDT-TTF two-dimensional molecular conductor.

6 Conclusions

Compounds with bis(ethylenedithio)tetrathiafulvalene molecules are prominent examples of quasi-2D systems with strong electron interactions. Conductance of these systems is strongly anisotropic, and resistivity in direction transversal to BEDT-TTF molecule plane is much greater of that in planes. For theoretical modeling of electronic properties of the noted compound the model [24], which contains four different transfer integrals for different direction in the plane, which is, in our opinion, an overdetalization. For adequate description of phase transition and anisotropy of the compounds under consideration, it suffices to introduce two distinct hopping integrals. In such a simplified effective model, standard approaches of strongly correlated electron system theories prove to work well, and the decisive role belongs to intra-atomic Coulomb correlation parameter and electron hopping anisotropy parameter. For consistent description of electron correlations and correlated hopping of electrons, we have used the configurational representation of the microscopic model with taking into account translation processes with nearest-neighbors and next-nearest-neighbors hopping parameters between $(\text{BEDT-TTF})_2$ complexes dependent on the applied external pressure or doping of anion subsystem as well as intra- and intersite Coulomb interactions and intersite exchange interaction. The projection procedure allows consistent description of the metal-insulator transitions as well as stabilization of magnetic orderings in the generalized Hubbard model (with electron-hole asymmetry).

Concentration dependence induced by the correlated hopping allows qualitative interpretation of the fact that electron interactions in κ-phase have greater effect than in α-phase of BEDT-TTF family. In the phase diagram, application of the external pressure is equivalent to the composition changes (chemical pressure), which leads to the change of conduction bandwidth. Therefore, taking into account the correlated hopping of electrons is important for the correct interpretation of experimental results on the basis of theoretical models of electronic subsystem of quasi-two-dimensional organic conductor.

References

1. Powell BJ, McKenzie RH (2006) Strong electronic correlations in superconducting organic charge transfer salts. J Phys: Condens Matter 18:R827–R866
2. Scriven E, Powell BJ (2009) Toward the parametrization of the Hubbard model for salts of bis(ethylenedithio)tetrathiafulvalene: a density functional study of isolated molecules. J Chem Phys 130:104508
3. Ivanov VA, Ugolkova EA, Zhuravlev ME (1998) Electronic structure and superconductivity of κ-(BEDT-TTF)2X salts. Zh Eksp Teor Fiz 113:715–733
4. Lebed AG (2008) The physics of organic superconductors and conductors. Springer series in materials science, vol110. Springer, Berlin, Heidelberg
5. Skorenkyy Yu, Kramar O (2006) Energy spectrum of the organic quasi-1D conductors with NNN and correlated hopping. Condens Matter Phys 9:161–168
6. Skorenkyy Yu, Kramar O (2016) Antiferromagnetic ordering and pseudogap in a model of quasi-1D organic superconductor electronic subsystem. Mol Cryst Liq Cryst 639:24–32
7. Kubo K, Miyasaka H, Yamashita M (2010) Crystal structure and electrical conductivity of α"'-[BEDT-TTF.12[Cu2Br 4.3 (BEDT-TTF = bis(ethylenedithio)tetrathiafulvalene). Physica B 405:S308–S312
8. Ishiguro T, Yamaji K, Saito G (1998) Organic superconductors. Springer series in solid-state sciences, vol 88. Springer, Berlin
9. Commeau B, Geilhufe RM, Fernando G, Balatsky AV (2017) Structural and electronic properties of α-(BEDT-TTF)$_2$I$_3$, β-(BEDT-TTF)$_2$I$_3$, and κ-(BEDT-TTF)$_2$X$_3$ (X = I, F, Br, Cl) organic charge transfer salts. Phys Rev B 96:125135
10. Momma K, Izumi F (2011) VESTA 3 for three-dimensional visualization of crystal, volumetric and morphology data. J Appl Crystallogr 44:1272–1276
11. Ito H et al (2005) Charge carriers in the divalent conductor (BEDT-TTF)Cu2Br 4. Phys Rev B 71:085202
12. Maesato M, Kaga Y, Kondo R, Kagoshima S (2001) Control of electronic properties of α − (BEDT − TTF)2MHg(SCN)4 (M = K, NH4) by the uniaxial strain method. Phys Rev B 64:155104
13. Pratt FL et al (1992) Magnetotransport and Fermi-surface topology of [bis(ethylenedithio)tetrathiafulvalene.$_2$KHg(SCN)$_4$. Phys Rev B 63:13904–13912
14. Choi ES et al, Magnetothemopower study of quasi two-dimensional organic conductor -(BEDT-TTF) KHg(SCN). Phys Rev B 65:205119
15. Tanatar MA et al (2002) Pressure-temperature phase diagram of the organic superconductor κ − (BEDT − TTF)2Cu[N(CN)2.I. Phys Rev B 65:064516
16. Miyazaki A et al (1997) Phase transition of (BEDT-TTF)$_3$(HSO$_4$)$_2$. Phys Rev B 55:6847–6855
17. Sasaki T et al (2004) Electronic correlation in the infrared optical properties of the quasi-two-dimensional κ-type BEDT-TTF dimer system. Phys Rev B 69:064508
18. Sekiyama A et al (1997) High-resolution photoemission study of metallic, insulating, and superconducting BEDT-TTF salts. Phys Rev B, 56:9082–9090

19. Kawamoto A, Honma Y, Kumagai K (2004) Electron localization in the strongly correlated organic system κ-(BEDT-TTF)$_2$X probed with nuclear magnetic resonance. Phys Rev B 70:060510
20. Larkin MI et al (2001) Pressure dependence of the magnetic penetration depth in κ-(BEDT-TTF)$_2$Cu(NCS)$_2$. Phys Rev B 64:144514
21. Kanoda K (1997) Electron correlation, metal-insulator transition and superconductivity in quasi-2D organic systems, (ET)2X. Phys C 282–287:299–302
22. Yong-Nian Xu, Ching WY, JeanY C, Lou Y (1995) First-principles calculation of the electronic and optical properties of the organic superconductor κ-(BEDT-TTF)$_2$Cu(NSC)$_2$. Phys Rev B 52:12946–12950
23. Hofstetter W, Vollhardt D (1998) Frustration of antiferromagnetism in the *t-t'*-Hubbard model at weak coupling. Cornell University Library. E-print cond-mat/9802233
24. Kino H, Fukuyama H (1996) Phase diagram of two-dimensional organic conductors (BEDT-TTF)$_2$X. J Phys Soc Jpn 65:215821–215869
25. Demiralp E, Goddard WA (1997) Conduction properties of the organic superconductor κ-(BEDT-TTF)$_2$Cu(NCS)$_2$ based on Hubbard-unrestricted-Hartree-Fock band calculations. Phys Rev B 56:11907–11919
26. McKenzie R (1998) A strongly correlated electron model for the layered organic superconductors κ-(BEDT-TTF)$_2$X. Comments Cond Matt Phys 18:309–328
27. Didukh L, Skorenkyy Yu, Dovhopyaty Yu, Hankevych V (2000) Metal-insulator transition in a doubly orbitally degenerate model with correlated hopping. Phys Rev B 61:7893–7908
28. Skorenkyy Yu et al (2007) Mott transition, ferromagnetism and conductivity in the generalized Hubbard model. Acta Phys Pol, A 111:635–644
29. Didukh L, Skorenkyy Yu, Kramar O (2008) Electron correlations in narrow energy bands: modified polar model approach. Condens Matter Phys 11:443–454
30. Parcollet O, Biroli G, Kotliar G (2004) Cluster dynamical mean field analysis of the Mott transition. Phys Rev Lett 92:226402
31. Kuroki K, Aoki H (1999) Superconductivity and spin correlation in organic conductors: a quantum Monte Carlo study. Phys Rev B 60:3060–3063
32. Skorenkyy Y, Kramar O, Didukh L, Dovhopyaty Y (2018) Electron correlation effects in theoretical model of doped fullerides. In: Fesenko O, Yatsenko L (eds) Nanooptics, nanophotonics, nanostructures, and their applications. NANO 2017. Springer proceedings in physics, vol 210. Springer, Cham
33. Skorenkyy Y (2019) Phase transitions in a model of BEDT-TTF compound electron subsystem. Mater Today: Proc https://doi.org/10.1016/j.matpr.2019.10.164
34. Gebhard F (1997) The Mott metal-insulator transition: models and methods. Springer, Berlin
35. Georges A, Kotliar G, Krauth W, Rozenberg M (1996) Dynamical mean-field theory of strongly correlated fermion systems and limit of infinite dimensions. Rev Mod Phys 68:13–125
36. Anderson PW (1961) Localized magnetic states in metals. Phys Rev 124:41–53
37. Georges A, Krauth W (1993) Physical properties of the half-filled Hubbard model in infinite dimensions. Phys Rev B 48:7167–7182
38. Kajueter H, Kotliar G, Moeller G (1996) Doped Mott insulator: results from mean-field theory. Phys Rev B. 53:16214–16226
39. Pruschke Th, Kox DL, Jarrell M (1993) Hubbard model at infinite dimensions: thermodynamics and transport properties. Phys Rev B. 47:3553–3565
40. Zhang XY, Rozenberg M, Kotliar G (1993) Mot transition in the $d\to\infty$ Hubbard model at zero temperature. Phys Rev Lett 70:1666–1669
41. Caffarel M, Krauth W (1994) Exact diagonalization approach to correlated fermions in infinite dimensions: Mott transition and superconductivity. Phys Rev Lett 72:1545–1548
42. Noack RM, Gebhard F (1999) Mott-Hubbard transition in infinite dimensions. Phys Rev Lett 82:1915–1918
43. Bulla R (1999) Zero temperature metal-insulator transition in the infinite dimensional Hubbard model. Phys Rev Lett 83:136–139

44. Górski G, Mizia J, Kucab K (2014) New Green's function approach describing the ferromagnetic state in the Hubbard model with correlated hopping. Physica Status Solidi (B) 251:2294–2301
45. Górski G, Mizia J, Kucab K (2016) Modified equation of motion approach for metallic ferromagnetic systems with the correlated hopping interaction. Physica Status Solidi (B) 253:1202–1209
46. Górski G, Kucab K (2018) Effect of assisted hopping on spin-dependent thermoelectric transport through correlated quantum dot. Physica B 545:337–345
47. Górski G, Mizia J, Kucab K (2019) Influence of assisted hopping interaction on the linear conductance of quantum dot. Physica E 111:190–200
48. Kramar O, Skorenkyy Yu, Dovhopyaty Yu (2019) Effective masses of carriers in the degenerate conduction band: interplay of density of electronic states peculiarities and magnetization. J Nano-Electron Phys 11:05030(6)
49. Didukh L, Skorenkyy Yu (2000) Electron correlations in narrow energy bands: ground state energy and metal-insulator transition. Cond Matt Phys 3:787–798
50. Didukh L, Skorenkyy Yu, Kramar O, Dovhopyaty Yu (2006) Effect of magnetic field, pressure and correlated hopping of electrons on conductivity of Mott-Hubbard material. Physica B 378–380:321–322
51. Didukh L, Skorenkyy Yu, Hankevych V, Kramar O (2001) Ground state ferromagnetism in a doubly orbitally degenerate model. Phys Rev B 64:144428
52. Didukh L, Hankevych V, Kramar O, Skorenkyy Yu (2002) Itinerant ferromagnetism of systems with orbital degeneracy. J Phys: Condens Matter 14:827–835
53. Didukh L, Kramar O (2002) Metallic ferromagnetism in a generalized Hubbard model. Fizika Nizkikh Temperatur (Kharkov) 28:42–50
54. Didukh L, Kramar O, Skorenkyy Y (2002) Ground state energy of metallic ferromagnet in a generalized Hubbard model. Physica Status Solidi (B) 229:1241–1254
55. Didukh L, Kramar O (2005) Metallic ferromagnetism in the systems with strongly correlated electrons. Condens Matter Phys 8:547–564

Modeling Self-organization of Adsorbate at Chemical Vapor Deposition in Accumulative Ion Plasma Devices

Vasyl O. Kharchenko and Alina V. Dvornichenko

1 Introduction

Thin film presents a layer of any material with a thickness from one atomic layer (several angstroms) to several micrometers. Nowadays, nano-structured thin films are used as an integral part of modern technology, having applications in modern microelectronics and miniature devices [1]. They are exploited in a wide range of applications, for example, optical and decorative coatings and solar cells, or as diffusion layers in integrated circuits. During preparation of thin films, its morphology and the corresponding microstructure depend on the growing temperature, type of substrate and growing conditions that defines properties of thin films [2]. The bounding between deposited atoms and between adatom and substrate defines the growth scenarios: two-dimensional layer-by-layer growth (Frank–van der Merve model); three-dimensional island growth (Volmer–Weber model); and mixed growth scenario (Stranski–Krastanov model) [3]. For the case of the two-dimensional growth, the bonding between adatoms and substrate is stronger than the bonding between adatoms. In the opposite case, adatoms are able to construct three-dimensional structures. These islands grow during exposing in both lateral direction and direction normal to the surface and coalesce. In the mixed growth scenario for the adatoms on first several layers counted from substrate, the bonding between adatoms and substrate is stronger leading to layer-by-layer growth of one or two layers. Then, bonding between adatoms on a fully covered layer leads to self-organization of adatoms into islands. Adsorbate structures attain much attention fields of electronics, semiconductors, biomagnetics and magnetism [4–7].

The growth of thin film can be carried out by chemical or physical vapor deposition [1, 8]. In the first case, chemical reactions precede deposition and the chemical

V. O. Kharchenko (✉)
Institute of Applied Physics, National Academy of Sciences of Ukraine,
58 Petropavlovskaya St., Sumy 40000, Ukraine
e-mail: vasiliy@ipfcentr.sumy.ua

A. V. Dvornichenko
Sumy State University, 2 Rimskii-Korsakov St., Sumy 40007, Ukraine
e-mail: alina.dvorni4enko@ukr.net

O. Fesenko and L. Yatsenko (eds.), *Nanooptics and Photonics, Nanochemistry and Nanobiotechnology, and Their Applications*, Springer Proceedings in Physics 247, https://doi.org/10.1007/978-3-030-52268-1_8

bonding state of the deposit is different from the precursor gases; in the second case, the material from a vapor is deposited by physical means. Among them, one can issue sol-gel synthesis [9, 10], electron beam deposition [11], sputtering [12], pulsed laser deposition [13], ultrasonic spray pyrolysis [14–17] and spray deposition [18]. These techniques are used to produce ordered pattern of vacancies inside adsorbate matrix [19], elongated adsorbate structures [20, 21] and nano-dots [22, 23].

Plasma-condensate devices serve a useful technique to produce separated adsorbate islands with small linear size. There ions, sputtered by magnetron, attain growing surface, located in a hollow cathode, and become adatoms. At the same time, a presence of the electric field can induce desorption of adatoms, their additional ionization and finally their adsorption on the high layers of multi-layer growing surface [24]. Such anisotropy in transferring of adatoms between layers with preferential bottom-up motion can be controlled by the strength of the electrical field. These systems were mostly studied in the framework of experimental methods [24, 25], where three-dimensional adsorbate islands are characterized by hundred nanometers in a linear size.

Processes of thin-film growth with the nano-sized adsorbate islands cannot always be easily studied experimentally. In order to perform a comprehensive study detail of dynamics of self-organization of adatoms into cluster, one exploits numerical simulations [26]. In theoretical studies, the authors deal with the reaction–diffusion models by taking into account adsorption, desorption and diffusion of adatoms [27–32]. These studies allow one to predict a change in the surface morphology type and linear size of surface structures by varying deposition conditions [33–36].

In this work, we will construct the accurate model, describing spatiotemporal evolution adsorbate concentration on an intermediate layer of multi-layer plasma-condensate system. We will take into account the anisotropic bottom-up motion of adatoms between layers induced by the electric field near substrate. We will discuss first-order phase transitions in homogeneous system, define values of main system parameters, reduced to adsorption rate, proportional to the pressure inside a chamber, interaction strength (energy) between adatoms and anisotropy strength, proportional to the strength of the electrical field, when the growing surface will characterized by the stable surface structures. In the framework of numerical simulations, we will discuss dynamics of pattern formation and a possibility to control the morphology of the growing surface, type and linear size of surface structures during condensation.

The chapter is organized as follows. In the next section, we construct the one-layer model for the adsorbate evolution on the intermediate layer by deriving the functional dependence of the adsorbate concentration on neighbor layers on the concentration on the current layer. In Sect. 3, we consider the homogeneous system and discuss a possibility of first-order phase transition realization. In Sect. 4, we perform stability analysis in order to define ranges of the main system parameters, when pattern formation is possible. Numerical simulation of the self-organization of adsorbate will be done in Sect. 5, where we discuss a possibility of control, a surface morphology and statistical properties of the surface structures. In Sect. 6, we construct three-dimensional Volmer–Weber islands from obtained two-dimensional patterns and estimate obtained results. We conclude in the last section.

2 Mathematical Model

To provide theoretical studies of processes of adsorbate island formation at condensation, we will monitor the dimensionless concentration of adsorbate x on each nth layer of multi-layer system. We will define it in the unit cell with the linear size ℓ on each nth layer as the ratio between a number of adsorbed particles in the each unit cell N_{ap} and possible sites for adsorption N_{ps}, $x_n \equiv N_{ap}/N_{ps}$, giving $x_n(\mathbf{r}, t) \in [0, 1]$ in each unit cell on each nth layer; $\mathbf{r} = \{x, y\}$ is the space coordinate, and t is the time variable. We will consider the system with N total number of layers, $n = 1 \ldots N$, which is continuous in the horizontal direction (parallel to the substrate) and discrete in vertical direction. We will exploit the reaction–diffusion model for the adsorbate concentration on each nth layer of multi-layer system in the standard form:

$$\partial_t x_n(\mathbf{r}, t) = R(x_n(\mathbf{r}, t)) - \nabla \cdot \mathbf{J}(x_n(\mathbf{r}, t), \nabla). \tag{1}$$

The first term in the right-hand side of (1) corresponds to the quasi-chemical reactions on the nth layer, $R(x_n(\mathbf{r}, t)) = R_a + R_d + R_t$, describing adsorption R_a, desorption R_d and transference of adatoms between layers R_t. The second term, $\mathbf{J}(x_n(\mathbf{r}, t), \nabla)$, describes the lateral diffusion of adsorbate on the nth layer; $\nabla = \partial/\partial_{\mathbf{r}}$. Ions from a plasma can attach the surface (substrate or any layer) and become adatoms with the adsorption coefficient $k_a = \nu p \mathrm{e}^{-Ea/T}$, defined through the frequency factor ν, pressure inside a chamber p, activation energy for adsorption Ea and temperature T, which is scaled here in energetic units. For the adsorption in each unit cell on the nth layer here should be free cites for adsorption on the current layer, free cites on the up $(n + 1)$th layer and a presence of adsorbate on the $(n - 1)$th layer, serving a substrate for adsorption. Therefore, for the adsorption term one has $R_a = k_a x_{n-1}(1 - x_n)(1 - x_{n+1})$. Adatoms can desorb back to the plasma from the layer with the desorption coefficient $k_d = k_d^0 \exp(U_n(\mathbf{r})/T)$. Here, $k_d^0 = \nu \mathrm{e}^{-Ed/T}$ corresponds to the desorption coefficient of non-interacting adatoms and relates to the lifetime of adatoms: $\tau_d = [k_d^0]^{-1}$; Ed is the activation energy for desorption. The interaction potential of adsorbate $U_n(\mathbf{r})$ gives a correction of desorption coefficient due to interaction-induced localization of adatoms. Desorption processes require free cites on the up $(n + 1)$th layer and nonzero adsorbate concentration on the precursor layer, giving: $R_d = -k_d^0 x_n x_{n-1}(1 - x_{n+1}) \exp(U_n(\mathbf{r})/T)$.

Processes of transferring of adatoms between neighbor layers R_t are possible onto free cites only. For the isotropic systems, one gets the standard vertical diffusion, $R_t^0 = k_\updownarrow [x_{n+1} + x_{n-1} - 2x_n]$, defined by the diffusion coefficient $k_\updownarrow$. In ion plasma devices, a transference of adatoms between layers is anisotropical due to the presence of the electrical field near substrate. Here, some part of adatoms can desorb back to plasma, ionized there and adsorb on the high layers of the growing surface [24]. Such process can be represented as induced by electrical field bottom-up motion of adatoms from lower layers toward upper layers. These processes are characterized by the rate k_E, which is proportional to the electrical field strength $|\mathbf{E}|$. Therefore, the

transference of adatoms between neighbor layers is described by the reaction term: $R_t = R_t^0 + k_E[x_{n-1}(1-x_n) - x_n(1-x_{n+1})]$.

Next, let us define the mathematical model for the lateral diffusion flux of adsorbate on each nth layer $\mathbf{J}(x_n(\mathbf{r},t),\nabla)$. This flux contains the standard diffusion part $\mathbf{J}_0 = -k_{\leftrightarrow}\nabla x_n$, with the diffusion coefficient $k_{\leftrightarrow} = D_0 e^{-E_D/T}$, defined through the prefactor $D_0 = a^2\nu$ with the lattice constant a and the activation energy for diffusion $E_D \simeq Ea/3$. Interaction of adatoms with the potential U_n induces the flux $(k_{\leftrightarrow}/T)F_n x_n$, defined by the force $F_n = -\nabla U_n$, affecting adatom. Therefore, the total adsorbate flux on nth layer is defined by the equation:

$$\mathbf{J} = -k_{\leftrightarrow}[\nabla x_n + T^{-1}x_n(1-x_n)\nabla U_n]. \tag{2}$$

According to the self-consistent approximation, one can represent the interaction potential U_n through the binary attractive potential $u_n(r-r')$ in the following way: $U_n = x_{n-1}\left\{-\int u_n(r-r')x_n(r')\mathrm{d}r'\right\}$ [34, 35, 37]. Here, $x_0 = 1$ represents the substrate, the integration is provided over the whole layer and the interactions are assumed to be mediated by the precursor layer. The binary interaction potential $u(r)$ we choose in the symmetrical form with the property $\int r^{2n+1}u(r)\mathrm{d}r = 0$. As a simplest approximation, we use the Gaussian form: $u(r) = 2\varepsilon[4\pi r_0^2]^{-1/2}\exp\left(-r^2/(4r_0^2)\right)$, defined through the interaction energy of adsorbate ε and the interaction radius r_0. By taking into account that the concentration of adsorbate evolves much slow than $u(r)$ on a distance of interaction radius, one can put: $\int u(\mathbf{r}-\mathbf{r}')x_n(\mathbf{r}')\mathrm{d}\mathbf{r}' \simeq \int u(\mathbf{r}-\mathbf{r}')\sum_m \frac{(\mathbf{r}-\mathbf{r}')^m}{m!}\nabla^m x_n(\mathbf{r})\mathrm{d}\mathbf{r}'$, that gives:

$$U_n(\mathbf{r}) \simeq -\varepsilon x_{n-1}(\mathbf{r})\left\{x_n(\mathbf{r}) + (1+r_0^2\nabla^2)^2 x_n(\mathbf{r})\right\}. \tag{3}$$

Her, we assume $r_0^n = 0$ at $n > 4$. Such self-consistent approximation is general and was widely used by studying pattern formation processes [30–33, 38–41] and epitaxial growth of surface structures [42–44].

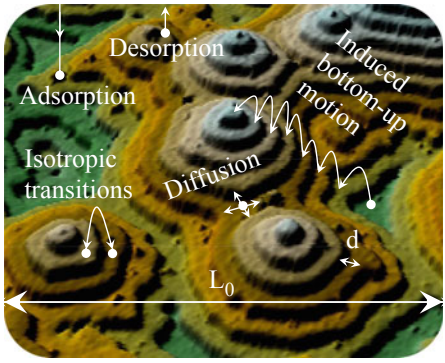

Fig. 1 Schematic presentation of the main processes realized on a growing surface with the linear size L_0 during condensation. Here, d corresponds to the width of terrace of multi-layer pyramidal-like structures

By studying multi-layer growth at condensation $N \gg 1$, reaction–diffusion equation type of (1) should be solved simultaneously. At the same time, the larger the number of layers, the larger the calculation time. Theoretical and numerical studies of formation of surface structures during condensation for multi-layer systems, containing several layers, were done in [34, 35, 37]. In order to save time and perform comprehensive study of surface pattern formation for the problem under consideration, we are aimed to construct the appropriate one-layer model, allowing one to modelize pattern formation processes on the intermediate layer of N-layer adsorptive system. To that end, we should take into account that the concentration of adsorbate on a layer should decrease with the growth in the layer number, counted from the substrate, according to the minimization of the surface energy. To proceed, we need to express the adsorbate concentration on both precursor and the next layers through one on the current layer. Let us define the adsorbate concentration on any nth layer as $x_n = S_n/S_0$, where $S_0 \propto L_0^2$ corresponds to the area of the substrate and $S_n = \sum_i^M s_{ni} = \pi \sum_i^M r_{ni}^2$ defines the area, covered by adsorbate on the nth layer; here, sum is taken over all M structures. The linear size of any ith multi-layer pyramidal-like adsorbate structure should decrease with the layer number growth by the value of the width of terrace d (see scheme in Fig. 1). By combining all structures of adsorbate on the nth layer into one structure with the linear size r_n, one can put: $S_n \propto r_n^2$. The quantity r_n should decrease with increase in the number of layers n by the terrace width Δ of the constructed structure. As a simplest expression, one can use $r_n = r_1 - (n-1)\Delta$ that gives the relation between the areas covered by adsorbate on the first layer and any nth layer, as: $S_n \propto S_1[1-(n-1)\Delta/r_1]^2$. Hence, the concentration of adsorbate on the current nth layer and both precursor $(n-1)$th and next $(n+1)$th layers is expressed as:

$$\begin{aligned} x_n =& \frac{S_1}{S_0}\left[1-(n-1)\frac{\Delta}{r_1}\right]^2 \\ x_{n\pm1} =& \frac{S_1}{S_0}\left\{\left[1-(n-1)\frac{\Delta}{r_1}\right] \mp \left[\frac{\Delta}{r_1}\right]\right\}^2 \\ =& \underbrace{\frac{S_1}{S_0}\left(1-(n-1)\frac{\Delta}{r_1}\right)^2}_{x_n} \mp 2\frac{\Delta}{r_1}\underbrace{\frac{S_1}{S_0}\left(1-(n-1)\frac{\Delta}{r_1}\right)}_{\sqrt{x}\sqrt{S_0/S_1}} + \frac{S_1}{S_0}\left(\frac{\Delta}{r_1}\right)^2. \end{aligned} \tag{4}$$

From (4), one immediately finds:

$$x_{n\pm1} = \left(\sqrt{x_n} \mp \beta/2\right)^2, \quad \beta = 2\Delta/L_0 < 1. \tag{5}$$

By using (5), one can write the evolution equation for adsorbate concentration $x \equiv x_n$ on the intermediate layer of multi-layer system in the form:

$$\begin{aligned}\partial_t x = {} & \alpha(1-x)\nu(x) - x\nu(x)\mathrm{e}^{-2\varepsilon x(\sqrt{x}+\beta/2)^2} \\ & + \frac{1}{2}\beta^2 + u_E\left[\beta\sqrt{x}(1-2x) + \frac{1}{4}\beta^2\right] \\ & + L_D^2\nabla\cdot\left[\nabla x - \varepsilon\gamma(x)\nabla\{x + \mathscr{L}_{SH}x\}\right] + \xi(t).\end{aligned} \tag{6}$$

Here, time is scaled in units $t' \equiv tk_d^0$ and distance is scaled in units $r' = r/L_D$, where $L_D = \sqrt{k_{\leftrightarrow}/k_d^0}$ is the diffusion length. We use dimensionless constant parameters $\varepsilon \equiv \varepsilon/T, \alpha \equiv k_a/k_d^0, k_t \equiv k_{\updownarrow}/k_d^0, u_E \equiv k_E/k_d^0$, introduce: $\nu(x) = (\sqrt{x} + 1/2\beta)^2 \left[1 - (\sqrt{x} - 1/2\beta)^2\right], \gamma(x) = \mu(x)(\sqrt{x} + 1/2\beta)^2, \mu = x(1-x)$; $k_t = 1$ and exploit the Swift–Hohenberg operator $\mathscr{L}_{SH} = (1 + r_0^2\nabla^2)^2$ [45], widely used in problems of pattern formation [46, 47]. The last term in (6) is the zero-mean delta-correlated Gaussian white noise with intensity σ^2 proportional to the bath temperature. The derived one-layer model has one limitation: the maximal value of the adsorbate concentration on the precursor layer, $x_{n-1} = 1$ that corresponds to the substrate. Hence, the maximal value of the concentration of adsorbate on the current layer is $x_{\max} = (1 - 1/2\beta)^2$. Therefore, from the relation $R(x_{\max}) = 0$ one gets the minimal value of the anisotropy strength u_E.

3 First-Order Phase Transitions

In this section, we will study homogeneous system (6) by setting $\nabla x = 0$. It is known that adsorptive bi-stable systems undergo first-order gas-condensate phase transitions (see, e.g., [30–33, 40, 41]). Here, we will discuss the possibility of the anisotropy strength, proportional to the strength of the electrical field near the substrate in plasma-condensate system to induce such transitions. The stationary value of the adsorbate concentration can be found from the relation $\partial_t x = 0$, or $R(x) = 0$. Obtained dependencies $x_{\mathrm{st}}(u_E)$ for different values of adsorption coefficient α are shown in Fig. 2.

Here, $u_{\min}(\alpha, \varepsilon, \beta)$ limits the stationary value of adsorbate concentration x by the quantity $x_{\max}$. From Fig. 2, one gets that for the small values of adsorption coefficient an increase in the anisotropy strength leads to the first-order phase transition from dense toward diluted phase at $u = u_1$ (see Fig. 2 at $\alpha = 0.04$). At intermediate values of the adsorption coefficient α, one gets more complicated scenario of phase transformations with an increase in the anisotropy strength (see Fig. 2 at $\alpha = 0.06$). In such a case, dense-diluted phase transition is realized at $u_E = u_{E1}$; at $u_E = u_{E3}$, phase transition from low- to high-density state is realized. With further growth in adsorption coefficient with an increase in anisotropy strength, one gets first-order phase transition from diluted phase to dense phase at $u_E = u_{E1}$ (see Fig. 2 at $\alpha = 0.15$). For the case of large values of α, adsorbate concentration monotonically decreases with u_E growth.

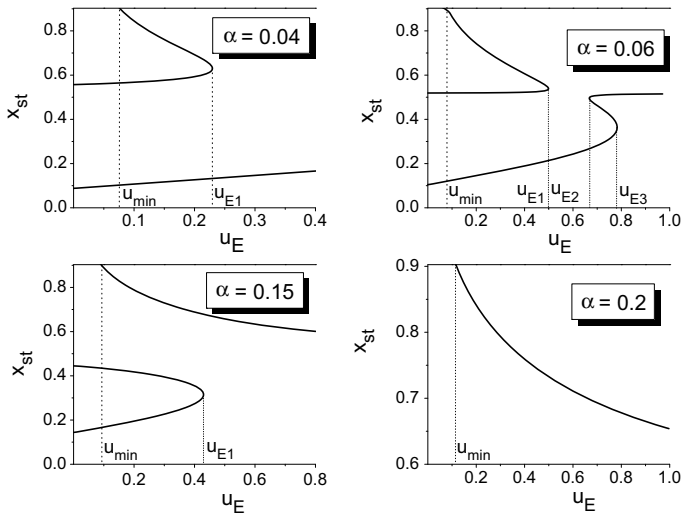

Fig. 2 Dependencies of the stationary values of adsorbate concentration x_{st} on the anisotropy strength u_E at $\varepsilon = 4.0$, $\beta = 0.1$ and different values of the adsorption coefficient α

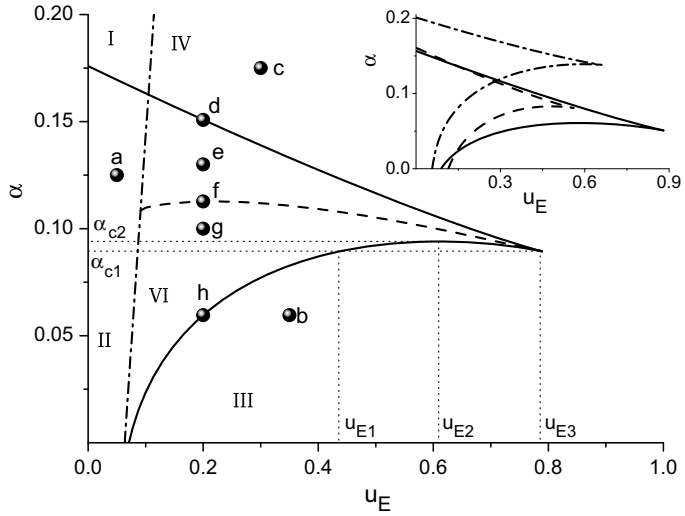

Fig. 3 Phase diagram $\alpha(u_E)$ for the homogeneous system (6) calculated at $\varepsilon = 3.5$ and $\beta = 0.1$. Inset corresponds to: $\varepsilon = 4$, $\beta = 0.1$ (solid curves); $\varepsilon = 3$, $\beta = 0.1$ (dash-dot curves); $\varepsilon = 3$, $\beta = 0.15$ (dash curves)

In Fig. 3, we show the phase diagram in plane (u_E, α) illustrating domain of system parameters, where the system is bi-stable.

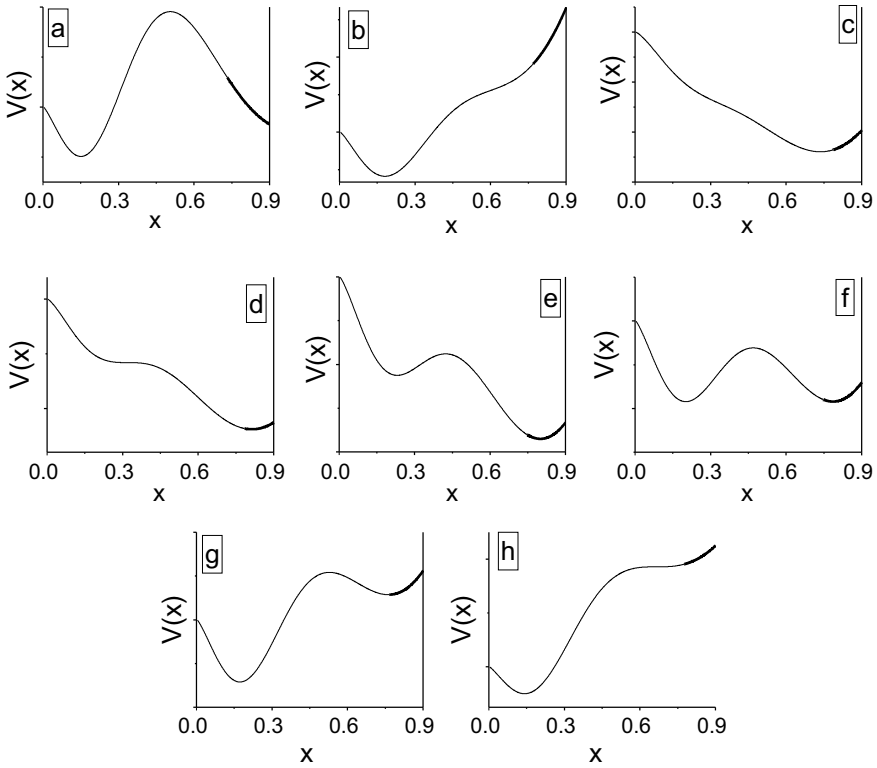

Fig. 4 Effective potentials $V(x)$ at different values of α and u_E. Other parameters are: $\varepsilon = 3.5$, $\beta = 0.1$

Here, the whole plane (u_E, α) is divided by four curves into six different domains. Solid lines correspond to binodals and define the range of the system parameters when the system is bi-stable (domains V and VI). Dash curve corresponds to the spinodal. Dash-dot curve relates to the limitation $x \leq x_{\max}$: Inside the domain I, no physically realized stationary value of adsorbate concentration does exist.

Inside the domain VI, one can define the critical values of the adsorption coefficient: $\alpha_{c1} = \alpha(u_{E1}) = \alpha(u_{E3})$ and $\alpha_{c2} = \alpha(u_{E2})$, related to the complex picture of first-order phase transitions shown in Fig. 2 at $\alpha = 0.06$.

Inset in Fig. 3 shows an influence of the interaction strength ε and parameter β onto the bi-stability domain: Here, solid curves were obtained at $\varepsilon = 4$, $\beta = 0.1$; dash-dot curves correspond to $\varepsilon = 3$, $\beta = 0.1$; dash curves relate to $\varepsilon = 3$, $\beta = 0.15$. It follows that an increase in β leads to a shrink of the bi-stability domain (compare dash-dot and dash curves). With an increase in the interaction strength, the bi-stability domain extends in anisotropy strength but shrinks in adsorption coefficient. Moreover, at elevated values of ε the reentrant first-order phase transitions can realize (see solid curve in the inset in Fig. 3).

Stability of the stationary states of the homogeneous system can be studied with the help of the effective potential $V(x) = -\int R(x)\mathrm{d}x$. It is shown in Fig. 4 at different values of the system parameters corresponding to the black circles in the phase diagram in Fig. 3. As usual, minima of $V(x)$ correspond to the stable states. It follows that in domain II the system is characterized by one stable and one unstable state (see Fig. 4a). In domains III and IV, the system is characterized by one stable stationary state with small and large values of adsorbate concentration, respectively (see plots b and c in Fig. 4). In the case of values of system parameters from the domains V and VI, there are two stable states and the depth of the corresponding minimum of $V(x)$ defines the more stable state (see plots e and g in Fig. 4). In the point f in Fig. 3 corresponding to the spinodal, the two minimums of the potential $V(x)$ are equivalent (see plot f in Fig. 4).

4 Stability Analysis

In order to define conditions of pattern formation in this section, we will study a stability of the stationary homogeneous states x_{st} to inhomogeneous perturbations. To this end, we will use linear stability analysis by considering the deviation from the stationary state δx in the form: $\delta x = x - x_{\mathrm{st}} \propto \mathrm{e}^{\lambda(k)t}\mathrm{e}^{ikr}$, where $\lambda(k)$ is the stability exponent defined through the wave number k. By making linearization of the reaction term of (6), one gets the equation for the stability exponent λ in the form:

$$\lambda(\kappa) = \left.\frac{\mathrm{d}R}{\mathrm{d}x}\right|_{x=x_{\mathrm{st}}} - \kappa^2\left[1 - \varepsilon\gamma(x_s t)\left\{1 + (1 - \rho_0^2\kappa^2)^2\right\}\right],$$

where $\rho_0 = r_0/L_D$ and $\kappa = kL_D$. By varying system parameters and by analyzing the dependence $\lambda(\kappa)$, one can define a range of system parameters, when pattern formation is possible. In the case $\lambda(\kappa) \leq 0$ at $\kappa \in [0, 2\pi L_D]$, any spatial instability realized at initial stages of the system evolution will disappear and stationary structures cannot be realized. It is possible if $\lambda(\kappa) > 0$ at $\kappa \in [\kappa_1, \kappa_2]$ with $\kappa_{1,2} \neq 0$. The stability diagram $\alpha(u_E)$ indicating domains of system parameters, when stable structures can be formed, is shown in Fig. 5a.

Here, the domain I corresponds to the system parameters when stationary surface structures will appear. Outside domain I (in the domain II), adsorbate will homogeneously cover the substrate. One should indicate that in the isotropic system with $u_E \to 0$ no stable patterns are possible. In such system, only transient patterns can be formed. In order to stabilize these transient structures, the non-equilibrium reactions $-k_r x^n$ were used [31, 32, 40, 41]. From the diagram in Fig. 5, it follows that at fixed value of adsorption coefficient $\alpha = \alpha_0$ an increase of the anisotropy strength u_E induces pattern formation at $u_E = u_{E1}$. In the case of strong anisotropy, $u_E > u_{E2}$, adsorbate covers substrate homogeneously. At fixed u_{E0}, an increase in the adsorption coefficient results in formation of stable structures at $\alpha > \alpha_1$. At large values of

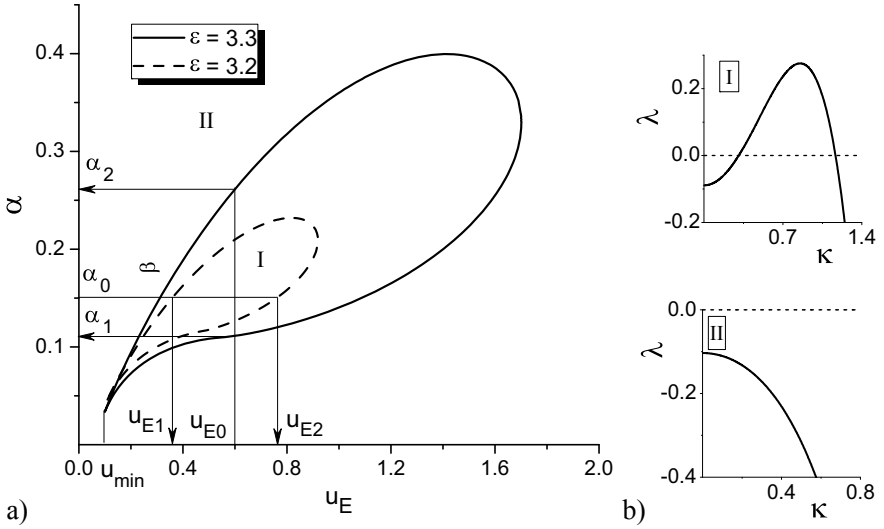

Fig. 5 Stability diagram at $\beta = 0.1$. **a** In the domain I, stationary patterns are realized; in domain II, one gets the homogeneous distribution of the coverage field. **b** Typical dependencies of the stability exponent in domains I and II

the adsorption rate, $\alpha > \alpha_2$, one gets homogeneous distribution of the coverage field. Same influence of the adsorption coefficient onto picture of pattern formation gas-condensate systems was observed in [33, 34]. From the obtained results, it follows that an increase in the values of the interaction energy ε results in an extension of the domain of pattern formation (compare solid and dash curves in Fig. 5a). Typical dependencies of the stability exponent $\lambda(\kappa)$ in both domains of the stability diagram of Fig. 5a are shown in Fig. 5b.

5 Numerical Simulations

In this section, we will perform numerical simulation by solving numerically (6) on two-dimensional triangular lattice $L_0 \times L_0$ with $L_0 = 256$ sites, time-step $\Delta t = 10^{-3}$ and mesh size $\Delta x = 0.5$. Boundary conditions are periodic. In numerical scheme, we put $L_D/r_0 = 12.6$, giving $L_0 = 40L_D$. For the initial conditions, we put $x(\mathbf{r}, 0) = 0$. In all simulations, we use $\sigma^2 = 0.01$.

In Fig. 6a, b, we show snapshots of the system evolution at different values of the anisotropy strength u_E. Here, black color corresponds to the diluted phase with small concentration of adsorbate; white color corresponds to the dense phase with large values of the adsorbate concentration. In Fig. 6c, d, we show evolution of the mean adsorbate concentration $\langle x \rangle$ and dispersion $\langle (\delta x)^2 \rangle$, at different values of system parameters. In problems of pattern formation, the quantity $\langle (\delta x)^2 \rangle$ can be considered

as a control parameter [29, 32, 33, 48–50]. It is seen that at initial stages of the system evolution the mean adsorbate concentration grows (see Fig. 6c), whereas the order parameter $\langle(\delta x)^2\rangle$ equals zero (see Fig. 6d), meaning homogeneous distribution of adsorbate. At $t = t_c$, the adsorbate concentration attains saturation and order parameter $\langle(\delta x)^2\rangle$ increases. The last means self-organization of adsorbed particles into separated structures. At late stages of the system evolution, both quantities $\langle x\rangle$ and $\langle(\delta x)^2\rangle$ attain their stationary values and depending on values of system parameters stationary surface structure types of nano-holes (Fig. 6a) or nano-dots (Fig. 6b) are realized. By analyzing dependencies $\langle x\rangle(t)$ and $\langle(\delta x)^2\rangle(t)$, one gets that both stationary values $\langle x\rangle_{\rm st}$ and $\langle(\delta x)^2\rangle_{\rm st}$ and the time instant t_c depend on the main system parameters.

Lets us discuss an influence of control parameters onto both stationary values $\langle x\rangle_{\rm st}$ and $\langle(\delta x)^2\rangle_{\rm st}$, shown in Fig. 7.

It follows that an increase in the adsorption coefficient leads to monotonic growth of the stationary adsorbate concentration. Inside an interval $\alpha \in (\alpha_1, \alpha_2)$, surface patterns can be realized due to nonzero values of the stationary values of the order parameter (see Fig. 7a). Similar picture is realized with an increase in the values of the anisotropy strength (see Fig. 7b). With an increase in the interaction energy, stationary adsorbate concentration grows and no patterns can be formed while $\varepsilon < \varepsilon_1$; at $\varepsilon > \varepsilon_1$, an increase in ε leads to a decrease in adsorbate concentration $\langle x\rangle_{\rm st}$ with an increase in the stationary values of the dispersion meaning formation of the ordered surface (see Fig. 7c). It is important that the critical values $\alpha_{1,2}$, $u_{E1,2}$ and ε_1, obtained by using numerical simulations, correspond well to values calculated in the framework of stability analysis.

Next, let us analyze an influence of main system parameters onto the time instant t_c indicating a start of ordering processes. The corresponding dependencies are shown in Fig. 8.

It follows that with an increase in the adsorption coefficient inside the interval (α_1, α_2) the value of t_c decreases, attains the minimal value at α_m and then increases (see Fig. 8a). Analogous picture is realized with a variation in anisotropy strength u_E within the interval (u_{E1}, u_{E2}): Time instant t_c optimizes at $u_E = u_{Em}$ (see Fig. 8b). With an increase in the values of the interaction strength $\varepsilon > \varepsilon_1$, the time instant t_c monotonically decreases (see Fig. 8c). A decrease in t_c means accelerating of the ordering process; an increase in t_c means a delay in the processes of pattern formation.

A change in the surface morphology with variation in adsorption coefficient α, anisotropy strength u_E and interaction strength ε is shown in Fig. 9a, b, c, respectively.

From Fig. 9a, it follows that at small values of the adsorption coefficient $\alpha > \alpha_1$ separated adsorbate islands (nano-dots) are realized (see Fig. 9a at $\alpha = 0.13$). A growth of the adsorption coefficient leads to the formation of nano-holes inside adsorbate matrix (see Fig. 9a at $\alpha = 0.24$) through labyrinthine structure of elongated adsorbate islands (see Fig. 9a at $\alpha = 0.175$) and holes (see Fig. 9a at $\alpha = 0.2$). An increase in the anisotropy strength u_E leads to the opposite picture of the surface morphology transformations (see Fig. 9b). Here, nano-holes inside adsorbate matrix transform to separated adsorbate islands (nano-dots) with an increase in u_E. With an

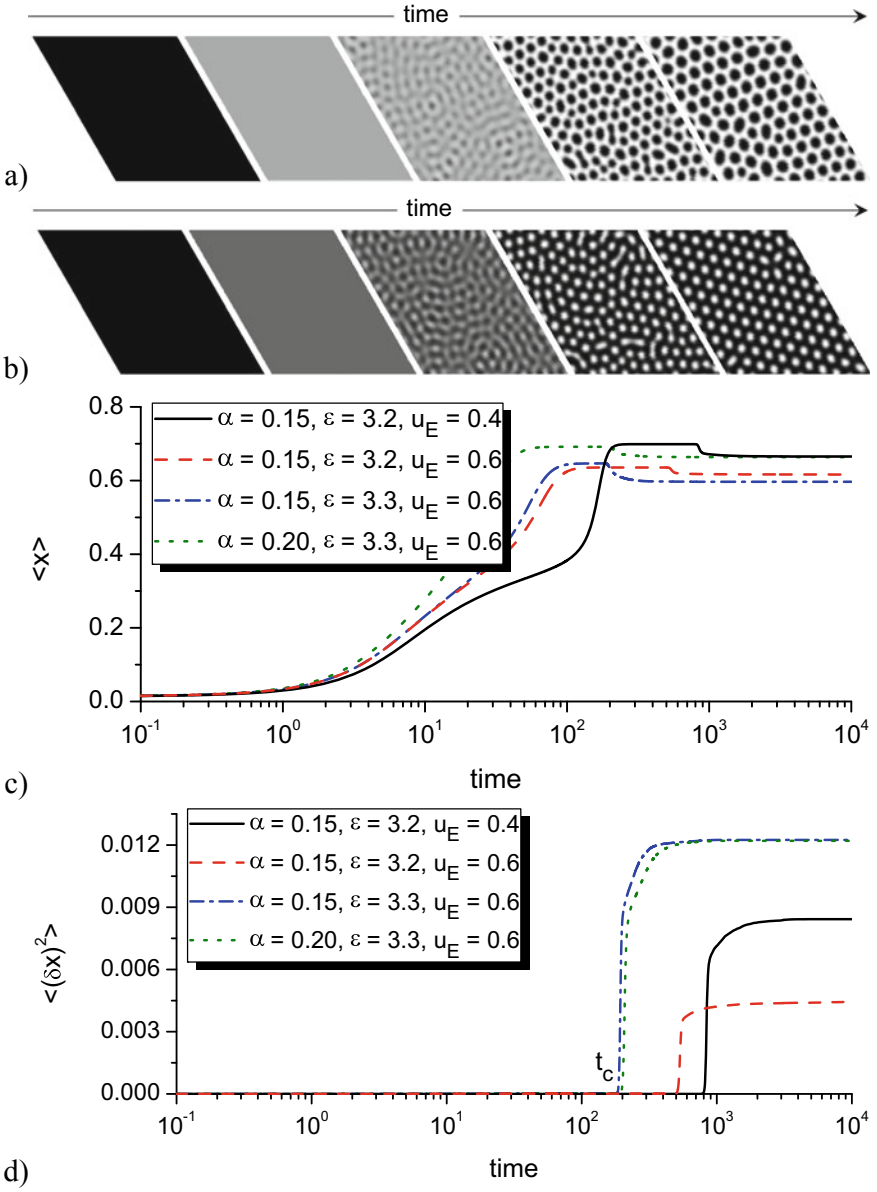

Fig. 6 Typical snapshots of the system evolution at $\alpha = 0.15, \varepsilon = 3.2$ and: **a** $u_E = 0.4$; **b** $u_E = 0.6$. Dynamics of the mean concentration of adsorbate (**c**) and the dispersion (**d**) at different values of the system parameters

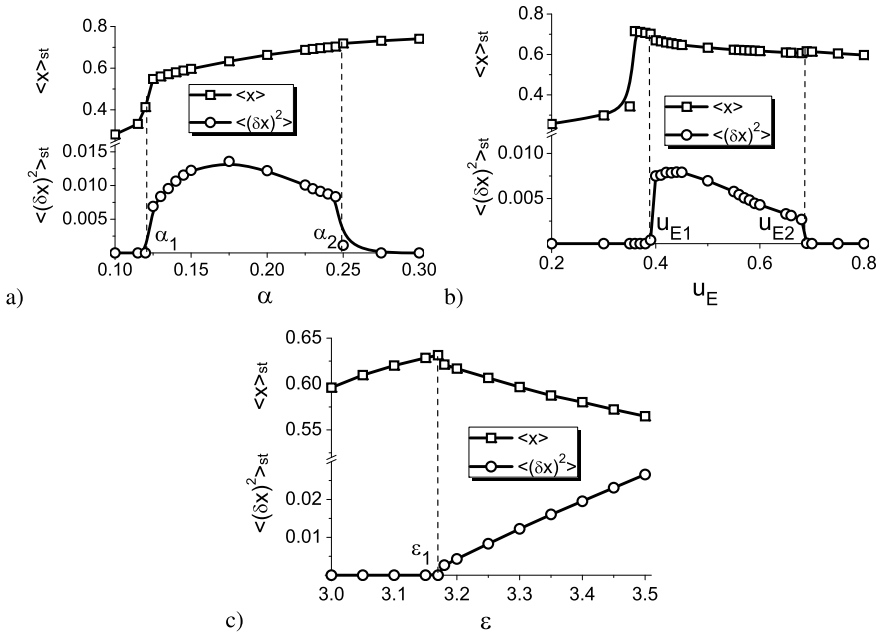

Fig. 7 Dependencies of the stationary values of the concentration of adsorbate $\langle x \rangle_{\rm st}$ and dispersion $\langle (\delta x)^2 \rangle_{\rm st}$ at: **a** $\varepsilon = 3.3$, $u_E = 0.6$; **b** $\varepsilon = 3.2$, $\alpha = 0.15$; **c** $\alpha = 0.15$, $u_E = 0.6$

increase in the interaction strength ε, separated spherical adsorbate islands formed at small ε become elongated (see Fig. 9c).

To characterize an influence of the main control parameters onto the linear size of the surface structures, we will use a percolation method and define the area s_i of each adsorbate/vacancy cluster in units L_D^2. Next, by considering each cluster as a disk with the same area, we define the linear size (radius) $R = \sqrt{s_i/\pi}$ in units L_D. From Fig. 8a, b, it follows that after an incubation period (formation and growth stages) the mean size attains the stationary value. In Fig. 10, we present dependencies of the number $N_{a,v}$ of separated surface structures and their mean size $\langle R_{a,v} \rangle$ on the adsorption coefficient α (Fig. 10a), anisotropy strength u_E (Fig. 10b) and interaction strength ε (Fig. 10c). First, let us discuss in detail dependencies $N_{a,v}(\alpha)$ and $\langle R_{a,v} \rangle(\alpha)$. Starting from the value $\alpha = \alpha_1$, the linear size of separated adsorbate islands $\langle R_a \rangle$ grows until $\alpha < \alpha_a$. The number of adsorbate islands N_a increases at small $\alpha > \alpha_1$. At $\alpha > a_c$, the number N_a decreases with α growth. Here, both spherical and elongated adsorbate islands are realized. In the interval $\alpha \in [\alpha_a, \alpha_v]$, labyrinthine structures are formed (see Fig. 9a at $\alpha = 0.175$). Separated spherical and elongated holes start to organize at $\alpha > \alpha_v$ (see Fig. 9a at $\alpha = 0.2$). A further increase in $\alpha < \alpha_2$ leads to formation of separated holes inside adsorbate matrix. The number of holes N_v monotonically increases with α, and their linear size $\langle R_v \rangle$ decreases. An increase in the anisotropy strength the number of separated holes deceases and they become larger (see Fig.

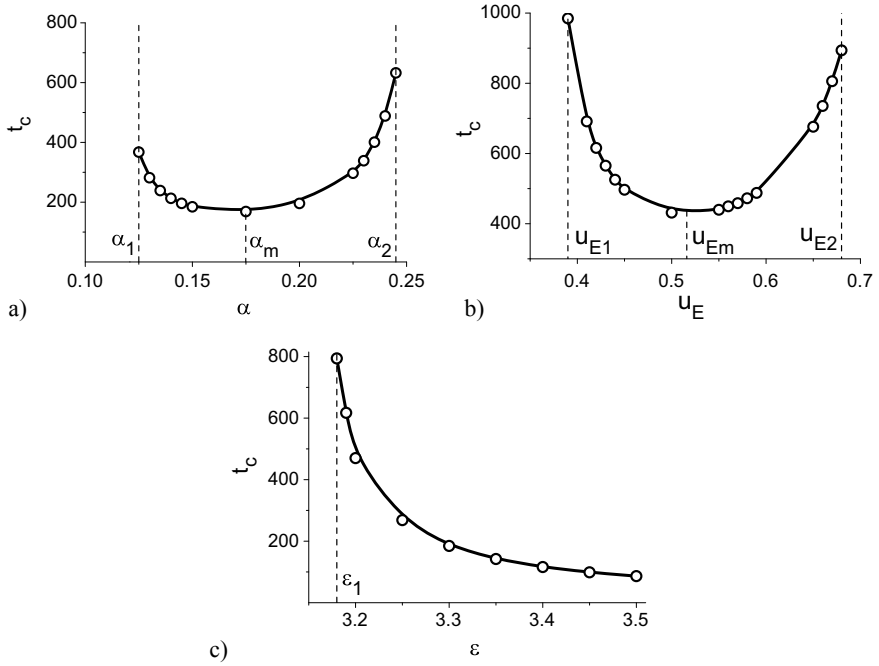

Fig. 8 Dependencies of the time instant t_c, indicating a start of ordering processes at: **a** $\varepsilon = 3.3$, $u_E = 0.6$; **b** $\varepsilon = 3.2$, $\alpha = 0.15$; **c** $\alpha = 0.15$, $u_E = 0.6$

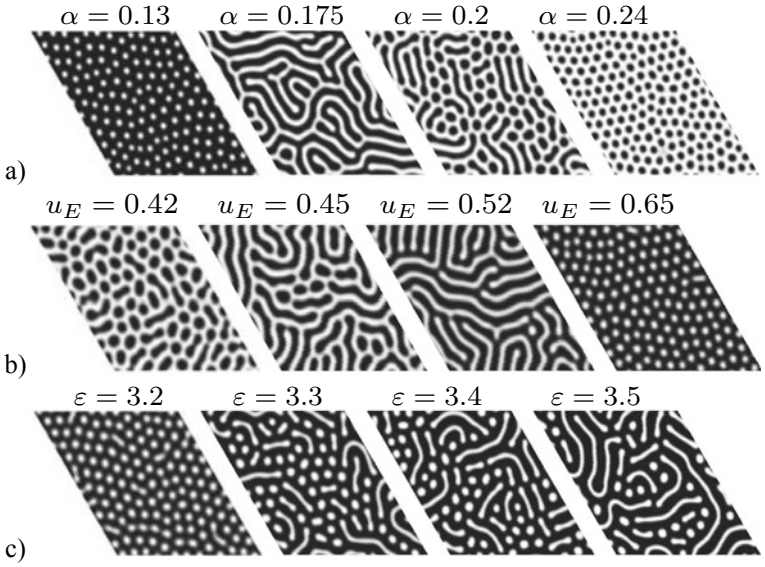

Fig. 9 Quasi-stationary snapshots obtained at **a** $\varepsilon = 3.3$, $u_E = 0.6$; **b** $\varepsilon = 3.2$, $\alpha = 0.15$; **c** $\alpha = 0.15$, $u_E = 0.6$

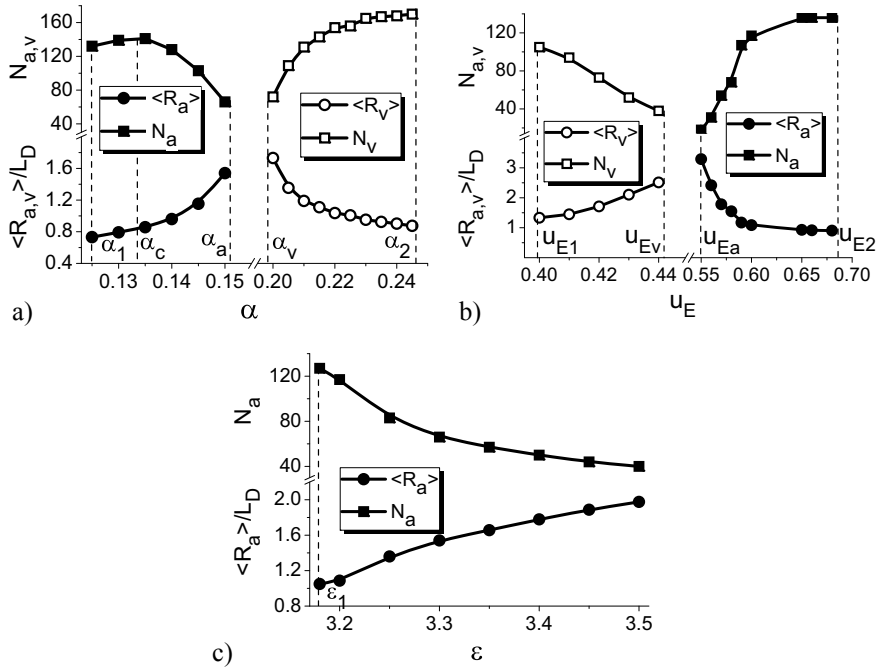

Fig. 10 Dependencies of the mean linear size of separated adsorbate islands $\langle R_a \rangle$ (filled circles) and holes $\langle R_v \rangle$ (empty circles) and the number of adsorbate islands N_a (filled squares) and holes N_v (empty squares) at: **a** $\varepsilon = 3.3$, $u_E = 0.6$; **b** $\varepsilon = 3.2$, $\alpha = 0.15$; **c** $\alpha = 0.15$, $u_E = 0.6$

10b and Fig. 9b at $u_E = 0.42$ and $u_E = 0.45$). In the interval $u_E \in (u_{Ev}, u_{Ea})$, the labyrinthine structures are realized. At elevated $u_E > u_{Ea}$, a growth in $u_E < u_{E2}$ results in an increase of the number of separated nano-dots with small size. An increase in ε provides formation of elongated adsorbate structures; their number decreases (see Fig. 10c).

6 Discussion

Obtained results correspond to the patterns, realized on an intermediate nth layer of the N-layer system. These structures allow one to construct the 3D pyramidal-like patters for the multi-layer system. To do this, we need to define the terrace width in units of computational grid. In the actual case with $L_0 = 256$ and $\beta = 0.1$, the parameter Δ which characterizes the width of terrace of structure, constructed from all islands, is $\Delta = 13$ in units of the grid. In order to calculate the terrace width d for the each pyramidal structure (see Fig.1), we proceed in the following way. By exploiting the formula for the total area, occupied by adsorbate on the current nth

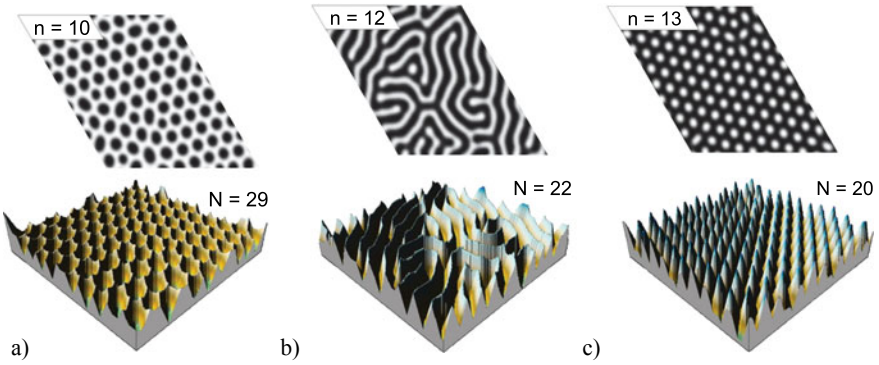

Fig. 11 Snapshots of the surface structures at $L_0 = 226$, $\beta = 0.1$, $\alpha = 0.15$, $\varepsilon = 3.2$ and: **a** $u_E = 0.4$, **b** $u_E = 0.5$, **c** $u_E = 0.6$. Top row corresponds to the two-dimensional structures on the nth layer (number n is shown in the left-top corner). Bottom row shows a constructed N-layer structures (number N is presented in the right-top corner)

layer, $S_n = \pi r_n^2$, one can define the total area on the previous $(n-1)$th layer as: $S_{n-1} = \pi r_{n-1}^2$. By using $r_{n-1} = r_n + \Delta$, one gets:

$$S_{n-1} = S_n + 2\Delta\sqrt{\pi S_n} + \pi\Delta^2. \tag{7}$$

At the same time, the linear size of the each ith structure r_{ni} on the precursor layer is larger than one on the current on the terrace width d: $r_{n-1,i} = r_{n,i} + d$. Therefore, for the area of each ith structure on the precursor $(n-1)$th layer, one has: $s_{n-1,i} = s_{n,i} + 2d\sqrt{\pi s_{n,i}} + \pi d^2$. By taking a sum over all M structures, we have:

$$S_{n-1} = S_n + 2d\sum_{i}^{M}\sqrt{\pi s_{ni}} + M\pi d^2. \tag{8}$$

Equations (7) and (8) give an expression for the terrace width d for the each pyramidal-like structure:

$$d = \frac{1}{\pi M}\left\{\left[\left(\sum_{i=1}^{M}\sqrt{\pi s_{ni}}\right)^2 + \pi M\left(2\Delta\sqrt{\pi S_n} + \pi\Delta^2\right)\right]^{1/2} - \sum_{i=1}^{M}\sqrt{\pi s_{ni}}\right\}. \tag{9}$$

For the fixed values of the control parameters, one can calculate areas of all structure s_{ni} and total number of structures M and fine the value of the terrace width d in units of the computational grid. For the case under consideration with $L_0 = 256$ and $\beta = 0.1$ for the terrace width d from (9), we get $d = 1$. It allows us to construct the N-layer surface structures. The corresponding results are shown in Fig. 11.

It follows that for the all cases one has the relation $n \simeq N/2$, meaning that the constructed one-layer model describes pattern formation processes on the half-height of the growing surface.

In order to estimate the obtained data for the linear size of the surface structures on the half-height level, we will use the formula for the diffusion length $L_D = \sqrt{k_{\leftrightarrow}/k_d^0} = a^2 \exp([E_d - E_D]/T)$ and experimental data from [51]: $E_D = 0.24$ eV and $Ed = 0.44$ eV at $T = 773$ K, giving $L_D \simeq 50$ nm. Therefore, from the data from Fig. 10 one gets: $\langle R_a \rangle \in (35 \div 150)$ nm (for separated adsorbate islands) and $\langle R_v \rangle \in (40 \div 125)$ nm (for separated holes inside adsorbate matrix). These results are in good correspondence with experimentally observed data [51–54].

7 Conclusions

We perform theoretical study of pattern formation at condensation in ion plasma devices. We construct a reaction–diffusion model by taking into account an influence of the electrical field near substrate leading to anisotropy of transference of adatoms between neighbor layers or the spatiotemporal evolution of adsorbate concentration on intermediate layer of multi-layer system. We discussed an influence of the adsorption coefficient, interaction energy of adsorbate and anisotropy strength, the dynamics of pattern formation and morphology of the surface.

We have found the conditions of the first-order phase transitions and obtained the phase diagram illustrating the range of system parameters, when pattern formation is possible. It is found that an increase in both adsorption rate and anisotropy strength leads to reentrant scenario of pattern formation. It is found that stable surface structures can be realized if the anisotropy strength exceeds the critical value.

We have shown that an increase in the adsorption coefficient leads to an increase in adsorbate concentration, accelerates processes of separated adsorbate island formation, promotes a growth of the linear size of adsorbate islands, induces formation of elongated patterns and slows down dynamics of separated hole formation. With an increase in the anisotropy strength, one gets transition from the separated holes inside adsorbate matrix toward separated nano-dots. Strong interaction between adatoms leads to formation of elongated adsorbate islands. It is shown that the derived model one layer allows one to construct the pyramidal-like structures, formed in multi-layer system.

Obtained results can be used to predict a change in the morphology of the growing surface during condensation in plasma-condensate devices by varying pressure inside a chamber and strength of the electrical field near substrate and to adjust the technological conditions of thin-film growth with predetermined statistical properties of the surface structures.

Acknowledgements Support of this research by the Ministry of Education and Science of Ukraine, project No. 0117U003927, is gratefully acknowledged.

References

1. Ohring M (2001) Materials science of thin films, 2nd edn. Academic press, p 794
2. Marchand P, Hassan IA, Parkin IP et al (2013) Dalton Trans 42:9406
3. Benning L, Waychunas G (2008) Nucleation, growth, and aggregation of mineral phases: mechanisms and kinetic controls. In: Brantley S, Kubicki J, White A (eds) Kinetics of water-rock interaction. Springer, New York, NY
4. Ferrando R, Jellinek J, Johnston RL (2008) Chem Rev 108:845
5. Jortner J (1992) Z Phys D At Mol Clusters 24:247
6. Chaudhuri RG, Paria S (2012) Chem Rev 112:2373
7. Johnston RL (1998) Philos Trans R Soc London Ser A 356:211
8. Campbell SA (1996) The science and engineering of microelectronic fabrication. Oxford University Press, New York
9. Masalski J, Gluszek J, Zabrzeski J et al (1999) Thin Solid Films 349:186
10. Vitanov P, Harizanova A, Ivanova T et al (2009) Thin Solid Films 517:6327
11. Chin AK (1983) J Vac Sci Technol B Microelectron Nanom Struct 1:72
12. Echigoya J, Enoki H (1996) J Mater Sci 31:5247
13. Gottmann J, Husmann A, Klotzbiicher T et al (1998) Surf Coatings Technol 100–101:415
14. Carmona-Tellez S, Guzman-Mendoza J, Aguilar-Frutis M (2008) J Appl Phys 103:34105
15. Aguilar-frutis M, Garcia M, Falcony C et al (2001) Thin Solid Films 389:200
16. Dhonge BP, Mathews T, Sundari ST et al (2011) Appl Surf Sci 258:1091
17. Ortiz JC, Alonso A (2002) J Mater Sci Mater Electron 13:7
18. Wu Y, Choy KL (2004) Surf Coat Technol 180–181:436
19. Pohl K, Bartelt MC, de la Figuera J et al (1999) Nature 397:238
20. Mo YW, Swartzentruber BS, Kariotis R et al (1989) Phys Rev Lett 63:2393
21. Cirlin GE, Egorov VA, Okolov LV, Werner P (2002) Semiconductors 36:1294
22. Bucher JP, Hahn E, Fernandez P et al (1994) Europhys Lett 27:473
23. Besenbacher F, Pleth Nielsen L, Spunger PT (1997) Chapter 6. Surface alloying in heteroepitaxial metal-on-metal growth. In: King DA, Woodruff DP (eds) The chemical physics of solid surfaces 8:207. Elsevier
24. Perekrestov VI, Olemskoi AI, Kosminska YuO, Mokrenko AA (2009) Phys Lett A 373:3386
25. Kosminska YA, Mokrenko AA, Perekrestov VI (2011) Tech Phys Lett 37:538
26. Sree Harsha KS (2006) Principles of physical vapor deposition of thin films. Elesevier
27. Batogkh D, Hildebrant M, Krischer F, Mikhailov A (1997) Phys Rep 288:435
28. Hildebrand M, Mikhailov AS, Ertl G (1998) Phys Rev Lett 81:2602
29. Hildebrand M, Mikhailov AS, Ertl G (1998) Phys Rev E 58:5483
30. Walgraef D (2002) Phys E 15:33
31. Kharchenko VO, Kharchenko DO, Kokhan SV et al (2012) Phys Scripta 86:055401
32. Kharchenko VO, Kharchenko DO (2012) Phys Rev E 86:041143
33. Kharchenko VO, Kharchenko DO, Dvornichenko AV (2014) Surf Sci 630:158
34. Kharchenko VO, Kharchenko DO (2015) Surf Sci 637–638:90
35. Kharchenko VO, Kharchenko DO, Yanovsky VV (2017) Nanoscale Res Lett 12:337
36. Dvornichenkoa AV, Kharchenkob DO, Lysenkob IO (2019) J Cryst Growth 514:1
37. Casal SB, Wio HS, Mangioni S (2002) Physica A 311:443
38. Mangioni SE, Wio HS (2005) Phys Rev E 71:056203
39. Mangioni SE (2010) Physica A 389:1799
40. Walgraef D (2003) Physica E 18:393
41. Walgraef D (2004) Int J Quant Chem 98:248
42. Kharchenko DO, Kharchenko VO, Lysenko IO (2011) Phys Scripta 83:045802
43. Kharchenko DO, Kharchenko VO, Zhylenko TI et al (2013) Eur Phys J B 86(4):175
44. Kharchenko VO, Kharchenko DO, Dvornichenko AV (2015) Eur Phys J B 88:3
45. Swift J, Hohenberg PC (1977) Phys Rev A 15:319
46. Kharchenko D, Lysenko I, Kharchenko V (2010) Physica A 389:3356

47. Elder KR, Grant M (2004) Phys Rev E 70:051605
48. Kharchenko VO, Kharchenko DO (2012) Eur Phys J B 85:383
49. Kharchenko DO, Kharchenko VO, Bashtova AI (2014) Radiat Eff Defects Solids 169:418
50. Kharchenko VO, Kharchenko DO (2014) Phys Rev E 89:042133
51. Leonhardt D, Han SM (2009) Surf Sci 603:2624
52. Hunter KI, Held JT, Mkhoyan KA et al (2017) ACS Appl Mater Interf 9:8263
53. Perekrestov VI, Kosminska YO, Kornyushchenko AS et al (2013) Physica B 411:140
54. Kornyushchenko AS, Natalich VV, Perekrestov VI (2016) J Cryst Growth 442:68

Directional Synthesis of CdX (X = S, Se, and Te) Thin Films for Solar Cell Application

H. A. Ilchuk, R. Y. Petrus, I. V. Semkiv, and A. I. Kashuba

1 Introduction

Considering the development of modern electronic devices, polycrystalline films of semiconductors are most interesting for practical use than crystals. Unlike bulk crystals, the growth of polycrystalline films is a simpler and more productive production process, which does not require precision growth equipment and high-cost single crystal substrates. These factors make the semiconductor material and devices based on it cheaper. High interest in polycrystalline layers is expressed by developers of inexpensive solar cells for terrestrial applications. The authors' use of [1–3] rightfully affirms that the wide use of polycrystalline semiconductors in electronics was for a long time limited by the fact that numerous extended defects such as grain boundaries and dislocations exist in them. However, at present, a study of these objects has increased so that their polycrystallinity is more likely hope for the future rather than a problem. The grain boundaries in these semiconductors possess specific electrical and recombination characteristics, which can be interestingly implemented in a number of device applications. Being a serious quality violation of the crystal lattice, they play the role of an effective internal getter promoting the removal of residual impurities and point defects from the material bulk. This property of the intergrain boundaries is important in improving the exploitation characteristics, in particular, the thermal and radiation stability of semiconductor electronic devices [4].

Thin films of cadmium chalcogenides (CdS, CdSe, and CdTe) representative of the $A^{II}B^{VI}$ crystal group show semiconductor behavior. They are an important research field because of their wide application in various fields of optoelectronic devices.

H. A. Ilchuk (✉) · R. Y. Petrus · I. V. Semkiv · A. I. Kashuba
Department of General Physics, Lviv Polytechnic National University, S. Bandery Str., 12, 79013 Lviv, Ukraine
e-mail: ilchukg@gmail.com

O. Fesenko and L. Yatsenko (eds.), *Nanooptics and Photonics, Nanochemistry and Nanobiotechnology, and Their Applications*, Springer Proceedings in Physics 247, https://doi.org/10.1007/978-3-030-52268-1_9

The CdTe semiconductor compound has proven to be a leading compound for manufacturing cost-effective second-generation photovoltaic devices. CdTe-based solar cells are attracting attention since CdTe is characterized by a direct forbidden gap with an energy bandwidth of ~1.46 eV and a high absorbance (above 10^5 cm^{-1}) [5], which makes it an excellent light-absorbing layer of solar cells.

For the formation of high-efficiency heterojunctions based on *p*-CdTe for a window layer of a solar battery, cadmium sulfide is mainly used [6–8]. CdS is characterized by a high absorbance and high photoconductivity in the visible region. This is due to the fact that CdS is a direct band gap semiconductor and, accordingly, is characterized by the direct band–band optical transitions. The energy width of the band gap at room temperature is ~2.42 eV. The electrical properties of CdS are characterized by a resistivity value of about 10^6 Ω cm and the *n*-type conductivity.

CdS forms cubic and hexagonal phases, depending mainly on the choice of the method of synthesis and on the growth parameters [9–12]. In solar cells based on the CdS/CdTe heterojunction, the thickness of a CdS layer in most cases is about 150–300 nm [13]. Photogenerated charge carriers almost completely recombine inside the CdS film and do not generate photocurrent. Due to the absorption of light by the CdS film, no photocurrent appears in the structure. Therefore, it is desirable to use a CdS film with a thickness of less than 100 nm in order to fabricate high-efficiency CdTe-based solar cells [13–15].

These films have potential applications in many semiconductor devices such as γ-ray detector [16], sensors [17–19], and solar cells [20–23].

To prepare thin films of cadmium chalcogenides the different methods are used: physical vapor deposition, sputtering, spray pyrolysis, electrodeposition, close-space sublimation (CSS), etc [22–28]. Despite the significant number of methods for producing thin films, improving the technological parameters of the deposition process allows to obtain thin films of higher quality. It is the modified methods and characteristics of high-quality obtained films are described below.

2 Deposition Method of Cadmium Chalcogenides Thin Films

Cd*X* (*X* = S, Se, and Te) films were deposited on glass, quartz, silicon, sapphire, glass/ITO, and other substrates (20 × 10 × 1.1 mm^3 size substrates using in this work) by the high-frequency (HF) (13.6 MHz) magnetron sputtering using a VUP-5M vacuum station (Selmi, Ukraine) [5, 15]. A crystalline target of 99.999% purity for CdS and CdTe and 99.99% for CdSe purity (thickness—1 mm, diameter—40 mm) was used. The distance between the target and substrate was 60 mm. The thickness of thin films was controlled by the time of deposition. The beginning and end of sputtering were controlled by the shutter. The chamber where the sputtering was carried out was pre-evacuated. Inside the sputtering chamber pressure of 4 × 10^4 Pa was achieved. This was achieved through the use of polyphenyl ether 5Φ4E (diffusion

fluid) in the vacuum pump, which allows achieving low vapor pressures (9×10^7 Pa).

The thin films deposition was carried out in the argon (Ar) atmosphere at a pressure of 1.0–1.3 Pa. The power of the high-frequency magnetron was 30 W. The deposition occurred on the substrate which was heated to the temperature of 573 K. The heating of substrates was carried out by the tungsten heater (300 W). The temperatures, heating and cooling rates as well as providing the temperature conditions of deposition during the sputtering process were controlled by a proportional–integral–derivative controller (PID controller). The average rate of thin films deposition was 3.9–4.2 Å/s.

Another method of obtained thin films of cadmium chalcogenides is quasi-CSS method [1, 29–33] at pressure 1×10^{-6} Torr. As an example, the deposition of CdSe thin films was conducted on a quartz substrate. The source and substrate material temperature was 900 K and 700 K, respectively. The temperature was controlled using the PID-regulator of temperature PE-202 using a thermocouple of the type "K". The relative error of temperature didn't exceed 0.2%. The substrates were 14 mm in diameter that were used for deposition CdSe thin films. Before the CdSe film deposition, the substrate surface was cleaned by boiling in a high purity CCl_4 solution during 0.25 h.

We do not consider chemical method [34, 35] of obtaining CdX (X = S, Se, and Te) thin films in this work, because he wasn't given high-quality thin films with comparison to other methods listed here.

3 Methods of Characterization CdX (X = S, Se, and Te) Thin Films

The arrays of the experimental intensities and angles of reflection from the investigated samples were obtained using an STOE STADI P diffractometer with a linear position-sensitive detector (PSD) operating in the reflection Bragg–Brentano geometry arrangement (CuKα1 and FeKα1 radiation; concave Ge (111) monochromator of the Johann type; and the $2\theta/\omega$ scanning in the range of angles of $20.000° \leq 2\theta \leq 117.905°$ with increments of 0.015° at room temperature). The processing of the experimental diffraction arrays, the calculation of the theoretical X-ray diffractograms, the X-ray phase analysis, and the indexation of unit-cell parameters were carried out using the STOE WinXPOW and PowderCell software packages [15, 36].

The surface morphology of the obtained thin films was studied using a JSM 6700F scanning electron microscope. The spectral dependence of the optical transmittance (Shimadzu UV-3600) of the obtained samples in the visible and near infrared regions is studied at room temperature [15]. Using the interference pattern of the optical transmittance, the thickness of the CdX (X = S, Se, and Te) films is calculated.

To determine the thickness of the films under investigation, we can use the following equation:

$$d = \frac{M \cdot \lambda_1 \cdot \lambda_2}{2 \cdot (n(\lambda_1) \cdot \lambda_2 - n(\lambda_2) \cdot \lambda_1)} \quad (1)$$

where λ_1 and λ_2 are wavelengths corresponding to neighboring extreme points in the transmission spectrum and $M = 1$ for two neighboring maximum of one type (max–max, min–min) and $M = 0.5$ for two neighboring maximum of opposite types (max–min, min–max). The average thicknesses of the CdX thin films calculated by (1) are listed in Table 1.

4 Morphology Analysis Thin Films of Cadmium Chalcogenides

All the studied layers are polycrystalline and consist of randomly oriented crystallites irrespective of the conditions in which they were obtained (Fig. 1). We observed separate grains with clear intergrain boundaries and a "coalescence" of separate grains. A considerable portion of the crystallites is faceted, but another part is shapeless. There are multiformations in the form of a stack of hexagonal plates (Fig. 1a, c). In some of these layers, we found crystallites in the form of plates, which are, most often, regularly shaped (Fig. 1b). We also found regular-shaped faces such as hexagons, rectangles, triangles, and trapezoids (Fig. 1c).

Crystallites of cadmium chalcogenide CdX (X = S, Se, and Te) evenly cover the substrate and are characterized by the average grains size which are presented in Table 1. The uniform size of crystallites indicates homogeneous deposition conditions throughout the substrate. On the substrates also there are grains with a size of 300 nm, but they are uncommon.

5 Structure Analysis of CdX (X = S, Se, and Te) Thin Films

From the X-ray diffraction analysis of CdS thin films (Fig. 2(1)), it was established that the samples consist of a single phase. The cadmium sulfide (CdS) belongs to the space group $P6_3mc$. In Table 1 are given the parameters of the unit cell. A detailed comparison of the positions and intensities of experimental reflexes with theoretical peaks allowed establishing a strong preferential orientation of the grains in the deposited CdS film. In observed diffractogram, the reflexes from all planes with the *hkl* Miller indices are quenched in intensity, and the exception is the observed reflexes from the planes (001). Observed insignificant noise can be explained by reflexes from the substrate.

CdSe (see Fig. 2(2)) thin film crystallized in hexagonal structure (structure type—ZnO, space group $P6_3mc$ (No. 186), with unit-cell constants $a = 4.277(5)$ Å, $c = 6.981(8)$ Å, and $V = 110.6(2)$ Å^3). Anomaly reflexes from planes with the (10z) and (20z) *hkl* Miller indices are observed.

Table 1 Result of experimental characterization of CdX (X = S, Se, and Te) thin films

CdX	Method of deposition	Substrates	Crystal structure	Structure type	Crystal parameter, nm	Average crystallite size, μm	Method calculation thickness	d^{exp} (μm)	E_g^{exp} (eV)
CdS	HF magnetron sputtering	Glass/ITO	$P6_3mc$	Wurtzite	$a = 0.4048(16)$ $c = 0.666(4)$	30–40	Optical	0.380	2.39
CdSe	CSS	Quarts	$P6_3mc$	ZnO	$a = 0.4277(5)$ $c = 0.6981(8)$	2-5	Optical	1.875	1.68
CdTe	CSS	Glass/ITO	$F43m$	Cubic	$a =$ 0.64765(19)	20	Optical	3.5	1.40

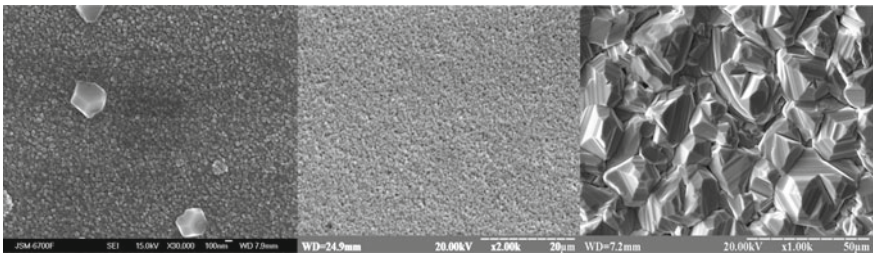

Fig. 1 Morphology of surface fragments of CdS (1 [15]: deposition by HF magnetron sputtering on glass/ITO substrates), CdSe (2: deposition by CSS method on quarts substrates), and CdTe (3 [31]: deposition by HF magnetron sputtering on mica substrates) samples

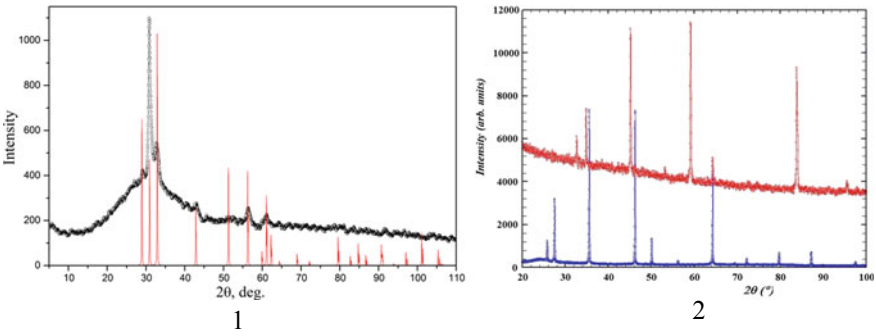

Fig. 2 X-ray diffractograms of CdS (1 [15]: deposition by HF magnetron sputtering on glass/ITO substrates) and CdSe (2: deposition by SCS method on quarts substrates) samples. Red lines are theoretical data

CdTe (not shown) thin film crystallize in cubic structure (structure type—ZnS, space group $F43m$, with unit-cell constants $a = 6.4765(19)$ Å and $V = 271.7(2)$ Å^3). In observed diffractogram, the reflexes from all planes with the *hkl* Miller indices are quenched in intensity, and the exception is the observed reflexes from the planes (111), (222), (333), (444).

6 Determination Band Gap Thin Films of Cadmium Chalcogenides

The transmission spectra $T(\lambda)$ of CdX (X = S, Se, and Te) thin films (Fig. 3(1)) are characterized by an appropriate fundamental absorption edge, with the values corresponding to the cadmium sulfide (CdS), cadmium selenide (CdSe), and cadmium telluride (CdTe). In the transmission spectra are also observed the interference

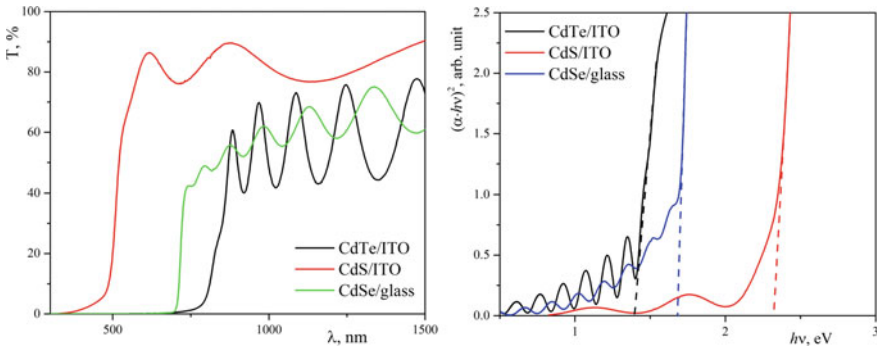

Fig. 3 Transmission spectra (1) and optical absorption (2) of CdX (X = S, Se, and Te) thin films

extremes, which characterize the perfection of the films. Interference maxima and minima in the range 300–1500 nm (Fig. 3(1)) are associated with the phase incursion for 2π in the phase thickness upon changing the light wavelength.

The spectral dependence of the optical absorption of CdX (X = S, Se, and Te) thin films presented in the $(\alpha h\nu)^2$–$h\nu$ coordinates characterized by the fundamental absorption edge (Fig. 3(2)). Extrapolation of the linear part of the observed spectra until the intersection with the energies axis was carried out by the method presented in [37]. The obtained optical band gap values of CdX (X = S, Se, and Te) films are presented in Table 1. The linear dependence of the $(\alpha h\nu)^2 = f(h\nu)$ curves indicates that the absorption edge is formed by direct inter-band transitions.

7 Theoretical Band Structure Calculation of CdX (X = S, Se, and Te) Thin Films

The theoretical calculations were performed within the framework of the density functional theory (DFT).

The models of CdX (X = S, Se, and Te) thin films were formed from a three-dimensional single crystals along the [0 0 1] axis. The distance between the formula units was increased by approximately 15 nm, thus forming a vacuum gap to avoid interaction between the layers. The energy band diagram of thin films with a thickness of near 10 nm (see Table 2) was theoretically calculated. Since ab initio calculations of films with a thickness of equaled of experimental results require considerable computational resources, the results shown below may reflect the effect of the film size on its properties.

To calculate we used structure parameters given in Table 1. Vanderbilt's ultrasoft pseudopotentials [38] were used for the ion potentials. To describe the exchange-correlation energy of the electronic subsystem, a functional in the approximation of

Table 2 Parameters used for calculation electron band structure and result of calculation (electron configuration of Cd–[Kr] $4d^{10}5s^2$)

Cd*X*	d^{teor} (nm)	Electron configuration	*k*—points by the Monkhorsta–Pack scheme	ΔE (eV)	$E_{cut\text{-}off}$ (eV)	E_g^{teor} (eV)
CdS	~10	S–[Ne] $3s^2 3p^4$	2 × 2×2	0.73	290	1.66
CdSe	~9.5	Se–[Ar] $4s^2 4p^4$	4 × 1×2	0.71	260	0.97
CdTe	~10	Te–[Kr]$5s^2 5p^4$	2 × 2×2	0.797	290	0.653

generalized gradient (GGA) in the Purdue–Burke–Ernzerhof (PBE) parameterization [39] was used. As a correlation potential, the Ceperlay–Alder and Gell–Mann–Brueckner equations were applied to the high-electron density boundaries. Details used in the electron band energy calculation are listed in Table 2.

8 Electron Energy Band Structure of Cd*X* (*X* = S, Se, and Te) Thin Films

Figure 4 presents the electronic band structure of the Cd*X* (*X* = S, Se, and Te) thin films built along the symmetric lines of the Brillouin zone (tetragonal). The energy during the calculation was counted from the zero point which corresponds to the Fermi level.

Based on the theoretical calculations of the electronic band structure can be seen that all samples are characterized by the smallest band gap which is localized in the point Γ of the Brillouin zone (center of a zone). In accordance with the obtained results, we can conclude that all samples are characterized by a direct band gap. Considering the results of theoretical calculation and the experimental data [15, 31–36], we can see that the use of GGA PBE approximations for calculations of the band structure leads to underestimated band gap value.

An analysis of the partial contributions of individual levels to the function of the total density of states (Fig. 5) and the partial contributions of individual bands to the

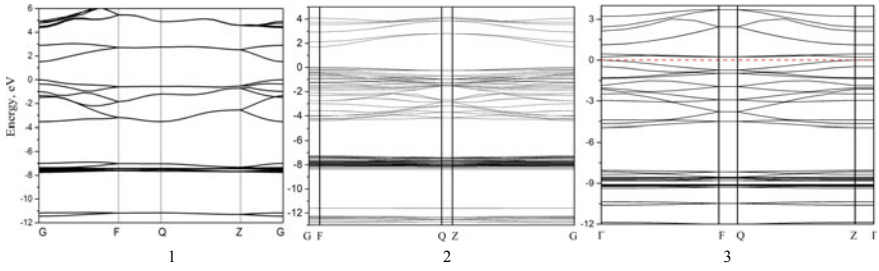

Fig. 4 Electron band energy of Cd*X* (*X* = S (1 [15]), Se (2), and Te (3 [31])) thin films

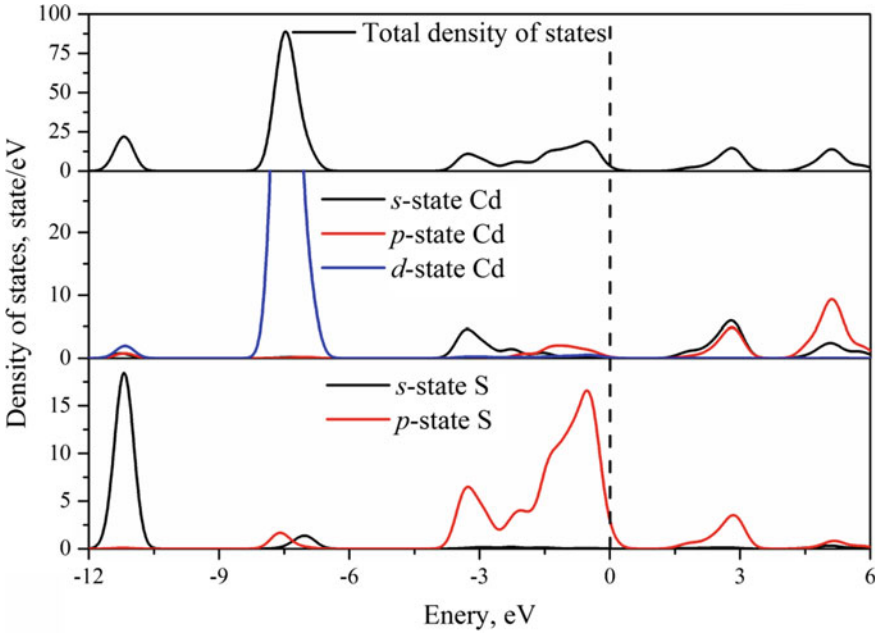

Fig. 5 Density of states of CdS thin films [15]

electronic density allowed us to determine the genesis of the valence and conduction bands of the CdX (X = S, Se, and Te) thin film. In the case of CdS thin films, the *s*-states of S are responsible for the formation of lowest bands in the range from –12 to –10 eV. The next bands localized at the energy range from –9 to –6 eV are formed by the contributions of cadmium *d*-states. The overlapping of the *p*-states of S and the *p*-states of Cd forms the top of the valence bands. In turn the bottom of conduction band basically is formed by overlapping the *s*-states of cadmium as well as *p*-states of sulfur and cadmium. Considering the results of theoretical calculation of electronic structure, density of electronic states, and the selection rules, we can assume that the smallest band gap is formed by the direct *s*–*p* transitions. In case of other compounds (CdSe and CdTe thin films), significant changes weren't observed. For all compounds, the top level of valence bands complex is basically formed by the *p*-states of chalcogenides (S, Se, Te). We can assume that the chalcogenides–cadmium linkages are responsible for forming the direct band transition (point Γ of the Brillouin zone).

9 Conclusions

Methods of deposition of thin films of cadmium chalcogenides are analyzed. The quasi-CSS growth method was optimized and was used to grow CdTe and CdSe thin films on non-orienting (glass and ITO-coated glass) and orienting (sapphire and silicon) substrates. Another method of deposition CdX (X = S, Se, and Te) thin films which used in this work is high-frequency magnetron sputtering. Microphotographs of the cadmium chalcogenide films showed uniform distribution of grains and indicate the formation of homogeneous films obtained by both deposition methods. The average crystallite size obtained by morphology analysis of the surface was determined. With increasing deposition temperature, the average grain size in the films increases. The X-ray diffraction analysis confirmed the synthesis of the semiconductor compounds, and their structural parameters were obtained.

The optical transmittance spectra are characterized by the fundamental absorption edge with the wavelength position of which is typical for the cadmium chalcogenides compounds. Using the interference behavior of the optical spectra, the thickness of the CdX (X = S, Se, and Te) films is calculated. We observed a tendency for the grain size to increase with increasing film thickness.

On the basis of theoretical calculations of electron energy structure for CdX (X = S, Se, and Te) thin film established localization of a direct band gap at the Γ point of the Brillouin zone. The nature of the conduction band, valence bands, and the band gap is established. The substitution of chalcogenides in CdX (X = S, Se, and Te) does not make significant changes in the density of states.

References

1. Kurilo IV, Ilchuk HA, Lukashuk SV, Rudyi IO, Ukrainets VO, Chekaylo NV (2011) Morphology, elemental composition, and mechanical properties of polycrystalline CdTe layers. Semiconductors 45(12):1531–1537
2. Medvedev SA, Klevkov YV, Kolosov CA, Krivobok VS, Plotnikov AF (2002) Photoconductivity of the coarse-grained polycrystals of CdTe. Fiz Tekh Poluprovodnikov 36(8):937–940
3. Sermakasheva NL, Novikov GF, Shul'ga YuM, Semenov VN (2004) Microwave photoconductivity and photodielectric effect in thin PbS films obtained from thiocarbamide coordination compounds. Semiconductors 38(4):380–386
4. Mil'vidskii MG (1986) Semiconductor materials in modern electronics. Nauka, Moscow (in Russian)
5. Romeo N, Bosio A, Tedeschi R, Canevari V (2000) Growth of polycrystalline CdS and CdTe thin layers for high efficiency thin film solar cells. Mater Chem Phys 66(2):201–206
6. Basola BM, McCandless B (2014) Brief review of cadmium telluride-based photovoltaic technologies. J Photon Energy 4(1):040996
7. Romeo N, Bosio A, Canevari V, Podestá A (2014) Recent progress on CdTe/CdS thin film solar cells. Sol Energy 77(6):795–801
8. Paudel NR, Xiao C, Yan Y (2014) Close-space sublimation grown CdS window layers for CdS/CdTe thin-film solar cells. J Mater Sci Mater Electron 25(4):1991–1998

9. Averin SV, Kuznetsov PI, Zhitov VA, Alkeev NV, Kotov VM, Zakharov LY, Gladysheva NB (2012) Metal-semiconductor-metal photodiodes based on ZnCdS/GaP wide-gap heterostructures. Tech Phys 57(11):1514–1518
10. Bhattacharya RN, Contreras MA, Egaas B, Noufi RN, Kanevce A, Sites JR (2006) High efficiency thin-film $CuIn_{1-x}Ga_xSe_2$ photovoltaic cells using a $Cd_{1-x}Zn_xS$ buffer layer. Appl Phys Lett 89(25):253503
11. Oladeji IO, Chow L (2005) Synthesis and processing of CdS/ZnS multilayer films for solar cell application. Thin Solid Films 474(1–2):77–83
12. Mahmood W, Ali J, Zahid I, Thomas A, Haq A (2018) Optical and electrical studies of CdS thin films with thickness variation. Optik 158:1558–1566
13. Bosio A, Romeo N, Mazzamuto S, Canevari V (2006) Polycrystalline CdTe thin films for photovoltaic applications. Prog Cryst Growth Charact Mater 52(4):247–279
14. McCandless BE, Dobson KD (2004) Processing options for CdTe thin film solar cells. Sol Energy 77(6):839–856
15. Petrus RYu, Ilchuk HA, Kashuba AI, Semkiv IV, Zmiiovska EO (2019) Optical-energy properties of CdS thin films obtained by the method of high-frequency magnetron sputtering. Opt Spectrosc 126(3):220–225
16. Roth M (1989) Advantages of limitations of cadmium selenide room temperature gamma ray detectors. Nucl Instrum Methods UK 283(2):291–298
17. Joshi SS, Lokhande CD, Han SH (2007) A room temperature liquefied petroleum gas sensor based on all-electrodeposited *n*-CdSe/*p*-polyaniline junction. Sens Actuators B Chem 123(1):240–245
18. Smyntyna VA, Gerasutenko V, Kashulis S, Mattongo G, Reghini S (1994) The causes of thickness dependence on the sensitivity of CdSe and CdS gas sensors to oxygen. Sensors Act B 19(1–3):464–465
19. Potyrailo RA, Leach AM (2006) Selective gas nanosensors with multisize CdSe nanocrystal/polymer composite films and dynamic pattern recognition. Appl Phys Lett 88(13):134110
20. Chu CS, Chuang CY (2015) Optical fiber sensor for dual sensing of dissolved oxygen and Cu^{2+} ions based on PdTFPP/CdSe embedded in sol–gel matrix. Sens Actuators B Chem 209:94–99
21. Ding L, Fan C, Zhong Y, Li T, Huang J (2013) A sensitive optic fiber sensor based on CdSe QDs fluorophore for nitric oxide detection. Sens Actuators Chem 185:70–76
22. Guminilovych RR, Shapoval PI, Yatchyshyn II, Ilchuk GA, Kusnezh VV (2013) Chemical surface deposition and growth rate of thin CdSe films. Russ J Appl Chem 86(5):696–702
23. Nair PK, Nair MTS, Garcia VM, Arenas OL, Peña Y, Castillo A, Ayala IT, Gomezdaza O, Sánchez A, Campos J, Hu H, Suárez R, Rincón ME (1998) Semiconductor thin films by chemical bath deposition for solar energy related applications. Sol Energy Mater Sol Cells 52(3–4):313–344
24. Kariper IA, Baglayan Ö, Gödec F (2015) Fabrication and optical characterization of CdSe thin films grown by chemical bath deposition. Acta Phys Pol, A 128(2):19–221
25. Baban C, Rusu GI (2003) On the structural and optical characteristics of CdSe thin films. Appl Surf Sci 211(1–4):6–12
26. Tepantlan CS, Gonzalez AMP, Arreola IV (2008) Structural, optical and electrical properties of CdS thin films obtained by spray pyrolysis. Rev Mex Fis 54(2):112–117
27. Baban C, Rusu GI, Prepelita P (2005) On the optical properties of polycrystalline CdSe thin films. J Optoelectronics Adv Mater 7(2):817–821
28. Chikwenze RA, Nwofe PA, Agbo PE, Nwankwo SN, Ekpe JE, Nweke FU (2015) Effect of dip time on the structural and optical properties of chemically deposited CdSe thin films. Int J Mater Sci Appl 4(2):101–106
29. Il'chuk GA, Kurilo IV, Petrus RY, Kus'nezh VV (2014) Growth of CdTe films on Ni-coated microtextured silicon substrates. Inorg Mater 50(6):559–565
30. Il'chuk GA, Kurilo IV, Kus'nezh VV, Petrus RY, Kogut IT, Stan'ko TN (2013) Morphology, structure, and composition of polycrystalline CdTe films grown on three-dimensional silicon substrates. Inorg Mater 49(4):329–334

31. Ilchuk HA, Petrus RY, Kashuba AI, Semkiv IV, Zmiiovska EO (2018) Optical-energy properties of CdS single crystal and thin films. Nanosistemi, Nanomateriali, Nanotehnologii 16(3):519–533
32. Il'chuk GA (2000) Model of quasi-equilibrium mass transfer of cadmium telluride sublimated in closed volume. Semiconductor Sci Technol 15(12):1141–1143
33. Il'chuk GA, Kurilo IV, Kus'nezh VV, Petrus' RYu, Shapoval PI, Guminilovich RR, Partyka MV, Tokarev SV (2014) Growth of thin CdS films on glass substrates via reaction of thiourea with cadmium acetate in aqueous solution. Inorg Mater 50(8):762–767
34. Il'chuk GA, Ukrainets VO, Rud' YuV, Kuntyi OI, Ukrainets NA, Lukiyanets BA, Petrus RYu (2004) Electrochemical synthesis of thin CdS films. Technical Physics Letters 30(8):628–630
35. Il'chuk GA, Kusnezh VV, Rud' VYu, Rud' YuV, Shapowal PYo, Petrus' RYu (2010) Photosensitivity of *n*-CdS/*p*-CdTe heterojunctions obtained by chemical surface deposition of CdS. Semiconductors 44(3):318–320
36. Kraus W, Nolze G (1996) POWDER CELL - A program for the representation and manipulation of crystal structures and calculation of the resulting X-ray powder patterns. J Appl Crystallogr 29(3):301–303
37. Bloom S, Bergstresser TK (1968) Band structure of α-Sn, InSb and CdTe including spin-orbit effects. Solid State Commun 6(7):465–467
38. Vanderbilt D (1990) Soft self-consistent pseudopotentials in a generalized eigenvalue formalism. Phys Rev B 41(11):7892–7895
39. Perdew JP, Burke K, Ernzerhof M (1996) Generalized gradient approximation made simple. Phys Rev Lett 77(18):3865–3868

Smart Nanocarriers for Delivery of Anticancer Drugs: Recent Advances and Disadvantages

Nataliya Kutsevol and Antonina Naumenko

1 Introduction

Nowadays, chemotherapy is the major cancer treatment. However, low selectivity and wide side effect give additional problem to the clinical application of antitumor drugs. Chemotherapy damages both normal and tumor cells. Therefore, it is important to develop novel drug delivery systems for overcoming side effect and to improve the efficacy of anticancer drugs [1]. Nanotechnology is a promising approach for creation of highly efficient nanocarriers for modern cancer therapy, including dendrimers, polymeric nanoparticles, liposomes, etc. Polymer nanoparticles are considered as promising nanoplatform and nanocarrier for drug delivery [2]. Current reviews have demonstrated that polymer molecules have possibility to be accumulated by tumors [3]. However, most of water-soluble polymers cannot provide controllable drug release. To overcome this problem, stimuli-sensitive polymer as thermosensitive and pH-sensitive can be used for controlled release of drugs [4]. Such approach gives possibility to decrease the dosage of toxic drugs, although the drug concentration in tumor can be maintained for a much longer time [5].

Thus, such nanocarriers are considered as smart ones. However, for engineering of effective stimuli-responsive nanosystems, it should be deep knowledge on nanosystem biocompatibility and its capacity to load of antitumor drugs, stability, and toxicity of nanosystems. In this work, we summarized our recent research on the creation and characterization of nanocomposites synthesized into stimuli-responsible polymers and some advantages and possible disadvantages for their use in chemotherapy and photodynamic antitumor therapy.

N. Kutsevol (✉) · A. Naumenko
Taras Shevchenko National University of Kyiv, Kiev, Ukraine
e-mail: kutsevol@ukr.net

O. Fesenko and L. Yatsenko (eds.), *Nanooptics and Photonics, Nanochemistry and Nanobiotechnology, and Their Applications*, Springer Proceedings in Physics 247, https://doi.org/10.1007/978-3-030-52268-1_10

Table 1 Molecular characteristics of D-*g*-PAA determined by SEC

Sample	$M_w \times 10^{-6}$ (g mol^{-1})	R_g (nm)	M_w/M_n
D-*g*-PAA	2.15	85	1.72

2 Stimuli-Responsive Polymers Nanocarriers

2.1 pH-Sensitive Polymer

The pH-responsive polymers have attracted attention as promising approach for applications in cancer therapy. The normal tissues and blood have pH value of 7.4, but the pH of tumors is from 6.0 to 6.5 [4]. Thus, the use of pH-sensitive nanocarriers can target deliver of the encapsulated antitumor drugs to cancer cells.

A star-like copolymer with dextran (D) core and polyacrylamide (PAA) grafts was used for preparation of pH-sensitive nanocarrier. This polymer was synthesized by grafting PAA chains onto dextran with $M_w = 7 \times 10^4$ g/mol, using a ceric-ion-reduce initiation method [6]. The synthesis, characterization, and analysis of polymer structure were reported in [7]. The theoretical number of grafts for this polymer was equal to 5. Further, this copolymer was referred as D-*g*-PAA. This copolymer was chosen based on our previous research as the most efficient polymer nanocarrier for photodynamic therapy [8].

For transformation of the D-*g*-PAA copolymer in anionic form, the alkaline hydrolysis was used. The anionic polymer was referred as D-*g*-PAA (PE) throughout [7]. The degree of hydrolysis of PAA chains was determined by potentiometric titration and was equal to 43%.

The molecular characteristics of the D-g-PAA copolymer, according to size-exclusion chromatography, are shown in Table 1.

2.2 Thermosensitive Polymer

Poly(*N*-isopropylacrylamide) (PNIPAM) is referred in several reviews as attractive polymer for biomedical application. PNIPAM is soluble in water and has lower critical solution temperature (LCST) close to physiological temperatures [9, 10], that is why drug delivery, biosensors, and bioimaging can be the most promising areas of this polymer application. Below LCST the polymer is soluble, above LCST undergoes a phase transition; then collapse and form aggregates. Linear PNIPAM has an LCST value of approximately 32 °C, its phase transition observes at physiological temperature (37 °C), and therefore, it can be used for controlled release of the drug for cancer therapy [11].

Table 2 Molecular characteristics of D-*g*-PNIPAM determined by SEC

Sample	$M_w \times 10^{-6}$ (g/mol)	M_w/M_n	Dh^{25C} (nm)
D-*g*-PNIPAM	1.03	1.52	40

A star-like copolymer dextran-graft-PNIPAM (D-g-PNIPAM) was referred as efficient nanocarrier for delivery of doxorubicin (Dox) [12]. D-g-PNIPAM is star-like with dextran core and PNIPAM grafts. The conformational transition for this copolymer was registered within the temperature range of 32.6–33.4 °C that was higher than LCST point for linear PNIPAM of similar molecular weight and polydispersity and is closer to physiological temperature (37 °C). A possible tuning of the hydrophobicity of star-like polymer, the regulation of the region of phase transition and size of hydrophobic domains by variation of copolymer internal structure were reported [13]. The number of grafting sites per dextran backbone was equal to 15. The sample was designated as D-*g*-PNIPAM.

The molecular characteristics of D-*g*-PNIPAM copolymer are given in Table 2.

2.3 Preparation of Nanosystems

2.3.1 Reagents

Photosensitizer chlorine e6 (Ce6) from Santa Cruz Biotechnology (USA); doxorubicin hydrochloride (Dox) from Sigma-Aldrich (USA); cisplatin (CPt) from "EBEVE" (Austria); $NaBH_4$; $AgNO_3$; $HAuCl_4$; Hank's balanced salt solution from Sigma-Aldrich (USA); dimethyl sulfoxide (DMSO) from Serva (Germany) were used for nanosystems preparation.

2.3.2 Nanosystem Polymer/AgNPs/CPt

Silver nanoparticles (AgNPs) were synthesized in situ in polymer solution of $AgNO_3$. 2 mL of $AgNO_3$ aqueous solution ($C = 0.1$ M) was added to 5 mL of aqueous solution of polymer ($C = 1 \times 10^{-3}$ g/mL) and stirred for 20 min. Then, 2 mL of aqueous solution of $NaBH_4$ ($C = 0.1$ M) was added and stirred for 30 min. The color of solution turned reddish brown that indicated the formation of AgNPs. 1 mL of *C*Pt ($C = 0.5$ mg/mL) was added to the 1 mL of prepared solution of D-*g*-PAA/AgNPs under stirring for 30 min. A basic solution of nanocomposite containing polymer/AgNPs/CPt was diluted by water to achieve needed concentration of CPt for cytotoxicity experiments.

2.3.3 Nanosystem Polymer/AuNPs

For in situ AuNPs synthesis into polymer solution, tetrachloroauric acid and $NaBH_4$ (reductant) were used. The synthesis process was reported in [14].

2.3.4 Nanosystem Polymer/AuNPs/Ce6/Dox

Ce6 was dissolved in DMSO ($C = 0.182$ mg/mL). Then, 0.55 mL of Ce6 solution was added to 0.27 mL of distilled water. This mixture was added to 1.15 mL of polymer/AuNPs nanosystem, and then, Dox was added. The concentration of Dox in nanocomposite was equal to 0.20 m kg/mL.

2.4 Methods

2.4.1 Fourier Transform Infrared (FTIR) Spectroscopy

Nicolet NEXUS-475 (USA) spectrophotometer was used to obtain FTIR spectra in the range 4000–400 cm^{-1}. The thin films ($l = 6$–9 μm) were fabricated from aqueous solutions of polymer and solution of polymer with addition of CPt or Dox.

2.4.2 Transmission Electron Microscopy (TEM)

The analysis of the nanoparticles was carried on two TEMs, Tecnai G2 or CM12 (FEI, Eindhoven, Netherlands). The images were acquired with a ssCCD Eagle camera on the Tecnai and a Megaview SIS camera. 400 mesh Cu grids with plain carbon film were used for samples preparation (Elmo, Cordouan Technologies, Bordeaux, France).

2.4.3 Quasi-Elastic Light Scattering and Determination of Zeta Potential

Size distribution of scattering objects and zeta potential for nanosystems were performed by quasi-elastic light scattering (QELS) on a Zetasizer Nano-ZS90 (Malvern, Worcestershire, UK) at $T = 298$ K. The instrument was equipped with a He–Ne laser (5 mW) operating at the wavelength of 633 nm. The autocorrelation function of the scattered light intensity was analyzed.

2.5 Biological Examination

2.5.1 Cell Culture

Cell lines were obtained from culture collection of Institute of Molecular Biology and Genetics of NASU (J-774 (murine macrophage cell line), K-562 (human chronic myelogenous leukemia cell line), and U-937 (human histiocytic lymphoma cell line)). All cell lines were maintained in Dulbecco's modified Eagle medium (DMEM) containing 4.00 mM L-glutamine, 4500 mg/mL glucose, and sodium pyruvate. 10% fetal bovine serum (GE Healthcare) and 1% penicillin/streptomycin were added to the culture medium. The cells were cultured in a humidified atmosphere at 37 °C and 5%.

R. E. Kavetsky Institute for Experimental Pathology, Oncology, and Radiobiology NASU provided the MT-4 cells (human T cell leukemia) from The Bank of Cell Lines from human and animal tissue. Cells were maintained in RPMI-1640 containing 10% FBS at 37 °C in humidified atmosphere and 5% CO_2.

Sublines of breast carcinoma MCF-7 cells, namely MCF-7/S—sensitive to cytostatics; MCF-7/Dox—resistant to doxorubicin (Dox), were obtained from the culture bank of the same Institute. Cells were maintained in RPMI-1640 medium containing 10% fetal bovine serum at 37 °C in 95% air and 5% carbon dioxide (CO_2).

2.5.2 In Vitro Study of Nanosystems Cell Viability

MTT assay was used to determine cell viability. Cells were seeded at cell density of 1–105 cells/mL, 100 μL in each of 96 wells. The incubation period was 16 h. Various concentrations of the nanoparticles were used. 10 μL of MTT reagent was added to each well after 48 h incubation and incubated for 4 h. The optical density was measured at 570 nm for the control.

2.5.3 Photodynamic Activity Test

Cell suspensions were prepared from a culture of the malignant cell lines in a log phase of growth. For the preparation, the Hank's balanced salt solution was used. The 1.5-h incubation period for cells in nanocomposite ($t = 37$ °C) was used. After that, the cells were washed twice with fresh Hank's solution. The prepared samples were irradiated with red laser excitation ($\lambda = 658$ nm, power density $= 1.1$ mW/cm^2, dose $= 1$ J/cm^2). After irradiation, the cells were replaced to growth medium, incubated for 18 h ($t = 37$ °C) to finished apoptosis process. The trypan blue dye exclusion test was used to estimate the viability of cells. MTT test was used to determine of the evaluation of dark cytotoxicity of nanocomposites.

3 Results and Discussion

As it was mentioned above, the goal of modern cancer treatment is to kill cancer cells effectively, leaving healthy cells intact. Our research revealed the efficiency of anticancer nanosystems combined the branched copolymer dextran-graft-polyacrylamide and cisplatin. The further attempt was made to improve this nanosytem by adding of silver nanoparticles to nanocomposite.

It was reported that the pH-sensitive copolymer nanocontainers D-g-PAA(PE) was absorbed by macrophages (J-774) and was not cytotoxic [15]. Polymer nanocontainers were completed with the cisplatin-cytotoxic chemotherapy drugs. Complexes of copolymer D-g-PAA(PE)/CPt were synthesized. The FTIR spectra confirmed the complex formation. The FTIR spectra of individual polymer and D-g-PAA(PE)/CPt are represented in Fig. 1.

A nanocomposite polymer/AgNPs and triple nanocomposite polymer/AgNPs/CPt were prepared. The TEM image of these nanosystems is shown in Fig. 2.

Figure 2a demonstrates the presence of nanoparticles with two sizes: 10–15 nm and 2–5 nm due to the interaction of silver ions with carbamide (as in nonionic polymers) and carboxylate groups of the anionic polymer matrix. From Fig. 2b, one can see the partial decreasing of polymer solubility in ternary system polymer/AgNPs/CPt due to complex formation between functional groups of polymer matrix and CPt.

The cytotoxic effects of these nanosystems were tested (Fig. 3).

As it was reported in [16] the results of MTT assays revealed a dose-dependent decrease in viability for both cell lines exposed to either silver- or cisplatin-conjugated nanoparticles. In the study, as anticipated, copolymers did not exhibit any toxicity to both cell types. At the same time, the polymer nanoparticles loaded with cisplatin caused the cytotoxic effect in cell lines at 10 μg/mL (40–44% in U-937),

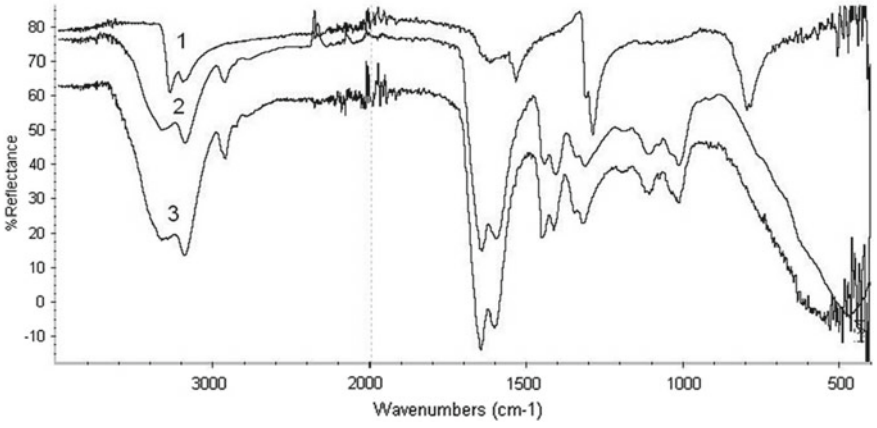

Fig. 1 FTIR spectra for CPt (1), D-*g*-PAA(PE) (2), and D-g-PAA(PE)/CPt (3)

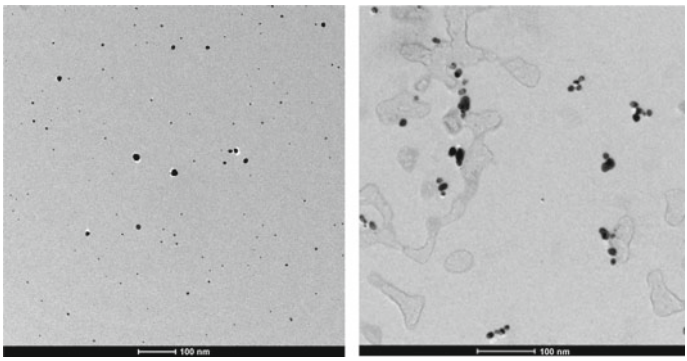

Fig. 2 TEM images of nanosystems polymer/AgNPs (**a**) and polymer/AgNPs/CPt (**b**)

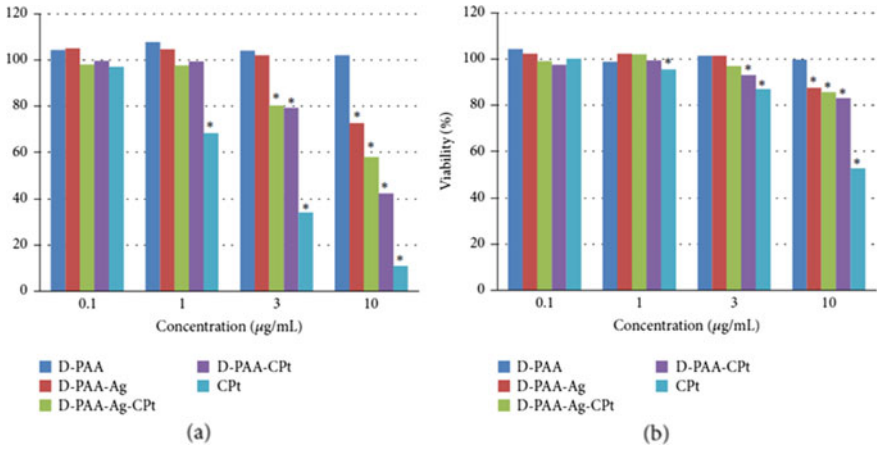

Fig. 3 Viability of the U-937 cells (**a**) and K-562 cells (**b**) after cultivation with the nanoparticles at different concentration for 48 h measured by MTT assay. Mean values of triplicates with standard derivation are shown. $^*P < 0.05$ compared to the untreated control

and so did silver nanoparticles (polymer/AgNPs) at the same concentration (72–76% in U-937 and 86–92% in K-562 provided by MTT assay), although the toxic effect of nanosilver on a cell viability was greater than ones of polymer/cisplatin. Figure 3 demonstrates that a nanosystem where the copolymers were conjugated to both nanosilver and cisplatin displayed less cytotoxic effect compared to the conjugates of dextran-polyacrylamide and cisplatin. It can be deal with some aggregation process which takes place in the ternary nanosystem polymer/AgNPs/CPt (Fig. 2).

A modern trend in photodynamic therapy (PDT) is to use the multifunctional polymer nanocarrier for enhancing target-oriented PDT. The goal of this study was to create hybrid nanocarriers based on the stimuli responsible branched copolymers

D-*g*-PAA(PE) and dextran-*g*-PNIPAM and incorporated AuNPs and photosensitizer, also to try combine PDT with chemotherapy by adding Dox to polymer/AuNPs/Ce6 nanosystem. MT-4 cells were used for testing the ability of these nanosystems onto photodynamic damage. It is very important to estimate the effectiveness of the interaction of the dye molecule with the nanocarrier in nanocomposite photosensitizers (NCPS). That is why we studied how the mass ratio of tetrachloroauric acid to sodium borohydride, which was used as a reducing agent in the synthesis of AuNPs, affects the resulting photodynamic activity of polymer/AuNPs/Ce6 NCPS. The mass ratio of Ce6:AuNPs in all tested samples was 1:10. And the concentration of Ce6 in all samples was equal to 0.1 μg/ml. Figure 4 demonstrates that AuNPs nanocomposite obtained when mass ratio of $HAuCl_4$:$NaBH_4$ during synthesis was 1:2 showed higher photodynamic activity, than Ce6 itself. Nanoparticles synthesis under increase of $NaBH_4$ concentration during the process doesn't affect photodynamic efficacy of nanosystems D-*g*-PNIPAM/AuNPs/Ce6 in comparison with free photosensitizer. However, nanocomposite D-*g*-PAA(PE)/AuNPs/Ce6 ($HAuCl_4$:$NaBH_4$ mass ratio 1:2) demonstrated high enhancement of photodynamic activity in comparison with Ce6 itself.

Namely, this composite has been chosen for preparation of the nanosystem with Dox to combine PDT and chemotherapy. The nanosystems were tested in vitro for its PDT efficiency on the malignant MCF-7/S and MCF-7/Dox cell lines (Fig. 5). The laser irradiation of polymer/AuNPs/Ce6 nanosystem caused the death of 68.4% MCF-7/S cells (Fig. 5a). For MCF-7/Dox cells, nanosystem caused the death of 24.9% (Fig. 5b). However, the activity of nanocomposites containing polymer/AuNPs/Ce6 and Dox for both cell lines was much less.

To understand this phenomenon the three-component nanosystem polymer/AuNPs/Ce6 and four-component nanosystem polymer/AuNPs/Ce6/Dox were studied by DLS at 37 °C. For correct analysis of processes occurring in

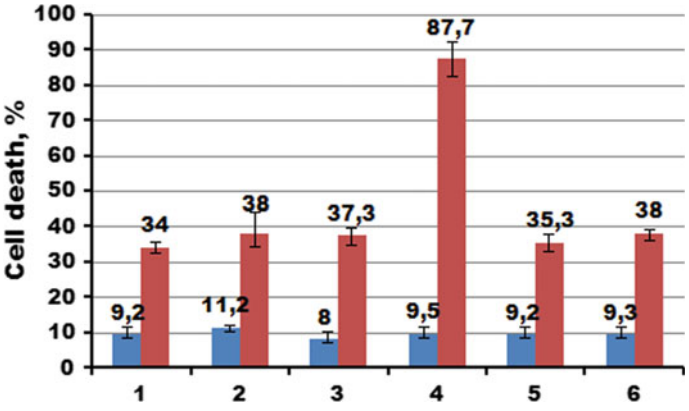

Fig. 4 Dark cytotoxicity and photodynamic activity of polymer/AuNPs/Ce6 nanosystems with different HAuCl4: $NaBH_4$ mass ratios during their synthesis. 1—Ce6 alone; 2—D-*g*-PNIPAM (1:2); 3—D-*g*-PNIPAM (1:4); 4—D-*g*-PAA(PE) (1: 2); 5—D-*g*-PAA(PE) (1:4); 6—D-*g*-PAA(PE) (1: 6)

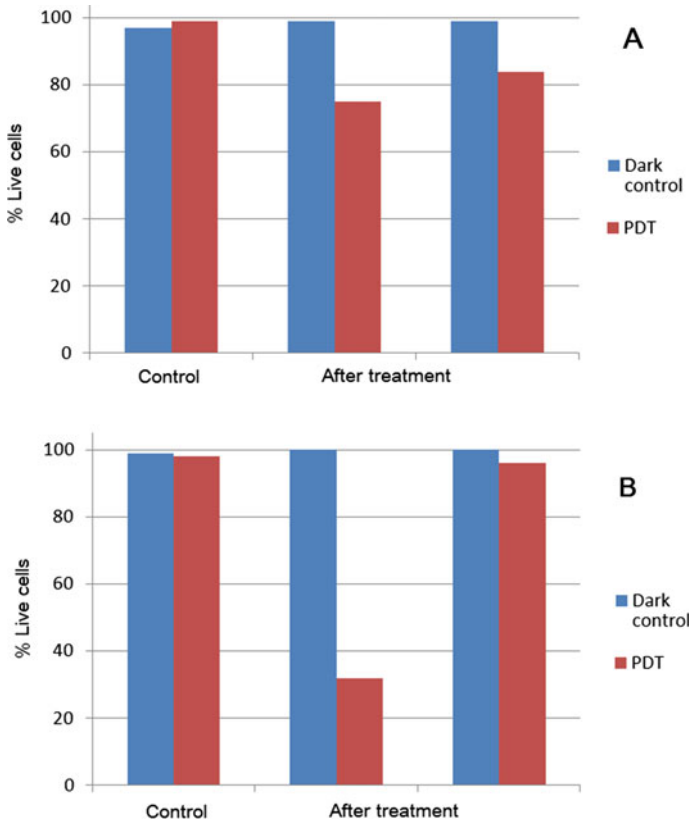

Fig. 5 Effect of PDT on survival of cells—MCF-7/S (**a**), MCF-7/Dox and MCF-7/Ce6 (**b**) lines after the influence of nanocomposites. Control—the same treatment of cells without nanocomposites

multicomponent nanosystems, the author's program for data treatment was used [13]. The size distributions of scattering nanoobjects are shown in Fig. 6.

For three-component nanosystems polymer/AuNPs/Ce6 at 37 °C (Fig. 6, black curve), DLS has revealed several types of scattering nanoobjects. The first maximum corresponds to AgNPs of 10 nm in size. The second maximum can be attributed to the individual macromolecules of 70–80 nm in size with incorporated AgNPs. The third maximum deals with the presence of aggregates of macromolecules of 200–500 nm in size. For four-component nanosystems polymer/AuNPs/Ce6/Dox (Fig. 6, blue curve), AuNPs of 10 nm in size, individual macromolecules, and large aggregates of 800 nm are observed. Obviously, the increased aggregation ability in this nanosystem compared to ones described above is the result of an increase in the number of components included into the macromolecule of the polymer. That leads to change in the hydrophobic-hydrophilic balance of the macromolecule. The strong aggregation process is evident in the TEM images of studied multicomponent nanosystems (Fig. 7).

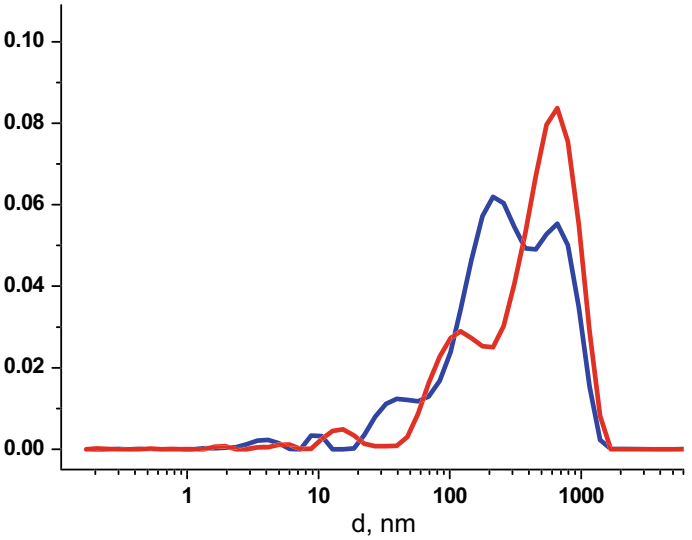

Fig. 6 The dependence of normalized intensity of scattering on hydrodynamic diameter of scattering objects for nanosystems polymer/AuNPs/Ce6 (blue), polymer/AuNPs (red) at 37 °C

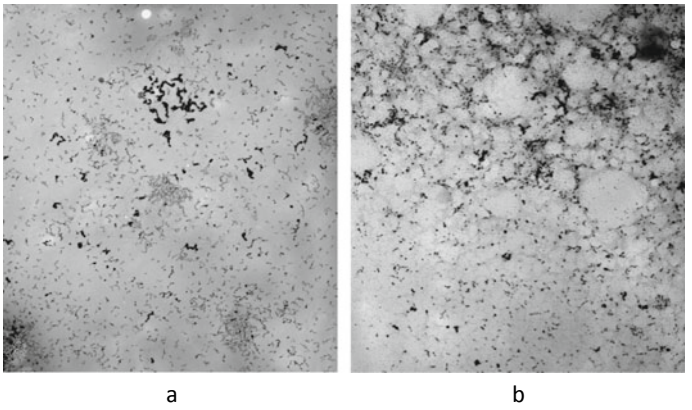

Fig. 7 TEM images of nanosystems: **a** D-*g*-PAA(PE)/AuNPs/Ce6; **b** D-*g*-PAA(PE)/AuNPs/Ce6/Dox

4 Conclusion

Thus, the decreasing of antitumor efficiency of hybrid multicomponent nanosystem synthesized in smart stimuli responsible polymer nanocarriers was registered due to an aggregation process caused by complex formation between functional groups of polymer matrix and encapsulated drugs. As a result, the partial decreasing of polymer

solubility was observed. Thus, we have demonstrated the advantages and possible disadvantages to use the multicomponent nanosystems for antitumor therapy.

Acknowledgements Authors are very grateful to academician V. F. Chekhun—the Director of R. E. Kavetsky Institute for Experimental Pathology, Oncology, and Radiobiology of the National Academy of Sciences of Ukraine, for fruitful collaboration.

References

1. Ganta S, Devalapally H, Shahiwala A, Amiji MJ (2008) A review of stimuli-responsive nanocarriers for drug and gene delivery. Control Releas 126(3):187–204
2. Taghizadeh B, Taranejoo S, Monemian SA, Salehi Moghaddam Z, Daliri K, Derakhshankhah H, Derakhshani Z (2015) Classification of stimuli-responsive polymers as anticancer drug delivery systems. Drug Deliv 22(2):145–155
3. Hatakeyama H (2017) Recent advances in endogenous and exogenous stimuli-responsive nanocarriers for drug delivery and therapeutics. Chem Pharm Bull (Tokyo) 65(7):612–617
4. Vijayakameswara Rao N et al (2018) Recent progress and advances in stimuli-responsive polymers for cancer therapy. Front Bioeng Biotechnol 6:110
5. Gil ES, Hudson SM (2004) Stimuli-responsive polymers and their bioconjugates. Prog Polym Sci 29:1173–1222
6. Bezuglyi M, Kutsevol N, Rawiso M, Bezugla T (2012) Water-soluble branched copolymers dextran-polyacrylamide and their anionic derivates as matrices for metal nanoparticles in-situ synthesis. Chemik 66(8):862–867
7. Kutsevol N, Bezuglyi M, Rawiso M, Bezugla T (2014) Star-like destran-graft-(polyacrylamide-co-polyacrylic acid) copolymers. Macromol Symp 335:12–16
8. Chumachenko VA, Shton IO, Shishko ED, Kutsevol NV, Marinin AI, Gamaleia NF (2016) Branched copolymers dextran-graft-polyacrylamide as nanocarriers for delivery of gold nanoparticles and photosensitizers to tumor cells. In: Fesenko O, Yatsenko L (eds) Springer proceedings in physics "nanophysics, nanophotonics, surface study, and applications", vol 183, pp 379–390
9. Chen S, Zhonh H, Gu B, Wang Y, Li X, Cheng Z, Zhang L, Yao C (2012) Thermosensitive phase behavior and drug release of in situ N-isopropylacrylamide copolymer. Mater Sci Eng C Mater Biol Appl 32:2199–2204
10. Bischofberger I, Trappe V (2015) New aspects in the phase behavior of poly-N-isopropylacrylamide: systematic temperature dependent shrinking of PNIPAM assemblies well beyond the LCST. Sci Rep 5:15520
11. Guan Y, Zhang Y (2011) PNIPAM microgels for biomedical applications: from dispersed particles to 3D assemblies. Soft Matter 7:6375–6384
12. Matvienko T, Sokolova V, Prylutska S, Harahuts Y, Kutsevol N, Kostjukov V, Evstigneev M, Prylutskyy Y, Epple M, Ritter U (2019) In vitro study of the anticancer activity of various Doxorubicin-containing dispersions. Bioimpacts 9(1):59–70
13. ChumachenkoV, Kutsevol N, HarahutsY, Rawiso M, Marinin A, Bulavin L (2017) Star-like dextran-graft-PNiPAM copolymers. Effect of internal molecular structure on the phase transition. J Mol Liq 235:77–82 (2017)
14. Kutsevol N, Glamazda A, Chumachenko V, Harahuts Y, Stepanian S, Plokhotnichenko A, Karachevtsev A (2018) Behavior of hybrid thermosensitive nanosystem dextran-graft-pnipam/gold nanoparticles: characterization within LCTS. J Nanopart Res 20:236
15. Telegeeva P, Kutsevol N, Filipchenko S, Telegeev G (2017) Dextran-polyacrylamide as nanocarrier for targeted delivery of anticancer drugs into tumor cells. In: Mukbaniany O, Abadie M,

Tatrishvili T (eds) Chemical engineering of polymers production of functional and flexible materials, Part 2, pp 183–195
16. Telegeev G, Kutsevol N, Chumachenko V, Naumenko A, Telegeeva P, Filipchenko S, Harahuts Y (2017) Dextran-polyacrylamide as matrices for creation of anticancer nanocomposite. Int J Polymer Sci Article ID 4929857

Natural Nanobentonites as Supports in Palladium(II)–Copper(II) Catalysts for Carbon Monoxide Oxidation with Air Oxygen

Tatyana Rakitskaya, Ganna Dzhyga, Tatyana Kiose, and Vitaliya Volkova

1 Introduction

Natural and differently modified bentonites mainly containing montmorillonite and silica phases (α-quartz, β-cristobalite, and α-tridymite) are among the most promising materials of the twenty-first century [1, 2] owing to their unique structural and physicochemical properties, wide-spread occurrence, low price, and environmentally friendly behavior. Bentonites are used in different fields of science and technology. In chemistry, they are mainly applied in catalytic reactions involving organic compounds [3] and for adsorption of heavy metal ions [4, 5]. Despite the fact that layered aluminosilicates from different deposits are well studied and results of their investigations are reported in many monographs [6–10] and reviews [11, 12], research continues to study physicochemical and structural properties of both natural and differently modified bentonites in order to extend their area of application. It should be noted that the bentonite origin is one of the most important factors influencing bentonite behavior [6, 7, 13, 14]. The data concerning the use of natural and modified bentonites as supports for metal complex compounds showing their catalytic properties in the removal of toxic gaseous substances, particularly, carbon monoxide, from air are scant. As previously reported [2, 13, 15–17], the main components of the anchored metal complex catalysts based on different supports for the low-temperature CO oxidation are palladium(II) and copper(II) complexes. The catalytic activity of supported Pd(II)–Cu(II) complexes was varied by changing the nature and concentrations of palladium(II) and copper(II) precursors and the nature of supports [15–20]. Depending on their origin, natural bentonites differ in their phase compositions, phase ratios, and the presence of impurities. These factors influence

T. Rakitskaya (✉) · G. Dzhyga · T. Kiose · V. Volkova
Odessa I.I. Mechnikov National University, Odesa, Ukraine
e-mail: tlr@onu.edu.ua

O. Fesenko and L. Yatsenko (eds.), *Nanooptics and Photonics, Nanochemistry and Nanobiotechnology, and Their Applications*, Springer Proceedings in Physics 247, https://doi.org/10.1007/978-3-030-52268-1_11

their physicochemical properties and thus the catalytic activity of palladium–copper complexes anchored on them in the reaction of CO oxidation with air oxygen [15].

The aim of the work was to determine the effect of structural and physicochemical properties of natural bentonites from three Ukrainian deposits on the activity of bentonite-based palladium(II)–copper(II) nanocatalysts in the process of CO oxidation with air oxygen.

2 Experimental

Natural bentonites (N-Bents) from three Ukrainian deposits, i.e., Gorbskii, N-Bent(G) (TU U 26.8-05792908.005:2005), Dashukovskii, N-Bent(D) (TU U 14.2-00223941-006:2010), and Kirovogradskii, N-Bent(K) (TU U 14.2-23231149-001-2002), were used in the research.

K_2PdCl_4-$Cu(NO_3)_2$-KBr/N-Bents were prepared by incipient wetness impregnation of each natural bentonite with aqueous-alcohol solution at certain ratios of the anchored compounds. The wet mass obtained was kept in a closed Petri dish at 20–25 °C for 24 h and then dried in an oven at 110 °C till constant weight. Palladium(II), copper(II), and KBr contents in the samples thus obtained were 2.72×10^{-5} mol/g, 2.90×10^{-5} mol/g, and 1.02×10^{-4} mol/g, respectively. The catalyst samples were denoted as Pd(II)–Cu(II)/N-Bents.

The X-ray powder diffraction analysis was carried out on a Siemens D500 diffractometer (CuK_α radiation, $\lambda = 1.54178$ Å) with a secondary beam graphite monochromator. For data recording, the samples crumbled in a porcelain mortar were placed into a glass cell with an enclosed volume of $2 \times 1 \times 0.1$ cm^3. XRD patterns were measured in the angle range of $3° < 2\theta < 70°$ with the pitch of 0.03° and acquisition time of 60 s for each position.

The bentonite samples were also characterized by scanning electron microscopy using a JEOL-JSM5410 scanning microscope with an AZtech Energy X-max^n 50 energy dispersive spectrometer. An accelerating voltage was 15 kV.

Analysis of FT-IR spectra in the range from 400 to 4000 cm^{-1} with resolution of 4 cm^{-1} was carried out using a Perkin Elmer FT-IR spectrometer. All spectra were recorded using pellets consisting of 1 mg of the material under study and 200 mg of KBr compressed under pressure of 7 tons/cm^2 for 30 s.

Water vapor ad/desorption was studied gravimetrically using a vacuum setup temperature controlled at 21 ± 0.2 °C and containing a conventional McBain-Bakr silica-spring balance [21].

The thermal behavior of the samples (0.25 g each) was investigated by DTG-DTA using a Paulik, Paulik and Erdey derivatograph in the temperature range from 25 to 1000 °C with a linear heating rate of 10 °C/min. A measurement error was ±5%.

Protolytic properties of the bentonite surface were estimated by measurement of equilibrium pH, pH_{eq}, values in aqueous suspensions of 0.2 g N-Bent in 20 mL of distilled water. pH values were measured by a pH-340 instrument with an ESL 43-07

glass electrode and an EVL 1M3 chlor-silver electrode under continuous stirring of the suspensions at 20 °C.

The samples (10 g) of K_2PdCl_4–$Cu(NO_3)_2$–KBr/N-Bent compositions were tested in a gas-flow setup with a fixed-bed glass reactor at an initial CO concentration in the gas–air mixture (GAM), C_{CO}^{in}, of 300 mg/m^3 and the following GAM parameters: temperature of 20 °C, relative humidity, RH, of 67%, a volume flow rate, w, of 1 L/min, a linear velocity, U, of 4.2 cm/s. By monitoring final CO concentrations, C_{CO}^{f}, a carbon monoxide conversion, η (%), was determined and η in a steady-state mode, η_{st}, serves as a parameter characterizing the catalytic activity of the compositions.

$$\eta = \frac{\left(C_{CO}^{in} - C_{CO}^{f}\right)}{C_{CO}^{in}} \times 100, \%, \quad (1)$$

where C_{CO}^{in}, C_{CO}^{f} are the initial and final CO concentrations, mg/m^3.

3 Results and Discussion

3.1 Chemical Compositions

The results of elemental analysis of natural bentonites from different deposits in terms of oxides are summarized in Table 1. N-Bent(D) is characterized by the minimum SiO_2/Al_2O_3 ratio and a high CaO content.

Table 1 Chemical compositions of natural bentonites from three Ukrainian deposits

Bentonite components	Content, wt%		
	N-Bent(G)	N-Bent(D)	N-Bent(K)
SiO_2	63.18	52.23	62.12
Al_2O_3	25.70	22.58	22.84
Fe_2O_3	8.23	10.17	8.39
TiO_2	1.09	1.44	1.37
CaO	0.54	11.15	0.74
MgO	0.66	1.94	1.56
Na_2O	–	0.26	0.99
K_2O	0.60	0.22	1.53
SiO_2/Al_2O_3	2.45	2.31	2.72

3.2 Phase Compositions

XRD patterns of natural bentonites and Pd(II)–Cu(II)/N-Bent nanocompositions are shown in Fig. 1a, b, respectively. By identification of XRD patterns, it has been found that these bentonites are polyphase minerals containing montmorillonite, M, (layered aluminosilicate with 2:1 structure) and α-quartz, Q ($2\theta = 20{,}855°$, $d = 4.258$ Å and $2\theta = 26.630°$, $d = 3.346$ Å). Impurities of kaolinite, K ($2\theta = 12.470°$, $d = 7.096$ Å and $2\theta = 25.080°$, $d = 3.550$ Å) and α-tridymite, α-tr, ($2\theta = 21.828°$, $d = 4.068$ Å and $2\theta = 35.954°$, $d = 2.497$ Å) are sharply defined for N-Bent(G) but absent for N-Bent(D) and N-Bent(K). Calcite, C, ($2\theta = 29.405°$, $d = 3.035$ Å and $2\theta = 48.523°$, $d = 1.874$ Å) is present in significant quantities in N-Bent(D), whereas its reflections are very weak for N-Bent(G) and N-Bent(K). Amorphous SiO_2 is present in all these bentonites, and impurities of anatase and goethite are observed as very weak reflections (not more than two in each XRD pattern). No additional reflection was found for the nanocompositions (Fig. 1b) signifying that crystalline phases of initial salts, oxide (PdO, CuO) or reduced (Pd^0, Cu^0) forms are absent. X-ray spectral parameters for N-Bents and Pd(II)–Cu(II)/N-Bents are presented in Table 2. As can be seen, the positions and intensities of the first reflection, d_{001}, for the montmorillonite phase are different: d_{001} basal spacing is largest for N-Bent(D); the absolute intensities for this reflection and other montmorillonite phase reflections for N-Bent(K) are half as high as those for N-Bent(G) and N-Bent(D) (Fig. 1a) being evidence for amorphization of the montmorillonite phase. The shift of d_{001} reflection to a higher basal spacing also indicates some destruction in the montmorillonite lattice. From d_{001} values and a depth of the aluminosilicate peak (9.6 Å), Δd values ($\Delta d = d_{001} - 9.6$ Å) characterizing distances between the layers were calculated, and N-Bent(D) was found to have the largest Δd. Crystallite sizes, D (nm), calculated

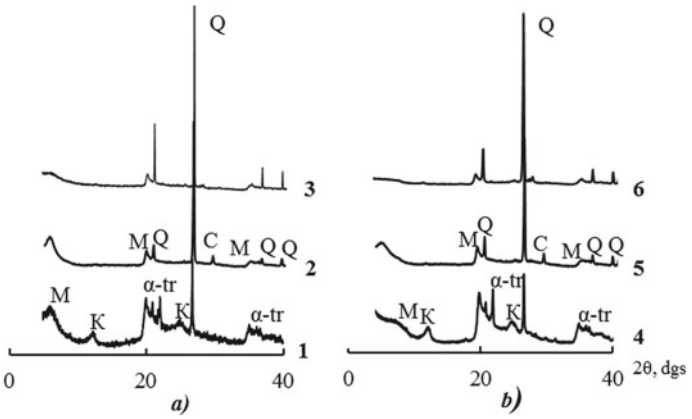

Fig. 1 XRD patterns of natural bentonites **a** N-Bent(G) (1), N-Bent(D) (2), and N-Bent(K) (3) and nanocompositions **b** Pd(II)–Cu(II)/N-Bent(G) (4), Pd(II)–Cu(II)/N-Bent(D) (5), and Pd(II)–Cu(II)/N-Bent(K) (6)

Table 2 X-ray spectral parameters for natural bentonites and Pd(II)–Cu(II)/N-Bent nanocompositions

Sample	d_{001} (Å)	Δd (Å)	d_{006} (Å)	D (nm)
N-Bent(G)	13.817	4.22	1.500	28
N-Bent(D)	15.387	5.79	1.501	14
N-Bent(K)	14.297	4.70	1.540	20
Pd(II)–Cu(II)/N-Bent(G)	12.047	2.45	1.503	27
Pd(II)–Cu(II)/N-Bent(D)	14.345	4.75	1.501	30
Pd(II)–Cu(II)/N-Bent(K)	11.594	1.99	1.541	19

by using the Scherrer formula and taking into account d_{001} parameters, also depend on the bentonite origin. N-Bent(D) was also found to have the largest crystallite size.

Due to Pd(II) and Cu(II) anchoring, a decrease in the d_{001} basal spacing of the montmorillonite phase is observed in all cases. This indicates the contraction of aluminosilicate layers as a result of displacement of water molecules from the interlayer space, penetration of metal ions into hexagonal structure cavities of bentonite and their distribution over the outer bentonite surface. The crystallite sizes for the bentonite samples depend on their origin and are not significantly changed after Pd(II) and Cu(II) anchoring, except for N-Bent(D).

Thus, N-Bent(G) and N-Bent(D) have been found to have the most ordered crystalline structures. The basal spacing values increase in the order N-Bent(G) < N-Bent(K) < N-Bent(D) suggesting different amounts of water molecules in their interlayer spaces [5, 22–26]. For instance, two water layers are possible for air-dry N-Bent(D) [26].

3.3 Morphology

Electron microscopic data for structures of N-Bents and Pd(II)–Cu(II)/N-Bents are shown in Fig. 2. It can be seen that the natural bentonite samples are in a flake-like form characteristic of the montmorillonite phase, although other montmorillonite morphotypes can also occur depending on bentonite origins [27]. An irregular arrangement of globular agglomerations characteristic of an opal-tridymite-cristobalite phase formed from inorganic silica is observed for N-Bent(D) and N-Bent(K) [28]. Tubular structures (Fig. 2a) with slot-like pores (Fig. 2b) are distinctly apparent for N-Bent(G) being evidence for the biogenic silica presence in the opal-tridymite-cristobalite phase [29].

The phase morphology is not changed for the nanocompositions (Fig. 2c, f, i). We can only note compaction of montmorillonite flake-like forms due to contraction of the aluminosilicate layered structure (Table 2).

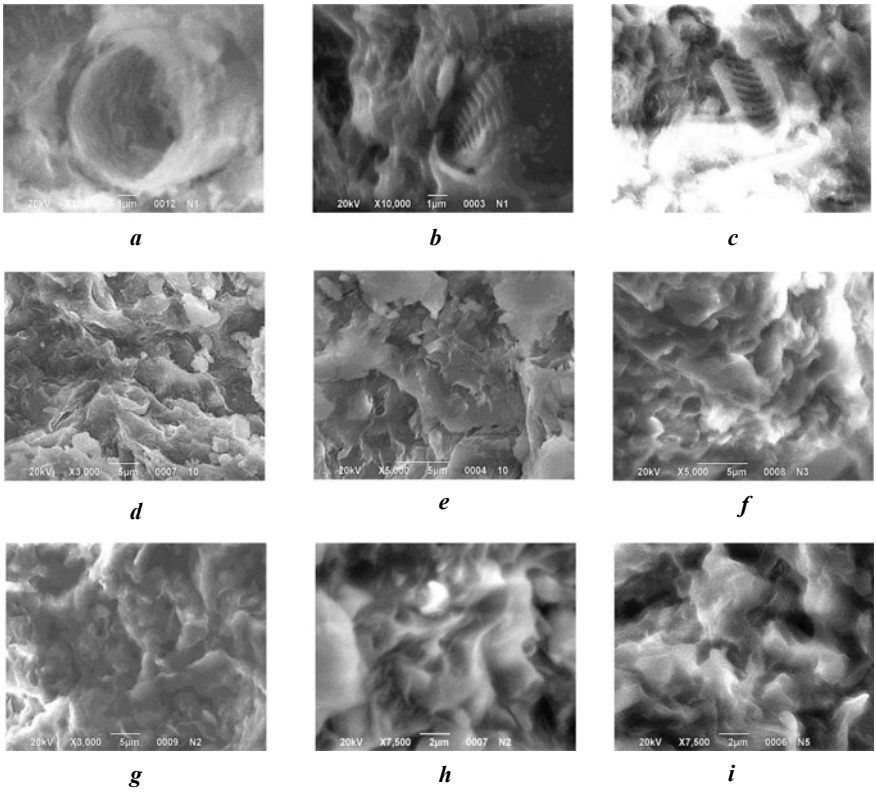

Fig. 2 SEM images of natural bentonites: N-Bent(G) (**a**, **b**), N-Bent(D) (**d**, **e**), N-Bent(K) (**g**, **h**), and nanocompositions: Pd(II)–Cu(II)/N-Bent(G) (**c**), Pd(II)–Cu(II)/N-Bent(D) (**f**), Pd(II)–Cu(II)/N-Bent(K) (**i**)

3.4 FT-IR Spectral Investigation

Figure 3 shows FT-IR spectra indicating polyphasicity of natural bentonites from three Ukrainian deposits. This is evident from the bands characteristic of the main montmorillonite phase in the region of stretching (ν) and deformation (δ) vibrations of its structural groups as well as the bands assigned to impurities, i.e., kaolinite, α-quartz, and calcite. Interpretation of FT-IR spectra for N-Bents (Table 3) was carried out by their comparison with the data reported [6–8, 30–33]. A sharp and intense band at 3697 cm^{-1} in the region of stretching vibrations of OH groups bound with octahedral cations along with a band of deformation vibrations at 913 cm^{-1} for N-Bent(G) indicates the presence of crystalline kaolinite. The intensity of these bands is significantly weaker for N-Bent(K) whereas, for N-Bent(D), only a shoulder at 3692 cm^{-1} is observed being evidence for the small kaolinite content in the latter. Thus, kaolinite content in N-Bents is different and decreases in the order N-Bent(G) > N-Bent(K) $\gg$ N-Bent(D). This sequence is confirmed by a change in intensity

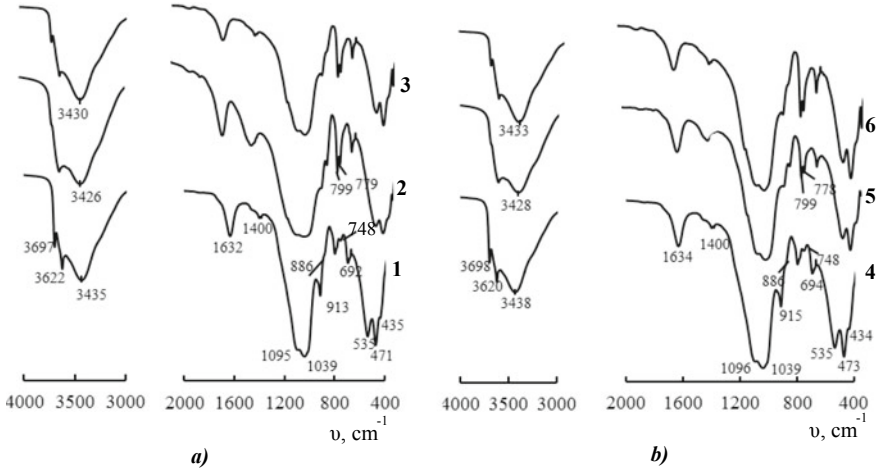

Fig. 3 FT-IR spectra of natural bentonites. **a** N-Bent(G) (1), N-Bent(D) (2), and N-Bent(K) (3), and nanocompositions, **b** Pd(II)–Cu(II)/N-Bent(G) (4), Pd(II)–Cu(II)/N-Bent(D) (5), and Pd(II)–Cu(II)/N-Bent(K) (6)

of a band at 748 cm^{-1} characteristic of Si–O deformation vibrations in kaolinite. A sharp band of moderate intensity at 748 cm^{-1} is observed only for N-Bent(G) characterized by a high kaolinite content and is absent for other two N-Bents. The presence of a characteristic doublet at 798 and 779 cm^{-1} shows that N-Bent(K) and N-Bent(D) contain an α-quartz phase. For N-Bent(G), this doublet is overlapped by a wider band of amorphous SiO_2 near 800 cm^{-1} and, instead of the doublet, a wide band at 797 cm^{-1} with a shoulder at 778 cm^{-1} is observed. The presence of calcite is indicated by a band at 1400 cm^{-1} for N-Bent(G), a band at 1421 cm^{-1} for N-Bent(D), and the most intense band at 1400 cm^{-1} for N-Bent(K).

Analyzing the FT-IR spectra in the range of stretching and deformation vibrations of OH groups bound with octahedral cations and OH groups in the associated water molecules, we can notice that a band characteristic of Al–Al–OH is clearly defined; a band at 913 cm^{-1} is very intense for N-Bent(G) due to the largest kaolinite content (see Fig. 1), whereas it is registered only as a bend for N-Bent(D) and N-Bent(K). A band at 886–876 cm^{-1} can be assigned to deformation vibrations of OH groups in Al–Fe^{3+}–OH structural fragments and it is the clearest for N-Bent(D). For other two N-Bents, instead of this band, only a shoulder is observed. The IR data concerning phase compositions of N-Bents agree with the results of the XRD (Fig. 1) and elemental analysis (Table 1).

As can be seen from Fig. 3 and Table 3, FT-IR spectra remained unchanged after Pd(II) and Cu(II) anchoring on N-Bents except for the position of an absorption band assigned to CO_3^{2-} group for Pd(II)–Cu(II)/N-Bent(D). Its shift to higher frequencies ($\Delta\nu = +9\ cm^{-1}$) is due to formation of carbonates of the corresponding metals [34].

Table 3 Wave numbers (cm^{-1}) for absorption maxima in FT-IR spectra of N-Bents and Pd(II)–Cu(II)/N-Bents

Structural group	N-Bent(G)		N-Bent(D)		N-Bent(K)	
	ν	δ	ν	δ	ν	δ
M–OH	3697	–	3692 sh	–	3697	–
Al–Al–OH	3622	913	3622	915 bend	3621	915 bend
Al–Fe^{3+}–OH	–	886 sh	–	876	–	876 sh
H_2O	3435	1632	3426	1634	3430	1633
Si–O–Si (tetrahedron)	1095 sh, 1039	471	1163 sh, 1096 sh, 1039	468	1163 sh, 1087 sh, 1038	468
Si–O–Al	–	535	–	519	–	519
Si–O–Mg	–	435	–	434 sh	–	431
α-SiO_2 (α-quartz)	–	797,778 sh, 748, 692	–	799, 779, 695	–	798, 778, 694
CO_3^{2-}	–	1400	–	1421	–	1400
Structural group	Pd(II)–Cu(II)/N-Bent(G)		Pd(II)–Cu(II)/N-Bent(D)		Pd(II)–Cu(II)/N-Bent(K)	
M–OH	3698	–	3694 sh	–	3697	–
Al–Al–OH	3620	915	3620	917 bend	3623	917 bend
Al–Fe^{3+}–OH	–	886 sh	–	876	–	876 sh
H_2O	3438	1634	3428	1636	3433	1632
Si–O–Si (tetrahedron)	1096 sh, 1039	473	1165 sh, 1095 sh, 1038	469	1163 sh, 1086 sh, 1039	468
Si–O–Al	–	535	–	520	–	521
Si–O–Mg	–	434	–	432 sh	–	433
α-SiO_2 (α-quartz)	–	798,779 sh, 748,694	–	798, 779, 694	–	799, 777, 695
CO_3^{2-}	–	1400	–	1430	–	1401

3.5 Water Vapor Adsorption

Bentonites are marked by their high affinities to water molecules. The bentonite origin [26, 35–38] and their modification with acids and metal salts [26, 36] have a considerable effect on structural-adsorption parameters of bentonites, which can be followed by collecting the isotherms of water vapor ad/desorption. Figure 4 shows isotherms of water vapor ad/desorption by N-Bents and Pd(II)–Cu(II)/N-Bents. All isotherms are S-shaped with well-defined loops of capillary condensation hysteresis notable for their anomalous forms: they exist at very low P/P_s values. A sharp rise observed for all isotherms at $P/P_s \rightarrow 1$ indicates that these bentonites and nanocompositions contain large pores with $r \geq 300$ Å. Generally, bentonites are structurally nonuniform and contain micro-, meso-, and macropores [6–10]. The isotherms were quantitatively evaluated using the BET equation [26] (Table 4).

Table 4 also presents values of a thermodynamic activity of adsorbed water, $a_{H_2O} = P/P_s$, [2] at adsorption, a, values of 2 and 4 mmol/g. As can be seen from Table 4, the water monolayer capacity, a_m, the BET constant, C, and the heat of water adsorption for the first layer, Q_1, decrease in the order N-Bent(D) > N-Bent(G) > N-Bent(K). The thermodynamic activity of adsorbed water increases in the order N-Bent(D) < N-Bent(G) < N-Bent(K) and correlates with the decrease in Q_1. For Pd(II)–Cu(II)/N-Bents, specific surface area, S_{sp}, decreases relative to that of their natural counterparts, whereas a_{H_2O} values are practically unchanged except for Pd(II)–Cu(II)/N-Bent(D).

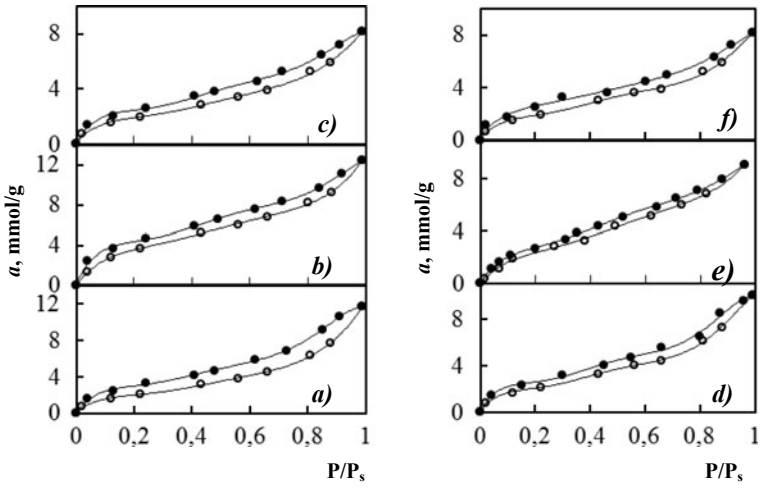

Fig. 4 Isotherms of water vapor adsorption (○) and desorption (●) by natural bentonites: N-Bent(G) (**a**), N-Bent(D) (**b**), and N-Bent(K) (**c**), and nanocompositions: Pd(II)–Cu(II)/N-Bent(G) (**d**), Pd(II)–Cu(II)/N-Bent(D) (**e**), and Pd(II)–Cu(II)/N-Bent(K) (**f**)

Table 4 Structural-adsorption parameters of N-Bends and Pd(II)–Cu(II)/N-Bents

Sample	BET equation constants		Q_1 (J/mol)	S_{sp} (m^2/g)	a_{H_2O}	
	a_m (mmol/g)	C			$a =$ 2.0 mmol/g	$a =$ 4.0 mmol/g
N-Bent(G)	1.96	26.92	8180	127	0.19	0.56
N-Bent(D)	3.11	32.78	8610	202	0.06	0.26
N-Bent(K)	1.79	25.81	8080	117	0.22	0.67
Pd(II)–Cu(II)/N-Bent(G)	1.85	14.29	6637	120	0.18	0.56
Pd(II)–Cu(II)/N-Bent(D)	2.34	13.09	6422	152	0.14	0.46
Pd(II)–Cu(II)/N-Bent(K)	1.71	15.44	6826	111	0.22	0.66

3.6 Thermochemical Properties

Figure 5 shows a representative derivatograms in the range from 25 to 1000 °C for N-Bent(G) and Pd(II)–Cu(II)/N-Bent(G). A TG curve for N-Bent(G) shows that its dehydration is a three-stage process. According to the conventional view [7, 39, 40], the dehydration process consists of removal of physically adsorbed water, removal of interlayer water and, finally, removal of water formed as a result of surface dehydroxylation. The results of thermogravimetric analysis of N-Bents and Pd(II)–Cu(II)/N-Bents demonstrate two endothermic effects: the first one in the range from 120 to 150 °C (removal of physisorbed and interlayer water) and the second one in the range from 580 to 600 °C (surface dehydroxylation). The results of the thermogravimetric analysis for all derivatograms (not shown here) are summarized in Table 5.

The maximum temperature of the first endothermic effect is the highest (150 °C) for N-Bent(D) whereas the maximum temperature of the second one is the highest (600 °C) for N-Bent(G) (for other N-Bents it is lower by 20 °C). Pd(II) and Cu(II) anchoring does not result in significant changes in the positions of both endothermic effects. Values of a total weight loss depend on the bentonite origin and decrease

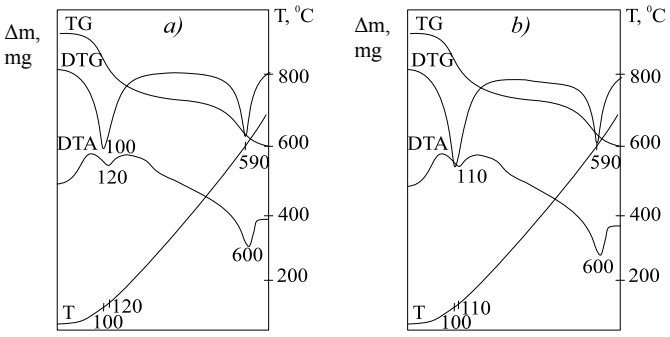

Fig. 5 Derivatograms for N-Bent(G) (**a**) and Pd(II)–Cu(II)/N-Bent(G) (**b**)

Table 5 Results of thermogravimetric analysis of N-Bents and Pd(II)–Cu(II)/N-Bents

Sample	Endothermic effect (T_{max}, °C)	Weight loss (%), in the range of			Total weight loss (%)	m_{sp} (mmol/g)
		25–110 °C	25–300 °C	300–800 °C		
N-Bent(G)	120	4.2	7.8	5.2	13.6	2.0
	600					
N-Bent(D)	150	4.8	11.0	4.0	15.2	3.4
	580					
N-Bent(K)	120	3.2	6.8	3.0	10.0	2.0
	580					
Pd(II)–Cu(II)/N-Bent(G)	110	4.4	7.8	5.0	13.0	1.9
	600					
Pd(II)–Cu(II)/N-Bent(D)	140	4.2	10.8	5.2	14.0	3.7
	570					
Pd(II)–Cu(II)/N-Bent(K)	110	3.4	7.0	3.3	9.8	2.0
	580					

in the order N-Bent(D) > N-Bent(G) > N-Bent(K) from 15.2 to 10%. N-Bent(D) contains the largest amount of water, which correlates with its highest basal spacing, i.e., $d_{001} = 15.387$ Å (Table 2). For Pd(II)–Cu(II)/N-Bents, the weight loss values are slightly lower in comparison with corresponding N-Bents. It should be noted that the N-Bent(D) and Pd(II)–Cu(II)/N-Bent(D) samples are also characterized by the largest content of irreducible water, m_{sp}, after their drying at 110 °C till constant weight.

3.7 Protolytic Properties

Figure 6 shows time dependences of pH level for aqueous suspensions of three natural bentonites. Equilibrium pH, pH_{eq}, values are quickly attained and stay unchanged for long periods of time. Interaction between water molecules and a bentonite surface results in the formation of acid or alkaline medium. pH_{eq} decreases in the order N-Bent(D) (pH 8.97) > N-Bent(K) (pH 6.21) > N-Bent(G) (pH 4.88).

The considerable difference in protolytic properties of natural bentonites seen from Fig. 6 can influence the compositions of the anchored Pd(II)–Cu(II) complexes and their activity in the reaction of carbon monoxide oxidation with air oxygen [2, 15].

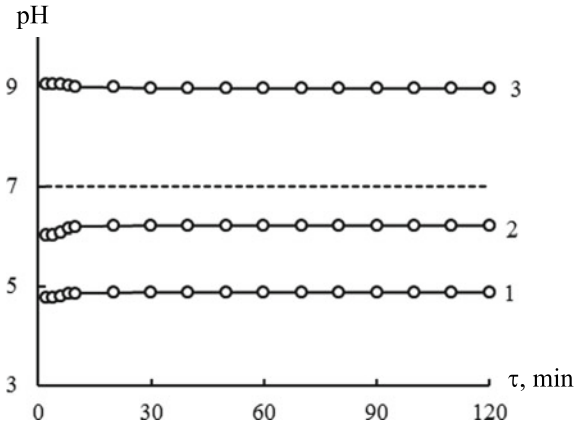

Fig. 6 Time dependences of pH for aqueous suspensions of: N-Bent(G) (1), N-Bent(K) (2), and N-Bent(D) (3)

3.8 Pd(II)–Cu(II)/N-Bent Nanocomposition Testing in the Reaction of CO Oxidation with Air Oxygen

Pd(II) and Cu(II) complex compounds with bromide ions as an efficient additive anchored on different supports are active catalysts for the reaction of CO oxidation [2, 15–20]. The nature of a support is a significant factor influencing the activity of these catalysts in the reaction. Figure 7 shows time dependencies of a CO conversion, η, %, for CO oxidation over the Pd(II)–Cu(II)/N-Bent nanocompositions. As can be seen from Fig. 7, the kinetic curve profiles depend on bentonite origins. For the Pd(II)–Cu(II)/N-Bent(D) nanocomposition, η value quickly reduces to zero as opposed to the Pd(II)–Cu(II)/N-Bent(G) and Pd(II)–Cu(II)/N-Bent(K) nanocompositions, for

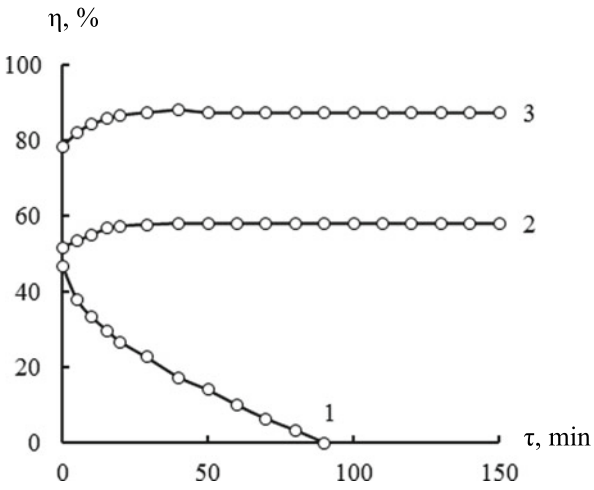

Fig. 7 Time dependences of C^{f}_{CO} for CO oxidation by air oxygen over K_2PdCl_4–$Cu(NO_3)_2$–KBr/$\bar{S}$ nanocompositions where $\bar{S}$: N-Bent(D) (1), N-Bent(K) (2), and N-Bent(G) (3)

which η values initially increase and then become constant and equal to 87% and 58%, respectively.

Thus, for the latter two nanocompositions, the steady-state mode of the process is established, and the numbers of catalytic cycles, n (a ratio of CO oxidized for the experimental period, Q_{exp} (moles of CO), to the amount of Pd(II) in the compositions) exceeds one (Table 6), showing the truly catalytic nature of the process. Consequently, the catalytic activity of Pd(II)–Cu(II)/N-Bent(G) is higher than that of Pd(II)–Cu(II)/N-Bent(K), whereas Pd(II)–Cu(II)/N-Bent(D) is not a catalyst.

Other structural, physicochemical, and stoichiometric parameters of natural bentonites and the Pd(II)–Cu(II)/N-Bent nanocompositions also presented in Table 6 are very different causing the differences in their catalytic activity in the reaction of CO oxidation. As can be seen, both a crystallite size, D, and a specific surface area, S_{sp}, are not the parameters determining the catalytic activity of Pd(II)–Cu(II)/N-Bents because they do not correlate with the order of catalytic activity. Similar observations were made for some other supports [2, 15].

Based on the data presented in Tables 4 and 5, it can be stated that amount of irreducible water, m_{sp}, after drying the Pd(II)–Cu(II)/N-Bent nanocompositions at 110 °C until constant weight is very close to their water monolayer capacities, a_m. Thereupon, it is possible to consider the Pd(II)–Cu(II)/N-Bent compositions as heterogenized systems where a support significantly influences a thermodynamic activity of adsorbed water molecules, a_{H_2O}, and their ability to dissociate with establishment of pH_{eq} ($a_{H_3O^+}$). As can be seen from Table 6, these parameters are very different for bentonites of different origin and the compositions based on them. Hence, an integrated thermodynamic parameter (ITP) can be calculated as follows $ITP = lg a_{H_2O}/a_{H_3O^+} \cdot a_{Br^-}$, where a_{Br^-} is an activity of bromide ions (KBr concentration in all compositions under study was 1.02×10^{-4} mol/g).

ITP increases from 3.84 to 9.53 in the order N-Bent(G) < N-Bent(K) < N-Bent(D). The catalytic activity, η_{st}, and the number of catalytic cycles, n, on the contrary, decrease in the same order. In our opinion [2, 15], differences in ITP values (we observed ITP ranging from 3.0 to 8.5 for active Pd(II)–Cu(II) compositions on various supports [2, 15–17]) influence both a degree of hydrolysis for Pd(II) and Cu(II) and formation equilibriums for palladium–copper complexes. Moreover, the lack of catalytic activity of Pd(II)–Cu(II)/N-Bent(D) may be due to a very high calcite content in N-Bent(D) and its ability to form inactive carbonates of Pd(II) and Cu(II).

Thus, the most active Pd(II)–Cu(II)/N-Bent(G) composition differs by the lowest ITP and calcite phase content, and, as opposed to other two bentonites, by biogenic origin of its silica phase.

4 Conclusions

K_2PdCl_4–$Cu(NO_3)_2$–KBr/N-Bent nanocompositions based on three natural bentonites, i.e., N-Bent(G), N-Bent(K), and N-Bent(D), from different Ukrainian deposits were prepared. Both the supports and the compositions based on them

Table 6 Structural, physicochemical, and stoichiometric parameters of N-Bents and Pd(II)–Cu(II)/N-Bents

Parameter	Composition		
	Pd(II)–Cu(II)/N-Bent(G)	Pd(II)–Cu(II)/N-Bent(K)	Pd(II)–Cu(II)/N-Bent(D)
D (nm)	27.0	19.0	30.0
S_{sp} (m^2/g)	120	111	152
a_{H_2O} at $a = 2$ mmol/g	0.18	0.22	0.14
pH^a_{eq}	4.88	6.21	8.97
$\lg a_{H_2O}/a_{H_3O^+} \cdot a_{Br^-}$	3.84	5.38	8.53
η_{st} (%)	87.0	58.0	–
n	4.9	3.3	0.5
C^a_{CaO} (wt%)	0.54	0.74	11.15

A parameter was measured for the support

were investigated by a combination of methods, i.e., XRD, SEM, FT-IR, DTG-DTA, water vapor adsorption, and pH-metry, and, as a result, their phase composition and morphology as well as physicochemical, structural, thermochemical, ad/desorption, and protolytic properties were determined. Effects of all these factors on the activity of K_2PdCl_4–$Cu(NO_3)_2$–KBr/N-Bents in the reaction of CO oxidation with air oxygen at 20 °C and RH of 67% were evaluated. It has been found that in the order N-Bent(G)/N-Bent(K)/N-Bent(D), the integrated thermodynamic parameter and calcite phase content increase from 3.84 to 8.53 and from 0.54 to 11.15 wt%, respectively, while CO conversion value and the number of catalytic cycles decrease from 87% to 0 and from 4.9 to 0.5, respectively.

References

1. Bergaya F, Lagaly G (2006) General introduction: clays, clay minerals, and clay science. Developments in clay science. In: Handbook of clay science, vol 1. Elsevier, Amsterdam, pp 1–18. https://doi.org/10.1016/S1572-4352(05)01001-9
2. Rakitskaya TL, Dzhyga GM, Kiose TA et al (2019) Pd(II), Cu(II), and pillared clay based nanocatalysts for low-temperature CO oxidation. SN Appl Sci 1:291. https://doi.org/10.1007/s42452-019-0314-x
3. Centi G, Parathonor S (2008) Catalysis by layered materials. A review. Micropor Mesopor Mater 107:3–15. https://doi.org/10.1016/j.micromeso.2007.03.011
4. Gupta SS, Bhattacharyya KG (2012) Adsorption of heavy metals on kaolinite and montmorillonite: a review. Phys Chem Chem Phys 14:6698–6723. https://doi.org/10.1039/c2cp40093f
5. Zhu R, Chen Q, Zhou Q et al (2016) Adsorbents based on montmorillonite for contaminant removal from water: a review. Appl Clay Sci 123:239–258. https://doi.org/10.1016/j.clay.2015.12.024
6. Tarasevich YuI, Ovcharenko FD (1975) Adsorbtsiya na glinistyih mineralah (Adsorption on Clay Minerals). Kiev, Nauk. Dumka
7. Tarasevich YuI, Ovcharenko FD (1988) Stroenie i himiya poverhnosti sloistyih silikatov (Structure and Chemistry of the Layer Silicate Surface). Kiev, Nauk. Dumka
8. Tarasevich YuI (1981) Prirodnyie sorbentyi v protsessah ochistki vodyi (Natural sorbents in water treatment processes). Kiev, Nauk. Dumka
9. Tarasevich YuI (2011) Poverhnostnyie yavleniya na dispersnyih materialah (Surface phenomena on dispersed materials). Kiev, Nauk. Dumka
10. Al-Ani T, Sarapää O (2008) Clay and clay mineralogy. Physical-chemical properties and industrial uses. GTK Espoo
11. Bish DL (2013) Parallels and distinctions between clay minerals and zeolites. Develop Clay Sci 5:783–800. https://doi.org/10.1016/b978-0-08-098258-8.00026-2
12. Rouquerol J, Llewellyn P, Sing K (2014) Adsorption by clays pillared clays zeolites and aluminophosphates. In: Adsorption by powders and porous solids principles methodology and applications, 2nd edn. pp 467–527. https://doi.org/10.1016/b978-0-08-097035-6.00012-7
13. Rakitskaya TL, Kiose TA, Zryutina AM et al (2013) Solid-state catalysts based on bentonites and Pd(II) Cu(II) complexes for low-temperature carbon monoxide oxidation. Solid State Phenom 200:299–304. https://doi.org/10.4028/www.scientific.net/ssp.200.299
14. Bineesh KV, Cho DR, Kim SY, Jermy BR, Park DW (2008) Vanadia-doped titania-pillared montmorillonite clay for the selective catalytic oxidation of H_2S. Catal Commun 9:2040–2043. https://doi.org/10.1016/j.catcom.2008.03.048

15. Rakitskaya TL, Ennan AA, Volkova VY (2005) Nizkotemperaturnaja kataliticheskaja ochistka vozduha ot monooksida ugleroda (на англ). Odessa, Ekologiya
16. Rakitskaya TL, Kiose TA, Voloschuk AG et al (2009) Effect exerted by acid modification of bazalt tuff on catalytic activity of fixed acido complexes of palladium(II) and copper(II) in the reaction of carbon(II) oxide oxidation with air oxygen. Russ J Appl Chem 82(2):204–208. https://doi.org/10.1134/s1070427209020074
17. Rakitskaya TL, Kiose TA, Golubchik KO et al (2017) Acid modified clinoptilolite as a support for palladium–copper complexes catalyzing carbon monoxide oxidation with air oxygen. Chem Cent J 11:28. https://doi.org/10.1186/s13065-017-0256-6
18. Radkevich VZ, Sen'ko TL, Khaminets SG et al (2008) Catalytic systems based on carbon supports for the low-temperature oxidation of carbon monoxide. Kinet Catal 49(4):545–551. https://doi.org/10.1134/s0023158408040149
19. Shen Y, Lu G, Guo Y et al (2010) A synthesis of high-efficiency Pd–Cu–Clx/Al_2O_3 catalyst for low temperature CO oxidation. Chem Commun 6:8433–8435. https://doi.org/10.1039/c0cc02776f
20. Wang Y, Shi J, Wu R et al (2016) Room-temperature CO oxidation over calcined Pd–Cu/palygorskite catalysts. Appl Clay Sci 1196:126–131. https://doi.org/10.1016/j.clay.2015.08.034
21. Rakitskaya TL, Truba AS, Ennan AA, Dlubovskii RM, Volkova VY (2017) Water vapor adsorption by nanostructured polyphase compositions based on the solid component of welding aerosol. Adsorpt Sci Technol 35:389–395. https://doi.org/10.1177/0263617416688691
22. Volzone C, Ortiga J (2004) Influence of the exchangeable cations of montmorillonite on gas adsorptions. Process Saf Environ Prot 82(2):170–174. https://doi.org/10.1205/095758204322972807
23. Kharroubi M, Balme S, Henn F et al (2009) Dehydration enthalpy of alkali-cations-exchanged montmorillonite from thermogravimetric analysis. J Colloid Interface Sci 329(2):339–345. https://doi.org/10.1016/j.jcis.2008.09.058
24. Fu MH, Zhang ZZ, Low PF (1990) Changes in the properties of a montmorillonite-water system during the adsorption and desorption of water: hysteresis. Clays Clay Miner 38(5):485–492. https://doi.org/10.1346/ccmn.1990.0380504
25. Kadoura A, Nair AKN, Sun S (2016) Adsorption of carbon dioxide, methane, and their mixtute by montmorillonite in the presence of water. Microporous Mesoporous Mater 225:331–341. https://doi.org/10.1016/j.micromeso.2016.01.010
26. Rakytskaya TL, Dzhyga GM, Kiose TO (2017) Adsorbtsiini ta fizyko-khimichni vlastyvosti pryrodnykh ta modyfikovanykh form montmorylonitu (Adsorption and physicochemical properties of natural montmorillonites and their modified forms). Visnyk ONU Chem 22(1):38–54 http://dx.doi.org/10.18524/2304-0947.2017.1(61).94710
27. Makhnach AA, Streltsova HD, Hulys LF et al (2004) Morfolohyia stroenye sostav y proyskhozhdenye zalezhy sylytsytov na mestorozhdenyy Stalnoe (Morphology structure composition and origin of silicites deposits at the field Stalnoe). Litasfera 2(21):63–71.
28. Keller WD, Reynolds RC, Inoue A (1986) Morphology of clay minerals in the smectite-to-illite conversion series by scanning electron microscopy. Clays Clay Miner 34(2):187–197. https://doi.org/10.1346/ccmn.1986.0340209
29. Alyosef HA, Ibrahim S, Welscher J et al (2014) Effect of acid treatment on the chemical composition and the structure of Egyptian diatomite. Int J Miner Process 132:17–25. https://doi.org/10.1016/j.minpro.2014.09.001
30. Reddy CR, Bhat YS, Nagendrappa G et al (2009) Brønsted and Lewis acidity of modified montmorillonite clay catalysts determined by FT-IR spectroscopy. Catal Today 141(1–2):157–160. https://doi.org/10.1016/j.cattod.2008.04.004
31. Madejová J, Bujdak J, Janek M et al (1998) Comparative FT-IR study of structural modifications during acid treatment of dioctahedral smectites and hectorite. Spectrochim Acta Part A Mol Biomol Spectrosc 54(10):1397–1406. https://doi.org/10.1016/S1386-1425(98)00040-7
32. Bradley SM, Kydd RA, Brandt KK (1992) Pillared clay minerals as catalysts and catalyst supports. Stud Surf Sci Catal 73:287–290. https://doi.org/10.1016/S0167-2991(08)60826-5

33. Vicente-Rodriguez MA, Suarez M, Bafiares-Mufioz MA et al (1996) Comparative FT-IR study of the removal of octahedral cations and structural modifications during acid treatment of several silicates. Spectrochim Acta Part A Mol Biomol Spectrosc 52:1685–1694. https://doi.org/10.1016/S0584-8539(96)01771-0
34. Shashkova IL, Ratko AI, Milvit NV (2000) Izvlechenie ionov tyazhelyih metallov iz vodnyih rastvorov s ispolzovaniem prirodnyih karbonat-soderzhaschih trepelov (Extraction of heavy metal ions from aqueous solutions using natural carbonate-containing tripoli). J Appl Chem 73(6):915–919
35. Cao L, Li Z, Xiang S, Huang Z et al (2019) Preparation and characteristics of bentonite–zeolite adsorbent and its application in swine wastewater. Biores Technol 284:448–455. https://doi.org/10.1016/j.biortech.2019.03.043
36. Krupskaya V, Novikova L, Tyupina E et al (2019) The influence of acid modification on the structure of montmorillonites and surface properties of bentonites. Appl Clay Sci 172:1–10. https://doi.org/10.1016/j.clay.2019.02.001
37. Bieseki L, Treichel H, Araujo AS et al (2013) Porous materials obtained by acid treatment processing followed by pillaring of montmorillonite clays. Appl Clay Sci 85:46–52. https://doi.org/10.1016/j.clay.2013.08.044
38. Pálková H, Hronský V, Bizovská V et al (2015) Spectroscopic study of water adsorption on Li^+, TMA^+ and $HDTMA^+$ exchanged montmorillonite. Spectrochim Acta Part A Mol Biomol Spectrosc 149:751–761. https://doi.org/10.1016/j.saa.2015.04.065
39. Dellisanti F, Minguzzi V, Valdre G (2006) Thermal and structural properties of Ca-rich montmorillonite mechanically deformed by compaction and shear. Appl Clay Sci 31:282–289. https://doi.org/10.1016/j.clay.2005.09.006
40. Nogueira FGE, Lopes JH, Silva AC et al (2011) Catalysts based on clay and iron oxide for oxidation of toluene. Appl Clay Sci 51:385–389. https://doi.org/10.1016/j.clay.2010.12.007

Effect of Temperature on Formation of Nanoporous Structure of Granule Shell in Technology of Obtaining Organo-mineral Fertilizers

Mykola Yukhymenko, Ruslan Ostroha, Artem Artyukhov, and Jozef Bocko

1 Introduction

Currently, the role of organic fertilizers is growing [1]. Demand for two-component fertilizers, which are granules with a solid mineral core and a porous organic shell is constantly increasing [2, 3]. At the same time, the effective time of encapsulated fertilizers is important, which is determined by the release time of the target components from the shell. Depending on the characteristics of the shell porous structure, there appear diffusion of the target components through micropores and macropores with an effective pore radius of less than 10^{-9} m and more than 10^{-7} m, respectively. Thus, by changing size of pores and their specific surface, we can obtain several types of encapsulated granules.

Formation of the shell porous structure with various modification features is primarily affected by the temperature regime of the granulation process. Similar works [4–6] were carried out to study the nanoporous structure of porous ammonium nitrate granules as a component of industrial explosives. However, further study of the process kinetics of nanoporous structure obtaining in other applications (production of granular products) requires further study. In [7], one studied influence of the temperature potential of a drying agent in a laboratory fluidized bed granulator, on non-porous glass particles and on the formation of a porous structure of aluminum oxide. In this paper, it is proposed an expression for the kinetics of granule growth, which takes into account acceleration of the growth rate due to the formation of porous structure. It is stated that using of shell porosity value when calculating the growth kinetics makes it possible to evaluate calculation results more correctly. In

M. Yukhymenko · R. Ostroha (✉) · A. Artyukhov
Sumy State University, Sumy, Ukraine
e-mail: r.ostroga@pohnp.sumdu.edu.ua

J. Bocko
Technical University of Košice, Košice, Slovak Republic

O. Fesenko and L. Yatsenko (eds.), *Nanooptics and Photonics, Nanochemistry and Nanobiotechnology, and Their Applications*, Springer Proceedings in Physics 247, https://doi.org/10.1007/978-3-030-52268-1_12

the work, it is also showed that the process conditions affect the method of droplet drying and, therefore, the formation of granules of different porosity.

2 Theoretical Laws of Temperature Profile in Two-Layer Granule "Solid Core–Porous Shell"

The two-layer granule with an organic shell is a solid core, that is, the primary granule of nitrogen fertilizers namely ammonium nitrate or urea. In the process of granulation in a fluidized bed, a layer of organic suspension, such as chicken manure, is applied on the core. By thermal drying of the granule outer shell, one obtains a porous shell of a certain structure. Size of pores, shape of their surface and nature of the curves, porosity of the shell depends on the temperature of the gas flow and duration of granules heating.

The process of heat transfer inside the granule, assuming its spherical shape, is described by the Fourier differential heat equation [8]:

$$\frac{\partial t(r,\tau)}{\partial \tau} = a_T\left(\frac{\partial^2 t(r,\tau)}{\partial r^2} + \frac{2}{r}\frac{\partial t(r,\tau)}{\partial r}\right), \tag{1}$$

where $t\,(r,\tau)$ is granule temperature at a point with the current radius r during the time τ, °C; r—current radius of the granule, m; a_{T}—coefficient of thermal conductivity of the granule material, m^2/s; τ—granule heating time, s.

The well-known [8] solution of (1) at:Initial conditions (the initial temperature distribution over volume of the granule is considered to be uniform)

$$\tau > \tau_0, \quad 0 < r < R, \quad t(r,\tau_0) = f(r); \tag{2}$$

Symmetry conditions

$$t(0,\tau) \neq \infty, \quad \frac{\partial t(0,\tau)}{\partial r} = 0; \tag{3}$$

Boundary conditions of the third kind, providing for the equality of heat flows from the gas to the surface of the granule and from it into the middle of the core

$$\lambda_{\mathrm{T}}\frac{\partial t(r,\tau)}{\partial r} = \alpha[t(r,\tau) - t_{\mathrm{med}}]; \tag{4}$$

Look like:

$$\frac{t_{\mathrm{med}} - t(r,\tau)}{t_{\mathrm{med}} - t_i} = \sum_{n=1}^{\infty} A_n \frac{\sin\left(\mu_n \frac{r}{R}\right)}{\mu_n \frac{r}{R}} \exp\left(-\mu_n^2 \cdot Fo\right), \tag{5}$$

where t_i is the initial temperature of the granule, °C; t_{med}—temperature of the gas medium, °C; R—granule outer radius, m; Fo—Fourier criterion; A_n, μ_n—constant and root of the equation, $A_1 = f(Bi)$, $\mu_1 = f(Bi)$; Bi—Biot criterion; λ_T—thermal conductivity coefficient of the particle material, W/(m K).

Since the process of granule heating during granulation is quite long ($Fo \geq 0.3$), the infinite series in (5) quickly converges, and we can restrict ourselves to only the first member of the series ($n = 1$) in this equation.

Then, (5) takes the form:

$$\frac{t_{med} - t(r, \tau)}{t_{med} - t_i} = A_1 \frac{\sin\left(\mu_1 \frac{r}{R}\right)}{\mu_1 \frac{r}{R}} \exp\left(-\mu_1^2 \cdot Fo\right). \tag{6}$$

Equation (6) makes it possible to determine the temperature profile by the granule radius when it is heated with gas from the surface to the center of the granule. Then, from (6), temperature of the granule along its current radius is:

$$t(r, \tau) = t_{med} - (t_{med} - t_i) A_1 \frac{\sin\left(\mu_1 \frac{r}{R}\right)}{\mu_1 \frac{r}{R}} \exp\left(-\mu_1^2 Fo\right). \tag{7}$$

Since the granules are small in size, within 1–4 mm, to determine the temperature profile it is enough to determine the temperature on the surface of the granule, in the center of the granule and the average integral in the volume of the granule.

In the first case, assuming $r = R$ (granule surface) from (7), we obtain the expression for determining the temperature on the granule surface

$$t_P(r, \tau) = t_{med} - (t_{med} - t_i) A_1 \frac{\sin \mu_1}{\mu_1} \exp\left(-\mu_1^2 Fo\right). \tag{8}$$

In the second case, assuming $r \to 0$ (center of the granule) from (7), we obtain the expression for determining the temperature in the center of the granule

$$t_C(r, \tau) = t_{med} - (t_{med} - t_i) A_1 \exp\left(-\mu_1^2 Fo\right). \tag{9}$$

Using the formula for the integral average temperature in the volume of the granule

$$t_{ia}(\tau) = \frac{3}{R^3} \int_0^R r^2 \cdot t(r, \tau) \mathrm{d}r. \tag{10}$$

in the third case, one obtains the expression for determining the volume-averaged temperature of the granule:

$$t_{ai}(r, \tau) = t_{med} - (t_{med} - t_i) \frac{6A_2}{\mu_1^2} \exp\left(-\mu_1^2 Fo\right). \tag{11}$$

3 Influence of the Granule Shell Porous Structure on the Nature of Thermal Conductivity

The rate of granules heating and, accordingly, the rate of temperature profile change according to formula (7), is also determined by the thermal conductivity value of the granule material. This parameter is included in the Biot criterion and in the Fourier criterion through the thermal conductivity coefficient.

It is important to present a significant picture of the thermal conductivity of the granule material dependence on the structural characteristics of the porous shell. Structure diagram of the two-layer granule "solid core–porous shell" (Fig. 1) provides that the solid core occupies 70% of the granule's volume, and the porous layer—30% of the volume [2].

Based on the presented structure of the two-layer granule, it follows that the thermal conductivity of the granule material is not the same: The thermal conductivity is lower in the porous shell than that in the solid core, since in the porous layer, the heat transfer by thermal conductivity decreases due to pores filled with gas. That is, in a porous shell, the resulting coefficient of thermal conductivity is always less than the corresponding coefficient in a solid body. This is explained by the following reasons:

(1) Part of the outer layer is covered with gas pores, wherein thermal conductivity of gas is considerably lower than the coefficient of thermal conductivity of a continuous body. Therefore, the heat flow taken relative to cross-sectional area of the porous shell forms a certain fraction of the flow that would be transported in the absence of pores in the shell. This fraction is equal to the fraction of the free section of the total number of pores, that is, the porosity of the layer;
(2) Since pores are of irregular geometric shape, namely in the form of channels, alternating narrowing and expansion zones of the pore cross sections, additional resistance to heat transfer by thermal conductivity arises;

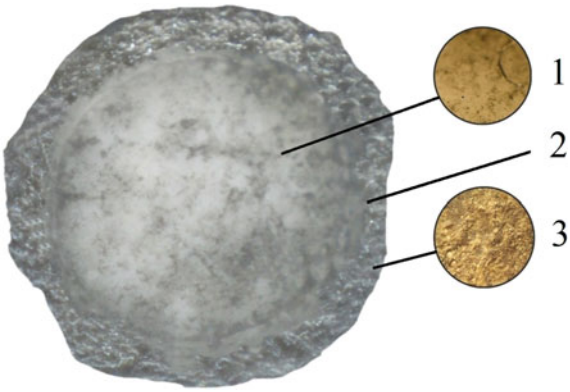

Fig. 1 Structure of organo-mineral granules: 1—mineral core (urea); 2—transition section; 3—dry organic shell (chicken manure)

(3) Wavy porous channels lengthen the path of heat transfer by thermal conductivity through the gas layer;
(4) The smaller the pore size, the greater the number of pores per unit volume of the granule with the same total porosity. It reduces value of the thermal conductivity coefficient.

Considering the above, the modified coefficient of "limited" thermal conductivity through the porous layer is

$$\lambda_{CT} = \frac{\lambda_E}{k_{sh} \cdot k_w \cdot k_p}, \tag{12}$$

where λ_E is the effective coefficient of thermal conductivity, depending on the porosity of the layer ε, $\lambda_E = f(\varepsilon)$, $0 < \varepsilon < 1$; k_{sh}—pore shape coefficient; k_w—coefficient of pore weaving; k_p—pore size coefficient.

Thermal conductivity of the porous layer is an effective value that is intermediate between the thermal conductivity of the granule solid core and the thermal conductivity of the gas contained in the pores.

One proceeds from the simplified model of Kriescher [9], according to which the porous body in the section is alternating layers of a solid body and gas layers. In this case, the heat flow moves both parallel to the layers and perpendicular to them.

In the first case, one obtains:

$$\lambda_E = (1 - \varepsilon)\lambda_T + \varepsilon\lambda_G. \tag{13}$$

In the second case:

$$\lambda_E = \frac{\lambda_T \cdot \lambda_G}{(1 - \varepsilon)\lambda_G + \varepsilon\lambda_T}, \tag{14}$$

where λ_T, λ_G—thermal conductivity of the granule material and gas in the pores, respectively, W/(m K).

Then, the average value of the effective thermal conductivity is

$$\lambda_E = \frac{0.5[(1 - \varepsilon)\lambda_T + \varepsilon\lambda_G)][(1 - \varepsilon)\lambda_G + \varepsilon\lambda_T] + \lambda_T\lambda_G}{(1 - \varepsilon)\lambda_G + \varepsilon\lambda_T}. \tag{15}$$

Analyzing (13)–(15), it can be seen that with increasing porosity of the layer, the thermal conductivity value decreases. Clarification of the nature and rate of this decrease is of a great interest, since thermal conductivity of the solid granule skeleton is tens of times higher than thermal conductivity of the gas inside pores. For example, mineral solid component parts of granules have thermal conductivity in the range of 0.15–0.45 W/(m K), and thermal conductivity of air at 0 °C is equal to 0.024 W/(m K). Thermal conductivity of air is theoretically the lowest limit of the porous layer thermal conductivity. Values of the thermal conductivity coefficient can approach this limit when the heat transfer in the granule is minimized due to the

presence of only touch contacts between the adjacent sections of the solid skeleton, i.e., in a layer with high porosity. These touch contacts have significant thermal resistance to heat transfer. Influence of the main solid skeleton is insignificant. Only at low porosity influence of continuous contact can be decisive, since a significant part of the heat flow is transferred inside the granule by its solid constituent parts.

Thus, taking into account these features, it should be noted that values of the coefficients k_{sh}, k_w, k_p included in formula (12) should be greater than 1.

Formulas (12) and (15) are used to determine the surface temperature of a two-layer granule according to (8) and the temperature profile within $0.7R < r < R$ according to (7). When determining temperature in the center of the granule with (9) of the temperature profile for $r < 0.7R$ using (7), the thermal conductivity λ_T of the granule solid component is taken into account. When determining the volume-averaged temperature of a two-layer granule according to (11), the reduced thermal conductivity coefficient according to the equation is:

$$\lambda_R = 0.7\lambda_T + 0.3\lambda_E. \tag{16}$$

4 Discussion of the Results

The results of mathematical modeling are obtained in comparison with a continuous granule with porosity $\varepsilon = 0$ and a porous granule with values of $0.1 \leq \varepsilon \leq 0.7$.

The graph (Fig. 2) shows the dependence $S_S = f(d_p)$, according to the equation

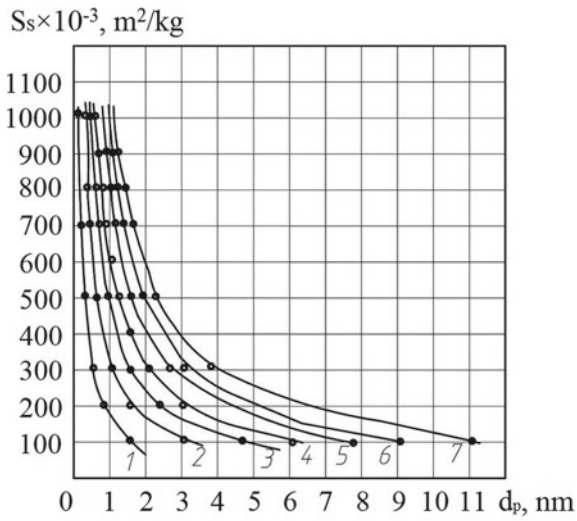

Fig. 2 Dependence of the specific pore surface on pore size: 1—$\varepsilon = 0.1$; 2—$\varepsilon = 0.2$; 3—$\varepsilon = 0.3$; 4—$\varepsilon = 0.4$; 5—$\varepsilon = 0.5$; 6—$\varepsilon = 0.6$; 7—$\varepsilon = 0.7$

$$S_S = \frac{2\varepsilon}{d_p \cdot \rho_g}, \tag{17}$$

where S_S is the total specific pore surface, m^2/kg; ε—granule porosity, $0 < \varepsilon < 1$; d_p—equivalent pore size, m; ρ_g—density of the granule material, kg/m^3.

Graphs of the dependence $S_S = f(d_p)$ show definite relationship between the specific surface of pores with their size and granule porosity. With the specific pore surface in the range (100–1000) $\times$ 10^{-3} m^2/kg and with ε = 0.1–0.7, we have micropores with a size d_p = 0.2–10 nm. With the decrease of the specific surface of pores to less than 10 $\times$ 10^{-3} m^2/kg and at $\varepsilon > 0.5$–0.7, there appear intermediate pores (mesopores) of size d_p = 50–100 nm and we approach the initial boundary of appearing macropores of size $d_p > 100$ nm.

Dependence of the effective coefficient of the granule thermal conductivity on its porosity, according to (15), first shows a rapid decrease of the thermal conductivity coefficient value during transition from the continuous structure of the granule ($\varepsilon = 0$) to the beginning of the porous structure formation ($\varepsilon = 0.1$), and then a proportional decrease in thermal conductivity within the change in the porosity of the granule $0.1 < \varepsilon < 0.7$.

The volume-averaged temperature of granule heating to a certain temperature is defined as

$$t = t_{med} - (t_{med} - t_i)\frac{6A_2}{\mu_1^2}\exp\left(-\mu_1^2\frac{\lambda_E \cdot \tau}{c \cdot \rho \cdot R^2}\right), \tag{18}$$

and granule heating time

$$\tau_h = \frac{R^2 \cdot c \cdot \rho}{\lambda_E \cdot \mu_1^2}\ln\left[\frac{6A_2}{\mu_1^2\left(\frac{t_{med}-t}{t_{med}-t_i}\right)}\right]. \tag{19}$$

where in addition to the above designations, c—the specific heat of the granule, J/kg K; ρ—granule density, kg/m^3.

The numerical values of the constants A_1, A_2 and the root μ_1 are found from the tables or graphically using the nomograms [8, 10]. This determination method makes it difficult to use a computer in an engineering calculation algorithm. Therefore, the authors using the least squares method processed the data of the monograph tables [8] and obtained regression equations to determine the constants A_1, A_2 in the range $0.1 < Bi < 4.0$, which is typical for suspended and fluidized beds:

$$A_1 = 0.274(Bi) + 1.0, \quad \text{at } 0 < Bi \leq 0.1; \tag{20}$$

$$A_1 = 0.29(Bi) + 1.0, \quad \text{at } 0.1 < Bi \leq 1.0; \tag{21}$$

$$A_1 = 0.183(Bi) + 1.1, \quad \text{at } 1.0 < Bi \leq 2.0; \tag{22}$$

$$A_1 = 0.13(Bi) + 1.22, \quad \text{at } 2.0 < Bi \leq 4.0; \tag{23}$$

$$A_2 = 0.47(Bi) + 0.01, \quad \text{at } 0.1 < Bi \leq 0.5; \tag{24}$$

$$A_2 = 0.325(Bi) + 0.06, \quad \text{at } 0.5 < Bi \leq 1.0; \tag{25}$$

$$A_2 = 0.30(Bi) + 0.1, \quad \text{at } 1.0 < Bi \leq 2.0; \tag{26}$$

$$A_2 = 0.25(Bi) + 0.05, \quad \text{at } 2.0 < Bi \leq 4.0; \tag{27}$$

Root μ_1 is determined:

$$\mu_1 = \frac{в + \sqrt{в^2 - 4c}}{2}, \tag{28}$$

or

$$\mu_1 = \sqrt{\frac{Bi^2}{A_2} - Bi^2 + Bi}, \tag{29}$$

where

$$в = \frac{2Bi}{A_1}; \tag{30}$$

$$c = \frac{\left(Bi^2 - Bi\right)(2 - A_1)}{A_1}. \tag{31}$$

Dependence of the granule heating time on its porosity, according to (19), shows a sharp increase in the heating time of the granule (approximately 2 times) during the transition from a continuous granule ($\varepsilon = 0$) to a granule with initial porosity ($\varepsilon = 0.1$). Then, heating time gradually increases and granule porosity reaches the level $0.1 < \varepsilon < 0.3$; further rapid increase of granule heating time causes porosity in range $0.3 < \varepsilon < 0.6$. The latter is caused by a significant decrease of areas of the granule solid skeleton that has less resistance to the heat conductivity process. This is proved by the nature of curves in the dependence $t = f(\tau)$ (Fig. 3) during heating of granules in the gas medium with an initial temperature of 65 °C.

During laboratory studies, film coating of an organic suspension was applied on mineral granules [11], and temperature of gas medium in the fluidized bed of granules was maintained in the range of 40–80 °C. The following temperature conditions of the granulation process were established experimentally [12]:

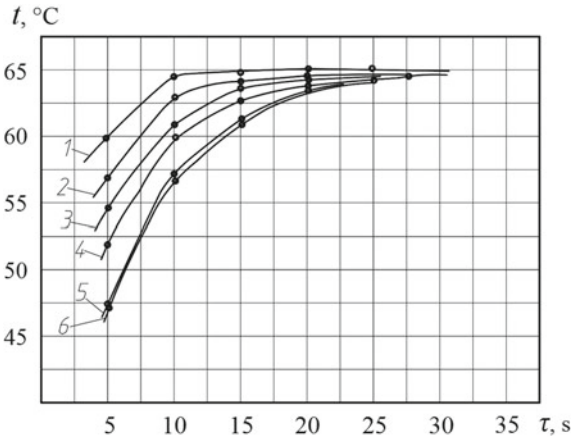

Fig. 3 Dependence of the granule heating temperature on time: 1—$\varepsilon = 0.1$; 2—$\varepsilon = 0.2$; 3—$\varepsilon = 0.3$; 4—$\varepsilon = 0.4$; 5—$\varepsilon = 0.5$; 6—$\varepsilon = 0.6$

1. At the temperature within 40–50 °C, droplets of the suspension do not spread over the surface of the granule, but attach to one side of the granule, and form a big growth which is as big as a drop itself (Fig. 4a).
2. When temperature of the fluidized bed is 60–65 °C, droplets of the suspension spread over the surface of the mineral granules and liquid starts to evaporate intensively, forming a thin solid layer of dry organics (Fig. 4b). As it can be seen from the graphs in Fig. 3, at 20–25 s of heating the granules, their temperature reaches 65 °C and then remains constant, that is, the indicated value is the limiting temperature of granule heating. Moreover, the granule outer shell is of sufficiently dense structure with micro- and mesopores on its surface.
3. Increase of the fluidized bed temperature above the limiting value, namely, up to 70–80 °C, causes the formation of irregular surface with deep cracks which is

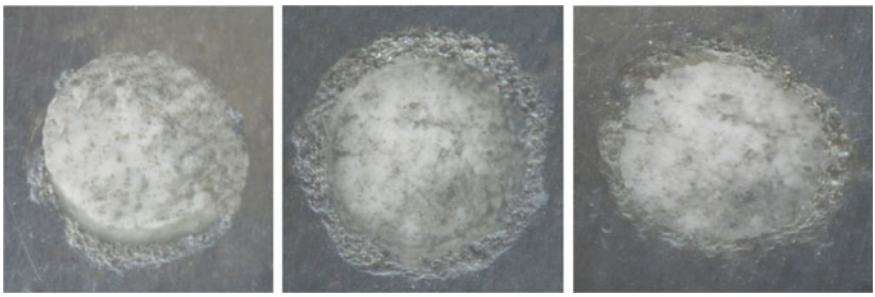

Fig. 4 Cut of the carbamide granule, encapsulated with chicken manure at the appropriate temperature: **a** 40–50 °C; **b** 60–65 °C; **c** 70–80 °C

accompanied with chipping of organic substance in separate places of the granules and thus new organic cores appear (Fig. 4c). The porosity of such granules increase, macropores are formed.

5 Conclusions

1. Nanoporous structure of organic fertilizer granules is described and the presence of micropores with a size of 0.2–10 nm and mesopores with a size of 50–100 nm in the solid skeleton of the granules are grounded.
2. Influence of granule solid skeleton porosity on the process of its thermal conductivity during heating of the granule in a gas medium is shown. One proposed formula for determining the effective coefficient of thermal conductivity depending on the porosity of the granule and true thermal conductivity coefficients of the solid skeleton and gas in the hollow sections of the granule. Decrease of heat conductivity with increasing of granule porosity is shown.
3. Analytical expressions for determining of the temperature profile and granule heating time, taking into account its porosity are obtained. It is explained that high granule porosity cause increase of the heating time and decrease of the granule temperature.
4. Optimal temperature regime to obtain granules with sufficient porous organic shell was grounded theoretically and experimentally and it is in range of 60–65 °C.

Acknowledgements This research work has been supported by the Ministry of Science and Education of Ukraine under the project "Small-scale energy-saving modules with the use of multifunctional devices with intensive hydrodynamics for the production, modification and encapsulation of granules," project No. 0119U100834.

References

1. Saeid A, Chojnacka K (2019) Fertilizers: need for new strategies. In: Organic farming. Global perspectives and methods. Elsevier Science Publishing Company, Inc., Amsterdam
2. Ostroha R, Yukhymenko M, Mikhajlovskiy Y, Litvinenko A (2016) Technology of producing granular fertilizers on the organic basis. Eastern-Eur J Enterprise Technol 1/6(79):19–26
3. Artyukhov A, Sklabinskiy V, Goncharov A (2018) Development of technology for obtaining N_4HNO_3 multilayer granules with nanostructured porous layers. J Nano Electron Phys 10(5), 05013
4. Artyukhov AE, Sklabinskyi VI (2013) Experimental and industrial implementation of porous ammonium nitrate producing process in vortex granulators. Nauk Visnyk Nats Hirnychoho Univ 6:42–48
5. Artyukhov AE, Sklabinskyi VI (2017) Investigation of the temperature field of coolant in the installations for obtaining 3D nanostructured porous surface layer on the granules of ammonium nitrate. J Nano Electron Phys 9(1):01015-1–01015-4
6. Artyukhov AE, Artyukhova NO (2019) Technology and the main technological equipment of the process to obtain N_4HNO_3 with nanoporous structure. Springer Proc Phys 221:585–594
7. Hoffmann T, Rieck C, Bück A, Peglow M, Tsotsas E (2015) Influence of granule porosity during fluidized bed spray granulation. Procedia Eng 102:458–467
8. Luikov A (1968) Analytical heat diffusion theory. Academic, New York
9. Krischer O (1978) Trocknungstechnik: Die Wissenschaftlichen Grundlagen der Trocknungstechnik. Springer, Berlin
10. Lykov A (1967) Theory of heat conduction. Vysshaya Shkola, Russia
11. Ostroha R, Yukhymenko M, Yakushko S, Artyukhov A (2017) Investigation of the kinetic laws affecting the organic suspension granulation in the fluidized bed. Eastern-Eur J Enterprise Technol 4/1(88):4–10
12. Ostroha R, Yukhymenko M, Lytvynenko A, Bocko J, Pavlenko I (2019) Granulation process of the organic suspension: fluidized bed temperature influence on the kinetics of the granule formation. Lecture Notes Mech Eng F2:463–471

Final Drying of Ammonium Nitrate with Nanoporous Structure in Gravitational Shelf Dryers: Hydrodynamic and Thermodynamic Conditions

N. O. Artyukhova, A. E. Artyukhov, and J. Krmela

1 Introduction

Some granular materials used for special industries must have a developed network of different-size pores (including nanoporous structure). The presence of pores allows increasing the specific surface of the mass transfer, providing absorption of the required amount of liquid material, etc. At the same time, important porosity properties include pore sizes and pores network configuration [1]. It is necessary to distinguish separately such feature of the porous surface as the ratio of the pore area on the surface of the granules in the mass unit of granular material. This property lets to provide the liquid (gaseous) phase penetration into the granules to carry out the target process [2, 3].

It is important to provide the required size (size range) of pores in terms of their ratio to the substance molecule size that must penetrate these pores. The size and configuration of the pores must be ensured by the optimal selection of the technology to form porous structure and the design of the main equipment to implement this process [4].

The individual granular materials to which the porous ammonium nitrate (PAN) belongs should have a nanoporous structure to provide the main function–absorption and retention of diesel fuel distillate. These PAN properties are necessary for its successful use as a component of the ANFO industrial explosive [5–10].

N. O. Artyukhova · A. E. Artyukhov (✉)
Processes and Equipment of Chemical and Petroleum-Refineries Department, Sumy State University, 2, Rymskogo-Korsakova str, 40007 Sumy, Ukraine
e-mail: a.artyukhov@pohnp.sumdu.edu.ua

J. Krmela
Department of Numerical Methods and Computational Modeling, Alexander Dubcek University of Trencin, 491/30 I. Krasku, 02001 Puchov, Slovak Republic
e-mail: jan.krmela@fpt.tnuni.sk

O. Fesenko and L. Yatsenko (eds.), *Nanooptics and Photonics, Nanochemistry and Nanobiotechnology, and Their Applications*, Springer Proceedings in Physics 247, https://doi.org/10.1007/978-3-030-52268-1_13

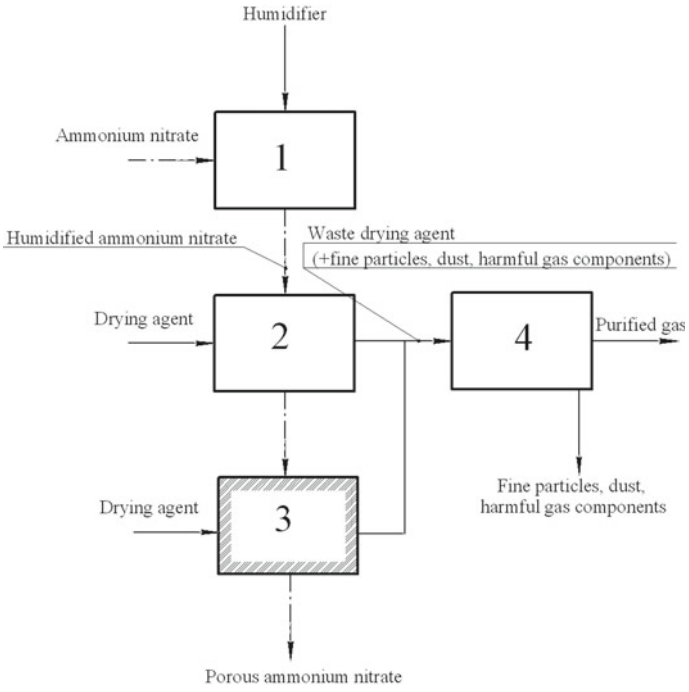

Fig. 1 Scheme of PAN obtaining process [15]: 1—humidification of ammonium nitrate granule; 2—granulation-drying; 3—final drying; 4—cleaning of waste gas

A number of works by the authors of this article [11–16] are devoted to the theoretical description and experimental study of the nanoporous structure formation in devices with intensive hydrodynamics–vortex granulators and gravitational shelf dryers. Therefore, the stages of the granule formation process are clearly separated, as shown in Fig. 1. The process of humidification and heat treatment of ordinary ammonium nitrate granules (it is used as an original stock to produce PAN in the scheme below) with the allocation of the surface moisture in a highly turbulent vortex flow enables you to form up to 75% of all pores inside the granule and on the surface of it. The remaining number of pores can be formed in two ways:

1. In the same vortex granulator, with the less twisting degree. The reduction of the twisting degree is caused by the high probability of granule core destruction and a significant decrease in its strength. It is also necessary to perform changeover of the vortex granulator and to convert it from cyclic to periodic mode.
2. In a shelf dryer; at the same time, due to the decrease of the flow twisting degree and to the complete preserving of the active hydrodynamic mode, the removal of bound moisture is not accompanied by the granules destruction.

Thus, two-stage heat treatment (drying + final drying), despite some increase of the energy amount to implement the process (which, however, can be solved by

the introduction of the Maisotsenko Cycle [17]) lets fully to form the nanoporous structure of the granule without losing its strength.

The influence made by the hydrodynamic modes of gravitational shelf dryer operation on the nanoporous granule structure nature is described in detail in [18, 19]. The aim of this research is to evaluate the effect made by the structural features of the gravitational shelf dryer (and the proper hydrodynamic and thermodynamic parameters of its operation) on the peculiarities of nanopore network formation on the PAN granules surface.

2 An Overview of the Basic Constructions of Gravitational Shelf Dryers and Features of Their Operation

Within the framework of the research and scientific works "Investigation of hydrodynamic and heat-mass transfer features of devices with vortex and highly turbulent single and two-phase flows," "Hydrodynamic parameters of two-phase flows of heat-mass transfer, granulation and separation equipment" at the department "Processes and Equipment of Department and Petroleum," a stand of multistage gravitational shelf dryer (Fig. 2) has been created.

Two shelf dryer constructions have been proposed for research (a general view of the dryer is shown in Fig. 3a):

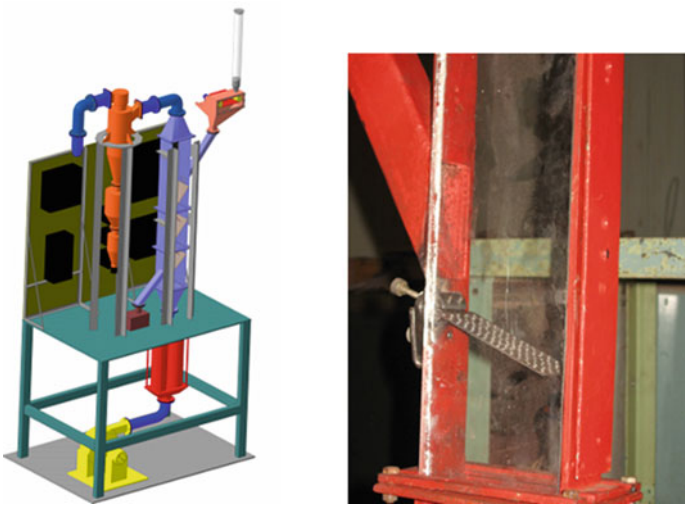

a b

Fig. 2 Gravitational shelf dryer: **a** stand diagram; **b** a shelf dryer element

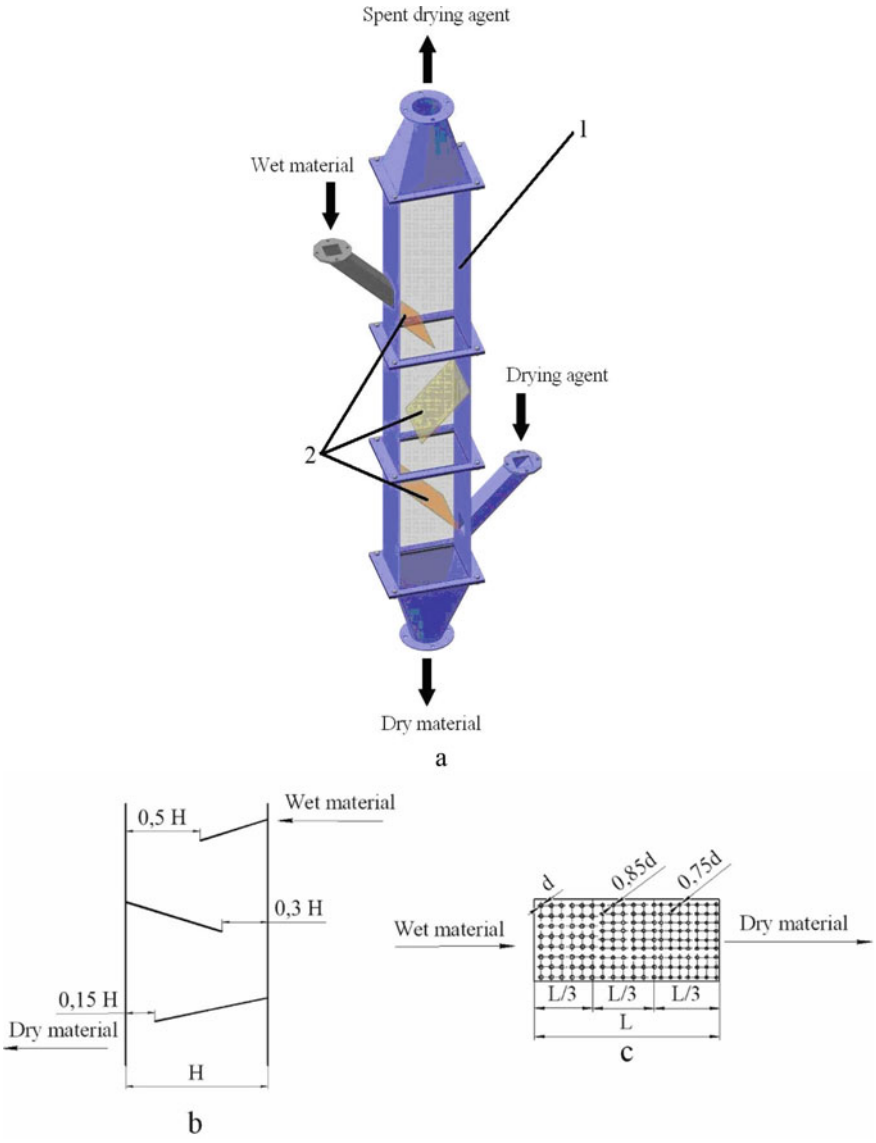

Fig. 3 Shelf dryer: **a** principle device; **b**, **c** design modifications; 1—case; 2—shelf

1. A dryer with a variable gap between the end of the shelf contact and the wall (Fig. 3 b) [20].
2. Sectioned shelf dryer with replaceable perforation (Fig. 3c) [21].

A general idea of the effect made by the gravitational shelf dryer on the hydrodynamic and thermodynamic conditions of the nanoporous surface layer formation of

the PAN granule can be obtained by describing the process in a dryer with different gaps between the end of the shelf and the wall. In the weighted layer mode, the efficiency of moisture removal from the material is greatly enhanced by the intensification of the phase contact. The particles are actively interacting with the airflow on the surface of the perforated shelf and in the outloading space. As the gap between the end of the shelf and the wall of the device decreases, the velocity of the drying agent increases. This is a major factor in the intensification of phase contact and the heat-mass transfer process. The increase of the residence time of the particles due to their circulation in the zone above the outloading space causes the increase in the moisture content of the particles of the material in the weighted layer mode. In this mode, drying of wet material in periods of constant (first period) and falling velocity (second period) is quite effective.

Thanks to changes in the constructive parameters of the shelf contacts in the dryer, the necessary hydrodynamic conditions of material motion on each shelf of the cascade are provided. When constructing a gravitational shelf dryer, one should provide the steadiness of the drying agent's contact with the disperse material on each shelf. This uniformity makes it possible to regulate the residence time of the particles on the shelves, taking into account their physicochemical properties. Any irregularity of the drying agent's contact with the disperse material can lead to underheating (with insufficient drying) or to overheating with undesirable destruction of the particles and a decrease of their consumer qualities.

On the upper contact shelf (shelf is a conditional notion, depending on the conditions of the process, there may be several shelves in the cascade) by varying the length, angle of installation or degree of perforation, the minimum necessary contact time of the disperse material with certain physicochemical properties, fractional composition and the drying agent's parameters is provided. On this shelf (or top shelf, if it will be a cascade of shelves) a small fraction is deleted, i.e., it serves as a separator. On the middle contact shelf, the residence time of the disperse material and its contact with the drying agent increases, which contributes to a more intensive removal of moisture. On the lower contact shelf, the contact between the disperse material and the drying agent provides a long stay of particles on the shelf to remove moisture from the depth of the material.

In order to control the technological process of nanopores formation in PAN granules, it is necessary to provide:

1. The uniformity of the gas flow velocity profile in the above-shelf space at each cascade dryer.
2. The minimum residence time of the granules in the workspace of the dryer.
3. The required temperature and humidity properties of the drying agent and the disperse material.

The solution of task 1 is presented in Fig. 4. The analysis of the graph data shows that there is a decrease in the intensity of the drying agent's motion with any shelf structure in the central part. This disadvantage can be corrected by the local changing of the perforation diameter.

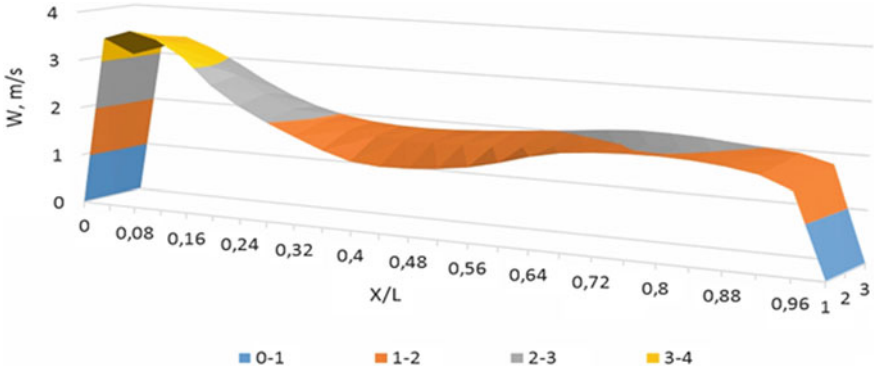

Fig. 4 The motion velocity curve of the drying agent along the relative length of the device: 1—shelf with constant perforation along the length; 2—sectioned shelf with variable perforation of sections; 3—sectioned shelf with constant perforation of sections and the changing tilt angle

It is possible to solve the task 2 through the use of the author's software Multistage Fluidizer© [22]. The main windows for calculating the residence time of the granules in the workspace of the dryer are shown in Fig. 5. The software product allows using different mechanisms to control the residence time of PAN granules (drying agent's velocity, number of shelf contacts, length of shelves, tilt angle and perforation degree) in the device both separately and in combination.

The solution of task 3 is presented in Figs. 6, 7, 8, 9. The data from these figures let us predict the change in the temperature and humidity features of PAN granules and a drying agent.

Comparing these data with the data from the hydrodynamic calculation, it is possible to create a reliable mechanism for controlling the pore-formation and nanoporous surface formation process. The results of the granule structure studies are presented in the next section.

3 Research Findings of the PAN Granule Structure

Having investigated a reliable mechanism for controlling the pore-formation and nanoporous surface formation process, PAN samples were obtained with different degrees of surface porosity and different pore structure. The porous surface photos were processed using the author's Converter Image software (Fig. 10).

The studies results of the porous structure of PAN granules are presented in Fig. 11. It should be noted that the granule samples obtained in the updated dryers are characterized by a more developed network of nanoscale pores on the surface. In this case, this network is a combination of straight and curved channels. The first type of channels lets diesel fuel distillate directly penetrate into the granules. The

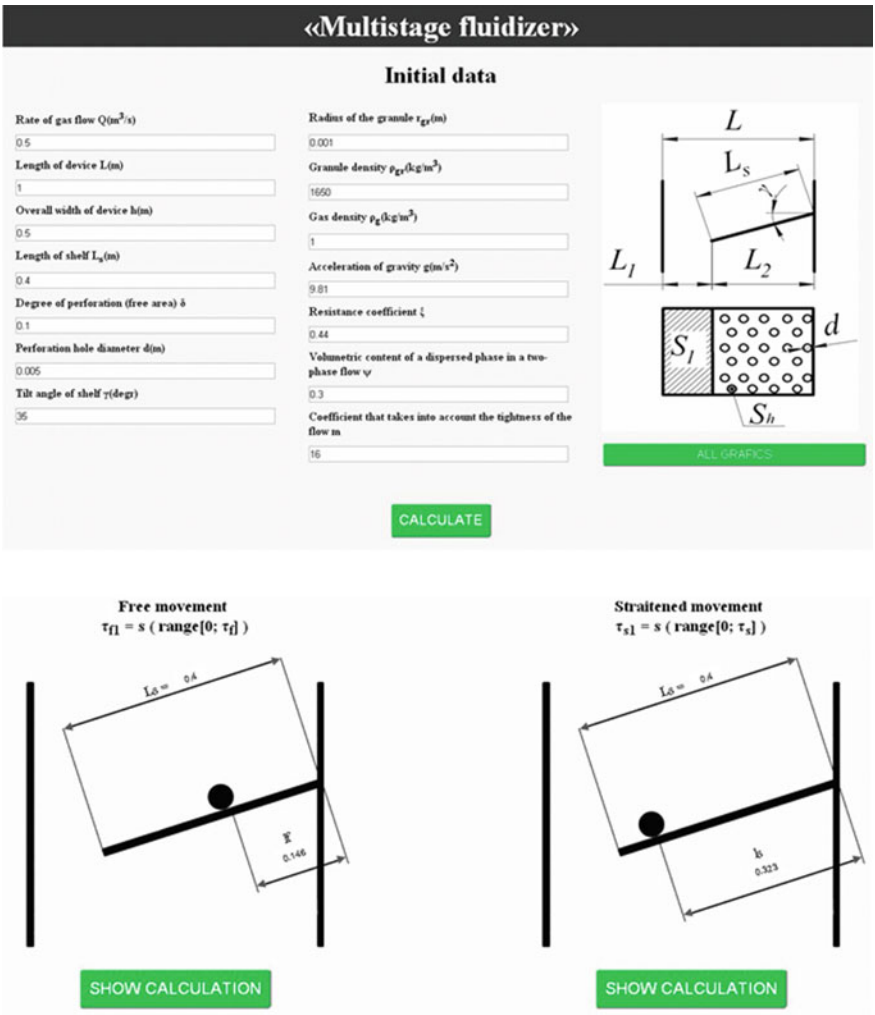

Fig. 5 Multistage Fliudizer© software windows

second type of channels lets successfully hold the diesel fuel distillate inside the granule thanks to the curvature.

The data from calculation of the porous surface relative area (according to the results from the calculation of the relative pore surface per area unit of the granules by the software Converter Image) are shown in Table 1. The results show a significant advantage to use the updated constructions of dryers in the implementation of the PAN obtaining method taking into account the optimal hydrodynamic and thermodynamic conditions, the mechanism to define which is presented in the previous section of this paper.

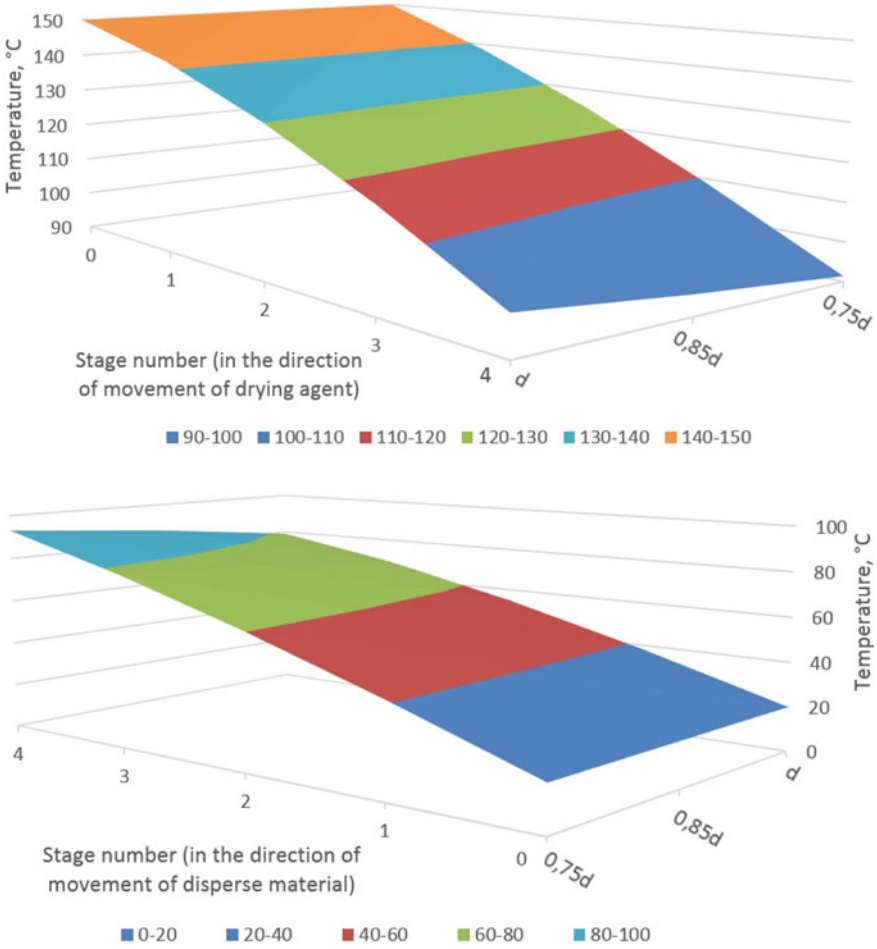

Fig. 6 Research findings of temperature features of flows in dryers with variable outloading gap: **a** drying agent; **b** PAN granules

The results of studies of the nanoporous structure of porous ammonium nitrate granules after the multistage drying stage showed the following patterns: an extensive network of deep curvilinear (winding) mesopores of a “modification” character is created; pores are evenly distributed over the entire surface of the granules; smaller pores practically do not merge into ensembles; the number of “mechanical” pores and destruction of the granules is significantly reduced.

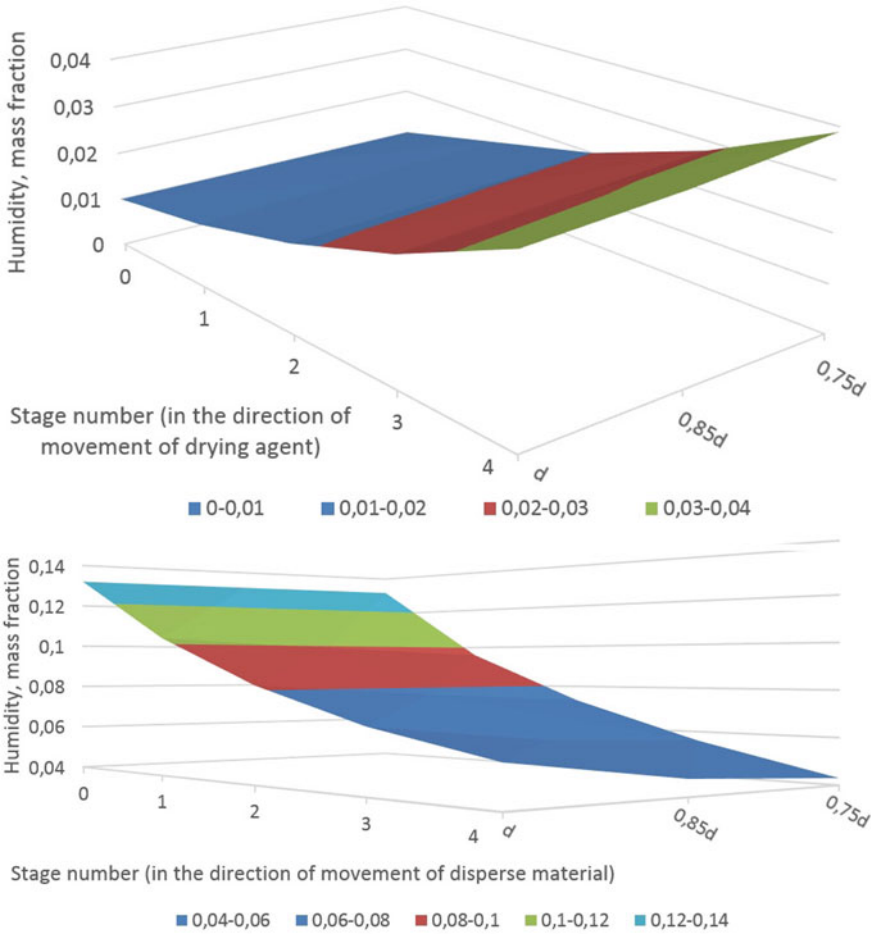

Fig. 7 Research findings of humidity features of flows in dryers with variable outloading gap: **a** drying agent; **b** PAN granules

4 Conclusions

The results of studies regarding the PAN granules structure showed that the additional stage of "soft" drying allows obtaining PAN with a developed network of surface pores, which successfully provide the necessary absorptivity and retentivity of this product. The ability to control the hydrodynamic and thermodynamic parameters of the PAN granules, as well as to control them, allows obtaining the predicted nanoporous structure.

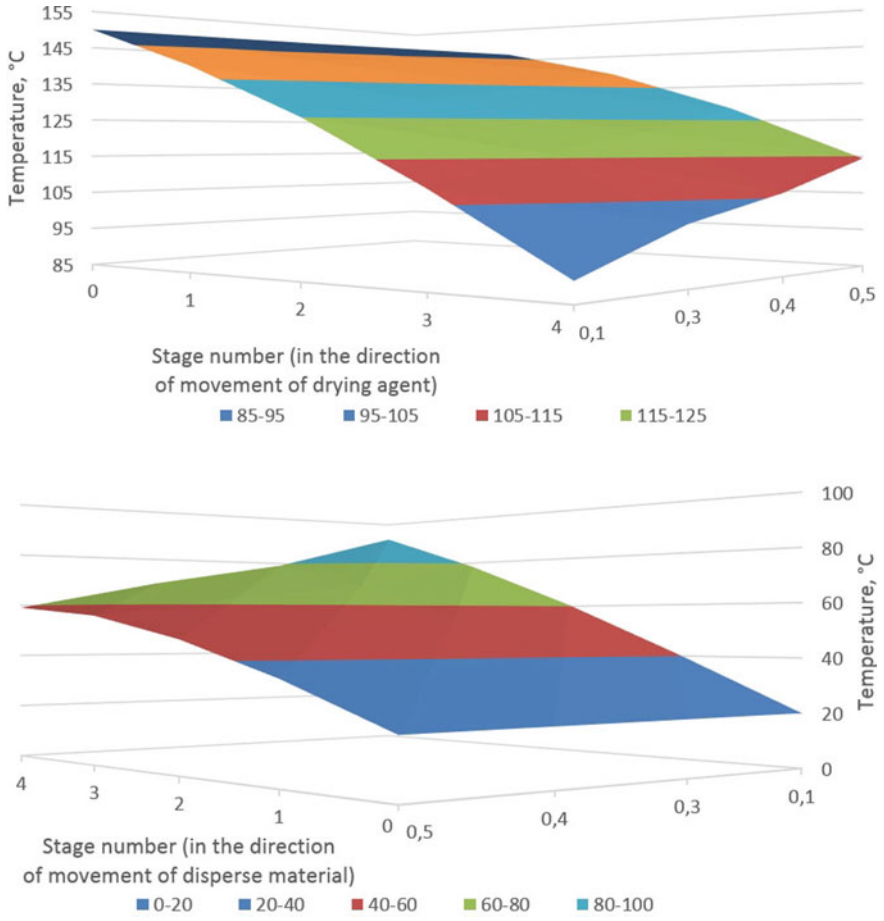

Fig. 8 Research findings of temperature features of flows in dryers with variable perforation of shelf contacts: **a** drying agent; **b** PAN granules

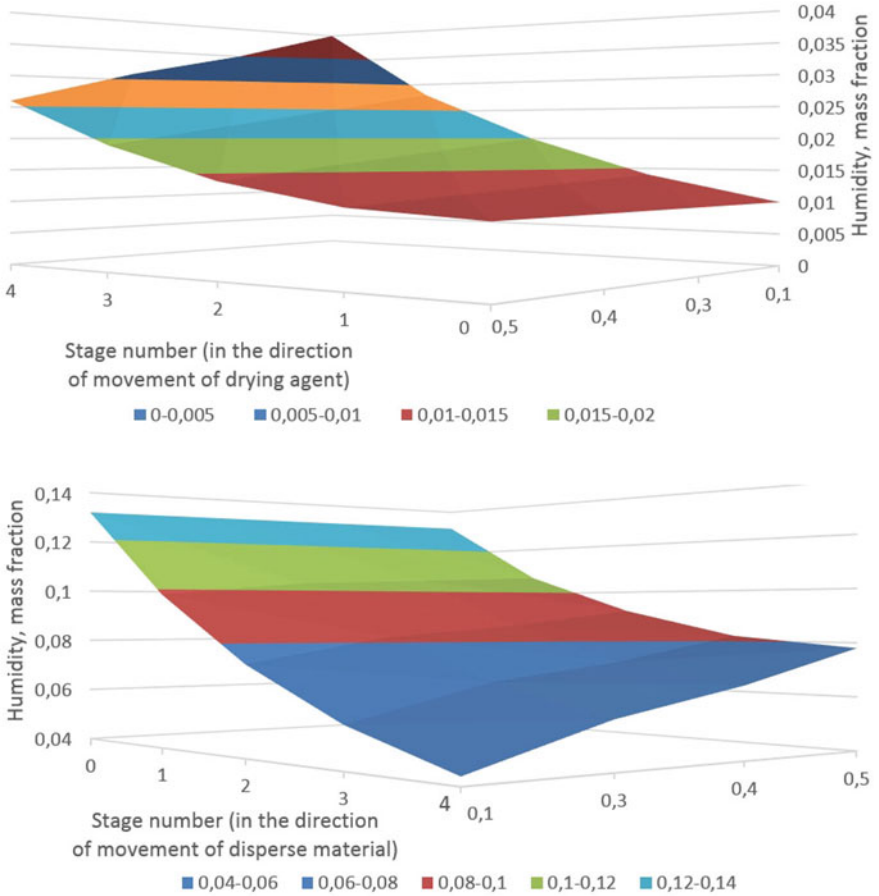

Fig. 9 Research findings of humidity features of flows in dryers with variable perforation of shelf contacts: **a** drying agent; **b** PAN granules

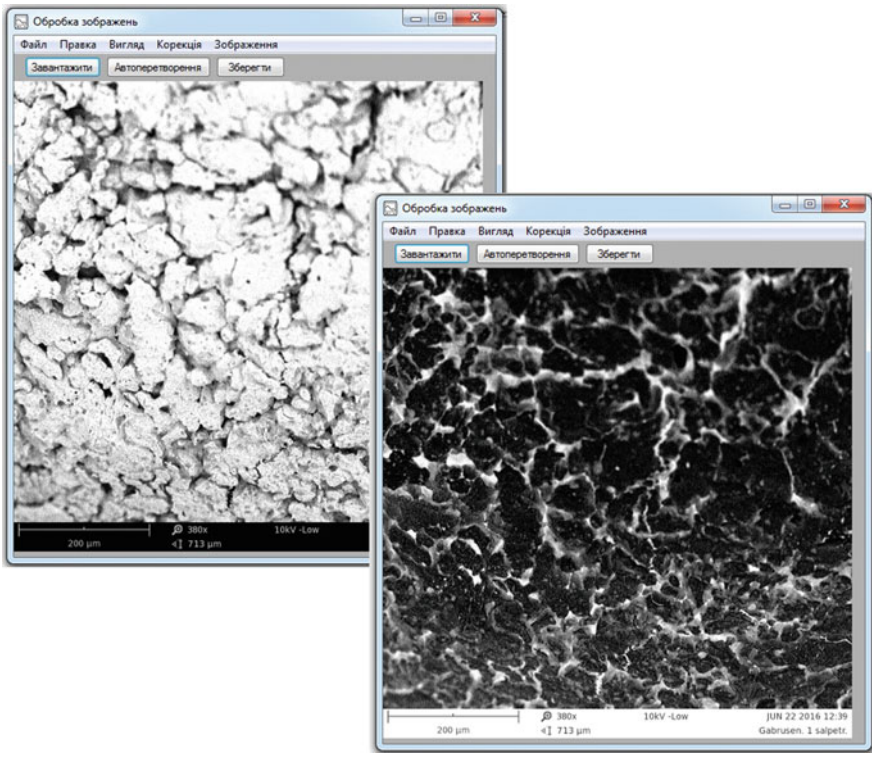

Fig. 10 Software product converter image

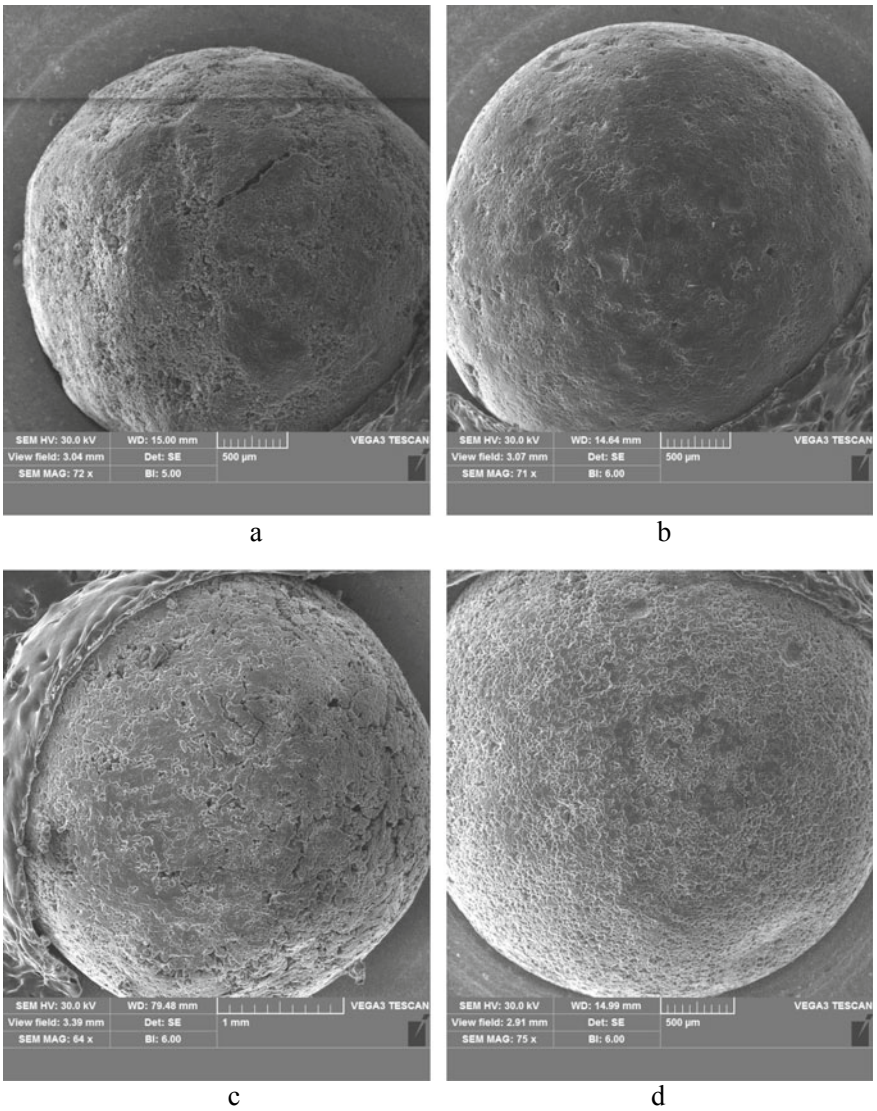

Fig. 11 PAN granule samples: **a** after vortex granulator; **b** after the dryer with shelves with the same outloading gap and constant perforation along the length; **c** after the dryer with shelves with different outloading gap; **d** after dryer with shelves with the same outloading gap and sectioned shelves with variable perforation of sections

Table 1 The relative area of the porous surface on the PAN granule

Constructive properties of the dryer	The size of the granule of commodity fraction, mm	The relative surface of pores, m^2/m^2	The relative area of the porous surface, m^2/kg
Dryer with shelves with the same outloading gap and constant perforation along the length	2	0.36	1.96
Dryer with shelves with different outloading gap	2	0.44	2.64
Dryer with shelves with the same outloading gap and sectioned shelves with variable perforation of sections	2	0.47	2.82

Acknowledgements This research work had been supported by the Ministry of Science and Education of Ukraine under the project "Technological bases of multistage convective drying in small-sized devices with utilization and heat recovery units", project No. 0120U100476 and by the cultural and Educational Grant Agency of the Slovak Republic (KEGA), project No. KEGA 002TnUAD-4/2019.

References

1. Artyukhov AE, Sklabinskyi VI (2016) 3D Nanostructured porous layer of ammonium nitrate: influence of the moisturizing method on the layer's structure. J Nano Electron Phys 8(4) 04051–1–04051–5
2. Artyukhov AE (2016) Kinetics of heating and drying of porous ammonium nitrate granules in the vortex granulator. In: Abstracts of the 6th international conference nanomaterials: application and properties (NAP-2016), vol 5(2), pp 02NEA02
3. Artyukhov AE, Voznyi AA (2016) Thermodynamics of the vortex granulator's workspace: the impact on the structure of porous ammonium nitrate. In: Abstracts of the 6th international conference nanomaterials: application and properties (NAP-2016), vol 5(2), pp 02NEA01
4. Artyukhov AE, Sklabinskyi VI (2016) Thermodynamic conditions for obtaining 3D nanostructured porous surface layer on the granules of ammonium nitrate. J Nano Electron Phys 8(4):04083–1–04083–5
5. Erode GM (2013) Ammonium nitrate explosives for civil applications: slurries, emulsions and ammonium nitrate fuel oils. Wiley-VCH and Co, Weinheim
6. Zygmunt B, Buczkowski D (2007) Influence of ammonium nitrate prills' properties on detonation velocity of ANFO. Propellants Explos Pyrotech 32(5):41–414
7. Lipinska K et al (2005) Demilitarized propellants as ingredients in commercial explosives. In: European Federation of Explosives Engineers: Brighton conference proceedings, Brighton, pp 493–498
8. Martin G, Barbour W (2003) In: Industrial nitrogen compounds and explosives. Chemical manufacture and analysis. Watchmaker Publishing

9. Kubota N (2015) Propellants and explosives: thermochemical aspects of combustion, 3rd edn. Wiley-VCH and Co, Weinheim
10. Janssen TJ (2011) In: Explosive materials: classification. Composition and properties, Nova Science Publishers Inc
11. Artyukhov AE, Sklabinskyi VI (2013) Experimental and industrial implementation of porous ammonium nitrate producing process in vortex granulators. Nauk Visnyk Nats Hirnychoho Univ 6:42–48
12. Artyukhov AE, Sklabinskyi VI (2017) Investigation of the temperature field of coolant in the installations for obtaining 3D nanostructured porous surface layer on the granules of ammonium nitrate. J Nano Electron Phys 9(1) 01015–1–01015–4
13. Artyukhov A, Gabrusenoks J (2018) Phase composition and nanoporous structure of core and surface in the modified granules of NH_4NO_3. Springer Proc Phys 210:301–309
14. Artyukhov AE, Artyukhova NO (2019) Technology and the main technological equipment of the process to obtain N_4HNO_3 with nanoporous structure. In: Springer proceedings in physics, vol 221, pp 585–594
15. Ivaniia AV, Artyukhov AY, Olkhovyk AI (2019) Hydrodynamic and thermodynamic conditions for obtaining a nanoporous structure of ammonium nitrate granules in vortex granulators. Springer Proc Phys 221:257–268
16. Artyukhov AE, Sklabinskyi VI (2015) Theoretical analysis of granules movement hydrodynamics in the vortex granulators of ammonium nitrate and carbamide production. Chem Chem Technol 9(2):175–180
17. Artyukhov AE, Levchenko DO, Yurko IV (2017) Maisotsenko cycle applications in multi-stage ejector recycling module for chemical production. In: IOP conference series: materials science and engineering vol 233(1), pp 012024
18. Artyukhov AE, Krmela J, Gavrylenko OM (2019) Evaluation of the impact made by the hydrodynamic regime of the granulation equipment operation on the nanoporous structure of N_4HNO_3 granules. J Nano-Electron Phys 11(4): 03033
19. Artyukhova NO, Krmela J (2019) Nanoporous structure of the ammonium nitrate granules at the final drying: the effect of the dryer operation mode. J Nano-Electron Phys 11(4): 04006
20. Artyukhova NO et al (2012) Prystriy dlya sushinnya dyspersnych materialiv (Device for drying of disperse materials) UA Patent 74070, 10 Oct 2012
21. Artyukhova NO et al (2013) Prystriy dlya sushinnya dyspersnych materialiv (Device for drying of disperse materials) UA Patent 81720, 10 July 2013
22. Artyukhov AE et al (2018) Computer program Multistage fluidizer UA Certificate for registration of copyright 52659, 17 May 2018

Study of the Producing Ferrite–Chromite by Coprecipitation

L. Frolova, O. Kushnerov, and O. Khmelenko

1 Introduction

In the technology of inorganic materials in recent decades, interest has increased in relation to oxide systems of the composition $FeFe_{2-x}Cr_xO_4$ (with spinel structure. Traditionally, ferrites and chromites are widely used as catalysts for various chemical processes [1–3]. In this regard, interest in such systems is growing. In addition, based on the analysis of available experimental studies, it can be noted that ferrites and chromites are also used as sensors [4], ceramic pigments [5–7], bactericidal materials [8], photocatalysts [9, 10].

Despite the rapidly developing new technologies for the synthesis of nanostructured materials, classical ceramic technology is still widely used [11, 12]. It allows you to get coarse materials of controlled chemical composition. One of the significant drawbacks of ceramic technology is the length of the production cycle and the need to use high heat treatment temperatures, which leads to an increase in specific costs for the production of materials.

In this regard, the development of the scientific foundations of hydrophase methods for producing spinel at low temperature with a shorter duration is an urgent task of the chemical technology of inorganic substances [13–15].

The purpose of the work is to study the optimal conditions for obtaining magnetic spinel ferrites, to determine their magnetic characteristics.

L. Frolova (✉)
Ukrainian State University of Chemical Technology, Dnipro, Ukraine
e-mail: 19kozak83@gmail.com

O. Kushnerov · O. Khmelenko
Oles Honchar Dnipro National University, Dnipro, Ukraine

O. Fesenko and L. Yatsenko (eds.), *Nanooptics and Photonics, Nanochemistry and Nanobiotechnology, and Their Applications*, Springer Proceedings in Physics 247, https://doi.org/10.1007/978-3-030-52268-1_14

2 Methodology of the Experiment

The starting reagents used were iron(II) sulfate seven-water ($FeSO_4.7H_2O$), chromium(III) sulfate eighteen-water ($Cr_2(SO_4)_3\ 18H_2O$), sodium hydroxide (NaOH). All reagents analytical qualification. Prepared model solutions based on chromium(III) sulfate and iron(II) sulfate with a concentration of 0.5 mol/l. The effect of temperature, the ratio of cations and the duration of the process on the residual concentration of chromium and iron ions in model solutions was studied.

The cation ratio was calculated by the Formula:

$$K = \frac{C_{Fe^{2+}}}{C_{Cr^{3+}}}, \tag{1}$$

where is the concentration of $C_{Fe}{}^{2+}$ cations, mol/l;
$C_{Cr}{}^{3+}$ concentration of cations Cr^{3+} mol/l.

The values of K were 1.0; 1.5; 2.3; 4.0; 9.0; 11.5; 15.7; 19.0; 24.0.

The temperature was kept constant using the UT-5 thermostat. The experiments were carried out in a thermostatically controlled cell at temperatures of 15, 30, 60, 70, 80, 90 °C. The concentration of chromium cations in the solution was determined photometrically using a KFK-2 photocolorimeter, and iron cations—permanganometrically. The phase composition of the precipitates was studied using a DRON-2.0 diffractometer with Co_α radiation. The relative magnetic properties of the suspensions were determined by the method of increasing the inductance of the coil when a sample of a ferrite suspension was introduced into its working volume.

It consists in setting up a series of experiments in which the total amount of cations is constant for all experiments and a certain amount of precipitant is set for the same total solution volume. According to the analysis of solutions, diagrams were made of the composition of the system—the residual concentration of cations in the solution and the dependence of the composition of the system—the apparent height of the precipitate.

Model solutions of iron and chromium sulfate (5 ml) were mixed in a certain ratio ($K = 1\ldots 24$) and precipitated with 1 M NaOH solution. Next, the suspension was heated to the required temperature (60–90 °C) and kept constant. The ferritization time was determined by measuring the value of the redox potential of the ionomer. After completion of the ferrite formation process, the magnetic characteristics of the suspension and the apparent volume of sediment were measured. The average sediment compaction rate was determined by the Formula:

$$V_{cp} = \frac{\Delta V}{\Delta \tau} \tag{2}$$

ΔV where is the change in sediment volume over a period of time, cm^3
$\Delta \tau$ selected time interval, min.

The precipitate was separated from the mother liquor, washed to a negative reaction to a sulfate ion, dried at 180 °C and the phase composition was determined. In the filtrate, the residual concentrations of chromium and iron were determined by the methods described above.

3 Results and Discussion

The first part of the research was devoted to the analysis of potentiometric titration curves. It is known that the formation of chemical compounds corresponds to jumps on the pH $= f(n)$ curve. The results of the analysis of a solution of iron Fe^{2+} and chromium Cr^{3+} in the ratio $K = 1$ with the addition of NaOH on a pH meter are shown in Fig. 1.4 large jumps corresponding to a high rate of change in pH can be observed. In Fig. 1, the first is visible—in the range of pH 2–4, and the second—at pH = 5–6, the third pH = 6–7.8 and the most mild at pH = 10.5. Jumps at low pH values correspond to the formation of a prestructure (polyhydroxocomplexes). It is obvious that the formation of hydroxides occurs at pH = 10.5.

pH is the value of the medium; n is the ratio of hydroxide added to the solution to the metal cations; $y'(x)$ is a derivative of pH.

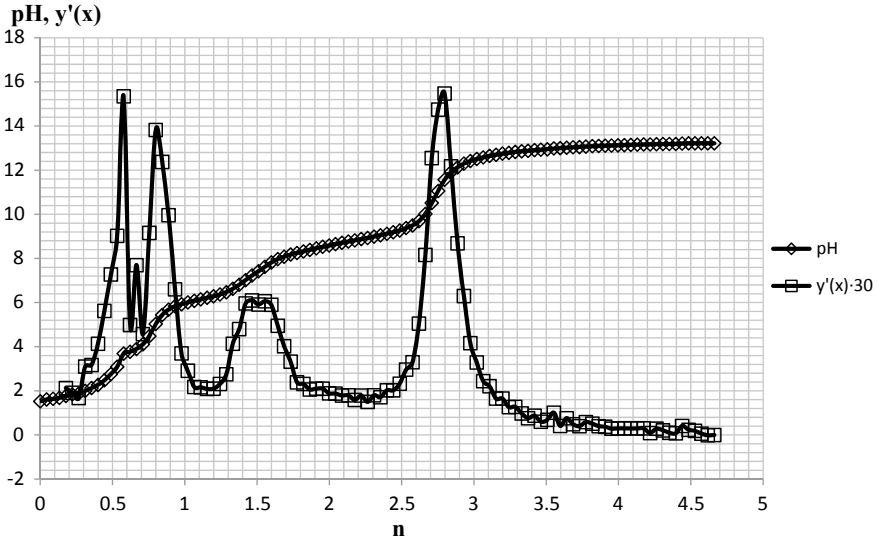

Fig. 1 The dependence of the pH of the solution ($K = 1$) and the rate of change ($y'(x)$) on the ratio of hydroxide added to the solution to the metal cations

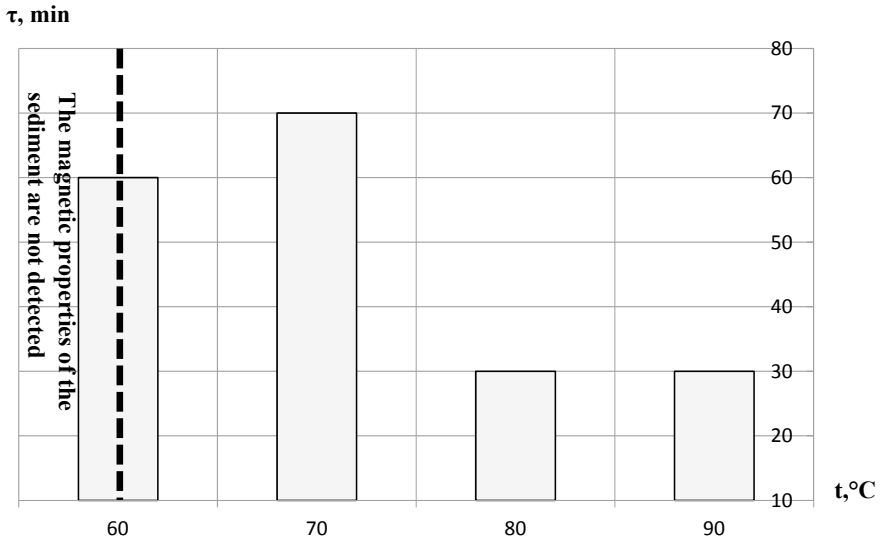

Fig. 2 Temperature dependence of ferritization time

It is also very important to study the process of ferritization of the resulting suspension when heated. As studies have shown, the suspension exhibits magnetic properties at a temperature of 60 °C. The dependence of ferritization time is extreme. In the first section, 60–70 °C increases, which can be explained by a decrease in oxygen solubility with increasing temperature (Fig. 2). With a further increase in temperature, the ferritization time decreases by half. This is due to the acceleration of the catalytic process according to the Shikorra reaction.

We can assume the following ferritization scheme in an alkaline medium at temperatures up to 65 °C:

$$(3-x)Cr^{3+} + xFe^{2+} + 6OH^- + 0.5O_2 => Fe_xCr_{3-x}O_4 + 3H_2O \quad (2)$$

$$Fe_xCr_{3-x}(OH)_6 + 1/2O_2 => Fe_xCr_{3-x}O_4 + 3H_2O \quad (3)$$

Products are ferrites or chromites, depending on the value of *x*.

With a further increase in temperature, the ferritization time decreases by half. It can be assumed that oxidation proceeds according to the reaction:

$$(3-x)Cr^{3+} + xFe^{2+} + (9-x)OH^- => (3-x)Cr(OH)_3 + xFe(OH)_2 \quad (4)$$

$$(3-x)Cr(OH)_3 + xFe(OH)_2 \xrightarrow{t \geq 50\,^\circ C} Cr_{3-x}Fe_xO_4 + (5-x)H_2O + 2H_2 \quad (5)$$

Next, experiments were carried out to establish the dependence of the residual concentrations of chromium and iron in solutions on the ratio K after heating (Table 1). Since the use of an alkaline agent leads to almost complete precipitation of cations in the form of the corresponding sparingly soluble hydroxocomplexes, there should be no metal ions in the filtrate. Experimental data show that the residual concentrations of chromium in the entire range of changes in K are low and do not depend on it. The residual concentrations of iron cations increase with increasing K, which is primarily due to the formation of amorphous colloidal precipitates of ferric compounds that do not have magnetic properties (Fig. 3).

Table 1 shows the results of measurements of the rate of compaction of sediments, which were obtained within 70 min of sedimentation at various ratios of Fe^{2+}/Cr^{3+}.

It is known that the average rate of sediment compaction corresponds to the degree of crystallinity and magnetization of the product; the formation of ferrites leads to a decrease in sediment volume by 1.5–2.0 times. The obtained dependences became the basis for establishing a correlation between the height of the sediment and its magnetic characteristics (Fig. 4). Curves 1 and 2 in Fig. 4 are similar in nature to the curve with two maxima.

The sediment exhibits magnetic properties in the entire studied range. However, two peaks are found in the graph: the first at $K = 1.5$, the second at $K = 19$. According to x-ray phase analysis (Fig. 5), the first peak in Fig. 4 corresponds to the formation of a mixture of $Fe_2(Cr_2O_4)_3\ 3H_2O$ hydrochromite and $FeCrO_3$ chromite, the second to the formation of a spinel structure of the $Cr_{3-x}Fe_xO_4$ type. In this case, the oxidation state of iron in chromite is equal to three, and in ferrite, it is equal to two, while the formation of $Cr_{3-x}Fe_xO_4$ occurs by the mechanism of magnetite formation.

To precipitate common trivalent metal ions (Cr^{3+} and Fe^{3+}) in the form of a ferrite-type compound, the weight ratio of Fe^{2+}/Me^{3+} was varied in the range from 2 to 7. This explains the high degree of suspension ferritization. A further decrease

Table 1 Characteristics of the ferritization process carried out at different values of K

K	Time, min	t, °C	Degree of purification for iron cations, %	Degree of purification for chromium cations, %	Apparent precipitate layer height, cm		Vcp, cm^3/min
					1 h	1 day	
10	30	80	100	9992	87	52	0.11.941
15	30	80	100	9986	95	75	0.048.849
23	30	80	9932	9984	92	74	0.081.416
40	30	80	9880	9980	92	63	0.168.259
90	30	80	9664	9984	102	58	0.037.994
115	30	80	7720	9986	90	54	0.056.991
157	30	80	7160	9988	94	62	0.092.271
190	40	80	7440	9992	89	50	0.200.825
240	30	80	7120	9984	96	66	0.092.271

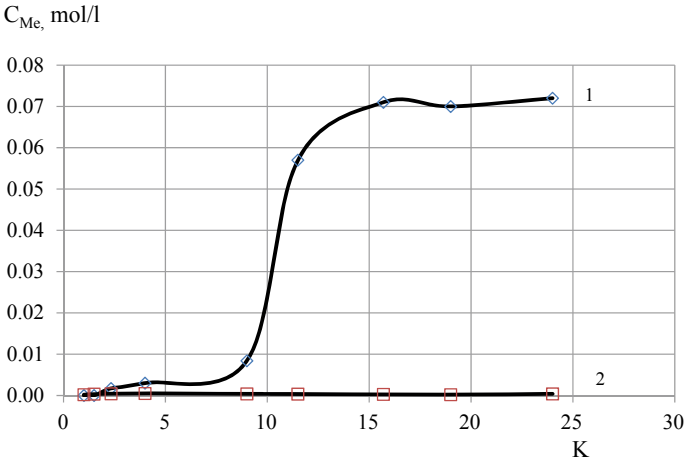

Fig. 3 The dependence of the residual concentration of cations in the filtrate depending on the ratio of cations *K*: 1—concentration of iron cations (II); 2—concentration of chromium cations (III); $t =$ 80 °C

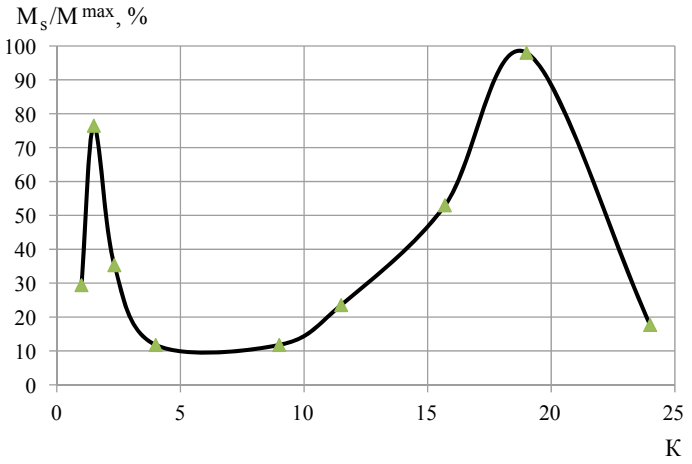

Fig. 4 The dependence of the saturation magnetization on the ratio *K*

in magnetic properties is explained by the formation of amorphous compounds of the type of maghemite.

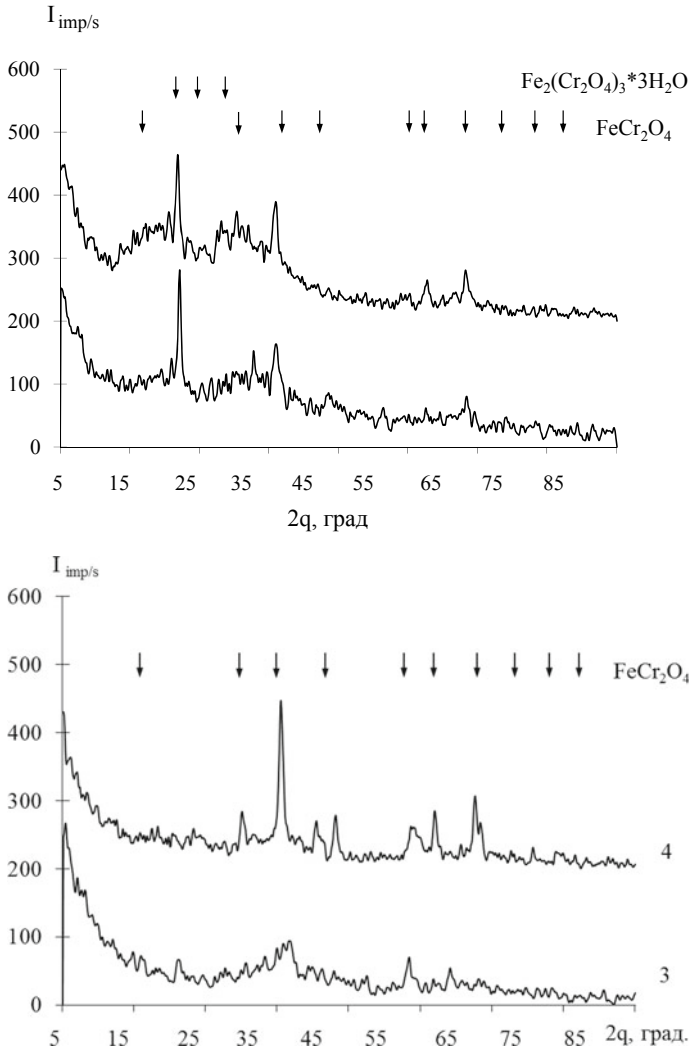

Fig. 5 X-ray diffraction patterns of samples at different values of K: 1—$K = 1$; 2—$K = 1.5$; 3—$K = 9$; 4—$K = 19$

4 Conclusions

1. An effective technology for producing ferrites and chromites has been shown. The degree of conversion is 99%.
2. The maximum magnetic characteristics are observed at a cation ratio of 18–25, corresponding to the formation of $Cr_{3-x}Fe_xO_4$ by the magnetite mechanism.

3. The phase composition of the precipitate at $K = 1–1.5$ is hydrochromites ($Fe_2(Cr_2O_4)_3$ $3H_2O$) and chromites of the composition $FeCrO_3$, and at $K = 18–25$, spinels with the general Formula $Cr_{3-x}Fe_xO_4$.

References

1. Minyukova TP et al (2016) Catalytic properties of copper chromite ferrites in water gas shift reaction and hydrogen oxidation. Kinet Catal 57(2):224–228
2. PalDey S et al (2005) Evaluation of a spinel based pigment system as a CO oxidation catalyst. Appl Catal B 56(3):241–250
3. Basak J et al (2007) Vapor-phase catalytic synthesis of 2-methylpyrazine over a nanocrystalline ferrite catalyst. Ind Eng Chem Res 46(22C):7039–7044
4. Gadkari AB, Shinde TJ, Vasambekar PN (2010) Ferrite gas sensors. IEEE Sens J 11(4C):849–861
5. Wang W et al (2013) Synthesis of ultrafine copper chromite black pigment by chemical coprecipitation using SBDS-assisted urea. CIESC J 5:49
6. Maslennikova GN (2001) Pigments of the spinel type. Glass Ceram 58(5–6C):216–220
7. Frolova L, Pivovarov A, Butyrina T (2017) Synthesis of pigments in Fe_2O_3-Al_2O_3-CoO by co-precipitation method. Pigment Resin Technol 46(5C):356–361
8. El-Bassuony AAH (2019) Influence of high annealing temperature on structural, magnetic and antimicrobial activity of silver chromite nanoparticles for biomedical applications. J Inorg Organomet Polym Mat 1–8
9. Vader VT (2017) Ni and Co substituted zinc ferri-chromite: a study of their influence in photocatalytic performance. Mat Res Bull 85:18–22
10. Patil SP, Sanadi KR, Helavi VB (2017) Impact of Ni substitution on structural electrical and thermoelectrical properties of zinc aluminium chromites synthesized by sol-gel route and their photocatalytic investigation. Mat Res 20(6):1445–1453
11. Valenzuela R (2005) Magnetic ceramics. vol 4, Cambridge University Press
12. Singh RK et al (2011) Thermal, structural and magnetic studies on chromite spinel synthesized using citrate precursor method and annealed at 450 and 650 C. J Therm Anal Calorim 107(1):197–204
13. Matulkova I et al (2015) On preparation of nanocrystalline chromites by co-precipitation and autocombustion methods. Mat Sci Eng B 195:66–73
14. Barbu M et al (2011) New synthesis method for M (II) chromites/silica nanocomposites by thermal decomposition of some precursors formed inside the silica gels. J Therm Anal Calorim 108(3):1059–1066
15. Shafqat MB et al (2019) Structural, morphological and dielectric investigation of spinel chromite (XCr2O4, X = Zn, Mn, Cu and Fe) nanoparticles. J Mat Sci Mat Electron 30(19):17623–17629

Adsorption Mechanisms of Gemcitabine Molecules on the Surface of Fe_3O_4 Nanoparticles with Biocompatible Coatings

P. P. Gorbyk, A. L. Petranovska, O. P. Dmytrenko, O. L. Pavlenko, I. P. Pundyk, T. O. Busko, T. M. Pinchuk-Rugal, A. I. Lesiuk, N. A. Goncharenko, O. O. Honcharova, L. V. Denis, V. V. Strelchuk, and M. P. Kulish

1 Introduction

Gemcitabine is the synthetic drug, in which chemical structure is an analogue of the pyrimidine bases of nucleic acids. It is primarily used for anticancer therapy of hepatocellular carcinoma (HCC) and intrahepatic cholangiocarcinoma (VPHC), which are the most common malignant neoplasms of the liver [1, 2].

The drug exhibits cyclic specificity, acting on cells in S- and C1/S-phases [3, 4]. At the same time, gemcitabine is characterized by a number of disadvantages due to their high toxicity and low chemical resistance. Among the combination of methods aimed at overcoming the adverse manifestations of antitumor medications, the most important place is taken by methods of directed local delivery of drugs to tumors. This delivery requires solving a few important issues.

Among them, it is important to study the nanochemical processes of synthesis of highly dispersed forms of magnetically sensitive nanocomposites with biocompatible coatings and their stabilization for following chemical modification of the surface with oncological preparations of chemo-immunotherapeutic action. Each of the steps in the synthesis of functionalized magnetically sensitive nanocomposites requires a complex of physico-chemical studies aimed at optimizing the antitumor

P. P. Gorbyk · A. L. Petranovska
Chuiko Institute of Surface Chemistry of NAS of Ukraine, Kyiv, Ukraine

O. P. Dmytrenko · O. L. Pavlenko (✉) · I. P. Pundyk · T. O. Busko · T. M. Pinchuk-Rugal · A. I. Lesiuk · N. A. Goncharenko · O. O. Honcharova · L. V. Denis · M. P. Kulish
Taras Shevchenko National University of Kyiv, Kyiv, Ukraine
e-mail: olpavl57@gmail.com

V. V. Strelchuk
V.E. Lashkaryov Institute of Semiconductor Physics, NAS of Ukraine of Kyiv, Kyiv, Ukraine

O. Fesenko and L. Yatsenko (eds.), *Nanooptics and Photonics, Nanochemistry and Nanobiotechnology, and Their Applications*, Springer Proceedings in Physics 247, https://doi.org/10.1007/978-3-030-52268-1_15

properties of gemcitabine, which is part of the magnetic-sensitive nanocomposites as new generation drugs with the possibility of their directed transport, fixation, and deposition in place of HCC and VPHC tumors localization [5].

Also, the determination of binding mechanisms of gemcitabine with functionalized magnetic nanocomposites and the influence on the change in the electronic structure of the drug is important for pharmacology kinetic activity.

The purpose of this work is to study mechanisms for the gemcitabine molecules interaction with biocompatible coatings of magnetic Fe_3O_4 nanoparticles using the study of adsorption characteristics, changes in the electron, and vibrational spectra.

2 Experimental Studies

Fe_3O_4 magnetic particles (8–12 nm) were used. The specific surface area of magnetite particles was S_{surf} ~110 m^2/g. The concentration of hydroxyl groups on the surface was 2.4 mmol/g. The nanosize particles stabilization and their encapsulation were carried out using a coating with hydroxyapatite (GA) or carbon (C) which are biocompatible with the tissues of living organisms. The biocompatible nanocomposites Fe_3O_4/GA and Fe_3O_4/C were formed. The thickness of the hydroxyapatite layer on the magnetic surface was ~4 nm. The thickness of biocompatible coating Fe_3O_4/C was ~2 nm. The specific surface area of Fe_3O_4/GA was S_{surf} ~105 m^2/g., and it was S_{surf} ~60 m^2/g for Fe_3O_4/C. The hydroxyl groups concentration on the surface was 2.2 mmol/g and 20 mmol/g, respectively for Fe_3O_4/GA and Fe_3O_4/C. Subsequently, the cytostatic gemcitabine molecules were immobilized on the Fe_3O_4, Fe_3O_4/GA and Fe_3O_4/C nanocomposites surface.

Gemcitabine belongs to antimetabolites of pyrimidine antagonists group, and its molecular formula has the form: $C_9H_{11}F_2N_3O_4$.

The study of gemcitabine molecules was carried out in solutions of distilled water (pH = 7) and in powder.

The absorption spectra of solutions were obtained using the UNICCO Spectro-Quest 4802 dual-channel spectrophotometer (United products and Instrument USA) over a near UV range of wavelengths in 1 nm steps.

Infrared transmission, absorption, and attenuated total reflectance (ATR) spectra in the average IR range (400–4000 cm^{-1}) were measured using the vacuum Fourier spectrometer Bruker Vertex 70v. DLaTGS detector was used for spectra registration, and the number of scans was 64, and resolution is -1 cm^{-1}. The diamond prism was used for ATR measurements.

Raman scattering spectra were obtained at room temperature in the inverse scattering geometry using Horiba Jobin Yvon T64000 spectrometer. The Ar–Kr laser (wavelength excitation $\lambda_{exc} = 488$ nm) and He–Cd laser ($\lambda_{exc} = 325$ nm) were used for excitation. The focusing of laser radiation on a sample in a spot with a diameter of < 1 μm was carried out using Olympus BX41 confocal microscope (lens 100×, aperture 0.90). Cooled CCD detector was used for registration.

Quantum chemical calculations of electronic transitions energy and vibrational modes of gemcitabine were performed with semi-empirical AM1 method, Hartree–Fock HF/6-31 (d, p), and DFT/B3LYP//6-31(d, p) methods. The first stage of molecular geometry was optimized and after that the electron transitions were calculated with ZINDO method.

3 Results and Discussion

The energy, molecular orbitals form, and vibrational frequency of the gemcitabine molecule were determined by quantum chemical calculations. It was shown that HOMO and LUMO are localized on a six-membered ring. Calculated optical density spectrum is in good agreement with experimental measurements of optical densities spectra, but the bands are shifted toward smaller wavelengths. At the same time, the convergence is sufficient for the interpretation of the electronic transitions type. They belong to the $\pi \rightarrow \pi$ type in the electronic subsystem localized on the hexadecimal ring of the gemcitabine molecule.

Figure 1 shows optimized geometry of gemcitabine molecule $C_9H_{11}N_3O_4F_2$. It contains one nitro group 1 and two hydroxyl groups (13, 15). It can be seen that the rotations around N–C (5,6) bond can lead to significant changes in the conformation states of the molecule.

Figure 2 shows spectra of the optical density of the solution of gemcitabine molecules in water with different concentrations. These spectra are described by two bands with maxima at $\lambda = 200$ nm and $\lambda_2 = 268$ nm.

Aqueous solutions of gemcitabine of various concentrations were prepared by sequential dilution. The optical absorption spectra of tenfold diluted solutions of gemcitabine of various concentrations were analyzed before magnetite or its nanocomposite added and after magnetic extraction from a solution of the magnetic component. Tenfold diluting was used for linearity optical density.

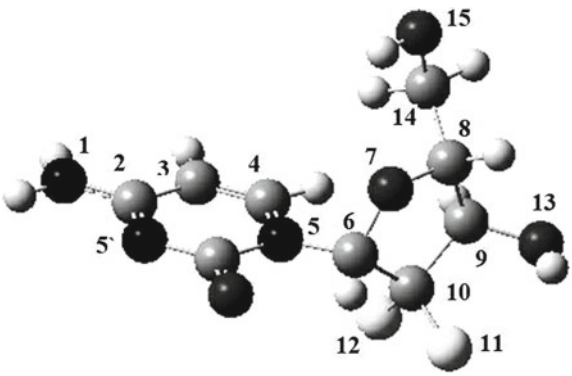

Fig. 1 Optimized geometry of gemcitabine molecule (2,3,4,6,8–10,14 balls correspond carbon atoms, 1,5-nitrogen atoms, 7,13,15-oxygen atoms, 11,12-fluorine atoms, respectively, small balls correspond to hydrogen atoms, and numbers indicate the numbers of individual atoms)

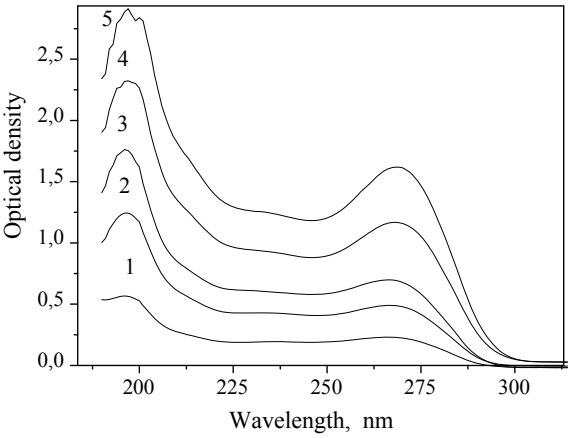

Fig. 2 The optical density of the solution of gemcitabine molecules in water with different concentrations 0.02 (1), 0.03(2), 0.04(3), 0.06(4), and 0.08 mg/ml (5)

Spectrophotometric method of studying the optical density of water solutions of gemcitabine molecules in the range of concentrations from 0.02 to 0.10 mg/ml was used before and after adsorption (mass $g = 0.03$ g, $V = 5$ ml, pH 7.0) to determine adsorption on the surface of nanoparticles of magnetite or its nanocomposites.

The quantum of adsorbed material on the surface of nanoparticles was determined by changing the optical density for $\lambda = 268$ nm using the calibration dependence D at $\lambda = 268$ nm on the concentration of gemcitabine molecules (C_p). The optical density at $\lambda = 268$ nm increases linearly in accordance with the Bouguer–Lambert–Beer in the range of concentrations from 0.02 to 0.10 mg/ml. The calibration graph is shown in Fig. 3.

The study of the gemcitabine adsorption on the surfaces of Fe_3O_4 nanoparticles and Fe_3O_4/Ga, Fe_3O_4/C nanocomposites were carried out by determining the adsorption capacity A and the degree of molecules removal from the solution (R).

The adsorption capacity of nanostructures A (mg/g) was calculated as follows:

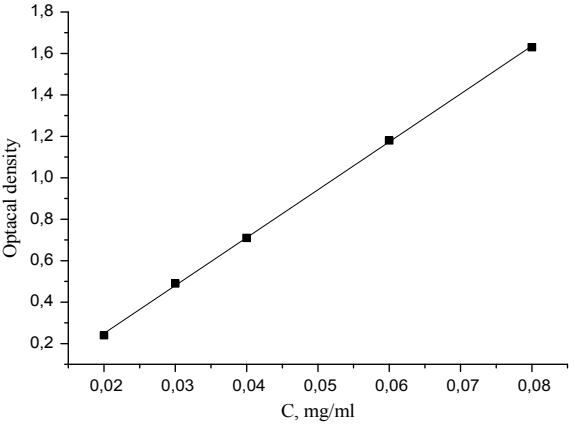

Fig. 3 Concentration dependence of the absorption intensity of gemcitabine: the points correspond to the values of the optical density of aqueous solutions at wavelength $\lambda = 268$ nm

$$A = \left(C_0 - C_p\right) \cdot \frac{V}{m},$$

where C_0 *i* C_p, the initial solution concentration and concentration of the solution after adsorption (mg/l), V—volume of the solution (ml), and m—mass of sorbent (g).

Degree of withdrawal R (%) was calculated as follows:

$$R = \left(1 - C_p/C_0\right) * 100\%.$$

The optical density spectra of the solutions after adsorption on Fe_3O_4, Fe_3O_4/GA, Fe_3O_4/C surfaces were investigated to determine the concentration of gemcitabine molecules in the solution (C_p) after adsorption.

The adsorption capacity isotherms are presented on Fig. 4. There are significant changes in the adsorption capacity depending on the concentration C_p. The curve A is saturated for all adsorbents surfaces with increasing content of deposited molecules.

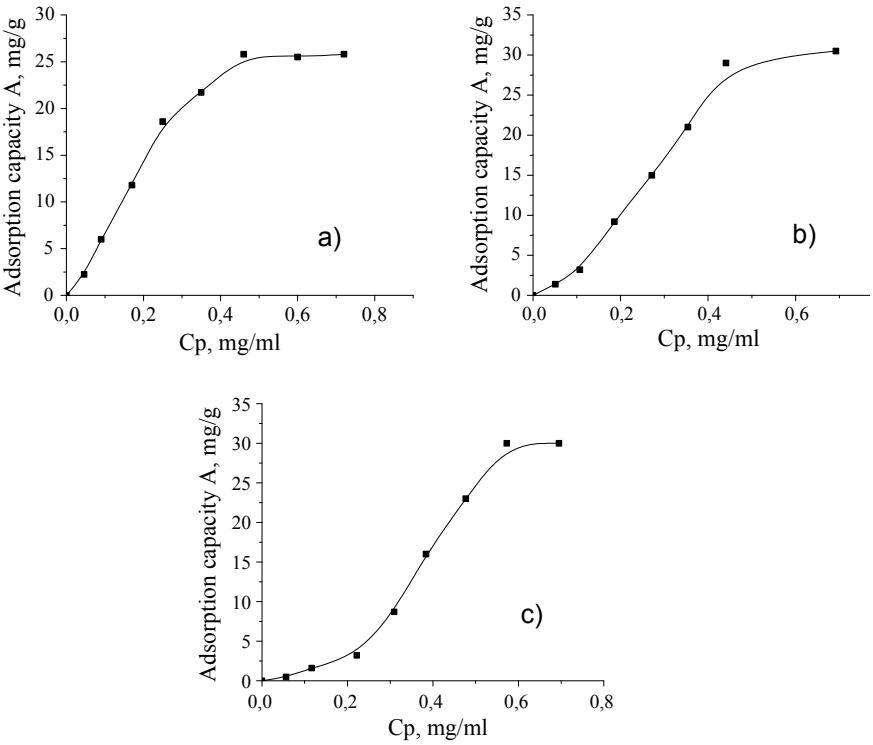

Fig. 4 Adsorption capacity isoterms of Fe_3O_4 **a** magnetic nanoparticles surfaces and Fe_3O_4/Ga **b** nanocomposites, Fe_3O_4/C **c** nanocomposites upon gemcitabine concentration in water solutions after adsorption (Cp)

The yield on the saturation is more slowed for Fe_3O_4 nanoparticles compared with Fe_3O_4/GA, Fe_3O_4/C nanocomposites, while retaining high affinity of molecules to all of the surfaces.

At the same time, weak interaction of gemcitabine molecules with the surfaces of nanocomposites is observed at low concentrations in contrast to the behavior of A with a change in the concentration of C_p for the Fe_3O_4. However, the degree of extraction of molecules is more prominent for the Fe_3O_4/Ga nanocomposite. It is evident that the adsorption of gemcitabine molecules as a result of their interaction with the surface of nanoparticles should affect the vibrational modes of infrared absorption and Raman scattering. In this case, it is important to establish functional groups, which are primarily responsible for the specified interaction and the nature of the restructuring of their oscillating modes.

Vibrational IR transmittance and ATR spectra of gemcitabine are shown in Fig. 5. Observed bands are in good agreement with the results of previous studies of gemcitabine and its conjugates [4, 6–12].

In the gemcitabine molecule, the bands at 3400 cm^{-1} (symmetric and asymmetric valence modes −OH), 3287 cm^{-1} (symmetric and asymmetric valence modes of the amino group $-NH_2$), 1718 cm^{-1} (valence modes C–O and deformation vibrations in plane of the ring with 3 nitrogen atoms), 1679 cm^{-1} (valence oscillations of the carbonyl group and deformation oscillation s of H–N–H and H–C–C–H), and 1537 cm^{-1} (bending oscillation s of the amino group $-NH_2$ and deformation vibrations H–C–C–H) are the most sensitive to their binding.

In the formation of conjugates of gemcitabine molecules with other molecules, the most sensitive to their binding are volatile modifications corresponding to hydroxyl (−OH), carbonyl (C=O), amid ($CONH_2$), and amino groups ($-NH_2$).

Also, altering the symmetric and antisymmetric modes of methyl (CH3) and methylene groups (CH2) at the frequency range 2800–3000 cm^{-1} and the band at 1089 cm^{-1} (valence fluctuations of the group C–O–C) is possible under binding.

The oscillation spectra were calculated using the electron density functional method with the B3LYP hybrid potential using the 3–21G basis. In general, the results obtained from the experiment and the calculated spectra coincide. At the same time, the bands in these spectra are shifted, which is characteristic of the chosen method of calculation.

The most intense of the calculated modes is experimentally observed in the vibration spectra of gemcitabine. For example, bands with maximums of 1255 and 1285 cm^{-1} are caused by C−N tensile vibrations. Bands with a maximum emission on 1678.5 cm^{-1} are generally associated with the C=O and C–N bond oscillations. Intense bands are observed in the region of 2700–3050 cm^{-1}, which correspond mainly to CH_2 oscillatory modes of elongation, oscillations in OH groups, and amine modes of oscillations of elongation ($-NH_2$). The wide structured band in the region of 3100–3500 cm^{-1} is traditionally associated with the vibrations of OH, NH, and NH_2 groups.

The ATR spectrum of Fe_3O_4 nanoparticles is presented at Fig. 6. In the low-frequency region of ATR spectrum, there is a series of bands in the range of 380, 436, 545, 629 cm^{-1}. The indicated bands correspond to different vibrational modes

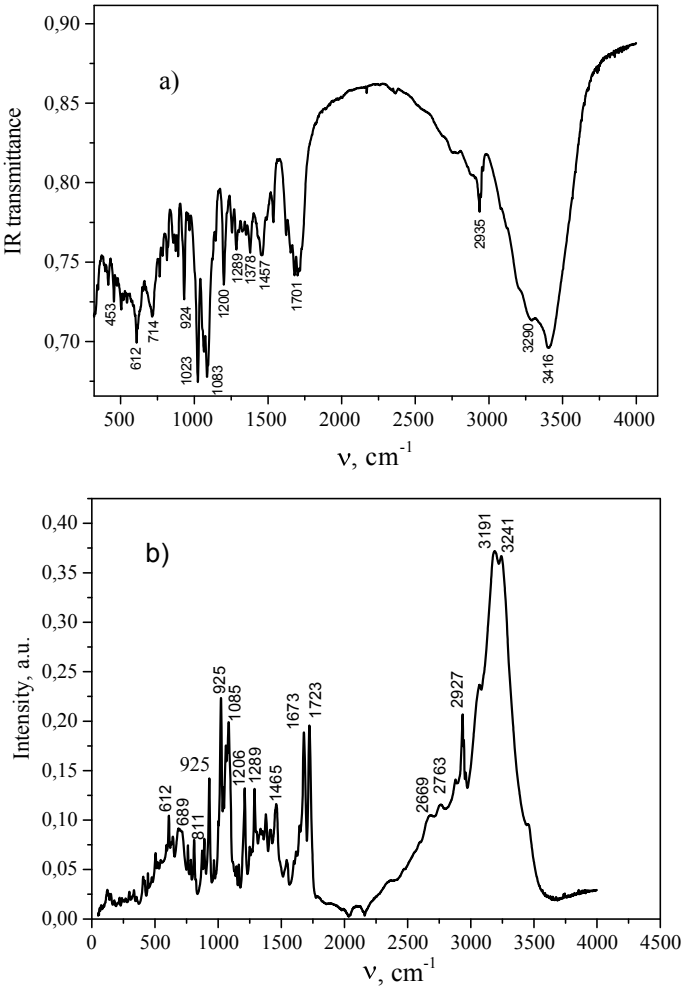

Fig. 5 IR transmittance and ATR spectra of gemcitabine

of Fe–O bonds [4]. The bands on 904 cm^{-1} is due to Fe–OH group deformation oscillations. The band at 1635 cm^{-1} belongs to a set of oscillating modes of water molecules adsorbed on the magnetite nanoparticles surface. In addition, a broad band at 3423 cm^{-1} corresponds to the oscillation of the hydroxyl group −OH on the Fe_3O_4 surface.

Figure 7 shows the IR transmittance and ATR spectra of Fe_3O_4 nanoparticles immobilized on their surface by gemcitabine molecules. It should be noted that as a result of the adsorption of gemcitabine molecules on the Fe_3O_4 surface, the vibrational spectrum differs significantly from the analogous spectra of its components in

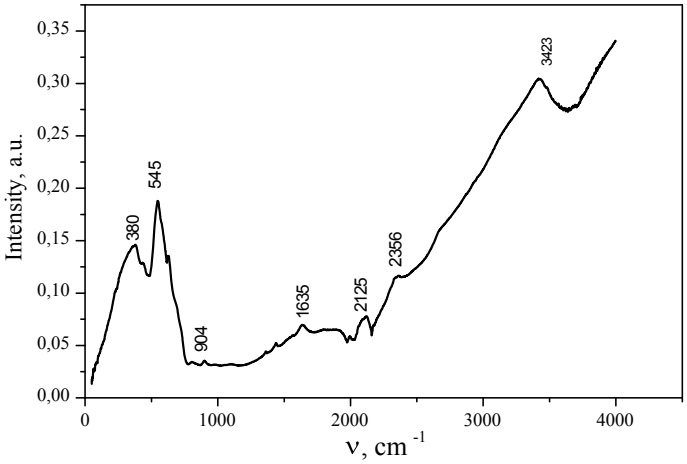

Fig. 6 ATR spectra of magnetic nanoparticles Fe_3O_4

the frequency range 1624–1718 cm^{-1}. Two narrow bands appear near the frequencies 1612 and 1647 cm^{-1}.

This means that an important place in binding the surface of Fe_3O_4 and molecules of gemcitabine is the amide bond of the aminogroup $-NH_2$. Significant is the restructuring of the IR spectrum in the region of 3200–3500 cm^{-1}. In contrast to the wide band for gemcitabine molecules in the formation of which involved valency displacement in the groups $-OH$, $-NH$, $-NH_2$ in the case of Fe_3O_4-gemcitabine, this band becomes narrower with a shift to higher frequencies.

Thus, in the adsorption of gemcitabine molecules on the nonfunctional surface, the main role is played by amide and hydrogen bonds with the participation of the hydroxyl and amino groups of both components. It is confirmed by a substantial restructuring of vibrational bands associated with these groups (Fig. 8).

There are differences due to the passivation of the Fe_3O_4 surface by carbon atoms. It leads to both changes in the frequencies of the fluctuations of the Fe_3O_4, as well as the displacements, changes in the shape of other bands characteristic of the nonfunctionalized Fe_3O_4 particles. For the Fe_3O_4/C system, there are practically no bands near 1617, 3424 cm^{-1}, which is due to a decrease in the effect on the change in the oscillating spectrum of water molecules and hydroxyl groups $-OH$ adsorbed on the surface of the nanoparticles. Low-intensity bands in the frequency range of the C–H bonds appear.

Infrared transmittance and ATR spectra of Fe_3O_4/C-gemcitabine nanosystems are shown in Fig. 9. The functional rearrangement of the vibrational spectra of gemcitabine molecules is also observed for functionalized magnetite due to their adsorption.

The infrared transmittance and ATR spectra of the Fe_3O_4/GA nanocomposite are shown in Fig. 10.

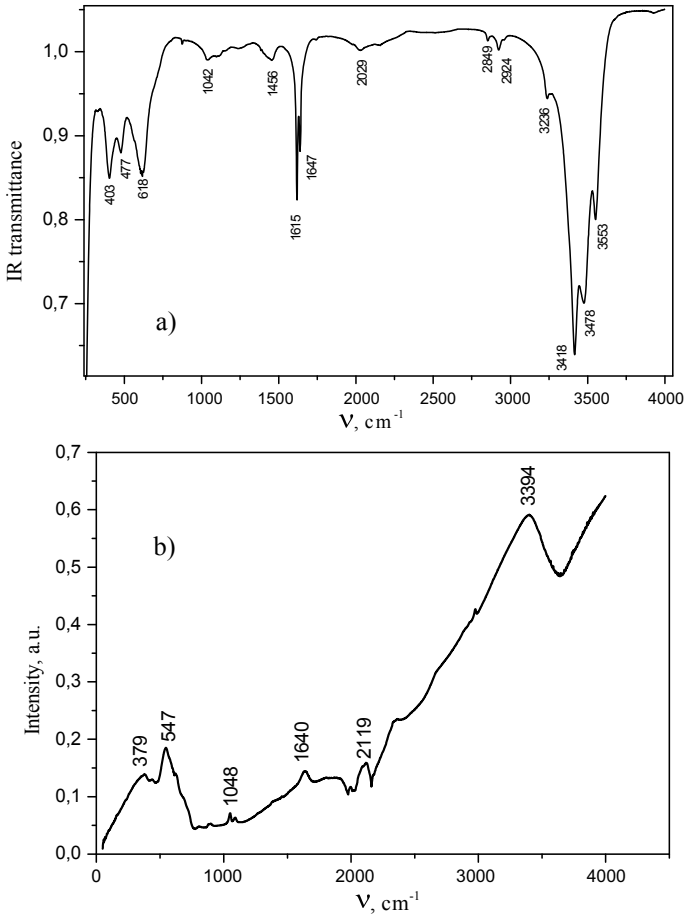

Fig. 7 IR transmission and ATR spectra of magnetic Fe_3O_4 nanoparticles immobilized on their surface by gemcitabine molecules

It was seen that the infrared and ATR spectra of Fe_3O_4-hydroxyapatite system differ significantly from analogous spectra of Fe_3O_4 nanocomposites. The IR absorption bands occur at 601, 633, 877, 962, 1032, 1095 cm^{-1} in the case of hydroxyapatite coating. The bands in the 600–1032 cm^{-1} range belong to the deformation oscillation of the Fe–OH group. The last group is responsible for the formation of hydrogen bonds with the cation hydroxyapatite. A significant absorption in this interval indicates a significant amount of hydrogen bond. Other bands in the 900–1200 cm^{-1} frequency range belong to the C_{sp3}=C_{sp3} group. The wide absorption band in the 1353–1459 cm^{-1} range corresponds to hydroxyl group, and also to the group CO_3^{2-} in the hydroxyapatite structure. The absorption band corresponding to the deformation fluctuations of water molecules at 1635 cm^{-1} is more intense than the analogous band for Fe_3O_4–C spectrum.

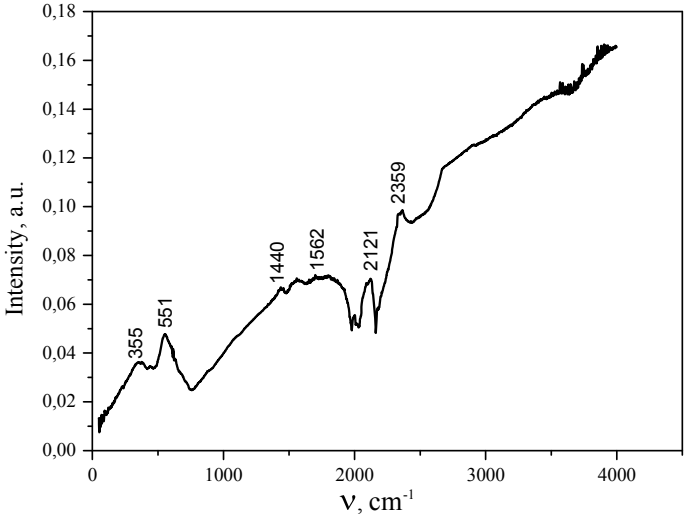

Fig. 8 ATR spectra of magnetic nanoparticles Fe_3O_4/C

The presence of hydroxyapatite also manifests itself in the appearance of a spectral band at 1028 cm^{-1}, more intensive bands in the 1500–2500 cm^{-1} region and at 3500 cm^{-1} in the ATR spectrum.

As shown in Fig. 11, the general form of the spectra after adsorption is retained for Fe_3O_4-hydroxyapatite nanocomposite. At the same time, the absorption in the marked strips is greatly reduced. There is the separation of the bands, similar to that of the spectra with the gemcitabine molecules for the other two magnetics: Fe_3O_4 and Fe_3O_4–C.

Thus, in spite of the different nature of spectrum changes of Fe_3O_4–hydroxyapatite–gemcitabine system in comparison with the spectra for Fe_3O_4 and Fe_3O_4–C nanoparticles with adsorbed molecules of the drug, an important role in binding to all systems plays hydrogen bonds involving the groups $-NH_2$ and $-OH$, which affect the fluctuations of carbonyl and amino groups as well as C_{sp3}=C_{sp3} conjugated bonds [13–15].

4 Conclusions

To establish the adsorption characteristics on the Fe_3O_4 nanoparticles surface and Fe_3O_4–C and Fe_3O_4/GA nanocomposites, a linear region of concentration dependence of the optical density of a water solution of gemcitabine molecules was used in the absence and presence of these nanoparticles. The adsorption capacity for all nanoparticles corresponds to a close range in the range of 25.8–30.5 mg/g, and the

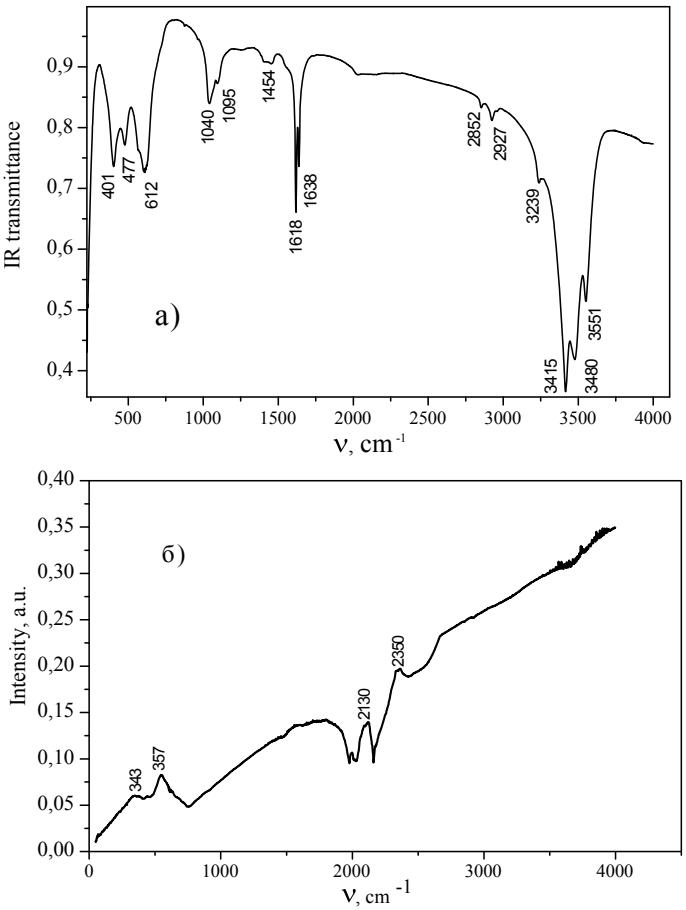

Fig. 9 IR transmittance and ATR spectra of magnetic Fe_3O_4/C nanoparticles immobilized on their surface by gemcitabine molecules

degree of extraction R from the solution increases significantly for the nanocomposite Fe_3O_4/GA to a value of 38.5%.

Mechanisms of gemcitabine adsorption on the magnetic nanoparticles surface were studied. Quantum chemical calculation of IR absorption spectra and Raman spectra of gemcitabine molecules was analyzed, and experimental studies of IR, ATR and Raman spectra of powdered gemcitabine and Fe_3O_4, Fe_3O_4–C, Fe_3O_4/GA without and with adsorbed molecules of the drug were performed.

The presence of gemcitabine molecules on the surface of nanoparticles leads to the rearrangement of the vibrational bands related to the carbonyl and amino groups of gemcitabine molecules, as well as the hydroxyl group on the surface of magnets and their nanocomposites. The conjugate group C=C also contributes to the restructuring of the vibrational spectra.

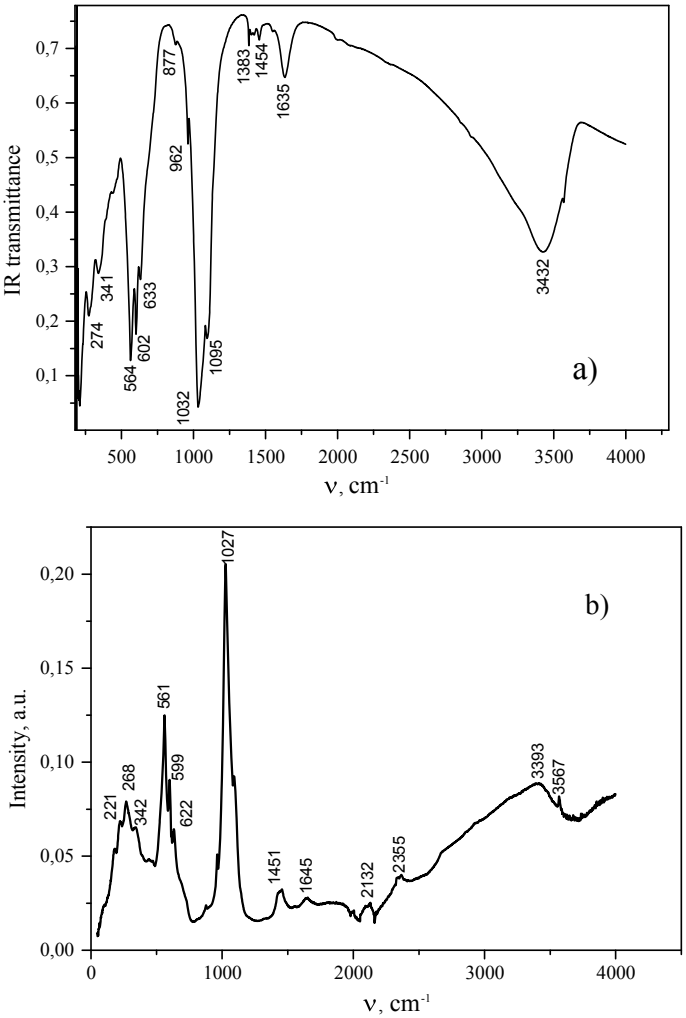

Fig. 10 IR **a** and ATR spectra **b** of Fe_3O_4-hydroxyapatite nanocomposite

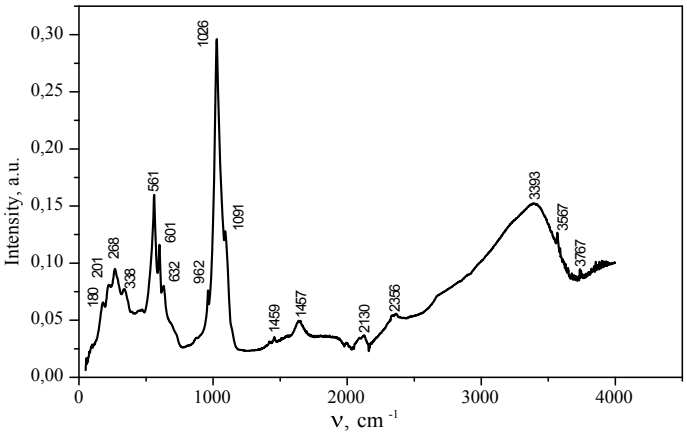

Fig. 11 ATR spectra of Fe_3O_4–hydroxyapatite–gemcitabine nanocomposite

References

1. Das S, Desai JL, Thakkar HP (2013) Gemcitabine hydrochloride-loaded functionalised carbon nanotubes as potential carriers for tumour targeting. Indian J Pharm Sci 75(6):707–715; Ishii R, Mori H, Matsumura K, Hongo N (2012) Molecular interactions between anticancer drugs and iodinated contrast media: an in vitro spectroscopic study. J Biomed Sci Eng 5:24–33
2. Mallaredy V, Sahoo SK (2010) Long circulation and cytotoxicity of PEGylated gemcitabine and its potential for the treatment of pancreatic cancer. Biomaterials 31(35):9340–9356
3. Lee NC, Bouvet M, Nardin S, Jiang P, Baranov E, Rashidi B, Yang M, Wang X, Moossa AR, Hoffma RM (2008) Antimetastatic efficacy of adjuvant gemcitabine in a pancreatic cancer orthotopic model. Clin Exp Metastasis 18(5):379–384
4. Jose L, Arias L, Reddy H, Couvreur P (2012) Fe_3O_4/chitosan nanocomposite for magnetic drug targeting to cancer. J Mater Chem 22(15):7622–7632
5. Khare V, Sakarchi WA, Prem N, Gupta B, Curtisa ADM, Hoskins C (2016) Synthesis and characterization of TPGS—gemcitabine prodrug micelles for pancreatic cancer therapy. RSC Adv 6(65):60126–60137
6. Hosseini Motlagh NS, Parvin P, Ghasemi F, Atyabi F, Jelvani S, Abolhosseini S (2016) Laser induced fluorescence spectroscopy of chemo-drugs as biocompatible fluorophores: irinotecan, gemcitabine and navelbine. Laser Phys Lett 13(7):075604–075612
7. Lee NC, Bouvet M, Nardin S, Jiang P, Baranov E, Rashidi B, Yang M, Wang X, Moossa AR, Hoffman RM (2001) Antimetastatic efficacy of adjuvant gemcitabine in a pancreatic cancer orthotopic model. Clin Exp Metastasis 18(5):379–384
8. Vandana M, Sahoo SK (2010) Long circulation and cytotoxicity of PEGylated gemcitabine and its potential for the treatment of pancreatic cancer. Biomat 31(35):9340–9356
9. Khare V, Kour S, Alam N, Dubey RD, Saneja A, Koul M, Prakash Gupta A, Singh D, Singh SK, Saxena AK, Gupta PN (2014) Synthesis, characterization and mechanistic-insight into the antiproliferative potential of PLGA-gemcitabine conjugate. Int J Pharm 470(15):51–62
10. Srinivas P, Sai Preeti K (2014) Formulation and evaluation of gemcitabine hydrochloride loaded solid lipid nanoparticles. JGTPS 5(4):2017–2023
11. Kaur T, Kaur S, Kaur P (2017) Development and validation of UV-spectrophotometric methods for determination of gemcitabine hydrochloride in bulk and polymeric nanoparticles. Int J Appl Pharm 9(5):0975–7058

12. Parsian M, Unsoy G, Mutlu P, Yalcin S, Tezcaner A, Gunduz U (2016) Loading of Gemcitabine on chitosan magnetic nanoparticles increases the anti-cancer efficacy of the drug. Eur J Pharm 784(5):121–128
13. Vandana M, Sahoo SK (2009) Optimization of physicochemical parameters influencing the fabrication of protein-loaded chitosan nanoparticles. Nanomed (Lond) 4(7):773–785
14. Cavallaro G, Mariano L, Salmaso S, Caliceti P, Gaetano G (2006) Folate-mediated targeting of polymeric conjugates of gemcitabine. Int J Pharm 307(2):258–269
15. Das S, Desai JL, Thakkar HP (2013) Gemcitabine hydrochloride-loaded functionalised carbon nanotubes as potential carriers for tumour targeting. Indian J Pharm Sci 75(6):707–715

The Study of Ultrasonic Treatment Influence on the Physical–Chemical Properties of $TiO_2/SnO_2 = 1:1$ Composition

O. V. Sachuk, V. A. Zazhigalov, O. A. Diyuk, V. L. Starchevskyy, P. Dulian, and M. M. Kurmach

1 Introduction

The development and manufacturing of single nanostructural materials with multiple applications has been attracting significant attention due to unique properties. Among of all nanomaterials, TiO_2 is widely used due to its high photocatalytic activity, non-toxicity, environmentally friendliness and long term chemical and catalytic stability. Despite wide range practical application of TiO_2, such as in solar energy harvesting, wastewater management, gas sensing, and organic transformation, because of their openness and attractive physico-chemical properties [1–5], a lot of investigations are concentrated on increasing its efficiency and improvement of physico-chemical properties. The effective resolution of these problems involves coupling TiO_2 with another nanosized metal oxide semiconductor in order to enhance its selectivity and to increase the surface area by avoiding grain growth [6]. Titanium dioxide is usually coupled with M_xS_y or M_xO_y type semiconducting materials in various systems such as TiO_2/CdS [7], TiO_2/ZnO [8], TiO_2/CeO_2 [9], TiO_2/Fe_xO_y [10], TiO_2/WO_3 [11, 12], TiO_2/MoO_3 [13], etc. that can increase its activity by increasing its active surface

O. V. Sachuk · V. A. Zazhigalov (✉) · O. A. Diyuk
Institute for Sorption and Problems of Endoecology, National Academy of Sciences of Ukraine, Naumova Str 13, Kiev 03164, Ukraine
e-mail: zazhigal@ispe.kiev.ua

V. L. Starchevskyy
National University Lviv Polytechnic, S. Bandery Str 12, Lviv 79013, Ukraine

P. Dulian
Faculty of Chemical Engineering and Technology, Cracow University of Technology, 24, Warszawska Str, 31-155 Cracow, Poland

M. M. Kurmach
L. V. Pisarzhevskii Institute of Physical Chemistry, National Academy of Sciences of Ukraine, Pr. Nauki 31, Kiev 03028, Ukraine

O. Fesenko and L. Yatsenko (eds.), *Nanooptics and Photonics, Nanochemistry and Nanobiotechnology, and Their Applications*, Springer Proceedings in Physics 247, https://doi.org/10.1007/978-3-030-52268-1_16

area. In particular, SnO_2 is a suitable material for coupling with TiO_2 because of its useful physical properties, and thus it is employed in a variety of commercial devices [14]. Furthermore, the similarities in the structure of TiO_2 and SnO_2 allow them to form a heterojunction hybrid between the two oxides [15]. This can lead to the formation of intermixed electronic density states and reduce the grain size to allow appropriate separation of the photogenerated electrons and holes, which facilitates the degradation of organic pollutants [16, 17] as well as providing the capacity to sense various gases [18]. On the other hand, any information connected with the catalytic properties of this composition on the other catalytic reactions exists in the literature. A considerable number of works are devoted to by traditional methods synthesis of TiO_2/SnO_2 systems (sol/hydrothermal, laser pyrolysis, hydrolysis processes) as photocatalysts for organic dyes degradation [5, 19–24]. However, ultrasonic treatment is a more promising method for the synthesis of nanocomposites. Ultrasonic activation is one of the modern ways of accelerating the flow of physical and chemical processes in heterogeneous systems. It is well known that the use of ultrasound not only increases the rate of chemical reaction but also increases the completeness of the reaction due to the effect of acoustic cavitation.

In this paper, the influence of ultrasonic treatment on the physical-chemical of TiO_2/SnO_2 system with an equimolar ratio of initial oxides and its catalytic properties in the ethanol selective oxidation was studied.

2 Experimental

The preparation of complex oxide titanium-tin composition with a molar ratio of $TiO_2/SnO_2 = 1{:}1$ was realized by mixing of TiO_2 and SnO_2 powders in an agate mortar. All reagents employed were commercially available and directly used without further purification. The dispersant UZDN-2T was used for the sonochemical modification of this mixture. The powder mixture (10 g) was placed in stainless reactor and treated in the aqueous medium during 2 h in the effect of acoustic cavitation at a frequency of 22–40 kHz and a load of 3 W/cm^2. The temperature of the reaction medium maintained at 80°C by circulating cold water around the reactor. Obtained suspensions were dried in air at 120 °C.

Physical-chemical parameters of initial and modified samples were determined by the following techniques. X-ray diffraction measurements for structural phase analysis of the samples were carried out with Bruker D8 Advance X-ray diffractometer using Cu Kα radiation. The average crystallite sizes (L) was estimated by the Sherrer formula. FTIR spectra were recorded on a Perkin-Elmer Specrtum-One Fourier spectrometer in the 4000–400 cm^{-1} range at sample/KBr mass ratio 1/20. The porous structure of the samples was determined from the isotherms of low-temperature nitrogen adsorption on the Quantachrome NOVA-2200e instrument. The TEM images have been obtained on a JEM 1230 («Jeol») instrument (300 kV) transmission electron microscope. Thermogravimetric analysis of the synthesized sample was carried out on the apparatus Derivatograph-Q in the temperature range

from room temperature up to 900 °C at a rate of 10 °C min^{-1}. Catalytic activity of the samples in the ethanol oxidation was tested in a flow fixed-bed stainless steel microreactor at atmospheric pressure in the temperature range of 25–410 °C. The catalyst (V = 0.5 cm^3 with fraction 0.25–0.50 mm) was loaded into a reactor. Gas mixture which contains 1 vol.% C_2H_5OH in the air was passed through the reactor at a total flow rate of 20 cm^3/min. Initial components and reaction products have been analyzed by on-line with the use of two gas chromatographs—Chrom-5 with the use of flame ionization detector (FID) and Selmi-Chrom-1 with thermal conductivity detector (TCD).

3 Results and Discussion

Results of XRD analysis of the $TiO_2/SnO_2 = 1{:}1$ samples are presented in Fig. 1. The X-ray pattern of initial mixture $TiO_2/SnO_2 = 1{:}1$ (Fig. 1a) shows the characteristic titanium oxide peaks of rutile crystal structure and reflexes of tin oxide which are attributed to the tetragonal modification of cassiterite/rutile with maximum reflex intensity from the plane (101). The obtained peaks were comparable to the TiO_2 and SnO_2 JPCDS cards no: 88–1175 and 41–1445, respectively. It should be noted that the XRD spectra both in the initial sample and the modified one are characterized by the presence of strong peaks for SnO_2 located at $2\Theta = 26.52°$, 33.89° and 51.82° corresponding to reflections from (110), (101) and (211) planes, respectively. These data show that after treatment the reflex of SnO_2 from the plane (110) becomes dominant with can be connected with anisotropic deformation of tin oxide in the sonochemical process (Fig. 1b). It is possible to note that similar changes were observed at the ultrasonic treatment of complex $CeO_2/MoO_3 = 1{:}1$ composition [25, 26]. This fact can indicate that the formation of anisotropic structure in multicomponent compositions can be accompanied by a significant increase of electrical and thermal conductivity and give it erosion resistance.

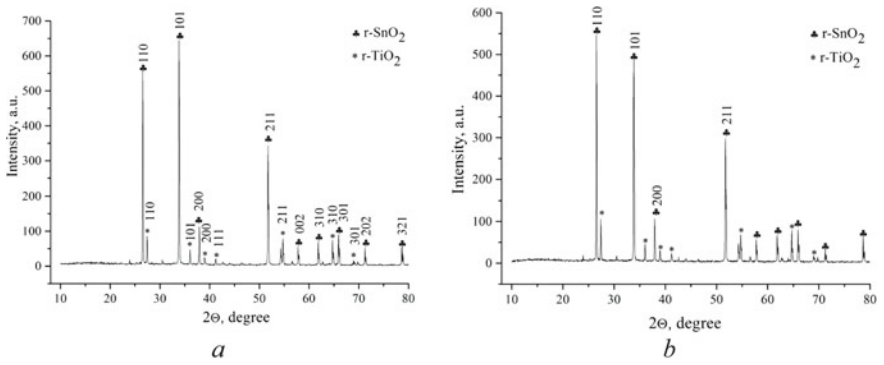

Fig. 1 XRD pattern of $TiO_2/SnO_2 = 1{:}1$ composition: initial **a** and after UST during 2 h-**b**

Table 1 Some properties of $TiO_2/SnO_2 = 1{:}1$ system

Sample	L (SnO_2)[a], nm		d, nm		S_{BET}, m^2/g	V_Σ, cm^3/g
	110	101	110	101		
Initial	60	53	0.32	0.25	2	0.02
After UST	58	50			4	0.03

[a]L—average particle sizes for maximum reflex, calculated to use Scherer's equation, d—interplanar distance to the most intense reflexes of SnO_2 determined from the Wolf-Bragg's equation, S_{BET} is a specific surface area (BET) of the sample, V_Σ—total pore volume

The obtained results indicate also that the calculated average crystallite sizes for dominant reflexes of SnO_2 from the planes (101) and (110) remain practically unchanged (the results are presented in Table 1) that is due to anisotropic destruction of SnO_2. This fact has been emphasized in a number of works on the dimensional stability of SnO_2 crystallites at the thermal treatment process [27, 28]. It should be noted that the intensities of TiO_2 phase reflexes remain unchanged except the reflex from the plane (101) at $2\Theta = 27.4°$ which intensity insignificant increases as a result of an increase of sample crystallinity and size of particles from 56 to 64 nm.

The studies of the samples by FT-IR method confirm some changes in their structure after treatment. The FT-IR spectra both initial (spectrum is not given) and modified (Fig. 2) composite clearly show 3 broad absorption bands (the position of the adsorption bands in the spectrum of initial sample coincides with the same in the spectrum of treated composition). The first band is in region 3670–3250 cm^{-1} with several peaks (at 3544, 3466 and 3414 cm^{-1}) corresponds to the stretching vibrations of the νO-H group of the TiO_2 nanoparticles which take part in intensive hydrogen bonding. The second observed adsorption band around 1630 cm^{-1} corresponds to bending modes of water $\delta(H_2O)$ which can indicate the interaction of water molecules

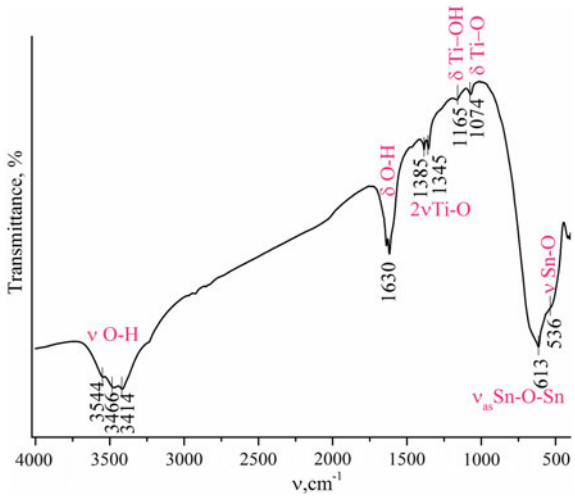

Fig. 2 FT-IR spectrum of initial $TiO_2/SnO_2 = 1{:}1$ composition

with elements of the titanium oxide structure with the possible formation of a Ti-OH bond. The very strong intense peak is observed at 613 cm^{-1} and its can be attributed to antisymmetric vibrations of Sn-O-Sn bond. The weak peaks at 1385 and 1345 cm^{-1} related to the stretching Ti-O modes.

It is necessary to note that the sonochemical treatment leads to some changes in FT-IR spectrum. Thus, a decrease in band intensity at 1165 cm^{-1}, which can be due to the vibrations of δ (TiOH) in the hydrated $TiO_2 \cdot H_2O$ phase and represented in the spectrum as a weakly expressed shoulder was observed. In the spectra of both samples, the absorption band at 1074 cm^{-1} indicates the presence of δ Ti-O modes in the TiO_6 octahedron [29]. Some changes in FT-IR spectrum for tin oxide should be noted after a sonochemical treatment also. There is a slight shift of the absorption band of ν Sn-O bond in the short-wave region (from 536 up to 522 cm^{-1}), which is due to the strengthening of this bond and the decrease in the intensity of the Sn-O-Sn band at 613 cm^{-1} what correspond to the XRD analysis data which demonstrate the anisotropic destruction of SnO_2 [30].

BET surface area analysis shows that the initial powder TiO_2/SnO_2 has isotherm type II (according to IUPAC classification) which was evaluated from the adsorption curves. Type II isotherms are normal forms of isotherms obtained with a nonporous and macroporous solid. It was found that after UST some changes of porous structure occur. Hence, the nitrogen adsorption isotherm of modified powder has a type III which is observed in the adsorption process on non-porous and macroporous solids with low adsorption. The existence of micro-porous structure in the studied samples is evidenced by the maximum values of the main pore volume in the region of 1.8–3.7 nm and $n > 95$ nm on the curves of pore size distribution.

It is known that anisotropic deformation leads to the low changes of the specific surface area of the samples and their porous structure. In the studied case the observed anisotropic destruction of SnO_2 and low agglomeration of TiO_2 (the process can be accompanied by an increase of the sample macropores volume) determine little changes these parameters of solids mixture. Some increases of specific surface area from 2 up to 4 m^2/g and macropores volume were observed. On the other hand, the anisotropic destruction of the solid leads to the formation of the dominant plane of the oxide and this plane can contain the most active centers for the catalytic process. Analogous results were described in [31] for V-containing catalyst. So, the obtained results which show the anisotropic deformation of SnO_2 permit to estimate the changes of catalytic properties of the oxides mixture after sonochemical treatment.

The data of microstructure of $TiO_2/SnO_2 = 1{:}1$ samples investigation by TEM analysis presented on Fig. 3. It is possible to see that treatment accompanied by a decrease of particles size which corresponds by XRD analysis. In the same time, it was shown that the sample after treatment contains many uniform agglomerated nanoparticles having nearly spherical nanocrystals with diameters of 30-50 nm. It is necessary to note that an increase of agglomeration degree can reduce surface energy [32].

The thermogravimetric results of activated $TiO_2/SnO_2 = 1{:}1$ composition are presented in Fig. 4. The results show that nanoparticles undergo some steps of

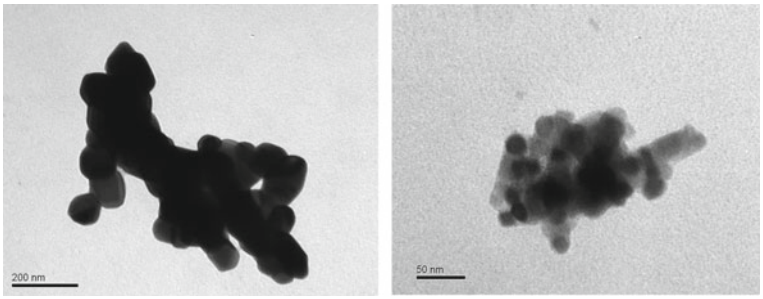

Fig. 3 TEM images of $TiO_2/SnO_2 = 1{:}1$ samples: initial (**a**) an after UST (**b**)

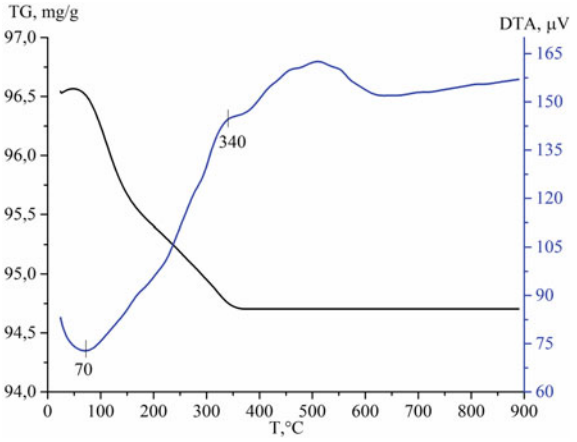

Fig. 4 DTA-TG curves of $TiO_2/SnO_2 = 1{:}1$ composition after UST

transformations in powders. Hence, DTA curves of the sample demonstrate two thermal effects (these peaks were observed in the initial sample also). The first one endothermic peak at 70 °C is related with remove of chemical and physical absorbed water with the mass lost about 1% and the second one exothermic effect at 340 °C is due to a phase change in the powder or due to conversion of $Sn(OH)_2$ to SnO_2 [33]. Literature data for comparison in the paper are not presented. But it is known that bound water difficult removes from SnO_2, which is a product of the tin acid thermolysis and occurs by (1):

$$Sn(OH)_4 \rightarrow SnO_2 + 2H_2O \tag{1}$$

It has been observed that there is no weight loss in the TG curve indicating the onset of oxide formation and expected changes in the crystal. It should be noted that the explanation of thermal analysis results is deficient. This process is more complicated. The actual decomposition process can be explained by the primary

decomposition of hydroxide at 70 °C with the formation of α-tin acid $SnO_2{\cdot}xH_2O$ ($1 < x < 2$).

Further heating of α-tin acid leads to the gradual removal of water, the formation of β-tin acid ($x < 1$) and its subsequent gradual dehydration. Both tin acids have a variable water content of $SnO_2{\cdot}xH_2O$ and lose water continuously [28]. There any peaks on the DTA curve were observed that is due to the high thermal stability of the sample.

The catalytic properties of oxide Ti/Sn = 1:1 composition in the reaction of partial oxidation of ethanol (POE) were studied. The obtained results show that the acetic aldehyde, carbon oxides, ethylene and hydrogen are the products of the reaction.

It is possible to note that at present the production of hydrogen from alcohol in the presence of oxygen is of great interest for many reasons. At first, this reaction takes place at much lower temperatures than reforming of ethanol (RE), steam reforming of ethanol (SRE) and autothermal reforming of ethanol (ATRE), does not require indirect heat addition to use heat exchanger, and allows the design of the reactor to be more compact that is a very desirable feature for mobile applications on fuel cells than steam reformers. Secondly, this reaction does not require an inert medium or a vacuum. However, with the wide variety of systems which are used to produce hydrogen via RE, SRE and ATRE, there are only a few publications reporting about active systems in the reaction of POE.

The following (2–5) proceed in this reaction probably best describe the ideal processes:

$$CH_3CH_2OH(g) + 1/2O_2 \rightarrow 3H_2 + 2CO(g) G_f^\circ = -105.9\,\text{kJmol}^{-1} \quad (2)$$

$$CH_3CH_2OH(g) + 3/2O_2 \rightarrow 3H_2 + 2CO_2(g) G_f^\circ = -620.3\,\text{kJmol}^{-1} \quad (3)$$

$$CH_3CH_2OH(g) + 2O_2 \rightarrow 3H_2O(g) + 2CO(g) G_f^\circ = -517.3\,\text{kJmol}^{-1} \quad (4)$$

$$CH_3CH_2OH(g) + 3O_2 \rightarrow 3H_2O(g) + 2CO_2(g) G_f^\circ = -1306.1\,\text{kJmol}^{-1} \quad (5)$$

The most desirable is the obtaining of the catalyst capable oriented preferably on the reaction (3) [34].

The obtained results show that treated samples are most effective in this reaction as initial mixture or individual oxides. According to obtained results it was found (Fig. 5) that activated sample TiO_2/SnO_2 at 185 °C shows 100% selectivity of acetic aldehyde formation but the ethanol conversion at this temperature does not exceed 18%. In the same time at this reaction temperature, initial oxides mixture demonstrates near-zero conversion of ethanol.

It was found that on the sonochemical activated composition TiO_2/SnO_2 at 220 °C the hydrogen begins to form and its maximum yield is 41% at 360 °C. However, the further temperature increase accompanied by a decrease of hydrogen and carbon oxides amount (Fig. 5) and increase selectivity of ethylene formation. In the case

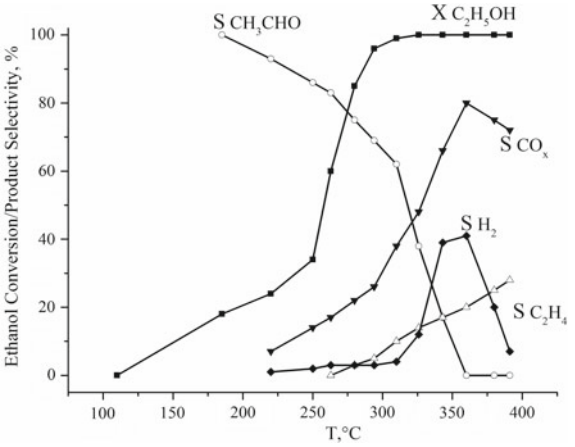

Fig. 5 Temperature dependence of ethanol conversion and selectivity of reaction product formation on the sample after 2 h UST

of initial oxides mixtures (it is the compilation of individual oxides properties) the formation of ethylene without hydrogen formation was observed. So, the formation of different products can be connected with different mechanism reaction and their deposit in the course of reaction at different temperatures.

In temperature range 310–380 °C the main reaction can proceeds accords to (6) and (7):

$$CH_3CHO + 1/2O_2 \rightarrow 2CO + 2H_2 \quad (6)$$

$$CH_3CHO + 3O_2 \rightarrow 2CO_2 + 2H_2O \quad (7)$$

Comparing of some catalytic indicators for initial and modified samples (Table 2) it was found that ultrasonic treatment allows to decrease the temperature reaction (about 60 °C) with simultaneous of increasing of selectivity formation of its products.

It worth noting that the hydrogen productivity in activated sample is 10 $L/kg_{kat} \times h$ while in an initial sample this indicator doesn't exceed 4 $L/kg_{kat} \times h$. Because the experiment was conducted more 10 h without loss of catalyst activity then during this time can be obtained 100 L of hydrogen.

These results in partial ethanol oxidation show the promising for using of this system for obtaining of hydrogen compare with well known but more expensive

Table 2 Catalytic properties of $TiO_2/SnO_2 = 1{:}1$ sample in ethanol oxidation reaction

Sample	$T_{reaction}$, °C		Selectivity at $X^a = 100\%$		
	$X_{50\,\%}$	$X_{100\,\%}$	CH_3CHO	C_2H_4	H_2
Initial	280	360	24	9	7
After UST	258	326	38	14	12

[a]X—ethanol conversion

catalysts (Rh/CeO_2, Pt/CeO_2, Ir/CeO_2 [35–37]) and characterized by cheap and non-toxicity.

4 Conclusion

The presented results show that ultrasonic treatment of oxide TiO_2/SnO_2 composition leads to grinding of initial oxides with nanosize particle formation. The increase of specific surface area, specific SnO_2 crystals orientation as a result of anisotropic destruction under treatment lead to increase of catalytic activity and selectivity in selective ethanol oxidation reaction where the acetic aldehyde and hydrogen are main products.

Acknowledgements This work was financially supported by NASU Program "New functional substances and materials of chemical production" (project 13–19).

References

1. Nuno M, Ball RJ, Bowen CR, Kurchania R, Sharma G (2015) Photocatalytic activity of electrophoretically deposited (EPD) TiO_2 coatings. J Mater Sci 50:4822–4835
2. Velazquez J, Fernandez-Gonzalez R, Díaz L, Melian EP, Rodríguez V, Núnez P (2017) Effect of reaction temperature and sacrificial agent on the photocatalytic H_2-production of Pt-TiO_2. J Alloy Comp 721:405–410
3. Mahadik MA, An GW, David S, Choi SH, Cho M, Jang JS (2017) Fabrication of A/RTiO_2 composite for enhanced photoelectrochemical performance: solar hydrogen generation and dye degradation. Appl Surf Sci 426:833–843
4. Patil SM, Deshmukh SP, Dhodamani AG, More KV, Delekar SD (2017) Different strategies for modification of titanium dioxide as heterogeneous catalyst in chemical transformations. Curr Org Chem 21:821–833
5. Dulian P, Nachit W, Jaglarz J, Kanak P, Zukowski W (2019) Photocatalytic methylene blue degradation on multilayer transparent TiO_2 coatings. Opt Mat 90:264–272
6. Ruiz AM, Cornet A, Morante JR (2004) Study of La and Cu influence on the growth inhibition and phase transformation of nano-TiO_2 used for gas sensors. Sens Actuators B Chem 100:256–260
7. Bai S, Li H, Guan Y, Jiang S (2011) The enhanced photocatalytic activity of CdS/TiO_2 nanocomposites by controlling CdS dispersion on TiO_2 nanotubes. Appl Surf Sci 257:6406–6409
8. Pant HR, Park CH, Pant B, Tijing LD, Kim HY, Kim CS (2012) Synthesis, characterization, and photocatalytic properties of ZnO nano-flower containing TiO_2 NPs. Ceram Int 38:2943–2950
9. Karunakaran C, Gomathisankar P (2013) Solvothermal synthesis of CeO_2–TiO_2 nanocomposite for visible light photocatalytic detoxification of cyanide. ACS Sustain Chem Eng 1:1555–1563
10. Peng L, Xie T, Lu Y, Fan H, Wang D (2010) Synthesis, photoelectric properties and photocatalytic activity of the Fe_2O_3/TiO_2 heterogeneous photocatalysts. Phys Chem Chem Phys 12:8033–8041
11. Hunge YM (2017) Sunlight assisted photoelectrocatalytic degradation of benzoic acid using stratified WO_3/TiO_2 thin films. Ceram Int 43:10089–10096

12. Hunge Y, Mahadik M, Moholkar A, Bhosale C (2017) Photoelectrocatalytic degradation of oxalic acid using WO_3 and stratified WO_3/TiO_2 photocatalysts under sunlight illumination. Ultrason Sonochem 35:233–242
13. Li N, Li Y, Li W, Ji S, Jin P (2016) One-step hydrothermal synthesis of TiO_2@MoO_3 core–shell nanomaterial: microstructure growth mechanism and improved photochromic property. J Phys Chem C 120(6):3341–3349
14. Moharrami F, Bagheri-Mohagheghi MM, Azimi-Juybari H (2012) Study of structural electrical optical thermoelectric and photoconductive properties of S and Al codoped SnO_2 semiconductor thin films prepared by spray pyrolysis. Thin Solid Films 520:6503–6509
15. Ponja S, Sathasivam S, Chadwick N, Kafizas A, Bawaked SM, Obaid AY, AlThabaiti S, Basahel SN, Parkin IP, Carmalt CJ (2013) Aerosol assisted chemical vapour deposition of hydrophobic TiO_2–SnO_2 composite film with novel microstructure and enhanced photocatalytic activity. J Mater Chem A 1:6271–6278
16. Hunge Y, Mahadik M, Moholkar A, Bhosale C (2017) Photoelectrocatalytic degradation of phthalic acid using spray deposited stratified WO_3/ZnO thin films under sunlight illumination. Appl Surf Sci 420:764–772
17. YM Hunge (2017) Photoelectrocatalytic degradation of 4-chlorophenol using nanostructured α-Fe_2O_3 thin films under sunlight illumination. J Mater Sci Mater Electron 1–8
18. Vanalakar SA, Patil VL, Harale NS, Vhanalakar SA, Gang MG, Kim JY, Patil PS, Kim JH (2011) Controlled growth of ZnO nanorod arrays via wet chemical route for NO_2 gas sensor applications. Sens Actuators B Chem 221:1195–1201
19. Patil SM, Dhodamani AG, Vanalakar SA, Deshmukh SP, Delekar SD (2018) Multi-applicative tetragonal TiO_2/SnO_2 nanocomposites for photocatalysis and gas sensing. J. Phy Chem Solids 115:127–136
20. Sheng J, Tong H, Xu H, Tang C (2016) Preparation and photocatalytic activity of SnO_2@TiO_2 core–shell composites modified by Ag. Catal Surv Asia 20:167–172
21. Kutuzova AS, Dontsova TA (2019) Characterization and properties of TiO_2–SnO_2 nanocomposites obtained by hydrolysis method. Appl Nanosci 9(5):873–880
22. Scarisoreanu M, Fleaca C, Morjan I, Niculescu A-M, Luculescu C, Dutu E, Ilie A, Morjan I, Florescu LG, Vasile E, Fort CI (2017) High photoactive TiO_2/SnO_2 nanocomposites prepared by laser pyrolysis. Appl Surf Sci 418(1):491–498, Part B
23. Guo H, Zhang H, Yang J, Chen H, Li Y, Wang L, Niu X (2018) TiO_2/SnO_2 Nanocomposites as electron transporting layer for efficiency enhancement in planar $CH_3NH_3PbI_3$-based perovskite solar cells. ACS Appl Energ Mater 1(12):6936–6944
24. Huang M, Yu J, Li B, Deng C, Wang L, Wu W, Dong L, Zhang F, Fan M (2015) Intergrowth and coexistence effects of TiO_2–SnO_2 nanocomposite with excellent photocatalytic activity. J Alloy Compd 629:55–61
25. Zazhigalov VA, Sachuk OV, Diyuk OA, Starchevskyy VL, Kolotilov SV, Sawlowicz Z, Shcherbakov SM, Zakutevskyy OI (2018) The ultrasonic treatment as a promising method of nanosized oxide CeO_2-MoO_3 composites preparation. Nanochem Biotechnol Nanomater Appl 214:297–309
26. Zazhigalov VA, Diyuk OA, Sachuk OV, Diyuk NV, Starchevsky VL, Sawlowicz Z IV, Bacherikova SM Shcherbakov (2019) The effect of mechanochemical and ultrasonic treatments on the properties of composition CeO_2-$MoO_3 = 1{:}1$. Nanochem Biotechnol Nanomater Appl 221:109–123
27. Rumyantseva MN (2009) Chemical modification and sensory properties of nanocrystalline tin dioxide: author disscussion for the science degree doctor chemical sciences. Moscow, pp 46
28. Ivanov VV, Sidorak IA, Shubin AA, Denisova LT (2010) Synthesis of SnO_2 powders by decomposition of thermally unstable compounds. J. Siberian Federal University Eng Technol 2(3):189–213
29. León A, Reuquen P, Garín C, Segura R, Vargas P, Zapata P, Orihuela PA 2017 FTIR and raman characterization of TiO_2 nanoparticles coated with polyethylene glycol as carrier for 2-methoxyestradiol. Appl Sci 7(49). https://doi.org/10.3390/app7010049

30. Bahade ST, Lanje AS, Sharma SJ (2017) Synthesis of SnO_2 thin film by sol-gel spin coating technique for optical and ethanol gas sensing application. IJSRST 3(7):567–575
31. Zazhigalov VA, Wieczorek-Ciurowa K (2014) Mechanochemiczna aktywacja katalizatorów wanadowych. Krakow: Wydawnictwo PK, pp 454
32. Ayeshamariam A (2013) Synthesis, structural and optical characterizations of SnO_2 nanoparticles. J Photon Spintron 2(2):4–8
33. Nithiyanantham U, Ramadoss A, Kundu S (2016) Synthesis and characterization of DNA fenced self-assembled SnO_2 nano-assemblies for supercapacitor applications. Dalton Trans 45:3506–3521
34. Sheng P-Y, Yee A, Bowmaker GA, Idriss H (2002) H_2 Production from ethanol over Rh–Pt/CeO_2 catalysts: the role of Rh for the efficient dissociation of the carbon–carbon bond. J Catal 208:393–403
35. Pirez C, Fang W, Capron M, Paul S, Jobic H, Dumeignil F, Jalowiecki-Duhamel L (2016) Steam reforming, partial oxidation and oxidative steam reforming for hydrogen production from ethanol over cerium nickel based oxyhydride catalyst. Appl Catal A V 518:78–86
36. Mattos LV, Noronha FB (2005) Hydrogen production for fuel cell applications by ethanol partial oxidation on Pt/CeO_2 catalysts: the effect of the reaction conditions and reaction mechanism. J Catal 233:453–463
37. Cai W, Wang F, Zhan E, Van Veen AC, Mirodatos C, Shen W (2008) Hydrogen production from ethanol over Ir/CeO_2 catalysts: a comparative study of steam reforming partial oxidation and oxidative steam reforming. J Catal V 257:96–107

Heat Resistance of Nanocrystalline Powders, Single Crystals, and Coatings of $CrSi_2$ Obtained from Molten Salts

Oleg Sapsay, Dmytro Shakhnin, Tetiana Lukashenko, Viktor Malyshev, and Marcelle Gaune-Escard

1 Introduction

Chromium disilicide is the subject of many investigations [1] due to its valuable physical and chemical properties: high strength, corrosion resistance, thermal stability, etc. Furthermore, $CrSi_2$ demonstrates attractive semiconducting and thermoelectric properties due to p-type conductivity allowing to use it in photovoltaic cells and optoelectronic devices and as anode material for Li–ion batteries [2, 3]. It is promising thermoelectric material used for energy conversion at high temperature [4]. Specific properties of silicides are caused by their crystal structure and the presence covalent bonds Me–Me, Me–Si, and Si–Si in their structure.

Besides, chemical properties of construction materials could be significantly improved by coating deposition onto their surface. Due to the formation of an impervious, self-healing layer of SiO_2 on these materials at high temperature, chromium silicides are the most suitable materials for use as surface coatings on the refractory

O. Sapsay (✉) · D. Shakhnin · T. Lukashenko · V. Malyshev
Open International University of Human Development "Ukraine", 23 Lvivska St., Kiev 03115, Ukraine
e-mail: sapsay@email.ua

D. Shakhnin
e-mail: shakhnin@ukr.net

T. Lukashenko
e-mail: taniainst@gmail.com

V. Malyshev
e-mail: viktor.malyshev.igic@gmail.com

M. Gaune-Escard
Ecole Polytechnique, CNRS, UMR 6595, Technopôle de Chateau Gombert, 5 rue Enrico Fermi, 13453 Marseille Cedex 13, France
e-mail: mgescard@gmail.com

O. Fesenko and L. Yatsenko (eds.), *Nanooptics and Photonics, Nanochemistry and Nanobiotechnology, and Their Applications*, Springer Proceedings in Physics 247, https://doi.org/10.1007/978-3-030-52268-1_17

metals in oxidizing atmosphere [1]. In microelectronic devices, thin silicides layers are used for contacts and interconnections protection since they have lower electrical resistivity than crystalline silicon [5].

Until recently, one of the most used methods of $CrSi_2$ synthesis was high-temperature electrochemical synthesis in melts [6, 7]. Therefore, the purpose of this work was synthesis of heat resistant chromium disilicide nanocrystalline powders, single crystals, and coatings by metallothermic reduction.

2 Materials and Methods

2.1 Experiment 1

$CrSi_2$ as nanocrystalline powder was synthesized by co-reduction of anhydrous $CrCl_3$ and Na_2SiF_6 with Na according to the reaction (1):

$$CrCl_3 + 2Na_2SiF_6 + 11Na = CrSi_2 + 12NaF + 3NaCl \quad (1)$$

Since the reaction between reduced Cr and Si occurs in molten salt system, it probably leads to nanocrystalline particles formation [7].

2.2 Experiment 2

Single crystals were obtained by solution growth method using molten Sn–Zn (1:10 by weight) system as a flux. Cr and Si powders of 99.9% purity (1:2 by molar ratio) were added to Sn–Zn melt (1:10 by weight vs. solvent). Selection of the Sn–Zn solvent was driven by the fact that chromium forms no binary phases with tin [8], and there is only one phase in Zn–Cr system [9]. Besides, the solvent characterized by the following properties: low melting point, measurable solubility of compounds in the solvent, easy separation of the crystals, and low toxicity and cost.

2.3 Experiment 3

$CrSi_2$ coatings were obtained by electroless deposition of Si onto pure chromium substrate in molten KCl–NaCl–NaF–Na_2SiF_6–Si system. Pure Cr plate was immersed into the molten salt. Mechanism of deposition was described earlier [10]. Because of the proportionation–disproportionation reactions between Si (Si powder) and Si^{4+} (Na_2SiF_6) ions, Si was deposited onto Cr plate (2). Deposited Si diffuses into the Cr surface and forms silicide alloy $CrSi_2$ (3)

Table 1 Melts composition (mol.)

Experiment 1		Experiment 2		Experiment 3	
$CrCl_3$	0.01	Cr	0.045	NaCl	0.4
Na_2SiF_6	0.02	Si	0.09	KCl	0.4
Na	0.11	Sn	0.35	Na_2SiF_6	0.05
		Zn	0.07	NaF	0.2
				Si	0.2

$$Si + 6F^- + SiF_6^{2-} \leftrightarrow 2SiF_6^{4-} \tag{2}$$

$$4SiF_6^{4-} + Cr \rightarrow CrSi_2 + 12F^- + 2SiF_6^{2-} \tag{3}$$

The reaction is possible due to difference between the thermodynamic activity of pure silicon and siliconized layer [11].

Melts compositions that were used in experiments presented in Table 1. The mixture was filled into the alumina crucible. The alumina crucible was put into a stainless-steel container and heated at 600–800 °C for 10–12 h under Ar atmosphere. After that, container was cooled to room temperature in the furnace. The obtaining powder was washed solute HCl, NaOH, distilled water, and ethanol. Single crystals were separated by dissolving the tin-zinc melt in 0.1 M HCl. Cr plate with deposited Si was washed several times with distilled water to remove the salt.

Finally, all samples were dried in vacuum at 80 °C for 8–10 h.

The morphology, cross-section and the impurity of the obtained samples were investigated by scanning electron microscopy (SEM). The crystal structure was analyzed by X-ray powder diffractometer using Cu Kα radiation (wavelength λ = 1.54178 Å). The thermogravimetric analysis (TGA/DTA) was performed on a thermal analyzer NETZSCH STA 449 F1 Jupiter below 1000 °C in air at a rate of 10 °C min^{-1} to study the oxidation behavior of $CrSi_2$.

3 List of Abbreviations

CNRS the National Center for Scientific Research of the French Ministry of Education and Research
SEM scanning electron microscopy
DSC differential scanning calorimetry
TGA thermogravimetric analysis
XRD X-ray diffraction

4 Results and Discussion

XRD pattern indicated that all obtained samples were of hexagonal phase of $CrSi_2$. The lattice parameters are: $a = 4.31$ Å, $i\,c = 6.31$ Å) for nanocrystalline powder: $a = 4.34$ Å, $i\,c = 6.25$ Å for single crystals and $a = 4.35$ Å, $c = 6.35$ Å for coatings which are consistent with the values ($a = 4.42$ Å, $i\,c = 6.35$ Å) reported [1]. According to X-ray diffraction analysis, other phases of silicide or Cr, Cr_2O_3, SiO_2, Sn or Zn impurities were not found.

The results of scanning electron microscopy (SEM) show (Fig. 1a) that nanocrystalline powder with particles size 35–70 nm were obtained.

Direct synthesis using the Sn–Zn melt leads to obtaining the chromium disilicide as acicular crystals 150–200 μm long (Fig. 1b). Crystals are slightly agglomerated with each other.

On the cross-section of Cr substrate with $CrSi_2$ coating, three zones are evident (Fig. 1c) in radiation characteristic for chromium: Cr substrate (1), Kirkendal zone (2), and $CrSi_2$ layer (3). In radiation for chromium, it clearly shows the presence of zones that differ in the ratio of chromium and silicon in their composition. The ratio of chromium and silicon is obvious from the density of bright spots corresponding to chromium. Chromium lining (1) contains no silicon. Kirkendal zone (2) has an intermediate intensity between the metallic substrate and the silicide layer > 25 μm

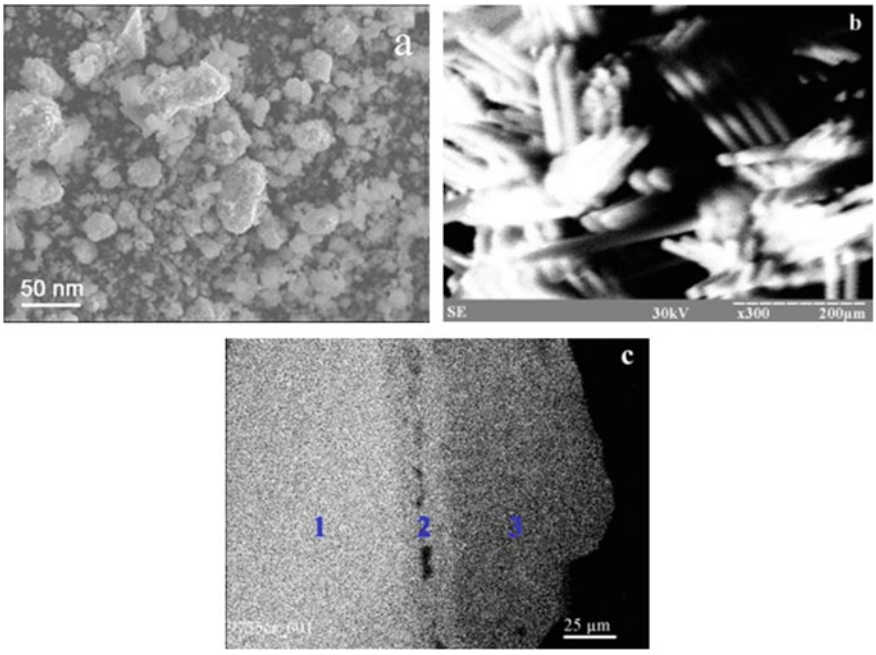

Fig. 1 SEM images of $CrSi_2$: **a** nanocrystalline powder; **b** crystals; **c** coating

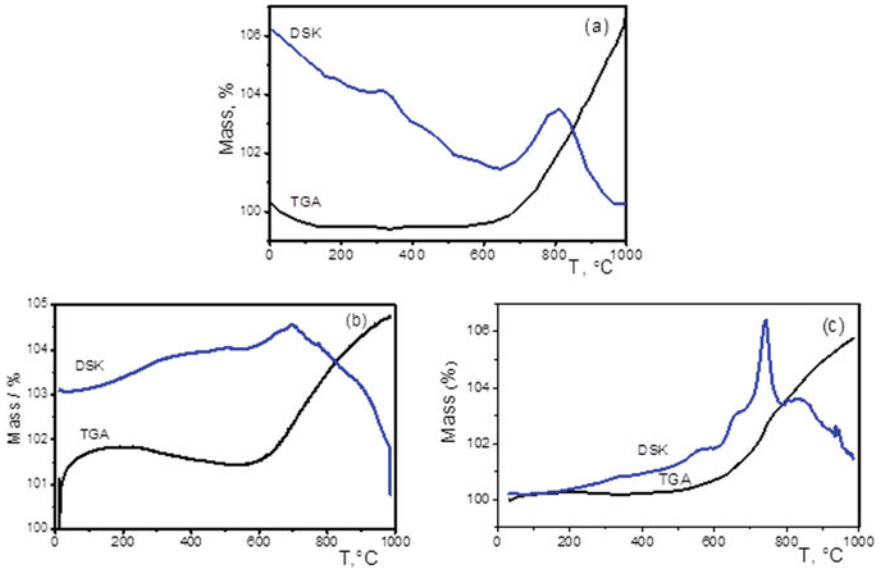

Fig. 2 DSC/TGA curves for heating in air of: **a** nanocrystalline powders; **b** crystals; **c** coating of $CrSi_2$

thick. Silicide layer (3) has the lowest density of bright spots corresponding to the chromium (Fig. 1c).

4.1 Heat Resistance

The stability of the nanocrystalline powders, single crystals, and coatings to oxidation in air at elevated temperatures was studied by differential scanning calorimetry (DSC) and thermogravimetric analysis (TGA) methods.

TGA curves show that masses of all $CrSi_2$ samples do not change up to temperature of 600 °C. Within the range of 600–1000 °C, masses gradually increased by 6.8% for nanopowders, by 4.6% for the crystals, and up to 5.3% for coatings (due to surface minor oxidation). With temperature further increase, samples surface oxidation was observed. DSC curve for the nanoparticles shows a major exothermic peak at the temperature close to 800 °C, whereas exothermic peak at DSC curves for crystals and coatings was observed at the temperature of about 700 °C. The correlation of TGA and DSC curves data suggested that the samples were not oxidized up to the temperature of 600 °C.

The intense oxidation process takes place at a temperature of 810–820 °C for nano-sized powders and of 700 °C for crystals and coatings of $CrSi_2$, which is consistent with previous studies [12] results for this compound. Later on, the samples surface formed a protective oxide layer of SiO_2.

5 Conclusions

1. The highest oxidation resistance in air has nanocrystalline $CrSi_2$ powders (800 °C). Single crystals and coatings were resistant up to 700 °C. This is due to fact that protective oxide layer of SiO_2 was formed on samples surface.
2. Obtained values of temperature resistance for nanocrystalline powders, single crystals, and coatings were different. It can be related with size and morphology of synthesized samples and also with the method of product obtaining.
3. Due to high oxidation resistance, obtained samples could be used as heat resistant details and coating for devices working at elevated temperatures.

Acknowledgements Authors of the present paper acknowledge support of all the Ecole Polytechnique and the University "Ukraine" staff in conducting scientific researches and writing this paper.

Competing Interests Authors of the present paper have no competing interests.

Funding Authors of the present paper have not used any external sources of funding in addition to regular financing for scientific investigations provided by CNRS and the University "Ukraine".

Authors' Contributions Authors of the present paper have made equal contributions in conducting scientific researches and writing this paper.

References

1. Lu J, Yang H, Liu B, Han J, Zou G (1999) Preparation and physical properties of nanosized semiconducting $CrSi_2$ powders. Mater Chem Phys 59:101–106
2. Courtel FM, Duguay D, Abu-Lebden Y, Davidson IJ (2012) Investigation of $CrSi_2$ and $MoSi_2$ as anode materials for lithium-ion batteries. J Power Sources 202:269–275
3. Henrion W, Lange H, Jahne E, Giehler M (1993) Optical properties of chromium and iron disilicide layers. Appl Surf Sci 70(71):569–572
4. Seo K, Varadwaj KSK, Cha D, In J, Kim J, Park J, Kim B (2007) Synthesis and electrical properties of single crystalline $CrSi_2$ nanowires. J Phys Chem 111:9072–9076
5. Murarka SP (1995) Silicide thin films and their applications in microelectronics. Intermetallics 3:173–186
6. Malyshev V, Shakhnin D, Gab A, Astrelin I, Molotovska L, Soare V, Donath C, Constantin V, Popescu AM (2016) Electrochemical synthesis of borides and silicides of chromium, molybdenum and tungsten in molten salts. Rev Roum Chim 67:2490–2500
7. Ma J, Gu Y, Shi L (2004) Synthesis and thermal stability of nanocrystalline chromium disilicide. J Alloys Comp 376:176–179
8. Molotovska LA, Shakhnin DB, Malyshev VV (2014) Metallothermic reduction and direct synthesis techniques in production of chromium disilicide. Powder Metall Met Ceram 53:386–391
9. Su X, Liu Y, Liu DYH, Tedenac JC, Yin F, Wang J (2010) Experimental investigation and thermodynamic assessment of the Zn–Cr system. J Alloys Comp 496:159–163
10. Ilyuhshchenko NG, Afinogenov AI, Shurov NI (1991) Vzaimodejstvie metallov v ionnyh rasplavah (Interaction of metals in ionic melts). Nauka, Moscow

11. Tatemoto K, Ono Y, Suzuki RO (2005) Silicide coating on refractory metals in molten salt. J Phys Chem Solids 66:526–529
12. Feng T, Li HJ, Fu QG, Yang X, Wu H (2011) The oxidation behavior and mechanical properties of $MoSi_2$–$CrSi_2$–SiC–Si coated carbon/carbon composites in high-temperature oxidizing atmosphere. Corros Sci 53:4102–4108
13. Molotovska L, Shakhnin D, Uskova N, Nikulina G, Cherednik V, Stukota S, Malyshev V (2016) Synthesis of VI group metals silicides dispersed powders by electrolysis of halide-oxide melts. J Chem Chem Eng 1:7–12. https://doi.org/10.17265/1934-7375/2016.01.002

Dezinvasion Efficiency of Colloidal Solutions of Metal Nanoparticles Against Helminth's Eggs

E. V. Semenko and O. V. Shcherbak

1 Introduction

The perspectives of livestock industry functioning depend on many factors, including the quality and usefulness of feed, breeding formulation, raising and management conditions, animal welfare. Herewith, a special place takes effective functioning of an antiparasitic measures system [1–5]. Strategy for prevention of animals' helminthiasis should be based on a set of measures aimed at efficient destruction of pathogens at different stages of their development. In deworming, one of the most effective methods of prevention is desinvasion. The main problem in the fight against invasive disease is high viability of pathogens, the ability of helminth eggs and larvae to survive after exposure to chemical disinfectants at concentrations and exposure, destructive for pathogenic microorganisms. As a result of the high stability of helminth eggs and larvae to natural factors, the accumulation of invasive material in the environment takes place, as well as their long-term storage and creating the risk of contamination of animals and humans [6–8].

Creating of a product with the active agent and an effective delivery system that would have a large antiparasitic effect on worms and will reduce to a minimum negative impact on animals and people is of essential theoretical and practical importance [1, 2, 6–11]. In the realization of helminths' eggs and larvae elimination effect promising is the use of nanomaterials, including nanometals [6–8]. The most promising nanotechnology products are biocidal metal nanoparticles (Ag, Cu,

E. V. Semenko (✉)
Institute of Veterinary Medicine, Quality and Safety of Animal Products, National University of Life and Environmental Sciences of Ukraine, Building No 12, Potehin str. 16, Kiev 03127, Ukraine
e-mail: eleora@ukr.net

O. V. Shcherbak
Institute of Animals Breeding and Genetics nd.a. M.V. Zubets, National Academy of Agrarian Sciences of Ukraine, Pogrebnjaka, 1, v. Chubinsky, Boryspil District, Kyiv Region 08321, Ukraine

O. Fesenko and L. Yatsenko (eds.), *Nanooptics and Photonics, Nanochemistry and Nanobiotechnology, and Their Applications*, Springer Proceedings in Physics 247, https://doi.org/10.1007/978-3-030-52268-1_18

Mg, Zn). Unique physical, chemical and biological properties of the biocidal metal nanoparticles (Ag, Cu, Mg, Zn) open up wide prospects of their use for diagnosis and treatment of diseases of animals. However, therapeutic and diagnostic applications of nanoparticles are often hampered by lack of information about their mechanism of action on animals and humans at the cellular and molecular levels. Stating of the value of natural systems and nanostructured nanomechanism in physiological, biochemical, immunological and genetic processes in the body requires a deep understanding of natural laws of functioning of living systems [5, 9–12].

2 Materials and Methods

The study was performed on a State Enterprise "Khrystynivske" of Institute of Animal Breeding and Genetics and a. M. V. Zubets of the National Academy of Agrarian Sciences of Ukraine (Cherkasy region) and at Laboratory of Parasitology and Tropical Veterinary Medicine Department of the National University of Life and Environmental Sciences of Ukraine (Kyiv).

To study the desinvasion effect of colloidal solutions of nanoparticles of metals on eggs and larvae of helminths, faeces were collected from an animal with a high intensity of invasions (85 eggs of *Strongylidae sp.* type in 1 g of faeces). The feces were placed in four Petri Dishes of 15 g each.

The first Petri Dishes were irrigated with anion-like magnesium nanoakvachelate. Second—nanocomposite "Shumerian silver". Third Petri Dishes were irrigated anionsimilar polymetallic agglomerates of nanoparticles Ag, Cu, Mg, Zn. The concentration of nanoparticles in colloidal solutions was about 100 dm^3. Calculation of the working solution was 0.01 dm^3 for 1 cm^2. The control Petri Dishes was irrigated with saline.

After that, the Petri Dishes were closed with lids and placed in a thermostat at 27 °C for 10 days. This material was used for cultivating of larva stage according to the method of Petrov and Gagarin [13]. This method is used to grow larvae of *Strongylidae* sp. type to the infection stage (stage 3 larva). Every day Petri Dishes were opened to aerate and moisten the faeces with saline. On day 7 and day 10 of cultivation, faeces were extracted from Petri Dishes and examined by method G. Baermann (larvae) (1917) and method A. Korchagin (1986) and F. Fulleborn methodology in the modification of W. Tracz (1992) (eggs) [14, 15]. Microscopy was performed under small and medium magnification of the microscope.

The second stage found the level of contamination of the environment with helminth eggs. The purpose of our study was to determine the effectiveness of desinvasion effect of colloidal solutions of nanoparticles of metals. To do that, the scrapings were taken from the animals, feeders, drinking bowls, floor and stall walls, metal grids. Taken samples were investigated due to A. Korchagin (1986) and F. Fulleborn methodology in the modification of W. Tracz (1992), followed by microscopy. For the determination of desinvasion effectiveness of colloidal solutions of nanoparticles of metals, there were formed three experimental and one control groups of

animals with 10 animals each. Animals were kept by group method in stalls of 20 m^2 each. The first stall was treated with anion-like magnesium nanoakvachelate. Second—with nanocomposite "Shumerian silver" with biocide properties of nanomaterials based on the mutual application of nanoparticles of silver and copper as silver-copper nanoagglomerates, resulted in erosion-explosive method due to "Nanomaterials and Nanotechnology" Ltd technology. A new nanomaterial has a wide antibacterial, antiviral and antifungal spectrum of activity (neutralizes over 1000 species of bacteria, viruses, fungi). Its efficiency is achieved through its unique set of properties of a composite "silver + copper" in nanoscale form. Small size (2–10 × 10–9 nm) silver nanoparticles have a very large specific surface area (1000 m^2/g or more), which increases the contact area of silver with bacteria and viruses, and significantly improves, thus, its antibacterial properties. Besides this, silver nanoparticles compared to their ions are less toxic [9]. The presence of copper in the colloidal solution "Shumerian silver" increases the antibacterial properties of silver and enhances antiviral and antifungal spectrum of action [6, 10]. The third stall was treated with anionsimilar polymetallic agglomerates of nanoparticles Ag, Cu, Mg, Zn.

The concentration of nanoparticles in colloidal solutions was about 100 dm^3. The control stall was watered with water. Before dezinvasion one made mechanical cleaning of each stall. The treatment was carried out in the presence of animals by using spray irrigation. Calculation of the working solution was 1 dm^3 for 1 m^2 stall. In 7 days after treatment carried out sampling for the sanitary and parasitological monitoring of the effectiveness of dezinvasion was made. After treatment constant clinical observation for the animals in these stalls were set.

3 Results and Discussion

The first stage of the study was to determine the effect of AgNPs' addition on the prior to the production testing of the drugs; we conducted studies on the effect of nanoavacellates on the culture of eggs of the *Strongylidae* sp. Type.

In the study of the effects of various nanoakvachelates: anion-like magnesium nanoakvachelate, nanocomposite "Shumerian silver" and anionsimilar polymetallic agglomerates of nanoparticles Ag, Cu, Mg, Zn on the culture of eggs and larvae of *Strongylidae* sp. type «in vitro» after 30 min of exposure, they were to have a detrimental effect on helminths eggs, causing their deformation and completely destroying them in 120 min. The results of the studies are shown in Table 1.

As can be seen from the table, all three nanocomponents understudy had a 100% detrimental effect on helminth eggs and their embryos.

So they can be used to destroy helminth eggs and their embryos as dezinvasion means (disinfectants).

The next stage of our research was to determine the dezinvasion effect of these agents in livestock farming. According to the held parasitological study, we've found that all of the objects investigated, in different degrees, were contaminated with the eggs of parasites. In samples taken from the floor, there were found eggs of

Table 1 The effect of nanoparticles on the culture of eggs of the *Strongylidae sp.* type

Test substance	Exposition (min)	Research day/changes		
		1	7	14
Control group	–	Eggs oval, average size (0.06–0.08) × (0.035–0.045) mm, the shell is smooth, inside is 6–18 blastomeres of gray color	Mobile larvae length 0.29–0.42 mm	Mobile larvae 0.50 mm
1. Magnesium nanoakvachelate	30	85% deformed eggs with an unusual color (dark gray with metallic luster)	Eggs are round in shape, with a discolored color and a broken shell	No eggs or larvae were detected
2. Shumerian silver		95% deformed eggs with an unusual color (dark gray with metallic lustre)		
3. Anionsimilar polymetallic agglomerates of nanoparticles Ag, Cu, Mg, Zn		95% deformed eggs with an unusual color (dark gray with metallic luster)		
1. Magnesium nanoparticles	60	Color change, egg shape, shell destruction and embryo death	Destruction of 100% of eggs	No eggs or larvae were detected
2. Shumerian silver				
3. Anionsimilar polymetallic agglomerates of nanoparticles Ag, Cu, Mg, Zn				
1. Magnesium nanoparticles	120	No eggs or larvae were detected	No eggs or larvae were detected	No eggs or larvae were detected
2. Shumerian silver				

(continued)

Table 1 (continued)

Test substance	Exposition (min)	Research day/changes		
		1	7	14
3. Anionsimilar polymetallic agglomerates of nanoparticles Ag, Cu, Mg, Zn				

Strongylidae sp. in average 1.4 ind./G (in 1 g of tested material) and oocyst of *Eimeriaα* sp.—1.0 ind./G. In samples selected from the surface of the walls, it was found larvae of *Strongylidae* type—1.8 ind./G (Fig. 1). In feeders and surface of drinking bowls, there were found only larvae of *Strongylidae* type (Fig. 2). At the skin of animals, there were found eggs of *Strongylidae* spp. with nematode embryos 0.8 ind./G and oocysts of *Eimeria spp.* 0.9 ind./G in average.

In 7 days after treatment carried out sampling for sanitary and parasitological monitoring of the effectiveness of dezinvation—at the scrapings, we have found rare eggs of nematode (strongylidosis) and oocysts of protozoosis (eimeriosis), all of which were unviable. Visually we've noted a change in their color, with distinct destructive changes within the eggs. Plasma inside the eggs became dark, and some nematode embryos had significantly shrinkage blastomeres (Figs. 3 and 4). It should be noted that no helminth larvae were found. This indicates eggs elimination effect of nanoparticles of metals and stopping of eggs development before the larval stage.

In the control stall objects were contaminated with eggs and larvae *Strongylidae*spp. and *Eimeria* spp. The most contaminated with invasive elements was the floor. Eggs and larvae of worms were viable. During the whole period of studies,

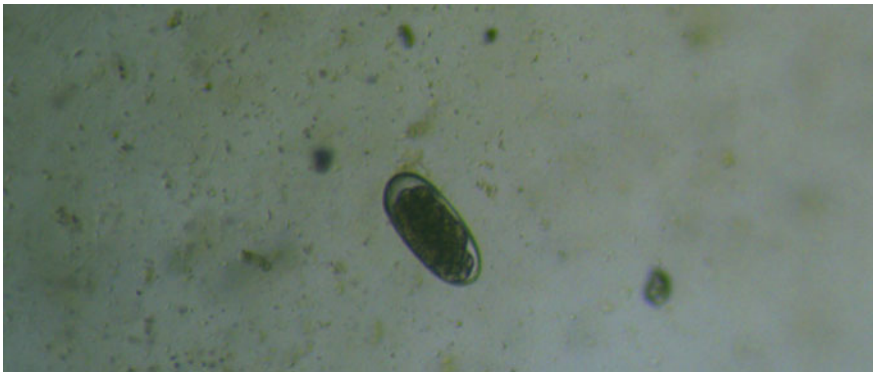

Fig. 1 Eggs of *Strongylidae* spp. (microscope magnification ×100)

Fig. 2 Larvae of *Strongylidae* type (microscope magnification ×40)

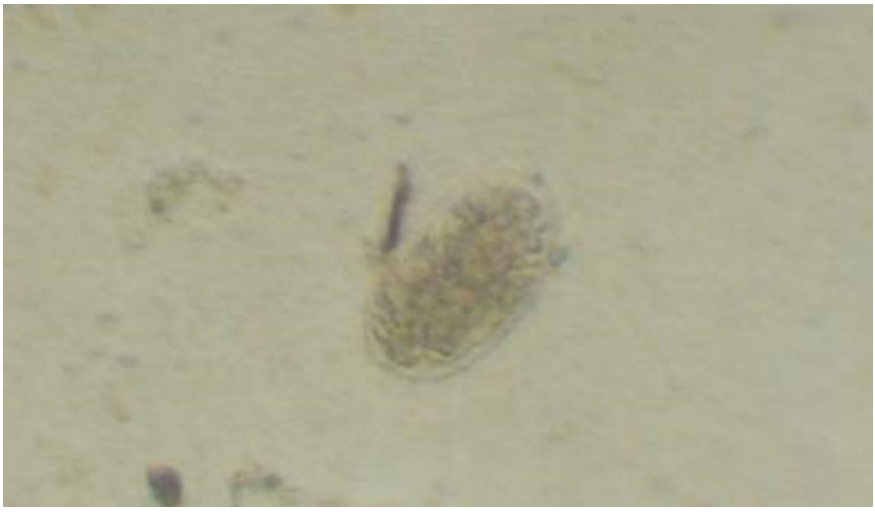

Fig. 3 The eggs of *Strongylidae* spp. were rounded, in many cases observed discoloration and destruction of the shell (microscope magnification ×400)

there were found with clinical observation no deviations from the animals' physiological norm. We assume that the mechanism of action of eggs elimination effect of biocidal metal nanoparticles (Ag, Cu, Mg, Zn) is linked with the effect of selective adhesion of metal nanoparticles to the surface of live eggs of worms and with the influence of a powerful electric field, formed by charged nanoparticles. All investigated nanocomposite metals showed 100% dezinvation effect. Electrically charged metal nanoparticles create conditions for continuous disinfection of viable parasitic

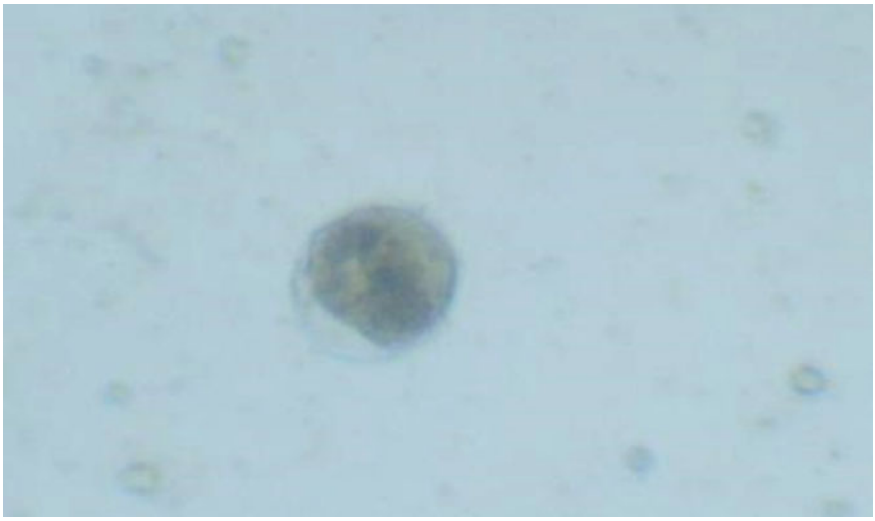

Fig. 4 There is a change in color, egg shape, destruction of the shell and death of the embryo (microscope magnification ×400)

elements excreted by diseased animals. This property of nanosubstance facilitates to profitability by saving of dezinvation solutions. Taking into account the maximum permissible concentrations of metals in the environment, the most environmentally friendly is the use of nanomagnesium because it is the maximum permissible concentration (MPC) is highest compared to other nanoparticles. Eggs elimination biocidal properties of the metals tested and validated in laboratory and industrial conditions and can be recommended for dezinvation of livestock buildings. Important from a practical point of view is that the metal nanoparticles besides the stated dezinvation properties have a broad spectrum of biocidal properties against pathogens (*bacterias: such as Escherichia coli, Streptococcus, Staphylococcus, Bacillus blue purulent; viruses and mold*). In general, it should be noted that the results widen the promising directions for further study of properties of metal nanoparticles and methods for their implementation in the diagnosis and prevention of parasitic diseases in particular. Eggs elimination mechanism of nanoparticles lays in the effect of "selective sedimentation" of anion similar nanoakvachelate metals to the surface of eggshell of only viable parasites and in the action of the electric field nanoelements. The advantages of the proposed product of dezinvasion at the base of nanoparticles are their environmental safety, the ability to interact only with viable parasite embryos and save eggs elimination properties with repeated use.

4 Conclusion

Biocidal metal nanoparticles at a concentration of 100 mg/dm^3 have highly expressed dezinvasion effect against viable pathogens of parasitic diseases of cattle. In particular, colloid nanoparticles of magnesium are the most environmentally friendly ones compared to other metal nanocomposite that allows extensive use of it in livestock buildings.

In the environmental objects of the researched groups after conducted dezinvation there were not found viable eggs and larvae of nematodes. All investigated nanocomposite metals showed 100% dezinvasion effect regardless of the stage of embryonic development of parasite embryos. Electrically charged metal nanoparticles create conditions for continuous disinfection of viable parasitic elements that are excreted by diseased animals.

Due to nanostructure availability in biological materials, the principle of natural high-energy is realized that requires further research.

References

1. Adamen FF (2007) Vysnuk Ukrainu 9:15–17 (in Ukraine)
2. Dolbin DA, Khayrullin RZ (2012) Resistance of helminth eggs to unfavorable physical and biological factors of the environment (Literature review). Russian J Parasitol 39(1):14–19
3. Borysevich VB (2009) The achievements of nanotechnology in the treatment and prevention of animal diseases. Nanoveterynariya (innovative technologies), pp 1–181 (in Ukraine)
4. Koval O (2005) Infekcijnyj control 4:19–21 (in Ukraine)
5. Cherepanov AA, Novikov NL (2003) Scientific papers. All-Russian Inst Helminthol 39:268–287 (in Russian)
6. Voloshina NO, Gorgol AV, Suchenko TV (2008) Veterynarna biotechnologyia 13(2):67–70 (in Ukraine)
7. Faunce T, Watal A (2010) Nanosilver and global public health: international regulatory issues. Nanomedicine 5(4):617–632
8. Zhang T, Wang L, Chen Q, Chen C (2014) Cytotoxic potential of silver nanoparticles. Yonsei Med J 55(2):283–291
9. Burmystrov VA (2007) Nanotekhnologii i nanomaterialy dlia biologii i mediciny 2:64–70 (in Russian)
10. Voloshina NO, Petrenko OF, Kaplunenko VG, Kosionov MV (2008) Veterynarna medicina Ukrainy 9:32–34 (in Ukraine)
11. Cherepanov AA, Kumbov PK, Novikov NL, Grygojev AG (2002) The theory and practice of control of parasitic diseases (zoonoses) 3:371–374 (in Russian)
12. Gerwert S, Failing K, Bauer C (2004) Dtsch Tierarztl Wochenschr 111(10):398–403
13. Zubarev IM, Vasilevich IF, Donchenko AS (2016) Aspekty jepizootologii invazionnyh boleznej. Uchebnoe posobie, pp 1–275 (in Russian)
14. Galat VF, Berezovs'kij AV, Prus MP, Soroka NM (2004) Parazy'tologiya ta invazijni xvoroby' tvary'n. Prakty'kum: Navchal'ny'j posibny'k, pp 1–238 (in Ukraine)
15. Parazitologicheskie metody laboratornoj diagnostiki gel'mintozov i protozoozov, Metodicheskie ukazanija, MUK 4.2.735–99, 1999. https://files.stroyinf.ru/Data2/1/4293790/4293790006.htm

Mechanisms of Tryptophan Transformations Involving the Photochemical Formation of Silver Nanoparticles

O. Smirnova, A. Grebenyuk, Iu. Mukha, and N. Vityuk

1 Introduction

Amino acid tryptophan (Trp, $C_{11}N_2H_{12}O_2$) is an advantageous reagent for the preparation of noble metal nanoparticles due to its multifunctionality and biocompatibility. It allows us to obtain stable colloids of mono- and bimetallic nanoparticles of gold and silver with prolonged stability, inherent optical properties and huge perspective for applications in cancer treatment without the need of further functionalization [1–3]. Researchers have shown interest in this problem since at least the middle of the last century [4, 5].

However, there is a need to reveal the mechanism of metal reduction and particles stabilization in such systems [6]. The quantum mechanical calculations are a useful tool to investigate the properties of metal/Trp systems starting from the single molecules [7].

The interaction of tryptophan molecules with solvent molecules or a solid surface under UV irradiation can lead to the formation of a tryptophan radical cation. For example, in [8] it was assumed that such a process is possible in a reaction with water molecules as a solvent (in this case solvated electrons are formed) or with transition metal cations, in particular, uranyl cations. Further transformations of the formed tryptophan radical cation with the participation of oxygen molecules lead to the formation of an intermediate consisting of tryptophan molecules with a peroxide bridge. This intermediate is converted to N′-formylkynurenine with cleavage of the C–C bond, which subsequently passes into kynurenine. The question of whether the counterparty should participate in these transformations remains debatable, that is, can the radical cation itself ensure the course of the described process.

O. Smirnova (✉) · A. Grebenyuk · Iu. Mukha · N. Vityuk
Chuiko Institute of Surface Chemistry, NAS of Ukraine, 17 General Naumov Str., Kiev 03680, Ukraine
e-mail: olsmirnova2001@ukr.net

O. Fesenko and L. Yatsenko (eds.), *Nanooptics and Photonics, Nanochemistry and Nanobiotechnology, and Their Applications*, Springer Proceedings in Physics 247, https://doi.org/10.1007/978-3-030-52268-1_19

It was experimentally shown in [9] that silver ions can participate as counterparties in the above reaction. In the present work, using quantum chemical calculations, we study the mechanism of the described transformations based on an analysis of the energy of elementary stages, as well as the spatial and electronic structures of possible intermediates.

2 Experimental and Methods

2.1 Experimental

The silver nanoparticles (Ag NPs) were formed during the photochemical process under UV irradiation.

For the synthesis of Ag NPs silver nitrate ($AgNO_3$) and amino acid tryptophan (Trp) were used in aqueous medium with a concentration of metal $C = 2 \times 10^{-4}$ M and a molar ratio of components Ag:Trp = 1:1. The pH = 10 of the system was reached with the 1 N solution of NaOH.

The initial solutions of Trp and $AgNO_3$ after mixing were irradiated applying UV-C LED source (LGInnotek) with the wavelength of $\lambda = 278$ nm at output optical power density of $P = 3.0 \pm 0.1$ mW/cm^2 during 5 h in quartz glass at the temperature $T = 25$ °C.

The absorption spectra of colloids were recorded in the UV-visible region (200–1000 nm) by a spectrophotometer Lambda 35 (Perkin-Elmer, United States) in 1 cm quartz cells.

2.2 Models and Methods

The spatial and electronic structure of the tryptophan molecule, its radical cation, and complexes with an oxygen molecule and silver particles, possible intermediates, and also conversion products were studied: N'-formylkynurenine, kynurenine (kyn) (Fig. 2).

The calculations have been carried out by density functional theory (B3LYP/SBKJC and B3LYP/3-21G*) method using the PC GAMESS software package [10]. The electronic absorption spectra of the studied structures were calculated by the TDDFT [11, 12] method. The influence of the aquatic environment on the spatial structure and absorption spectrum was taken into account in the framework of the continual PCM model [13].

3 Results and Discussion

The optical spectrum of silver nanoparticles (Ag NPs) is characterized by an absorption band of localized surface plasmon resonance (LSPR) in a visible range with a maximum of about 400 nm. For the Ag/Trp system, as we showed earlier [3], it is possible to obtain stable silver colloids with plasmon band maximum at 417 nm.

Such colloids are formed during the photochemical reaction between Ag^+ and Trp in alkaline medium from boiling solution (Fig. 1). The bands in UV region, namely at 270–290 nm, corresponding to the absorption of Trp and its oxidation products formed during reaction.

The oxidation of amino acid in studied systems in chemical process proceeds through indole ring cleavage, as was shown by authors in [8]. During photochemical process, the direct activation occurs with a precise wavelength that corresponds to the indole ring band. Thus, we assumed that the photochemical oxidation of Trp occurs via the kynurenine pathway through indole ring cleavage as well.

Figure 2 shows the spatial structure (B3LYP/SBKJC) of molecules and absorption spectra (TDDFT/B3LYP/3-21G*) of tryptophan and its conversion products (N′-formylkynurenine, kynurenine) based on the results of quantum chemical calculations.

The calculated values of the geometric parameters of the studied molecules practically (up to 0.001 Å) coincide with the calculation results by various methods

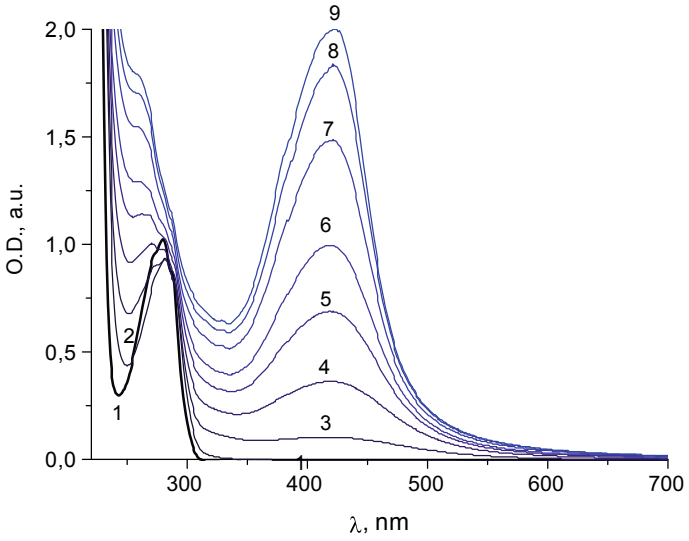

Fig. 1 Optical spectra of stable colloid of silver nanoparticles obtained in the presence of tryptophan: 1—refers to control solution of amino acid, 2—Ag^+/Trp system under UV irradiation during 5 min, 3—30 min, 4—1 h, 5—1 h 30 min, 6—2 h, 7—3 h, 8—4 h, 9—5 h

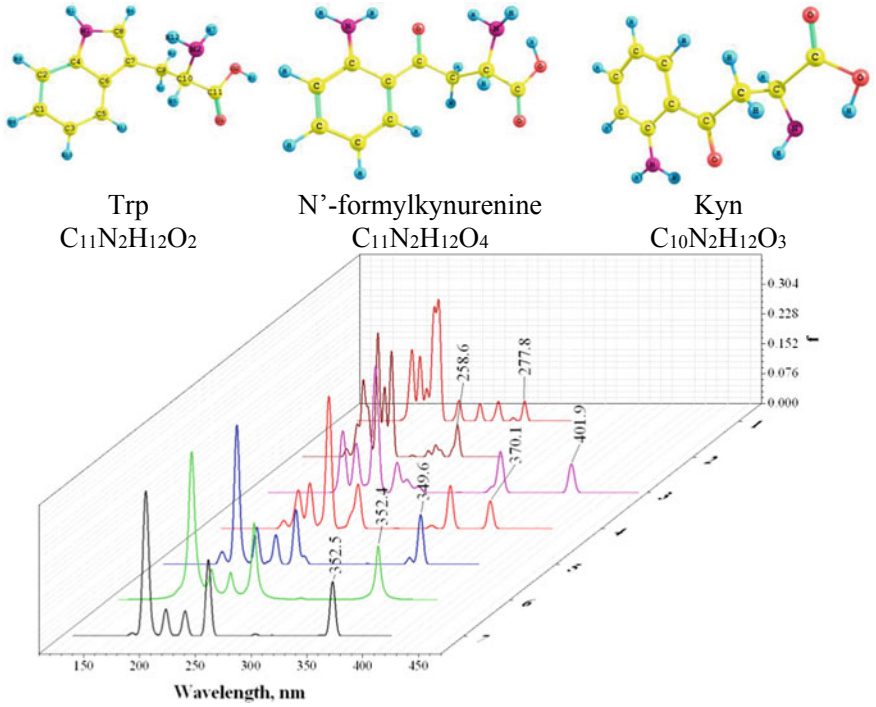

Fig. 2 Spatial structures and electronic absorption spectra of tryptophan and relative oxidation products in vacuum and in water: 1—Trp, 2—Trp in water, 3—N′-formylkynurenine, 4—N′-formylkynurenine in water, 5—kyn, 6—kyn in water, 7—Trp zwitter-ion in water

[14] (including B3LYP/3-31G*) and are very close to experimental data [15]. Therefore, the experimental geometric parameters and spectral characteristics of the above molecules are well reproduced by the calculation methods used (Fig. 2).

The absorption spectrum of tryptophan molecules in a vacuum has absorption bands (Fig. 2), of which the first (278 nm) corresponds (with a coefficient of 0.89) to the transition of the electron from the highest occupied to the lower free molecular orbital (B-band). In a polar solvent medium (water, pcm model), a hypsochrome shift of this absorption band to 258 nm occurs. This shift is due to an increase in the width of the orbital energies difference from 5.01 to 5.27 eV due to a decrease in the level of HOMO (localized on the benzene core and carboxyl group) from −5.40 to −5.56 eV and an increase in LUMO (localized only on the benzene core) from −0.39 to −0.29 eV (Fig. 3). Thus, this spectral shift is mainly due to the interaction of the polar carboxyl group with a polar solvent (water).

In accordance with the data described in [14], in an aqueous medium, tryptophan can transform into a zwitterion. The absorption spectrum calculated for this structure, also shown in Fig. 2, differs significantly from the experimental data. Therefore, the zwitterions are present in solution in small amounts.

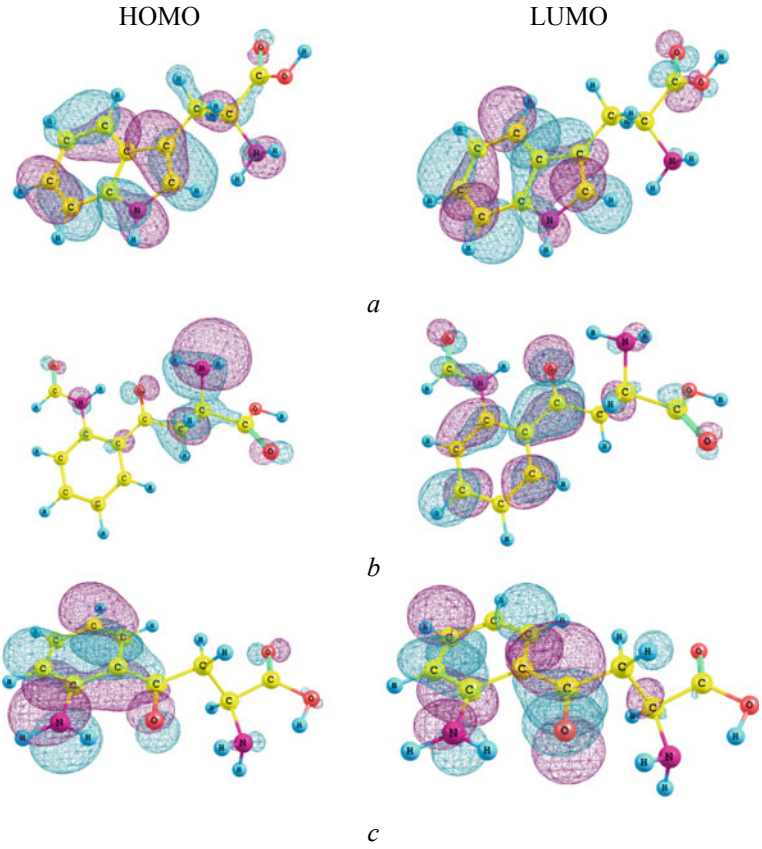

Fig. 3 Distribution of HOMO and LUMO in the molecules of tryptophan (**a**), N′-formylkynurenine (**b**), kyn (**c**)

Similarly, for the N'-formylkynurenine molecule, a hypsochromic shift (from 402 to 371 nm) is also observed upon transition from vacuum to an aqueous solution, and orbital energies difference changes from 3.76 to 4.07 eV due to a decrease in the HOMO level (localized mainly on the polar amino group of aromatic ring) from −5.95 to −6.15 eV and an increase in LUMO (localized mainly on the aromatic nucleus) from −2.20 to −2.08 eV (Fig. 3).

Thus, the spectral shift is mainly due to the interaction of the amino group of the aromatic nucleus with a polar solvent (water). However, the kynurenine spectrum upon transition to a polar solvent is characterized by a slight bathochromic shift (from 358 to 361 nm), due to a decrease in the orbital energies difference width from 3.87 to 3.82 eV, since both HOMO and LUMO are almost completely localized on the benzene core (Fig. 3). Thus, in this case, the spectral shift is mainly due to the interaction of the aromatic nucleus with a polar solvent (water).

The experimental maximum value of the first absorption band of the tryptophan molecule corresponds to 280 nm. Therefore, the proposed model satisfactorily describes the experiment and can be used for further studies.

Based on the experiment, it was found in [4] that the oxidation of tryptophan into N′-formylkynurenine is accompanied by a shift of the absorption band to 315–320 nm. Further hydrolysis of N′-formylkynurenine leads to a decrease in the band at 315 and the appearance of the band at 360 related to kyn [5].

According to the calculation results, the ionization of the tryptophan molecule is accompanied by the absorption of energy of 7.04 eV, and the recovery of the silver ion releases 4.82 eV of energy, which is for 2.22 eV less than that for tryptophan.

In the tryptophan/silver ion complex, the redox process (the transition from a singlet to a triplet) occurs under the effect of UV radiation) requires 1.94 eV of the energy that can be obtained by absorbing radiation.

When passing from a silver ion to charged silver clusters, the aforementioned value changes slightly (1.8 eV for Ag_3^+ and 1.7 eV for Ag_5^+). Thus, silver ion acts as an effective counterparty in the formation of tryptophan radical cation.

In the complex of tryptophan radical cation—oxygen molecule, both participants are at a great distance (more than 3 Å) and no covalent bond is formed. However, the $(Trp–O_2–Ag–H_2O)^+$ complex appeared to be stable. In the singlet state, a peroxide group is formed covalently bonded to a carbon atom adjacent to the imide group (Fig. 4). Upon transition to the triplet state (which requires absorption of 0.5 eV), this bridge breaks with the formation of two C=O groups in the five-membered nucleus of the tryptophan molecule. At the same time, the C–C bond length between these groups increases by 0.054 Å (from 1.551 to 1.605 Å). This suggests a possibility of a subsequent break in communication with the formation of the N′-formylkynurenine molecule.

The energy effect of the oxidation reaction (1) is −292 kJ/mol

$$\text{Trp} + O_2 = \text{N}'\text{-formylkynurenine} \tag{1}$$

The energy effect of the hydrolysis of N′-formylkynurenine to form kinurenine and formic acid (2) is −39 kJ/mol.

$$\text{N}'\text{-formylkynurenine} + H_2O = \text{Kyn}+ \tag{2}$$

So, these processes are thermodynamically profitable.

4 Conclusions

In this work, within the framework of the theoretical methods and models used, the available experimental data (spatial structure and electronic absorption spectra) are satisfactorily reproduced. An explanation is given of the direction of the spectral shifts of these three molecules upon transition to an aqueous medium from the point

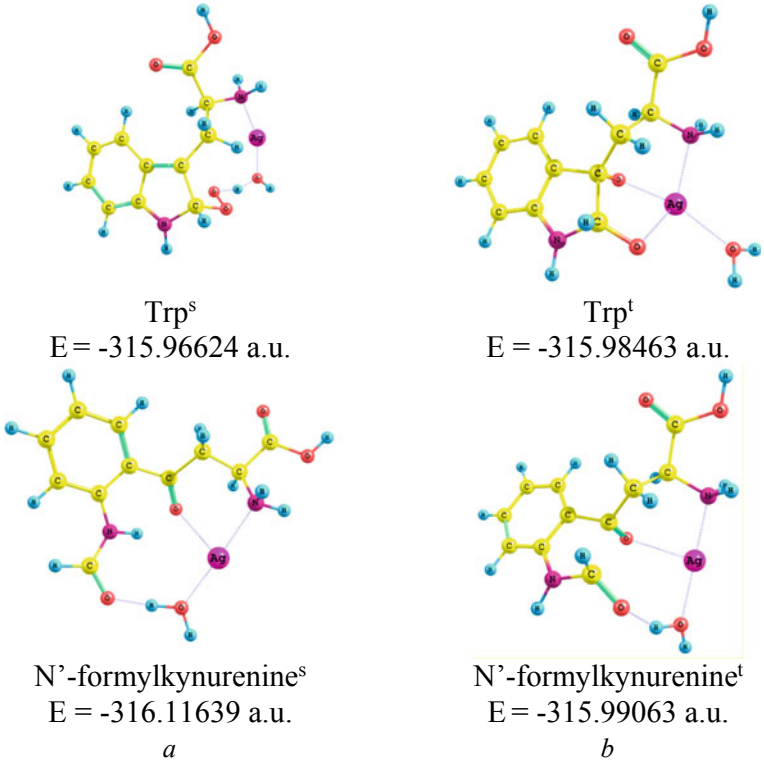

Fig. 4 The complex $(Trp–O_2–Ag–H_2O)^+$ in the singlet (**a**) and triplet (**b**) states

of view of the composition of the frontier orbitals. The energy effects of tryptophan oxidation and N′-formylkynurenine hydrolysis reactions have been determined. The role of charged silver clusters and water molecules in the formation of tryptophan radical cation under UV irradiation is revealed.

References

1. Mukha Iu, Vityuk N, Grodzyuk G, Shcherbakov S, Lyberopoulou A, Efstathopoulos EP, Gazouli M (2017) Anticancer effect of Ag, Au, and Ag/Au bimetallic nanoparticles prepared in the presence of tryptophan. J Nanosci Nanotech 17(12):8987–8994
2. Shmarakov I, Mukha Iu, Vityuk N, Borschovetska V, Zhyshchynska N, Grodzyuk G, Eremenko A (2017) Antitumor activity of alloy and core-shell-type bimetallic AgAu nanoparticles. Nanoscale Res Lett 12:333
3. Katifelis H, Lyberopoulou A, Mukha Iu, Vityuk N, Grodzyuk G, Theodoropoulos GE, Efstathopoulos EP, Gazouli M (2018) Ag/Au bimetallic nanoparticles induce apoptosis in human cancer cell lines via P53, CASPASE-3 and BAX/BCL-2 pathways. Artificial Cells, Nanomed Biotechnol 46(sup3): S389–S398
4. Alan H, Mehler W, Knox E (1950) The conversion of tryptophan to kynurenine in liver I. The coupled tryptophan peroxidase-oxidase system forming formylkynurenine. J Biol Chem 187:419–430

5. Alan H, Mehler W, Knox E (1950) The conversion of tryptophan to kynurenine in liver II. The enzymatic hydrolysis of formylkynurenine. J Biol Chem. 187:431–438
6. Makarov VV, Love AJ, Sinitsyna OV, Makarova SS, Yaminsky IV, Taliansky ME, Kalinina NO (2014) "Green" nanotechnologies: synthesis of metal nanoparticles using plants. Acta Naturae 6(1)(20):37
7. Mitrić R, Petersen J, Kulesz A, Bonačić-Koutecký V, Tabarin Th, Compagnon I, Antoine R, Broyer M, Dugourd Ph (2007) Photoabsorption and photofragmentation of isolated cationic silver cluster–tryptophan hybrid systems. J Chem Phys 127(13):134301
8. Kazakov VP, Ostakhov SS, Osina IO, Sultanbaev MV (2010) The intracomplex radical-cation chain oxidation of tryptophan photosensitized by uranyl ion. High Energy Chem 44(4): 297–303
9. Mukha Iu, Vityuk N, Khodko A, Kachalova N, Fedyshyn O, Malysheva M, Eremenko A (2019) Photo- and temperature-dependent formation of tryptophan/silver nanoparticles. Res Chem Intermediates 45(8):4053–4066
10. Schmidt M, Baldridge K, Boatz J, Elbert S, Gordon M, Jensen J, Koseki S, Matsunaga N, Nguyen K, Su S, Windus T, Dupuis M, Montgomery J (1993) General atomic and molecular electronic structure system. J Comput Chem 14:1347
11. Becke A et al (1993) Density-functional thermochemistry. III. The role of exact exchange. J Chem Phys 98(7):5648
12. Runge E, Gross EKU (1984) Density-functional theory for time-dependent systems. Phys Rev Lett 52(12):997
13. Wang Y, Cheng X, Yang X, Yang X (2006) DFT study of solvent effects for some organic molecules using a polarizable continuum mode. J Solution Chem 35:869–878
14. Krauklis IV, Tulub AV, Shtyrov AA (2017) Comparative characteristics of a tryptophan molecule in the gas phase and water. J Struct Chem 58(7):1263–1269
15. Görbitz CH, Törnroos KW, Day GM (2012) Single-crystal investigation of L-tryptophan with $Z = 16$. Acta Cryst B 68:549–557

Mechanisms of Stack Interaction in Polymer Composites of Polyvinylchloride with Methylene Blue

T. M. Pinchuk-Rugal, O. P. Dmytrenko, M. P. Kulish, M. A. Alieksandrov, O. L. Pavlenko, A. P. Onanko, Yu. E. Grabovskiy, V. V. Strelchuk, and O. F. Kolomys

1 Introduction

Polymers play an important role in various science-intensive industries. At the same time, they have a number of disadvantages, including those caused by low mechanical, electrically conductive properties. Overcoming these disadvantages is realized through the synthesis of polymers with internal conductivity or by filling the polymer matrix with conductive particles, including various carbon nanostructures to create external electrical conductivity and improve mechanical characteristics [1, 2]. The filling with the carbon nanostructures, primarily nanotubes and graphene plates leads to the percolation effect of increasing electrical conductivity by many orders of magnitude [3, 4]. In this case, we obtained nanocomposites with multi-walled carbon nanotubes characterized by low percolation threshold values. This concentration behavior of the electrical conductivity of these nanocomposites is a consequence of the segregated nanotube distribution. On the other hand, the increase in electrical conductivity at concentrations above the percolation threshold is limited due to the high value of the contact resistance due to the adsorbed layers of polymer on the fillers [5–10].

Of particular interest is the modification of polymers by conjugated systems. However, these structures can occur as an integral part of the molecular structure of polymer chains. An example of such systems is the formation of polyene structures in polyvinyl chloride (PVC) due to dehydrochlorination [11, 12]. In addition, it is possible to modify the filling of polymers with various conjugated systems. Thus,

T. M. Pinchuk-Rugal · O. P. Dmytrenko · M. P. Kulish · M. A. Alieksandrov (✉) · O. L. Pavlenko · A. P. Onanko · Yu. E. Grabovskiy
Taras Shevchenko National University of Kyiv, Kyiv, Ukraine
e-mail: mrmarafon@gmail.com

V. V. Strelchuk · O. F. Kolomys
V.E. Lashkaryov Institute of Semiconductor Physics, Kyiv, Ukraine

O. Fesenko and L. Yatsenko (eds.), *Nanooptics and Photonics, Nanochemistry and Nanobiotechnology, and Their Applications*, Springer Proceedings in Physics 247, https://doi.org/10.1007/978-3-030-52268-1_20

the modification of the PVA/PVP mixture with methylene blue leads to an increase in electrical conductivity while increasing the content of the doping dye molecules [13–15]. Graphene filling of polymer matrices leads to a significant drop in electrical resistance and the appearance of stack interaction [4–16]. The mechanisms of stack interaction in polymer composites and their effect on properties, including contact resistance were not studied sufficiently.

The purpose of this article is the installation of stack interaction mechanisms in polyvinyl chloride composites filled with one of the representatives of linear conjugate systems—methylene blue.

2 Experimental Studies

To prepare a PVC-MWCNTs nanocomposite, PVC powder of C-7058 grade with $M_W = 157 \times 10^3$ and methylene blue $C_{16}H_{18}ClN_3S$ powder with a density of $\rho = 1.0$ g/cm^3 were used. The composites were obtained by hot pressing. The PVC powder was mixed thoroughly with the addition of the appropriate amount of the dye. The temperature was 120 °C. PVC-MB composites in the form of the discs had a diameter of 30 mm. The concentrations of the dye in the polymer matrix were 0; 0.005; 0.03; 0.05; 0.07 vol. fract.

Crystalline structure of PVC-MB nanocomposites has been determined by means of X-ray diffractometer (DRON-3 M) with the usage of monochromatic CrK_α ($\lambda = 0.154178$ nm) irradiation.

For the investigation of the mechanical properties of nanocomposites PVC- MB, an ultrasonic KERN-4 computerized velocity meter was used. The dynamic elastic Young's modulus was determined by the formula: $E' = \rho V_l^2$, where ρ is the sample density, V_l is the velocity of quasi-longitudinal ultrasonic elastic waves. The dynamic shear modulus was obtained by the formula:

$G' = \rho V_{tr}^2$, where V_{tr} is the velocity of quasi- transverse ultrasonic elastic waves.

Raman spectra and luminescence were measured with a reflective geometry method at the room temperature by means of a triple spectrometer (Horbia Jobin Yvon T64000, Japan), provided with a cooled CCD detector. To excite Raman scattering spectra, Ar-Kr ionic laser was used with the wavelength $\lambda = 488$ nm. Excitation of the photoluminescence spectra was performed with He–Cd laser, wavelength $\lambda = 325$ nm. Irradiation with 1–2 MW laser power was focused at the specimen to a spot of 1 μm in dimension.

3 Results and Discussion

Polyvinyl chloride (PVC) is a carbon-chain polymer in which the supramolecular organization of the structure is poorly expressed. At the same time, as the predominantly amorphous phase in PVC, a crystalline structure emerges at the stage of

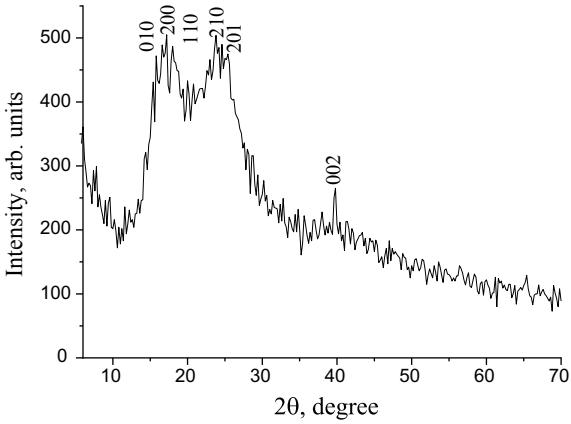

Fig. 1 X-ray diffraction spectra for PVC ($\lambda_{CuK\alpha} =$ 0.154178 nm)

synthesis, the diffraction pattern for which involves several sufficiently intense interference maxima (Fig. 1). PVC has an orthorhombic structure with the lattice parameters $a = 1.06$ nm, $b = 0.54$ nm, $c = 0.51$ nm.

With the filling of the PVC matrix by methylene blue (MB) ($C_{16}H_{18}ClN_3S$), the lattice symmetry remains unchanged and its parameters change little. To a greater extent, the degree of crystallinity is restructured (Fig. 2).

It is seen that in the initial state the degree of crystallinity is low ~21%. With the filling of the matrix of MB only at low concentrations (0.01 vol. fract.) the increase in the degree of crystallinity up to 30% is observed. At higher concentrations up to 0.03 vol. fract. the crystallinity decreases to ~26% and does not change further. It can be assumed that the aggregates of MB are the centres of crystallization of PVC, which is especially manifested in the low content of the dye when the size of its aggregates is small.

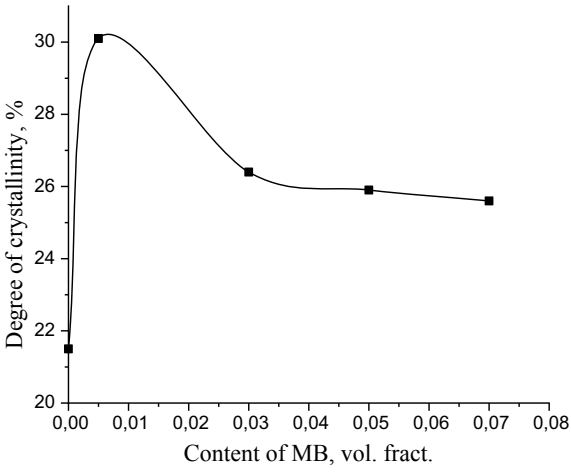

Fig. 2 Crystallinity degree of PVC as a function of MB content

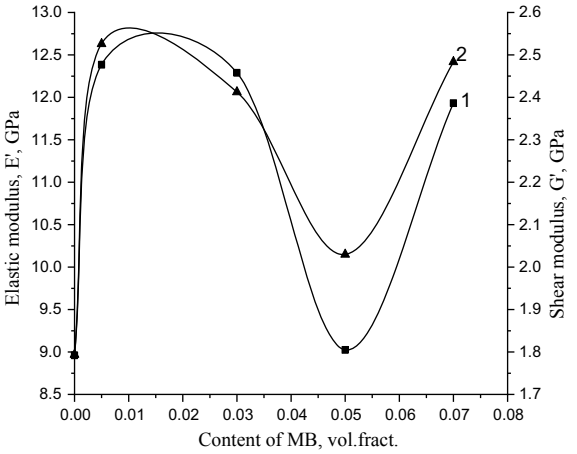

Fig. 3 Dynamic elastic ($f \approx$ 1.0 MHz) and shear ($f \approx$ 0.7 MHz) modules dependencies for PVC-MB composites depending on the content of the methylene blue modifier ($T = 25$ °C)

The presence of modifiers has a complex effect on the dynamic elastic and shear modulus. It is necessary that the composite PVC-MB is in a state of glass transition (Tg (PVC) = 87 °C) [6]. For a short time of dynamic loading, the considered modules act as characteristics of relaxation processes related to the conformational rearrangement of monomer units (β (transitions), whose relaxation time is insignificant ($\tau \approx$ 10–12 s). For the β-transition, the values of both modules are quite high with smaller values of the shear modulus (Fig. 3). The concentration dependences of the dynamic of elastic and shear modulus are similar and are characterized by the presence of a broad maximum in the low content of conjugated MB molecules, a minimum of about 0.05 vol. fract. and their further growth at higher dye concentrations. The minimum depth for the elastic modulus is higher. When comparing the curves of both modules with the curves of the degree of crystallinity, their correlation is observed in the region of low MB content. This suggests that the growth of modules in this concentration range is due to the existence of intermolecular bonds in the crystalline phase, which reduce the possibility of configurational reorganization of monomer units. As the degree of crystallinity decreased, the possibility of conformational transformations in the links increases and the modules fall. The role of the intermolecular bonds considered is higher for the dynamic modulus of elasticity. For higher MB concentrations, the degree of crystallinity remains unchanged, and both modules increase, which is a manifestation of the interaction between the macromolecules and the modifier.

For the establishment of mechanisms of such interaction, the Raman spectra and photoluminescence (PL) for both pure components and their composites were investigated. In Fig. 4, the Raman spectrum for pure PVC is given.

In this spectrum, there are all lines characteristic of PVC. The most important is the stretching oscillations ν (C–Cl) at 363, 639, 696, 853 cm^{-1}, bending oscillations w (CH_2) at ν (CH_2) = 1433 cm^{-1}, the stretching oscillations of methylene CH- group at ν (CH) = 2841 cm^{-1}, the stretching oscillations of the methylene CH_2-group at ν (CH_2) = 2917 cm^{-1}, ν (CH_2) = 2978 cm^{-1}. Particularly, important are oscillatory

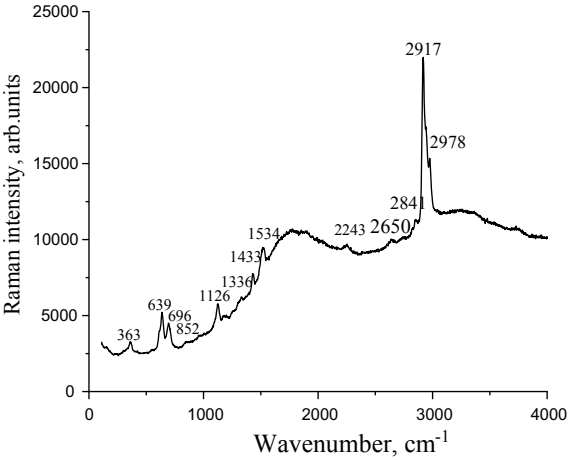

Fig. 4 Raman spectrum for pure PVC ($\lambda_L = 488$ nm, $T = 300$ K)

modes, which are characteristic of polyene structures formed in PVC. These oscillatory modes are observed at ν_1 (C–C) = 1126 cm^{-1}, ν_2 (C=C) = 1534 cm^{-1}, $2\nu_1$ (C–C) = 2243 cm^{-1}, ν_1 (C–C) + ν_2 (C=C) = 2650 cm^{-1}. For higher wavenumbers, more complex overtones and complex tones of oscillatory polyene modes are observed. The confirmation of the existence of polyene structures in PVC is also an increase in the Raman background, due to the manifestations of electronic excitations and, as a consequence, the subsequent emission of radiation. For this sample, the intensity of the polyene bands is less pronounced, as compared to the thermally or radiation degraded samples of PVC, for which the Raman spectrum consists mainly only of the bands of the oscillatory polyene modes [11].

Figure 5a–c shows the Raman spectra in different ranges for a PVC composite with 0.005 vol. fract. MB. At this concentration, there is a significant increase in the crystallinity degree, which is accompanied by the growth of dynamic modules. Figure 5 Raman spectra for PVC composite with 0.005 vol. fract. MB ($\lambda_L = 488$ nm, $T = 25$ °C, the designations correspond to the vibrational modes and their wavenumbers).

The spectra are characterized by a more sharp background growth while maintaining the bands of oscillation modes in PVC. First of all, this refers to the region of low wavenumbers in which the bands of stretching oscillation ν (C–Cl) are concentrated. At the same time, at high wavenumbers, where the bands ν (CH), ν (CH_2) are concentrated, the shape of the lines changes very much. The major changes in the Raman spectrum for a given composite occur in the domain of oscillating bands $\nu 1$ (C–C) and $\nu 2$ (C=C) of polyene structures. The relative intensities of PVC bands are greatly reduced. There is a sharp increase in the intensity of the band ν_1 (C–C) = 1129 cm^{-1}. The widths of both bands ν_1 (C–C) and ν_2 (C=C) decrease. The position of the band ν_2 (C=C) is shifted from 1534 cm^{-1} for PVC to 1518 cm^{-1} for the composite.

These results indicate that the conjugated structure of the MB modifier not only contributes to the formation of the crystalline phase in PVC but as a consequence leads

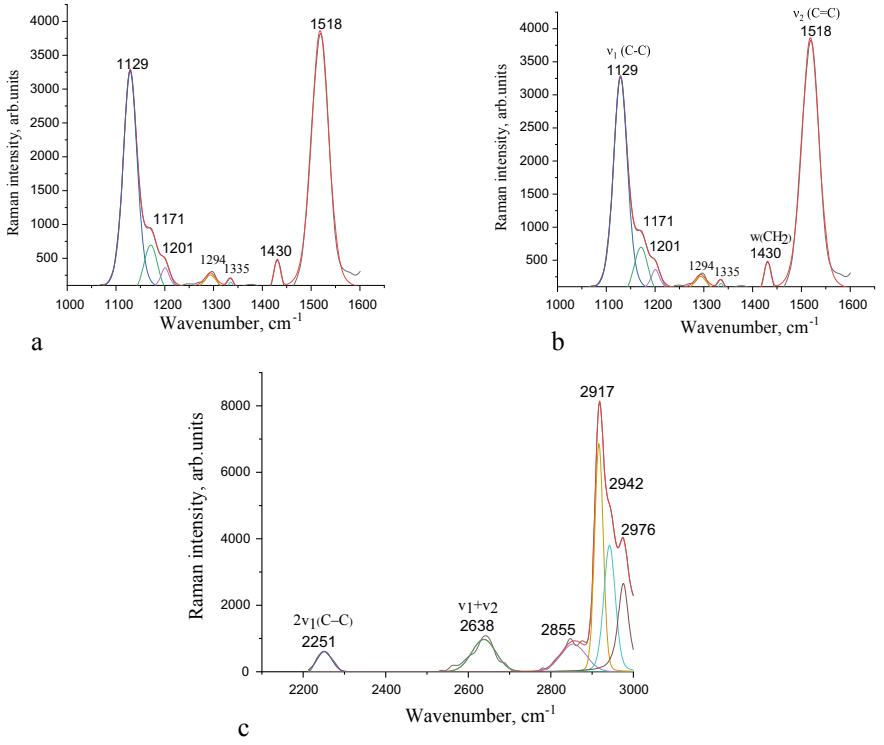

Fig. 5 Raman spectra for PVC composite with 0.005 vol. fract. MB in different ranges a–c ($\lambda_L =$ 488 nm, $T = 300$ K, the designations correspond to the oscillation modes and their wavenumbers)

to the emergence of polyene structures. Due to such structures, dynamic modules grow significantly as a result of the restructuring of the configuration of the monomer units of PVC. The appearance of such defective polyene systems is a consequence of the dehydrochlorination of the PVC units, which is stimulated by the conjugated MB molecules and may cause the stack interaction between the conjugated systems of the PVC-MB composite components.

With the increase of the MB concentration in the composite to 0.03 vol. fract., the degree of crystallinity and the values of the modules fall, the formation of polyene structures continues, but to a lesser extent, Fig. 6.

The positions of the peaks ν_1 (C–C) and ν_2 (C=C) differ from their locations in PVC and hardly change in comparison with the composite containing 0.005 vol. fract. MB. At the same time, the relative line intensities of about 1131 cm^{-1} become much less than the band intensities of 1522 cm^{-1}, similar to their PVC values. All PVC bands are suppressed. It can be assumed that with increasing content of MB there is a partial aggregation of dye molecules, which impairs the formation of the crystalline phase and, as a consequence, polyene structures. Due to the suppression of these processes, the magnitudes of the dynamic modules decrease. At the same

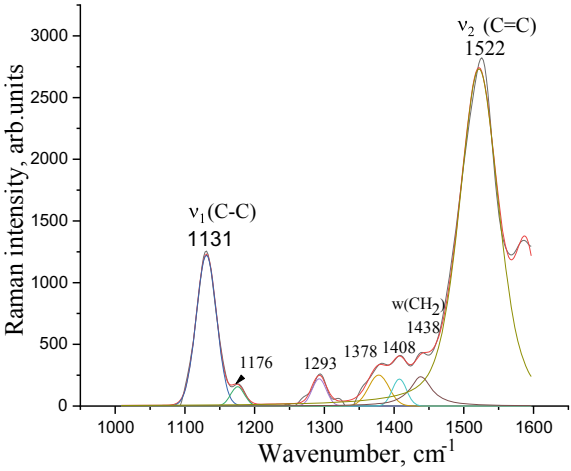

Fig. 6 Raman spectrum for PVC composite with 0.03 vol. fract. MB ($\lambda_L =$ 488 nm, $T = 300$ K, the designations correspond to the oscillation modes and their wavenumbers)

time, the formation of defects with conjugated structure is accompanied by degradation of the polymer molecules and therefore, the bands inherent in PVC are almost non-existent. With the further increase in the MB concentration in the composite with the available crystalline phase, the generation of polyene systems can be expected to continue, but together with the degradation of PVC chains due to the structure dehydrochlorination of the monomer units. Such degradation of the molecular structure while maintaining the crystalline phase and the presence of polyene structures should be accompanied by a drop in mechanical properties, hence a decrease in the dynamic modules responsible for the relaxation of these links. Figure 7 shows the Raman spectra for a PVC composite with 0.05 vol. fract. MB.

It is seen that, while maintaining low-intensity bands in the region of oscillation modes for the C–Cl functional group, bands ν (CH), ν (CH_2) is not observed, which indicates degradation of the molecular structure of PVC. At the same time, the formation of polyene structures continues, as evidenced by intense bands not only of the fundamental oscillation modes ν_1 (C–C) and ν_2 (C=C) but also of the overtones $2\nu_1$, $2\nu_2$, $3\nu_1$ and the folded mode $\nu_1 + \nu_2$. It is necessary to pay attention to the insignificant half-width of the bands of fundamental oscillation modes and to preserve their position in comparison with the placement of these bands in composites with 0.005 and 0.03 vol. fract. The shape and position of the bands indicate the generation of polyene structures with almost the same linear dimensions.

It can be assumed that the simultaneous existence of degradation processes of polymer macromolecules and the formation of polyene systems in PVC-MB composites leads to a minimum value of dynamic modules at a concentration of MB in the composite of 0.05 vol. fract. Further increase in the MB concentration, despite the possible aggregation of molecules, should lead to an increase in the content of polyene structures against the background of degradation of PVC macromolecules.

Figure 8 shows the Raman spectra of PVC composite with 0.07 vol. fract. MB modifier.

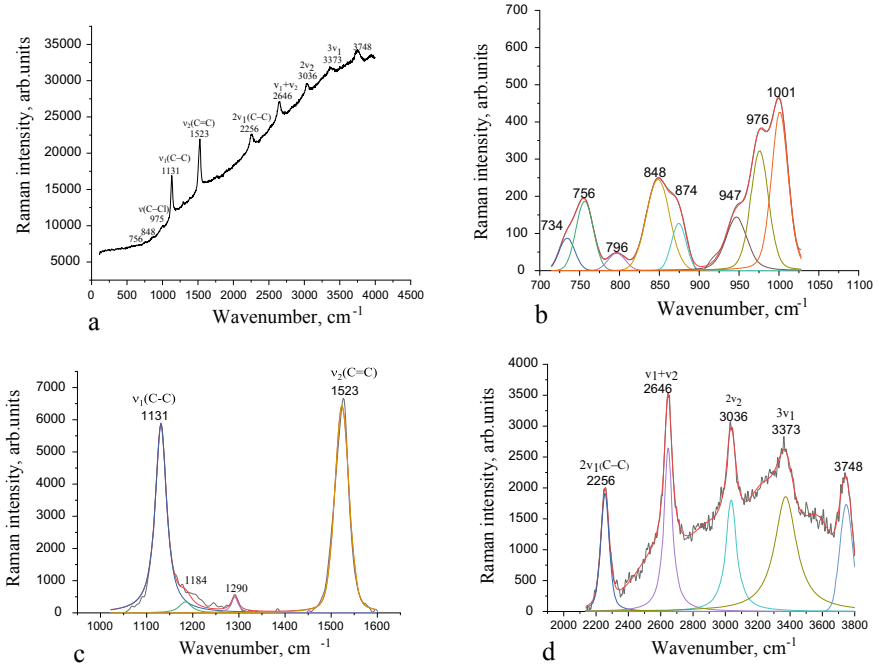

Fig. 7 Raman spectra for PVC composite with 0.05 vol. fract. MB in different ranges **a**–**d** ($\lambda_L =$ 488 nm, $T = 300$ K, the designations correspond to the oscillation modes and their wavenumbers)

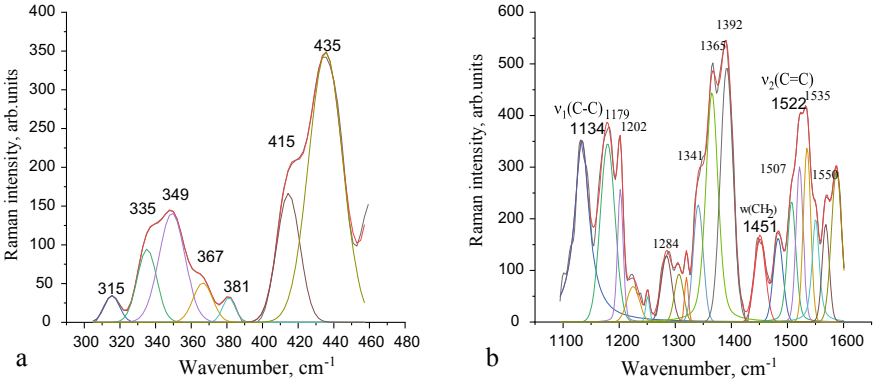

Fig. 8 Raman spectra for PVC composite with 0.07 vol. fract. MB in different ranges **a**, **b** ($\lambda_L =$ 488 nm, $T = 300$ K, the designations correspond to the oscillation modes and their wavenumbers)

Raman spectrum for composite with 0.07 vol. fract. MB undergoes significant changes compared to similar spectra for composites with less dye content. Only bands of deformation oscillation modes of PVC can be observed in this spectrum. Raman spectrum in the range of fundamental modes of polyene structures undergoes significant changes. First of all, there is a sharp increase in the intensity of the bands characteristic of PVC (1179, 1202, 1284, 1341, 1365, 1392, 1451 cm^{-1}). Compared to the CRC spectrum, many of these bands undergo significant shifts compared to their position for pure PVC. In addition, the band of fundamental oscillations ν_2 (C=C) undergoes significant changes. If it was narrow enough for composites with less MB content, then in the case of a composite of 0.07 vol. fract. It is highly expandable, allowing you to select several peaks at 1522, 1535, 1550 cm^{-1}. The considered transformations in the Raman spectrum allow us to point to a significant restructuring of molecular structures in this composite not only of the monomer units of PVC but also of polyene systems. This restructuring of the spectra, on the one hand, is associated with more profound destruction of PVC and the emergence of polyene structures with different numbers of conjugated links in them. The emergence of different polyene systems leads to a sharp increase in dynamic modules while maintaining the degree of crystallinity.

4 Conclusions

Composites PVC-MB dye with increasing modifier content have complex changes in crystallinity and dynamic modulus of elasticity and shear. These changes include the appearance of a maximum degree of crystallinity at a concentration close to 0.01 vol. fract. MB. In composites with MB content in the range of 0.04–0.07 vol. fract. it remains almost unchanged but remains larger than similar value for pure PVC. Maximums also occur for dynamic modules, but they occupy a wider concentration range from 0.005 to 0.04 vol. fract. MB. In addition, at a concentration of MB about 0.05 vol. fract. there is a minimum value of modules. In the composite with 0.07 vol. fract. MB is seeing a noticeable increase in the size of both dynamic modules.

The study of the Raman spectra for pure PVC and composites PVC-MB in a wide concentration range (0.005–0.07 vol. fract.) shows that together with the formation of the crystalline phase in the composites, the generation of polyene structures occurs due to the dehydrochlorination of the monomer units of PVC. Synthesis of polyene systems occurs with the simultaneous destruction of polymer macromolecules. With the increase of MB content in the composites, the degradation of PVC monomer units increases with the restructuring of polyene systems.

An important feature of the effect of a modifier with a conjugated system of chemical bonds in a molecule (MB) on the molecular structure of PVC is the generation in this polymer of polyene structures, which are also characterized by the presence of π-bonds in the structure of PVC macromolecules, creating opportunities for stack interaction between the components of the composite.

References

1. Garnier F (1989) Les polymeres conducteurs. Physics—Uspekhi 157:513–527 (in Russian)
2. Eletskii A (2007) Mechanical properties of carbon nanostructures and related materials. Physics—Uspekhi 50:225–261 (in Russian)
3. Min C, Shen H, Shi Z et al (2010) The electrical properties and conducting mechanism of carbon nanotube/polymer nanocomposites: a review. Polym-Plast Technol Eng 49:1172–1181
4. Lentzakis H, Moghimian N, Saeidlou S, Song N et al (2017) Mechanical, thermal and electrical property enhancement of graphene-polymer nanocomposites. SPE ANTEC Anaheim 2169–2173
5. Lisunova M, Mamunya Y, Lebovka N, Melezhyk A (2007) Percolation behaviour of ultra-high molecular weight polyethylene/multi-walled carbon nanotubes composites. Eur Polymer J 43:949–958
6. Ye Mamunya, Levchenko V, Lebedev E, Boiteux G (2008) Termomechanical and electrical properties of segregated polymer nanocomposites based on polyvinyl chloride and carbon nanotubes. Polimer 30:324–330 (in Ukrainian)
7. Lysenkov E, Klepko V, Yakovlev Yu (2016) Osobennosti perkolyatsionnogo povedeniya system na osnove poliefirov I uglerodnyih nanotrubok s dobavleniem $LiClO_4$. Surface Eng Appl Electrochem 52:324–330 (in Russian)
8. Lysenkov E, Yakovlev Yu, Klepko V (2013) Electric and optical percolation of systems based on polypropylenglicol and carbon nanotubes. Polimer 35:259–264 (in Ukrainian)
9. Lysenkov E, Klepko V (2013) Features of charges transfer in the polyethylene glycol/carbon nanotubes system. J Nano-Electron Phys 5:03052 (in Ukrainian)
10. Gagolkina Z, V. Lobko E, Yakovlev Y, Lysenkov E, Klepko V (2015) Electrical and mechanical properties of the systems based on the cross-linked polyurethanes modified with multiwalled carbon nanotubes. Polimer 37:157–161 (in Ukrainian)
11. Pinchuk-Rugal TM, Dmytrenko OP, Kulish MP, Prylutskyy YuI, Nychyporenko OS, Shut MI, Tkach VM, Shlapatska VV (2017) The electron radiation effect on polyvinylchloride (PVC) nanocomposites with multiwalled carbon nanotubes. Springer Proc Phys 195:757–770
12. Pinchuk-Rugal TM, Dmytrenko OP, Kulish MP, Nychyporenko OS, YuYe Grabovskyy, Strelchuk VV, Nikolenko AS, Shut MI, Shlapatska VV (2015) Structure and electronic properties of nanocomposites of polyvinylchloride with carbon nanotubes under an irradiation. Nanosistemi, Nanomateriali, Nanotehnologii 13:325–336 (in Ukrainian)
13. Zidan HM, El-Ghamaz NA, Abdelghany AM, Lotfy A (2016) Structural and electrical properties of PVA/PVP blend doped with methylene blue dye. Int J Electrochem Sci 11:9041–9056
14. Zidan HM, Abu-Elnader M (2005) Structural and optical properties of pure PMMA and metal chloride-doped PMMA films. Physica B 355:308–317
15. Zidan HM, El-Khodary A, El-Sayed IA, El-Bohy HI (2010) Optical parameters and absorption studies of UV-irradiated azo dye-doped PMMA films. J Appl Polymer Sci 117:1416–1423
16. Kachkovsky AD, Pavlenko EL, Sheludko EV, Kulish NP, Dmitrenko OP, Sendyuk VA, Smertenko PS, Kremenitsky VV, Tarasyuk OP, Rogalsky SP (2019) Composite 'graphene nanoplatelets - fluorine-containing polyamide': synthesis, properties and quantum-chemical simulation of electroconductivity. Funct Mater 26:1–7

Clay, Hydroxyapatite and Their Composites—Brief Review

E. Broda and E. Skwarek

1 Clays

According to the nomenclature of AIPEA (Association Internationale pour l'Etude des Argiles) and CMS (Clay Mineral Society) clay can be defined as naturally occurring material composed primarily of fine-grained minerals. Clay minerals are generally plastic after the appropriate water content addition and will harden with drying or firing. Clays usually contain phyllosilicates, but they can also contain other materials which impart plasticity and harden when dried or fired. The associated phases in clay can include materials which do not impart plasticity and organic matter [1]. The particle size of clay has no upper limit, although some branches set a maximum size—e.g. in pedology the 'clay fraction' refers to the particles smaller than 4 μm, in geology, sedimentology and geoengineering the particles should be smaller than 2 μm, and in colloid chemistry, the limit is 1 μm [2].

1.1 Mechanism of Formation and Spread in Nature

Three mechanisms of clay minerals formation process can be distinguished: detrital inheritance, transformations and neoformations, operating in three geological environments: weathering, sedimentary and diagenetic-hydrothermal [3]. Clay mineral originated by inheritance remain in a natural deposit and originate from the reactions which proceeded during the previous stage of the rock cycle in another area.

E. Broda · E. Skwarek (✉)
Department of Radiochemistry and Environmental Chemistry, Institute of Chemical Sciences, Faculty of Chemistry, Maria Curie-Sklodowska University, Maria Curie-Sklodowska Sq. 3, 20 031 Lublin, Poland
e-mail: ewunias@hektor.umcs.lublin.pl

O. Fesenko and L. Yatsenko (eds.), *Nanooptics and Photonics, Nanochemistry and Nanobiotechnology, and Their Applications*, Springer Proceedings in Physics 247, https://doi.org/10.1007/978-3-030-52268-1_21

Inheritance clays are inert in nature due to slow reaction rates or chemical equilibrium. Clays formed by inheritance can indicate their provenance. Clay precipitated from solution or formed from reactions of amorphous material is clay originated by neoformation. Transformation means that the clay preserves some of its inherited structure intact when chemical reactions were taking place. There are two types of reactions: ion exchange (exchange of loosely bound atom) or layer transformation (an arrangement of tightly bound octahedral, tetrahedral of fixed interlayered cations are relocated and reconstructed) [4]. Determination of clay deposition mechanism provided us with the information about environmental conditions in the area of sediment source (inheritance and transformation mechanism), and changes in the environmental (transformation and neoformation) [3].

Clay minerals occur in a narrow range of geologic conditions. Clay formation is influenced by such environmental factors as soil horizons, continental and marine sediments, geothermal fields, volcanic deposits and weathering rock formation. The erosion as a process of clay formation is based on the transport and deposition of clay and clay minerals produced by eroding continental and marine rocks and soils which is an important part of sedimentary rock formation cycle. The ancient sedimentary rock record is composed mainly (about 70%) of mudstones in which about 50% constituted clay-sized fragments. Nowadays the sedimentary environments containing muds cover 60% of marine continental shelves and 40% of deep oceans basins. Similarly, continental aquatic environments (e.g. lakes, rivers, estuaries and deltas) contain a large abundance of fine-sized particles. Diagenesis when the mineral metamorphose into a more stable form (excluding surface alteration—weathering), is a different clay formation process. The exposition of mineral stable in one depositional environment to another one by burial and compaction is the example of diagenesis. Common silicate materials (e.g. quartz, feldspar, and volcanic glasses), carbonates, nanocrystalline iron oxides and primary clay minerals are transformed into more stable clay minerals by dissolution and recrystallization. Bentonite and Fuller's earth formation occur mainly by diagenesis, however, some deposits can be formed by the hydrothermal process. The weathering process, which also leads to clay formation, involves physical disaggregation and chemical decomposition. Rock weathering depends on the initial type of rock, the amount of water, the temperature, organism and organic material presence and the time of process [4].

1.2 Different Types of Clay According to Their Structure

Due to a small size of clay particles (not exceeding a few micrometres), clay shapes can be studied by means of an electron microscope X-ray diffraction is also used for clay study and identification. The basic organization level of phyllosilicates is the sheets, formed by three ionic planes. Depending on the coordination type (difference in an ionic diameter) three elementary polyhedra can be distinguished. The fourfold coordination determines SiO_4^{4-} or AlO_4^{5-} tetrahedron, the sixfold coordination determines octahedron whose centre is occupied by Al^{3+}, Fe^{3+}, Fe^{2+} or Mg^{2+} cation and

the vertices are formed by O^{2-} or OH^{-} anions. The 12-fold coordination is determined by dodecahedron with the centre occupied by a wide-diameter cation, e.g. K^{+}, Na^{+}, Ca^{2+} and the vertices are formed by the anions O^{2-} of opposite tetrahedral sheets [5].

As a result of several ionic sheets association, there are formed the layers which can be divided into two basic types. In 1:1 layer one tetrahedral and one octahedral sheet are bonded. In 2:1 layers, one octahedral sheet is placed between two tetrahedral sheets. Theoretical structures (without deformations) of both types of layers depend on the hexagonal symmetry of linked tetrahedral and octahedral sheets. The tetrahedra apical oxygen becomes the octahedra vertices. In 1:1 layers, six vertices of the octahedra are formed by four OH^{-} radicals and two apical oxygens of the tetrahedra. In 2:1 layers vertices of the octahedra are formed only by two OH^{-} radicals, as four vertices form the apical oxygens of the two tetrahedral sheets. Because of different dimensions, a and b of tetrahedral and octahedral sheets, linkage of the sheets takes place with deformation of angles and lengths of chemical bonds. The deformations are more significant in dioctahedral than trioctahedral layers. The sixfold symmetry becomes threefold symmetry. The way of 1:1 or 2:1 layers stacking determines which symmetry group phyllosilicates belong to. The two vicinal layers can be stacked in three possible ways:

- no shift, then the symmetry is orthorhombic, pseudohexagonal or hexagonal,
- a:3 shift, the symmetry can be monoclinic, if there are no rotations, or the symmetry can be close to orthorhombic if rotation takes place and the angle β is close to 90°.
- b:3 shift, the symmetry is monoclinic without rotation, or the symmetry can be close to orthorhombic if rotation takes place and the angle α is close to 90° (Fig. 1).

The next organization level of clays are crystals, composed of a varying number of layers. Shape and dimensions of crystalline phases depend on the growth process. The crystal thickness depends on the number of stacked layers. Simple-species crystals are composed of chemically identical layers. Specified composition can be diversified by different stacking modes, which corresponds to the polytypes. In different types of clay observed in the rocks, crystals exhibit different sizes. The statistical distribution of crystal dimensions provides information about the crystallization process. Several crystals can form a mono or polyphase particle (characterized by re-entrant angles) by coalescence or epitaxy on the (001) faces. When crystals or particles are bound by weak bonds or by hydroxide or organic matter deposits, aggregates are formed [5].

1.3 Adsorption Properties. Application of Clays in Industry

Nowadays clays and clay minerals usage is growing due to the development of many branches of industry. The usage of clay is determined by crystallinity and morphological properties. Largely contaminated clays are suitable only for industrial

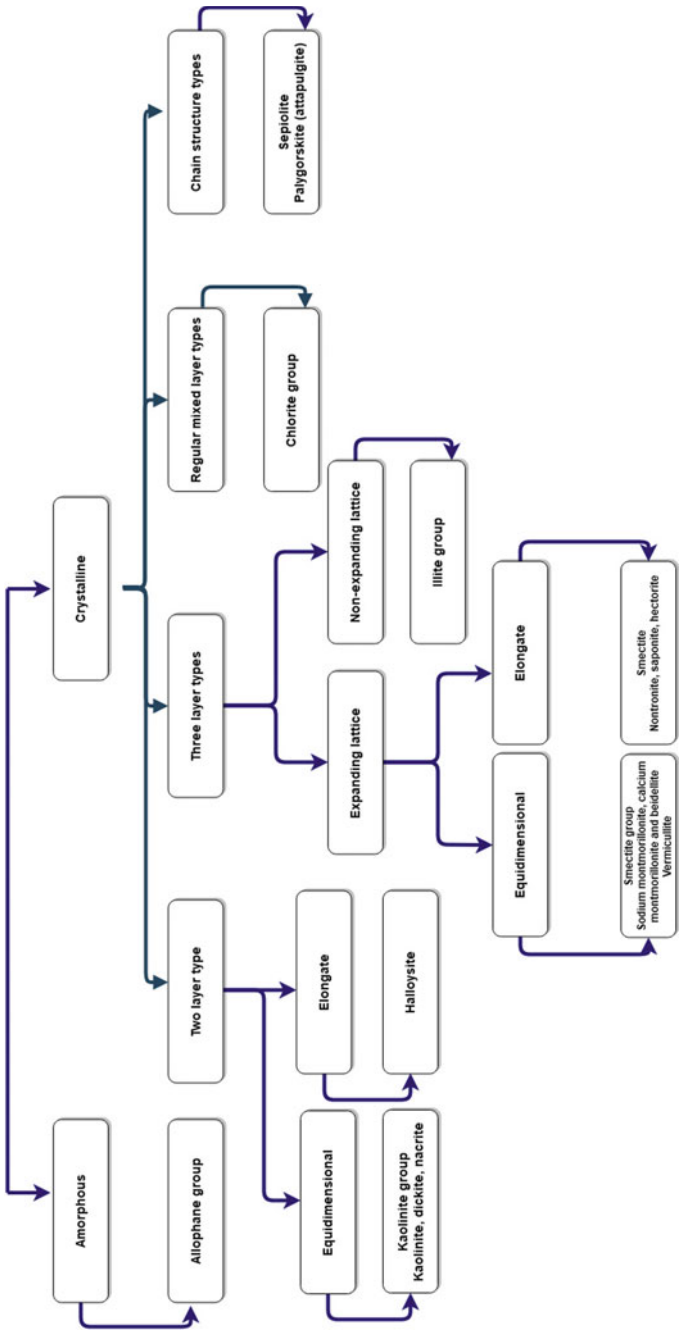

Fig. 1 Classification of the clay minerals [6]

ceramics. Poorly crystallized clays can be used as pottery basic and building materials (e.g. bricks) [7].

Mainly kaolins, bentonites, sepiolites/palygorskite's, common clays and shales are applied in industry. Their physical and chemical properties depend on the fine-grained clay minerals, the type of non-clay minerals, and the presence/absence of organic matter, the type of exchangeable ions as well as soluble salts and clay texture. Clays may be used in either bulk form or after application of various processing techniques (e.g. wet grinding, magnetic separation, flocculation, flotation or treatment with organic and inorganic compounds). These processes remove clay impurities, modify their properties, and increase the mineral content [8].

Wastes management in one of clay application of clays is widely used natural materials for constructing mineral barriers within the engineered sealing layers. Clays are used in in situ geological barriers. Soil barrier constituents in the appropriate amount in clay minerals, which provide low permeability, are used to prevent rapid advective migration of various leachates from waste disposal sites. Clay attracts water, other polar liquids and cations [2]. These properties are exploited in wastes management, e.g. adsorption of heavy metals from wastewaters.

Numerous studies were carried out in order to characterize the adsorptive properties of clays. One of them is the removal of heavy metals, for instance: Ni(II), Pb(II), Zn(II), Cu(II), Cd(II), Hg(I), As(V), Cr(VI), Mn(II), Fe(III), Cd(II), Co(II), Cs(I), Sr(II), Pu(V). [9] Adsorption of different dyes on different types of clays was also studied to examine the possibility of dyes removal from wastewaters. The major classes of acid dyes are azine, xanthene, anthraquinone, triphenylmethane, nitroso and nitro and azo dyes (i.e. acid blue 2, acid red 57, methyl orange, orange (I, II)). The major classes of basic dyes are cyanine, thiazine, acridine, oxazine, hemicyanine and diazahemicyanine (i.e. basic red 46, malachite green, basic yellow 28, crystal violet, methylene blue, basic brown and basic red 9).

Based on the tests it was stated that clays are appropriate adsorbents for dyes removal under proper conditions [10]. The important parameters affecting adsorption on clay minerals are initial solution pH, initial concentration of tested pollution and clay dosage, contact time.

Clays are also used as a host rock and material for engineered barriers. They play an important role in the safest long-term management solution for higher-activity radioactive wastes. Many countries dispose of their radioactive wastes in the facilities at proper depth in stable geological formation. In this application, the important clay properties are very small water movements in clays, diffusive transport, retention capacity, buffer effect, self-sealing capacity, stability, vertical homogeneity, lateral continuity [11].

Besides the application as an adsorbent, clay minerals find many other applications, in which we can distinguish:

- materials based on kaolin used as refractory materials—due to high alumina and silica contents, kaolin should have a low iron and titanium content for proper refractory properties [12]

- animal nutrition (improved feed efficiency comes from sepiolite sorptive, free-flowing, anticaking, non-toxic properties as well as chemical inertness) [13]
- paper industry (kaolin usage in paper filing and coating) [14]
- ceramic and related refractories industry (usage of all clay types)
- plastic industry—as fillers in plastic (kaolin usage in thermoplastics, it improves the strength and electrical insulation of thermoplastics, clays in plastics contribute to the products a smooth surface finishing, cause low water absorption, improve mechanical properties, increase chemical and weathering resistance [15]
- medicine and cosmetics (these applications are described in the next chapter)
- kaolin can be used in gardening as a "natural pesticide"

1.4 Applications in Natural Medicine and Cosmetics. History of Clays Usage

Minerals have been applied for medicinal purposes since the prehistorically times. Homo erectus and Homo Neanderthalensis used ochres in combination with water and muds as the preparation for wounds cure, irritations soothing and skin cleaning. This could be a result of observation of animal's behaviour, which instinctively uses minerals. In ancient Egypt and Mesopotamia, medicinal earth were also used, the example can be the Nubian earth used as an anti-inflammatory or mud materials for mummification of cadavers. In Ancient Greece, muds were used as antiseptic cataplasms to cure skin mal and cicatrises or as a cure for snake bites. Hippocrates and Aristotle classified the medicinal earth, the majority of which are clays. Cleopatra the Egypt Queen used muds from the Dead Sea for cosmetics purposes. Marco Polo described meeting Muslim pilgrims who used "pink earth" in order to cure fever. The first written reports about the use of minerals as a cure come from on 60 BC, Roman Timed, in "De Materia Medica" by Dioscorides. Avicenna and Averroes in the ninth and tenth centuries classified and encourages the use of medicinal muds. Clays were used for malaria cure by Galeno, the Arabic doctor. Later, there appeared "Lapidarios", which partially incorporated the description of minerals used as a part of the therapy. Pharmacopoeia which appeared during the Renaissance also included the texts classifying different minerals for the medical application. The regulations related to medicine production were described. In the seventeenth century, Scientific Academies worked to supply documentary evidence of medical and pharmaceutical advances of mineralogy. In the eighteenth and nineteenth centuries, the knowledge of raw minerals used in medicine and cosmetics developed due to progress in crystallography and mineralogy. Development of chemistry in the twentieth century enabled the synthesis of numerous minerals and had an influence on reduction using natural minerals [16].

Nowadays a lot of minerals are used as active ingredients in pharmaceutical preparations and cosmetic products. Among them, phyllosilicates can be distinguished (smectite, palygorskite, sepiolite, kaolinite, talc, mica). Their therapeutic

activity is determined by their chemical composition and physicochemical properties. For example, minerals composed of non-toxic ions capable of reacting with acids can be used as antiacids, antidiarrhoeics, osmotic oral laxatives and mineral supplements (because of the reaction with gastric acid HCl, cations disposable for absorption or effective in the intestine are liberated). The clays with the high sorption capacity and the large specific surface area can be also used as gastrointestinal and dermatological protectors, anti-inflammatories and local anaesthetics. The minerals with high astringency are used as antiseptics and disinfectants. Minerals with the high refraction index are used as sun protectors. The clays also find the application as bathroom salt and toothpaste ingredients (minerals with an appropriate hardness level). The minerals with the large specific surface area are used in creams, emulsions and powders. The clays as a therapeutic substance can be administered orally or topically [17]. Clays are also used as excipients in pharmaceutical preparations (palygorskite, sepiolite, kaolinite, talc, montmorillonite, saponite and hectorite). The above-mentioned minerals are characterized by structural and physico-chemical properties:

- high adsorption capacity and specific surface area—minerals used as carriers and releasers of active ingredients and flavour correctors
- tendency to take up water and to decompose in acidic media—minerals used as disintegrates and desiccants
- unctuousness—minerals used as lubricants
- thixotropic and colloidal properties—minerals used as emulsifying, thickening and anticaking agents
- slight reactivity under alkaline conditions and plasticity—minerals used as diluents and binders
- solubility water the obtained solution should have osmotic pressure—minerals used as isotonic agents
- opaqueness and colour—minerals used as pacifiers and pigments [18].

2 Hydroxyapatite

With the increasing demand for biomaterials in medicine, their application develops in many areas of science. This contributes to the development of knowledge in the area of the mechanism of biodegradation and corrosion as well as behaviour of such type of synthetic materials in the natural environment and biological one which is the human organism. Special attention should be paid to hydroxyapatite which is a very important ceramic material applied in biomedicine. It is the main component of inorganic bones and teeth constituting about 70 wt.% of bones and as much as 90 wt.% of tooth enamel. Taking into account the fact that the adult bone system constitutes about 30% of the whole body mass, each of us contains much of this material. It constitutes a mineral scaffold for the connective tissue which is responsible for the mechanical strength of bones. Natural hydroxyapatite occurs mainly in sedimentary rocks. However, synthetic hydroxyapatite is the most exploited one. It should be

emphasized that the attempts at its modification and improvement should follow the development of knowledge about its structure, composition and behaviour in colloidal systems. If the notion "phosphate" enters the scientific database, e.g. of Scopus type, the number of literature reports on 07.08.2017 was 1,338,792, biomaterials: 507,323, for "hydroxyapatite 145,302 in the general sense. This is the evidence of great interest in this type of investigations and technological solutions as proved by numerous papers prepared in famous scientific centres at home and abroad. These figures prove that this research subject is still of significant importance.

2.1 Hydroxyapatite (HAP) $Ca_{10}(OH)_2(PO_4)_6$ Synthesis

The next issue of my investigations was the synthesis of hydroxyapatite, modified hydroxyapatite materials and its composites with metal oxides and polysaccharides to obtain materials of the best adsorption properties. Optimization of hydroxyapatite preparation is still an important scientific problem. Hydroxyapatite of the best physicochemical properties and high purity can be obtained by many methods which can be classified as wet [19–24], dry [25], hydrothermal, sol–gel [22, 26], emulsion and those based on co-precipitation [24]. There are also mechanochemical and from natural raw materials methods but they are not applied on a large scale [27–29]. In all methods, the reagents, which are a source of calcium, phosphorus and regulate reaction pH, are used. Wet methods have become more common. The solid product obtained from such reactions was washed with redistilled water to obtain its steady conductivity and dried [30]. The hydroxyapatite crystals obtained by this method can be amorphous or of a small crystallinity degree. The advantage of the wet method is the possibility of introducing sodium, magnesium, potassium ions or carbonate groups into the hydroxyapatite structure. In my studies, there were applied wet methods described in the papers [31–35]. Ca (OH) $_2$ and H_3PO_4 were used for the synthesis of hydroxyapatite. In [32, 35–38] there was also used the wet method but different reagents: calcium acetate $(CH_3COO)_2Ca$ and dipotassium biphosphate K_2HPO_4. The successive synthesis was conducted based on the procedure worked out in the Institute of Surface Chemistry in Kiev [39]. The synthesis reaction proceeded according to the equation:

$$10Ca(NO_3)_2 + 6(NH_4)_2HPO_4 + 8NH_4OH \rightarrow Ca_{10}(PO_4)_6(OH)_2 + 20NH_4NO_3 + 6H_2O$$

The hydrothermal synthesis was conducted in the autoclave at 120–130 °C and under the water vapour pressure in the range 2–85 atmospheres. Using this method it is possible to obtain large, single crystals. In my studies, there was also applied the hydrothermal method of synthesis which proceeded according to the reaction equation: [25, 31, 32, 40–43]

$$6CaHPO_4 \cdot 2H_2O + 4Ca(OH)_2 \rightarrow Ca_{10}(PO_4)_6(OH)_2 + 18H_2O$$

Besides the preparation of hydroxyapatites by different methods, the addition of "foreign" ions, which occur, among others, in biological apatites in the synthesis process became also a subject of my scientific interest. I started to synthesize hydroxyapatite with the addition of Ag, Ca (Ca-HAP), P (P-HAP), carbonates (C-HAP) [44]. $Ca_{10-x}Ag_x(PO_4)_6(OH)_2$ of the silver ions concentrations x_{Ag}= 0.4 x_{Ag} = 0.8; were prepared (Ca/P molar ratio: 1.67 by co-precipitation using $Ca(NO_3)_2 \cdot 4H_2O$ and $(NH_4)_2HPO_4$. The Ca + Ag]/P ratio in the nanoparticles of hydroxyapatite with the addition of silver was 1.67. Carbon apatite was prepared by the wet method in the paper [33]. In the synthesis there were applied the following 1-mole solutions of reagents: $Ca(OH)_2$—calcium hydroxide of 95% purity, orthophosphoric acid H_3PO_4 of 85% purity, calcium carbonate $CaCO_3$ prepared in the Department of Radiochemistry and Chemistry of Colloids. The paper presents the studies carried out using the samples of hydroxyapatite of increased contents of calcium and phosphorus prepared by the wet method [33, 45]. In the case of powders with larger amounts of calcium and phosphorus, the solutions were prepared of two or four times larger concentrations: 0.12 mol/dm^3—K_2HPO_4 or 0.2 mol/dm^3—$(CH_3COO)_2Ca$.

The synthesis of hydroxyapatite composites with metal oxides was conducted by the wet method [38]. In order to obtain samples of synthetic hydroxyapatite aqueous solutions of calcium acetate $(CH_3COO)_2Ca$ and potassium biphosphate, K_2HPO_4 were prepared. The synthesis of hydroxyapatite on metal oxides was performed using the reagents and methods presented in the paper [38]. It was conducted for five oxides: ST20 (20% TiO_2; 80% SiO_2); A300 (100% SiO_2); A90 (100% SiO_2); Al_2O_3 and AST1(89% Al_2O_3;10% SiO_2; 1% TiO_2).

The composite of hydroxyapatite and nanotubes (ordinary and oxidized) was prepared due to the precipitation of Ca $(OH)_2$ and H_3PO_4 in the presence of nanotubes [34]. In the synthesis, there were applied two types of nanotubes (ordinary and oxidized) obtained in the Institute of Surface Chemistry in Kiev.

The samples of nanohydroxyapatite/polysaccharide composites were synthesized by mixing particles of hydroxyapatite and polysaccharides in two stages [46]. In the first stage, the hydroxyapatite synthesis was conducted by the wet method. There were applied the following reagents: $(CH_3COO)_2Ca$ and K_2HPO_4. The second stage included the synthesis of hydroxyapatite/polysaccharides composites. To prepare these composites there were used the following polysaccharides: chitosan; apple pectin APA 103; apple pectin APA 300 FB; sodium alginate. Hydroxyapatite composites were synthesized by mixing particles of hydroxyapatite and polysaccharides in two stages. The polysaccharide solution of the concentration of 2% and 4 wt.% was subjected to the action of ultrasounds in the redistilled water for 3 min. The same procedure was applied for the earlier obtained hydroxyapatite. Then they were mixed in the desired proportions to obtain the hydroxyapatite/polysaccharide 1:1, 4:1 composites. After being mixed they were gently stirred for 30 min. Then the hydroxyapatite/polysaccharide suspensions were placed on the Petri plates and dried at 40 °C.

All hydroxyapatite deposits and its components prepared by me were washed many times with redistilled water to obtain the stable value of supernatant in order to clean it from impurities. To sum up the part of autopresentation on syntheses, it can be stated that the synthesis of hydroxyapatite composite with nanotubes (ordinary and oxidized), metal oxides and polysaccharides is a scientific novelty. The synthesis methods presented above can have significant applications.

Instrumental methods particularly spectroscopic and electrochemical ones are an invaluable tool for studies on metal phosphates with particular consideration of hydroxyapatite and its composites. Combination of various types of radiation with different ways of its interactions with the studied sample makes it possible to obtain information about the studied substance: from its atomic composition through the chemical structure up to that of surface and behaviour in the colloidal systems. The research methods applied in the papers dealing with metal phosphates, hydroxyapatite and its composites can be divided into two groups. The first group includes the standard methods: powder diffraction, electron microscopy, IR spectroscopy and elementary analysis. The second group includes the radioisotope method for measurement of ions adsorption zeta potentials and grains size which is definitely a novelty in this area.

2.2 *Studies of Structure Diffraction of X-Ray Radiation (XRD)*

Hydroxyapatite used practically has a hexagonal structure, though perfectly stoichiometric hydroxyapatite crystallizes in the monoclinic system. $P6_3/m$ is a point group of hydroxyapatite in the hexagonal system and the elementary cell parameters are $a = 0.9423$ nm, $c = 0.6875$ nm, $\gamma = 120°$. A rhombic prism constitutes an elementary cell. In this system the hydroxyapatite structure is as follows: PO_4^{3-} ions in the tetrahedron shape are kept together owing to the calcium ions interlaced between them. Calcium ions occur in two distinctly different positions. Some of them take the Ca(I) position. They are set up precisely in columns and surrounded by oxygen atoms originating from PO_4^{3-} ions. Some of them fill up the Ca(II) position. They form groups in the equilateral triangle shape concentrated around the screw axis. In relation to each other, they are shifted by 60° and surrounded by oxygen atoms with PO_4^{3-} ions. Figure 2 presents the orientation distribution of calcium atoms. The OH^- groups are situated on the screw axis in the plane of triangles formed by calcium. Those in the vicinity are reversible towards each other [42, 43]. Stoichiometric hydroxyapatite crystallizes in the monoclinic system in the spatial $P2_1/b$ group. A cube is an elementary cell and its parameters are $a = 0.9421$ nm, $b = 2a$, $c = 0.6881$ nm, $\gamma = 120°$. In this form, hydroxyapatite is thermodynamically stable even at room temperature. Despite that, it occurs occasionally because even slight departure from stoichiometry results in crystalline structure change. The main difference between

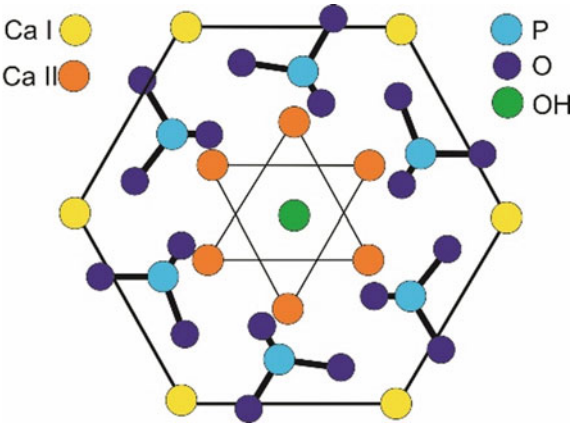

Fig. 2 Distribution of atoms in hydroxyapatite crystallizing in the hexagonal system

the monoclinic and hexagonal forms of hydroxyapatite consists of a different orientation of hydroxyl groups. In the monoclinic HAP, all groups in a given column are one direction oriented but in the next column, the direction is a reversal, etc. They are shifted, positioned either above or below the plane of triangles built of calcium atoms [42].

The diffractogram of pure hydroxyapatite presented in my papers indicate that the samples are of crystalline form as evidenced by the following peaks and their intensities: 25.75–40%; 32–100%; 34; 15–25%; 39.85–20%; 46.85–30%; 49.5–30% [32, 41, 42]. Based on the obtained results the crystallites size was calculated in some papers being, e.g. 36, 48.4, and 28 nm depending on the preparation method [32]. As follows from the size of crystals the hydroxyapatite molecules are composed of an enormous number of crystals which join to form a porous structure. One case in which the adsorbed ions built into the hydroxyapatite structure were Zn(II) ions and new crystallographic forms of zinc phosphate were created [31]. In the paper on cadmium adsorption on hydroxyapatite the results concerning the elementary structure of the crystalline cell were presented based on the results of XRD analysis: hydroxyapatite $a = 9.44038$ nm, $c = 6.87567$ nm [36]. The XRD studies of the hydroxyapatite sample with Cd(II) ion adsorbed from the solution show significant changes of crystalline cell parameters due to the Cd(II) ions adsorption on the surface of the hydroxyapatite sample. The crystal sizes determined by means of the Scherer method from the XRD data show that the molecules are composed of small crystals. The measurements method which is the laser diffraction shows larger molecules which could be formed due to dissolution, precipitation and their aggregation.

The cations smaller than Ca and low concentrations of slightly larger cations are replaced in CAI where interactions are stronger and larger cations should be placed in the CaII position even at high concentrations. The Sr^{2+} ions (radius 0.12 nm) can replace the Ca^{2+} ions (radius 0.099 nm) in the hydroxyapatite structure in the case of CaI and CaII substitutions. The Sr^{2+} ions are better substituted in the place of CaII but at low concentration, they are more often placed instead of CaI [39, 47].

The results of XRD investigations can contribute to understanding the BSA (bovine serum albumin) on hydroxyapatite [35, 48]. Adsorption of negatively charged BSA can proceed on different crystalline planes of hydroxyapatites depending on the synthesis method. The results indicate that hydroxyapatites richer in calcium ions attract better acidic, negatively charged albumins because they are adsorbed by the electrostatic attraction force as confirmed by the thermal studies.

In the paper [33] based on the comparison of the results obtained by the XRD method and the library of the apparatus data in both cases, the peaks characteristic of hydroxyapatite were observed. Moreover, the second phase which was calcium carbonate was found in the hydroxyapatite obtained with the concentration of carbonates. The sample contained 72.3% of hydroxyapatite and 27.7% of calcium carbonate. The crystallites size calculated from the results of X-radiation diffraction, based on the Rietveld line profile was: HAP = 18 nm, HAP + carbonates = 16.32 nm, $CaCO_3$ = 276.8 nm. Incorporation of carbonate ions into the crystalline structure of hydroxyapatite resulted in a slight decrease of crystallites size.

The peaks characteristic of fine—crystalline form of hydroxyapatite are presented in the paper [45]. Based on the XRD analysis it was found that after uranyl nitrate adsorption on the hydroxyapatite surface there is formed a new compound which is hydrated calcium uranyl hydroxyapatite $Ca(UO_2)_2(PO_4)_2$, $(H_2O)_{11}$ amounting to 68.9% and hydroxyapatite constitutes 31%. The formed deposit is more stable in the acidic and inactive media and proves the possibility of hydroxyapatite application for removal of U (VI) from aqueous solutions. The HAP-P/U(VI) sample is of low crystallinity, amorphous also after U(VI) ions adsorption. In the other sample HAP-C/U (VI), a new compound 51% of $CaCO_3$ and 47% of HAP were formed on the initial sample surface due to adsorption. The size of crystallites calculated by means of the

Scherer method was as follows: HAP = 20 nm; HAP-P-impossible to determine; HAP-C = 22 nm; HAP/U(VI) = 13.7 nm; HAP-P/U (V) - impossible to determine, HAP-C/U(VI) = 11 nm.

The paper, written for the Willey publishers, shows that the peaks characteristic of hydroxyapatite overlaps those with inbuilt Ag^+ ions independent of the silver content (0.8 Ag, 0.4 Ag) and a too-small amount of silver may not be responsible for differences [44]. It should be stressed that the studied samples are fine crystalline. Besides the crystalline phase of hydroxyapatite, no others were found for these samples. The size of crystallites calculated by the Retvield methods is HAP = 31.3 nm, HAP/0.8Ag = 35.56 nm, HAP/0.4Ag = 33.2 nm so they are very similar. The diffractograms obtained after Ag(I) ions adsorption on pure hydroxyapatite indicate something quite different that is the presence of additional peaks, in the case of HAP/Ag 58.1% of the surface is silver phosphate and 41.9% is hydroxyapatite. The size of silver phosphate crystallites is 79.5 nm and that of HAP is 31.3 nm.

The results published in the paper prove the fine—crystalline structure of hydroxyapatite, differences in the size of crystallites and changes due to the presence of two kinds of carbon nanotubes. The oxidized nanotubes possess mainly hydroxyl groups in the surface layer containing oxygen and are characterized by lower concentrations of carboxyl and carbonyl groups [34].

The crystalline structure was analyzed also for hydroxyapatite composites with oxides [38]. The samples ST20, A300, A90 are amorphous but Al_2O_3 and AST1 are crystalline. The composites formed from the combination of hydroxyapatite and a suitable amorphous oxide are ST20/HAP, A300/HAP but the crystalline ones are A90/HAP, Al_2O_3/HAP, AST1/HAP. The diffractograms have very wide peaks which point out that the powder molecules are small and not fully crystallized. The presence of low crystallinity or amorphous hydroxyapatite can be favourable for some applications of biomaterials.

3 Composites of Clays and HAP

3.1 Clays

Clays and clay minerals are widely used materials in the industry, especially as adsorbents. A lot of studies were carried out to modify clay minerals obtaining composites and improve their surface properties. The first instance is the polymer-clay used in the removal of inorganic and organic pollutants from aqueous solutions. This kind of composites can be synthesized in three different ways: in situ polymerization, when a monomer is used as a mean for the clay (e.g. polypropylene)) dispersion; dispersion in solution, when the clay is exfoliated in a single layer using a polymer dissolved in solvent (water-soluble polymers are particularly used, e.g. polyvinyl alcohol); or intercalation in the molten state, when the clay is mixed with the molten thermoplastic polymer (e.g. polycaprolactone or thermoplastic polyurethane) matrix [49]. An example of a natural polymer used in the clay composites is a starch. After application the clay–starch composites as the filler, the paper strength has improved over 100% compared to the untreated clay at 20–30% clay loading [50]. The other kind of clay composites is clay–carbon nanocomposites. They can be synthesized during the hydrothermal carbonization of biomass, and find an application as adsorbents in the environment protection [51].

Of the clay–metal oxide nanocomposites, one can distinguish composites with iron oxide, whose advantages, besides nontoxicity and high affinities for pollutants, are superparamagnetic properties, enabling on the separation of the adsorbent through the external magnetic field [51]. More specific modification is the titanium-pillared clay (Ti-PLC) impregnated with potassium iodine synthesized to remove elementary mercury Hg^0 the larger BET surface area [52].

3.2 Hydroxyapatite

Hydroxyapatite is used as a biomaterial for orthopaedic and dental applications because of its chemical similarity to the bones and bioactive properties. Hap should

be mixed with other components to create a composite due to Hap reduced resistance. An example of such composite is that of Hap and stainless steel [53] or Titanium-Hap composite [54], Magnesium/Hap composite [55], Chitosan-Hap composite [56], polyethylene-Hap composite [57]. The potential in mimicking and replacing the bones is also exhibited by the Hap-collagen composite, both components are already used separately in bone tissue repair [58]. The other example of Hap composite is the graphene-based HA composite fabricated as powders, coatings and scaffolds used for orthopaedic applications [59].

3.3 Hap/Clay Composites

The research on the composite clays and hydroxyapatite is in the early stage of development but that kind of composites can also find different applications. Pazourková et al. prepared the composites, where montmorillonite and vermiculite were used as a matrix for preparation of HAp by two methods: the wet precipitation with mixing and ultrasound treatment. The obtained composites were carefully tested [60]. Nasir et al. tested the possibility of using the composites of Trong clay/Hap for the fabrication of bone tissue scaffold by two methods: the solvent casting/particulate leaching method and the indirect three-dimensional printing method. However, only the latter method was appropriated to fabricate tissue scaffolds [61]. Broda et al. synthesized and tested the properties of white clay/Hap composites and proved that the composites usually have properties intermediate between Hap and white clay [62]. Hokkanen et al. worked with the substances composed of Hap, bentonite clay and nanocellulose. They showed the possibility of applying the composite for Cd^{2+}, Ni^{2+} and PO_4^{3-} adsorption from the contaminated water [63] Ersan et al. applied the HAp/clay composite for tetracycline removal from aqueous solutions [64]. Bhowmick et al. proposed that organically modified montmorillonite clay supported chitosan/hydroxyapatite-zinc oxide nanocomposites has the potential to be applied in bone tissue engineering [65]. Thus, based on the experiments it can be stated that the composites of clays and hydroxyapatite are a promising material to be applied for adsorbents or in bone engineering [66–68].

4 Conclusions

The chapter has been devoted to nanomaterials, with the special focus on clay, hydroxyapatite and their composite in the nanometer scale. The synthesis routes, properties, and the most common applications in the fields were discussed.

The presented topic is very interesting and quite new. Up to now, clay has been well discussed in the literature but not the clay composite with hydroxyapatite. However, a still of research has to be carried out to fill a big gap in the area of modern nanotechnology, finding applications in many fields of science and industry. Nanotechnology

employing the nanomaterials: clay, hydroxyapatite and their composites is a very broad field of science, and many of its interesting aspects were omitted in this chapter. This was due to the fact that they were not directly connected with the discussed topic.

This short review presents the information on clays, hydroxyapatite and their composites. A particular emphasis is made on: mechanism of formation and spread of clay in nature; different types of clay according to their structure; adsorption properties, application of clays in the industry; application in natural medicine and cosmetics; the history of clays usage; hydroxyapatite application, synthesis and structures methods as well as and Hap/clay composites. This chapter can be treated as a source of collected documents, devoted to the development of modern nanotechnology, which can be useful for people interested in this area, particularly in nanomaterial's (clay, hydroxyapatite and their composites) and their applications in different fields.

References

1. Guggenheim S (1995) Definition of clay and clay mineral: joints report of the AIPEA nomenclature and CMS Nomenclature Committees. Clay Min 43(2):255–256
2. Bergaya F, Theng BKG, Lagaly G, (Eds) (2006) Development in clay science. Handbook of clay science, Elsevier, Amsterdam, ISBN: 9780080441832, 9780080457635
3. Eberl DD (1984) Clay mineral formation and transformation in rocks and soils. Phil Trans R Soc Lond A 311:241–257
4. Mukherjee S (2013) The science of clays: applications in industry, engineering, and environment. Springer Netherlands, pp 250–253, ISBN: 978-94-007-6682-2, 978-94-007-6683-9
5. Meunier A (2005) Clays. Springer, Berlin Heidelberg, pp 1–105, ISBN 978-3-540-27141-3, 978-3-540-21667-4
6. Murray HH (2006) Applied clay mineralogy. Occurrences, processes and applications of kaolins, bentonites, palygorskitesepiolite, and common clays. Elsevier Science, pp 7–31, ISBN: 9780444517012, 9780080467870
7. Hussin A, Rahman AHA, Ibrahim KZ (2018) Mineralogy and geochemistry of clays from Malaysia and its industrial application. IOP Conf Ser Earth Environ Sci 212(1):012040
8. Christidis GE (2013) Assessment of industrial clays. Dev Clay Sci 5:425–449
9. Uddin MK (2006) a review on the adsorption of heavy metals by clay minerals, with special focus on the past decade. Chem Eng J 308:438–462
10. Kausar A, Iqbal M, Javed A, Aftab K, Nazli ZH, Bhatti HN, Nouren S (2018) Dyes adsorption using clay and modified clay: a review. J Mol Liq 256:395–407
11. Norris S (2017) Radioactive waste confinement: clays in natural and engineered barriers—introduction. Geol Soc 443:1–8
12. Moreno-Tovar R, Pérez-Moreno F, Arenas-Flores A, Romero-Guerrero LM (2014) Thermal behaviour, chemical, mineralogical and optical characterization of clays (Kaolin) for industrial use as refractory material. Adv Mater Res 976:174–178
13. Galan E (1996) Properties and applications of palygorskite-sepiolite clays. Clay Miner 31:443–453
14. Kogel JE, Trivedi NC, Barker JM, Krukowski ST (2006) Industrial minerals & rocks: commodities, markets and uses. 7th ed, Society for Mining, Metallurgy and Exploration, pp 390–398
15. Mekhemer WK, Abou El-Ala AA, El-Rafey E (2006) Clay as a filler in the thermoplastic compounding. Molecular crystals and liquid crystal science and technology, Sect A. Mol Crys Liq Crys 354:1: 13–21

16. Carretero MI (2002) Clay minerals and their beneficial effects upon human health. Appl Clay Sci 21:155–163
17. Carretero MI, Pozo M (2010) Clay and non-clay minerals in the pharmaceutical and cosmetic industries part II. Active ingredients. Appl Clay Sci 47:171–181
18. Carretero MI, Pozo M (2009) Clay and non-clay minerals in the pharmaceutical industry: part I. Excipients and medical applications. Appl Clay Sci 46:73–80
19. Knychalska-Karwan Z, Ślósarczyk A, Sobierska E (1994) Hydroksyapatyt HA-Biocer w leczeniu ubytków kostnych przyzębia. Ceramics 46:47–51
20. Szymański A (1991) Biomineralizacja i biomateriały Państwowe Wydawnictwo Naukowe, Warszawa
21. Riman RE, Suchanek WL, Byrappa K, Wei Chen C, Shuk P, Oakes CS (2002) Solution synthesis of hydroxyapatite designer particulates. Solid State Ion 151:393–402
22. Guzman VC, Pina BC, de la Munguia N (2005) Stoichiometric hydroxyapatite obtained by precipitation and sol gel processes. Rev Mex Fis 51:284–293
23. Suzuki S, Ohgaki M, Ichiyanagi M, Ozawa M (1998) Preparation of needle-like hydroxyapatite. J Mater Sci Lett 17(5):381–383
24. Dean-Mo L (1996) Fabrication and characterization of porous hydroxyapatite granules. Biomaterials 17:1955–1957
25. Murugan R, Ramakrishna S (2007) Development of cell-responsive nanophase hydroxyapatite for tissue engineering. Am J Biochem Biotechn 3:118–124
26. Sopyan I, Singh R, Hamdi M (2008) Synthesis of nano sized hydroxyapatite powder using sol-gel technique and its conversion to dense and porous bodies Indian. J Chem 47:1626–1631
27. Rhee SH (2002) Synthesis of hydroxyapatite via mechanochemical treatment. Biomaterials 23:1147–1152
28. Sobczak A, Kowalski Z, Wzorek Z (2009) Preparation of HAp from animal bones. Acta Bioeng Biomech 11(4):23–28
29. Sobczak A, Błyszczek E (2009) Kierunki zagospodarowania produktów ubocznych z przemysłu mięsnego. Czas Techn Politechniki Krakowskiej 1-Ch: 141–151
30. Dorozhkin SV (2010) Nanosized and nanocrystalline calcium orthophosphates. Acta Biomater 6:715–734
31. Skwarek E (2014) Adsorption of Zn on synthetic hydroxyapatite from aqueous solution. Sep Sci Technol 49(11):1654–1662
32. Skwarek E, Janusz W, Sternik D (2014) Adsorption of citrate ions on hydroxyapatite synthetized by various methods. J Radioanal Nucl Chem 299(3):2027–2036
33. Skwarek E, Janusz W (2016) the influence of carbonate ions on the structure of the electrical double layer at the interface of hydroxyapatite/electrolyte solution Mater. Sci. Medzigory 22(2):174–178
34. Skwarek E, Bolbukh Y, Janusz W, Tertykh V (2017) Hydroxyapatite composites with multiwalled carbon Nanotubes Adsorp. Sci Technol. 35(5–6):534–544
35. Skwarek E, Janusz W, Sternik D (2017) the influence of the hydroxyapatite synthesis method on the electrochemical, surface and adsorption properties of hydroxyapatite. Adsorp Sci Technol 35(5–6):507–518
36. Skwarek E, Janusz W (2016) Adsorption of Cd (II) ions at the hydroxyapatite/electrolyte solution interface. Sep Sci Technol 51(1):11–21
37. Mostafa NY (2005) Characterization, thermal stability and sintering of hydroxyapatite powders prepared by different routes. Mater Chem Phys 94:333–341
38. Skwarek E, Janusz W, Gun'ko VM, Pakhlov EM, Zarko VI, Gdula K (2016) Characteristics of surface and electrochemical properties of composites with fumed metal oxides and hydroxyapatite. Adsorption 22(4–6): 725–734
39. Janusz W, Skwarek E (2016) Study of sorption processes of strontium on the synthetic hydroxyapatite. Adsorption 22(4–6):697–706
40. Earl JS, Wood DJ, Milne SJ (2006) 2D mapping of texture and lattice parameters of dental enamel. J Phys: Conf Ser 26:2681–2692

41. Skwarek E (2015) Adsorption of Cs^+ at the hydroxyapatite/aqueous electrolyte interface. Adsorp Sci Technol 33(6–8):575–580
42. Skwarek E (2015) Thermal analysis of hydroxyapatite with adsorbed oxalic acid. J Therm Anal Calorim 122(1):33–45
43. Jingbing L, Ye X, Wang H, Zhu M, Wang B, Yan H (2003) The influence of pH and temperature on the morphology of hydroxyapatite synthesized by hydrothermal method. Ceram Int 29:629–633
44. Skwarek E (2016) Application of silver tin research on hydroxyapatite Chapter 10 advanced ceramic materials. WILEY-Scrivener Publishing LLC, USA
45. Skwarek E, Gładysz–Płaska A, Bolbukh Y (2017) Adsorption of uranyl ions at the nano-hydroxyapatite and its modification. Nano Res Lett 12(1): Article number 278
46. Skwarek E, Goncharuk O, Sternik D, Janusz W, Gdula K, Gun'k VM (2017) Synthesis, structural, and adsorption properties and thermal stability of nanohydroxyapatite/polysaccharide composites nano. Res Lett 12(1) Article number 155
47. Boanini E, Gazzano M, Bigi A (2010) Ionic substitutions in calcium phosphates synthesized at low temperature. Acta Biomater 6:1882–1894
48. Zhuang Z, Aizawa M (2013) Protein adsorption on single-crystal hydroxyapatite particles with preferred orientation to a (b) - and c-axes. J Mater Sci Mater Med 24:1211–1216
49. Hernández- Hernández K, Illescas J, Díaz-Nava MdC, Muro-Urista CR, Martínez-Gallegos S, Ortega-Aguilar EE (2016) Polymer-clay nanocomposites and composites: structures, characteristics, and their applications in the removal of organic compounds of environmental interest. Med Chem 6:201–210
50. Yoon SY, Deng Y (2006) Clay-starch composites and their application in papermaking. J Appl Poly Sci 100:1032–1038
51. Sarkar B, Rusmin R, Ugochukwu UC, Mukhopadhyay R, Manjaiah KM (2018) Modified clay minerals for environmental applications. In: Mercurio M, Sarkar, B, Langella A (eds) Modified clay and zeolite nanocomposite materials. Environmental and pharmaceutical applications. Elsevier, pp 113–127, ISBN: 9780128146170, 9780128146187
52. Shen B, Chen J, Yue S (2015) Removal of elemental mercury by titanium pillared clay impregnated with potassium iodine. Micropor Mesopor Mater 203:216–223
53. Poinescu AA, Ion RM (2018) 316L Stainless steel/hydroxyapatite composite materials for biomedical applications. In: Thirumalai J (ed) Hydroxyapatite—advances in composite nanomaterials, biomedical applications and its technological facets. InTech, pp 137–155, IBSN: 9789535138051 9535138057
54. Moonchaleanporn P, Poolthong N, Tongsri R (2015) Sintered titanium-hydroxyapatite composites as artificial bones. Key Eng Mater 659:35–39
55. Aizat MMF, Liyana MRN, Khalijah KS (2018) Fabrication of magnesium-hydroxyapatite composites targeted for biodegradable implant application. AIP Conf Proc 2030:020082
56. Pighinelli L, Kucharska M (2014) Properties and structure of microcrystalline chitosan and hydroxyapatite composites. J Biom Nanobiotech 5:128–138
57. Fang L, Leng Y, Gao P (2006) Processing and mechanical properties of HA/UHMWPE nanocomposites. Biomaterials 27:3701–3707
58. Wahl DA, Czernuszka JT (2006) Collagen-hydroxyapatite composites for hard tissue repair. Eur Cells Mater 11:43–56
59. Li M, Xiong P, Yan F, Li S, Ren C, Yin Z, Li A, Li H, Ji X, Zheng Y, Cheng Y (2018) An overview of graphene-based hydroxyapatite composites for orthopaedic applications. Bioactive Mater 3:1–18
60. Pazourková L, Čech Barabaszová K, Hundáková M (2014) Preparation of hydroxyapatite/clay mineral nanpcomposite. Nanocon 2013:83–89
61. Nasir NM, Khan SF, Baling JS, Roslan MR, Cheng EM, Amin NM, Abdullah MN (2018) Preliminary study of trong clay-HA bone scaffold fabrication using solvent casting/particulate leaching method and indirect 3D-printing technique. J Eng Res Educ 10:83–90
62. Broda E, Skwarek E, Payentko VV, Gunko VM (2019) Synthesis and selected physicochemical properties of hydroxyapatite and white clay composite. Physicochem Probl Miner Process 55(6):1475–1483

63. Hokkanen S, Bhatnagar A, Srivastava V, Suorsa V, Sillanpää M (2018) Removal of Cd^{2+}, Ni^{2+} and PO_4^3 from aqueous solution by hydroxyapatite-bentonite clay-nanocellulose composite. Inter J Biol Macromolec 118:903–912
64. Ersan M, Guler UA, Acikel U, Sarioglu M (2015) Synthesis of hydroxyapatite/clay and hydroxyapatite/pumice composites for tetracycline removal from aqueous solutions. Process Safety Environ Prot 96:22–32
65. Bhowmick A, Banerjee SL, Pramanik N, Jana P, Mitra T, Gnanamani A, Das M, Kundu PP (2018) Organically modified clay supported chitosan/hydroxyapatite-zinc oxide nanocomposites with enhanced mechanical and biological properties for the application in bone tissue engineering. Inter J Biol Macromolec 106:11–19
66. Ambre A, Katti KS, Katti DR (2011) In situ mineralized hydroxyapatite on amino acid modified nanoclays as novel bone biomaterials. Mater Sci Eng C 31:1017–1029
67. Madusanka N, Sandaruwan C, Kottegoda N, Sirisena D, Munaweera I, Alwis AD, Karanaratne V, Amaratunga GAJ (2017) Urea-hydroxyapatite-montmorillonite nanohybrid composites as slow release nitrogen composition. Appl Clay Sci 150:303–308
68. Millot G (1970) Geology of clays: weathering sedimentology geochemistry. Springer, Berlin, Heidelberg, pp 302–322, ISBN: 978-3-662-41611-2, 978-3-662-41609-9

Synthesis of Molybdenum and Tungsten Silicides Nanopowders from Ionic Melts

Arkadii Tretiakov, Angelina Gab, Tetiana Lukashenko, Viktor Malyshev, and Marcelle Gaune-Escard

1 Introduction

Silicon compounds of VI-B group metals belong to an important class of inorganic compounds with a range of valuable properties. Their powders can be converted into construction materials with desired electrophysical, fire resistance, corrosion resistance, and wear resistance properties, which makes them promising inorganic materials for new developing areas of technology.

Disilicides MSi_2 (M = Cr, Mo, W) are the most studied and practically important ones. The most common method for their preparation is synthesis from elementary substances under inert gas atmosphere at temperature 1273–1373 K. Other known methods include thermal reduction by magnesium and aluminum from oxides at temperature 1873–2573 K, chemical vapor deposition of halides, and finally electrolysis of molten salt, which is of the most promising ones [6, 7]. Information regarding obtaining Cr, Mo, and W silicides by electrolysis of molten salts is scarce. Method

A. Tretiakov (✉) · A. Gab · T. Lukashenko · V. Malyshev · M. Gaune-Escard
University "Ukraine", 23 Lvivska St., 03115 Kiev, Ukraine
e-mail: a.tretiakov@meta.ua

A. Gab
e-mail: lina_gab@ukr.net

T. Lukashenko
e-mail: taniainst@gmail.com

V. Malyshev
e-mail: viktor.malyshev.igic@gmail.com

M. Gaune-Escard
e-mail: mgescard@gmail.com

Ecole Polytechnique, CNRS, UMR 6595, Technopôle deChateau Gombert, 5 rue Enrico Fermi, 13453 Marseille Cedex 13, France

O. Fesenko and L. Yatsenko (eds.), *Nanooptics and Photonics, Nanochemistry and Nanobiotechnology, and Their Applications*, Springer Proceedings in Physics 247, https://doi.org/10.1007/978-3-030-52268-1_22

for chromium silicides obtaining in silicate (borate)-fluoride melts is described [3], and for molybdenum silicides obtaining in alkali metal chlorides-fluorides melts[4].

Development of practical applications of method of synthesis by electrolysis of melts was hampered by the data lack on electrochemical behavior of compounds used as sources of metal and silicon. Electrochemical behavior of Na_2MO_4 (MO_3) (M = Mo, W), and also of K_2CrO_4 in molten NaCl–Na_3AlF_6 and of SiO_2 in the same melt, was studied [1, 2, 4].

2 Materials and Methods

For synthesis of Cr, Mo, and W silicides, their oxygen compounds were used dissolved in KCl–KF and NaCl–Na_3AlF_6 mixtures. It enables us to realize large current densities and to use graphite as anode material without risk of anode effect.

To study joint electroreduction of synthesis components, voltammetry method was used. Methodology of current–voltage studies, and also design of electrochemical cell and of electrodes, were similar to those described [1, 4]. Reference electrode was platinum wire immersed into studied melt.

Deposition of fine powders by electrolysis was carried out in a quartz reactor. Anode was graphite crucible MPG-7, and cathode was tungsten rod. Product was extracted together with the working cathode, mechanically separated from it, and ground.

Silicides are separated by consecutive leaching of salts with hot water and with 10% solution of H_2SO_4 heated up to 50–60 °C. Then, precipitate was washed with distilled water, filtered, and dried to constant weight at 100–105 °C.

Bulk properties were determined by analytical methods, and surface ones were controlled by physical methods: X-ray diffraction, thermogravimetric analysis, and low-temperature adsorption of argon. Phase composition of the powders was determined using DRON-2 device and Cu Kα radiation, and specific surface area—by BET method through low-temperature adsorption of argon. Contents of Cr, Mo, and Si, and also of main impurities, were found in powders by atomic absorption spectroscopy method using Pye-Unicam spectrometer; tungsten was determined by the gravimetric method.

3 List of Abbreviations

CNRS the National Center for Scientific Research of the French Ministry of Education and Research.
TG thermogravimetric analysis
DTG differential thermogravimetric analysis
DTA differential thermal analysis.

4 Results and Discussion

4.1 Synthesis of Silicides of Molybdenum and Tungsten

Preliminary experiments on electrolysis of chromium (molybdenum, tungsten) and silicon containing melts make it possible to generalize findings (Table 1).

In current–voltage curves for chloride-cryolite melts, under joint presence of sodium molybdate and silicon oxide, two waves are observed (Fig. 1a). The first of them is caused by electroreduction of molybdenum oxyfluoride complex, and the second one—by oxyfluoride complex of silicon. Difference between half-wave potentials is 0.8–0.9 V. Similar situation is observed in presence of sodium tungstate (Fig. 1b), with the only difference that difference of half-wave potential is 100–150 mV lower. These data confirm that silicides synthesis could be carried out by electrolysis alone in kinetic regime [2].

It causes the following sequence of steps for electrosynthesis of silicides of molybdenum and tungsten: I—deposition of more electropositive metals (molybdenum or tungsten); II—deposition of the second component-silicon-on the surface of Mo or W deposited earlier; III—silicon reaction diffusion into the depth of metal-salt "pear" with formation of silicides phases of different compositions up to higher silicides.

Silicides synthesis process can be described by the electrochemical and chemical (1–4) [1, 2]:

at the cathode:

$$MO_3F_2^{2-} + 6\bar{e} \rightarrow M + 3O^{2-} + 2F^-, \quad (1)$$

$$SiO_2F_2^{2-} + 4\bar{e} \rightarrow Si + 2O^{2-} + 2F^-, \quad (2)$$

Table 1 Electrochemical systems and melt electrolysis conditions for synthesis of VI-B group metals silicides

Electrolyte	Refractory metal containing component	Silicon containing component	U, V	T, K	Cathode product	Literature
Na_2SiF_6 (K_2SiF_6)	Cr_2O_3, Cr fluorides	Na_2SiF_6 (K_2SiF_6)	1.9–2.1	1273	$CrSi_2$	[2]
Li, Na, K/F	Mo fluorides	K_2SiF_6	1.9–2.2	1273	$MoSi_2$	[2]
NaCl–Na_3AlF_6	Na_2MoO_4 (Na_2WO_4)	SiO_2	1.8–2.2	1173	Mo_3Si_5, $MoSi_2$, W_3Si_5, WSi_2	[1, 2]
NaCl–Na_3AlF_6	K_2CrO_4	SiO_2	2.5–3.0	1173	Cr_3Si, CrSi, Al compd.	[2]
KCl–KF	K_2CrO_4	K_2SiF_6 (SiO_2)	3.0–4.0	1173	Cr_3Si, $CrSi_2$	[1, 2]

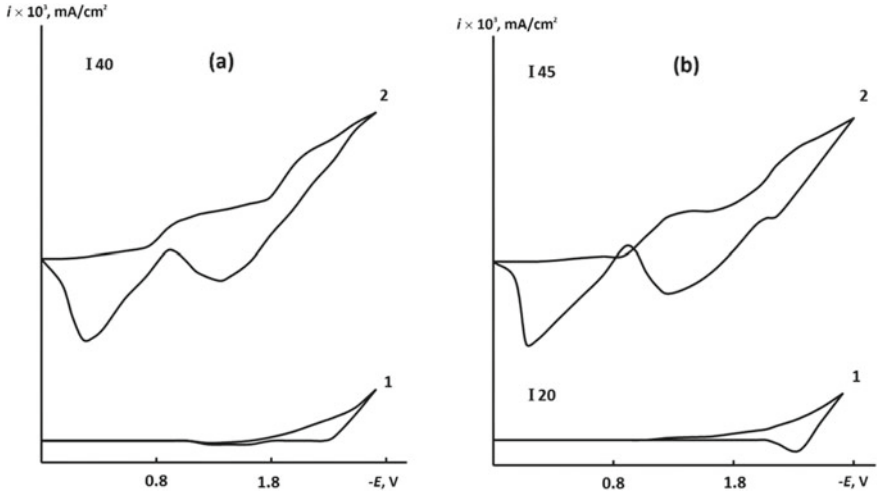

Fig. 1 Voltammograms of melt NaCl–Na_3AlF_6 (50/50 wt%) (1) containing 2.3×10^{-5} mol/cm^3 Na_2MoO_4 and 14.0×10^{-5} mol/cm^3 SiO_2 (**a**) and 2.3×10^{-5} mol/cm^3 Na_2WO_4 and 24.0×10^{-5} mol/cm^3 SiO_2. **b** Polarization rate 0.1 V/s; electrode–platinum-oxygen, $T = 1173$ K

$$\mathrm{M} + \mathrm{zSi} \rightarrow \mathrm{MSi}_z; \tag{3}$$

at the anode:

$$2\mathrm{O}^{2-} - 4\bar{\mathrm{e}} + \mathrm{C} \rightarrow \mathrm{CO}_2. \tag{4}$$

Duration of the first stage of synthesis depends on amount of refractory metal in system and on cathode current density. To obtain molybdenum or tungsten in form of fine powder, current density should be the maximum possible one.

The second stage begins with exhausting of electropositive component. Synthesis of silicides can be carried out only under conditions that molybdenum or tungsten powders deposit at cathode surface in form of metal-salt "pear" of such size and shape which allow it to be held firmly at the cathode without breaking. In case of the metal (W or Mo) powders falling out to the electrolyzer bottom, synthesis components are not in contact with each other, and silicides synthesis does not occur.

Temperature of electrochemical synthesis of molybdenum and tungsten silicides is 850–900 °C. Gain in energy of interaction compared with known synthesis processes is provided by interaction of deposited at cathode fine powders of Mo (W) and silicon at atomic level.

Optimization of process of electrochemical synthesis of silicides of molybdenum or tungsten is reduced to determination of concentration ratio, current density and temperature values, and also of process duration.

Choice of concentration ratios of components was guided by the following considerations. Silicon dioxide has a limited solubility in molten cryolite (8.82 wt%) at 1010 °C [8]. Addition of sodium chloride to cryolite results in lower mixture melting temperature and higher solubility of SiO_2. In eutectic melt (737 °C; 68.5 wt% NaCl and 31.5 wt% Na_3AlF_6), its solubility is about 1.0 wt%. Maximal content of cryolite in binary system NaCl–Na_3AlF_6 which allow to carry out electrolysis at 900 °C is 70 wt% with the SiO_2 solubility in melt of such composition 2.0 wt%. Concentration of sodium molybdate (tungstate) is determined by value of SiO_2 solubility, which provide for stoichiometric composition silicides obtaining. Choosing the concentration of the refractory metal oxysalt, one should also take into account the first stage of electrochemical synthesis. The first stage is formation of metal-salt "pear," and process of deposition of silicon starts after salt exhaustion. Salt concentration in melt (with $i_k = \text{const}$) defines duration of metal deposition at cathode and size of metal-salt "pear." For complete siliconizing of deposited molybdenum or tungsten, content of Na_2MO_4 in melt should not exceed 2 wt%.

Essential role in electrochemical synthesis of silicides of Mo and W is played by temperature and current density values. Lowering the temperature below 850 °C does not ensure completeness of interaction of Mo (W) and Si, and temperature rise above 950 °C reduces stability of metal-salt "pear" due to which silicides are not formed. With optimal melt composition, pure products were obtained with current density 0.5–1.2 A/cm^2 for $MoSi_2$ and 0.5–1.5 A/cm^2 for WSi_2. With $i_k < 0.5$ A/cm^2, obtained product is contaminated with Mo or W. Within the range of current density 0.5–1.5 A/cm^2, with current density increase, dispersity of Mo and W silicides increases.

During electrochemical synthesis of silicides of Mo and W, as well as during direct interaction of simple substances, main process is silicon diffusion through metal layer. In such a case, metal is weakly involved in diffusion, and higher silicides are formed in such a system from lower ones. Therefore, obtained products composition is influenced significantly by process duration. Thus, melt having a composition wt%: NaCl—49; Na_3AlF_6—49.0; Na_2MoO_4—1.0; SiO_2—1.0, at 900 °C and with current density 1.0 A/cm^2, depending on electrolysis duration, different products are produced:

Duration (min)	10	20	30	45	60
Phase composition	Mo	Mo, Mo_5Si_3	Mo_5Si_3, $MoSi_2$	$MoSi_2$	$MoSi_2$, Si

Similar dependence of phase composition on electrolysis duration is observed in $NaCl–Na_3AlF_6–Na_2WO_4–SiO_2$ system. Thus, optimal electrolysis duration is 45–50 min.

Washed free of salts and silicon and dried silicides of Mo and W are fine powders with particle size of 0.1–5 μm. The main parameters characterizing experimental samples are presence of free silicon and impurities content, as well as specific surface area of samples.

According to X-ray analysis data, in some cases products contained free silicon, which was removed by treatment with hot sodium hydroxide solution. Degree of free silicon removal was controlled by X-ray diffraction data (Fig. 2).

Washed free from silicon molybdenum and tungsten disilicides have content of impurities (Si, Na, Al) at level of hundredths of a percent. Specific surface of Mo_2Si and WSi_2 is 6–15 m^2/g.

It is known that Group VI silicides are highly chemically stable compounds, and $MoSi_2$ is the most oxidation-resistant one among oxygen-free compounds. Temperature of beginning of active oxidation of $MoSi_2$ is 1600 °C, and of WSi_2—1400 °C

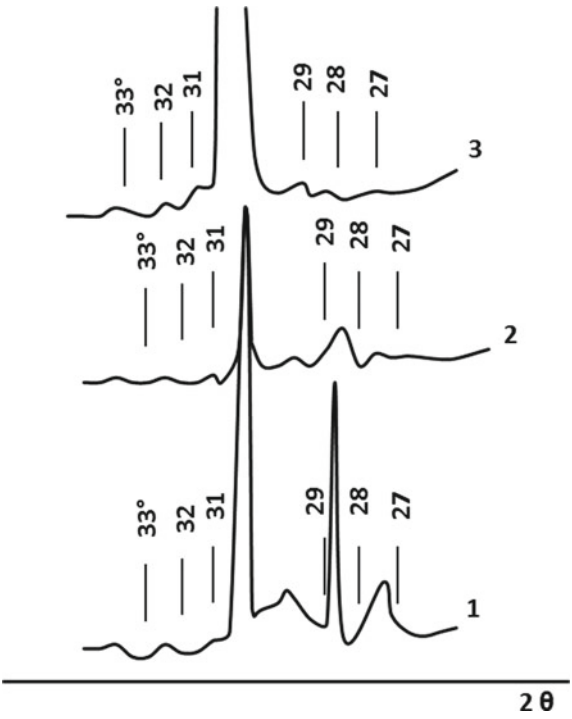

Fig. 2 Diffractograms of powders of Mo_2Si: 1—initial; 2, 3—after treatment with NaOH solution for 20 min and 120 min, respectively

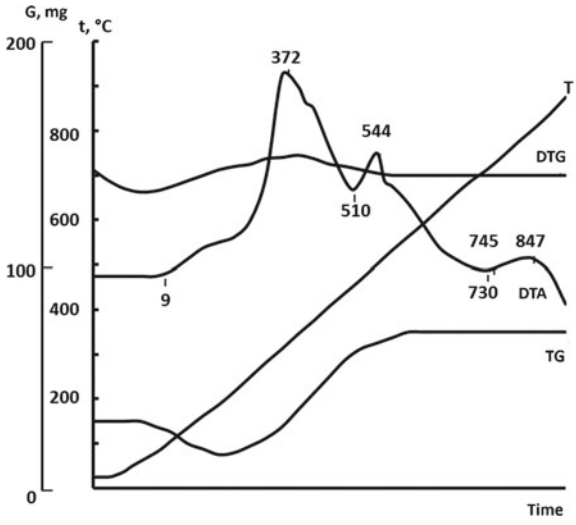

Fig. 3 Derivatograms of heating of fine powder of $MoSi_2$ in air

Murarka [5]. However, fine powders of $MoSi_2$ are oxidized in air at about 370 °C (Fig. 3) to form MoO_2, MoO_3, SiO_2.

4.2 Electrochemical Synthesis of Chromium Silicide

Initially, high-temperature electrochemical synthesis of chromium silicide is carried out from a mixture of molten NaCl–Na_3AlF_6–K_2CrO_4–SiO_2. Voltammetric curves show reduction waves of oxyfluoride complexes of Cr and Si at significantly different potentials (0.7–0.9) V and (1.6–1.9) V, respectively. Depending on composition and electrolysis parameters, Cr_2O_3, higher silicide $CrSi_2$, and silicide Cr_3Si phases were obtained as a mixture with aluminum compounds.

To optimize synthesis conditions for chromium silicides containing no aluminum compounds, electrochemical synthesis was carried out in KCl–KF–K_2SiF_6–K_2CrO_4 system. The resulting current–voltage dependences (Fig. 4) show reduction waves for oxyfluoride complexes of Cr and Si at significantly different potentials.

Depending on electrolyte composition and electrolysis parameters, both individual phases Cr_2O_3, Cr_3Si, and $CrSi_2$, and also mixtures of these phases with low silicon content were obtained (Table 2). Choosing concentrations of CrO_4^{2-} and SiO_2 (K_2SiF_6), it should be taken into account that, at the first stage of electrolysis, Cr_2O_3-salt "pear" is formed which starts to become siliconized during exhaustion of the refractory metal. Unlike high-temperature electrochemical synthesis of silicides of molybdenum and tungsten, during this synthesis, one of components are not deposited in elementary form but rather in oxide form, and the other acts as a reducing agent of the mentioned oxide to form binary compounds.

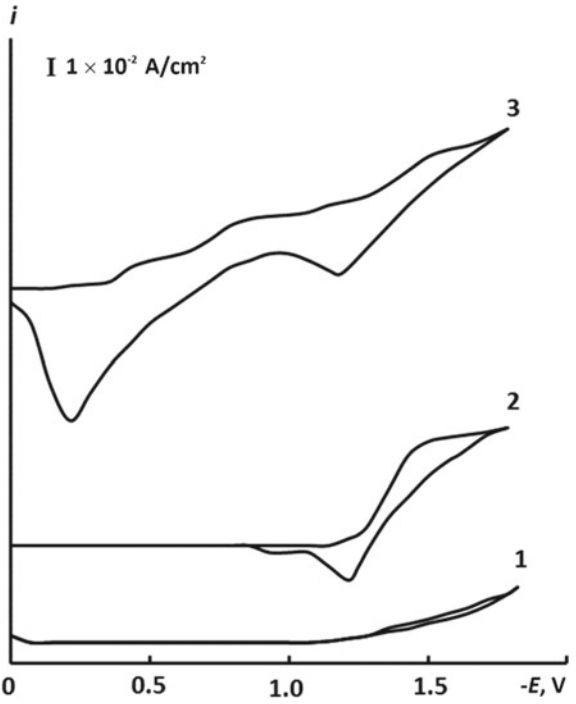

Fig. 4 Voltammograms of molten KCl–KF (1:1)-K_2SiF_6-K_2CrO_4 system. K_2SiF_6: 1–0; 2, 3–2 $\times 10^{-5}$ mol/cm^3. K_2CrO_4: 1, 2–0; 3–5 $\times 10^{-5}$ mol/cm^3. $T = 1173$ K, cathode material-platinum, polarization rate-0.1 V/s

Table 2 Phase composition of electrolysis products of system KCl–KF(25 wt%)–K_2SiF_6(1 wt%)–SiO_2–K_2CrO_4 ($T = 900$ °C, U = 3–4 V)

K_2CrO_4 (wt%)	The duration of electrolysis (min)				
	5	10	15	30	60
0.5	Cr_2O_3	Cr_3Si; Si	Cr_3Si; $CrSi_2$	$CrSi_2$	$CrSi_2$; Si
1.0	Cr_2O_3	Cr_3Si; Si	Cr_3Si; Si	Cr_3Si; $CrSi_2$	$CrSi_2$; Si

5 Conclusions

1. During electrolysis of chromium (molybdenum, tungsten) and silicon containing melts, high-temperature electrochemical synthesis of nanopowders of silicides of chromium, molybdenum, and tungsten was realized.
2. Sequence of stages of electrosynthesis of silicides of chromium, molybdenum, and tungsten was studied.
3. Optimal values of concentrations ratio, current density, temperature, and duration of electrosynthesis were found.

Acknowledgements Authors of the present paper acknowledge support of all the Ecole Polytechnique and the University "Ukraine" staff in conducting scientific researches and writing this paper.

Competing Interests Authors of the present paper have no competing interests.

Funding Authors of the present paper have not used any external sources of funding in addition to regular financing for scientific investigations provided by CNRS and the University "Ukraine."

Authors' Contributions Authors of the present paper have made equal contributions in conducting scientific researches and writing this paper.

References

1. Malyshev V, Gab A (2011) High-temperature galvanic coatings of molybdenum, tungsten, and their carbides from ionic melts. Phys Chem Surfaces Protection Mater 47:525–533
2. Malyshev V, Kushkov H, Shapoval V (2002) High-temperature electrochemical synthesis of carbides, silicides, and borides of VI-a group metals in ionic melts. J Appl Electrochem 32:573–579
3. Molotovska L, Shakhnin D, Podyman O, Malyshev V (2014) Electrochemical synthesis of silicides from molten salts. J Chem Chem Eng 8:845–848
4. Molotovska L, Uskova N, Malyshev V (2011) Electroreduction of silicon ions against the background of the melt NaCl-Na_3AlF_6. Voprosy khimii i khimicheskoy tekhnologii [Prob Chem Chem Technol] 4:75–76
5. Murarka SP (1983) Transition metal silicides. Annu Rev Mater Sci 13:117–137
6. O'Mara WC, Herring RB, Hunt LP (1990) Handbook of semiconductor silicon technology, 1st ed. Noyes Publications
7. Roesky HW (2017) Efficient methods for preparing silicon compounds, 1st ed. Academic Press
8. Zaikov Y, Redkin A, Apisarov A (2013) Silica solubility in molten fluoride-chloride electrolytes. J Chem Eng Data 58:932–947

Regulation of Biological Processes with Complexions of Metals Produced by Underwater Spark Discharge

Anatoly Veklich, Tetiana Tmenova, Oksana Zazimko, Valentyna Trach, Kostyantin Lopatko, Luiudmyla Titova, Viacheslav Boretskij, Yevgen Aftandiliants, Serafim Lopatko, and Ivan Rogovskiy

1 Introduction

Studies of the electric spark dispersion processes have been in the focus of attention for a while. Significant contribution into development of pulse engineering and technology was made in [1–4]. Modern technological units with stabilization of impulse parameters allow to achieve desirable process efficiency [5]. However, implementation of a complex physical phenomenon such as underwater electric discharge requires both the corresponding equipment and the detailed investigation of the process itself.

Electric spark dispersion of conducting materials in liquid media has been extensively studied by another research group [6, 7]. Specifics of this process lie in the possibility of a direct synthesis of colloidal solutions with potential to control the degree of nanomaterials' dispersion. A colloidal solution, sometimes also known as a colloidal suspension, is a solution in which a material is evenly suspended in a liquid. Nevertheless, due to the physical reasons, the dispersed matter tends to consolidate, which does not allow the dispersed powders to remain isolated. Colloidal solutions, in turn, do not have this disadvantage. In case of their inherent stability, colloids ensure the dispersed-isolated state of a solid phase.

Colloidal solutions as nanofertilizers offer a wide range of promising options for improving the quantities and quality of plants and seeds grown for consumption, reducing the costs of production as well as negative impacts on the environment, to achieve sustainable food development. It is well known that there are about two tens

A. Veklich (✉) · T. Tmenova · V. Boretskij
Taras Shevchenko National University of Kyiv, 60 Volodymyrska Street, Kyiv 01033, Ukraine
e-mail: van@univ.kiev.ua

V. Trach
Institute of Physiology of Plants and Genetic of National Academy of Science of Ukraine, 31/17 Vasylkivska Street, Kyiv 03022, Ukraine

O. Zazimko · K. Lopatko · L. Titova · Y. Aftandiliants · S. Lopatko · I. Rogovskiy
National University of Life and Environmental Sciences of Ukraine, 15 Geroiv Oborony Street, Kyiv 03041, Ukraine
e-mail: zazimko@nubip.edu.ua

O. Fesenko and L. Yatsenko (eds.), *Nanooptics and Photonics, Nanochemistry and Nanobiotechnology, and Their Applications*, Springer Proceedings in Physics 247, https://doi.org/10.1007/978-3-030-52268-1_23

of nutrient elements required for growth of plants [8]. They increase plant growth as micronutrients and perform special functions as cofactors for enzymes. Of course, depending on the plant species, they may not require all of these elements and the necessary quantities may also vary.

Because of the small size and physicochemical characteristics of nanoparticles (NPs), such as shape, surface chemistry, electrical charge, and agglomeration, NPs can be synthesized depending on the requirements and needs of each crop. The main characteristics of NPs are their size, shape, superficial charge, chemical composition, concentration, stability, and availability. These characteristics have effects on the properties of the NPs, i.e., they should be taken into account in the exact applications and various uses of NPs. For example, with regard to size, some studies of Ag NPs (spherical shaped) have shown that particles measuring <40 nm can penetrate the skin, with a critical size of 70 nm, so bigger particles have been shown to be less toxic and cause less damage to the skin than smaller particles [9]. Such results suggest size-dependent toxicity and reactivity of smaller NPs. With regard to shape, [10] studied different shapes of Ag NPs with equal surface areas and found that truncated triangular nanoplates with a {111} lattice plane as the basal plane had higher reactivity than NPs with fewer facets, such as spherical or rod-shaped particles. With regard to surface charge, according to [11], a positive charge in NPs may produce severe effects such as cytotoxicity, genotoxicity, and mutagenicity. It was stated in [12] that NPs with a positive charge are more toxic than negatively charged ones. Therefore, this must be taken into consideration as an important factor when NPs are released into the environment.

Over the past decades, worldwide research community has made numerous contributions into better understanding of the plasma–liquid interactions and all the subsequent phenomena. A vast base of theoretical works and topical reviews has been created focusing on classification of plasma discharges in and in contact with liquids depending on their configuration, type of the liquid media, specifics of chemical and physical processes occurring in the plasma–liquid interface, etc. Such global interest is explained by the variety of practical applications and emerging technological opportunities for the plasma community.

Intense UV radiation, electric field, shock waves and active species (OH radicals, atomic oxygen, hydrogen peroxide, etc.) generated in plasma–liquid systems are effective agents against many biological and chemical matters which make liquid plasmas particularly suitable for decontamination and sterilization purposes. Studies of the environmental and biotechnological applications of pulsed discharges in water [13] have demonstrated that bubbling of oxygen through a hollow needle electrode in a point-to-plane electrode system is an effective way to decompose organic materials due to the active species originating from oxygen gas. A unique method for deactivation of microorganisms by means of microplasmas generation in saline solution has been presented in [14]. It was employed *Escherichia coli* to bacteria to investigate the disinfection efficiency of the developed approach. More than 99.5% of *E. coli* was deactivated in 180 s as a result of electrolysis in NaCl aqueous solution. The production of reductive species by high-voltage electric discharges in water and their effectiveness for water purification was qualitatively studied in [15]. It was shown

that the rate of the formation of reductive species in the pulsed streamer discharge increased as the input power to the system increased, offering a possibility that in a mixture of aqueous contaminants some pollutants or a component of certain pollutants could degrade by reductive mechanisms, thereby increasing the degradation efficiency of the process.

On the other hand, another major application of plasmas in and in contact with liquids is nanomaterial (NM) synthesis through plasma–liquid interactions that represents a separate research branch [16]. At present, immersed arc discharge presents one of the most common approaches to NPs synthesis. Otherwise known as the electrical condensation method, it has been further developed, and, it has been successfully used to synthesize carbon nanostructures from nanotubes to complex structures with embedded metals. It was a famous work on synthesis of carbon 'onions' in water [17] that served as a starting point to investigate the possibilities of application of an immersed electric discharge for generation of non-carbon structures, including metals [18], silicon [19], oxides [20], and carbides [21].

While application of plasma–liquid interface for water purification has longer history compared to its use in NM synthesis, some of the reactor configurations reviewed in [22–24] can be as well applicable for NM generation. Additionally, a substantial number of reviews on NM synthesis by using in-liquid plasma techniques have been published recently. These works mostly focus on certain types of plasma, namely microplasmas, electric arc discharge in liquids, glow discharge plasma electrolysis, and atmospheric pressure plasma–liquid interactions. These reports, in combination with general reviews covering a variety of plasma types, provide in-depth information about each plasma type [25, 26].

The arc discharge method in liquid, on the other hand, simply requires a DC power supply and an open vessel full of deionized water, alcohol, or other liquid of a choice. It does not require vacuum equipment, reactive gas, a high temperature furnace, or a heat exchanging system. Consequently, such approach is extremely simple and cheap comparing to laser ablation [27, 28] or chemical vapor deposition techniques [29–32]. Application of an electric discharge in liquid can be characterized by high productivity, relatively low costs, possibility of scaling and performing one-stage synthesis of NMs. However, one of the disadvantages of the electrical condensation method is a generation of NPs with a broad size distribution. At the same time, it is possible to carry out directed synthesis of a variety of NMs by regulating the process of interaction between the medium and the particles formed under the influence of the arc discharge. Moreover, the simplicity of this method allows scaling up for mass production of NPs.

More specifically, the pulsed low-voltage electric discharge immersed in water is used for synthesis of metal colloidal solutions in the field of biology and agriculture [33]. As it was shown, the application of colloidal solutions Mo, Fe, Mo, Cu, Ag, Zn NPs in agriculture and biotechnology has physiological, fungicidal, and bactericidal effect on soil, foliar, seed, crops growth, and grain nutrient enrichment [34–36]. The fungi leaf spot decreases in 2.5–3 times, the reduction on 60–95% of pathogenic microorganisms, and 15–20% yield increasing on winter wheat under

trace amount of nano-active ingredients. NPs application through seed treatment and foliar applications reduced fertilizer rates to 20–30%.

Such idea constitutes the main motivation for this investigation: since main properties of the obtained NPs are formed on the stage of their synthesis, it is reasonable to study the qualitative and quantitative correlations between parameters of the electric discharge plasma and resulting NMs [37, 38]. Taking into account, that the physical state, structure, and morphology of metal particles are directly related to their biological functionality, another, equally important, component of the motivation of our study is to identify the possibility of regulating biological processes with the involvement of metal complexes generated by underwater electric spark discharge. Therefore, this paper deals with complex investigation of peculiarities of metal NPs generation and their application for regulation of biological processes.

2 Experimental Setup Description

2.1 Experimental Arrangement

The volumetric electric spark destruction of metal granules was used to produce the suspensions of nanodimensional metal particles in water. The method consists in simultaneous formation of spark channels in contacts between the metal granules. Due to the spark erosion, the part of metal granules evaporates and, becoming tempered in a liquid, forms fine dispersion fraction of particles. In this study, special thyristor generators of discharge pulses with capacitor stores of energy were used [3, 39] to initiate the discharge between metal (molybdenum, copper, silver, iron, zinc, etc.) granules dipped into the deionized water.

Processing unit for implementation of the electrical spark dispersion regime for synthesis of metal colloidal solutions is shown in Fig. 1. The arrangement consists of impulse generator, discharge chamber, and auxiliary devices for registration of electric parameters, such as Rogowsky coil, voltage divider, and oscilloscope. Simplified schematics of the impulse generator's power circuit can be also seen in Fig. 1. Generator feeds from the single-phase 220 V alternating current network of 50 Hz frequency. The supply voltage is being rectified, filtered, and regulated by phase rectifier, which consisting of power diodes (VD_1 and VD_2), power thyristors (VD_3 and VD_4), and working capacitor C_1. The control board regulates periodical charging and discharging of the working capacitor that has a discretely variable capacity from 25 to 650 μF.

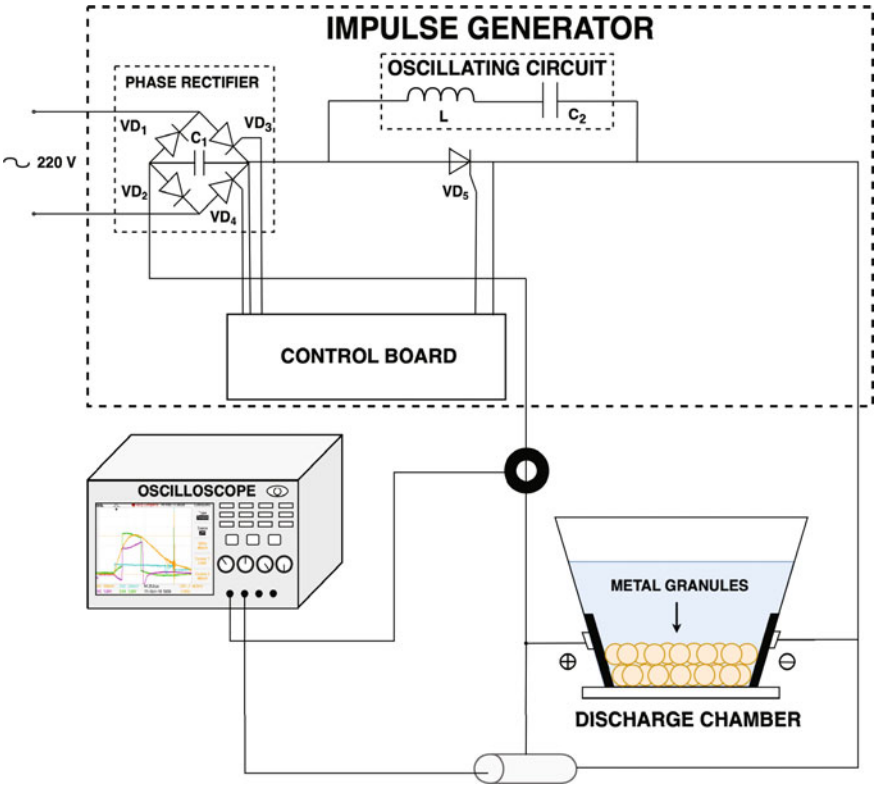

Fig. 1 Experimental arrangement for multiple-pulse underwater electrical discharge investigation

2.2 Plasma Emission Registration

The arrangement for the registration of the electric spark discharge plasma emission is shown in Fig. 2. The setup consists of a discharge chamber, the bottom of which has been adjusted for the spectroscopic diagnostics through the quartz window. The spectrometer used in all the experiments is the high-aperture compact SDH IV spectrometer by Solar LS. The spectrometer is equipped with a four-position manually switch grating turret, consisting of diffraction gratings of 300, 400, 600, and 900 lines/mm. The technical specifications of the spectrometer are presented in Table 1. Plasma emission is registered using all four diffracting gratings. The exposure time for every measurement is 10 ms. The spectrometer was placed below the discharge chamber, with the entrance slit pointed directly at the quartz window in order to increase the possibility of capturing the light from the plasma channels.

The discharge chamber used in the experiments is shown in Fig. 3. It is designed specifically for these experiments and is made of polycarbonate. The outer surface of the chamber's walls is coated with a layer of silver paint and another layer of

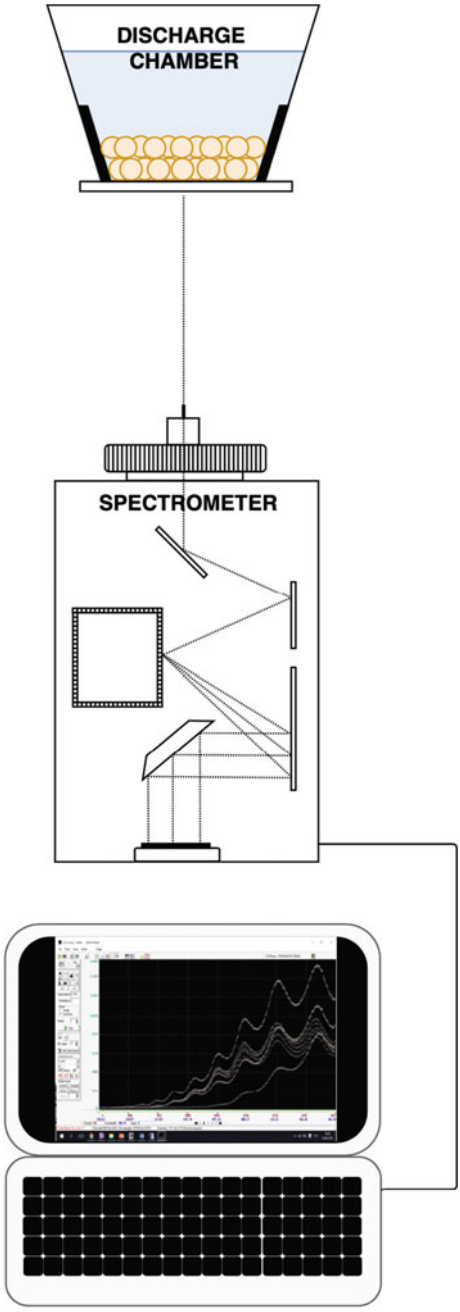

Fig. 2 Experimental arrangement for registration of plasma emission of multiple-pulse underwater electrical discharges

Table 1 Parameters of the spectrometer

Spectral range, nm	200–1100			
Linear image sensor	TCD1304 Toshiba			
Detectable spectral range, nm	200–390	300–600	450–900	600–1100
Diffraction gratings, lines/mm	900	600	400	300
Average linear dispersion, nm/mm	7.0	10.5	15.8	21.1
Spectral resolution (FWHM, average), nm	0.18	0.28	0.42	0.54

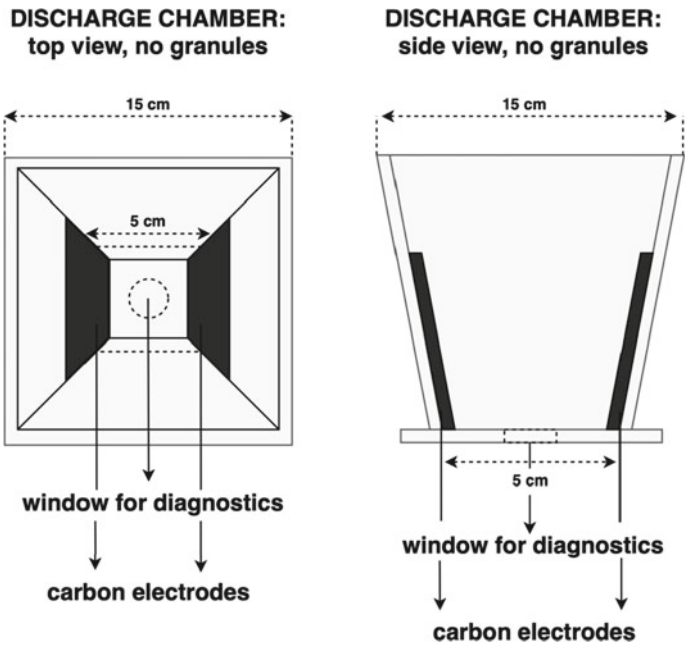

Fig. 3 Discharge chamber for registration of plasma emission of multiple-pulse underwater electrical discharges

black paint on top of it, in order to reduce the dissipation of plasma emission through it. The length of the side of the chamber's foundation is 5 cm, while the length of the top is 15 cm. Main electrodes embedded into the discharge chamber are flat carbon electrodes of 5 mm thickness. Carbon is used in order to avoid the necessity of replacing the main electrodes after every set of measurements.

In order to study the electric spark dispersion of a conducting materials, the layer of metal granules is placed at the bottom of the chamber in quantity of around 100 g. The chamber then is filled with a non-purified water. The average diameter of granule is 1.5 mm. The measurements are carried out involving the granules

of copper, aluminum, molybdenum, chromium, manganese, magnesium, argentum, cobalt, iron, zinc, and silicon.

The plasma emission registration is performed in regime of a constant water flow through the discharge chamber in order to avoid the excessive contamination of liquid with erosion products.

2.3 Electron Microscopy of Metal Nanoparticles

The size, shape, and chemical composition of the particles were determined by scanning electron microscopes Jeol 6490LV, Jeol JSM6360, Hitachi SU8000, or MIRA3 TESCAN. The study of grain and subgrain boundaries, and crystal structure defects were carried out by transmission electron microscope JEM-3010 JEOL with multiscan camera GATAN Orius SC200D. The phase composition, crystal lattice parameters of NPs, and size of subgrains were studied by X-ray diffraction in a monochromatic Cu Kα-radiation on the DRON-UM1 diffractometer. The chemical state of the surface of NPs was studied using X-ray photoelectron spectroscopy (XPS) on EC-2401 spectrometer. Study of the technological parameters' influence on dispersion and morphology of products of metal granules' erosion as a result of local electric spark discharges was performed through control over the discharge circuit's electrical parameters.

3 Results and Discussion

3.1 Peculiarities of Colloidal Nanoparticles Forming

Processes occurring during electric discharge in water have strong influence on the structural and phase composition of NPs, the micelle structure, and electrokinetic potential that further defines the functionality of the obtained colloidal systems. When plasma temperature in the discharge channel increases from 3000 to 8000 K, water vapor dissociates with formation of O_2, H_2, O^-, H^+, OH^-, H_3O^+ that can dissolve in crystal lattice of solid phase or create a layer on surface [6].

Colloidal solutions of metals, which were obtained by electrical discharge treatment, have aggregate stability, biological efficacy, and low toxicity. One of the most important parameters that characterize the agregate stability of the colloidal system is electrokinetic potential, which is approximately 40 mV for silver and copper [40]. Formation of colloidal particles occurs in harsh conditions of temperature—power influence as physical factor. High temperature in the zone of discharge, which is achieved during a few hundreds microseconds, combined with ultra-high-speed cooling and intense hydrodynamic processes significantly determines the kinetics of solid phase formation, which is not typical for equilibrium processes of chemical

synthesis of solid phase. The condensation of solid phase at the end of the plasma channel existence was shown in [40] during thermalization of the plasma discharge at the stage of voltage pulse decreasing.

The channel surface is a zone of most intense heat removal and most likely is the formation of a solid phase by condensing steam. Probably, formed crystals are negatively charged by electrons because of ambipolar diffusion drift to the periphery of the discharge channel. The adsorption leads to formation of the positive ions as layer (Stern layer) on the particle surface and negative counterions as layer (Helmholtz layer) (Fig. 4).

The micelle core and parts of the electrical double layer are formed at the trailing edge of discharge pulse. The disappearance of the gas space and getting of the formed solid phases in the water causes a diffusion layer concentration of ions in solution, degree of hydration, and the rate of occurrence of (layer Gouy).

The value of the diffusion layer will be determined by the dynamic equilibrium adsorption–desorption process, in which counterions adsorption and diffusion layers participate. This stage of the colloidal system formation is finished when micelles

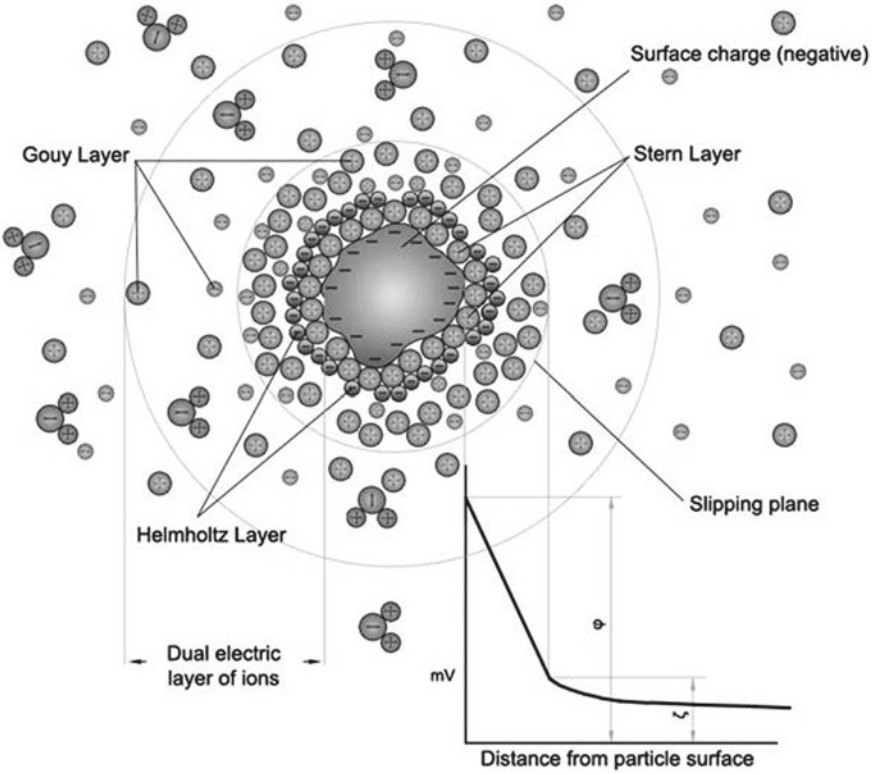

Fig. 4 Construction of the colloidal micelle obtained by electrical discharge method

substantially become electroneutral and characterized by satisfactory aggregative stability. Each metal or combination of metals has specific physical and biological properties, which can be used in biotechnologies. The formation of colloidal system under non-equilibrium conditions with characteristic properties and internal structure will differ from colloids obtained using traditional methods. For this process, brevity discharges and large temperature gradients that determine the intensity and other character of the disperse phase formation are characteristic features. Obtaining thermodynamically stable colloids that is practically impossible for condensation methods (solvent or chemical reactions substitution) to form an insoluble phase of microcrystal becomes possible during electric spark discharge in the water, when a solid phase synthesis from the metal vapor occurs. As a result, the formation of heterogeneous dispersed-isolated systems with satisfactory aggregative and kinetic stability is conditioned by the dimensional parameters of the synthesized solid phase, its structural and phase composition, and kinetics of the surface phenomena.

The obtained results of ζ potential show qualitative composition of adsorbed layer, which along with the aggregate (metal phase) forms a colloidal particle with a corresponding value of electrokinetic potential. It is shown that the magnitude and sign of electrokinetic potential are sensitive characteristics of colloidal systems, and its values for the study of metals vary both in sign and magnitude. Thus, the main condition for the formation of a stable or at least temporarily stable colloidal system is formation of electrical double layer, which is the result of a particle charge screening accumulated by other charged particles (ions) on its surface. The magnitude of ζ potential is directly affected by process parameters and its duration. At the agreed parameters of the process when the highest dispersion (for each metal separately) is reached, both dispersed phase concentration and electrokinetic potential are time functions of electric spark dispersion.

3.2 Optical Emission Spectroscopy of Underwater Discharge Plasma

The emission spectra of underwater electric spark discharge between copper, silver, iron, and molybdenum granules are shown in Figs. 5, 6, 7, and 8, respectively. As one can see, spectral lines of metals and hydrogen are emitted by plasmas. The presence of metal lines in the spectra confirms erosion of granules during discharge and contamination of evaporated metal atoms in the plasma volume of discharge gap. The evaporation and dissociation of water take place due to the plasma heating, which explains the presence of H_α in all the spectra.

Boltzmann plot method was used to estimate temperatures in plasma. The half-width of spectral lines was used to obtain electron densities in the discharge plasma. The excitation temperatures depend on material of granules and power input into the discharge and were in the range of 6500–14,000 K [41]. The electron densities were obtained from the width of H_α and, in the case of copper, were testified by comparing

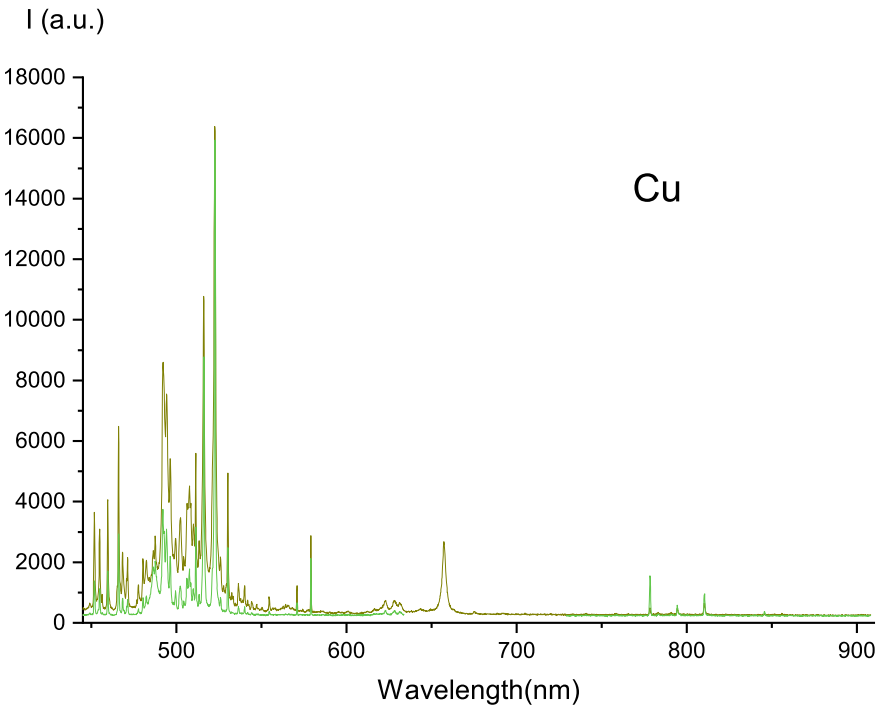

Fig. 5 Optical emission spectra of underwater electric spark discharge between copper granules

with values obtained from the Cu I 515.3 nm spectral line. Typical values of electron densities were in the range of 10^{17}–10^{18} cm^{-3} [41, 42].

We must note that the radiation of atomic and ionic spectral lines in plasma emission of underwater electric spark discharges confirms that metal NPs are condensated from vapor phase (metal and water vapors).

Results illustrate that even with the increase of initial power input of the system, temperature and electron density of the plasma channel do not vary sufficiently staying in the fixed range of values. That might mean that with increase of an input energy, energy dissipates on physical processes other than those related to plasma channel initiation and extension.

3.3 Crystal Structure of Metal Nanoparticles

The combination of intense heat and force action on the metal in the discharge chamber gives possibility during the ultrashort time intervals to obtain nanoparticles with non-equilibrium structure, increased level of free energy, and particles sizes in the range of 20–300 nm (see Fig. 9).

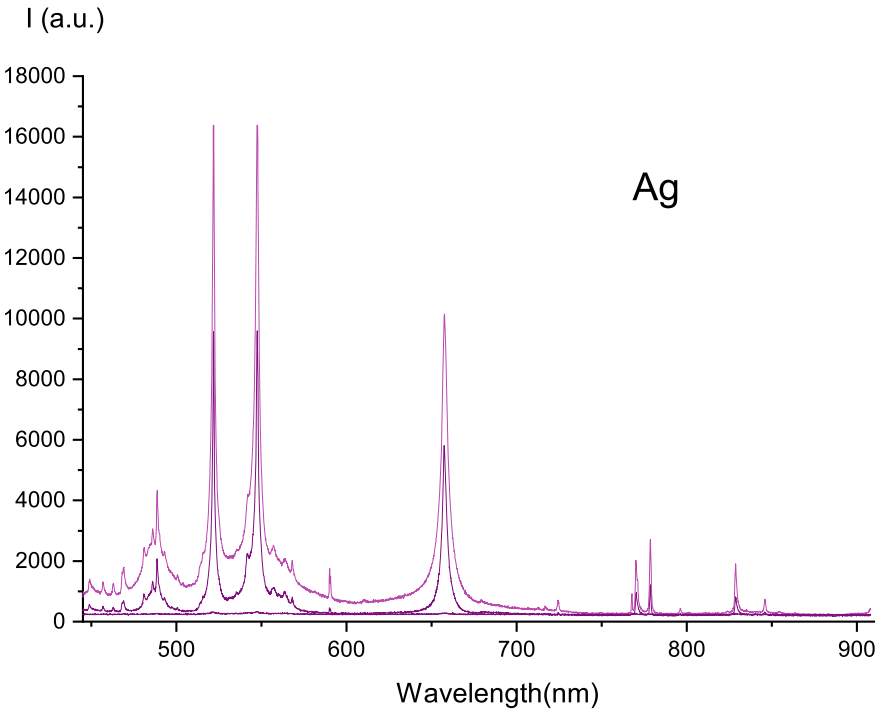

Fig. 6 Optical emission spectra of underwater electric spark discharge between silver granules

Most of the particles have a crystal structure that indicated on their condensation from gas to solid phase. Water was chosen as dispersion environment for nanoparticles due to its adaptability and convenience for future use. In the crystal structure of nanoparticles after spark processing levels of defects are significantly higher than in bulk metals. The high level of dislocation density in the nanoparticles determines their high energy saturation. The nanoparticles with defects in the crystal structure (dislocations, twins, and sources of generation of dislocations) are formed during electrical discharge treatment of metal granules. We can assume that dislocation density can be achieved to the theoretical limit ($\sim 10^{14}$ cm^{-2}) [43, 44], due to the joint action of shock waves, generated in the process of electric spark channel expansion, at the pressure in several hundred atmospheres, and high cooling rate [45].

In Fig. 10 the images of nanoparticles (a, b, e) and substructures of Fe nanoparticles (c, d) are shown by transmission electron microscopy. One can conclude from Fig. 6a, that Al nanoparticle has pronounced ordered (1) and unordered (2, 3) structures within its volume and periphery. Moreover, both of these structures are observed as well within nanoparticle of another elements (e) (e.g., Ag). As one can see in Fig. 10c, metal nanoparticles have a pronounced polycrystalline structure with a developed subgrains surface and available sources of Frank-Reid (4) dislocations ($\sim$10 atomic surfaces) and metastable phases (82% γ-Fe and 18% α-Fe according to [46]). In

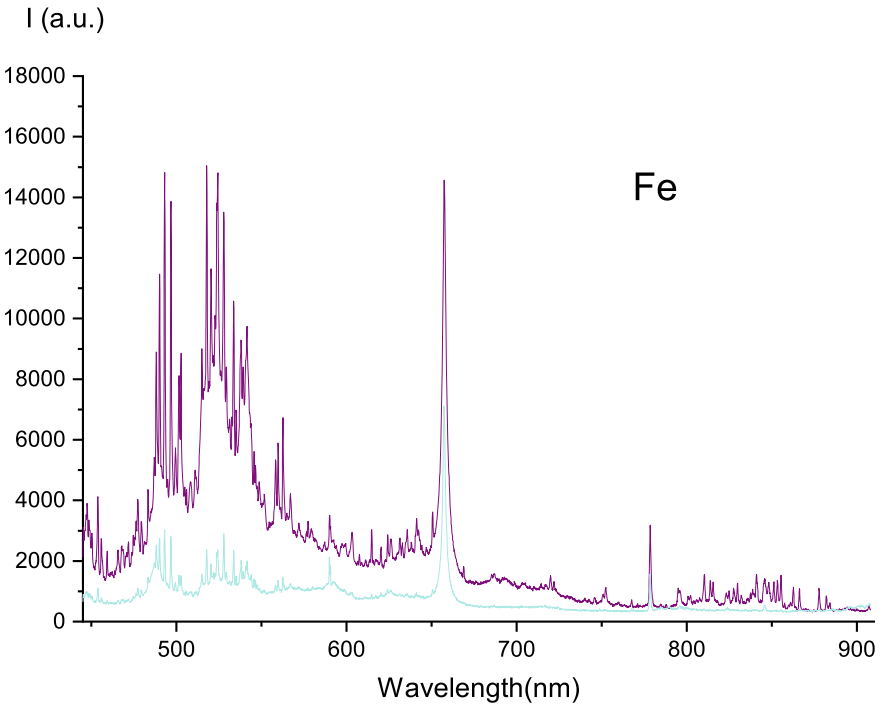

Fig. 7 Optical emission spectra of underwater electric spark discharge between iron granules

Fig. 10d, high-angle boundaries (5) are shown in Fe nanoparticles. Probable outputs of dislocation are located at the nanoparticle surface, which leads to its increased activity (see Fig. 10b). The structures within nanoparticle volume consist of main material (material of granules immersed into the water) and oxygen, originated from water dissociation, which is placed predominantly at the periphery.

3.4 Metal Nanoparticles for Laboratory Biological Testing

The results of the influence of multicomponent colloidal systems on the morphological parameters of the seedlings of crops give only a comparative assessment, since in the conditions of laboratory experiments do not take into account the developmental stages and stages of organogenesis, when the plants need certain composition of microelements. Thus, it is almost impossible to give an unambiguous assessment of the effectiveness of metal complexes in the conditions of short-term experience. We must note that in the presence of the second metal, the activity of the first one may change, that is, the antagonism or synergism of the microelements can be realized (Fig. 11). However, the data obtained indicate the preferential stimulation of growth

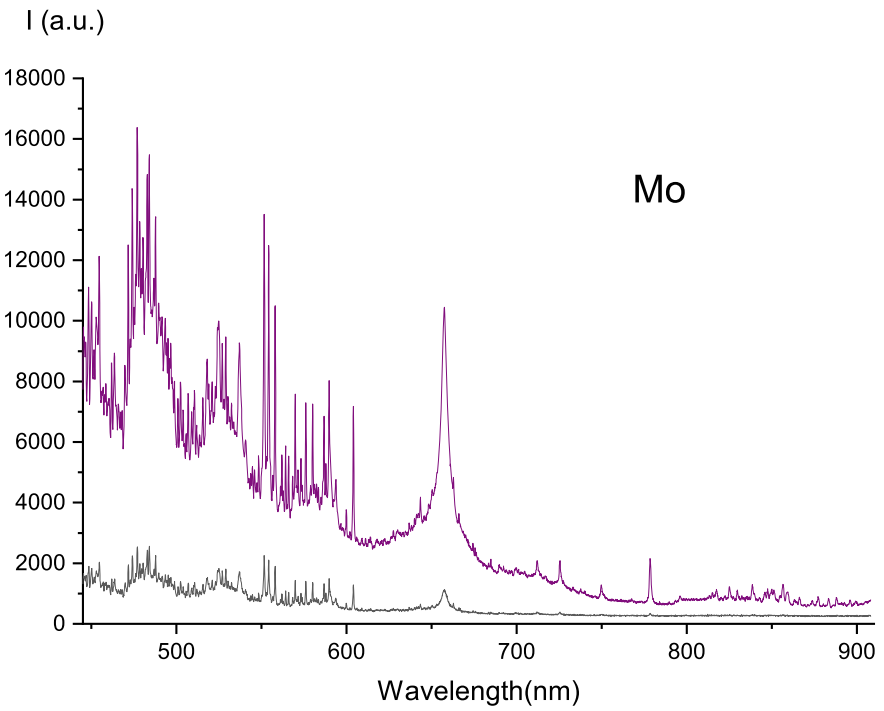

Fig. 8 Optical emission spectra of underwater electric spark discharge between molybdenum granules

processes in the studied cultures, which can be caused by purely physical factors of influence in addition to the probable participation of selected biogenic metals in plant-determining biochemical processes. In particular, at the stage of germination of seeds on the background of colloidal solutions, there is intense swelling of the seeds during one–two hours of exposition (Fig. 12).

It was shown earlier [47] that colloidal solutions of metals do not have a noticeable electrical conductivity, which characterizes the presence of a sufficient number of metal ions as current carriers. This fundamentally differs them from solutions of metal salts that have electrical conductivity, which is several orders of magnitude higher.

It must be noted, with the same concentration of the substance, partial concentration of the colloidal form in comparison with the salt will be several orders of magnitude lower, according to the comparison of the sizes of the ionic radius and the radius of a single particle corresponding to 20–50 nm. The diffusional mobility of such particles will decrease with increasing size of the dispersed phase, according to the Stokes–Einstein equation (1) and Einstein–Smoluchovsky:

$$D = \frac{RT}{N_A 6\pi\eta r} \tag{1}$$

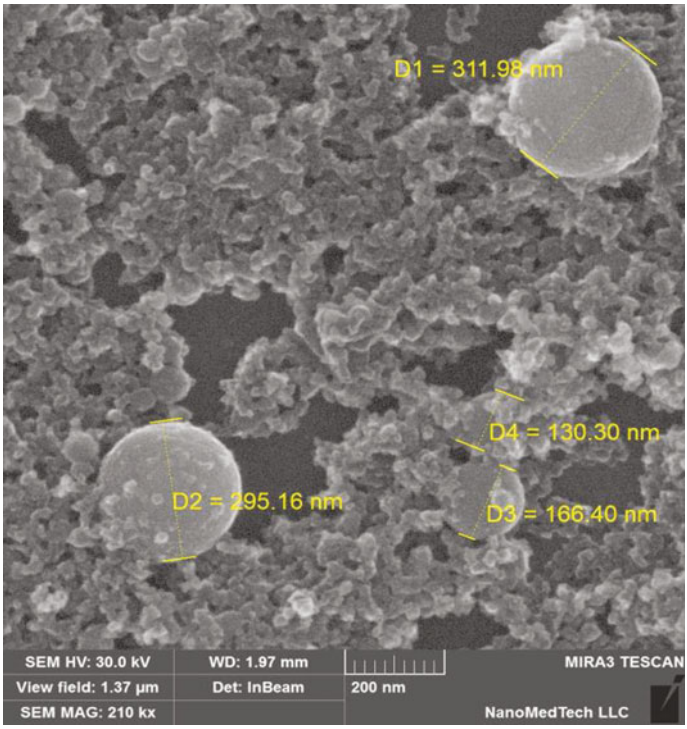

Fig. 9 Scanning electron microscopy of the nanoparticles of molybdenum

where r is the radius of the individual particle. These circumstances cause a decrease in the osmotic pressure of colloidal solutions in comparison with the salt form of metals, since the osmotic pressure in this case depends not so much on the nature of the solute, but on the partial concentration of the substance per unit volume. According to the van't Hoff equation, the osmotic pressure is equivalent to the partial and molar concentrations of a substance in solution:

$$\Pi = \frac{C}{M} RT \tag{2}$$

where C—particle concentration, g/dm^3; M is the molar mass of the solution, kg/mol

Accordingly, at the same metal concentrations, colloidal solutions, having significantly less osmotic pressure than similar solutions of metal salts, will contribute to the processes of water absorption and swelling. Thus, an important task in determining the concentrations of working solutions of metal colloids is to evaluate the degree of their isotonicity with respect to the cells of the biological object.

Characteristic particle compositions (in colloidal form) were used in vegetative experiments for growing winter wheat plants. The properties of iron and copper solutions were investigated, the dispersed phase of which differed in the content

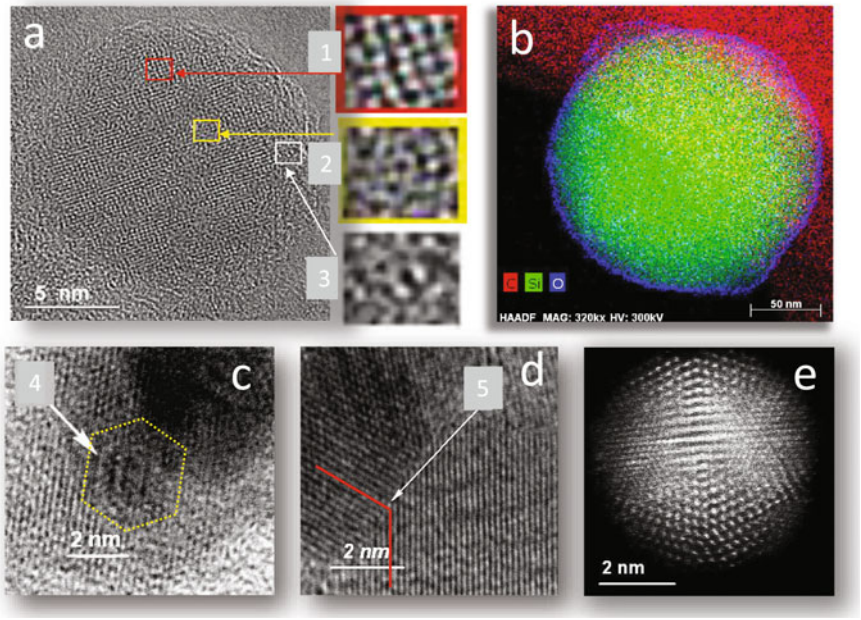

Fig. 10 TEM images of nanoparticles **a** (Al), **b** (Si), **e** (Ag) and substructures of Fe nanoparticles **c** and **d**

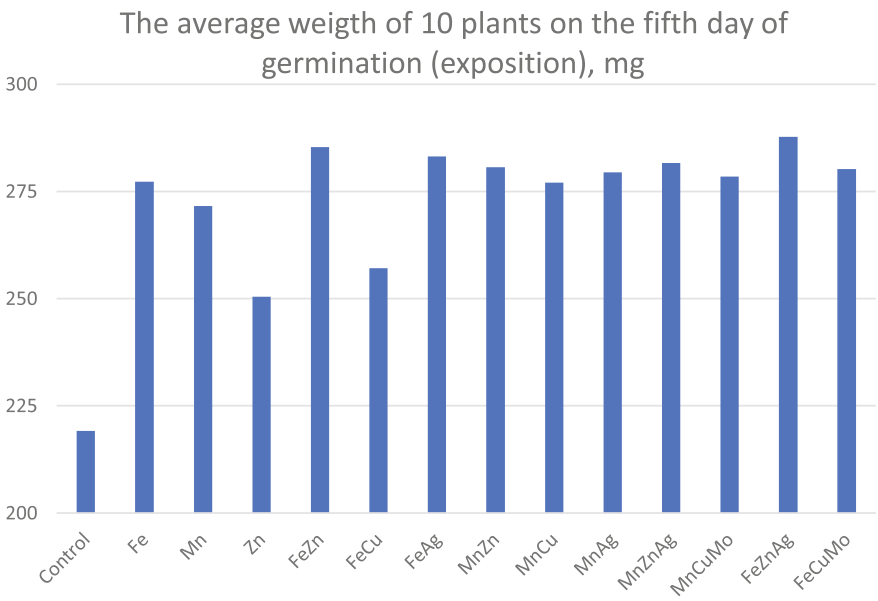

Fig. 11 Vegetative mass of watercress plants depending on the microelement background on the fifth day of germination

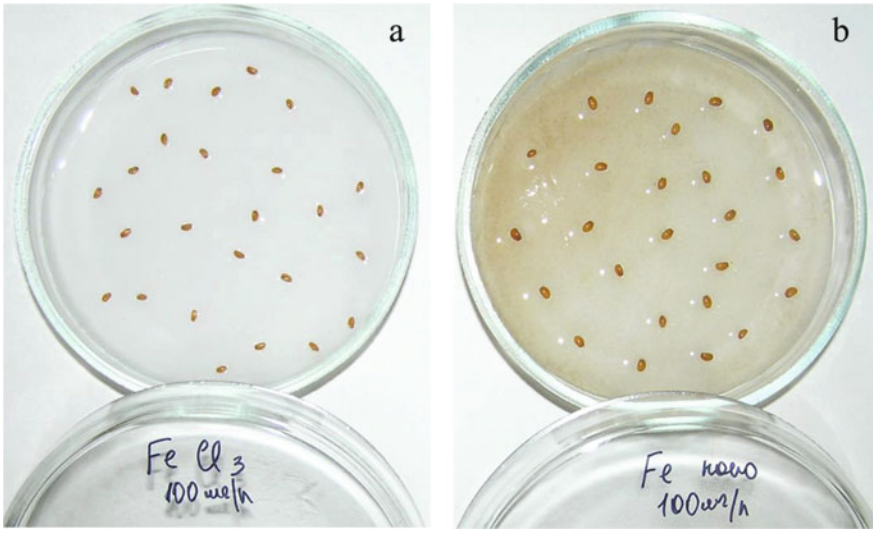

Fig. 12 Seed swelling by iron chloride (**a**) and iron colloid (**b**) solutions

Table 2 Influence of phase composition of Fe nanoparticles on biological activity

Phase composition od nanoparticles	Average weight of aboveground part of single plant	
	7 days exposure	11 days exposure
Control (water)	275 ± 5	294 ± 4
Fe (metal phase $\alpha + \gamma$, oxide phase (Fe_3O_4) less than 15%)	315 ± 6	342 ± 7
Fe (metal phase α, oxide phase ($Fe_3O_4 + FeO$) less than 80%)	270 ± 5	293 ± 5
Fe (metal phase $\alpha + \gamma$, oxide phase ($Fe_3O_4 + FeO$) less than 60%)	283 ± 5	327 ± 6

of metal and oxide phase. The question of the probable biological functionality of nano-sized objects is considered not only in connection with the preparative form of the microelements, but also in the structure of metal nanoparticles (Sect. 2.3). The biological activity of metal nanoparticles depends not only on the method of implementation, conditions of synthesis, their size, but on their complex structural-phase composition (see Table 2).

3.5 Metal Nanoparticles for Agronomy Testing

The experience of field testing of metal colloids shows that for cereals, in addition to pre-sowing seed treatment, the relevant stages of organogenesis are of particular

importance, when there is a greatest need for essential nutrients and microelements. This is the stage of sprouting (foliar feeding allows to prepare the plant for the winter), the stage of tillering (at this stage foliar feeding provides activation of morpho-physiological processes), and the stage of exit into the tube (during foliar feeding at this stage qualitatively improves the formation and development of grains) [48].

Taking into account the agrotechnological features of the culture during the autumn growing season, foliar treatment with a solution of manganese at a concentration of 1–3 mg/l was additionally carried out at the stage of sprouting. The treatment of plants with a colloidal solution of manganese during the autumn growing season is due to the fact that this metal promotes the absorption of nitrogen and phosphorus, participates in the synthesis and accumulation of carbohydrates, and enhances the overall metabolism in the plant [48]. The fungicidal and bactericidal properties of colloidal solutions of copper and silver were used to improve the phytosanitary condition of the crops at the tillering stage. Thus, at the beginning of spring, vegetation was additionally treated with a mixture of these metals with a total concentration of 0.5–1 mg/l. During the tube or flowering period, the mixture was treated with a mixture of zinc and iron with a total concentration of 1–3 mg/l (Fig. 13). A comparative analysis of the variants was carried out throughout the growing season. Seed observations indicated that field germination was at least 85–90% under pre-sowing, regardless of the variant. However, the subsequent development of seedlings, depending on the level of nutrition, pre-sowing treatment of seeds, and cultivation of vegetative plants, occurred with a significant difference in the intensity of growth processes (Fig. 14). Plants, in which seeds were treated by colloidal solutions, have the better developed aerial part and root system.

The data obtained from laboratory studies of the positive effect of metal colloids on the normalization of the osmotic properties of plants (Sect. 3.4, Fig. 12) indicate that seeds treated with colloidal solutions have a greater ability to absorb productive moisture. It can be assumed that the solid phase particle that attaches to the seed surface, because of its high sorption properties, acts as an additional acceptor that interacts with other cations and anions from the soil solution, thereby reducing its osmotic pressure. Probably, similar properties have any particles having a high specific surface area, regardless of their biogenicity. Reducing the osmotic pressure of the soil solution will help to improve the water regime and the faster germination of seeds. In addition, as has been repeatedly stated, a considerable amount of oxygen is adsorbed on the surface of a metal particle. In this case, the metal particle can be considered as a carrier or donor of oxygen necessary for the embryo, the presence of which together with water is a prerequisite for activating the processes of germination and the beginning of the development of the organism. Together with the protective properties (bactericidal and fungicidal) of individual metals, the implementation of the above mechanism may further explain the increase in adaptive capacity of winter wheat plants to adverse conditions and to ensure sustainable sprouting, even in dry years, which is unfortunately becoming the norm in recent years in Central European agriculture zone.

An analysis of the structure of direct costs in growing winter wheat indicates that its main items are mineral fertilizers, seeds, and fuel. Due to the more efficient use of

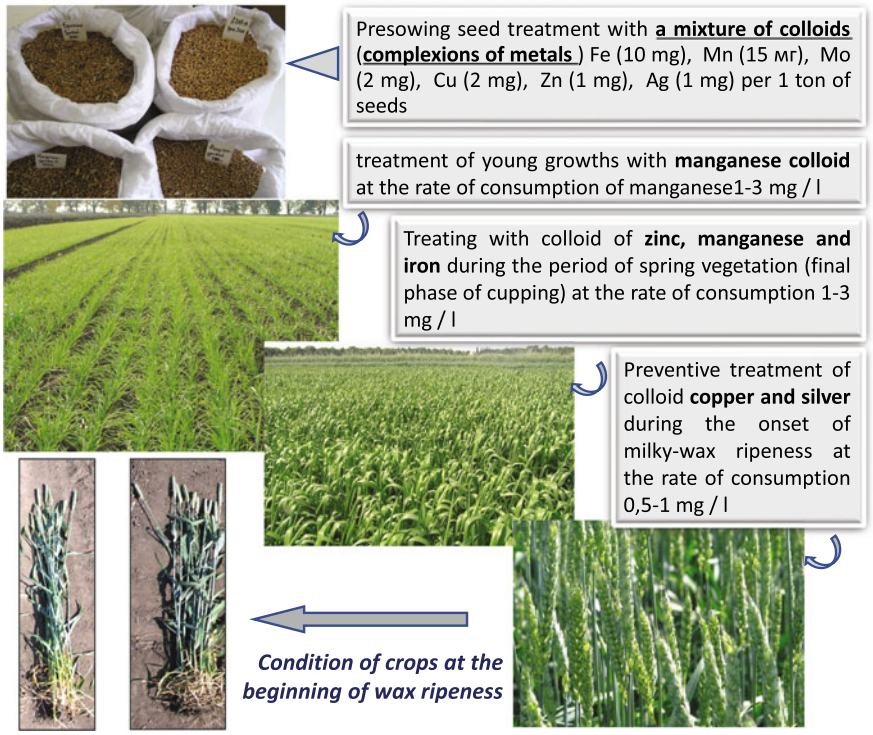

Fig. 13 Field tests of colloidal metal solutions

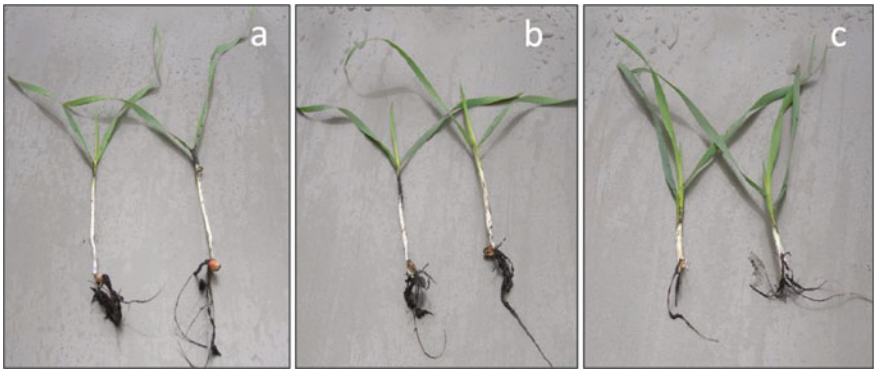

Fig. 14 Winter wheat seedlings in the 2–3 leaf stage after pre-sowing seed treatment: **a** control (without treatment), **b** chemical treatment, **c** colloidal solution of trace element mixtures

Table 3 Main quality indicators of food wheat grain

Wheat variety	Option	Protein (%)	Gluten (%)	Starch (%)
♯1	Base technology	17.3	10.7	60.7
	Treatment by metal colloids	17.6	11.1	60.1
♯2	Base technology	16.2	9.6	62.9
	Treatment by metal colloids	17.2	10.7	61.5

the basic mineral fertilizers, the doses of their application can be adjusted (reduced by 20–30% without loss of yield). Only saving of mineral fertilizers allows to increase the profitability of production of commodity grain by 20–30%.

The biological activity of nanoscale objects, which is manifested even at low concentrations of the solid phase, which do not bear the threat of biological background, actively influences the normalization of the physiological processes of plants in conditions of insufficient mineral nutrition and provides an economically valuable effect.

The obtained indicators of grain quality indicate (see Table 3) the direction of the biochemistry of the synthesis of dry substances and the redistribution of the content of hydrocarbons and proteins—there is a decrease in starch and an overall increase in proteins, in particular gluten, a substance that determines the quality of wheat, which gives a particularly valuable economic effect.

The practical implementation of the use of metal nanoparticles in colloidal form is: first, a significant reduction in the rates of application of traditional agrochemicals, including basic mineral fertilizers, secondly, the possibility of directional influence on the structural and functional self-regulation of plants, which enhances their natural resistance. With potentially broad biological effects, metal colloids can be used at different stages of organogenesis and at different technological operations.

4 Conclusions

The peculiarities of metal nanoparticle generation and their application for regulation of biological processes were investigated. It was shown that non-equilibrium conditions of particle synthesis are realized due to the short duration of the discharge and significant temperature gradients, which determines the polycrystalline nature of their structure, and the formation of metastable phase γ Fe (more than 80%) under conditions of underwater electric spark process in the mode of occurrence of a pulsed plasma channel. It was found from TEM imaging that the formation of Frank–Reed dislocations with 2 nm dimensions in Fe nanoparticles is generated by underwater electric spark discharge.

Optical emission spectroscopy results shown that metal NPs are condensated from vapor phase (metal and water vapors).

The regularities of the formation of colloidal systems for underwater electric spark discharge are analyzed and the model of colloidal micelles structure is proposed. It is shown that by optimizing the basic physical and technological parameters (in particular, parameters of discharge circuits, temperature, and electron density of plasma in discharge gap) of the process of underwater electro-spark discharge, the dispersed-isolated state of the solid phase with satisfactory aggregate stability ($\zeta \approx 40$ mV) is achieved.

The probable mechanism of biological action of metal nanoparticles, their influence on plant physiological processes, and normalization of metabolic processes is shown. It is proposed to consider the biological functionality of nanoparticles as a complex characteristic of nano-objects. Namely, the biological functionality of nanoparticles is a reflection of the nature of the basic synthesis process, its parameters, the chemical, structural and phase composition of the solid phase of its surface, the size (∼20–30 nm) and concentration of the dispersed phase in the dispersion medium, and the duration of interaction with the biological object. Field experiments showed that pre-sowing treatment of wheat seeds with colloidal solutions of metals (copper—2 mg, silver—1 mg, iron—10 mg, manganese—15 mg, zinc—1 mg, molybdenum—2 mg per 10 l of water per 1 ton of seeds) and two–three times the vegetation with manganese, zinc, iron, molybdenum, and copper solutions with a metal phase concentration of 50–200 mg/l (at the rate of consumption of 1–3 l/ha) provides a yield increase of 15–20%.

Due to the more efficient use of the basic mineral fertilizers, the doses of their application can be adjusted (reduced by 20–30% without loss of yield). In addition, the influence of metal colloids on winter wheat quality indicators is accompanied by an economically valuable physiological effect—an increase in the gluten content of the grain.

References

1. Shcherba AA, Suprunovska NI (2018) Cyclic transients in the circuits of electric discharge installations taking into account the influence of magnitude and rate of discharge currents rise on resistance of electric spark load. Tech Electrodyn 2:3–10
2. Shcherba AA, Suprunovskaya NI, Ivashchenko DS (2014) Modeling of nonlinear resistance of electro-spark load for synthesis of discharge circuit of capacitor by time parameters. Tech Electrodyn 3:12–18
3. Shcherba AA, Podoltsev AD, Zakharchenko SN, Kucheryavaya IN, Shevchenko NI, Suprunovskaya NI (2005) Progress in spark-eroded particle production: development of technological system for high-yield electrical-spark dispersion of metal granules in liquid. Tech Electrodyn 6:3–13
4. Shcherba AA, Zakharchenko SN, Suprunovskaya NI, Shevchenko NI (2006) The influence of repetition rate of discharge pulses on electrical resistance of current-conducting granular layer during its electric-spark treatment. Tech Electrodyn 2:10–14

5. Berkowitz AE et al (2003) Amorphous soft magnetic particles produced by spark erosion. J Magn Magn Mater 254:1–6
6. Lopatko KG et al (2013) Obtaining of metallic nanoparticles by plasma-erosion electrical discharges in liquid mediums for biological application. Ann Wars Univ Life Sci SGGW Agric 61:105–115
7. Taran N et al (2016) Colloidal nanomolybdenum influence upon the antioxidative reaction of chickpea plants (*Cicer arietinum L.*). Nanoscale Res Lett 11(1):476
8. Fernández-Luque F, López-Valdez F, Rodriguez MF (2015) Mineral fertilizers, bio-fertilizers and PGPRs: advantages and disadvantages of its implementation. Fertilizer technology II, biofertilizers. Studium Press, New Delhi, pp 277–294
9. Filon FL, Mauro M, Adami G, Bovenzi M, Crosera M (2015) Nanoparticles skin absorption: new aspects for a safety profile evaluation. Regul Toxicol Pharmacol 72(2):310–322
10. Pal S, Tak YK, Song JM (2007) Does the antibacterial activity of silver nanoparticles depend on the shape of the nanoparticle? A study of the gram-negative bacterium *Escherichia coli*. Appl Env Microbiol 73(6):1712–1720
11. Huk A et al (2015) Impact of nanosilver on various DNA lesions and HPRT gene mutations-effects of charge and surface coating. Part Fibre Toxicol 12(1):25
12. Abdelmonem AM, Pelaz B, Kantner K, Bigall NC, del Pino P, Parak WJ (2015) Charge and agglomeration dependent in vitro uptake and cytotoxicity of zinc oxide nanoparticles. J Inorg Biochem 153:334–338
13. Sato K, Yasuoka K, Ishii S (2010) Water treatment with pulsed discharges generated inside bubbles. Electr Eng Jpn 170(1):1–7
14. Sakiyama Y, Tomai T, Miyano M, Graves DB (2009) Disinfection of E. coli by nonthermal microplasma electrolysis in normal saline solution. Appl Phys Lett 94(16):161501
15. Locke BR, Thagard SM (2012) Analysis and review of chemical reactions and transport processes in pulsed electrical discharge plasma formed directly in liquid water. Plasma Chem Plasma Process 32(5):875–917
16. Svedberg T (1922) Herstellung Kolloider Liisungen Anorganischer Stoffe, Dresden/Leipzig
17. ChhowallaM A, Amaratunga GAJ (2001) Synthesis of carbon ‘onions’ in water. Nature 414:506–507
18. Ashkarran A (2012) Synthesis and characterization of gold nanoparticles via submerged arc discharge based on a seed-mediated approach. J Theor Appl Phys 6(1):14
19. Liu S-M, Kobayashi M, Sato S, Kimura K (2005) Synthesis of silicon nanowires and nanoparticles by arc-discharge in water. Chem Commun 37:4690–4692
20. Ashkarran AA, Iraji zad A, Mahdavi SM, Ahadian MM (2009) ZnO nanoparticles prepared by electrical arc discharge method in water. Mater Chem Phys 118(1):6–8
21. Parkansky N et al (2008) W-C synthesis in a pulsed arc submerged in liquid. Plasma Chem Plasma Process 28(3):365–375
22. Locke BR, Sato M, Sunka P, Hoffmann MR, Chang J-S (2006) Electrohydraulic discharge and nonthermal plasma for water treatment. Ind Eng Chem Res 45(3):882–905
23. Bruggeman P, Leys C (2009) Non-thermal plasmas in and in contact with liquids. J Phys Appl Phys 42(5):053001
24. Jiang B et al (2014) Review on electrical discharge plasma technology for wastewater remediation. Chem Eng J 236:348–368
25. Graham WG, Stalder KR (2011) Plasmas in liquids and some of their applications in nanoscience. J Phys Appl Phys 44(17):174037
26. Chen Q, Li J, Li Y (2015) A review of plasma-liquid interactions for nanomaterial synthesis. J Phys Appl Phys 48(42):424005
27. Tarasenko NV, Butsen AV, Nevar EA (2005) Laser-induced modification of metal nanoparticles formed by laser ablation technique in liquids. Appl Surf Sci 247(1–4):418–422
28. Burakov VS, Savastenko NA, Tarasenko NV, Nevar EA (2008) Laser-induced modification of composite Cu-C nanosized particles synthesized using a pulsed electrical discharge in a liquid. J Appl Spectrosc 75(3):394–401

29. Singaravelan R, Bangaru Sudarsan Alwar S (2015) Electrochemical synthesis, characterisation and phytogenic properties of silver nanoparticles. Appl Nanosci 5(8):983–991
30. Rodríguez-Sánchez L, Blanco MC, López-Quintela MA (2000) Electrochemical synthesis of silver nanoparticles. J Phys Chem B 104(41):9683–9688
31. Saedy S, Palagin D, Safonova O, van Bokhoven JA, Khodadadi AA, Mortazavi Y (2017) Understanding the mechanism of synthesis of Pt 3 Co intermetallic nanoparticles via preferential chemical vapor deposition. J Mater Chem A 5(46):24396–24406
32. Piszczek P, Radtke A (2018) Silver nanoparticles fabricated using chemical vapor deposition and atomic layer deposition techniques: properties, applications and perspectives: review. In: Seehra MS, Bristow AD (eds) Noble and precious metals-properties, nanoscale effects and applications. InTech
33. Lopatko KG, Aftandilyants EH, Scherba AA, Zakharchenko SM, Yatsuk SA (2009) Setup for synthesis of colloidal solutions of ultra-disperse metal powders, u200810312
34. Taran N, Gonchar O, Lopatko K, Batsmanova L, Patyka M, Volkogon M (2014) The effect of colloidal solution of molybdenum nanoparticles on the microbial composition in rhizosphere of *Cicer arietinum L.* Nanoscale Res Lett Springer Open J 9(1):289
35. Liu W (2006) Nanoparticles and their biological and environmental applications. J Biosci Bioeng 102(1):1–7
36. Roberson M, Rangari V, Jeelani S, Samuel T, Yates C (2014) Synthesis and characterization silver, zinc oxide and hybrid silver/zinc oxide nanoparticles for antimicrobial applications. Nano LIFE 04(01):1440003
37. Descoeudres A (2006) Characterization of electrical discharge machining plasmas (Thesis). EPFL, Lausanne (Switzerland)
38. Bruggeman P, Schram D, González MÁ, Rego R, Kong MG, Leys C (2009) Characterization of a direct dc-excited discharge in water by optical emission spectroscopy. Plasma Sources Sci Technol 18(2):025017
39. Ivanova OM, Danylenko MI, Monastyrskyy GE, Kolomytsev VI, Koval YuM, Shcherba AA, Zakharchenko SM, Portier R (2009) Investigation of the formation mechanisms for Ti-Ni-Zr-Cu nanopowders fabricated by electrospark Erosion method in cryogenic liquids. Metallofizika i Noveishie Tekhnologii 31(5):603–614
40. Kravchenko Y, Lopatko K, Aftandilyants Y, Trach V (2014) The effect of colloidal nanoparticles on plant growth, phytotoxicity and crop yields. Fertilizer Technol Synth 1:689–724
41. Boretskij VF, Veklich AN, Tmenova TA, Cressault Y, Valensi F, Lopatko KG, Aftandilyants YG (2019) Plasma of underwater electric discharges with metal vapors. In: Problems of atomic science and technology, 1. Series: plasma physics (25), pp 127–130
42. Tmenova T, Valensi F, Veklich A, Cressault Y, Boretskij V, Lopatko K, Aftandilyant Y (2017) Etude d'un arc impulsionnel immergélaide de deux dispositifs expérimentaux. Journal International de Technologie, de l'Innovation, de la Physique, de l'Energie et de l'Environnement 3(1):2428–8500. https://doi.org/10.18145/jitipee.v3i1.159
43. Lopatko KG, Aftandilyants YG, Zaulichnyy YV, Karpets MV, Sheretskyi AA (2012) The structure and phase transformation of nanoparticles produced by electrospark treatment of iron pellets. In: Electrical contacts and electrodes. Kyiv, pp 125–140 (in Russian)
44. Liangad XZ, Dodgeb MF, Jiangc J, Donga HB (2019) Using transmission Kikuchi diffraction in a scanning electron microscope to quantify geometrically necessary dislocation density at the nanoscale. Ultramicroscopy 197:39–45
45. Tanaka Y (2017) Synthesis of nano-size particles in thermal plasmas. In: Handbook of thermal science and engineering. Springer International Publishing AG, pp 1–38
46. Aftandilyants YG, Lopatko KG, Zaulichnyy YV, Karpets MV, Sheretskyi AA (2014) Phase transformations in nanoparticles produced by electrospark treatment of metallic granules. In: Electric contacts and electrodes. Kyiv, pp 112–128 (in Russian)

47. Natsuki J, Abe T (2011) Synthesis of pure colloidal silver nanoparticles with high electroconductivity for printed electronic circuits: the effect of amines on their formation in aqueous media. J Colloid Interf Sci 359(1):19–23
48. Taran N, Storozhenko V, Svietlova N, Batsmanova L, Shvartau V, Kovalenko M (2017) Effect of zinc and copper nanoparticles on drought resistance of wheat seedlings. Nanoscale Res Lett 12(1):60

Nanooptics and Photonics

Surface Plasmon Polariton Resonance Grating-Based Sensors Elements

V. Fitio, O. Vernyhor, I. Yaremchuk, and Y. Bobitski

1 Introduction

It is well known that resonance optical effects occur in the periodical and prism structures due to the excitation of the plasmon-polariton or waveguide resonances. Resonance excitation takes place at the phase-matching condition between the tangential component of the electromagnetic wave and wavenumber of the surface plasmon polariton. These conditions are expressed in features of the dependence of the reflectance on the angle of incidence or wavelength [1]. The incident light is combined with surface plasmons under certain conditions. It is due to the positive dielectric permittivity of the dielectric and the negative dielectric permittivity of the metal at optical frequencies. As a result, independent and propagating electromagnetic waves have been created. The high concentration of electromagnetic wave energy for this interface makes it possible to enhance the field at subwavelength scales, and the waves can propagate along with the interface for several hundred wavelengths [2]. Surface plasmon polaritons occur in conductors due to of collective vibrations of free electrons and form a hybrid wave. It provides the advantage to combine both photonic and electronic elements on the same platform. Surface plasmon polaritons decay exponentially with distance in both directions from the interface but propagate along with the interface [3]. Therefore, they transmit absorbed electromagnetic energy along with the interface and can reradiate electromagnetic wave under certain conditions. The ability to realize the transformation of light by the wave at the surface

V. Fitio (✉) · O. Vernyhor · I. Yaremchuk · Y. Bobitski
Department of Photonics, Lviv Polytechnic National University, S. Bandery Str., 12, 79013 Lviv, Ukraine
e-mail: v.m.fitio@gmail.com

Y. Bobitski
Faculty of Mathematics and Natural Sciences, University of Rzeszow, Pigonia Str.1, 35959 Rzeszow, Poland

O. Fesenko and L. Yatsenko (eds.), *Nanooptics and Photonics, Nanochemistry and Nanobiotechnology, and Their Applications*, Springer Proceedings in Physics 247, https://doi.org/10.1007/978-3-030-52268-1_24

and transformation of light by high localization of electromagnetic energy near the surface make plasmon polaritons promising for further miniaturization of integrated and optoelectronic circuits and increase their performance.

The application of surface plasmon polaritons usually attracts the attention of researchers for a number of reasons. One of the reasons for this great popularity is the high intensity of the evanescent waves at the metal-dielectric interface and the high-quality factor achieved under the conditions of surface plasmon polariton resonance. High intensity on the surface opens the way to nonlinear applications of surface plasmons [4]. On the other hand, the sharp resonance state makes it possible to produce highly sensitive sensors that are commonly used for biological or chemical detection [5–8]. Such sensors usually operate on the principle of measuring the change in the refractive index. The most modern ones have very high precision and sensitivity less than 10^{-5} units of refractive index [9]. The enhancement of the electromagnetic field due to surface plasmon polariton resonance allows enhancing such phenomena as Raman scattering, second harmonic generation, fluorescence, etc. [10]. Moreover, plasmon polaritons are of interest for various types of integral sensors. They are based on the fact that the dielectric permittivity of the surrounding medium influences on excitation of the plasmon polaritons. In additional, the electromagnetic field of the excited plasmon can interact with the surrounding medium.

Grating-based sensors are not as widely used as prismatic ones but their compatibility with mass production (in particular, replication into plastic) makes grating structures attractive for low-cost sensors elements [11]. High sensitivity of plasmonic grating sensors is provided, for example, by a metal [12, 13] or dielectric grating [14] together with a prism structure; using two-layer metal gratings [15, 16], dielectric gratings with metallic coatings [17–19], metal gratings [20] or semiconductor nanowires [21], semiconductor gratings [22] or grating based on composite materials [23] and nanoparticles [24, 25] and others. In addition, the sensitivity of the grating-based sensor can be enhanced by optimizing the grating geometry parameters such as period, depth, filling factor, and relief [26]. It was shown in [27] that the optimization of a rectangular metal grating resulted in the sensitivity increase of more than 3 times compared to the standard sensor.

Taking into account written above, it should be notified that further studies of grating structures are necessary in order to produce the available optoelectronic devices with both high resolution and sensitivity. Since they are critical elements that determine the work of such devices. In addition, the sensitivity of the grating-based sensor can be enhanced by optimizing the geometric parameters. Motivated by these ideas, we consider optimization of geometric parameters and application of special structures, namely metal gratings on the metal substrate and dielectric grating on the metal substrate to obtain the highly sensitive sensors element.

2 Theoretical Background

It is known that surface plasmon polariton wave can be excited at the metal/dielectric interface for TM polarization waves. The surface wave means that the electric field intensity vector is maximal at the boundary of two media and rapidly decays from the boundary, especially in metal [28]. The plasmon-polariton wave can be generated using the prism or grating [29]. The application of the metal/dielectric interface as a sensing element of the sensors is based on the dependence of the constant propagation of the surface wave on the dielectric permittivity of the dielectric as follows [30, 31]:

$$\beta \cong \frac{2\pi}{\lambda}\sqrt{\frac{\varepsilon_m \varepsilon_d}{\varepsilon_m + \varepsilon_d}}, \tag{1}$$

where ε_m is dielectric permittivity of metal, which has the negative real part and positive imaginary part, ε_d is dielectric permittivity of the dielectric, λ is the wavelength.

The propagation constant is $\beta \propto \sqrt{\varepsilon_d} = n_d$, as follows from (1). It is due to the fact that $\mathrm{Re}(\varepsilon_m) \gg \varepsilon_d$. Thus, the propagation constant of the surface plasmon polariton wave is linearly sensitive to change the refractive index of the dielectric.

Nowadays, nanotechnologies make it possible to produce perfect gratings with periods less than 1 μm. Therefore, it is advisable to study grating structures in which surface plasmon polariton waves can be excited. It is obvious that the metal planar surface can be used as gratings substrate. Rectangular gratings are easy to produce from a technology point of view. The test medium should contact the metal surface over the period of maximum area in order to obtain the high sensitivity of the sensor. It is advisable to use gold or silver as a metal substrate, so as they are chemically stable and have a small imaginary part of the dielectric permittivity. However, gold is more stable than silver. In fact, when we say "metal substrate", we mean a thin layer of gold or silver deposited on a fused silica substrate with thickness from 0.1 to 1 μm. This thickness of the metal film is sufficient since the depth of penetration of the field into the metal for the surface plasmon polariton wave is less than 10 nm (skin effect). It is known that the dielectric permittivity of metals depends strongly on the wavelength. Approximate analytical dependences for gold and silver on the basis of the experimental data for calculations have been used from [32].

The numerical calculations for the study of the plasmon-polariton resonance were carried out for gratings with a period of 1 μm and for this type of resonance; the following condition must be satisfied:

$$\frac{2\pi}{\lambda}\sqrt{\frac{\varepsilon_m \varepsilon_d}{\varepsilon_m + \varepsilon_d}} \cong \frac{2\pi}{\Lambda}. \tag{2}$$

That is, the surface plasmon polariton resonance will occur at the wavelength which is larger than the grating period. The grating plane disturbance decreases when the cross-section of the grating groove decreases. Therefore, the left part of

(2) approaches to the right part, and the resonant wavelength approaches the grating period.

The dielectric permittivity of gold and silver is equal $\varepsilon_{\mathrm{Ag}} = -51.53 + i1.17$ and $\varepsilon_{\mathrm{Au}} = -44.27 + i1.3863$ at the wavelength of 1 μm. Thus, propagation constants of the surface plasmon polariton wave for interface of the gold or silver/dielectric ($\varepsilon_d = 1.0$) are $\beta_{\mathrm{Ag}} = 6.345 + i0.00143$ μm^{-1}, $\beta_{\mathrm{Au}} = 6.355 + i0.0023$ μm^{-1} in accordance with (1). Propagation constants are $\beta_{\mathrm{Ag}} = 7.81 + i0.0027$ μm^{-1} and $\beta_{\mathrm{Au}} = 7.83 + i0.0043$ μm^{-1} if $\varepsilon_d = 1.5$.

The electric field intensity at the propagation of the surface plasmon polariton wave at the interface of two media can be described as follows:

$$E(x, z) = E_0 \exp(i\beta x). \tag{3}$$

The value of the imaginary part of the constant propagation determines the distance l at which the amplitude of the surface wave decreases e times based on the expression $\mathrm{Im}(\beta)l = 1$. Therefore, the propagation distance of the plasmon-polariton wave can be expressed as follows $l = 1/\mathrm{Im}(\beta)$. Thus, the propagation distance of the plasmon-polariton wave will be maximal for silver at $\varepsilon_d = 1.0$. In this case, $l = 1/0.00143 = 699$ μm ≈ 0.7 mm. The last number gives an estimate of the grating length when the calculation can be carried out as for periodic structure. If the grating length is comparable with l or less than l, then it cannot be considered as the periodic structure in the calculation. Thereby, the grating length must be much greater than l and then experimental results will be in the good fitting with the calculated ones for the gratings with an infinite number of periods.

3 Rectangular Gratings on the Metallic Substrate

The features of propagation and excitation of the surface plasmon polariton waves of metallic and dielectric gratings on the gold substrate have been studied. It is known that gold is more resistant to external influence, and its characteristics in terms of the resonance of plasmon-polariton waves is slightly worse than for silver. It is demonstrated in Fig. 1, where the real and imaginary parts of the constant propagation of the surface plasmon polariton wave, calculated by (1) for gold, silver and dielectric with dielectric permittivity of 1.0. The real parts of the constant propagation for the two metals are almost the same. The imaginary part of gold is slightly larger than for silver. It should be noted that the imaginary and real parts of the constant propagation decrease when the wavelength increases. It is in good agreement with (1).

There is the resonant absorption of electromagnetic wave energy in the grating at the carefully selected grating parameters and wavelength. In present work, there are determined grating parameters and wavelength to obtain maximal absorption of electromagnetic wave. The angle of incidence of the optical wave on the grating is normal in all calculations. The field distribution calculations were carried out using the finite element method. The metal grating and dielectric grating on the

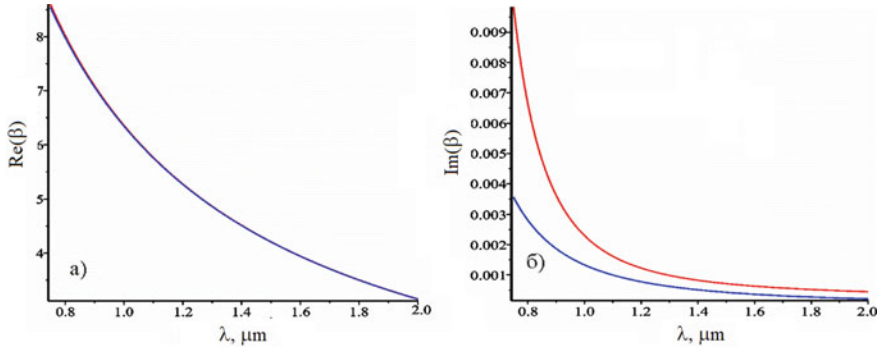

Fig. 1 Spectral dependences of the real and imaginary parts of constant propagation of the surface plasmon polariton waves for gold (red curve) and silver (blue curve)

metal substrate at different refractive indices of the surrounding medium have been researched.

Optimal parameters of the rectangular golden grating on a gold substrate were determined. The grating thickness is 14.81 nm, grating width is 500 nm, grating period is 1000 nm and the fill factor is 0.5. The refractive index of the surrounding medium is 1.0. The surface plasmon polariton resonance occurs at the wavelength of 1012.5 nm. The spectral half-width of the absorption spectrum is 1.3 nm.

The distributions of electric and magnetic fields in such a periodic structure at the resonant wavelength are shown in Fig. 2a, b, respectively.

It can be seen that the strongest electric field is concentrated at the corner of the golden grating. The maximum electric field is 1.5×10^6 r.u. The maximum value is 2.1×10^3 r.u. in the case of the magnetic field. It should be noted that the magnetic field is concentrated above the grating and into the grating slit. Generalized simulation results are presented in Table 1, structure No. 1.

In the next step, the optimal parameters of the dielectric grating on a gold substrate were founded. The grating thickness is 55 nm, grating width is 160 nm, the grating

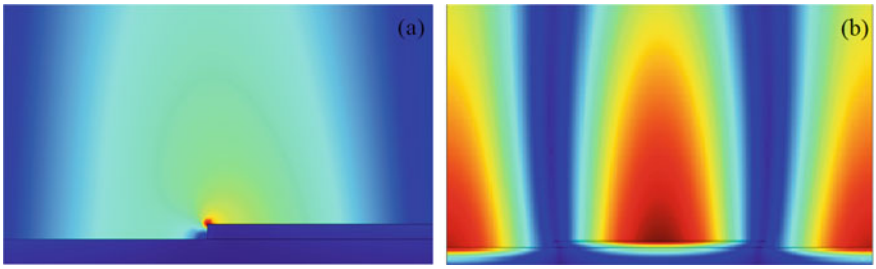

Fig. 2 The distribution of electric (**a**) and magnetic (**b**) fields by the golden grating on the gold substrate at the resonant wavelength of 1012.5 nm. The maximum electric field is 1.5×10^6 r.u. and the magnetic field is 2.1×10^3 r.u. Refractive index of the surrounding medium is 1.0

Table 1 Characteristics of the plasmon-polariton resonance of periodic structures with gold substrate

No structure	λ_{res}, μm	Δλ, nm	$\lvert E_{\max}\rvert$, r.u., contact	$\lvert H_{\max}\rvert$, r.u., contact
	2	3	4	5
1	1.0125	1.3	1.5×10^6, +	2.1×10^3, +
2	1.01342	2.6	5×10^5, +	4×10^3, −
3	1.0519	6.1	5×10^6, +	4×10^3, −

A "+" in the table indicates that the strong electric or magnetic field will contact the test substance

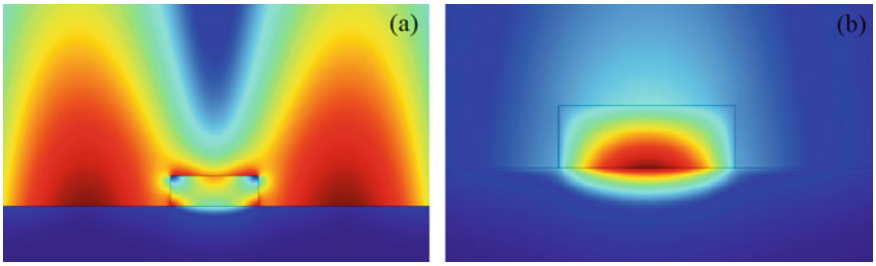

Fig. 3 The distribution of electric (**a**) and magnetic (**b**) fields by the dielectric grating on the gold substrate at the resonant wavelength of 1013.42 nm. The maximum electric field is 5.0×10^5 r.u. and the magnetic field is 4.0×10^3 r.u. Refractive index of the surrounding medium is 1.0

period is 1000 nm and the fill factor is 0.16. The refractive index of the surrounding medium is 1.0. The refractive index of the dielectric grating is 3.0. The surface plasmon polariton resonance occurs at the wavelength of 1013.42 nm. The spectral half-width of the absorption spectrum is 2.6 nm.

The distributions of the electric and magnetic fields in the periodic structure at the resonant wavelength are shown in Fig. 3. The electric field is concentrated above the grating and in the grating slits. Moreover, the strongest electric field is in the grating slit and the maximum value is 5×10^5 r.u. The magnetic field is concentrated inside the dielectric grating, as shown in Fig. 3b and maximal value of the magnetic field is 4×10^3 r.u. Generalized simulation results are presented in Table 1, structure No. 2.

Further, the optimal parameters of the dielectric grating on gold substrate in the surrounding medium with a refractive index of 1.777 were determined. The grating thickness is 55.3 nm, grating width is 90 nm, the grating period is 750 nm and the filling factor is 0.2. The refractive index of the dielectric grating is 3.0. The surface plasmon polariton resonance occurs at the wavelength of 1051.1 nm. The spectral half-width of the absorption spectrum is 6.1 nm.

The distributions of electric and magnetic fields in this periodic structure at the resonant wavelength are shown in Fig. 4. It can be seen from Fig. 4a that strongest electric field is concentrated above the grating and into the grating slit. Moreover, it penetrates into the dielectric grating for a short distance near the substrate. The

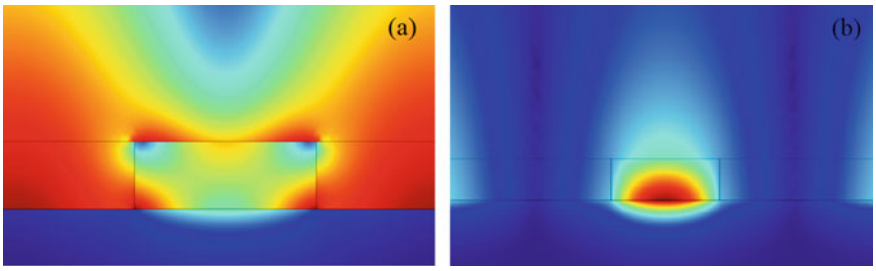

Fig. 4 The distribution of electric (**a**) and magnetic (**b**) fields by the dielectric grating on the gold substrate at the resonant wavelength of 1051.9 nm. The maximum electric field is 5.0×10^5 r.u. and the magnetic field is 4.0×10^3 r.u. Refractive index of the surrounding medium is 1.777

maximum electric field is 5×10^5 r.u. In the case of the magnetic field, its maximum value is 4×10^3 r.u. Magnetic field is concentrated inside the dielectric grating, as shown in Fig. 4b. Generalized simulation results are presented in Table 1, structure No. 3.

The strongest electric field is concentrated in a small volume near the corners of the rectangular grating in structure No. 1 (metal grating). Therefore, it will contact the test substance in a small volume. However, the magnetic field takes a large volume above the grating and will interact strongly with the test substance. Thus, such structure can be used for the study of luminescence excited by magnetic-dipole interaction under the condition of the plasmon-polariton resonance.

On cases of the dielectric gratings on the golden substrate (structure No. 2 and No. 3) the strong magnetic field is concentrated inside the dielectric grating. Therefore, this field will not come into contact with the test substance. However, in these structures, there is a strong electric field that takes a large volume above the grating. It is obvious that such structures under plasmon-polariton resonance should be used for Raman spectroscopy and for the study of luminescence excited by electro-dipole interaction. In additional, structure No. 3 can be used to study aqueous solutions of active substances since the wavelength of the resonance is determined by the refractive index of the solution.

Thus, the sensitivity of the sensor to change the refractive index of the surrounding medium was calculated. The dependences of the resonance wavelength on the refractive index of the surrounding medium for structures No. 2 and No. 3 are shown in Fig. 5a, b, respectively.

It can be concluded from Fig. 5 that the dependences of the change of the resonant wavelength on the change of the refractive index are linear. The sensitivity can be estimated as follows:

$$S = \frac{\Delta\lambda_{\text{res}}}{\Delta n}. \tag{4}$$

Therefore, the sensitivity of structure No. 2 will be 0.91 μm for gas medium and for it is 0.67 μm for aqueous solutions in case of structure No. 3.

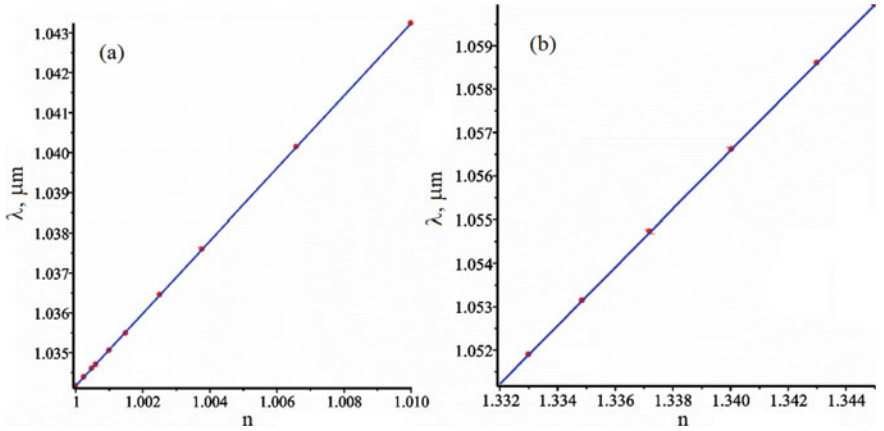

Fig. 5 Dependences of change of the resonance wavelength on the refractive index of the surrounding medium in contact with dielectric grating on a metal substrate for gas media (**a**), and for aqueous solutions (**b**)

4 Conclusions

Optimal parameters of the rectangular golden grating on the gold substrate and dielectric grating on the gold substrate to obtain a highly sensitive sensors element were founded.

It is shown that a strong electric field is concentrated in a small volume near the vertices of the rectangular grating in case of golden grating on the gold substrate. The magnetic field is concentrated above the grating and will strongly interact with the test substance. Therefore, such structure under plasmon-polariton resonance can be used to study luminescence, which is excited by magnetic-dipole interaction.

The strong electric field is concentrated above the gratings in dielectric grating on the gold substrate. At the same time, the strong magnetic field is concentrated into the dielectric. Thus, such structures under plasmon-polariton resonance can be used for Raman spectroscopy and luminescence studies, which are excited during the electric-dipole interaction. In addition, such structure can be used to study aqueous solutions of active substances, since the resonance wavelength is determined by the refractive index of the solution.

Sensitivity of surface plasmon polariton resonance grating-based sensors elements was researched. It is shown that the change of the resonant wavelength is proportional to the change of the medium refractive index. Thereby such periodic structures can be used as the sensitive element of sensors for measuring the refractive index of aqueous or other solutions exposed to various chemical reagents.

References

1. Maier SA, Atwater HA (2005) Plasmonics: localization and guiding of electromagnetic energy in metal/dielectric structures. J Appl Phys 98(1):011101-1–011101-9
2. Barnes WL, Dereux A, Ebbesen TW (2003) Surface plasmon subwavelength optics. Nature 424(6950):824–830
3. Gramotnev DK, Bozhevolnyi SI (2014) Nanofocusing of electromagnetic radiation. Nat Photon 8(1):13–22
4. Kauranen M, Zayats AV (2012) Nonlinear plasm. Nat Photon 6(11):737–748
5. Sinibaldi A, Danz N, Descrovi E, Munzert P, Schulz U, Sonntag F, Michelotti F (2012) Direct comparison of the performance of Bloch surface wave and surface plasmon polariton sensors. Sens Actuat B: Chem 174:292–298
6. Homola J (2008) Surface plasmon resonance sensors for detection of chemical and biological species. Chem Rev 108(2):462–493
7. Fitio V, Yaremchuk I, Bobitski Y (2011) Optical excitation of surface plasmon polariton and waveguide modes resonances on prismatic structures. Optica Aplicata 41(4):929–940
8. Yaremchuk I, Fitio V, Petrovska H, Bobitski Y (2019) The temperature impact on the characteristics of the surface plasmon resonance sensors element. Optik 192:162969-1–162969-8
9. Prabowo BA, Purwidyantri A, Liu KC (2018) Surface plasmon resonance optical sensor: a review on light source technology. Biosensors 8(3):80
10. Homola J, Yee SS, Gauglitz G (1999) Surface plasmon resonance sensors. Sens Actuat B: Chem 54(1–2):3–15
11. Zayats AV, Smolyaninov II, Maradudin AA (2005) Nano-optics of surface plasmon polaritons. Phys Rep 408(3–4):131–314
12. Singh P (2016) SPR biosensors: historical perspectives and current challenges. Sens Actuat B: Chem 229:110–130
13. Byun KM, Kim SJ, Kim D (2007) Grating-coupled transmission-type surface plasmon resonance sensors based on dielectric and metallic gratings. Appl Opt 46(23):5703–5708
14. Dhawan A, Canva M, Vo-Dinh T (2011) Narrow groove plasmonic nano-gratings for surface plasmon resonance sensing. Opt Expr 19(2):787–813
15. Pi S, Zeng X, Zhang N, Ji D, Chen B, Song H, Song Y (2016) Dielectric-grating-coupled surface plasmon resonance from the back side of the metal film for ultrasensitive sensing. IEEE Photon J 8(1):1–7
16. Hu C, Liu D (2010) High-performance grating coupled surface plasmon resonance sensor based on Al–Au bimetallic layer. Mod Appl Sci 4(6):8–13
17. Turker B, Guner H, Ayas S, Ekiz OO, Acar H, Guler MO, Dâna A (2011) Grating coupler integrated photodiodes for plasmon resonance based sensing. Lab Chip 11(2):282–287
18. Lu M, Peng W, Liu Q, Liu Y, Li L, Liang Y, Masson JF (2017) Dual channel multilayer-coated surface plasmon resonance sensor for dual refractive index range measurements. Opt Expr 25(8):8563–8570
19. Yaremchuk I, Petrovska H, Fitio V, Bobitski Y (2018) Optimization and fabrication of the gold-coated GaAs diffraction gratings for surface plasmon resonance sensors. Optik-Int J Light Electr Opt 158:535–540
20. Petrovska HA, Yaremchuk IY, Fitio VM, Suriadova OD, Bobitski YV (2016) Optimization metal-coated gratings for sensors applications. In: 2016 IEEE 13th international conference on laser and fiber-optical networks modeling (LFNM), pp 30–31
21. Hua-Jun Z (2012) High sensitivity refractive index gas sensing enhanced by surface plasmon resonance with nano-cavity antenna array. Chin Phys B 21(8):087104-1–087104-5
22. Jahanshahi P, Adikan FRM (2015) Sensitivity enhancement of graphene-based surface plasmon resonance biosensor using germanium nanowires grating. J Med Bioeng 4(2):145–149
23. Nikitin PI, Anokhin PM, Beloglazov AA (1997) Chemical sensors based on surface plasmon resonance in Si grating structures. In: International conference on solid state sensors and actuators, TRANSDUCERS'97, pp 1359–1362

24. Jandieri V, Meng P, Yasumoto K, Liu Y (2015) Scattering of light by gratings of metal-coated circular nanocylinders on a dielectric substrate. JOSA A 32(7):1384–1389
25. Okamoto T, Yamaguchi I, Kobayashi T (2000) Local plasmon sensor with gold colloid monolayers deposited upon glass substrates. Opt Lett 25(6):372–374
26. Yaremchuk I, Tamulevičienė A, Tamulevičius T, Tamulevičius S (2014) Optical properties of DLC-Ag nanocomposite and grating structures on their base. Appl Mech Mater 490:53–57
27. Søndergaard T, Bozhevolnyi SI (2009) Surface-plasmon polariton resonances in triangular-groove metal gratings. Phys Rev B 80(19):195407-1–195407-9
28. Ichihashi K, Mizutani Y, Iwata T (2014) Enhancement of the sensitivity of a diffraction-grating-based surface plasmon resonance sensor utilizing the first-and negative-second-order diffracted lights. Opt Rev 21(5):728–731
29. Martin J, Proust J, Gérard D, Plain J (2013) Localized surface plasmon resonances in the ultraviolet from large scale nanostructured aluminum films. Optic Mater Expr 3(7):954–959
30. Barnes WL, Preist TW, Kitson SC, Sambles JR, Cotter NPK, Nash DJ (1995) Photonic gaps in the dispersion of surface plasmons on gratings. Phys Rev B 51(16):11164
31. Bozhevolnyi SI, Erland J, Leosson K, Skovgaard PM, Hvam JM (2001) Waveguiding in surface plasmon polariton band gap structures. Phys Rev Lett 86(14):3008
32. Fitio V, Yaremchuk I, Vernyhor O, Bobitski Y (2018) Resonance of surface-localized plasmons in a system of periodically arranged gold and silver nanowires on a dielectric substrate. Appl Nanosci 8(5):1015–1024

Metamorphic InAs/InGaAs Quantum Dot Structures: Photoelectric Properties and Deep Levels

Sergii Golovynskyi, Oleksandr I. Datsenko, Luca Seravalli, Giovanna Trevisi, Paola Frigeri, Baikui Li, and Junle Qu

1 Introduction

In(Ga)As quantum dots (QDs) are used in photonic and electronic devices with novel functionalities [1–5], advanced energy-efficient 'green' communication systems with ultra-large bit rate such as energy-efficient lasers [6, 7] and QD optical amplifiers [1], solar cells [8–10], single-photon emitters [11–13].

Metamorphic InAs/InGaAs QD structures have wider tuning possibilities as compared to standard InAs QDs embedded into GaAs layers [14–16]. Due to the lower QD strain, caused by the reduced lattice-mismatch, their luminescence is shifted to the infrared (IR); this feature allows to obtain an efficient emission in the telecom windows at 1.3 and 1.55 μm ranges [14, 15]. It is also promising to use these structures as detectors of light in these wavelength ranges. Thus, it was reported earlier that vertical InAs/$In_{0.15}Ga_{0.75}As$ QD structures can maintain photosensitivity comparable to the GaAs-based ones [17]. However, there is a lack of photoelectric studies of metamorphic structures in lateral contact geometry, where the charge carriers flow in the plane of QD layers. Commonly, in such lateral-geometry designed

S. Golovynskyi (✉) · B. Li · J. Qu
Key Laboratory of Optoelectronic Devices and Systems of Ministry of Education and Guangdong Province, College of Physics and Optoelectronic Engineering, Shenzhen University, 518060 Shenzhen, People's Republic of China
e-mail: serge@szu.edu.cn

O. I. Datsenko (✉)
Physics Department, Taras Shevchenko National University of Kyiv, 01601 Kiev, Ukraine
e-mail: lesoto8g@gmail.com

L. Seravalli (✉) · G. Trevisi · P. Frigeri
Institute of Materials for Electronics and Magnetism, IMEM-CNR, 43124 Parma, Italy
e-mail: luca.seravalli@imem.cnr.it

O. Fesenko and L. Yatsenko (eds.), *Nanooptics and Photonics, Nanochemistry and Nanobiotechnology, and Their Applications*, Springer Proceedings in Physics 247, https://doi.org/10.1007/978-3-030-52268-1_25

structures, the QD layers associated with the WLs are known to be the main conductivity channels [18]. Because of this peculiar type of conductivity, QD photodetectors with the lateral transport of carriers are considered to have the potential for high photoresponsivity [19, 20].

An in-depth photoelectric study of metamorphic InAs/InGaAs QD nanostructures in the lateral configuration can give fundamental knowledge about the mechanism of photoconductivity and the efficiency of in-plane carrier transport. In this chapter, we summarize the results of earlier papers devoted to the study of lateral InAs/$In_xGa_{1-x}As$ QD structures with different In composition x using photocurrent (PC) and photoluminescence (PL) spectroscopies, lateral electrical measurements as well as modeling calculations at room and low temperatures. Moreover, we analyzed the defects in metamorphic QD structures, detected also in the lateral contact geometry by means of thermally stimulated current (TSC) spectroscopy of deep levels, and showed their effect on the luminescent and photoelectric properties. This fundamental investigation of the metamorphic structures is promising in terms of further improvements of novel light-sensitive devices, such as near-IR photodetectors, linear arrays and camera matrixes, by the implementation of metamorphic QDs. In particular, we reported on the redshift of QD photoresponse towards the IR range beyond 1.3 μm, while preserving responsivity similar to known GaAs-based QD structures. These investigations showing a high photoresponsivity in the IR range at room temperature indicate that metamorphic InAs/InGaAs QD heterostructures can be useful for photodetectors and other optoelectronic sensors based on interband transitions.

2 Sample Preparation and Methods

The structures were grown by molecular beam epitaxy and their design is given in Fig. 1a. As a first step, a semi-insulating (100) GaAs substrate was covered by a

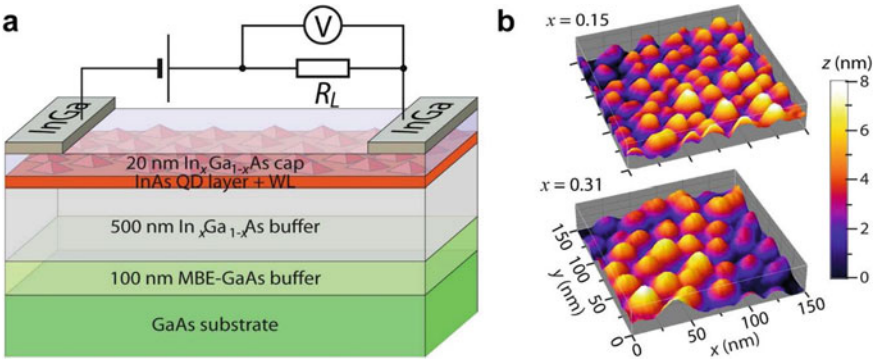

Fig. 1 Schematics of the InAs/InGaAs QD structures (**a**) and 150 × 150 nm AFM images (**b**) of the uncapped QDs in the structures with $x = 0.15$ and $x = 0.31$

100 nm-thick GaAs buffer at 600 °C, followed by the deposition of an undoped $In_xGa_{1-x}As$ metamorphic buffer (MB) 500 nm in thickness at 490 °C. Then, after a growth interruption of 210 s to cool down the substrate, 3.0 MLs (monolayers) of InAs were grown at 460 °C. Finally, these self-assembled QDs were covered by 20 nm of undoped $In_xGa_{1-x}As$. Four samples with In content x of 0.15, 0.24, 0.28 and 0.31 in $In_xGa_{1-x}As$ cladding layer were realized.

The atomic force microscopy topograms of the uncapped QDs (Fig. 1b) indicate that the surface density is similar for different x. InAs/$In_{0.15}Ga_{0.85}As$ structures have an average QD height of 4.9 ± 0.7 nm, diameter of 21 ± 3.7 nm and density of 1×10^{11} cm^{-2}, while the height and diameter of InAs/$In_{0.31}Ga_{0.69}As$ QDs were 4.3 ± 1.0 and 22.6 ± 3.6 nm, respectively, with a density of 1.5×10^{11} cm^{-2}. The same sizes were confirmed by HRTEM estimations (Fig. 2c).

For the photoelectric measurements, two ohmic InGa eutectic contacts were deposited over the surface of 5 × 2 mm pieces of the structures, the connection of the samples for the measurements is shown in Fig. 1a. The contact ohmicity was confirmed by measuring I–V characteristics (see below).

The current flowing through the samples was measured with a voltmeter, using a standard direct current technique [21–25], as a voltage drop across a series load resistance $R_L = 1$ MΩ being much less than the resistance of each sample. PC was

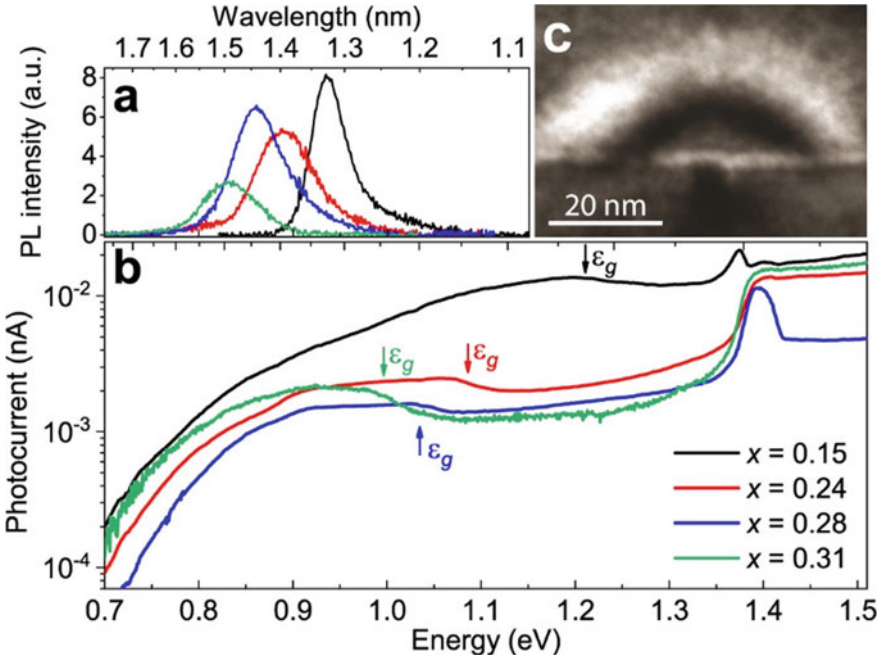

Fig. 2 **a** PL and, **b** PC spectra of the InAs/$In_xGa_{1-x}As$ QD structures with different In content at 300 K [24], the color arrows mark the bandgap of $In_xGa_{1-x}As$ buffer calculated following Paul et al. [33], **c** HRTEM image of a QD at a cross-section of the InAs/$In_{0.15}Ga_{0.85}As$ structure

excited with a 250 W halogen lamp light dispersed with a monochromator, and the spectra were obtained at room temperature (300 K) and 77 K and normalized to the excitation intensity of the light source. PL spectra were recorded at the same temperatures (300 K and 77 K) using an exciting 532 nm laser line with a power density of 5 W/cm^2.

Deep level TSC spectroscopy was used to obtain the spectrum of defect-related electron traps. The method and its application to metamorphic structures were described earlier [21, 25]. First, the temperature dependence of dark current (DC) was recorded during cooling from 300 K down to 77 K. Then, being cooled to 77 K, the sample was irradiated for preset time with fixed light energy. After the light was turned off and a delay in the dark for PC relaxation was applied, the sample was heated up to 300 K with a constant rate of 10 K/min, and the current temperature dependence was measured. On this curve, trap-related peaks in contrast to the background of DC were observed. For the acquisition of TSC spectra, the temperature dependence of DC was subtracted from the raw TSC dependencies.

3 Results and Discussion

3.1 Photoelectric Properties at Room Temperature

PL spectra of the studied metamorphic InAs/$In_xGa_{1-x}As$ QD structures at room temperature are shown in Fig. 2a, indicating the optical transitions between QD ground states, the top axes in both graphs are scaled in wavelengths for convenience. One can see that the PL band shifts to lower energies (redshifts) with increasing In content x in the confining InGaAs layers. The shift is attributed to the reduction in lattice mismatch between the materials of QD (InAs) and $In_xGa_{1-x}As$ layers with the increase in x, resulting in a decrease of the compressive strain in QDs.

This causes a reduction of the InAs QD bandgap and, then, a redshift of the PL as well as a change in the photoresponse onset toward IR [5, 17, 26–31]. An additional effect is the reduction of band discontinuities between QD and InGaAs confining layers, that causes a decrease of the confinement potentials. Also, the PL intensity tends to reduce for higher x. This is due to the fact that the increase in x reduces the confining potentials, facilitating the carrier leakage to InGaAs, an effect that can be considered as a non-radiative process.

The respective room temperature PC spectra of the structures are given in Fig. 2b. Features due to the QDs are also observed on the PC curves, as well as those related to InGaAs layers and GaAs bottom layer. The PC signal at the energies below the PL band onsets could be related to growth defects.

The investigated metamorphic InAs/$In_{0.15}Ga_{0.85}As$ QD structure was found to be photosensitive in the telecom range at 0.95 eV (1.3 μm). As x increased, a redshift was observed for all the samples: the structure with $x = 0.31$ was found to be sensitive near 0.8 eV (1.55 μm) (Fig. 2b), i.e., at the third telecom window [32]. In addition,

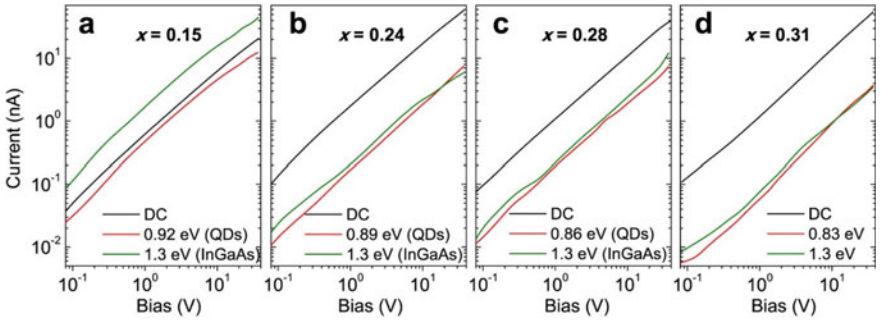

Fig. 3 Current versus voltage for the InAs/$In_xGa_{1-x}As$ structures with $x = 0.15$ (**a**), 0.24 (**b**), 0.28 (**c**) and 0.31 (**d**) at the dark (black) and PC under illumination of 300 mW/cm^2 at the energies of PL spectrum peaks (QD excitation) and 1.3 eV (InGaAs excitation) [24]

only a slight reduction of QD PC signal was detected, thus confirming preservation of a satisfactory photoresponsivity, comparable to the sample based on $In_{0.15}Ga_{0.85}As$. Recently, metamorphic QD heterostructures with $x = 0.15$ demonstrated a photoresponse similar to that in InAs/GaAs QD nanostructures under the same conditions [17]. Also, the PC reduction followed the trend of the PL one, as evidenced in Fig. 2.

The photoresponse reduction for increased x is most notable in Fig. 3, where the current-voltage dependences of DC and PC at different characteristic spectral ranges are presented. The PC value is just the photoinduced part of current obtained from the total current under illumination by subtracting DC (note the logarithm scale on X and Y axes). The mentioned spectral ranges are the QD PL peak positions and 1.3 eV, where the InGaAs MBs absorb efficiently. These dependencies are linear within the experimental error, similar to the dark I–V characteristics.

The best photoresponse was detected in the heterostructure with the lowest $x = 0.15$ in the confining layer that also revealed the lowest DC. At the applied level of MB excitation intensity (300 μW/cm^2), the PC value in the InAs/$In_{0.15}Ga_{0.85}As$ structure was 2–3 times above DC. When exciting at the QD energy, the photoresponse was comparable to DC: however, it should be considered that our structures have only one QD layer. Multilayered QD structures are expected to have a higher IR photoresponse. The structures with higher In content showed a lower PC: the detected values were approximately an order lower than DC magnitudes for all the applied voltages and different spectral points. The lowest PC was detected in the structure with the highest In content $x = 0.31$, despite the increase in the probability of carrier escape from QDs discussed above.

Apparently, the PC decrease was due to the presence of defects in MB, whose density increases with x, as known both from the structural analysis [26] and deep level transient TSC spectroscopy [21]. An InAs/$In_{0.15}Ga_{0.85}As$ QD structure was reported to have a total defect density near the QD layer comparable to that in InGaAs/GaAs ones; on the other hand, structures with higher x showed higher amounts of defects, as discussed below.

The photogeneration of carriers in MB occurs at energies above the bandgap ε_g of InGaAs confining layer: these values were calculated for different x by applying an empiric formula [33] and they are indicated by arrows in Fig. 2b. However, one can see a slight decrease in PC at excitation energies above ε_g. This confirms the conclusion [17, 29, 34] that metamorphic QDs are more effective contributors to PC than MB, despite the former being effective center of recombination [26, 27, 35, 36].

This PC peculiarity can be understood, if one considers the calculated QD band profiles along the growth direction [24] given in Fig. 4a. Furthermore, simulation of probability densities for confined carriers in Fig. 4b indicates a higher localization of heavy holes compared to that of electrons.

To contribute to the PC, electron–hole pairs photogenerated in QDs should thermally escape from QDs. It was established [37] that electrons and heavy holes escape from metamorphic QDs simultaneously, as correlated pairs, and the activation energy of the escape is the sum of the activation energies of two particles [38].

While studying the thermal dependence of PL emission in metamorphic QD samples [39, 40], it was shown that such activation energies correspond to the sum of energy distance from the WL levels and QD states. Being 250 meV for $x = 0.15$, the activation energy decreases to 150 meV for $x = 0.31$, thus the thermal escape of confined carriers caused a strong PL quenching at room temperature, as assumed in [24].

Based on these findings, one can suppose that carriers, after being excited in QDs, can thermally escape to WL and MB: there, the band bending in vicinity of QD (Fig. 4a) causes a separation of the electrons and heavy holes, as the holes are trapped back to QDs while the electrons remain outside due to the barrier inhibiting their re-trapping in QDs. As a result, heavy holes stay in the QD (Fig. 4b), whereas electrons can move along the potential well of WL and MB, participating in the conductivity [24]. This assumption is confirmed by discussions in [37], where the

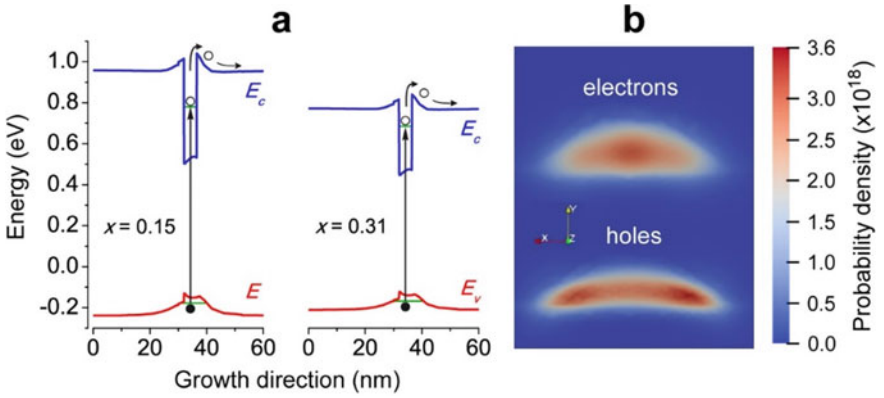

Fig. 4 Band profiles in the InAs/In$_x$Ga$_{1-x}$As QD structures with different x along the growth axis (**a**) and probability densities of the confined electrons and holes for the InAs/In$_{0.15}$Ga$_{0.85}$As QD (**b**) calculated with Tibercad software for 300 K [24]

escaped carriers at room temperature are not considered as excitons, as they can be separated in the vicinity of QDs by the band bending.

On the other hand, the non-equilibrium carriers generated in the confining layers have no obstacle to their recombination. It should be recalled here that WL was suggested to be the main conductivity channel in lateral metamorphic nanostructures [24, 25], alike InGaAs/GaAs ones [41], so the carriers are efficiently collected near the surface.

The decrease of PC signal above ε_g in Fig. 2b is followed by a slow rise at higher energies, e.g., above 1.3 and 1.1 eV for the structures with $x = 0.15$ and 0.31, respectively. This is probably caused by stronger optical absorption and, hence, generation of the carriers closer to the surface (and QD layer), thus involving shallower traps located there. Indeed, TSC spectroscopy [21] and deep level transient spectroscopy (DLTS) [42] have established that the shallower electron traps are concentrated near the surface of these structures (in relation to these samples, near the QD layer), unlike the deeper ones being located mainly in the InGaAs MB layer. From shallower traps, the thermal escape of electrons back to the conduction band is easier. Thus, the electrons excited near the QD layer are more mobile than those generated deeper in MB and, therefore, they give a higher contribution to the charge transport. Furthermore, the electrons generated near the surface are close to the QD layer and can freely transfer to the WL as a conductivity channel.

An increase in PC due to the absorption in GaAs (involving the defect states) is followed by a similar drop of PC near 1.4 eV. This effect is attributed to the photogeneration of carriers near the InGaAs/GaAs interface known to contain a high concentration of defects as traps and recombination centers.

The PC spectra can change with pumping intensity, as the relative contribution of different features to photoresponse varies with excitation density. Figure 5 shows PC values versus excitation intensity for the structures with $x = 0.15$ and $x = 0.31$ at different characteristic points of the spectra: the high-energy slope of the PL band related to the resonant excitation of the whole QD ensemble and the efficient edge absorption in InGaAs under 1.3 eV as well as GaAs under 1.5 eV [24].

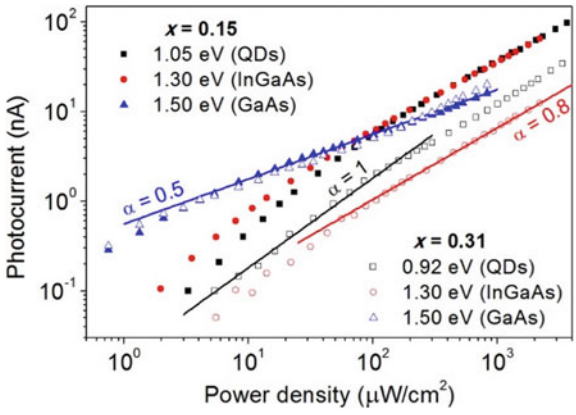

Fig. 5 PC versus the intensity of excitation at characteristic spectral points for the InAs/$In_xGa_{1-x}As$ structures with $x = 0.15$ and 0.31. The lines indicate fitting of data by power functions $f(x) \sim x^{\alpha}$ [24]

At the equivalent spectral ranges, both the structures demonstrated similar behavior of photoresponse. So, the band-to-band excitation in GaAs (1.5 eV) showed a square root dependence at most of the intensity range [24]. Such function is characteristic for the band-to-band recombination of non-equilibrium carriers in undoped semiconductors, where they highly dominate the equilibrium ones [43]. Otherwise, the dependencies for the QD and InGaAs excitation are linear at low carrier generation, transforming to sublinear at higher pumping. The linear dependence allowed to conclude that the carrier recombination proceeds through Shockley-Read centers [24]. It becomes sublinear since the center are saturated at higher intensities and, hence, carrier concentrations [44].

3.2 *Photoelectric Properties at Low Temperature*

When cooling the structures to liquid nitrogen temperatures, all the spectral features for PL and PC are expectably shifted to higher energies. The PL intensities, alike those for 300 K, keep the trend of decreasing with increasing the In content (Fig. 6a). However, their PC in Fig. 6b increases with x, unlike the room temperature data (Fig. 2b). This could be explained by a specific impact of the traps on the carrier mobility at lower temperatures, which manifests in the complex dynamics of PC increase.

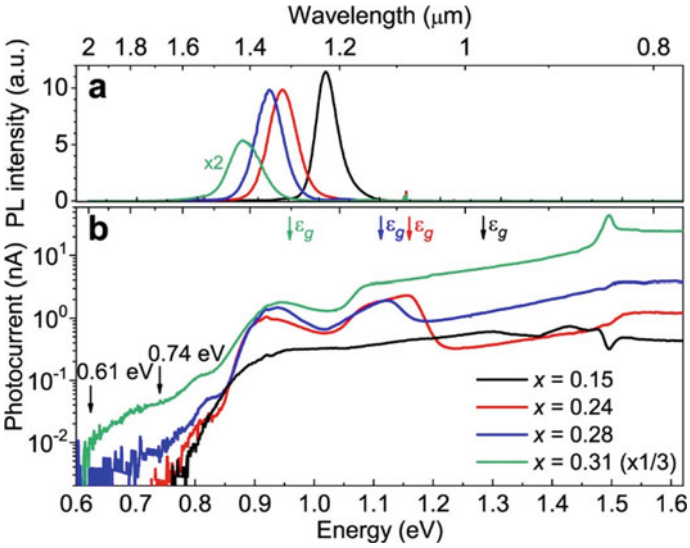

Fig. 6 PL (**a**) and PC (**b**) spectra of the InAs/$In_xGa_{1-x}As$ QD structures with different In content at 77 K [21]. The arrows mark the onsets of the defect responsivity

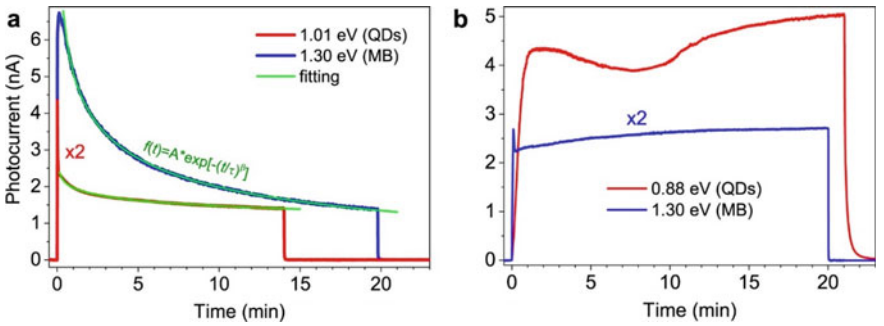

Fig. 7 Lateral PC versus time (77 K) in the InAs/$In_{0.15}Ga_{0.85}As$ (**a**) and InAs/$In_{0.31}Ga_{0.69}As$ (**b**) QD structures at the resonant QD excitation (red) and the simultaneous InGaAs and QD array excitation at 1.3 eV (blue). For the former structure (a), PC is fitted by allometric exponents (green curves). The point $t = 0$ corresponds to the start of illumination [25]

Switching the excitation on, a monotonous decrement of PC under a constant illumination is observed after the initial fast increase (Fig. 7a, b). This complex time dependence of PC was studied in detail for the structures with different x in [25]. In particular, it was found that the PC decrement depending on time under the excitation follows a stretched (allometric) exponent ~$\exp[(-t/\tau)^{\beta}]$, where τ is decay time and $\beta < 1$ is the dispersion factor. Allometric function (exponent or hyperbola) is observed in kinetic processes of structurally disordered systems. It is known [45] to originate from a continuous set of independent single functions with different decay times contributing to the amplitude decay as a result of the disordering, which is described by the dispersion factor β.

The PC decrement under illumination was attributed to an effect of electron traps, considering the WL to be a conductivity channel in the metamorphic QD array with in-plane bias. The traps near the QD array were confirmed by HRTEM microscopy [26, 42]. In particular, V-shaped dislocations originated at the large ('ripened') QDs were found to propagate towards the surface [46]; other extended defects (EDs), named as closed-shaped, were observed just above some QDs [26, 42]. Furthermore, various point defects (PDs) were detected near the QD layer by DLTS [42, 46–48]. The carriers trapped into the electron traps located just around QDs could induce a Coulomb potential, which draws the non-equilibrium electrons away from QDs and neighbor area of WL, thereby screening and narrowing the in-plane channel of conductivity [49]. Furthermore, under the MB excitation, this induced electric field may prevent non-equilibrium electrons which are coming from the embedding InGaAs layers to fall in WL, reducing photoresponse amplitude. The build-in electric field near QDs increases with the trapped charge at prolonged illumination. Various type of defects under various conditions should result in a set of exponents causing, in turn, the allometric function. It is noteworthy that no degradation of PC under excitation was observed at room temperature [25].

Quantitative analysis of the PC decrement curve was possible for the structure with $x = 0.15$, while it was more complex for the structures with higher x due to long-term

increase kinetics (Fig. 7b). This confirmed that the amount of traps increases with the In content in MB, as this feature was also found by both HRTEM observations [26, 42] and deep level spectroscopies [21, 42]. This is also seen in Fig. 6, where the contribution of the defects is observed at energies below the QD-related response. The band with onset at 0.74 eV is related to EL2-like PD [24], while the response at lower energies could be attributed to shallower defects, whose composition was found in the TSC studies.

3.3 Electron Traps

Four structures with $x = 0.15, 0.24, 0.28$ and 0.31 were studied by TSC spectroscopy earlier [21], and the total amount of traps in them was estimated by the total charge released through the thermal escape of carriers from traps. The values for the structures at identical conditions were 22, 145, 162, and 430 nC, respectively. The defect amount for the metamorphic structure with the lowest In content in MB ($x = 0.15$) was then shown to be comparable or lower than that in the best standard InGaAs/GaAs structure studied with this technique. However, a higher amount of defects has been found in other structures with InGaAs layers with higher x.

In Fig. 8 we show the results of the TSC technique applied to the structures with the highest and lowest values of x in order to obtain the energy spectrum of trap levels [25]. As the trap-related bands overlap each other, the energies of thermal activation of the traps were roughly estimated as $\varepsilon \approx 23 \times kT_m$, where T_m is the temperature at the maximum and k is the Boltzmann constant [21].

Signatures of such PDs as EL10, EL9, EL7, and EL6 were found in both the structures near 96 K (0.16 eV), 110 K (0.22 eV), 145 K (0.29 eV), and 190 K ($E_c -$ 0.37 eV), respectively. The energy of the shallowest trap EL10 (0.16 eV) was obtained more precisely by fitting the band onset by a function proportional to $\exp(-\varepsilon/kT)$. In the sample with $x = 0.31$, this band is lost against the background of the more intense EL9-related band that is very close at 111 K.

Furthermore, the bands of EDs near 267 K ($E_c - 0.53$ eV), 236 K (0.47 eV), and 218 K (0.42 eV) marked, respectively, as ED1, ED2 and ED3 were detected. Although the ED2 defect appears clearly only in the InAs/$In_{0.31}Ga_{0.69}As$ structure after QD resonant excitation (Fig. 8b), it was observed in other spectra, including those for $x = 0.15$, under different conditions [21]. These bands, considering their activation energies, could be also attributed to PDs EL3, EL4 and EL5, respectively [50], as it was done in both GaAs and related nanostructures [42, 47, 51]. The band attribution to either PDs or EDs was discussed in detail in [21].

Also, the InAs/$In_{0.15}Ga_{0.85}As$ QD structure revealed a set of new defects undetected in other samples. In particular, the band near 215 K, attributed earlier to ED3 [21], was found to split in two sharp peaks near 212 and 217 K which correspond to activation energies of, respectively, 0.42 and 0.43 eV. At the indicated measurement conditions, the split is notable only after the 1.3 eV excitation but was also observable under 1.01 eV excitation during a shorter time of 30 s [25].

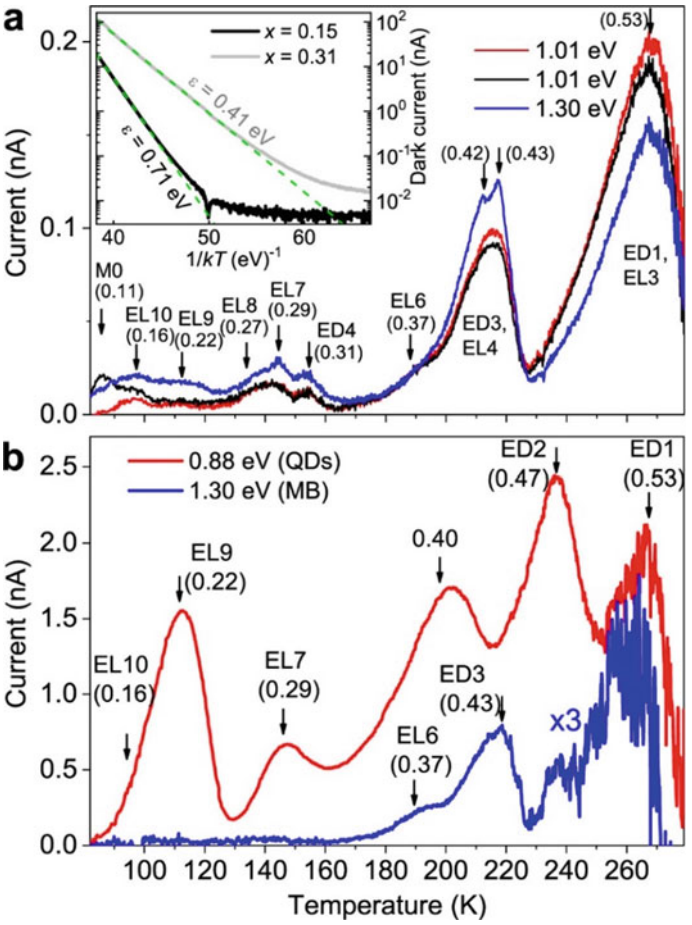

Fig. 8 TSC spectra of the InAs/$In_xGa_{1-x}As$ QD structures with $x = 0.15$ (**a**) and 0.31 (**b**) measured after the resonant QD excitation (1.01 and 0.88 eV, respectively) and the simultaneous InGaAs buffer and QD array excitation at 1.3 eV (b) with illumination time of 30 min and delay times of 5 min (red, blue) and 30 s (black); estimated activation energies of the traps in eV and their interpretations are given near the vertical arrows and bands. Inset: DC dependences on the temperature of the structures; the activation energies ε are derived from fitting the high-temperature ranges by functions $\sim e^{-\varepsilon/kT}$ (dash lines) [25]

These activation energies, as mentioned above, are very close to that of the PD EL5 at $E_c - 0.42$ eV [50] intrinsic in GaAs and found also in GaAs-embedded nanostructures [52]. The complexes based on Ga and/or As vacancies were considered [53] as possible origins of these defects. As vacancies could be arranged in a dislocation line, the components of the band at 215 K can be originated from EL5 defects both isolated (PDs) and related to dislocations (EDs). As different types of EDs, like closed-shaped defects near the QDs or threading and V-shaped dislocations

in the embedding layers, were observed by means of TEM in metamorphic nanostructures [26, 42], the activation energies can vary depending on the location in the sample volume, leading to the broadening or split of the TSC band.

Likewise, the unstructured band at 145 K, observed in the InAs/$In_{0.31}Ga_{0.69}As$ sample and attributed to EL7 (Fig. 8b), also splits when the In content is lower (Fig. 8a). In any spectrum, two components are distinguished near 145 and 155 K and related to, respectively, E_c – 0.29 eV and 0.31 eV. In addition, a shoulder is observed near 135 K after the excitation both at 1.01 and 1.3 eV. Its estimated activation energy of 0.27 eV is close to that of EL8 PD (0.275 eV) of GaAs [50]. The defects with similar activation energies were found in In(Ga)As/GaAs QD structures near the QD layers [51, 54], but were firstly detected in metamorphic structures in [25].

The deep traps at about 0.30 eV below the conductivity band were found in In(Ga)As/GaAs nanostructures mostly near QDs and attributed to PDs. In metamorphic QD structures, they were detected by DLTS in the upper part of InGaAs cap [42]. However, some traps with similar activation energy in InAs/GaAs QD structures were found to reveal logarithmic DLTS amplitude on filling pulse width [55, 56], that is usually considered as a sign of ED [57]. Thus, our component at 155 K (0.31 eV) was attributed to EL7 trap but possibly related to ED. Indeed, EL7 was assumed [58, 59] to originate from Frenkel pairs (V_{As}–As_i), and the vacancies, as mentioned above, could be related to a dislocation line. Following the numeration introduced in [21], we refer to this trap in Fig. 8a as ED4.

A response of a new trap level was also found after resonant QD excitation and short-time delay (30 s) near 85 K before the band of EL10 at 96 K (black curve in Fig. 8a). A similar signature at 85 K was also detected earlier in TSC spectra of InGaAs/GaAs QD samples after a short delay [60]. Its activation energy was estimated from the band onset to be 0.11 eV. This value corresponds to M0 PD intrinsic in GaAs material [61] and it has been repeatedly found in In(Ga)As/GaAs QD nanostructures [60, 62]. The traps found in the spectra of Fig. 8 and their interpretation are presented in Table 1 together with some references to similar interpretations of DLTS data both in InGaAs- and GaAs-based nanostructures.

The comparison of the TSC band amplitudes in Fig. 8a, b allows us to conclude that the structure with lower In content in MB has a much lower defect density. The same can be concluded if one compares the temperature dependences of DC in the structures of the inset of Fig. 8a. The InAs/$In_{0.31}Ga_{0.69}As$ nanostructure revealed higher DC over the whole temperature range and a lower conductivity activation energy of about 0.41 eV, a value that agrees well with the found trap E_c − 0.43 eV. Otherwise, the corresponding activation energy of conductivity in the InAs/$In_{0.15}Ga_{0.85}As$ structure was ~0.71 eV, this value is close to the depth of EL2 defect (~0.75 eV) characteristic for GaAs. This evidences a higher Fermi energy in the In-rich structure caused by a higher concentration of donor-like defects. It is noteworthy, however, that EL2 should not be considered as a defect related to MBE-grown metamorphic nanostructures, as it is commonly attributed to the GaAs substrate or the InGaAs/GaAs interface [25].

Table 1 Activation energies of the electron traps found in the metamorphic InAs/InGaAs QD structures and their location

Energy (eV)	Designation	Origin
0.11	M0	PDs located at InAs/InGaAs interface [60, 62]
0.16	EL10	PDs at InAs/InGaAs interface [22, 23, 42, 47, 48, 51, 60]
0.22	EL9	PDs at InAs/InGaAs interface [22, 23, 54, 60]
0.27	EL8	PDs at InAs/InGaAs interface [51, 54]
0.29	EL7	PDs at InAs/InGaAs interface [42, 54, 62]
0.31	ED4	EDs (clustered PDs) at InAs/InGaAs interface [55, 56]
0.37	EL6	PDs at InAs/InGaAs interface [22, 23, 48, 60]
0.42–0.43	ED3, EL5	EDs or related PDs in InGaAs MB [26, 42]
0.47	ED2, EL4	EDs or related PDs at InAs/InGaAs interface and in MB [47]
0.53	ED1, EL3	EDs or related PDs at InAs/InGaAs interface and in MB [42]

Summarizing the studies of lateral metamorphic QD structures as potential active structures for detectors in the near-IR telecom windows, we wish to highlight some relevant points: (i) for In-rich (x above 0.15) InGaAs embedding layers, advanced designs are needed to control strain-related defects; (ii) to increase the QD photoresponse, multilayer QD stacks (10 layers as a minimum) are necessary. We believe that these findings should be taken into account for the development of photodetectors based on metamorphic QDs.

However, a problem could arise in using the metamorphic QD structures as cooled detectors. The problem is related to the complicated PC kinetics after switching the illumination on and the large response time, which is observed at 80 K and related to the structural defects. This is more crucial for the structures with In-rich containing InGaAs layers, where a higher amount of the defects has been found. These defects also cause a redshift of the PC onsets toward IR due to additional optical transitions in MB and can act as (i) additional recombination centers resulting in a reduction of QD PL and PC; (ii) trap centers that can localize carriers and alter the carrier transport and lifetime. Thus, since the role of defects in the photoresponsivity at low temperatures is crucial, the control of defects should be one of the fundamental points to be addressed in the design of structures for further successful development of applications.

4 Conclusions

PL and PC characterizations on lateral metamorphic InAs/$In_xGa_{1-x}As$ QD nanostructures with different x were carried out at the room and liquid nitrogen temperatures, employing PL and PC spectroscopies, deep level transition spectroscopy by TSC technique, electrical measurements and theoretical simulations. At 300 K, the

metamorphic nanostructures revealed photosensitivity in the telecom windows at 1.3 ($x = 0.15$) or 1.55 μm ($x = 0.31$). The PC and PL efficiencies of QDs in the InAs/$In_xGa_{1-x}As$ structures with higher x were shown to be lower, but comparable to those of the structure with $x = 0.15$, whose sensitivity was estimated to be similar to InGaAs/GaAs QD structures. This PL and PC reduction was attributed to increased defect density in MB, found by TSC spectroscopy. At low temperatures, the traps caused a time-dependent PC with a reduction of photoresponse under constant illumination, which was explained by the Coulomb screening/narrowing of WL as a conductivity channel caused by the charged traps located near QDs. Furthermore, the traps can cause an increase in the response time of the samples with high x. All the reported data allow to conclude that metamorphic QDs with In-rich containing layers could be valid structures for optoelectronic IR-sensitive devices, but the design of the nanostructure should be optimized. Particular attention should be paid to reduce the amount of defects which can make difficult to use metamorphic InAs/$In_xGa_{1-x}As$ QD structures as cooled detectors.

Acknowledgements This work was supported in part by National Natural Science Foundation of China [61525503, 61620106016, 61604098]; Shenzhen University Scientific Research Start-up Foundation of China [860-000002110207]; and Ministry of Education and Science of Ukraine [0119U100308].

References

1. Bimberg D (2018) Semiconductor nanostructures for flying q-bits and green photonics. Nanophotonics 7:1245–1257. https://doi.org/10.1515/nanoph-2018-0021
2. Wu Y, Yan X, Zhang X, Ren X (2018) Photovoltaic performance of a nanowire/quantum dot hybrid nanostructure array solar cell. Nanoscale Res Lett 13:62. https://doi.org/10.1186/s11671-018-2478-5
3. González D, Braza V, Utrilla AD, Gonzalo A, Reyes DF, Ben T, Guzman A, Hierro A, Ulloa JM (2017) Quantitative analysis of the interplay between InAs quantum dots and wetting layer during the GaAs capping process. Nanotechnology 28:425702. https://doi.org/10.1088/1361-6528/aa83e2
4. Tiemeyer S, Bombeck M, Göhring H, Paulus M, Sternemann C, Nase J, Wirkert FJ, Möller J, Büning T, Seeck OH, Reuter D (2016) Polaron-induced lattice distortion of (In, Ga) As/GaAs quantum dots by optically excited carriers. Nanotechnology 27(42):425702. https://doi.org/10.1088/0957-4484/27/42/425702
5. Wu J, Yu P, Susha AS, Sablon KA, Chen H, Zhou Z, Li H, Ji H, Niu X, Govorov AO, Rogach AL, Wang ZM (2015) Broadband efficiency enhancement in quantum dot solar cells coupled with multispiked plasmonic nanostars. Nano Energy 13:827–835. https://doi.org/10.1016/j.nanoen.2015.02.012
6. Liao M, Chen S, Park JS, Seeds A, Liu H (2018) III–V quantum-dot lasers monolithically grown on silicon. Semicond Sci Technol 33:123002. https://doi.org/10.1088/1361-6641/aae6a5
7. Schmeckebier H, Fiol G, Meuer C, Arsenijevic D, Bimberg D (2010) Complete pulse characterization of quantum-dot mode-locked lasers suitable for optical communication up to 160 Gbit/s. Opt Expr 18:3415–3425. https://doi.org/10.1364/OE.18.003415
8. Zhang J, Ai L, Yan X, Wu Y, Wei W, Zhang M, Zhang X (2018) Photovoltaic performance of pin junction nanocone array solar cells with enhanced effective optical absorption. Nanoscale Res Lett 13:306. https://doi.org/10.1186/s11671-018-2727-7

9. Yu P, Wu J, Gao L, Liu H, Wang Z (2017) InGaAs and GaAs quantum dot solar cells grown by droplet epitaxy. Sol Energ Mat Sol C 161:377–381. https://doi.org/10.1016/j.solmat.2016.12.024
10. Cedola A, Cappelluti F, Gioannini M (2016) Dependence of quantum dot photocurrent on the carrier escape nature in InAs/GaAs quantum dot solar cells. Semicond Sci Technol 31:025018. https://doi.org/10.1088/0268-1242/31/2/025018
11. Carmesin C, Olbrich F, Mehrtens T, Florian M, Michael S, Schreier S, Nawrath C, Paul M, Hoschele J, Gerken B, Kettler J, Portalupi SL, Jetter M, Michler P, Rosenauer A, Jahnke F (2018) Structural and optical properties of InAs/(In)GaAs/GaAs quantum dots with single-photon emission in the telecom C-band up to 77 K. Phys Rev B 98:125407. https://doi.org/10.1103/PhysRevB.98.125407
12. Dusanowski Ł, Syperek M, Misiewicz J, Somers A, Höfling S, Kamp M, Reithmaier JP, Sęk G (2016) Single-photon emission of InAs/InP quantum dashes at 1.55 μm and temperatures up to 80 K. Appl Phys Lett 108:163108. https://doi.org/10.1063/1.4947448
13. Strauss M, Höfling S, Forchel A (2009) InAs/GaInAs(N) quantum dots on GaAs substrate for single photon emitters above 1300 nm. Nanotechnology 20:505601. https://doi.org/10.1088/0957-4484/20/50/505601
14. Balakrishnan G, Huang S, Rotter TJ, Stintz A, Dawson LR, Malloy KJ, Xu H, Huffaker DL (2004) 2.0 μm wavelength InAs quantum dashes grown on a GaAs substrate using a metamorphic buffer layer. Appl Phys Lett 84:2058–2060. https://doi.org/10.1063/1.1669067
15. Semenova ES, Zhukov AE, Mikhrin SS, Egorov AY, Odnoblyudov VA, Vasil'ev AP, Nikitina EV, Kovsh AR, Kryzhanovskaya NV, Gladyshev AG, Blokhin SA, Musikhin YG, Maximov MV, Shernyakov YM, Ustinov VM, Ledentsov NN (2004) Metamorphic growth for application in long-wavelength (1.3–1.55 μm) lasers and MODFET-type structures on GaAs substrates. Nanotechnology 15:S283–S287. https://doi.org/10.1088/0957-4484/15/4/031
16. Seravalli L, Minelli M, Frigeri P, Allegri P, Avanzini V, Franchi S (2003) The effect of strain on tuning of light emission energy of InAs/InGaAs quantum dot nanostructures. Appl Phys Lett 82:2341–2343. https://doi.org/10.1063/1.1566463
17. Golovynskyi S, Seravalli L, Datsenko O, Trevisi G, Frigeri P, Gombia E et al (2017) Comparative study of photoelectric properties of metamorphic InAs/InGaAs and InAs/GaAs quantum dot structures. Nanoscale Res Lett 12:335. https://doi.org/10.1186/s11671-017-2091-z
18. Kunets Vas P, Rebello Sousa Dias M, Rembert T, Ware ME, Mazur YuI, Lopez-Richard V et al (2013) Electron transport in quantum dot chains: dimensionality effects and hopping conductance. J Appl Phys 113:183709. https://doi.org/10.1063/1.4804324
19. Golovynskyi S, Datsenko OI, Seravalli L, Trevisi G, Frigeri P, Gombia E, Babichuk IS, Lin D, Li B, Qu J (2020) Near-infrared lateral photoresponse in InGaAs/GaAs quantum dots. Semicond Sci Tech 35(5):055029. https://doi.org/10.1088/1361-6641/ab7774
20. Golovynskyi SL, Dacenko OI, Kondratenko SV, Lavoryk SR, Mazur YI, Wang ZM et al (2016) Intensity-dependent nonlinearity of the lateral photoconductivity in InGaAs/GaAs dot-chain structures. J Appl Phys 119:184303. https://doi.org/10.1063/1.4948953
21. Golovynskyi S, Datsenko O, Seravalli L, Kozak O, Trevisi G, Frigeri P et al (2017) Deep levels in metamorphic InAs/InGaAs quantum dot structures with different composition of the embedding layers. Semicond Sci Technol 32:125001. https://doi.org/10.1088/1361-6641/aa91e7
22. Kondratenko SV, Vakulenko OV, Mazur YI, Dorogan VG, Marega E, Benamara M et al (2014) Deep level centers and their role in photoconductivity transients of InGaAs/GaAs quantum dot chains. J Appl Phys 116:193707. https://doi.org/10.1063/1.4902311
23. Vakulenko OV, Golovynskyi SL, Kondratenko SV (2011) Effect of carrier capture by deep levels on lateral photoconductivity of InGaAs/GaAs quantum dot structures. J Appl Phys 110:043717. https://doi.org/10.1063/1.3626051
24. Golovynskyi S, Datsenko OI, Seravalli L, Trevisi G, Frigeri P, Babichuk IS, Golovynska I, Qu J (2018) Interband photoconductivity of metamorphic InAs/InGaAs quantum dots in the 1.3–1.55 μm window. Nanoscale Res Lett 13:103. https://doi.org/10.1186/s11671-018-2524-3

25. Golovynskyi S, Datsenko OI, Seravalli L, Trevisi G, Frigeri P, Babichuk IS, Golovynska I, Li B, Qu J (2019) Defect influence on in-plane photocurrent of InAs/InGaAs quantum dot array: long-term electron trapping and Coulomb screening. Nanotechnology 30:305701. https://doi.org/10.1088/1361-6528/ab1866
26. Seravalli L, Frigeri P, Nasi L, Trevisi G, Bocchi C (2010) Metamorphic quantum dots: quite different nanostructures. J Appl Phys 108:064324. https://doi.org/10.1063/1.3483249
27. Gioannini M, Cedola AP, Di Santo N, Bertazzi F, Cappelluti F (2013) Simulation of quantum dot solar cells including carrier intersubband dynamics and transport. IEEE J Photovolt 3:1271. https://doi.org/10.1109/JPHOTOV.2013.2270345
28. Munoz-Matutano G, Barrera D, Fernandez-Pousa CR, Chulia-Jordan R, Seravalli L, Trevisi G et al (2016) All-optical fiber Hanbury Brown and Twiss interferometer to study 1300 nm single photon emission of a metamorphic InAs quantum dot. Sci Rep 6:27214. https://doi.org/10.1038/srep27214
29. Golovynskyi S, Seravalli L, Datsenko O, Kozak O, Kondratenko SV, Trevisi G et al (2017) Bipolar effects in photovoltage of metamorphic In As/InGaAs/GaAs quantum dot heterostructures: characterization and design solutions for light-sensitive devices. Nanoscale Res Lett 12:559. https://doi.org/10.1186/s11671-017-2331-2
30. Mi Z, Bhattacharya P (2008) Pseudomorphic and metamorphic quantum dot heterostructures for long-wavelength lasers on GaAs and Si (Invited paper). IEEE J Sel Top Quant 14:1171–1179. https://doi.org/10.1109/JSTQE.2008.923295
31. Seravalli L, Frigeri P, Minelli M, Franchi S, Allegri P, Avanzini V (2006) Metamorphic self-assembled quantum dot nanostructures. Mater Sci Eng C-Bio S 26:731–734. https://doi.org/10.1016/j.msec.2005.09.093
32. Song H-Z, Hadi M, Zheng Y, Shen B, Zhang L, Ren Z et al (2017) InGaAsP/InP nanocavity for single-photon source at 1.55-μm telecommunication band. Nanoscale Res Lett 12:128–131. https://doi.org/10.1186/s11671-017-1898-y
33. Paul S, Roy JB, Basu PK (1991) Empirical expressions for the alloy composition and temperature-dependence of the bandgap and intrinsic carrier density in $Ga_xIn_{1-x}As$. J Appl Phys 69:827–829. https://doi.org/10.1063/1.348919
34. Azeza B, Alouane MHH, Ilahi B, Patriarche G, Sfaxi L, Fouzri A et al (2015) Towards InAs/InGaAs/GaAs quantum dot solar cells directly grown on Si substrate. Materials 8:4544–4552. https://doi.org/10.3390/ma8074544
35. Seravalli L, Frigeri P, Trevisi G, Franchi S (2008) 1.59 μm room temperature emission from metamorphic InAs/InGaAs quantum dots grown on GaAs substrates. Appl Phys Lett 92:213104. https://doi.org/10.1063/1.2937095
36. Seravalli L, Trevisi G, Frigeri P, Rivas D, Munoz-Matutano G, Suarez I et al (2011) Single quantum dot emission at telecom wavelengths from metamorphic InAs/InGaAs nanostructures grown on GaAs substrates. Appl Phys Lett 98:173112. https://doi.org/10.1063/1.3584132
37. Sanguinetti S, Colombo D, Guzzi M, Grilli E, Gurioli M, Seravalli L et al (2006) Carrier thermodynamics in $InAs/In_xGa_{1-x}As$ quantum dots. Phys Rev B 74:205302. https://doi.org/10.1103/PhysRevB.74.205302
38. Le Ru EC, Fack J, Murray R (2003) Temperature and excitation density dependence of the photoluminescence from annealed InAs/GaAs quantum dots. Phys Rev B 67:1–12. https://doi.org/10.1103/PhysRevB.67.245318
39. Seravalli L, Minelli M, Frigeri P, Franchi S, Guizzetti G, Patrini M et al (2007) Quantum dot strain engineering of InAs/InGaAs nanostructures. J Appl Phys 101:024313. https://doi.org/10.1063/1.2424523
40. Seravalli L, Trevisi G, Frigeri P, Franchi S, Geddo M, Guizzetti G (2009) The role of wetting layer states on the emission efficiency of InAs/InGaAs metamorphic quantum dot nanostructures. Nanotechnology 20:275703. https://doi.org/10.1088/0957-4484/20/27/275703
41. Danil'tsev VM, Drozdov MN, Moldavskaya LD, Shashkin VI, Germanenko AV, Min'kov GM et al (2004) Electron transport effects in the IR photoconductivity of InGaAs/GaAs structures with quantum dots. Tech Phys Lett 30:795–798. https://doi.org/10.1134/1.1804599

42. Rimada JC, Prezioso M, Nasi L, Gombia E, Mosca R, Trevisi G et al (2009) Electrical and structural characterization of InAs/InGaAs quantum dot structures on GaAs. Mater Sci Eng B-Adv 165:111–114. https://doi.org/10.1016/j.mseb.2008.10.007
43. Sze SM, Ng KK (2006) Physics of semiconductor devices. Wiley-Interscience, New Jersey
44. Duboc CA (1955) Nonlinearity in photoconducting phosphors. Br J Appl Phys 6:107–111. https://doi.org/10.1088/0508-3443/6/S4/343
45. Linnros J, Lalic N, Galeckas A, Grivickas V (1999) Analysis of the stretched exponential photoluminescence decay from nanometer-sized silicon crystals in SiO_2. J Appl Phys 86:6128–6134. https://doi.org/10.1063/1.371663
46. Frigeri P, Nasi L, Prezioso M, Seravalli L, Trevisi G, Gombia E, Mosca R, Germini F, Bocchi C, Franchi S (2007) Effects of the quantum dot ripening in high-coverage InAs/GaAs nanostructures. J Appl Phys 102:083506. https://doi.org/10.1063/1.2795661
47. Kaniewska M, Engström O, Kaczmarczyk M (2010) Classification of energy levels in quantum dot structures by depleted layer spectroscopy. J Electron Mater 39:766–772. https://doi.org/10.1016/j.mssp.2006.01.004
48. Asano T, Fang Z, Madhukar A (2010) Deep levels in GaAs(001)/InAs/InGaAs/GaAs self-assembled quantum dot structures and their effect on quantum dot devices. J Appl Phys 107:073111. https://doi.org/10.1063/1.3359704
49. Prishchenko DA, Mazurenko VG, Katsnelson MI, Rudenko AN (2017) Coulomb interactions and screening effects in few-layer black phosphorus: a tight-binding consideration beyond the long-wavelength limit. 2D Mater 4:025064. https://doi.org/10.1088/2053-1583/aa676b
50. Martin GM, Mitonneau A, Mircea A (1977) Electron traps in bulk and epitaxial GaAs crystals. Electron Lett 13:191. http://doi.org/10.1049/el:19770140
51. Sobolev MM, Kochnev IV, Lantratov VM, Cherkashin NA, Emtsev VV (1999) Hole and electron traps in the InGaAs/GaAs heterostructures with quantum dots. Physica B: Cond Matter 273–274:959–962. https://doi.org/10.1016/S0921-4526(99)00577-3
52. Panepinto L, Zeimer U, Seifert W, Seibt M, Bugge F, Weyers M, Schröter W (1996) Temperature dependent EBIC and deep level transient spectroscopy investigation of different types of misfit-dislocations at MOVPE grown GaAs/InGaAs/GaAs-single-quantum wells. Mater Sci Eng, B 42:77–81. https://doi.org/10.1016/S0921-5107(96)01686-8
53. Reddy CV, Fung S, Beling CD (1996) Nature of the bulk defects in GaAs through high-temperature quenching studies. Phys Rev B 54:11290–11297. https://doi.org/10.1103/PhysRevB.54.11290
54. Iliash S, Kondratenko S, Yakovliev A, Kunets Vas P, Mazur YuI, Salamo GJ (2016) Thermally stimulated conductivity in InGaAs/GaAs quantum wire heterostructures. SPQEO 19:75–78. https://doi.org/10.15407/spqeo19.01.075
55. Walther C, Bollmann J, Kissel H, Kirmse H, Neumann W, Masselink WT (2000) Characterization of electron trap states due to InAs quantum dots in GaAs. Appl Phys Lett 76:2916–2918. https://doi.org/10.1063/1.126516
56. Walther C, Bollmann J, Kissel H, Kirmse H, Neumann W, Masselink WT (1999) Non-exponential capture of electrons in GaAs with embedded InAs quantum dots. Physica B 273–274:971–975. https://doi.org/10.1016/S0921-4526(99)00604-3
57. Wosiński T (1989) Evidence for the electron traps at dislocations in GaAs crystals. J Appl Phys 65:1566–1570. https://doi.org/10.1063/1.342974
58. Pons D, Bourgoin JC (1985) Irradiation-induced defects in GaAs. J Phys C: Solid State Phys 18:3839–3871. https://doi.org/10.1088/0022-3719/18/20/012
59. Bourgoin JC, von Bardeleben HJ, Stiévenard D (1988) Native defects in gallium arsenide. J Appl Phys 64:R65–R92. https://doi.org/10.1063/1.341206
60. Vakulenko OV, Golovynskyi SL, Kondratenko SV, Mazur YI, Wang ZM, Salamo G J (2011) Effect of interface defect states on photoelectric properties of $In_xGa_{1-x}As$/GaAs heterostructures with quantum dots. Ukr J Phys 56:940–947. http://archive.ujp.bitp.kiev.ua/files/journals/56/9/560910p.pdf
61. Lang DV, Cho AY, Gossard AC, Ilegems M, Wiegmann W (1976) Study of electron traps in n-GaAs grown by molecular beam epitaxy. J Appl Phys 47:2558–2564. https://doi.org/10.1063/1.322974

62. Krispin P, Lazzari JL, Kostial H (1998) Deep and shallow electronic states at ultrathin InAs insertions in GaAs investigated by capacitance spectroscopy. J Appl Phys 84:6135–6140. https://doi.org/10.1063/1.368927

Spectral Manifestations of Nonlinear Resonant Wave Interactions in the Vibrational Spectra of Transition Metal Dichalcogenides

N. E. Kornienko, A. P. Naumenko, V. O. Gubanov, L. M. Kulikov, V. E. Fedorov, and S. B. Artemkina

1 Introduction

The unique physicochemical properties of inorganic structural analogues of graphene and graphite—a wide family of two-dimensional (2D) transition metal dichalcnogenides (TMD) MeX_2 (Me = Mo, W, Ti, Nb, Zr, Ta, Hf; X = S, Se, Te) are determined not only by features from the two-dimensional structure, but also by the presence of the forbidden band E_g ~ 2 eV, which is associated with their semiconductor properties, and especially their exciton states A_1, B_1, associating with their resonance properties, which are often manifested in Raman spectra (RS). It is significant that TMD excitonic states, unlike traditional semiconductor Raman spectra, are well manifested at room temperatures. Note that this is the subject of scientific discussion to date. The essential role of d-states near the top of the valence band and the bottom of the conduction band, including strong phonon-electron interaction and spin-orbit coupling, in our opinion, is a characteristic feature of TMD. Owing to the combination of layers consisting of different atoms and the difference in charges on them, MeX_2 vibrations are well manifested not only in Raman spectra similar to carbon materials and nanostructures (graphene, fullerenes, nanotubes, onion-like structures, etc.), but also in IR absorption spectra. In addition, semiconductor-metal transitions are characteristic for TMD, as well as superconductivity (especially when they are

N. E. Kornienko (✉) · A. P. Naumenko · V. O. Gubanov
Taras Shevchenko National University of Kyiv, 64/13 Volodymyrska St, Kiev 01601, Ukraine
e-mail: nikkorn@univ.kiev.ua

L. M. Kulikov
Frantsevich Institute for Problems of Materials Science, National Academy of Science of Ukraine, 3 Krzhizhanovskyi Str 142, Kyiv-142 03680, Ukraine

V. E. Fedorov · S. B. Artemkina
Nikolaev Institute of Inorganic Chemistry SB RAS, 3, Acad. Lavrentiev Ave, Novosibirsk 630090, Russia

O. Fesenko and L. Yatsenko (eds.), *Nanooptics and Photonics, Nanochemistry and Nanobiotechnology, and Their Applications*, Springer Proceedings in Physics 247, https://doi.org/10.1007/978-3-030-52268-1_26

intercalated by alkali metal atoms). In connection with the noted above properties of TMD, they should be richer than the widely known carbon nanostructures in a purely scientific and technical-applied respects.

The characteristic features of TMD can also be associated with the unique properties of their excitonic states. In particular, in 2H–MoS_2, the excitons A_1 and B_1 are located at energies of 1.85 and 1.97 eV, respectively [1]. In 2H–WS_2, the exciton energies are 1.95 and 2.36 eV, while in 2H–WSe_2 they are 1.65 and 2.30 eV. It should be noted that MeX_2 is characterized by a large dependence of the intensities and energies of the exciton absorption bands on the number of 2D X–Me–X monolayers [2] and the sizes of nanocrystallites (dimensional quantization), as well as they manifest a strong temperature dependence. Therefore, in some publications on the Raman spectra of TMD, somewhat changed values of exciton energies are given, for example, for 2H–MoS_2 (1.89 and 2.06 eV) [3]. On the whole, a wide spectrum of the exciton states of TMD provides Raman spectra registration conditions close to resonance even for fixed excitation wavelengths of traditional continuous wave (cw) lasers (632.8; 514.5; 488 nm, etc.). For graphite-like structures, where there is a Kohn feature at point K of the Brillouin zone (BZ), the resonance conditions for Raman scattering are always automatically realized. But in the Raman spectra of MeX_2 family, it is possible to obtain both in resonant and nonresonant conditions, which allows a consistent and deeper study of the effect of resonances.

Currently, there is a tendency to study Raman spectra of TMD using a large number of laser excitation lines. For example, in [3], more than 20 laser lines with energies from 1.85 to 2.18 eV were used, which provides close to resonant conditions not only for exciting laser radiation, but also for scattered Stokes or anti-Stokes radiation (double resonant Raman processes). This leads to a variety of obtained spectral information with a large number of additional Raman lines, which are not yet fully understood [3, 4]. The richness of the experimentally observed features of resonance Raman scattering (RRS) is due to the appearance of reviews on this problem [5, 6], as well as a comparative study of Raman spectra of graphene and MoS_2-type TMDs [7].

To a large extent, the great interest in the spectral studies of TMD is due to the complexity of the Resonant Raman scattering phenomenon and the transition from spontaneous to stimulated Raman scattering even when excited by cw lasers. It should be noted that Raman spectra, when a sharp increase in the intensity of Raman scattering when the frequency of the exciting radiation approaches the electronic state is detected, was discovered in the pre-laser era (discovery diploma No. 151 (USSR) dated 1952, authors P. P. Shorygin and T. M. Ivanova). Upon excitation of RRS in the region of almost complete opacity of a substance, the ability of molecules to provide resonant Raman spectra turned out to be some orders of magnitude greater than under nonresonant conditions [8]. In the initial period, Raman spectra were studied for many semiconductors such as CdS, CdSe, ZnSe, GaAs, ZnTe, ZnO, GaP, etc. [9–11]. In many cases, the intensities of the RRS and Rayleigh scattering bands can be equally large. We point out that for a long time many of the specific regularities of RRS, including the period of development of quantum electronics and nonlinear optics, remained not entirely clear.

Extremely high intensities of the resonant Raman spectra (RRS), 10^3–10^9 times higher than the intensity of ordinary spontaneous scattering [8], as well as selective amplification of only some fundamental vibrations, for example, longitudinal optical (LO) phonons [9–11] and especially the observation of sequences of overtone lines of LO-phonons, intensities which can exceed the intensities of the main bands, the RRS with stimulated Raman scattering (SRS) is related.

Preresonance and resonant SRS scattering (SRS) in a number of liquids, including organic, and more complex molecules including dye molecules, were analyzed in reviews [12, 13]. It is characteristic that the SRS spectra showed the most intense vibrational lines of the substance, for example, in benzene, the fully symmetric vibrations $\nu_{1,2}$ (A_{1g}) with frequencies of 992 and 3064 cm^{-1}, respectively, as well as the harmonics $2\nu_1$, $3\nu_1$. In order to approach the resonance conditions for SRS excitation, we used the 2nd harmonic of a ruby laser (347.1 nm) and the 4th harmonic of a neodymium laser (265 nm). In this regard, for liquid nitrogen, as well as for gaseous hydrogen and deuterium, the SRS thresholds during UV excitation decreased by ~8 times [13], which in principle can be explained by the frequency dependence of the cross section RS~$(\nu_L - \nu_{vib})^4$.

The most convincing demonstration of the resonance SRS phenomenon is presented in [14]. To excite SRS in high-quality anthracene crystals at low temperatures (4.2–15 K), tunable dye laser radiation was used. As the excitation ν_L approaches from the bottom to the bottom of the lowest exciton band ($E_g = 3.11$ eV, frequency detunings $\Delta\nu = 100 - 40$ cm^{-1}), an increase in the intensity of the strongest RS line of anthracene (1402 cm^{-1}) was ~10^2 times, and when $\Delta\nu = 35 - 15$ cm^{-1} a sharp drop in the intensity of the RRS was detected. For $\Delta\nu < 40$ cm^{-1}, a band of intrinsic luminescence of the crystal appeared in the spectrum of the resonance RS, which was in 1404 cm^{-1} from the bottom of the exciton band. Note that photoluminescence quite often plays a key role for resonance RS playing the role of a seed for SRS amplification. Nonlinear dependence of the band intensity at 1402 cm^{-1} on the power of the excitation and crystal thickness, narrowing of the Stokes line at 1402 cm^{-1} (FWHM $\delta\nu \approx 1.5$ cm^{-1}) and suppression of other anthracene vibrations, as well as 20% conversion of laser radiation to Stokes line convincingly proved that in this case there was a resonant SRS (RSRS).

For a long time the experimental and theoretical studies of SRS in organic liquids (benzene, toluene, o- and m-xylenes, pyridine, bromoform, etc.), as well as metal vapors (including resonance conditions) were conducted in Taras Shevchenko National University of Kyiv, the results are reflected in a series of publications [15]. Among the basic fundamental results, we note the first observation in 1982 of SRS on polaritons in a number of organic liquids with registration of the frequency–angular structure of scattered radiation [19–26]. This explains the anomalous spectral broadening and conical radiation at the highly developed stage of stimulated Raman scattering, which did not find an adequate explanation for about 20 years. At the same time, significant excitation during SRS of higher vibrational states ($v =$ 2–10) was shown, and the polariton mechanism of vibrational relaxation in liquids was proposed. Thus, in addition to sequences of harmonics of fundamental vibrations, true overtones with shifted frequencies were observed. For the first time, the

resonance mutual focusing of waves during SRS was theoretically considered and the possibility of focusing Stokes radiation in the absence of self-focusing pumping was shown [16], and the excitation of higher vibrational states during SRS was also taken into account taking into account wave self-focusing [17].

It was proved in [18, 19] that the fine quasi-equidistant structure of the Stokes and anti-Stokes bands near the SRS threshold is due to the contribution of four-wave resonant parametric interactions (FWRPI). The influence of nonlinear parametric processes, for which the superposition of resonant and nonresonance electron nonlinear susceptibilities is significant, leads to a difference in the frequency shifts of the Stokes and anti-Stokes components during SRS [20]. Nonlinear parametric processes and a fine spectral structure are also observed in SRS on electronic states in alkali metal vapors (in the vicinity of doublet transitions) [21]. The fine structure of the generated radiation also arises with other FWRPI in metal vapors [22]. Along with polariton frequency–angular branches in liquids, very broadband purely parametric frequency–angular branches are also observed [23]. The development of several FWRPIs in self-focusing fibers, when the phase velocity of nonlinear polarization waves exceeds the phase velocity of emitted waves, leads to the observation of the Cherenkov-type frequency–angular structure in the anti-drain region [24]. The latter manifests itself in a smaller spectral range in comparison with polariton branches. The frequency–angular structure of scattered radiation in metal vapors, which is similar in appearance to scattering by polaritons in a liquid, was considered in [25]. The possibility of simultaneous observation of SRS and inverse RS was shown for the first time experimentally and theoretically in [26]. This may explain the change in the shape of the RRS with alternating positive and negative polarities of the bands when scanning the excitation in the region of a wide electronic absorption band [8].

We carried out a consistent theoretical analysis of the generation of Stokes and anti-Stokes components under SRS with allowance for strong pump depletion and population dynamics of resonance states, including saturation effects and changes in nonlinear resonance susceptibilities [27–36]. In this case, an exact analytical solution was obtained for the interaction of laser pump waves ν_L, Stokes ν_S and anti-Stokes ν_{AS} waves, taking into account the effects of saturation and changes in nonlinear resonance polarizabilities. Additionally, near the resonance an induced dispersion and changes in the phase synchronism (nonlinear quasisynchronism) were taken into account [31]. This extends the key concept of phase synchronism in nonlinear optics, which is applicable only in nonresonant conditions. The concept of nonlinear quasisynchronism was used when considering the generation of the third harmonic, which is attenuated as a result of the stimulated Raman scattering [32]. For the five-wave approximation in the SRS theory, together with cascade combination processes all possible types of FWRPI was theoretically taken into account in [33]. As a result of their large number, which significantly exceeds the number of step processes RS, a fundamentally new phenomenon of energy concentration on one of the Stokes SRS components is manifested [33, 37]. As a result of this, its intensity can significantly exceed the intensity of other components, which is often observed in the experiment [38].

In [34, 35], the SRS theory was developed for IR active vibrational modes (including their polariton nature) and the possibility of their efficient generation despite absorption was shown. It is significant that in these and other publications the possibility of wave enlightenment of the medium is shown, when the amplitudes of all waves are fixed when equilibrium is existed between all competing nonlinear processes. In this case, the nonlinear interactions seem to cease, which is manifested in the stabilization of the intensities of the interacting waves with increasing pump intensity [39]. Theoretical analysis of SRS for pulsed laser pumping showed that the medium-wave bleaching regime in the case of continuous excitation corresponds to the multiwave coupled SRS solitons together with the corresponding solitons of resonance state populations [36]. SRS theory was developed in [40, 41] with a substantial nonmonochromaticity of the pump and reproduction of its spectrum in the Stokes and anti-Stokes regions. In a series of theoretical articles [42–44], SRS is one of the concomitant nonlinear processes in the resonance generation of sum and difference frequencies under conditions of two-photon pump resonance.

Using our experience of studying SRS and understanding its fundamental patterns allowed us deeper approach to the study of RS TMD spectra, including resonant excitation conditions. Based on our own experimental studies of vibrational RS spectra of MoS_2, $MoSe_2$, $MoTe_2$, $MoSe_2$, etc., as well as the results of many publications by other authors, we analyzed the observed anomalies of changes in the intensities of fundamental vibrations and bands of overtones and composite tones. It is significant that we use not only the results of Raman spectroscopy, but also the data of our measurements of the IR spectra of TMD. This made it possible for the first time to distinguish two classes of nonlinear wave interactions in TMD: nonlinear resonance interactions of only 2H–MeX_2 vibrational modes and nonlinear resonance interactions involving laser and scattered radiation. When using 632.8 nm He–Ne laser radiation, which is close to the resonance conditions, we first observed in MoS_2 a giant amplification of the second Stokes component with a frequency of $2\nu_3$ (A_{1g}) and close spectral components.

2 Experimental Procedure

We studied Raman spectra of 2H–MoS_2 nanoparticles (NPs) with 6–8 S–Mo–S monolayers in thick and with sizes (4−5) × 17 (40−50) nm, natural microcrystallites (MK) with sizes of ~200 × 200 nm and more ("Climax Molybdenum Co.," USA), as well as synthesized MoS_2 single crystals and individual 1L monolayers or several MoS_2 layers on Si subtraction. The NPs sizes were determined by the data of precision X-ray studies (the full-profile method, using WinCSD computer structural calculation programs [39]), carried out by Akselrud L. G. (Lviv National University, Ukraine). In this case, the unit cell parameters correspond to the known published data [45]: $a = 0.315956$ (2) nm, $c = 1.22964$ (2) nm. Scanning electron microscopy of micron powders of layered molybdenum disulfide was performed on

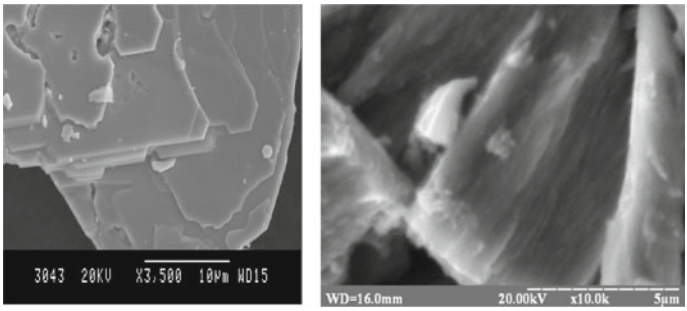

Fig. 1 Images of scanning electron microscopy for micron powders (**a**) and nanoparticles (**b**) of 2H–MoS_2

a JSM-820 Scanning Microscope electron microscope (Fig. 1a). An example of a scanning electron microscope image of LF 2H–MoS_2 is shown in Fig. 1b.

Raman spectra were studied using a modern Horiba Jobin Yvon T64000 spectrometer with a cooled CCD detector in photon counting mode. To excite the Raman spectra, we used radiation from an ion Ar^+ laser with a wavelength of $\lambda_L = 488$ nm near the edge of electronic absorption and radiation from a He-Ne laser $\lambda_L = 632.8$ nm resonant with the exciton states of MoS_2. The IR spectra of ATR and diffuse scattering were additionally studied using a Nicolet NEXUS-470 Fourier spectrometer (400–8000 cm^{-1} working area) using a Spectra-Tech Inc. cell, model 0001-397. For the D^4_{6h} symmetry group of the 2H–MoS_2 crystal structure for 18 normal vibrational modes, the following vibrational representation holds: $\Gamma = A_{1g} + 2A_{2u} + 2B_{2g} + B_{1u} + E_{1g} + 2E_{1u} + 2E_{2g} + E_{2u}$. The vibrations A_{1g}, E_{1g}, and E_{2g} are active in the Raman spectra, and A_{2u} and E_{1u} are active in the IR spectra (half of them relate to the acoustic modes TA, LA). In the case under consideration, just like for the C_6H_6 molecule, half of the vibrational modes are doubly degenerate and some of the vibrational modes (B_{2g}, B_{1u}, and E_{2u}) are inactive in the vibrational spectra.

In experimental studies of Raman spectra and their analysis, special attention was paid to low-frequency regions where difference tones of vibrations appear and acoustic modes can manifest themselves, as well as anomalous amplification of overtones and total tones of the main vibrational modes ν_1 (E_{1g}), ν_2 (E_{2g}) and ν_3 (A_{1g}) whose frequencies for 2H–MoS_2 single crystals are respectively equal to 287, 283, and 409 cm^{-1}. Naturally, in the region of higher vibrational states approaching to the electronic states, it is preferable to use IR spectra in which one can obtain the best signal-to-noise ratio. For 2H–MoS_2 nanoparticles, a decrease in the frequencies of fundamental vibrations $\nu_{1,2,3}$ in comparison with macrosamples is shown: $\nu_1 = 287 \rightarrow 279$ cm^{-1}, $\nu_2 = 383 \rightarrow 377$ cm^{-1}, $\nu_3 = 409 \rightarrow 403$ cm^{-1}.

The Raman spectra made it possible to establish changes in the states of NPs and 2H–MoS_2 microcrystallites (MC) upon exposure to exciting laser radiation. These state changes are associated with an increase in the intensities of the vibrational bands ν_1, ν_2, and ν_3 and a decrease in their frequencies upon amplification of the

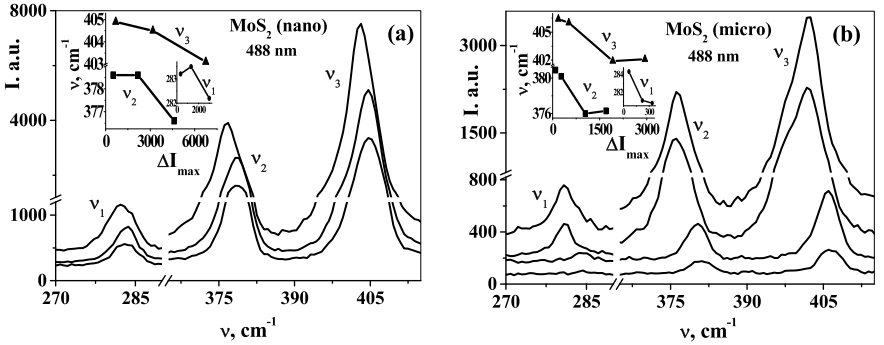

Fig. 2 Changes in the fundamental vibrational bands ν_1, ν_2, ν_3 in the Raman spectra of **a** nanoparticles and **b** 2H–MoS_2 microcrystallites upon 488 nm laser excitation and a change in the broadband background

broadband background (BB) in RS, which is shown in Fig. 2a, b upon excitation of 488 nm.

BB is the result of the emergence of new electronic states, which are also in the band gap of MoS_2 or other TMD, as a result of strong vibrational-electronic interactions (VEI) [38, 39, 41–53]. VEI is also associated with the known instability of the sublattices of metal atoms with the appearance of lines of stronger M–M bonds and charge density waves with a significant decrease in medium symmetry [54]. The dependences of the vibration frequencies ν_1, ν_2, ν_3 on the peak intensities of the corresponding bands minus the intensity BB $\Delta I_{\max}$ are shown in the insets in Fig. 1a, b. The increase of $\Delta I_{\max}$ is due to the redistribution of the electron density and the growth of its delocalized part while reducing the vibration frequencies $\nu_{1,2,3}$ and weakening the strength of chemical bonds (CB). We point out that in MC the changes $\Delta\nu_i$ ($i = 1, 2, 3$) reach 5 cm^{-1}, while in NPs they do not exceed 2 cm^{-1}. We attribute this to the great influence of vibrational-wave processes in micro- and macrocrystals, which will be discussed later. It should also be noted that the spectra of nanoparticles are more intense, which may be due to a lower absorption of 488 nm laser radiation as a result of a dimensional increase in the electron excitation energy

3 Results and Discussion

3.1 Differences in Raman Spectra for Nanoparticles, Micro- and Macrocrystals of MoS_2 at Resonance with Electronic and Exciton States

We compared the Raman scattering (RS) spectra of nanoparticles, natural microcrystals, and 2H–MoS_2 single crystals upon excitation by laser radiation of 488 and

632.8 nm. The Raman spectra upon excitation near the edge of electronic absorption ($\lambda_L = 488$ nm) for 2H–MoS_2 single crystals and nanoparticles (NP, inset) are shown in Fig. 3a. In this case, the spectra are relatively simple: in the fundamental region, there are three relatively narrow oscillation lines ν_1 (E_{1g}), ν_2 (E_{2g}) and ν_3 (A_{1g}), the intensities of which in most cases increase with increasing of vibrational frequency. But for the Raman spectrum of a single crystal, in addition to the dominance of the ν_3 (A_{1g}) = 407−409 cm^{-1} line, there are also cases of a decrease in the intensity of the ν_3 vibration as compared with the ν_2 (E_{2g}) = 282−283 cm^{-1} vibration, which will be analyzed in more detail below. For NPs and microcrystallites, according to the data in Fig. 2 and the insert in Fig. 3a, when the excitation is 488 nm, the ν_3 vibration always has the maximum intensity.

It is significant that for MoS_2 NPs, the frequencies of all vibrations are significantly reduced comparing with single crystals: ν_1 (287 → 280 cm^{-1}), ν_2 (383 → 275 cm^{-1}) and ν_3 (409 → 402 cm^{-1}). It should be noted that these frequency mitigations exceed the decrease in the vibration frequencies in nanoparticles and microcrystals associated with the amplification of the broadband background (see Fig. 2). We also

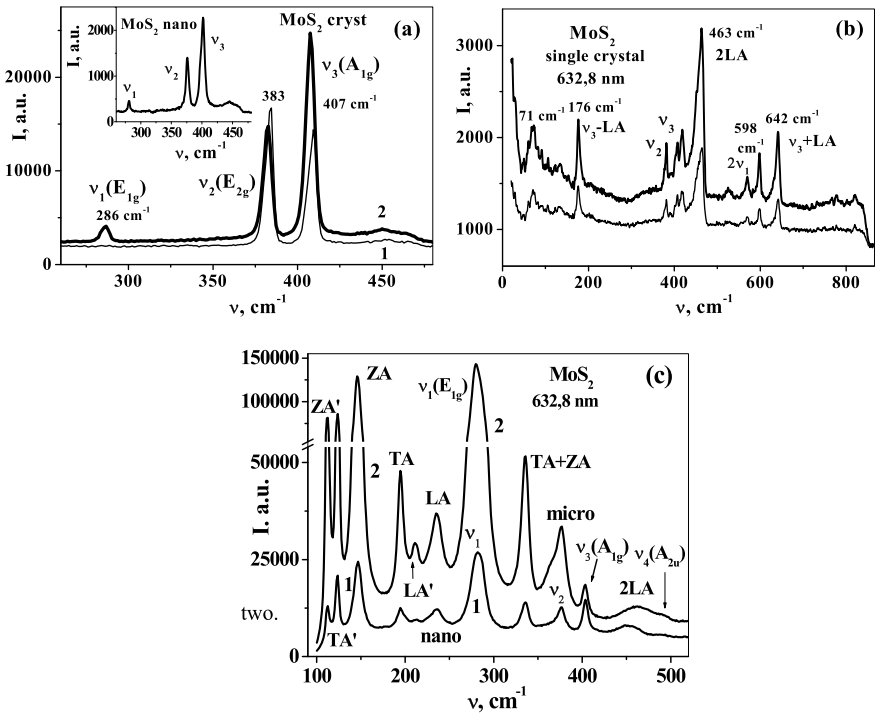

Fig. 3 Raman scattering spectra of single crystals (1, 2) and nanoparticles (insert) of 2H–MoS_2 upon excitation of 488 nm (**a**) and a significant complication of the spectra of single crystals (**b**), as well as nanoparticles (1) and microcrystallites (2) (**c**) at resonant excitation of 632.8 nm. In **b**, the excitation intensities differ by a factor of two

note that when using 488 nm radiation, the intensity of the overtone band of the acoustic vibrations 2LA~450 cm^{-1} in the RS spectra is very low. In the NPs spectra, the intensity of the 2LA band slightly increases, but it still remains much less than the vibrational band ν_3 (see inset in Fig. 3a).

In the case when $\lambda_L = 632.8$ nm line of He–Ne laser in resonance with exciton states, the Raman spectra are greatly complicated, as illustrated in Fig. 3b, c. For 2H–MoS_2 single crystals, a simpler situation is observed, as shown in Fig. 3b. First of all, a sharp amplification of the wide overtone band 2LA $\approx$ 463 cm^{-1}, the intensity of which significantly exceeds the intensity of the lines of the main vibrations ν_2 and ν=, should be noted. In addition, the low-frequency bands of difference tones (71 and 176 cm^{-1}) appear in the spectrum and the high-frequency bands of the sum tones ν_i + LA ($i = 1, 2, 3$) and overtone $2\nu_1$ are significantly amplified (see Fig. 3b). In this case, the ν_1 vibration is not observed in the spectra, as well as in spectrum 1 for the MoS_2 single crystal in Fig. 3a.

Even more radical changes in the RS spectra upon resonance excitation of 632.8 nm are observed for nanoparticles and natural microcrystallites of 2H–MoS_2, as shown in Fig. 3c. First of all, we note the manifestation in the spectra of distinct bands of transverse and longitudinal acoustic modes TA, LA, as well as the torsion mode ZA. A significant redistribution of the intensities of the vibrational bands ν_1, ν_2, and ν_3 is also significant: the very weak (or even unobservable) at 488 nm band ν_1 in the resonance case has a maximum intensity and noticeably broadens. And previously very strong bands ν_2 and ν_3 are significantly weakened, which is especially true of the previously strong band ν_3. The 2LA overtone band is also very weak. At the same time, the bands of sum tones and overtone $2\nu_3$ in the region of 600–1000 cm^{-1} are anomalously enhanced. We also point out that in RS of MoS_2 NPs, upon excitation of 632.8 nm, strong variations in the intensities of all vibrational bands appear. Such significant differences in the spectra of single crystals and 2H–MoS_2 nanoparticles in the case of quasiresonant radiation of 632.8 nm are associated not only with a change in the structure of NPs under the influence of laser radiation, but to a large extent with an exacerbation of resonance due to an increase in the energies of electronic and exciton states due to size quantization All the above significant changes in the resonance spectra of Raman scattering, including the strong redistribution of the intensities of the vibrational bands and the manifestations of acoustic vibrations, as well as the giant amplification of the bands of the second and higher orders, will be analyzed in detail in the following sections.

3.2 Observation in the Raman Spectra the Series of Acoustic Vibrations and Composite Tones with Their Participation

At resonant excitation ($\lambda_L = 632.8$ nm), the difference and sum tones with the participation of acoustic vibrations are well manifested in RS. They are especially clearly observed in the spectra of 2H–MoS_2 single crystals (Fig. 3b). First of all,

we are talking about the most high-frequency longitudinal acoustic mode LA. In the considered composite tones $\nu_i \pm$ LA ($i = 1, 2, 3$), vibrations appear in the region of oppositely directed wave vectors k at the boundary of the Brillouin zone (BZ, point M). Therefore, an analysis of the frequency positions of the bands $\nu_i \pm$ LA will allow us to clarify the frequencies ν_i(M) and LA(M).

Like the most intense strongly asymmetric band 2LA = 463 cm^{-1} in Fig. 3b, the considered composite tones $\nu_{1,2,3} \pm$ LA are characterized by significant asymmetry. It is due to the strong frequency dispersion of LA vibrations, in contrast to the much weaker phonon dispersion of optical vibrational modes. For bands of sum tones, as well as for the band of the overtone 2LA, low-frequency asymmetry is observed, and for difference frequencies it is observed the high-frequency asymmetry. Figure 4a shows the results of a numerical analysis of the shape of the ν_3(M) − LA(M) difference band. High-frequency asymmetry is manifested in the presence of additional spectral components of 181–183 cm^{-1}. It is significant that when the excitation power is doubled, not only does the intensity of the band 176 cm^{-1} double,

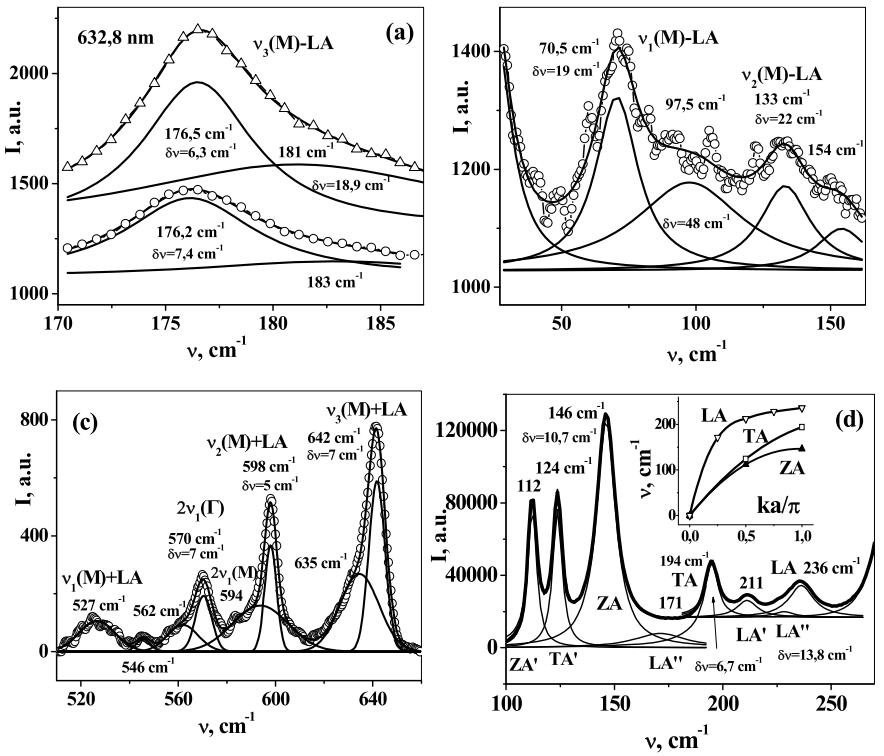

Fig. 4 The results of the numerical decomposition of the observed bands of the difference tones ν_3-LA (**a**) and ν_1-LA, ν_2-LA (**b**), as well as the total tones $\nu_{1,2,3}$ + LA (**c**) in the Raman spectra of 2H–MoS_2 single crystals, as well as nanoparticles (**d**) with resonance excitation of 632.8 nm into individual spectral components

but there is a slight decrease in its half-width $\delta\nu$ (7.4 $cm^{-1} \rightarrow$ 6.3 cm^{-1}). There is a narrowing and an additional band of 181–183 cm^{-1}. This decrease in $\delta\nu$~15% can characterize the transition regime from spontaneous to stimulated RS.

Figure 4b shows the results of the decomposition of lower-frequency difference frequencies into components of the Lorentz form. It is significant that two difference tones $\nu_1(M) - LA = 70.5\ cm^{-1}$ and $\nu_2(M) - LA = 133\ cm^{-1}$ and their additional high-frequency asymmetry satellites appear here. Figure 4c shows the results of a numerical analysis of the structure of the observed sum bands $\nu_{1,2,3} + LA$. Note that the low-frequency asymmetry of all the bands under consideration is clearly manifested here and the overtone $2\nu_2(M)$ overlaps with the low-frequency wing ~294 cm^{-1} of the total tone $\nu_2(M) + LA = 598\ cm^{-1}$. Moreover, the superposition of vibrational bands of the sum tone $\nu_1(M) + LA$ and overtone $2\nu_1$ is observed. The values of $\nu_{1,2,3}(M)$ and LA(M) were calculated from the observed frequency pairs $\nu_{1,2,3}(M) - LA$ and $\nu_{1,2,3}(M) + LA$, which are shown in Fig. 4a–c. The obtained value of the frequency $LA(M) \approx 232\ cm^{-1}$, up to small anharmonic corrections, correlates well with the value determined from the position of the overtone $2LA = 463\ cm^{-1}$. The following values were obtained for the frequencies of the main oscillations at the BZ boundary: $\nu_1(M) = 302.5\ cm^{-1}$, $\nu_2(M) = 366\ cm^{-1}$, and $\nu_3(M) = 409\ cm^{-1}$. Thus, a positive dispersion of phonon branches was obtained for KM ν_1, a negative dispersion for ν_2, and a very weak dispersion for ν_3 mode. The results obtained are in good agreement with the results of numerical calculations [5].

We proceed to the analysis of specific manifestations of acoustic modes in the RS spectra of nanoparticles and natural microcrystallites 2H–MoS_2, shown in *r* is 4*d*. Here are the results of numerical decomposition of the observed family of lines of acoustic vibrations into Lorentzian components, which indicates the absence of inhomogeneous broadening. Under these conditions, the manifestation of vibrational states at the BZ boundary is associated with a doubling of the size of unit cells (UC) and the process of addition of phonon dispersion branches. In this case, the vibrational states at the BZ boundary (point M) are transformed into the center of the BZ (point Γ) and can be observed in vibrational spectra. As a result, we observe the lines LA-mode = 236 cm^{-1}, TA = 194 cm^{-1} and the torsion mode lines ZA = 146 cm^{-1}. It is characteristic that the torsion mode ZA has the maximum intensity. The observation of additional spectral components $ZA' = 112\ cm^{-1}$, $TA' = 124\ cm^{-1}$ and $LA' = 211\ cm^{-1}$ (see Fig. 4d) is due to the repeated doubling of the size of the electron microscope. Isolation of weak additional components LA″ around 171 and 229 cm^{-1} indicates a third increase in the size of the UC. Thus, an increase in the sizes of 2H–MoS_2 by no less than 8 times is shown. According to the repeating scenario of disordering of the 2H–MoS_2 structure (premelting) under the influence of resonant laser radiation of 632.8 nm, the dispersion of phonon acoustic branches was reconstructed, which is illustrated by the inset in Fig. 4d. many lines of acoustic modes made it possible to identify the sharp peak TA + ZA with a frequency of 336 cm^{-1} in Fig. 3b, c. The intensity of this peak significantly exceeds the intensity of the main vibrations $\nu_{2,3}$. Consequently, the effect of resonant radiation on nanostructures can significantly increase their anharmonicity and enhance the nonlinear resonant interaction of CMs.

3.3 *Manifestation of Nonlinear Wave Interaction of Vibrational Modes in the IR Spectra of MoS_2*

To explain a number of detected anomalies in the Raman spectra of nanoparticles (NPs) and single crystals, we studied the IR spectra of diffuse scattering (DS) for NPs and microcrystallites of MoS_2. Because of their low frequencies, the vibrations of plurality MeX_2 structures are close to the average thermal vibrational energies kT $\approx$ 200 cm^{-1} at room temperature and can take an active part in creating nonequilibrium populations of higher vibrational states (HVS). For example, in a 2H–MoS_2 single crystal, low-frequency transverse and longitudinal acoustic vibrations TA $\approx$ 124 and 194 cm^{-1}, LA $\approx$ 171, 211 and 236 cm^{-1} and torsion ones ZA $\approx$ 112 and 146 cm^{-1}, as well as optical fundamental vibrations active in Raman scattering ν_1 $(E_{1g}) = 287$ cm^{-1}, ν_2 $(E_{2g}) = 383$ cm^{-1} and ν_3 $(A_{1g}) = 408$ cm^{-1} can take an active part in the nonlinear interaction of vibrational modes (NIVM) with the generation of higher-frequency excitations in the overtone region and total tones. interactions, thermal energy is converted into a high-energy region with the creation of excess populations of the HVS series. The latter approach electronic and exciton states, which leads to enhanced vibrational-electronic interactions (VEI) [49–53]. A clear confirmation of the key role of NIVM is the visible photoluminescence of porous silicon upon IR excitation, the frequency of which is seven times lower than the frequency of the emitted light [54].

A comparison of DS IR spectra for nano- and microsamples of MoS_2 is shown in Fig. 5a. It is characteristic that the recorded optical density D for the IR spectra of NPs (spectrum 1) is much higher than for MC (spectrum 2). This is especially significant for the region of overtones and sum tones ($\nu > 500$ cm^{-1}). Earlier, we observed a similar amplification of vibrational bands in the IR absorption and Raman spectra from C_{60} fullerite nanofilms with a thickness of 150–250 nm compared with the spectra of microfilms (1, 2–2, 0 μm) [3, 4, 55]. Anomalous amplification of vibrational bands in nanostructures is associated with a significant change in their electrophysical parameters as a result of weakening symmetry and strengthening anharmonicity, as well as NIVM. This leads to an increase in the VEI and a change in the electronic states, which has been studied very little previously. At the same time, the fundamental IR mode $\nu 4$ (A2u) with a frequency of 468.6 cm^{-1} and a half-width of $\delta\nu = 4.6$ cm^{-1} is much better manifested for MC MoS_2, as shown in the inset in Fig. 5a.

A comparison of the selected IR spectra of DS NPs and MCs of MoS_2 is shown in Fig. 5b. The separation of part of the vibrational bands of MC on BB in IR spectrum 2 is shown in Fig. 5a. It is seen that the spectra of nanosamples are more than three times more intense. But for the microsamples, the fine structure of the vibrational bands is better expressed, which is due to the smaller FWHM $\delta\nu$ of the individual spectral components. Figure 5b also gives an interpretation of the main vibrational bands. As in the RS spectrum in Fig. 4c, the sum tone ν_2 + LA, a series of sum frequencies with the participation of optical and acoustic VMs, as well as overtones $2\nu_2$, $2\nu_4$ (A_{2u}) and $3\nu_2$, $3\nu_3$ are shown here.

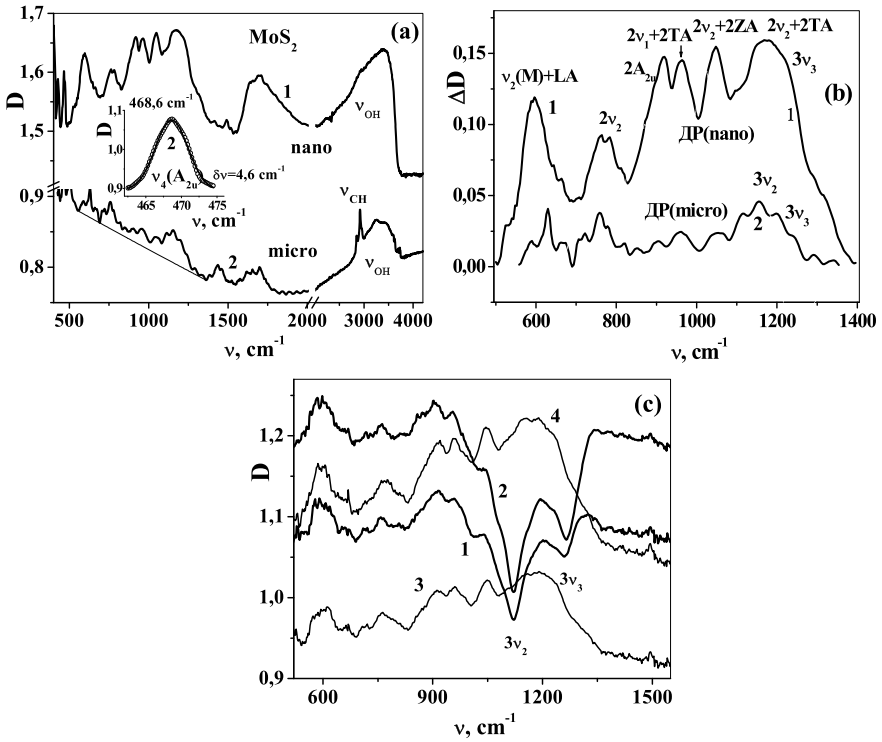

Fig. 5 Comparison of the IR spectra of diffuse scattering (DS) of nanoparticles (NP) (1) and microcrystallites (MC) (2) MoS_2 in a wide spectral region (**a**) and comparison of the IR bands DS NP (1) and MC (2) MoS_2 isolated on a broadband background in the mid-frequency region (**b**), as well as a comparison of the observed fragments of the IR spectra of DS NP with the negative polarity of the vibrational bands (1.2) and the usual positive polarity of the absorption bands (3.4) (**c**)

Figure 5c shows the observation of IR bands of negative polarity ($\Delta D < 0$) in the region of $3\nu_2$ and $3\nu_3$ MoS_2 overtones for spectra 1 and 2 DS NPs MoS_2 in comparison with similar spectra 3 and 4, in which the usual absorption spectra appear. The bands of negative polarity are due to the excessive inverse population of the vibrational levels $3\nu_2$ and $3\nu_3$, which is formed as a result of NIVM with lower frequencies. Although vibrational bands with $\Delta D < 0$ are observed an intense broadband background of electron absorption and overall absorption is manifested in general, their observation proves the key role of NVMCs. It is in the nanoparticles reached abnormally strong nonlinear susceptibility NIVM processes. The increasing role of radiation bands in DS spectra is associated with a longer optical path along which NIVM accumulation is realized. For the accumulation of nonlinear interactions, collective (wave) properties of vibrational modes are important. We point out that for the broadband electronic background in the IR spectra of DS LF, as well as for the IR glow, significant variations are characteristic intensity, which is partially

illustrated in Fig. 5c. This is due to the relationship between the HVS populations and the induced electronic states as a result of the action of strong VEIs. Both strong variations of the electronic background and the time-dependent IR emission of nanostructures are also associated with excessive variations in nonlinear wave interactions.

3.4 Change in the Ratio of the Intensities of the Fundamental Bands in the Raman Spectra of MeX_2, the Appearance of Their Fine Structure, and the Observation of the Phenomenon of Stimulated Scattering

Let us consider the ratio of the intensities of the vibrational bands ν_2 (E_{2g}) and ν_3 (A_{1g}) in the RS spectra upon excitation of 488 and 632.8 nm and a change in their shape for various transition metal dichalcogenides (TMD) MeX_2 samples, as well as with an increase in the laser excitation power. This analysis will establish the manifestation of characteristic patterns in the transition to the process of resonant stimulated RS (RSRS). Figure 6a–d show the results of a numerical analysis of the observed lines and more complex vibrational bands in the region of ν_2 and ν_3 2H–MoS_2 vibrations upon excitation of 488 nm. Figure 6a, b refer to the RS spectra of MoS_2 nanoparticles, and Fig. 6c, d—to the spectra of single crystals. At a very weak radiation power of 488 nm lazer line, the $\nu_{2,3}$ vibrational lines are also weak and their shape is close to Lorentzian (see Fig. 6a). In this case, the ratio of the peak intensities of the bands ν_3 and ν_2 $\zeta = I_{3\max}/I_{2\max} = 1.9$. Exactly the same value of ζ was observed in [56].

With an increase in the excitation power of 488 nm, the intensities of the ν_2 and ν_3 bands increase by more than an order of magnitude, as illustrated in Fig. 6b. In this case, the intensity ratio under consideration is $\zeta = 1.6$, but in the $\nu_{2,3}$ bands low-frequency satellites 366 and 398 cm^{-1} appear. As it was established in the previous Sect. 3, the 366 cm^{-1} component relates to the state of the ν_2(M) mode at the boundary of the BZ. But because of the very weak phonon dispersion of the ν_3 (A_{1g}) mode (ν_3 (Γ) $\approx$ ν_3(M)), the stronger component of 398 cm^{-1} should have a different nature. The tendency for ζ to decrease to 1.43 for the bulk sample upon excitation at 514.5 nm was observed in [57]. In the analyzed spectrum in Fig. 6b, a weak band ν_1 (E_{1g}) = 281 cm^{-1} (shown in the inset in Fig. 6b) with a FWHM $\delta\nu$ = 4.6 cm^{-1} shown in the inset in Fig. 5b is clearly observed. Its peak intensity is weaker than for ν_3 band by exactly 10 times.

In the RS spectrum of 2H–MoS_2 single crystal upon excitation of 488 nm, shown in Fig. 6c, the intensities of the ν_2 and ν_3 bands strongly increase compared to Fig. 6a, b as a result of an increase in the sample volume. In this case, the quantity $\zeta = 1.8$, and the band $\nu 1$ is weaker than the intensity $I_{3\max}$ by 12.7 times. An even more significant change in the ratio ζ of the peak intensities of the ν_3 and ν_2 bands is observed with an increase in the laser radiation intensity of 488 nm, as illustrated in

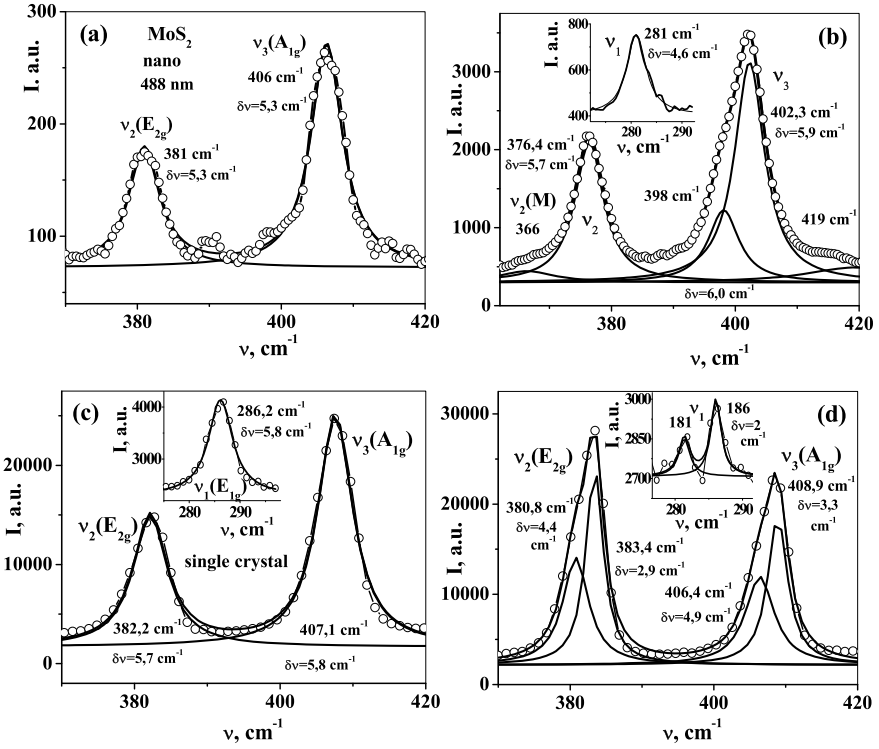

Fig. 6 The results of numerical approximation of the observed Raman scattering lines of nanoparticles (**a**, **b**) and 2H–MoS_2 single crystals (**c**, **d**) upon excitation of 488 nm by spectral components of the Lorentz form

Fig. 6d. In this case, the value of $I_{3\max}$ becomes noticeably less than $I_{2\max}$ and the value $\zeta = 0.8$ decreases in comparison with the cases considered earlier by more than 2 times. Similar decreases in the ratio of the peak intensities of the ν_3 and ν_2 bands to $\zeta = 1$ were observed in [58, 59], respectively, using excitations of 532 nm and 488 nm. Moreover, when using a low power of 0.23 mW excitation of 532 nm, stimulated RS processes should not develop.

Such changes in the ratio of the intensities of the fundamental bands $\nu_{1,2,3}$ in the RS spectra can be explained by a change in the differences in the populations of the ground state n_0 and the corresponding vibrational n_i levels ($i = 1, 2, 3$). It is known that in Raman processes, the Stokes wave growth rates $dE_{Si}/dz \sim A\Delta n_i |E_L|^2 E_{Si}$ (z-coordinate, $i = 1, 2, 3$), in addition to the amplitudes of the laser E_L and Stokes E_{Si} waves, depend on the population differences $\Delta n_i = n_0 - n_i$. In particular, when the populations of the ground state and ν_1 are equal, $E_{S1} \approx 0$, which is often observed. This accounts for the low intensities of the $\nu 1$ bands in Fig. 6b–d. An increase in the population n_3 of the ν_3 level leads to a weakening of the intensity of the ν_3 band, which is clearly shown in Fig. 6d. A change in the populations of vibrational

states occurs as a result of nonlinear resonant wave processes (NRWP) involving vibrational modes. This is confirmed by the results of IR spectroscopy of MoS_2 samples described in the previous section.

For a fragment of the RS spectrum in Fig. 6d, even more significant is the observation of the fine structure not only for the ν_2 and ν_3 bands, but also for the ν_1 band, as shown in the inset in Fig. 6d. It is significant that in this case the half-widths of the observed spectral components $\delta\nu$ decrease from 4.6–5.9 cm^{-1} to 2–3 cm^{-1}. Thus, there is a narrowing of individual lines by about 2 times, which is typical for stimulated RS (SRS) processes. An equally important evidence for the development of SRS is the observation of a thin line structure (TLS) of scattered radiation [18, 19]. This structure is especially clearly observed for the weak band ν_1 (inset in Fig. 6d), the intensity of which is 80 times lower than the value I_{3max}. The fine structure of the vibrational bands appears as a result of the influence of four-photon resonant parametric processes and is usually observed near the SRS threshold [18, 19]. It should be noted that for the transient processes from spontaneous to stimulated RS, the strongest vibrational lines are not yet distinguished and SRS signs (narrowing of lines and TLS) are observed for different vibrations. And this is especially important for the significant influence of four-photon resonant parametric processes. A distinctive feature of the SRS processes in layered MeX_2 crystals with low frequencies of fundamental vibrational modes (VM) is the mutual interweaving of the NIRS with the participation of only VM and with the participation of exciting laser and scattered radiation. For low-frequency VM, along with SRS processes, the role of nonlinear resonant parametric interactions also increases.

Let us proceed with the analysis of more complex 2H–MoS_2 Raman spectra excited by resonance radiation of 632.8 nm, as illustrated in Fig. 6a–d. Figure 7a shows the simplest Raman spectrum of a MoS_2 single crystal upon excitation of 632.8 nm. However, in contrast to the spectrum, upon excitation at 488 nm with approximately the same intensities (see Fig. 5c), a substantial redistribution of the

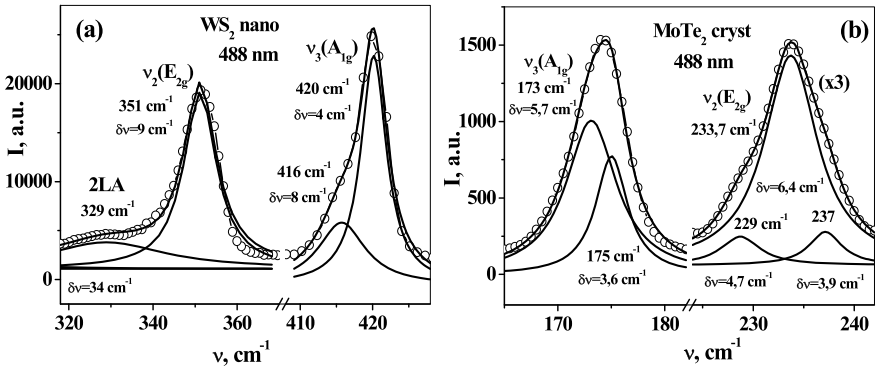

Fig. 7 The results of the numerical decomposition of the observed Raman scattering bands of 2H-WS_2 (**a**) nanoparticles and 2pH–$MoTe_2$ (**b**), **c** single crystals upon excitation of 488 nm into spectral components and Lorentzian shape

intensities of the ν_2 and ν_3 lines is observed here ($\zeta = 0.8$ as in Fig. 6d). The significant narrowing of the ν_2 and $\nu_3 - \delta\nu_2$ lines also decreases significantly from 5.7 cm^{-1} to 3.9 cm^{-1}, and $\delta\nu_2 = 5.8\ cm^{-1} \rightarrow 4.5\ cm^{-1}$. Thus, FWHM of the ν_3 and ν_2 bands narrow by 22 and 32%, respectively, which is also characteristic of SRS processes. But unlike pulsed high-power laser pumping for nonresonant SRS, upon resonant excitation in 2H–MoS_2 single crystals, the SRS process develops with low-power continuous excitation by He-Ne radiation of ~50 mW. We point out that it also begins to appear upon excitation at 488 nm, as shown in Fig. 6b.

Figure 7b shows the results of the numerical decomposition of a fragment of vibrational bands isolated in the RS spectrum of a 2H–MoS_2 single crystal at a maximum excitation power of $\lambda_L = 632.8$ nm (see Fig. 3b) into individual spectral components. In this case, the intensities of the 2LA overtone and composite tones $\nu_3 \pm$ LA increase significantly in the spectrum, which also confirms the development of SRS. As in Fig. 6d, a thin linear-frequent structure is also observed here, which has a nonlinear parametric nature [18, 19]. Moreover, this linear-frequent structure develops in the low-frequency direction, which is caused by the frequency dependence of the nonlinear cubic susceptibility $|\chi^{(3)}|^2$, which contains resonant Raman and nonresonant electron contributions [56]. Of particular note is the appearance of two new bands $\nu\ (E_{1u}) = 390$–$394\ cm^{-1}$ and $\nu\ (B_{1u}) = 413$–$428\ cm^{-1}$. These bands relate to the IR active vibration E_{1u} and silent vibration B_{1u}, which are forbidden in the RS spectra. However, as a result of changes in the properties of MoS_2 under the influence of resonant laser radiation, they are well manifested in the Raman spectra, and the B_{1u} band with a maximum of about 419 cm^{-1} even begins to dominate in the region of $\nu_{2,3}$ vibrations. It is characteristic that the B_{1u} band has a well-developed fine structure containing 5 quasi-equidistant components with small half-widths. As already mentioned above, this structure is due to nonlinear parametric processes.

Let us consider the resonance spectra of RS nanoparticles and microcrystallites 2H–MoS_2. With a low-power excitation of 632.8 nm in the relatively weak RS spectrum of MoS_2 nanoparticles in Fig. 7c, the intensity of the $\nu_3\ (A_{1g})$ band is 3.3 times higher than the intensity of the band, which was not previously observed. This is an indication of the gain of the full-symmetric A_{1g} vibrational band at SRS. In this case, the ν_3 band is approximated by the effective Lorentzian with a FWHM of $\delta\nu_3 = 9\ cm^{-1}$. However, a more detailed analysis of the $\nu_3\ (A_{1g})$ band showed the presence of its fine structure, which is shown by the inset in Fig. 7c. Significant amplification of the $\nu_3\ (A_{1g})$ band and its fine structure are characteristic features of the development of resonant SRS. In Fig. 7c, as in Fig. 6b, additional vibrational bands $\nu_2(M) = 362\ cm^{-1}$ and B_{1u}~$421\ cm^{-1}$ are observed.

With an increase in the resonance excitation power of 632.8 nm, the RS spectra of MoS_2 nanoparticles and microcrystallites radically change. This is manifested in an anomalous attenuation of the $\nu_3\ (A_{1g})$ band, which dominates the spectrum in Fig. 7c. A previously very weak or even unobserved band $\nu_1\ (E_{1g})$ of about 286 cm^{-1} is anomalously amplified. This band is shown in the inset in Fig. 7d, in which an additional, more intense spectral component of 279 cm^{-1} is observed. In this case, the intensity ratio $\zeta = I_{3max}/I_{2max} = 0.36$, i.e., compared to the low excitation power in Fig. 7c, the situation changes by 9.2 times.

An even stronger redistribution of intensities is observed for the ν_1 and ν_3 bands. In the previously considered spectra, the intensity of the ν_1 (E_{1g}) band was 10–80 times weaker than the ν_3 (A_{1g}) band. And in the spectrum in Fig. 7d, the peak intensity of the $\nu 1$ band is 17.75 higher than the ν_3 band. Consequently, the intensity of the ν_1 (E_{1g}) band can be increased in comparison with the ν_3 (A_{1g}) band by a factor of 1420. We explain the anomalous changes in the ratio of the intensities of the ν_1 and ν_3 bands (~10^2–10^3 times) with a change in the excitation power λ_L by the influence of the resonant stimulated RS in the anti-Stokes region. The spectral interval between the maximum spectral component of 279 cm^{-1} in the vibrational region ν_1 (E_{1g}) and the observed band ν_3 (A_{1g}) = 403 cm^{-1} is 124 cm^{-1}, which exactly corresponds to the TA′ state of the transverse acoustic mode (see Fig. 5d). When the TA′ state is overpopulated by comparing with the ground level, the initially very intense Stokes radiation ν_3 (A_{1g}) acts as a pump and anti-Stokes radiation is generated in the region of the ν_1 (E_{1g}) vibration. The efficiency of this process is facilitated by several important factors: (1) the approximation of the radiation in the $\nu_3 = 403$ cm^{-1} (1909 eV) line to the exciton resonance ($E_g = 1.89$ eV [3]) compared with the excitation of 632.8 nm (1959 eV); (2) the observed TA′ line is characterized by the smallest FWHM $\delta\nu \approx 5$ cm^{-1} in comparison with the vibrational modes LA, TA and ZA (see Fig. 4d), which is even smaller than the initial half-width of the ν_3 (A_{1g}) line $\delta\nu = 5.3$–5.8 cm^{-1} (Fig. 6a, c); (3) a very effective nonlinear resonance interaction of only the vibrational modes leads to a radical change in the equilibrium populations of the vibrational levels, which is confirmed by the observation of the "glow" of the IR bands $3\nu_2$ and $3\nu_3$. The relaxation of higher vibrational states can also lead to a nonequilibrium population of the TA′ mode (Figs. 8 and 9).

4 Conclusions

A brief analysis of the development of studies of resonance Raman scattering spectra is given, as well as stimulated Raman scattering (SRS) in various media, including wide families of semiconductors, organic substances and liquids, metal vapor and transition metal dichalcogenides (TMD) MeX_2. The main attention is paid to the resonance SRS in the TMD MeX_2. Characteristic features of stimulated scattering and nonlinear resonant parametric interactions (NRPI) were observed even before the development of quantum electronics and nonlinear optics, and because of their difficulties, they did not find a correct understanding for a long time. With SRS, it is essential to observe various frequency–angle branches (FAB) of scattered radiation (polariton, Cherenkov, and parametric types), including those associated with self-focusing and interfocusing waves. We pay attention to the fine line structure of the generated Stokes and anti-Stokes components near the SRS threshold, as well as the dynamics of the resonance state populations, changes in the nonlinear resonance susceptibilities, and the induced dispersion of the medium at the stage of the developed SRS, which leads to a change in the phase synchronism (FS) conditions for the NRPI (nonlinear quasisynchronism) [31, 32]. We especially note the possibility of

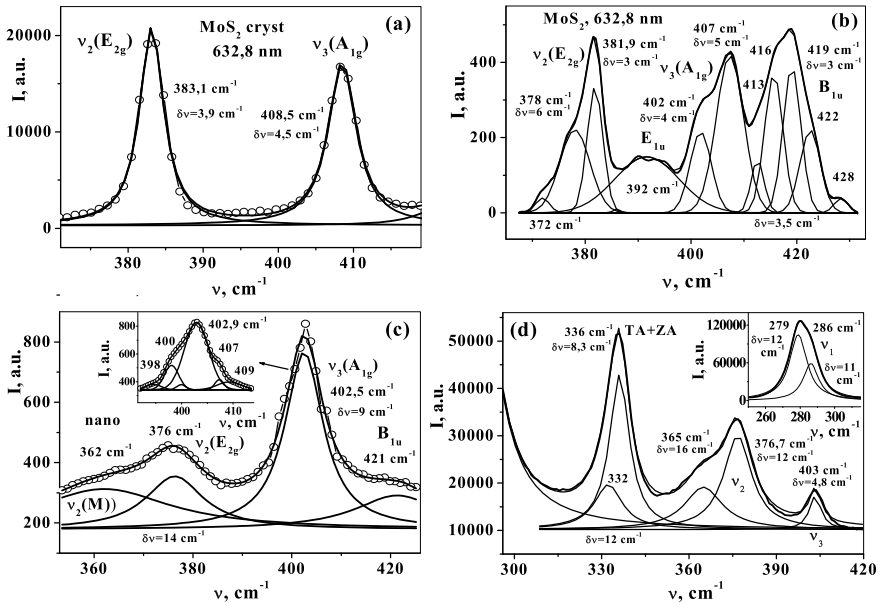

Fig. 8 The results of numerical decomposition of the observed Raman scattering bands of single crystals (**a**, **b**), nanoparticles (**c**) and natural 2H–MoS_2 (**d**) microcrystals upon excitation by radiation of 632.8 nm into spectral components and Lorentzian form

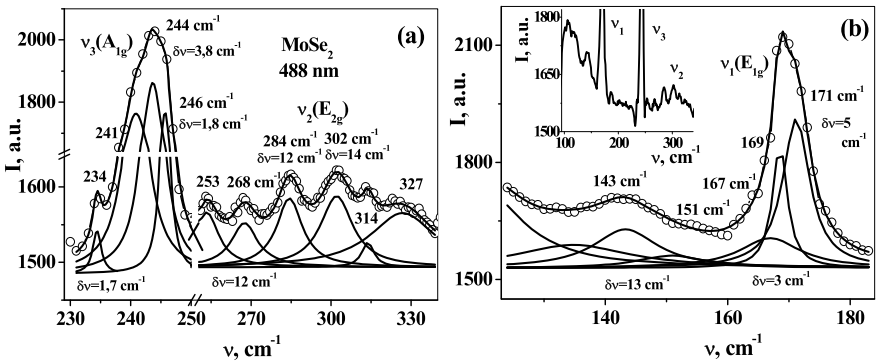

Fig. 9 The results of the numerical decomposition of the observed ν_3 (A_{1g}) and ν_2 (E_{2g}) (**a**) and ν_1 (E_{1g}) (**b**) bands of Raman scattering of 2H–$MoSe_2$ (d) microcrystals upon excitation of 488 nm into spectral components and Lorentzian form

establishing wave enlightenment of the medium for a set of interacting waves [27–36], which leads to the involvement of additional spectral components in the SRS process and significantly complicates the observed spectra, as well as the energy concentration on one of the scattered waves [33, 37]. The considered regularities and

features of the many-sided SRS processes, including resonance cases, open up new possibilities for explaining the experimental results.

In the process of studying resonant SRS in a number of TMD 2H–MeX_2, the following results were obtained:

1. The Raman spectra of nanoparticles (NPs), natural microcrystals (MC), and 2H–MoS_2 single crystals excited by 488 and 632.8 nm laser radiation were compared. It was shown that for MoS_2 NPs, the frequencies of all vibrations are significantly reduced compared with single crystals: ν_1 (E_{1g}) (287 $\rightarrow$ 280 cm^{-1}), ν_2 (E_{2g}) (383 $\rightarrow$ 275 cm^{-1}) and ν_3 (A_{1g}) (409 $\rightarrow$ 402 cm^{-1}). In addition, the vibrational frequencies in NPs and MCs still decrease with amplification of the broadband electronic background, which arises as a result of strong vibrational-electron interactions [49–53].
2. Under excitation 632.8 nm, which is resonant with excitonic states, the overtone of the longitudinal acoustic mode 2LA $\approx$ 463 cm^{-1}, as well as the total and difference tones $\nu_{1,2,3} \pm$ LA, are strongly amplified in the Raman spectra of 2H–MoS_2 single crystals. This allows us to determine the frequencies of the vibrational states at the boundary of the Brillouin zone (BZ) ν_1(M) = 302 cm^{-1}, ν_2(M) = 366 cm^{-1}, ν_3(M) = 409 cm^{-1} and LA(M) = 232 cm^{-1}, which corresponds to a positive dispersion ν (k) in the ΓM direction for the ν_1 mode, a negative dispersion for the ν_2 mode, and a very weak dispersion for the ν_3 mode.
3. A strong influence of 632.8 nm laser radiation on the change in the structure and properties of 2H–MoS_2 was established. In MoS_2 single crystals, this manifests itself in a significant amplification of the 2LA overtone and composite tones $\nu_{1,2,3} \pm$ LA, as well as the appearance of strong bands of previously inactive vibrations E_{1u}~390−394 cm^{-1} and B_{1u}~419 cm^{-1}. And in the Raman spectra of NPs and MCs MoS_2, very intense lines of transverse TA = 194 cm^{-1} and longitudinal LA = 236 cm^{-1} acoustic modes, as well as the torsion mode ZA = 146 cm^{-1}, are observed. This is due to the doubling of the size of unit cells (UC) and the mapping of vibrational states at the BZ boundary to its center. The observation of additional lines ZA′ = 112 cm^{-1}, TA′ = 124 cm^{-1} and LA′ = 211 cm^{-1} is associated with a repeated doubling of the size of the UC, and the components LA′ = 171 and 229 cm^{-1} indicate the third doubling of the UC. Thus, the disordering of the MoS_2 structure under the influence of resonance radiation of 632.8 nm occurs by increasing the size of the electron element by no less than 8 times. It is significant that, in contrast to the softening in the NPs of the frequencies of optical vibrational modes (VM) $\nu_{1.2.3}$ by 7–8 cm^{-1}, the frequency of the acoustic mode LA, on the contrary, increases 232 $\rightarrow$ 236–238 cm^{-1}.
4. Systematic studies have been carried out of the ratio of the peak intensities of the ν_3 (A_{1g}) and ν_2 (E_{2g}) $\zeta = I_{3max}/I_{2max}$ bands of the strong in Raman scattering (RS) spectra for NPs, MCs, and 2H–MoS_2 single crystals under excitation at λ_L = 488 and 632.8 nm, including power change λ_L. An initial decrease in ζ values from 1.9 to 0.8 and less was established, due to an increase in the

nonequilibrium populations of vibrational levels $\nu_{1,2,3}$ as a result of resonant nonlinear interaction of VM, which inhibits the development of stimulated RS (SRS). A subsequent increase in ζ to values of 2.2–5.9 and more, as well as a narrowing of the FWHM $\delta\nu$ of the vibrational lines, first by 20–30%, and then ~2 times characterize the development of SRS.

5. A characteristic manifestation of the SRS process is the observation of a thin line structure (TLS) of a number of vibrational bands at the initial stages of SRS development. The TLS in the SRS spectra arises as a result of the contribution of four-photon resonant parametric interactions (FRPI) and is caused by the dependence on the wave detuning frequency Δk (ν) in the phase synchronism factor (PS) [18, 19]. In the simplest case, the PS factor has the form $\sin^2(\tau)/\tau^2$, where $\tau = \Delta k_L/2$ and L is the length of the medium on which the nonlinear wave interaction occurs.
6. A change in ζ values, as well as the observation of TLS, is also characteristic of the processes of SRS development in NPs and 2H–WS_2, 2H–$MoSe_2$ and 2H–$MoTe_2$ crystals, which testifies to the commonality of the analyzed phenomena. The TLS is especially distinct for the weak bands ν_1 (E_{1g}) in MoS_2 and ν_2 (E_{2g}) in $MoSe_2$ (6 components), which are near the SRS threshold. In the case of resonance excitation of 632.8 nm in a 2H–MoS_2 single crystal, TLS is clearly manifested for an anomalously amplified band of inactive B_{1u} vibration in the region of 413–428 cm^{-1}. A characteristic feature of FRPI in layered MeX_2 media is the low frequency of VM, which facilitates the fulfillment of PS conditions.
7. The SRS phenomenon in TMD MeX_2 is characterized by the mutual interweaving of two types of nonlinear wave processes: (1) nonlinear interactions only of VM (NWVM) MeX_2 and (2) with the participation of exciting laser and scattered radiation. As a result of the NWVM, an increase in the unequal-weighted populations of vibrational states leads to a decrease in the Stokes radiation intensity even with the development of SRS. The essential role of the FRPI for low frequencies of MeX_2 VM leads to the manifestation of SRS properties for a large number of vibrational bands.
8. For TMD, the RS spectra and IR absorption spectra were compared. The IR spectra of diffuse scattering of 2H–MoS_2 NPs in the region of overtones and sum tones are approximately 3 times more intense than for MC. This is due to increased anharmonism and vibrational nonlinearity in nanostructures. The low vibrational frequencies of many MeX_2 structures are close to the average thermal vibrational energies kT $\approx$ 200 cm^{-1} and take an active part in the NWVM with the generation of populations of higher vibrational states. This is confirmed by the observation of the emission bands of overtones $3\nu_2$ and $3\nu_3$ (absorption bands of negative polarity) 2H–MoS_2, which is due to the inversion of the populations of these states. This proves the important role of NWVM in the structures of TMD. The observed strong changes in the shape and intensity of the infrared absorption bands of TMD, as well as of the broadband electronic background, are associated with excessive variations in the values of nonlinear wave interactions.

9. The strongest manifestations of SRS are associated with an anomalous increase in the intensities of a number of scattered radiation bands. A distinctive feature of the SRS phenomenon in TMD MeX_2 is the sharp amplification of not the strongest A_{1g} symmetry bands, but very weak ν_1 (E_{1g}) bands, which was first experimentally established using NP and MC 2H–MoS_2 and 2H–$MoSe_2$ crystals as an example. Moreover, an abnormal increase of ~10^2–10^3 times the intensity of the ν_1 (E_{1g}) band is accompanied by a simultaneous weakening of the ν_3 (A_{1g}) ($\zeta = 0.36$) MoS_2 band and the ν_2 (E_{2g}) band in $MoSe_2$. In 2H–MoS_2, the frequency difference of the most intense component of 279 cm^{-1} in the amplified band ν_1 (E_{1g}) and the attenuated band ν_3 (A_{1g}) = 403 cm^{-1} exactly corresponds to the frequency TA′ = 124 cm^{-1} of the transverse acoustic mode state, and in 2H–$MoSe_2$—mode frequency LA = 70−75 cm^{-1}. Thus, in the TMD series, we first observed the anti-Stokes SRS $\nu_L - \nu_3$ (ν_2) + TA′(LA) → $\nu_L - \nu_1$, which develops in the Stokes region.
10. Three important factors contribute to the high efficiency of the anti-Stokes SRS in the Stokes region: (1) the approximation of radiation in the ν_3 = 403 cm^{-1} (1909 eV) line to the exciton resonance in MoS_2 (E_g = 1.89 eV); (2) the TA′ line observed in SRS has the smallest FWHM $\delta\nu$, which is less than $\delta\nu$ for the amplified oscillation ν_3 (A_{1g}) at the initial stage of SRS; (3) the observation of the anti-Stokes SRS proves the population inversion at the levels of the TA and TA acoustic modes active in the RS spectra as a result of changes in the structure and properties of TMD MeX_2 induced by laser radiation.

References

1. Li H, Zhang Q, Chong C, Tay BK et al (2012) From bulk to monolayer MoS_2: evolution of Raman scattering. Adv Funct Mater 22:1385–1390
2. Zhaoa W, Ghorannevisa Z, Kumar AK, Pang JR, Tohd M, Zhange X, Klocd C, Tane PH, Edaa G (2013) Lattice dynamics in mono- and few-layer sheets of WS_2 and WSe_2. Nanoscale 5(20):9677–9683
3. Carvalho BR, Wang Y, Mignuzzi S, Roy D, Terrones M, Fantini C, Crespi VH, Malard LM, Pimenta MA (2017) Intervalley scattering by acoustic phonons in two-dimensional MoS_2 revealed by double-resonance Raman spectroscopy. Nature Commun. https://doi.org/10.1038/ncomms14670
4. Molas MR, Nogajewski K, Potemski M, Babiński A (2017) Raman scattering excitation spectroscopy of monolayer WS_2. Sci Rep 7:5036
5. Zhang X, Qiao XF, Shi W, Wu JB, Jiang DS, Tan PH (2015) Phonon and Raman scattering of two-dimensional transition metal dichalcogenides from monolayer, multilayer to bulk material. Chem Soc Rev 44:2757
6. Saito R, Tatsumi Y, Huang S, Ling X, Dresselhaus MS (2016) Raman spectroscopy of transition metal dichalcogenides. J Phys Condens Matter 28:35300
7. Pimenta MA, Corro E, Carvalho BR, Fantini C, Malard LM (2015) Comparative study of Raman spectroscopy in graphene and MoS+ type transition metal dichalcogenides. Acc Chem Res 48(1):41–47
8. Ivanova TM (1987) The resonance Raman light scattering in studies of the structures and functions of flavins and flavoproteins. Russ Chem Rev 56(2):182–201

9. Anderson A (1973) The Raman effect in two volumes, volume 2 Applications, University of Waterioo, Ontario, Canada, Marcel Dekker, Inc., New York
10. Валах МЯ, Стрельчук ВВ, Семенова ГН, Садофьев ЮГ (2004) Резонансное стоксовое и антистоксовое комбинационное рассеяние света в наноструктурах CdSe/ZnSe. ФТТ 46(1):174–176
11. Клочихин АА, Плюхин АГ, Суслина ЛГ, Шадрин ЕБ (1976) Резонансное комбинационное рассеяние света на продольных оптических фононах в смешанных кристаллах. ФТТ 18(7):1909
12. Bloembergen N (1967) The stimulated Raman effect. Amer J Phys 35(11):989
13. Бобович ЯС, Борткевич АВ (1977) РЕЗОНАНСНОЕ ВЫНУЖДЕННОЕ КОМБИНАЦИОННОЕ РАССЕЯНИЕ СВЕТА (ОБЗОР). Квантовая электроника 4(3): 485–512
14. Броуде ВЛ, Максимов АА, Тартаковский ИИ (1977) Резонансное комбинационное рассеяние света в кристаллах антрацена. Письма в ЖЭТФ 27(7):424–426
15. Корниенко НЕ, Малый ВИ, Понежа ГВ, Понежа ЕА (1983) Природа частотно-угловой структуры излучения при ВКР в жидкостях. Доклады АН УРСР, сер, А. 4:65-68
16. Корниенко НЕ, Гайдук ВФ (1987) Природа самофокусировки стоксового излучения при вынужденном комбинационном рассеянии света. УФЖ 32(9):1331–1334
17. Корниенко НЕ, Гайдук ВФ, Малый ВИ, Понежа ГВ (1993) Возбуждение обертонов колебательных возбуждений при вынужденном комбинационном рассеянии в самофокусирующих жидкостях, поляритонный механизм релаксации и измерение ангармонизма колебаний, Сб. научных трудов, Оптическая спектроскопия, АН Украины, Ин-т физики, Киев 171–176
18. Корниенко НЕ, Малый ВИ, Понежа ГВ, Федорченко АМ (1986) Тонкая структура и аномальное уширение спектров при вынужденном комбинационном рассеянии, Сб. Физика жидкого состояния, Киев, 14:41–54
19. Корниенко НЕ, Малый ВИ, Понежа ГВ, Федорченко АМ (1986) Параметрическая природа линейчатой структуры спектров ВКР, Оптика и спектроскопия 60(2):422–425
20. Корниенко НЕ, Малый ВИ, Понежа ГВ, Суровцев ДВ (1988) О различии частотных сдвигов стоксовых и антистоксовых компонент при вынужденном комбинационном рассеянии, VIII Всесоюзный симпозиум по спектроскопии высокого разрешения: Материалы, Томск 2:108–111
21. Корниенко НЕ, Федорченко АМ (1985) О влиянии параметрических процессов на электронное вынужденное комбинационное рассеяние, Оптика и спектроскопия 59(4):920–923
22. Корниенко НЕ, Корниенко МФ, Науменко АП, Федорченко АМ (1986) О четырехфотонном параметрическом преобразовании частоты в условиях двухфотонного резонанса накачки и сигнала, Оптика и спектроскопия, 60(3):650–654
23. Корниенко НЕ, Малый ВИ, Понежа ГВ, Дзюбан НВ (1986) Нерезонансные параметрические процессы при вынужденном комбинационном рассеянии, Украинский физический журнал, (письма в редакцию) 31(3):779–784
24. Корниенко НЕ, Малый ВИ, Понежа ГВ (1993) Черенковское излучение волн нелинейной поляризации, возбуждаемых при вынужденном комбинационном рассеянии света, Сб. научных трудов, Оптическая спектроскопия, АН Украины, Ин-т физики, Киев 161–165
25. Корниенко НЕ (1985) Частотно-угловая структура четырехфотонного резонансного параметрического рассеяния. Оптика и спектроскопия 58(4):924–927

26. Кондиленко ИИ, Корниенко НЕ, Малый ВИ, Понежа ГВ (1981) Некоторые закономерности в спектрах обращенного комбинационного рассеяния, Квантовая электроника, Москва 8(11):2447–2453
27. Корниенко НЕ, Стеба АМ, Стрижевский ВЛ (1982) Теория генерации и усиления стоксовой и антистоксовой волн в газообразных средах. Квантовая электроника, Москва 9(11):2271–2280
28. Корниенко НЕ, Стеба АМ, Стрижевский ВЛ (1982) Теория трехчастотного источника на основе комбинационного усиления. Оптика и спектроскопия 53:568–569
29. Корниенко НЕ, Стеба АМ, Стрижевский ВЛ (1983) Генерация стоксовой и антистоксовой волн, индуцируемая двухфотонной подсветкой. Квантовая электроника, Москва 10(2):300–307
30. Корниенко НЕ, Стеба АМ, Стрижевский ВЛ (1983) Генерация стоксовой и антистоксовой волн, стимулируемая двухфотонной подсветкой, Оптика и спектроскопия 54(5):555–557
31. Гречко ЛГ, Корниенко НЕ, Задорожный ВИ, Федорченко АМ (1983) Нелинейный квазисинхронизм в процессах параметрического преобразования оптических частот в резонансных средах. Оптика и спектроскопия 55(2):209–211
32. Корнієнко МЄ, Сіденко ТС (2004) Нелінійний квазісинхронізм при генерації третьої гармоніки в умовах двофотонного резонансу. Український фізичний журнал 49(11):1081–1089
33. Корнієнко МЄ (2002) П'ятихвильове наближення в теорії вимушеного розсіяння світла. УФЖ 47(5):435–440
34. Корнієнко МЄ, Міхницький СІ (2002) Хвильове просвітлення речовини при вимушеному комбінаційному розсіянні світла на дипольно-активних коливальних модах. УФЖ 47(6):545–551
35. Корнієнко МЄ, Міхницький СІ, Хвильове просвітлення речовини і високоефективна гене-рація випромінювання при вимушеному комбінаційному розсіянні світла на поляритонах. УФЖ 47(8): 726–737
36. Корнієнко МЄ, Міхницький СІ (1999) Динаміка встановлення хвильового просвітлення речовини і багатохвильові зв'язані солітони при вимушеному розсіянні світла, Проблеми оптики та її освітнього аспекту на порозі 3-го тисячоліття, Науково-практична конференція з міжнародною участю, присвячена 165-річчю Київського університету та 60-річчю кафедри оптики. Київ, 5–6 жовтня тези доповідей 17
37. Корниенко НЕ, Малый ВИ, Понежа ГВ, Михницкий СИ, Спектроскопия ВКР (2010) коллективные свойства жидкостей и явление концентрации энергии, Тезисы докладов XXIV Съезда по спектроскопии. Москва 187–188
38. Рагульский ВВ, Файзуллов ФС (1967) Распределение фотонов по компонентам вынужденного комбинационного рассеяния в жидком азоте, Письма ЖЭТФ 6:887–891
39. Сущинский ММ (1976) Спектры комбинационного рассеяния молекул и кристаллов, М., Наука 576 с
40. Корниенко НЕ, Стеба АМ, Стрижевский ВЛ (1982) Воспроизведение спектра немонохроматической накачки в стоксовой и антистоксовой областях. Украинский физический журнал 27(11):1721–1723
41. Корниенко НЕ, Стеба АМ, Стрижевский ВЛ (1984) Теория генерации стоксовой и антистоксовой волн при немонохроматической накачке, Оптика и спектроскопия, 56(3):514–522
42. Корниенко НЕ (1985) Пространственная эволюция амплитуд волн, устойчивость решений и бифуркации при генерации суммарных и разностных частот в условиях двухфотонного резонанса. Квантовая электроника, Москва 12(8):1595–1601

43. Корниенко НЕ, Стрижевский ВЛ (1982) Предельные коэффициенты преобразования при генерации суммарных и разностных частот в условиях двухфотонного резонанса по накачке. Оптика и спектроскопия 53:963–966
44. Корниенко НЕ, Бифуркации и (1986) предельные эффективности четырехфотонной резоансной генерации суммарных и разностных частот при бигармонической накачке. Оптика и спектроскопия 60(1):186–188
45. Akselrud L, Grin Y (2014) WinCSD: soft ware package for crystallographic calculations (Version 4). J Appl Crystallogr 47(2):803–805
46. Корниенко НЕ, Гайдук ВФ (1987) Природа самофокусировки стоксового излучения при вынужденном комбинационном рассеянии света. УФЖ 32(9):1331–1334
47. Lieth RMA, Terhell JCJM (1977) Transition metal dichalcogenides, "Preparation and crystal growth of materials with layered structures. In: Lieth RMA (ed) Dordrecht-Boston, pp 141–223
48. Naumenko A, Kulikov L, Konig N (2016) Ukr J Phys 61(6):556–561
49. Корниенко НЕ (2006) Ефекти сильної фонон-електронної взаємодії 1. Відкриття електронних смуг нового типу, Вестник Киевского универ., сер.физ.-мат. наук. 3:489–499
50. Kornienko NE, Kulish NP, Alekseev SA, Dmitrenko OP, Pavlenko EL (2010) Fine band structure of the vibrational spectra of fulle-rite C_{60} and enhancement of intermolecular interaction in high_temperature phase. Opt Spectr 109(5):742–752
51. Kornienko ME, Kulish MP, Alekseev SA, Dmitrenko OP, Pavlenko JL (2010) Fine structure of bands in vibrational spectra of C_{60} fullerite. Ukr J Phys 55(6):732–738
52. Kornienko M, Naumenko A (2014) The vibrational band enhancements for active and "silent" vibrations in the Raman and IR spectra of the fullerene C_{60} nanofilms. Ukr J Phys 59(3):339–346
53. Kornieko NE, Naumenko AP (2015) Collective nature of chemical bonds in fullerenes and fullerites C_{60}: vibrational resonances, vibrational-electronic interactions, and anomalous enhancement of bands in the vibrational spectra of nanofilms (Results of Vibrationsl Spectroscopy and quantum Chemical Calculations, pp 103–145. In: Vijay Kumar Thakur and Manju Kumari Thakur (eds) Chemical functionalization of carbon nanomaterials: chemistry and application, CRC Press, Taylor Francis Group, Boca Raton London New York, p 1077
54. Соболев ВВ, Немошкаленко ВВ (1990) Методы вычислительной физики в теории твердого тела, Киев, Изд. Наукова думка, 294 (in Russian)
55. Клочихин АА, Пермогоров СА, Резницкий АН (1976) Многофононные процессы в резонансном рассеянии и экситонной люминесценции кристаллов. ЖЭТФ 1976 71(6):2230–2251
56. Jimenez Sandoval S, Yang D, Frindt RF, Irwin JC (1991) Raman study and lattice dynamics of single molecular layers of MoS_2. Phys Rev B 44(8):3955–3962
57. Biswanath Chakraborty HS, Ramakrishna Matte S, Sooda AK, Rao CNR (2013) Layer-dependent resonant Raman scattering of a few layer MoS_2. J Raman Spectr 44:92–96
58. Zhang X, Han WP, Wu JB, Milana S, Lu Y, Li QQ, Ferrari AC, Tan PH (2013) Raman spectroscopy of shear and layer breathing modes in multilayer MoS_2. Phys Rev B 87:115413–115418
59. Li H, Zhang Q, Yap CC, Tay BK, Edwin TH, Olivier A, Baillargeat D (2012) From bulk to monolayer MoS_2: evolution of Raman scattering. Adv Function Mater 22(7):1385–1390

Structure, Morphology, and Optical-Luminescence Properties of Eu^{3+}- and Mn^{2+}-Activated $ZnGa_2O_4$ and $MgGa_2O_4$ Ceramics

O. Kravets, Y. Shpotyuk, O. Zaremba, K. Szmuc, J. Cebulski, A. Ingram, A. Luchechko, and O. Shpotyuk

1 Introduction

Up to date spinel oxide compounds activated with transition or rare-earth elements are well-known phosphor materials applied in the different spectral range [1–9]. For instance, doping with chromium ions gives a phosphor material with a persistence luminescence in the near-infrared spectral range. The near-IR emission going along with chemical resistance and biocompatibility of $ZnGa_2O_4$ and $MgGa_2O_4$ compounds and makes them suitable biomarker materials [6, 10–13]. Both $ZnGa_2O_4$ and $MgGa_2O_4$ spinels with manganese dopant are bright phosphors emitting in green spectral region [7, 14–17]. Spinels doped with rare-earth elements are a high-spot in display, WLED and solid-state lasers technologies [18–20].

Even though $MgGa_2O_4$ and $ZnGa_2O_4$ are compounds of the same structural type, they differ a lot with their properties. The most prominent difference is the spatial inversion of cation tetrahedral and octahedral sites in $MgGa_2O_4$ compound, while $ZnGa_2O_4$ is completely normal spinels structure material [7, 21–24]. The degree of inversion in magnesium gallate depends on the preparation conditions and the effect of its existence causes a high concentration of point defects involved in luminescence

O. Kravets (✉) · Y. Shpotyuk · O. Zaremba · A. Luchechko
Ivan Franko National University of Lviv, 79000 Lviv, Ukraine
e-mail: oleh.kravets@lnu.edu.ua

Y. Shpotyuk · K. Szmuc · J. Cebulski
University of Rzeszow, 35-959 Rzeszow, Poland

A. Ingram
Opole University of Technology, 45370 Opole, Poland

O. Shpotyuk
Jan Dlugosz University in Częstochowa, 42201 Czestochowa, Poland

Vlokh Institute of Physical Optics, 79005 Lviv, Ukraine

O. Fesenko and L. Yatsenko (eds.), *Nanooptics and Photonics, Nanochemistry and Nanobiotechnology, and Their Applications*, Springer Proceedings in Physics 247, https://doi.org/10.1007/978-3-030-52268-1_27

processes. At the same time, $ZnGa_2O_4$ is predisposed to evaporation of starting materials during annealing, for the most part, zinc oxide, which produces vacancy-type defects and leads to redistribution of excitation energy [5, 9, 17, 25]. From this point, the structure of these materials can be modified using different approaches giving control over light emission [4]. But for now, either the effects of inversion, evaporation and incorporation of activators into spinel host haven't been investigated in details and a lot of questions appear.

Comparing these materials at a nanoscale level with the specificity of their defect structure, we are trying to shed more light on the mechanisms that occur in $ZnGa_2O_4$ and $MgGa_2O_4$ spinels co-activated with Mn^{2+} and Eu^{3+} ions, employing multi-experimental approach.

2 Experimental Methods and Techniques

2.1 Material Synthesis

The $ZnGa_2O_4$, $MgGa_2O_4$ polycrystalline samples with Mn^{2+} and Eu^{3+} ions had been obtained with solid-state ceramic synthesis from powders of simple oxides (ZnO, MgO, β-Ga_2O_3, Eu_2O_3, MnO) with purity of $\geq$99.99%. The powders mixed in stoichiometric composition of $ZnGa_2O_4$ ($MgGa_2O_4$) matrix with corrected quantity of ZnO (MgO) and Ga_2O_3 on amount of MnO and Eu_2O_3 doping material, respectively. The $ZnGa_2O_4$:Mn^{2+}, Eu^{3+} and $MgGa_2O_4$:Mn^{2+}, Eu^{3+} ceramics were obtained after sintering at 1200 °C for 8 h in the air. The quantity Mn^{2+} and Eu^{3+} ions were chosen according to [23, 25, 26] and fixed to be 0.05 and 4 mol%, respectively.

2.2 Structure Analysis and Morphology Investigations

The X-ray diffraction (XRD) data were acquired using a STOE STADI P diffractometer. The setup is powered with an X-ray tube (copper $K\alpha_1$-radiation) and linear position-sensitive detector providing 0.005° step of scanning. The analysis of data arrays was done with STOE WinXPOW software.

The FEI Tecnai Osiris device was used for visualizing morphology of intrinsic grains. Imagining was performed with primary electrons accelerated by 200 kV. For more details, see [9].

2.3 Free-Volume Structure Studies

The free-volume structure of both ceramics was studied at room temperature (22 °C) and 35% humidity using PAL spectroscopy using the ^{22}Na isotope (~50 kBq) as a positron source, acquiring the statistics of for each measurement. The PAL spectra consisted of 1 M annihilation events were fit into three distinct exponentials using LT 9.0 software [27]. This allowed to cover channels originated from positrons annihilating in defect-free bulk, trapped in free-volume defects and forming bound positron-electron Ps (positronium) state. The uncertainties in lifetime τ_i and intensities I_i are ±0.005 ns and ±0.5%, respectively. The positron trapping was parameterized in defect-free bulk lifetime τ_b, trapping rate in defects κ_d, a mean lifetime τ_{av} and fraction η of trapped positrons defined within simple two-state trapping model [28], applied in addition to Ps-decaying channel [9, 29].

2.4 Optical-Luminescence Spectroscopy

Agilent Cary 5000 spectrophotometer powered with Agilent diffuse reflectance accessory was used to measure absorption properties of ceramic materials. Photoluminescence (PL) properties were investigated with spectrofluorometer SM 2203. For more details, see [4].

3 Results and Discussion

3.1 Crystalline Structure and Phase Analysis

Both compounds were studied with XRD spectroscopy for defining the phase purity of obtained samples. The XRD spectra with respect to standard diffraction pattern are depicted in Fig. 1. The character of XRD spectra follows the standard pattern, however unexpected peaks of additional phase were found as well.

The Rietveld analysis showed that $ZnGa_2O_4$:Mn^{2+}, Eu^{3+} ceramics consists of two different phases. $ZnGa_2O_4$ is the main phase with $MgAl_2O_4$ structure type. Additional $Eu_3Ga_5O_{12}$ phase with $Y_3Al_5O_{12}$ structure type was found to have concentration up to 2.1 mol%. Cell parameters with atomic coordinates for the major phase are given in Table 1.

The $MgGa_2O_4$:Mn^{2+}, Eu^{3+} ceramics also contained two phases. The main phase was well-defined as $MgGa_2O_4$ that belongs to the $MgAl_2O_4$ structure type (*cF*56 Pearson's symbol, *Fd*-3*m* (227) space group). About 2.3 mol% of additional $Eu_3Ga_5O_{12}$ phase with $Y_3Al_5O_{12}$ structure type was found as in the zinc gallate sample. The refined cell parameter with atomic coordinates for the major phase is presented in Table 2.

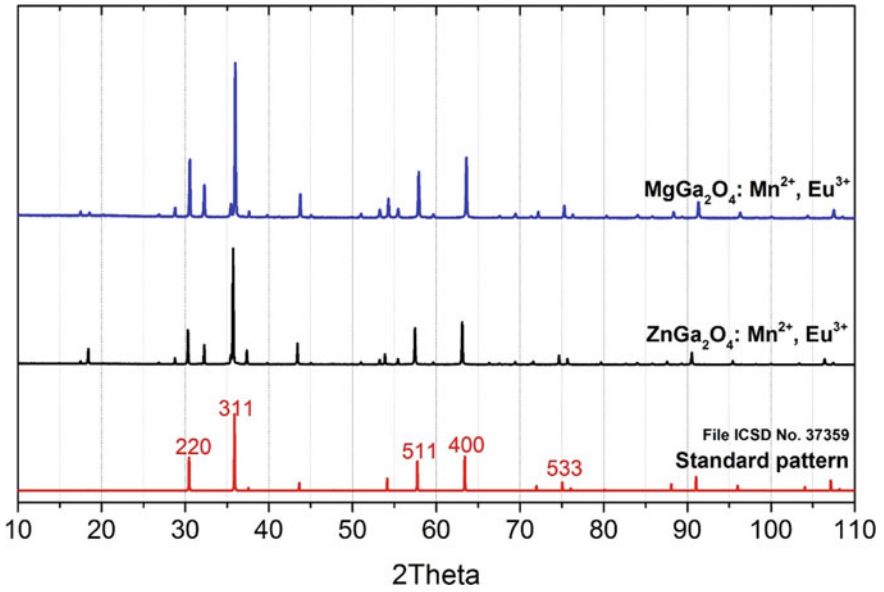

Fig. 1 X-ray diffraction spectra of magnesium and zinc gallate compounds accompanied with standard a pattern of spinel structure ICSD No 37359

Table 1 Refined lattice parameters of the spinel phase in $ZnGa_2O_4$:Mn^{2+}, Eu^{3+} ceramics (lattice constant $a = 8.3307(1)$ Å, Reliability-factor = 4.83) [9]

Site	Wyckoff position	Atomic coordinates			Occupancy
		x	*y*	*z*	
O	32*e*	0.2419	0.2419	0.2419	1
Ga	16*c*	0	0	0	1.00(1)
Zn	8*b*	3/8	3/8	3/8	0.99(1)

Table 2 Refined lattice parameters of spinel phase in $MgGa_2O_4$:Mn^{2+}, Eu^{3+} ceramics (lattice constant $a = 8.2726(1)$ Å, Reliability-factor = 3.17)

Site	Wyckoff position	Atomic coordinates			Occupancy
		x	*y*	*z*	
O	32*e*	0.2441	0.2441	0.2441	1
Mg1	16*c*	0	0	0	0.48(1)
Ga1	16*c*	0	0	0	0.52(1)
Mg2	8*b*	3/8	3/8	3/8	0.17(1)
Ga2	8*b*	3/8	3/8	3/8	0.83(1)

Reviewing earlier publications on spinel gallate compounds we have enough reasons to state that additional phase is a matter of preparation conditions and used methods. For instance, Zhang et al. reported single-phase $ZnGa_2O_4$ doped with an amount of Mn^{2+} or Eu^{3+} ions that don't exceed 5 mol% [30]. In that particular case, the synthesis was carried via a facile hydrothermal approach [30]. Concerning the $MgGa_2O_4$ obtained with a gel-assisted high-temperature calcination process reported by [31], the appearance of an additional phase was found at the concentrations of rare-earth ions at about 5 mol%.

From the refined parameters listed in Tables 1 and 2 is clearly seen that there is only one position occupied by Zn^{2+} cations and another type of position is filled with Ga^{3+} cations. Thus, ceramic samples of $ZnGa_2O_4$ with adds of Mn^{2+} and Eu^{3+} ions have a completely normal spinel structure [22, 25]. While in the structure of $MgGa_2O_4$ for Mg^{2+} and Ga^{3+} cations exist two types of sites, that testifies in favor of partial inversion spinel structure in magnesium gallate sample [23, 32]. Accordingly, in the structure of $MgGa_2O_4$:Mn^{2+}, Eu^{3+} a high number of antisite defects is expected.

Earlier, Sawada et al. reported Eu–Ga–O ternary system and showed that the $Eu_3Ga_5O_{12}$ garnet doesn't have emission observed in the investigated spinels [9, 33]. Taking into account the small relative amount of the additional phase, we can state that effect $Eu_3Ga_5O_{12}$ formations onto photoluminescent properties can be neglected and isn't under further consideration.

The nanoscale structure probes were obtained with a transmission electron diffraction technique on selected grains (Fig. 2). The $ZnGa_2O_4$:Mn^{2+}, Eu^{3+} electron diffraction pattern exhibits the almost single crystalline character of reflections. The electron diffraction of $MgGa_2O_4$:Mn^{2+}, Eu^{3+} shows a typical polycrystalline pattern of beam reflections forming circles around the center. The analysis of the brightest diffraction spots of both diffraction patterns showed that there are reflections from 422, 440, 444 and 731 planes belonging to atomic layers of spinel structure in both compounds [9].

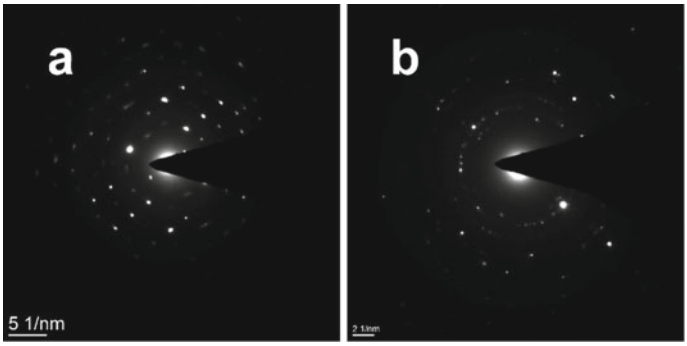

Fig. 2 Electron diffraction patterns of $ZnGa_2O_4$:Mn^{2+}, Eu^{3+} (**a**) and $MgGa_2O_4$:Mn^{2+}, Eu^{3+} (**b**) samples

3.2 *Morphology*

The transmission electron microscopy (TEM) had been applied to investigate the morphology of the obtained ceramics (Fig. 3). Figure 3a presents a single grain of $ZnGa_2O_4$:Mn^{2+}, Eu^{3+} ceramics. The observed grain has an irregular shape with about 200 nm transverse length.

The TEM image of $MgGa_2O_4$:Mn^{2+}, Eu^{3+} was taken with higher scale reveals the multiple grains of irregular shape and high distribution of crystallite sizes. The results of TEM microscopy presented in Fig. 3 are typical for ceramic materials.

The energy-dispersive X-ray (EDX) spectroscopy has been applied to investigate the elements' distribution in the ceramic grains. The EDX maps were obtained for all elements in the compositions of zinc and magnesium gallate spinels.

The elements of host materials (Zn, Mg, Ga, and O) exhibited highly homogeneous distribution in the grain volume (not presented) [9]. The EDX maps of Eu^{3+} ions in $ZnGa_2O_4$:Mn^{2+}, Eu^{3+} and $MgGa_2O_4$:Mn^{2+}, Eu^{3+} is presented in Fig. 4a, b,

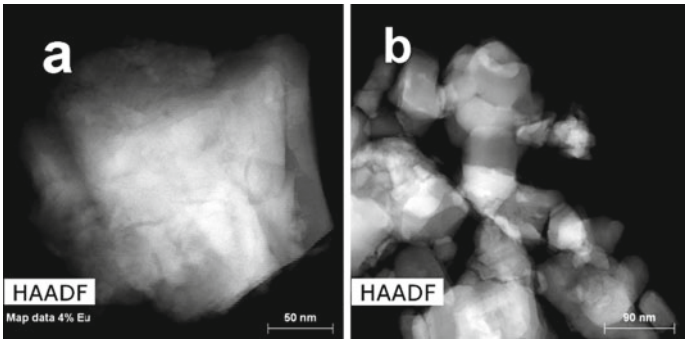

Fig. 3 TEM images of grains in zinc (**a**) and magnesium gallate (**b**) samples with manganese and europium activators

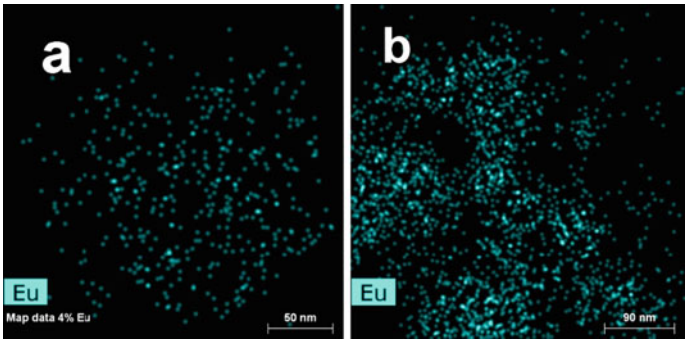

Fig. 4 EDX map images. Spreading of Eu^{3+} ions in the volume of crystallites of $ZnGa_2O_4$ (**a**) and $MgGa_2O_4$ (**b**) samples with Mn^{2+} and Eu^{3+} ions

respectively. It is clearly seen that the Eu dopant was well dissolved in the host material of both compounds even through that a part europium oxide formed the garnet phase.

3.3 *Free-Volume Structure by PAL*

The penetration of Eu^{3+} ions into the grains of $ZnGa_2O_4$:Mn^{2+} and $MgGa_2O_4$:Mn^{2+} spinel ceramics is studied by PAL spectroscopy.

In the case of $ZnGa_2O_4$:Mn^{2+} ceramics, the deep penetration of Eu ions into the grains is well confirmed by the obtained results of positron annihilation spectroscopy.

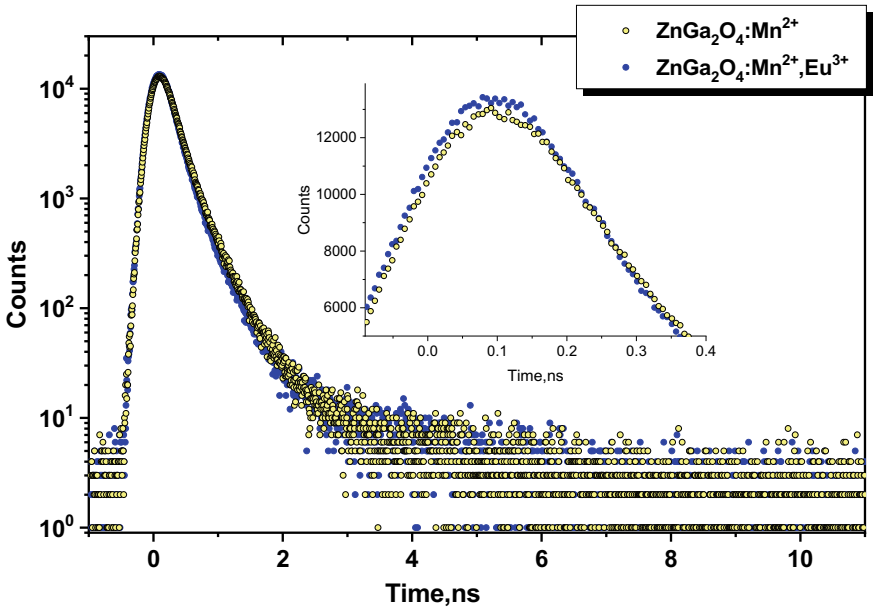

Fig. 5 The positron annihilation spectra of $ZnGa_2O_4$:Mn^{2+} and $ZnGa_2O_4$:Mn^{2+}, Eu^{3+} ceramics

Table 3 The fitting parameters of positron annihilation spectra of studied ceramics

Sample	Fitting parameters					
	τ_1, ns	τ_2, ns	τ_3, ns	I_2, a.u.	I_3, a.u.	τ_{av}, ns
$ZnGa_2O_4$:Mn^{2+}	0.156	0.329	1.967	0.230	0.010	0.215
$ZnGa_2O_4$:Mn^{2+}, Eu^{3+}	0.147	0.303	1.917	0.180	0.012	0.196

The compared PAL spectra both ceramics are shown in Fig. 5 and the fitting parameters are summarized in Table 3. The PAL spectrum of Eu-doped sample is sharper and slightly right-shifted causing the decrease in mean positron lifetime τ_{av}.

The second positron lifetime in the x3-decomposed spectrum corresponds to the trapping of positrons in vacancies and vacancy-like defects located near the boundaries of ceramics grains. In this regard, the defect-specific lifetimes $\tau_d = \tau_2$ reflects the character sizes of positron traps.

The third component in the x3-decomposed PAL spectrum with long-lived lifetime τ_3 is related to the Ps-decaying through pick-off annihilation of positron with an electron from surrounding [28, 29]. The Ps-states are localized in atomic-unoccupied free-volume holes in the intergranular space of the studied ceramics giving an indication of their mean radii R_3 in terms of long-lived τ_3 lifetime with respect to the known Tao-Eldrup equation. The intensity of this third component I_3 gives the density of Ps-decaying sites so that corresponding fractional free volume f_{v3} can be calculated in a spherical approximation with some empirical constant [29].

Since low contribution of Ps-states (because the I_3 intensity is no more than 1.2%), the physically realistic annihilation channels exploring two-state simple trapping model (STM) [28] in addition to the well-known three-state Ps-decay model [29] can be validated, the details of such parameterization being presented below in Table 4. It is obvious that Eu^{3+} doping results in the reduction of positron trapping rate κ_d in Eu^{3+}-doped ceramics (decrease in the κ_d value from 0.80 to 0.62 ns^{-1}), this effect being partially counterbalanced by increased fractional free volume f_{v3} in Ps-decay component. The free-volume traps with character defect-specific positron lifetimes τ_2 close to ~0.30–0.33 ns are expected (as for typical spinel structures with defect-free bulk positron lifetime τ_b approaching ~0.16–0.17 ns) as prototypes of multivacancy clusters (close to triple-quadruple vacancies) due to high enough value of difference $(\tau_2 - \tau_b) =$ ~0.14–0.15 ns and ratio $\tau_2/\tau_b =$ ~1.9 [28]. In contrast, the role of Ps-decay input is enhanced in Eu^{3+}-doped ceramics due to increased Ps formation probability, resulting from opposite trend in both I_3 and I_1 intensities in respect to I_2 intensity [34]. The effect of Eu^{3+} doping causes almost 11% rise in the fractional free volume f_{v3} in the studied $ZnGa_2O_4:Mn^{2+}$ ceramics. The Ps-related states are accommodated mainly in intergranular free-volume spaces having $R_3 =$ ~0.28 nm in a radius (Table 4).

Table 4 The positron annihilation modes in the studied samples treated within unconstrained x3-term decomposition

Sample	e^+-trapping modes						Ps-decaying modes	
	$\tau_{av.}^{tr}$, ns	τ_b, ns	κ_d, ns^{-1}	τ_2-τ_b, ns	τ_2/τ_b, a.u.	η, a.u.	R_3, nm	f_{v3}, %
$ZnGa_2O_4:Mn^{2+}$	0.197	0.178	0.80	0.151	1.85	0.125	0.285	0.18
$ZnGa_2O_4:Mn^{2+}$, Eu^{3+}	0.175	0.162	0.62	0.141	1.87	0.091	0.280	0.20

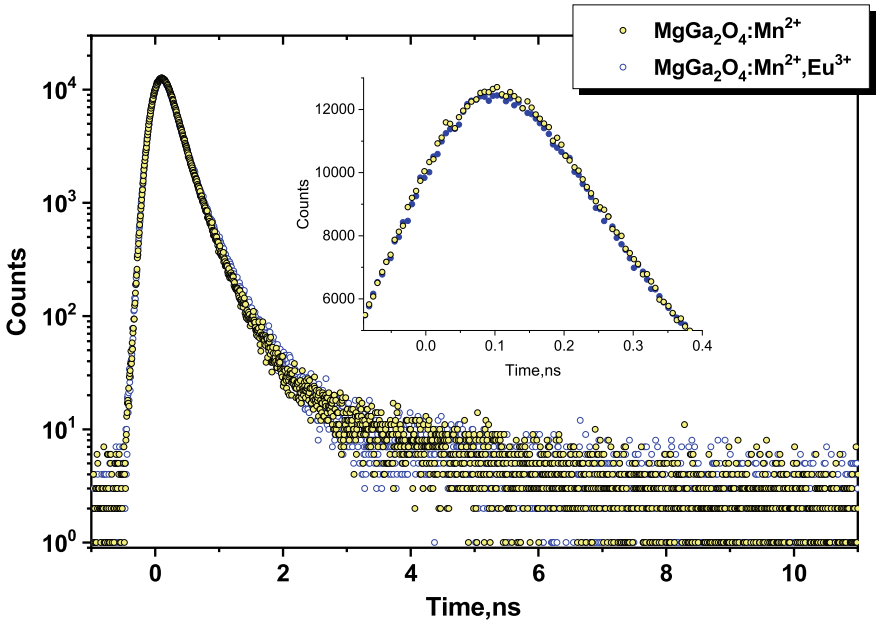

Fig. 6 PAL spectra of $MgGa_2O_4:Mn^{2+}$ and $MgGa_2O_4:Mn^{2+}$, Eu^{3+} ceramics

Within x3-x2-CDA (coupling decomposition algorithm) employed to the detected PAL spectra we come to conclusion that positron traps are located in ceramics grains. These defects occur to be occupied with Eu^{3+} ions, favored overall annihilation toward Ps-decay in free-volume holes, located mainly at the grain boundaries [9].

As to $MgGa_2O_4:Mn^{2+}$ and Eu-doped $MgGa_2O_4:Mn^{2+}$ ceramics, the PAL data testify that Eu^{3+} ions do not penetrate deeply into the grains of these spinel ceramics. The PAL spectra of both $MgGa_2O_4$ ceramics are reproduced in Fig. 6.

The fitting parameters of these spectra are gathered in Table 5. The results show only a slight growing tendency in the mean positron lifetime τ_{av} under Eu addition.

Since only low contribution arises from the third component (no more than 1.3%), the two-state positron trapping model could be applied to describe the effect of Eu-doping [28], applied in addition to Ps-decay model [29]. The results of such parameterization are gathered in Table 6. Such simplification allows to conclude

Table 5 The fitting parameters of positron annihilation spectra of studied ceramics

Sample	Fitting parameters					τ_{av}., ns
	τ_1, ns	τ_2, ns	τ_3, ns	I_2, a.u.	I_3, a.u.	
$MgGa_2O_4:Mn^{2+}$	0.172	0.322	2.142	0.180	0.013	0.224
$MgGa_2O_4:Mn^{2+}$, Eu^{3+}	0.166	0.339	2.162	0.230	0.011	0.227

Table 6 The positron annihilation modes of the studied samples treated within constraint-free x3-term decomposition

Sample	e$^+$-trapping modes						Ps-decaying modes	
	$\tau_{av.}^{tr}$, ns	τ_b, ns	κ_d, ns^{-1}	$\tau_2 - \tau_b$, ns	τ_2/τ_b, a.u.	η, a.u.	R_3, nm	f_{v3}, %
$MgGa_2O_4$:Mn^{2+}	0.199	0.188	0.50	0.134	1.71	0.086	0.301	0.26
$MgGa_2O_4$:Mn^{2+}, Eu^{3+}	0.206	0.188	0.72	0.151	1.80	0.120	0.302	0.22

Table 7 The PAL trapping modes of $MgGa_2O_4$:Mn^{2+}, Eu^{3+} ceramics in respect to $MgGa_2O_4$:Mn^{2+} one within x3-x2-CDA

First component		Second component		Trapping modes			
τ_n, ns	I_n, a.u.	τ_{int}, ns	I_{int}, a.u.	τ_{av}^m, ns	τ_b^m, ns	κ_d^m, ns^{-1}	$\tau_{\text{int}}/\tau_b^m$, ns
0.157	0.297	0.372	0.078	0.201	0.178	0.764	2.09

that Eu^{3+} doping enhances positron trapping in $MgGa_2O_4$:Mn^{2+} ceramics (due to increased trapping rate κ_d from 0.50 to 0.72 ns^{-1}). This increase in κ_d is followed by a decrease in fractional free volume f_{v3} calculated from Ps-related component. The high values of $(\tau_2 - \tau_b)$~0.13–0.15 ns and τ_2/τ_b~1.7–1.8 suggest multivacancy clusters with free volumes close to triple-quadruple vacancies [28] as prototypes of positron traps in both types of ceramics. The role of Ps-decay input is somewhat depressed in Eu^{3+}-doped ceramics due to decreased probability of Ps formation, as it follows from opposite trends in I_3 and I_1 intensities compared to I_2 [34].

The Ps-to-positron trapping interplay in $MgGa_2O_4$:Mn^{2+}, Eu^{3+} ceramics can be also analyzed with x3-x2-CDA [35, 36]. The comparison of positron annihilation parameters calculated with this approach is given in Table 7.

Since positive values of both I_n and I_{int} intensities, the overall free-volume evolution caused by Eu^{3+} doping can be described as replacement of Ps-trapping sites with character lifetime approaching $\tau_3 = 2.142$ ns (corresponding to spheres of ~0.30 nm in radius) by positron defect-related traps with $\tau_{\text{int}} = 0.372$ ns (equivalent of multivacancy clusters). Owing to close bulk positron lifetimes for modified ceramics (τ_b^m~0.18 ns) and spinel-structured compounds [35], we believe that extended traps (due to $\tau_{\text{int}}/\tau_b^m$~2.1) are located deeply in ceramics grains, while Ps-trapping holes are located mainly at grain boundaries. So, the obtained results suggest that relative input of positron traps in an overall annihilation process in the Eu-doped ceramics can be enhanced as result of Eu^{3+} ions localization in Ps-trapping holes near grain boundaries, which decreases their effective number and, consequently, the Ps-related lifetime component.

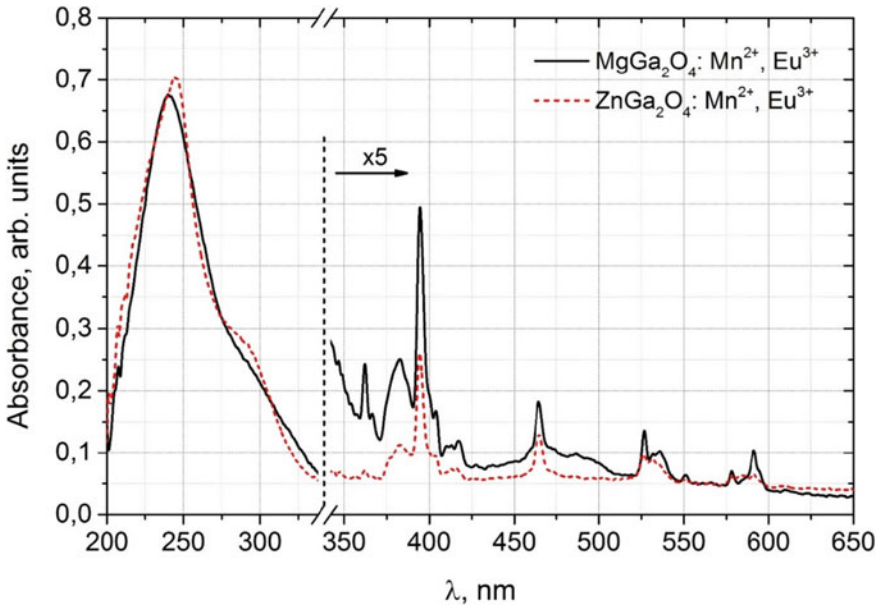

Fig. 7 Absorbance spectra of Mn^{2+} and Eu^{3+} co-doped spinel gallate ceramics. The right side of spectra was increased ×5 due to low relative intensity

3.4 Optical-Luminescent Spectroscopy

The optical absorption spectra of both $MgGa_2O_4$ and $ZnGa_2O_4$ ceramics co-doped with Mn^{2+} and Eu^{3+} ions are presented in Fig. 7. Strong absorption bands were found in the UV-spectral region as a result of "band-to-band" transitions in $MgGa_2O_4$ and $ZnGa_2O_4$ matrixes. These fundamental absorption bands overlap with much weaker bands around 280 nm which restrict the estimation of bandgap energies of Mn^{2+} and Eu^{3+} co-doped ceramics of magnesium and zinc gallate compounds.

Corresponding band gap energies of 4.8 and 4.6 eV were estimated for $MgGa_2O_4$:Mn^{2+} and $ZnGa_2O_4$:Mn^{2+}, respectively [9, 14]. The observed red shift of UV absorption bands of $ZnGa_2O_4$:Mn^{2+}, Eu^{3+} ceramics with respect to $MgGa_2O_4$:Mn^{2+}, Eu^{3+} is due to the difference in bandgap energies. From the earlier works, it is possible to associate the overlapping band which forms a shoulder at 280 nm to transfer of charges from 2*p* states of oxygen anions to 4*f* states of Eu^{3+} ions ($O^{2-} \rightarrow Eu^{3+}$) [4, 23, 25]. Several sharp lines are found in the absorption spectra (Fig. 7). These sharp lines correspond to *f*–*f* transitions of Eu^{3+} ions [4, 37]. Supreme intensity among the lines is at about 393 nm related to $^7F_0$–$^5L_6$ transitions. The rest of the lines are caused by $^7F_0$–^5D_j transitions. A redistribution of lines intensities above 500 nm for $MgGa_2O_4$:Mn^{2+}, Eu^{3+} and nGa_2O_4:Mn^{2+}, Eu^{3+} should indicate the difference of crystalline field symmetry around Eu^{3+} ions in those compounds [38, 39].

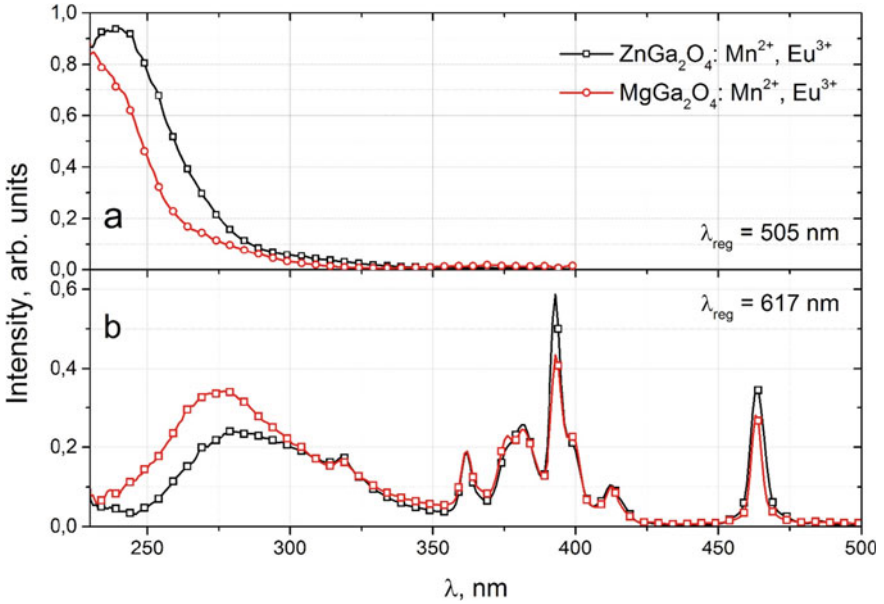

Fig. 8 Excitation spectra of manganese and europium ions in the zinc and magnesium gallate spinel matrix registered at 505 (**a**) and 617 nm (**b**), respectively

Luminescent properties of $MgGa_2O_4$ and $ZnGa_2O_4$ ceramics with Mn and Eu were investigated by the photoluminescence excitation (PLE) and photoluminescence (PL) spectroscopy at room temperature (Figs. 8 and 9).

Both gallate ceramics demonstrate strong excitation related to the fundamental absorption of host material under a monitoring wavelength of 505 nm (see Fig. 9a). This indicates a dominative contribution of the recombination mechanism to the excitation process of manganese ions in gallate spinel materials [17, 37, 40]. The efficient transfer of energy from $ZnGa_2O_4$ and $MgGa_2O_4$ matrixes to manganese ions is confirmed by an intense emission peak at 505 nm at 240 nm UV-light excitation [37]. The CTB from oxygen to manganese ions produces the shoulder around 275 nm which is better resolved in the spectrum of $MgGa_2O_4$:Mn^{2+}, Eu^{3+} (Fig. 8a). A strong charge transfer band from O^{2-} anions to Eu^{3+} ions and several excitation lines in the region from 350 to 480 nm (*f–f* transitions in Eu^{3+} ions), with strongest at 393 ($^7F_0 \rightarrow {}^5L_6$) and 462 ($^7F_0 \rightarrow {}^5D_2$) nm were found at 617 nm detection wavelength (Fig. 8b) [4, 23, 25].

The Mn^{2+} and Eu^{3+} gallate ceramics show emission mainly in two spectral regions of 475–550 nm and 575–650 nm that are related to activator ions, respectively [23, 41] (Fig. 9). The only small exclusion is a weak luminescence band of $ZnGa_2O_4$:Mn^{2+}, Eu^{3+} at about 380 under 280 nm excitation associated with vacancy type of defects (Fig. 9b) [17, 42]. The relative intensity of Mn^{2+} emission increases significantly with the excitation in the region of "band-to-band" transitions, which is indirect evidence of the recombination mechanism. According to [43, 44], luminescence at 505 nm is

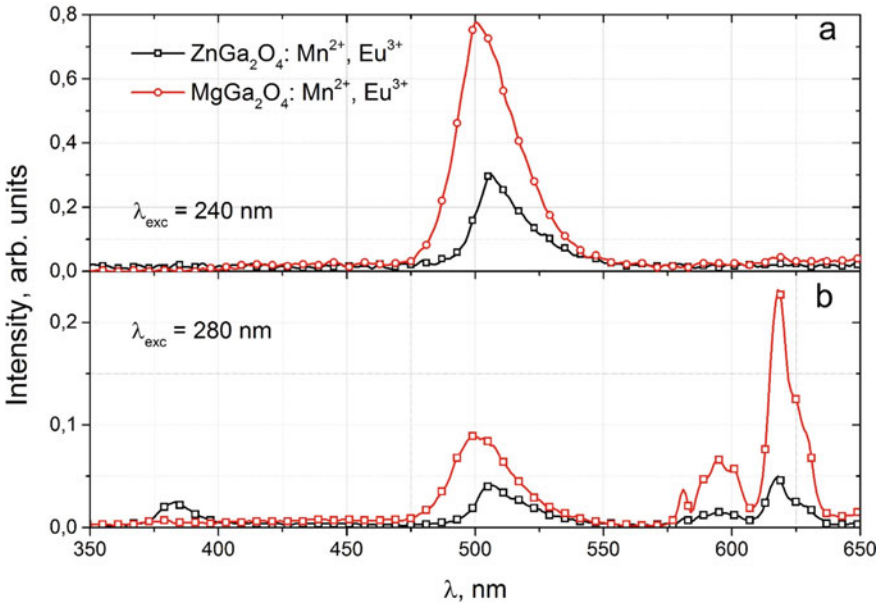

Fig. 9 PL spectra of $ZnGa_2O_4$ and $MgGa_2O_4$ spinels with Mn^{2+} and Eu^{3+} ions excited at 240 (**a**) and 280 nm (**b**), respectively

characteristic of the manganese ions in tetrahedral symmetry and corresponds to the $^4T_1(^4G) \rightarrow {}^6A_1(^6S)$ transition of Mn^{2+} (Fig. 9).

Except intense luminescence at 505 nm associated with the Mn^{2+} ions, both manganese and europium co-doped gallate ceramics show emission in 575–650 nm region, which belongs to the transitions from $^5D_0$ level to ^7F_J levels of the Eu^{3+} ions [4, 23, 45, 46]. The dominant red luminescence line at about 617 nm is due to the $^5D_0 \rightarrow {}^7F_2$ transitions of Eu^{3+}. It is well known that the local symmetry of Eu^{3+} sites in the lattice is reflected by a form of Eu^{3+} emission spectrum. Following the Judd–Ofelt theory [38, 39, 47] the local symmetry around Eu^{3+} ions in the lattice is reflected by a form of Eu^{3+} emission spectrum. In this case, the $^5D_0 \rightarrow {}^7F_1$ magnetic-dipole transitions are attributed to the ions located into positions with higher symmetry, while electric-dipole transitions $^5D_0 \rightarrow {}^7F_2$ originate mainly from the ions in the lower symmetry sites. The intense red emission of Eu^{3+} is indicated by domination of the electric-dipole transitions of Eu^{3+} ions dominate in the luminescence spectra. Thus, to estimate the degree of symmetry of Eu^{3+} sites the ratio between the magnetic-dipole and electric-dipole transitions was calculated. The values of asymmetry ratio $(^5D_0 \rightarrow {}^7F_2)/(^5D_0 \rightarrow {}^7F_1)$ for $MgGa_2O_4$:Mn^{2+}, Eu^{3+} and $ZnGa_2O_4$:Mn^{2+}, Eu^{3+} calculated as (I_{617}/I_{593}) are equal to 3.5 for both samples. The values of asymmetry suggest a strong disorder of coordination polyhedron around Eu^{3+} ions, i.e., the Eu^{3+} ions possess the sites in the spinel lattice with non-inversion symmetry.

Taking into consideration the relative intensities of gallate ceramics the emission efficiency of Mn^{2+} and Eu^{3+} ions in $MgGa_2O_4$:Mn^{2+}, Eu^{3+} sample is higher for about factor of 2 than in $ZnGa_2O_4$:Mn^{2+}, Eu^{3+} sample. A strong proof of weak penetration of Eu^{3+} ions into the volume of $MgGa_2O_4$ matrix and favorable location of europium in the grain boundaries explains the derived values of Judd–Ofelt parameters and strong disorder of the local symmetry. On the contrary, the europium in $ZnGa_2O_4$ is more predisposed to penetrate deeply into the volume of the grain. These results lead us to the conclusion that red emission of Eu^{3+} ions dominantly origins from the ions located in the grain boundaries.

Apart of that, higher PL intensity of Mn^{2+} ions at 505 nm for magnesium gallate can be considered in terms of different defect structure with respect to zinc gallate compound. As mentioned above, the $MgGa_2O_4$ is characterized by a significant amount of antisite structural defects that results in the creation of trap and/or recombination centers. Such centers are involved in recombination mechanism of green PL of Mn^{2+} ions leading to strong enhancement of emission intensity for $MgGa_2O_4$ ceramics.

4 Conclusions

Rietveld refinement analysis of XRD patterns of $MgGa_2O_4$:Mn^{2+}, Eu^{3+} and $ZnGa_2O_4$:Mn^{2+}, Eu^{3+} ceramics indicated spinel phase in both samples. TEM-EDX mapping shows that Eu^{3+} ions are homogeneously distributed in the crystallites of $MgGa_2O_4$:Mn^{2+}, Eu^{3+} and $ZnGa_2O_4$:Mn^{2+}, Eu^{3+} samples. The TEM morphology images show that particle sizes are in the scale from hundreds nano- to micrometers.

The Eu^{3+} ions penetration into the grains of $ZnGa_2O_4$:Mn^{2+} and $MgGa_2O_4$:Mn^{2+} spinel ceramics is studied by PAL spectroscopy. In the case of $ZnGa_2O_4$:Mn^{2+}, the analysis of PAL spectra decomposed into three unconstrained exponentials confirmed deep penetration of Eu^{3+} ions into the ceramics grains. The reduced positron trapping is observed under Eu addition owing to occupancy of vacancy-type defects in grains, while the Ps-decaying is enhanced mainly in the intergranular free-volume spaces. In the case of $MgGa_2O_4$:Mn^{2+}, the opposite effect of the inability of Eu ions to deeply penetrate into ceramic grains is confirmed by the results of PAL spectroscopy. The addition of Eu^{3+} results in the enhanced positron trapping due to preferential occupancy of vacancy-type defects near ceramic grains. This effect is counterbalanced by reduced Ps-decaying mainly in intergranular free-volume spaces.

Optical absorption spectra revealed strong UV absorption corresponding to "band-to-band" transitions together with sharp lines of f–f transitions of Eu^{3+} ions. Mn^{2+} ions demonstrate intense green luminescence dominantly under excitation in the region of "band-to-band" transitions, which indicates the favorable contribution of channels with recombination nature into this emission. Eu^{3+} ions are excited in wide-ranging CTB and narrow lines of f–f intracenter transitions of Eu^{3+} ions. Both excitation ways lead to the f–f characteristic emission of Eu^{3+} ions. Derived from luminescence spectra the Judd–Ofelt parameter was derived as the ratio between line

intensities of electric-dipole to magnetic-dipole transitions and reveal that the Eu^{3+} ions occupy sites with low symmetry in the $MgGa_2O_4$ and $ZnGa_2O_4$ lattices.

References

1. Valiev D, Stepanov S, Khasanov O et al (2019) Opt Mater 91:396–400
2. Wang S, Chen C, Li Ya, et. al (2019). J Electron Mater 48:6675–6685
3. Safeera TA, Anila EI (2019) J Lumin 205:277–281
4. Luchechko A, Kravets O (2017) J Lumin 192:11–16
5. Jain M, Manju M, Gundimeda A et al (2019) Appl Surf Sci 480:945–950
6. Fernández-Osorio A, Tapia M, Vázquez-Olmos AR et al (2019) J Solid State Chem 269:328–335
7. Luchechko A, Zhydachevskyy Ya, Maraba D et al (2018) Opt Mater 78:502–507
8. Kumari P, Dwivedi Y, Bahadur A (2018) Optik 154:126–132
9. Kravets O, Zaremba O, Shpotyuk Ya et al (2019) Appl Nanosci 9:907–915
10. Ma J, Qi G, Chen Y et al (2018) Ceram Int 44:11898–11900
11. Zhang Y, Huang R, Li H et al (2018) Acta Mater 155:214–221
12. Brik MG, Papan J, Jovanović DJ et al (2016) J Lumin 177:145–151
13. Mondal A, Das S, Manam J (2016) RSC Adv 6:82484–82495
14. Luchechko A, Kravets O, Tsvetkova O (2017) J Nano-Electron Phys 9:1–6
15. Ahn W, Im M, Kim YJ (2017) Mater Res Bull 96:254–257
16. Gu Zh, Liu F, Li X et al (2010) J Phys Chem Lett 1:354–357
17. Luchechko A, Zhydachevskyy Y, Ubizskii S et al (2019) Sci Rep 9:9544
18. Kumar M, Gupta SK, Kadam RM (2016) Mater Res Bull 74:182–187
19. Krishna KM, Anoop G, Jayaraj MK (2012) Phys Status Solidi A 209:2641–2645
20. Liu H, Yu L, Li F (2013) J Phys Chem Solids 74:196–199
21. Sakoda K, Hirano M (2014) Ceram Int 40:15841–15848
22. Viana B, Sharma SK, Gourier D et al (2016) J Lumin 170:879–887
23. Luchechko A, Kravets O, Kostyk L et al (2016) Radiat Meas 90:47–50
24. Sasajima N, Matsui T, Furuno S et al (2000) Nucl Instrum Methods Phys Res B 166:250–257
25. Luchechko A, Kravets O, Syvorotka II (2017) Spectrosc Lett 50:404–410
26. Uheda K, Maruyama T, Takizawa H et al (1997) J Alloys Compd 262–263:60–64
27. Kansy J (1996) Nucl Instrum Methods Phys Res Sect A 374:235–244
28. Krause-Rehberg R, Leipner HS (1999) Positron annihilation in semiconductors: defect studies. Springer, New York
29. Jean YC, Mallon PE, Schrader DM (2003) Principles and applications of positron and positronium chemistry. World Scientific
30. Zhang Ya, Wu Z, Geng D et al (2014) Adv Func Mater 24:6581–6593
31. Li Ya, Niu P, Hu L et al (2009) J Lumin 129:1204–1206
32. Galazka Z, Klimm D, Irmscher K et al (2015) Phys Status Solidi A 212:1455–1460
33. Sawada K, Nakamura T, Adachi S (2016) J Appl Phys 120:143102
34. Vijay YK, Wate S, Awasthi DK et al (2000) Indian J Eng Mater Sci 7:375–377
35. Shpotyuk O, Ingram A, Shpotyuk Y (2018) Nucl Instrum Methods Phys Res Sect B 416:102–109
36. Shpotyuk O, Filipecki J, Ingram A et al (2015) Nanoscale Res Lett 10:77
37. Luchechko A, Zhydachevskyy Y, Sugak D et al (2018) Latv J Phys Tech Sci 55:43–51
38. Judd BR (1962) Phys Rev 127:750–761
39. Jorgensen CK, Reisfeld R (1983) J The Less-Common Met 93:107–112
40. Luchechko A, Kravets O (2017) Phys Status Solidi C 14:1600146
41. Moon YM, Choi S, Jung HK et al (2008) J Lumin 128:1491–1495
42. Kim JS, Park HL, Chon CM et al (2004) Solid State Commun 129:163–167

43. Costa GKB, Pedro SS, Carvalho ICS et al (2009) Opt Mater 31:1620–1627
44. Mironova N, Skvortsova V, Smirnovs A et al (1996) Opt Mater 6:225–232
45. Tsai BS, Chang YH, Chen YC (2006) J Alloys Compd 407:289–293
46. Tsai BS, Chang YH, Chen YC (2004) J Mater Res 19:1504–1508
47. Ofelt GS (1962) J Chem Phys 37:511–520

Composite Titanium Dioxide Photocatalytically Active Materials: Review

A. Kukh, I. Ivanenko, and I. Asterlin

1 Introduction

Numerous treatment methods and processes have been used in water treatment processes. However, using only one treatment method for complete purification of water with a complex composition of pollutants or pollutants of complex chemical structure rarely demonstrates great results, neither it can be deemed economic, thus industrial-scale application is limited.

Titanium dioxide has been exploited as photocatalytic material for water treatment widely. This material can remove various hazardous pollutants of organic and inorganic origin on the high rate. The general approach towards the understanding of the photocatalytic degradation of organic substances includes the following:

(1) irradiation with suprabandgap photons;
(2) excitation of the active sites of photocatalyst;
(3) charge separation and diffusion of the positive and negative charge carriers to the surface of the photocatalyst.

There, the holes get trapped by H_2O or OH^-, adsorbed to the surface and as a result hydroxyl radicals are formed. For the majority of organic materials, destruction occurs as a result of the oxidation process where hydroxyl radicals enter the redox reaction with the organic compound. It results in the formation of organo-radicals that get involved in secondary reactions to form CO_2 and H_2O, although reduction mechanisms have a tendency to occur in the case of compounds containing halogen groups. Photodegradation kinetics is adsorption-dependent process. Even though the possibility of diffuse charge transfer onto the aqueous media is possible and observed in laboratory studies, and as a result secondary destruction of the compounds in

A. Kukh (✉) · I. Ivanenko · I. Asterlin
National Technical University of Ukraine "Igor Sikorsky Kyiv Polytechnic Institute, 37 Prosp Peremohy, Kiev 03056, Ukraine
e-mail: angela.kukh@gmail.com

O. Fesenko and L. Yatsenko (eds.), *Nanooptics and Photonics, Nanochemistry and Nanobiotechnology, and Their Applications*, Springer Proceedings in Physics 247, https://doi.org/10.1007/978-3-030-52268-1_28

the solution volume takes place, it has minor influence on the overall efficiency of the photodegradation process. As a result of this obstacle, photodegradation of molecules, especially the ones, that hardly adsorb on the polar TiO_2 is extremely difficult. Unfortunately, an extensive amount of hazardous pollutants belongs to this category.

Thus, certain drawbacks exist, that limit the use of bare TiO_2 in large-scale industrial water treatment. In order to be photocatalytically active and effective in the treatment process particles of relatively small size (4–30 nm) should be evenly distributed in the volume of the treated water. Due to small particle size suspended TiO_2 tend to aggregate rapidly. As a result, effective surface area as well as catalytic efficiency is greatly decreased. Due to the crystalline structure and thus non-porous surface, TiO_2 photocatalysts demonstrate low overall adsorption activity, especially towards organic molecules. Moreover, industrial wastewaters that need to undergo treatment are of the complex composition and contain several contaminants at the time. As a result, molecules in the system compete on the already limited number of adsorptive sites of the photocatalyst. Due to this fact applicability of laboratory-scale experiments than involve a limited number of components for simulation of complex systems that appear during practical use is limited. In addition, the tendency towards the formation of toxic by-products and intermediates of photocatalytical degradation of organic compounds is often observed.

Immobilization of the photocatalyst particles onto the surface of inert support is a technique that has the potential to improve the efficiency of photocatalytic process. The fundamental concept behind this idea is that inert domains are used for the adsorption of target compounds that generally hardly adsorb on the photocatalyst particles. As a result, within a small distance from photocatalytically active site, the area of increased concentration of pollutants is formed. Once the pollutant molecule is absorbed, the surface diffusion of the molecules towards photocatalytic sites is possible.

Even though the concept of the use of composite catalytic materials in the industry is nothing new, the possibility of use of composite photocatalysts is a subject of the great interest in the scientific community.

The proposed review article takes a look at the actions taken within recent decades on the development and use of composite photocatalytically active materials containing titanium dioxide as well as photodegradation processes where these composites may be exploited. The sole properties of inert domains are left behind the scope of the proposed paper and addressed only in terms of their effect on overall mass transport effect in the process involving composite material.

2 Synthesis and Characterization of Composite Photocatalysts

2.1 Types of Inert Supports

The amount of materials that are used as inert supports for preparation of composite photocatalysts, are quite limited. These materials can be separated into several groups, taking into consideration their properties and chemical nature:

(1) carbonaceous materials;
(2) oxides;
(3) metals;
(4) polymers.

The most widely exploited group of materials used for the preparation of composite photocatalytically active materials is carbonaceous materials. Materials that this group includes are represented by graphene, fullerenes, carbon nanotubes [1], however, the most used among all is activated carbon. Activated carbon attracts the attention of scientific community and industry due to exceptional adsorption properties, highly developed surface area, ability to adsorb different types of hazardous pollutants and relative economical efficiency combined with availability and ease of modification. Furthermore, activated carbon together with TiO_2 in photocatalytic processes demonstrates the development of the synergetic effect of two that result in an overall increase of efficiency of the photocatalytic process. It is reported, that a physical mixture of activated carbon and titanium dioxide particles demonstrated enhanced degradation rates [2].

As for the group collectively referred to as oxides, it includes silica [3, 4], alumina [5], glass and clays. The adsorption ability of this material is usually determined by their structural characteristics that largely determine their physical-chemical properties and areas of application. The type of active sites on the surface of these materials, that are responsible for adsorption properties, differ for various types of aluminosilicates and often may be a result of modifying agents used during synthesis process. As for natural clays, the adsorption properties maybe not evenly distributed and depend on the source, formation process and excavation methods. Being highly suitable for the adsorption of contaminants of polar nature, materials of this group generally cause secondary contamination of treated water due to the low stability of the particles.

Use of metal support for the TiO_2 in photocatalytic process is generally considered to be a way to determine the selectivity of photodegradation process. It is obvious, that metals are unable to demonstrate adsorption properties, but rather are used for irreversible chemisorption of the contaminants, and thus in-depth discussion of this topic is out of the scope of the proposed review.

Combination of polymer materials with TiO_2 has many possibilities of use but at the same time is linked to the variety of limitations [6, 7]. Organo-silanes and polymers used as inert supports in composites with TiO_2 result in efficient material proven to be highly effective in the degradation of specific types of pollutants, such

as insoluble in water pesticides. Such combination materials allow achieving great operational advantages for industrial-scale use. Low-temperature synthesis methods allow to control and determine adsorption characteristics, the shape of particles, etc. However, one of the major drawbacks that limit the use of polymer-TiO_2 composite materials is the tendency of the inert material attached directly to the photocatalyst to be degraded during the photocatalytic process. The attempts to overcome this obstacle result in complex synthesis approach and additional expenses [8].

2.2 Preparation Methods

The variety of methods have been proposed for the preparation of composite materials. The synthesis method regardless of the operation sequence and technological regime should ensure:

1. good adherence of photocatalyst particles onto the surface of inert support;
2. size of particles and crystalline structure of photocatalyst;
3. preserving of adsorption properties of inert support.

In the majority of cases in situ preparation of one of the components of the composite material can achieve stated above goals. Usually, in situ formation of photocatalyst (for instance, by a sol–gel method) takes place. Oftentimes such methods require thermal post-synthesis treatment (normally at high temperatures ranging from 300 °C to possibly 650 °C). Thermal treatment is necessary in order to form active anatase phase of titanium dioxide, as well as remove solvents and chelating agents. Interaction between titanium dioxide particles and inert support is expected and reported. It is reported, that immobilization of TiO_2 particles onto the surface of silica increases the overall thermal stability of anatase phase [9].

Despite the fact, that sol–gel method is the most frequently used preparation method due to its simplicity, relative economic efficiency and possibility to control properties of resulting material through synthesis conditions, it is important to mention, that the calcination step, which oftentimes is essential for obtaining desired photoactive anatase phase, may result in a decrease of surface area of the inert component, especially if activated carbons are used. However, the reduction of surface area generally is compensated by the improvement of crystallinity of the photocatalyst. Also, it is observed that often calcination temperatures in the range below anatase rutile transition temperature may be used.

Attempts were made towards the preparation of photocatalytic active composite materials with activated carbon by temperature inducted sol–gel method without calcination stage. The proposed method results in obtaining of photocatalytic active composite material without significant decrease of surface area and porosity of inert support [10].

Another method commonly used for the preparation of the composites is hydrothermal. This method utilizes the same principle of in situ preparation of TiO_2

particles and capable of the provision of good adherence between photocatalyst particles and inert support, normally activated carbon. During this process formation of Ti-O-C bonds was reported [11]. Supercritical treatment with isopropanol was also used in order to achieve a desirable degree of bonding between the photocatalyst particles and activated carbon. However, the maximum mineralization rates were less than 50% compared with those for a physical mixture of AC and TiO_2 [17]. Hydrothermal method allows exploitation of alternative approach, where in situ preparation of carbonaceous support is used, for instance by thermally driven carbonization of polyvinyl alcohol under N_2 environment [12].

As an approach to reduce time and apparatus needed for the preparation of composite materials pre-prepared or commercially available titanium dioxide particles may be used. In this case, thermal treatment is still used in order to increase adherence between TiO_2 particles and support. In order to reduce the temperature that is required to guarantee good adherence between components of composite material, Ionized Cluster Beam (ICB) method may be employed. In order to achieve in situ immobilization on an inert substrate of titanium dioxide particles, oxidation of ICB titanium by gaseous oxygen at a temperature about 250 °C is used. Activated carbon fibers, as well as porous silica, are the most commonly used inert supports in this case [13].

Besides the undoubtful influence of synthesis process of photocatalytical part of composite, the synthesis method of the activated carbon appears to have a great impact on materials' properties as well. In fact, the properties of inert support may govern the enhancement ratio of the treatment process. It was observed, that high enhancement ratio in the degradation of such common aromatic alcohols as phenol and 4-chlorophenol (as high as 2,5) were achieved with activated carbons physically treated by CO_2 or steam [14]. On the other hand, ACs chemically treated, for instance with H_3PO_4, tend to demonstrate no synergism and in fact, an adverse effect reducing the overall effcicency is observed. As a result, the presence of a detrimental doping effect was suggested, that occurs as a result of low dry ash content.

Electrospinning is another preparation method that may be used for the production of composite fibers that contain titanium dioxide. This rater simple method is based on the charging of electrostatic surface of a viscous solution that draws a jet moving at a high speed towards a stationary or rotating surface. This technique has been used to produce TiO_2 nanofibers, [15] as well as synthesis of fibers containing both TiO_2 and polymers such as poly(vinyl alcohol) [16] or poly(acrylonitrile) [1].

2.3 Adsorption Properties of Composites

Due to poor adsorption properties of crystalline titanium dioxide particles, it is self-evident that the adsorption properties of inert support determine the overall adsorption properties of composite phocatalytically active material. However, immobilization on the surface of inert support of titanium dioxide particles causes a significant decrease in surface area of the adsorbent even in cases when the percentage of photocatalyst

Table 1 Structural-adsorption characteristics of activated carbon—TiO_2 composites (based on data from [10])

Sample	$S_{BET.}^{N_2}$, $\frac{m^2}{\Gamma}$	$\bar{V}_{\sum}$, $\frac{cm^3}{g}$	V_{meso}, $\frac{cm^3}{\Gamma}$	V_{micro}, $\frac{cm^3}{g}$	r_{av}, nm
1	2	3	4	5	6
AC bare	1277	126	082	035	198
AC–TiO_2 (nh)	1143	099	058	035	17
AC–TiO_2 (2F)	1110	091	5	036	16
AC–TiO_2 (7F)	899	073	041	029	16
AC–TiO_2 (15F)	1143	098	058	035	17
AC–TiO_2 (prec)	1116	103	064	029	18

part is low. This is a result of clogging of pores of adsorbent, that is responsible in majority of cases for the adsorption properties of adsorbent [10, 17]. Adsorption properties of resulting material are usually lower comparing to the bare adsorbent. The degree of reduction in the surface area tends to be higher in cases of in situ formations of TiO_2 from the viscous liquid phase, for instance by sol–gel process. During this process viscosity of liquid media assists in bridging over small pores (Table 1).

One major drawback exists with an estimation of surface area and absorptivity of composites (which should supposedly lead to enhanced degradation rates). Traditional approach towards the measurement of the surface area of porous materials includes measurement by BET isotherm. Normally, small molecules are used, such as nitrogen. The main obstacle is that small-sized spherical nitrogen molecules vary in size and shape from the model pollutants that are commonly used for studies of photocatalytic activity. Usually, model pollutants are not symmetrical, thus the area per each molecule is highly dependent on orientation and packing relative to the surface. This is greatly influenced by the physical and chemical characteristics of the surface. It is obvious, for instance, that nearly planar aromatic molecule will adsorb onto alumina in a different orientation as on carbonaceous substrate. Taking this into consideration, the calculated BET surface area is unable to provide neither accurate nor even relative estimation of the amount of adsorbed model contaminants.

3 Photocatalytic Experiments

3.1 Photocatalytic Experiments

Different approaches exist towards the realization of photocatalytic experiments in terms of apparatus. It was established, that composite photocatalitically active materials play major role not only in changes in degradation rates but modify the character of the degradation process in terms of intermediate and end products. Large number

of factors are claimed to cause this effect: surface area, adsorption characteristics of the surface, loading of photocatalyst, domain size as well as operational parameters such as humidity and temperature. In most cases during the studies composite and bare TiO_2 prepared in the same manner are being compared. While it generally allows obtaining a good impression and allows study the influence of different effects, in terms of commercial use the comparison must be made against other commercially available product.

The vast majority of works on photocatalytically active composite materials is generally focused on the enhancement of the photodegradation efficiency as it is. Oftentimes more deep and complex analysis whether the introduction of inert support can influence other aspects of the process are left out of the scope of the research.

3.2 Model Contaminants

General approach towards the selection of substances for photodegradation may be divided into several equally applicable:

(1) use of model well-described and studied contaminant, like methylene blue;
(2) use of compounds known to be difficult to adsorb onto the surface of titanium dioxide;
(3) use of compounds known to be difficult to remove in general (whether adsorption will require complex regeneration scheme or degradation using bare TiO_2 appears to have low efficiency).

The number of contaminants used as a model for the purposes of photocatalytic studies is quite extensive. Among the list propioaldehyde [18], pyridine [19], dyestuff [20, 21], herbicides [22] and insecticides, heavy metals ions, simulants of nerve gases, chlor-organic substances such as 1, 2-dichloroethane [23, 24], pharmaceutical substances (antibiotics [25], anti-inflammatory agents, etc.) and many more classes.

3.3 Enhancement of Degradation Rate

One of the most obvious and most addressed benefits of the use of a composite of photocatalysts is the enhancement of the degradation rate of pollutants. The calculation of this factor is made either by the direct or indirect measure of the concentration of the contaminants. Quantitative aspect of this enhancement is often described as an enhancement factor, also known as enhancement ratio. The definition of enhancement factor can be described as « the ratio between the rate constant with the composite photocatalyst to the reaction rate constant with titanium dioxide having the same weight as the TiO_2 in the composite » [26]. Though, this definition is accurate for a probable first-order kinetics model. Oftentimes observed enhancement factors for composite photocatalysts are in the range between 2 and 7.

It may be nothing unexpected, that photocatalytically active composite materials containing activated carbon as inert support demonstrate impressive and high enhancement factors regardless of the synthesis route employed. Composite material consisting of commercial mesoporous carbon and titanium dioxide was used by Park et al. [27] to achieve constant of pseudo-first-order kinetic model in the process of photocatalytic degradation of dye Rhodamine 6G, which known to have limited adsorption on titanium dioxide. The obtained constant was 5 times larger than that of commercially available commonly used photocatalyst P25 [27]. The experimental procedure included the formation of mesoporous structure on a silica-rods template by HF etching using furfuryl alcohol to obtain activated carbon. It is important to note that there is a potential effect of doping of the surface of the AC with fluorine ions, during pre-treatment of silica before etching. First-order reaction model was also obtained by the kinetic data of RhB photodegradation [28].

A variety of parameters determine the enhancement ratio of composites. Some of them include the characteristics of the photocatalyst, while the experimental conditions are being demonstrated by others:

(1) the differences in extent of adsorption (per unit of area) between the inert supports and the photocatalyst;
(2) the surface area of the inert support of composite;
(3) the ratio (gram per gram) of the photocatalyst loaded onto the inert material;
(4) the ability of contaminants and active oxidizing species to effectively diffuse on and inside the inert substrates;
(5) the average diffusion distance that the pollutants or active particles (radicals) have to overcome in order to reach active sites of the photocatalyst;
(6) temperature;
(7) pH;
(8) contact time.

3.4 Loading

Immobilization of titanium dioxide particles onto the surface of inert support affects both the surface area and average diffusion distance. The optimal amount varies. It is not clear if any systematic work towards the establishment of correlation between the optimal TiO_2/inert support ratio and the type of contaminant had been made so far. Nevertheless, it is the factor that should be addressed in future research. Since strong interaction between the adsorbate and adsorbent takes place, it is likely that optimal loading lays in the range of low percentage of photocatalitically active component in composite material. It may be linked to the fact, that low TiO_2/inert support ratio, resulting in an excessive amount of the inert material might result in a way too large diffusion distance. Furthermore, the effect of TiO_2/inert support ratio can be linked to the structural or morphological variations of the composite photocatalytic materials.

For instance, it is demonstrated that photodegradation of propionaldehyde results in the formation of CO_2 tends to increase for ratios up to 50% of TiO_2 in the structure of composite [29]. And after that the tendency to decrease is observed.

It is logically to expect, that the diffusion distance are significantly shorter and the "adsorb and shuttle" effect is stronger in composites with relatively smaller active sites—TiO_2 particles.

3.5 Photodegradation Pathway

Photodegradation of contaminants usually goes through the formation of intermediate products, that may be released into media and then adsorb onto the composite photocatalyst again and undergo another cycle of degradation that might result in the formation of actual end products. Majority of works link the degradation pathway to the TiO_2 domains. In many cases, intermediate products, that are formed during the degradation process are a separate issue to address, due to their potential toxicity. For degradation of dyes potential by-products are not a big concern, however, during the photocatalytical treatment of pharmaceutical compounds or pesticides the attention of researchers is often driven towards degradation mechanism and intermediate compounds that may form. It is noteworthy to say, that oftentimes the formation of intermediates is determined by overall chemical structure of the treated molecule, however, in many cases, the formation of intermediates is unpredictable and requires further research. In this case, during the treatment of diclofenac with TiO_2 formation of 6 different intermediate compounds observed (Fig. 1), that demonstrate a great extent of toxicity [30].

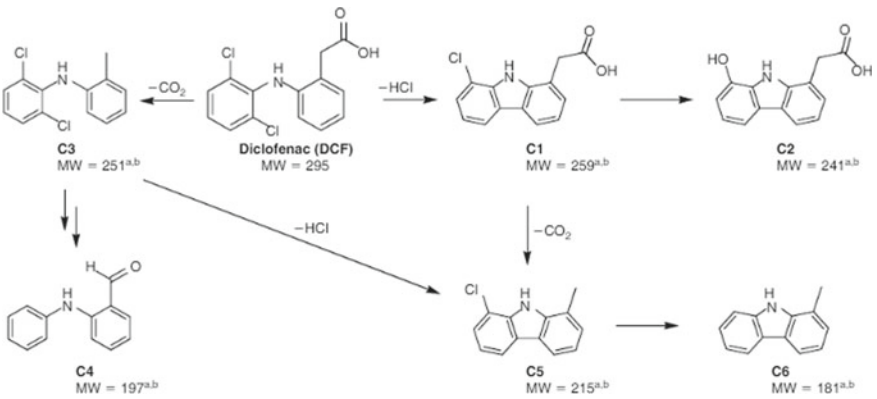

Fig. 1 Degradation scheme for 2—[(2,6-dichlorophenyl)-amino]phenylacetic acid (DCF, diclofenac) [30]

Along this line, only minute amounts of the intermediate products hydroquinone and benzoquinone were found in the degradation of phenol [31] and 4-chlorophenol [32] by a suspension made of P25 particles and activated carbon [33].

4 Conclusions

The use of composite photocatalytically active materials has a great potential for use, especially if their benefits are taken into consideration. The most important is that use of composites allows to overcome several problems, like limited control over the formation of intermediate products and difficulty in removal of pollutants that hardly adsorb onto the surface of the polar photocatalytically active materials. Adsorption, especially onto the activated carbon, may be considered a mature fully-formed well-studied technology that allows to remove an extensive amount of contaminants with high TiO_2/inert support ratio. That allows to project photodegradation with composite photocatalysts as a significant improvement of existing adsorption methods.

There is solid evidence that materials that consist of inert supports and TiO_2 are able to affect the photocatalytic properties of the latter in photocatalytic processes. It is apparent that the most significant effect is defined as enhancement of photodegradation rate, due to concomitant adsorption of pollutant molecules onto the surface of inert support and their diffusion towards photocatalitically active domains. The efficiency of this process and the extent of enhancement is dependent on number of factors, like surface area, adsorption properties of inert supports, ratio in content between titanium dioxide and inert domain, the size of active sites and operational parameters (temperature, humidity), as well as the type of pollutant.

With the stated above, composite photocatalytically active materials become more and more extensively studied which tends towards the development of effective materials capable of resolving numerous industrial problems and challenges.

References

1. Kedem S, Schmidt J, Paz Y, Cohen Y (2005) Composite polymer nanofibers with carbon nanotubes and titanium dioxide particles. Langmuir 21(12):5600–5604
2. Matos J, Laine J, Herrmann J-M, Uzcategui D, Brito JL (2007) Influence of activated carbon upon titania on aqueous photocatalytic consecutive runs of phenol photodegradation. Appl Catal B: Environ 70:1–4
3. Hendrix Y, Lazaro Garcia A, Yu Q, Brouwers HJH (2015) Titania-Silica composites: a review on the photocatalytic activity and synthesis methods. World J Nano Sci Eng 5(4):161–177
4. Yan Y, Parr J (2011) Preparation and properties of TiO_2/fumed silica composite photocatalytic materials. Procedia Eng 27
5. Miyake M, Takahashi A, Hirato T (2017) Electrodeposition and anodization of Al-TiO_2 composite coatings for enhanced photocatalytic activity. Int J Electrochem Sci 12(2017):2344–2352

6. Chaudhari SB, Shaikh TN, Pandey P (2013) A review on polymer Tio_2 nanocomposites. Int J Eng Res Appl 3(5):1386–1391
7. Segura Gonzalez E, Olmos D, Lorente MA, Velaz I, Gonzalez-Benito J (2018) Preparation and characterization of polymer composite materials based on PLA/TiO_2 for antibacterial packaging. Polymers 10:1365
8. Naoki T, Katsuyuki T, Sei S, Shinichi I, Takahiro O, Hideki S, Masumi K, Masahiko A (2007) Synthesis and properties of a microtube photocatalyst with photoactive inner surface and inert outer surface. J Photochem Photobiol A Chem 185:133–139
9. Cheng Y, Luo F, Jiang Y, Li F, Wei C (2018) The effect of calcination temperature on the structure and activity of TiO_2/SiO_2 composite catalysts derived from titanium sulfate and fly ash acid sludge. Colloids Surf A: Physicochem Eng Aspects 554:81–85
10. Kukh AA, Ivanenko IM, Astrelin IM (2018) TiO_2 and its composites as effective photocatalyst for glucose degradation processes. Appl Nanosci 9(5):677–682
11. Liu SX, Chen XY, Chen X (2007) A TiO_2/AC composite photocatalyst with high activity and easy separation prepared by a hydrothermal method. J Hazard Mat 143(1–2):257–263
12. Tsumura T, Kojitani N, Izumi I, Iwashita N, Toyoda M, Inagaki M (2002) Carbon coating of anatase-type TiO_2 and photoactivity. J Mat Chem 12(5):1391–1396
13. Yamashita H, Harada M, Tanii A, Honda M, Takeuchi M, Ichihashi Y, Anpo M, Iwamoto N, Itoh N, Hirao T (2000) Preparation of efficient titanium oxide photocatalysts by an ionizedcluster beam (ICB) method and their photocatalyticreactivities for the purification of water. Catal Today 63:63–69
14. Matos J, Laine J, Herrmanna J-M (1999) Association of activated carbons of different origins with titania in the photocatalytic purification of water. Carbon 37(11):1870–1872
15. Li D, Xia Y (2003) Fabrication of titania nanofibers by electrospinning. Nano Lett 3(4):555–560
16. He C-H, Gong J (2003) The preparation of PVA–Pt/TiO_2 composite nanofiber aggregate and the photocatalytic degradation of solid-phase polyvinyl alcohol. Polym Degrad Stab 81(1):117–124
17. Avraham–Shinman A, Paz Y (2006) Photocatalysis by composite particles containing inert domains. Israel J Chem 46:33–43
18. Torimoto T, Okawa Y, Takeda Y, Yoneyama H (1997) Effect of activated carbon content in TiO2-loaded activated carbon on photodegradation behaviors of dichloromethane. J Photochem Photobiol A Chem 103(1–2):153–157
19. Tian F, Zhu R, Ouyang F (2013) Synergistic photocatalytic degradation of pyridine using precious metal supported TiO_2 with KBr O_3. J Environ Sci 25(11):2299–2305
20. Xing B, Shi C, Zhang C, Yi G, Chen L, Guo H, Huang G, Cao J (2016) Preparation of TiO_2/activated carbon composites for photocatalytic degradation of RhB under UV light irradiation. J Nanomat 2016:10
21. Ghosh G, Basu S, Saha S (2018) Photocatalytic degradation of textile dye using TiO_2-activated carbon nanocomposite. In: International conference on inventive research in material science and technology AIP conference proceedings 1966, American Institute of Physics, pp 1–9. 020027-1–020027-8
22. Asilturk M, Sener S (2012) TiO_2-activated carbon photocatalysts: preparation, characterization and photocatalytic activities. Chem Eng J 180:354–363
23. Mohsenzadeh M, Mirbagheri S-A, Sabbaghi S (2019) Degradation of 1, 2-dichloroethane by photocatalysis using immobilized PAni-TiO_2 nano-photocatalyst. Environ Sci Pollut Res 26(30)
24. Guidetti G, Pogna E, Lombardi L et. al. (2019) Photocatalytic activity of exfoliated graphite–TiO_2 nanoparticle composites. Nanoscale 2019(41)
25. Martins AC, Cazetta AI, Pezoti O, Souza JRB, Zhang T, Pilau E, Asefa T, Almeida VC (2016) sol–gel synthesis of new TiO_2/activated carbon photocatalyst and its application for degradation of tetracycline. Ceram Int 1–8
26. Paz Y (2010) Composite titanium dioxide photocatalysts and the "Adsorb and Shuttle" approach: a review. Solid State Phenom 162(2010):135–162
27. Park I-S, Choi SY, Ha JS (2008) High-performance titanium dioxide photocatalyst on ordered mesoporous carbon support. Chem Phys Lett 456(4):198–201

28. Mao K et al (2019) New efficient visible-light-driven photocatalyst of chitin-modified titanium dioxide/carbon fiber composites for wastewater. Sci Rep 9
29. Takeda N, Torimoto T, Youneyama H (1999) Effects of mordenite support on photodegradation of gaseous organic compounds over TiO2 photocatalyst. Bull Chem Soc Japan 72:1615–1621
30. Kanakaraju D (2014) Photolysis and TiO_2-catalysed degradation of diclofenac in surface and drinking water using circulating batch photoreactors. Environ Chem 11(1):51–62
31. Matos J, Laine J, Herrmann JM (1998) Synergy effect in the photocatalytic degradation of phenol on a suspended mixture of titania and activated carbon. Appl Catal B: Environ 18(3):281–290
32. Mahrouqi HKN, Nawi MA, Nawawi WI (2014) Photodegradation of 4-chlorophenol using carbon coated TiO_2 under solar irradiation. Int J Sci Res Publ 4(6):1–7
33. Paz Y (2010) Composite titanium dioxide photocatalysts and the adsorb and shuttle approach: a review. Solid State Phenom 162:135–162

Core–Shell Nanostructures Under Localized Plasmon Resonance Conditions

I. Yaremchuk, T. Bulavinets, V. Fitio, and Y. Bobitski

1 Introduction

Localized surface plasmon resonance is the most strongly pronounced optical property of the noble metallic nanostructures. It is appeared in the collective oscillation of conduction electrons excited by an electromagnetic field [1]. The electronic oscillations cause an electric field around the nanoparticle in the case of metallic nanoparticles, where electrons are in three dimensions. This field can be much more intense than the incident light [2]. Plasmon resonance is one of the best examples of how the material properties on a nanoscale differ from a bulk material. When the size of the metallic nanoparticles is reduced to a few nanometers, the optical properties are dramatically modified due to appearance of plasmon resonance. The optical properties of nanoparticles are completely different in comparison to bulk metal.

The near-field enhancement around metallic nanostructures, induced by irradiation in the visible and near infrared ranges, allows them to be used in various optoelectronic applications [3–6]. The enhanced field is localized on the nanostructures surface. Thus, they can be used in the detection changes of the local refractive index for biological sensors applications [7, 8]. In addition, the local reaction of metallic nanostructures can be applied to enhance the input and formed fields by nonlinear processes [9]. Metallic nanoparticles have found wide application in microscopy [10, 11], biosensors [12, 13], near-field optics [14, 15], medicine [16–18], and others

I. Yaremchuk (✉) · T. Bulavinets · V. Fitio
Department of Photonics, Lviv Polytechnic National University, S. Bandery Str. 12, 79013 Lviv, Ukraine
e-mail: iryna.y.yaremchuk@lpnu.ua

Y. Bobitski
Lviv Polytechnic National University, S. Bandery Str. 12, 79013 Lviv, Ukraine

Faculty of Mathematics and Natural Sciences, University of Rzeszow, Pigonia Str.1, 35959 Rzeszow, Poland

O. Fesenko and L. Yatsenko (eds.), *Nanooptics and Photonics, Nanochemistry and Nanobiotechnology, and Their Applications*, Springer Proceedings in Physics 247, https://doi.org/10.1007/978-3-030-52268-1_29

due to some special properties. The first one is that the absorption or scattering cross section resonantly increases, which can exceed its geometric dimensions many times. The second one is that field is enhanced near the surface of nanoparticle compared to the field of incident wave. The third one is spatial localization of the field at nanoscales which is much smaller than the wavelength of incident wave. The last one is possibility of transfer plasmon excitation between particles. In general, the noble metallic nanoparticles are characterized by unique electronic, optical, and magnetic properties under localized plasmon resonance conditions [19–21].

In recent years, more and more scientists have been paying attention to metallic nanoshells, the uniqueness of which is the presence of pronounced surface plasmon resonance and an even more efficient possibility of its application [22]. This perspective is associated with the ability to control the optical and plasmonic properties of structurally modified nano-objects with predicted geometry. The position of the plasmon resonance peak can be varied widely from visible to near-infrared spectrum region by changing the morphology and size of the particles, creating their aggregates and more complex nanostructures and changing the dielectric constant of the medium in which they are placed. Controlled change of parameters allows to adjust plasmonic nanostructures for specific practical applications, for instance, the "optical window" of living organisms [23]. In addition, nanoshells are expected to be more sensitive to change refractive index of the surrounding medium, allow to controlled redirection of electromagnetic radiation, and facilitate the study of multipole surface plasmon resonances [24]. It should be noted that growing interest in the use of the optical properties of plasmonic nanoshells is a functional component in various optical, biomedical systems [25]. The development of nanoshell synthesis technology in recent years has enabled researchers to study nanoshells of various shapes, ranging from nanowires and ending with exotic nanostar or nanorice structures [26].

The study of the interaction of laser radiation with nanostructures, the synthesis of optical elements with given geometric parameters on their base and, accordingly, the required optical properties played the key role from the point of view of fundamental science. Therefore, this work is devoted to the study of the spectral characteristics of the core–shell-type nanostructures, namely silver–copper, silver–titanium dioxide, and copper–cupric in the conditions of localized plasmon resonance for the purpose of their further photonics and plasmonics applications.

2 Mathematical Background

In general, the plasmon resonance frequency is determined by many factors, which are the concentration and effective mass of the conduction electrons, the shape, structure and size of the nanoparticles, the interaction between the nanoparticles, and the influence of the refractive index of the surrounding medium. However, for the elementary description of optics of the plasmon resonance nanoparticles, a combination of Rayleigh approximation and Drude theory is sufficient [27]. In this case, the absorption and scattering of light by a small particle are determined by its electrostatic

polarizability α, which is calculated using optical dielectric constant $\varepsilon(\omega)$ or $\varepsilon(\lambda)$, where ω is the angular frequency and λ is the wavelength in vacuum. Polarizability for small sphere of radius R in a homogeneous dielectric medium with dielectric permittivity ε_h can be written as follows:

$$\alpha = 4\pi R^3 \frac{\varepsilon_i - \varepsilon_h}{\varepsilon_i + 2\varepsilon_h}, \tag{1}$$

where ε_i is nanoparticle dielectric permittivity and R is nanoparticle radius.

Absorption and scattering cross section of small nanoparticles can be defined as follows [28]:

$$C_{\text{abs}} = \pi R^2 4 \times \text{Im}\left\{\frac{\varepsilon_i - \varepsilon_h}{\varepsilon_i + 2\varepsilon_h}\right\}, \tag{2}$$

$$C_{sca} = \pi R^2 \frac{8}{3} x^4 \left|\frac{\varepsilon_m - \varepsilon_h}{\varepsilon_m + 2\varepsilon_h}\right|^2 \tag{3}$$

where $x = \frac{2\pi\sqrt{\varepsilon_h}R}{\lambda}$.

Polarizability in case of coated sphere (nanoshell) can be written as follows [28]:

$$\alpha = 4\pi R_2^3 \frac{(\varepsilon_2 - \varepsilon_h)(\varepsilon_1 + 2\varepsilon_2) + f(\varepsilon_1 - \varepsilon_2)(\varepsilon_h + 2\varepsilon_2)}{(\varepsilon_2 + 2\varepsilon_h)(\varepsilon_1 + 2\varepsilon_2) + f(2\varepsilon_2 + 2\varepsilon_h)(\varepsilon_1 - \varepsilon_2)}, \tag{4}$$

where ε_1 and ε_2 are dielectric permittivity of the core and shell, correspondingly; $f = R_1^3/R_2^3$, R_1 and R_2 are radii of the core and nanoshell, correspondingly.

More detailed description of the derivation of (4) can be founded in [27]. In addition, it should be noted that in the same way equation can be obtained for multilayer nanoparticles.

3 Optical Properties of the Core–Shell Nanostructures Under Localized Plasmon Resonance Condition

3.1 Bimetallic Nanoshells

The noble metals Au and Ag are the most widely used as plasmon materials. However, using other materials such as Cu can reduce production costs and extend the spectral range of the plasmonic effect [29, 30]. Therefore, these three materials were used for modeling of nanoparticles optical characteristic. Firstly, modeling characteristics of bimetallic nanoshells Ag–Au and Ag–Cu were carried out. Refractive indices of Ag, Au, and Cu were used from [31, 32]. Refractive index of surrounding medium is 1.33. The core size is 30 nm for all calculations. It is known that there is possible to

obtain plasmonic peak at the given wavelength by changing geometrical parameters of nanoshell. Thus, the thickness of shell was varied from 2 to 10 nm.

In case of Ag–Au nanoshells, the spectral position of absorption and scattering cross-sectional plasmonic peaks is shifted to long-wavelength region when shell thickness increases (Fig. 1). In both absorption and scattering cross section, this shift is about 10 nm at change of shell thickness in 8 nm. However, there is additional plasmon peak at wavelength of 380 nm for shell thickness of 2 nm. This additional peak does not observe when shell thickness increases and the amplitude of the main peak increases.

It can be seen from Fig. 2 that there is opposite situation for nanoshells Ag–Cu. The absorption and scattering cross-sectional peaks are clearly defined at the wavelength of 385 nm when the shell thickness is 2 nm and as the shell thickness increases their amplitude increases. At the same time, the second peak located in the region of

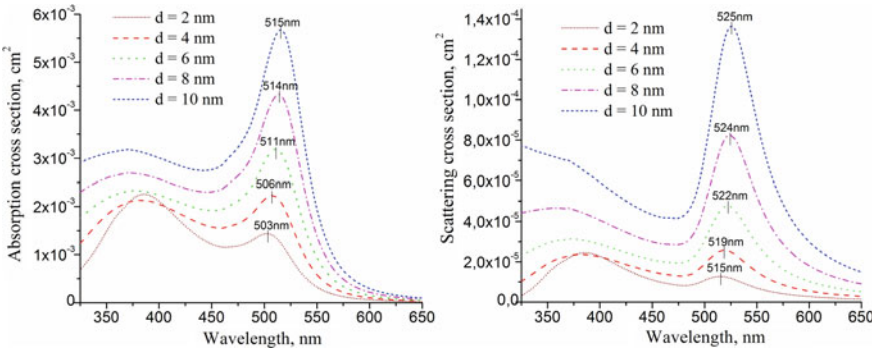

Fig. 1 Dependence of absorption and scattering cross sections on wavelength for nanoshells Ag–Au. Core (Ag) thickness is constant and equal to 30 nm. Shell (Au) thickness is varied from 2 to 10 nm. Refractive index of surrounding medium is 1.33

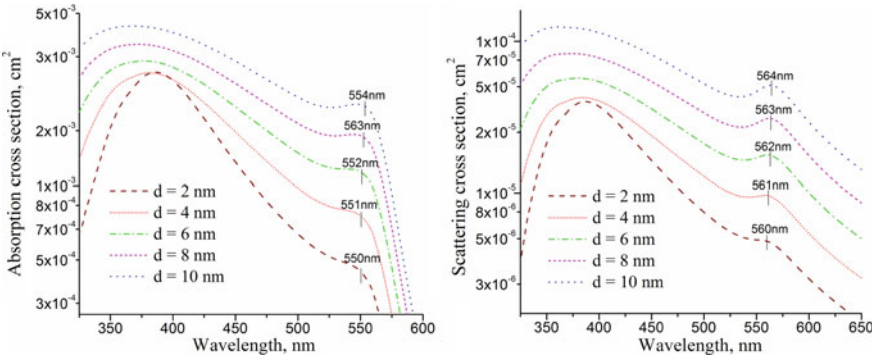

Fig. 2 Dependence of absorption and scattering cross sections on wavelength for nanoshells Ag–Au. Core (Ag) thickness is constant and equal to 30 nm. Shell (Cu) thickness is varied from 2 to 10 nm. Refractive index of surrounding medium is 1.33

longer wavelengths can be visually identified only by the shell thickness of 4 nm. In addition, the amplitude of the second peak is much lower than the amplitude of the first peak. Moreover, the absorption and scattering cross-sectional second peaks are shifted not significantly, about 4 nm.

Consequently, it can be concluded that shell thickness up to 10 nm will have a small impact on resulting optical response in case of Ag–Cu nanoshells comparing to Ag–Au nanoshells.

3.2 Metallic Nanoparticles with Oxide Shell

Recently, high interest has been focused on copper and copper oxide materials due to their use in semiconductors, gas sensors, energy storage, catalysts, antimicrobial programs, and others [33]. Copper-based nanocomposites materials have also been extensively studied, for example, nanocomposites based on matrix silicon dioxide, fluoropolymer matrix, cellulose, and diamond-like carbon matrix [34]. However, it is known that Cu nanoparticles are inclined to rapid oxidation upon interaction with air and humid surrounding medium. Moreover, in the oxidation process, the formation of Cu_2O compound is dominant reaction product in the copper nanoparticle surface layer. Therefore, it is advisable to simulate the optical characteristics of nanoshells, where pure Cu is the core and the shell is formed by Cu_2O.

As it will be noted previously, the absorption spectrum of nanoshells depends primarily on the ratio of the thickness of the core–shell, as well as the surrounding medium. Therefore, the dependence of the absorption and scattering cross sections of Cu–Cu_2O nanoshells on wavelength at different core and shell thicknesses was calculated. Diamond-like carbon film was used as surrounding medium. The refractive index of the diamond-like carbon film was obtained from [30].

The dependence of absorption and scattering cross-sectional Cu–Cu_2O nanoshells in diamond-like carbon matrix on wavelength at a constant shell thickness 2 nm and different radii of core is shown in Fig. 3. It can be seen that the absorption and scattering cross-sectional peaks are shifted to the short wavelengths when core thickness increases. In particular, the absorption cross-sectional peaks of Cu–Cu_2O nanoshells with the core radius of 10 nm are at the wavelength of 613 nm, with the core size of 50 nm at a wavelength of 589 nm. In case of scattering cross section, there is smaller shift from 600 to 588 nm.

In the next step, the calculations of the absorption and scattering cross-sectional spectra of Cu–Cu_2O nanoshells in diamond-like carbon were carried out at different thickness of the Cu_2O shell and constant core Cu radius. The simulation results are presented in Fig. 4. It can be seen that the absorption cross-sectional peak shifts to the region of longer wavelengths when shell thickness increases. Its shift is from 590 to 619 nm in case of absorption cross section and from 592 to 620 nm for scattering cross section. The shell thickness was varied from 1 to 5 nm. The intensity of both absorption and scattering cross sections increases as the thickness of the shell increases. It should be noted that the full width at half the maximum of the absorption

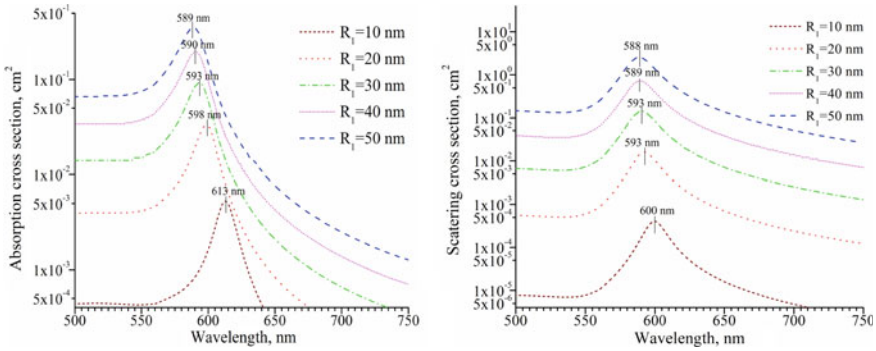

Fig. 3 Dependence of absorption and scattering cross sections on wavelength for nanoshells Cu–Cu_2O. Core (Cu) radius is varied from 10 to 50 nm. Shell (Cu_2O) thickness is constant and equal to 2 nm

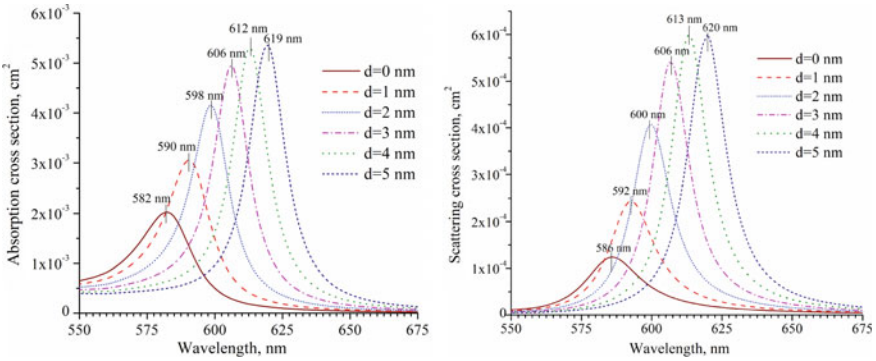

Fig. 4 Dependence of absorption and scattering cross sections on wavelength for nanoshells Cu–Cu_2O. Core (Cu) radius is constant and equal to 10 nm. Shell (Cu_2O) thickness is varied from 0 to 5 nm

and scattering cross sections does not depend on the shell thickness for researched diapason.

It should be noted that, shift of absorption cross-sectional peak of Cu–Cu_2O nanoshells is smaller in comparison to pure Cu nanoparticles, where it is about 200 nm [30].

3.3 Metal/Semiconductors Nanoshells

In the next stage of work, the absorption and scattering cross-sectional spectra of a spherical nanoparticle with a semiconductor shell have been simulated in a dipole approximation [27, 28]. Titanium dioxide was used as material of shell since lately

it is a subject of huge attention due to its optical properties, high photoactivity, non-toxicity, and chemical stability. Refractive index of titanium dioxide is used from [35]. The influence of the thickness of the semiconductor shell TiO_2 on the spectral position and amplitude of the plasmon resonance peak of the spherical Ag nanoparticle has been researched (Fig. 5). The results showed that the absorption and scattering cross-sectional peak of the Ag–TiO_2 nanostructure shift to the long-wave region when the shell thickness increases from 2 to 10 nm. It should be noted that the amplitude of the absorption cross section increases when shell thickness increases. However, in case of scattering, cross-sectional situation is opposite.

Further, the spectral characteristics of the inverted nanostructure, namely the core is semiconductor and the shell is metal, have been considered. Therefore, the absorption and scattering cross sections of the spherical semiconductor nanoparticle (TiO_2) with metallic shell (Ag) were simulated using dipole approximation. Research effect of the metal shell thickness on the spectral position of the plasmon resonance and its amplitude showed that such nanoshells would be characterized by two peaks of the absorption and scattering cross sections, as shown in Fig. 6. Such a two-peak nature can be explained by the excitation of localized plasmons at two interfaces titanium dioxide–silver and silver/surrounding media.

It should be noted that the position of the first resonant peak, which is approximately at a wavelength of 350 nm, is practically insensitive to change in the thickness of the shell. Absorption and scattering cross-sectional first peaks are shifted by a few nanometers to the long wavelength spectrum region. In this case, only the amplitude increases when shell thickness increases. The second resonant peak shifts to the short wavelength spectrum region, and shift of peak position is large enough. The second resonance peaks of the absorption and scattering cross sections of nanoshell are at the wavelength of 870 nm for shell thickness of 2 nm and for shell thickness of 10 nm resonance wavelength equal to 502 nm. The amplitude of the second peak increases when shell thickness increases.

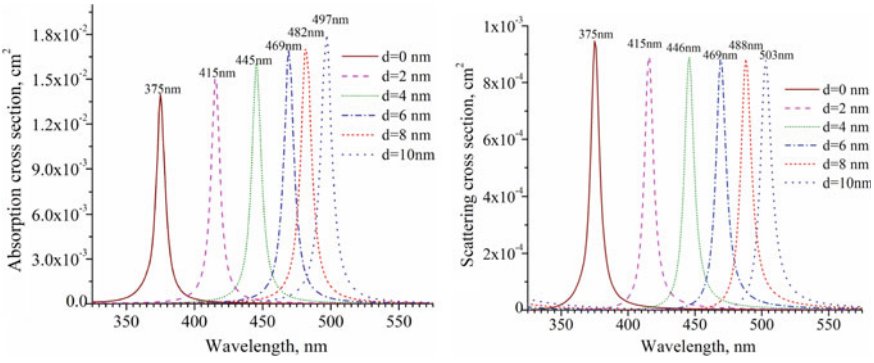

Fig. 5 Dependence of absorption and scattering cross sections of nanoshells Ag–TiO_2 on wavelength. Core (Ag) radius is constant and equal to 15 nm. Shell (Ti_2O) thickness is varied from 0 to 10 nm. Refractive index of surrounding medium is 1.33

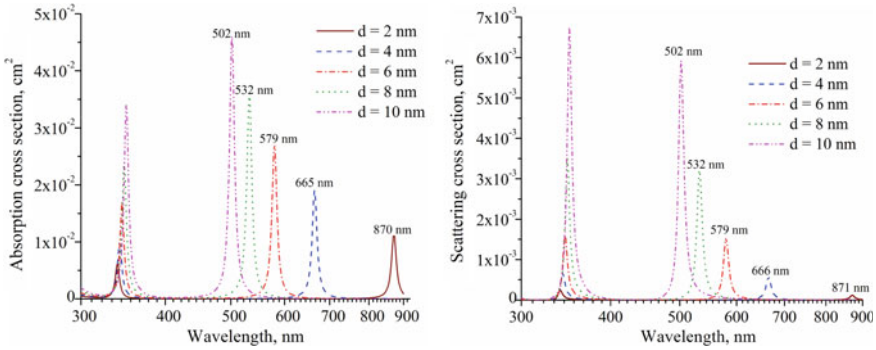

Fig. 6 Dependence of absorption and scattering cross sections of nanoshells TiO_2–Ag on wavelength. Core (TiO_2) radius is constant and equal to 15 nm. Shell (Ag) thickness is varied from 2 to 10 nm. Refractive index of surrounding medium is 1.33

It can be assumed that the both peaks will be fitted at the certain shell thickness. In this case, nanoshell will have characteristics similar to silver nanoparticles, that is, the metal properties will dominate.

4 Conclusions

The spectral characteristics of core–shell nanostructures, namely silver–gold, silver–copper, and titanium dioxide–silver, were calculated.

It is shown that in the case of bimetallic structures, the spectral position of the absorption and scattering cross-sectional peaks is not sensitive to the shell thickness changing, but only their amplitude changes.

Metallic nanoparticles with oxide shell, namely copper oxide–copper nanoshells, have been researched. It is established that for such nanoshells the plasmon peak shifts to the short wavelengths region when core thickness increases and shifts to the long wavelengths region when thickness of the shell increases.

In the case of silver–titanium dioxide nanostructures, the spectral position of the absorption and scattering cross-sectional peaks is shifted to the long-wavelength spectrum region when shell thickness increases. Titanium dioxide–silver nanoshells are characterized by two plasmonic resonance peaks. The first plasmonic peak is not sensitive to change of shell thickness. The second one is shifted to the short-wavelength spectrum region. It should be noted that such nanoshells will have spectral characteristics similar to the characteristics of the silver nanoparticles at the certain shell thickness.

References

1. Maier SA (2007) Plasmonics: fundamentals and applications. Springer Science and Business Media
2. García MA (2011) Surface plasmons in metallic nanoparticles: fundamentals and applications. J Phy D Appl Phys 44(28):283001
3. Salem JK, El-Nahhal IM, Najri BA, Hammad TM (2016) Utilization of surface plasmon resonance band of silver nanoparticles for determination of critical micelle concentration of cationic surfactants. Chem Phys Lett 664:154–158
4. Barnes WL, Dereux A, Ebbesen TW (2003) Surface plasmon subwavelength optics. Nature 424(6950):824–830
5. De Aberasturi DJ, Serrano-Montes AB, Liz-Marzán LM (2015) Modern applications of plasmonic nanoparticles: from energy to health. Adv Opt Mater 3(5):602–617
6. Lesyuk R, Klein E, Yaremchuk I, Klinke C (2018) Copper sulfide nanosheets with shape-tunable plasmonic properties in the NIR. Nanoscale 10:20640–20651
7. Stuart DA, Haes AJ, Yonzon CR, Hicks EM, Van Duyne RP (2005) Biological applications of localised surface plasmonic phenomenae. IEEE Proc-Nanobiotechnol 152(1):13–32
8. Sperling RA, Gil PR, Zhang F, Zanella M, Parak WJ (2008) Biological applications of gold nanoparticles. Chem Soc Rev 37(9):1896–1908
9. Kauranen M, Zayats AV (2012) Nonlinear plasmonics. Nature Photon 6(11):737–748
10. Artur CG, Womack T, Zhao F, Eriksen JL, Mayerich D, Shih WC (2018) Plasmonic nanoparticle-based expansion microscopy with surface-enhanced Raman and dark-field spectroscopic imaging. Biomed Opt Expr 9(2):603–615
11. Wu Z, Yang R, Zu D, Sun S (2017) Microscopic differentiation of plasmonic nanoparticles for the ratiometric read-out of target DNA. Sci Rep 7(1):14742
12. Xavier J, Vincent S, Meder F, Vollmer F (2018) Advances in optoplasmonic sensors–combining optical nano/microcavities and photonic crystals with plasmonic nanostructures and nanoparticles. Nanophotonics 7(1):1–38
13. Yaremchuk I, Tamulevičienė A, Tamulevičius T, Tamulevičius S (2014) Optical properties of DLC-Ag nanocomposite and grating structures on their base. Appl Mech Mater 490:53–57
14. Du L, Lei DY, Yuan G, Fang H, Zhang X, Wang Q, Yuan X (2013) Mapping plasmonic near-field profiles and interferences by surface-enhanced Raman scattering. Sci Rep 3:3064
15. Lin HY, Huang CH, Chang CH, Lan YC, Chui HC (2010) Direct near-field optical imaging of plasmonic resonances in metal nanoparticle pairs. Opt Expr 18(1):165–172
16. Lim WQ, Gao Z (2016) Plasmonic nanoparticles in biomedicine. Nano Today 11(2):168–188
17. Bulavinets T, Yaremchuk I, Bobitski Y (2016) Modeling optical characteristics of multilayer nanoparticles of different sizes for applications in biomedicine. In: Nanophysics nanophotonics, surface studies and applications. Springer, Cham, pp 101–115
18. Mlalila NG, Swai HS, Hilonga A, Kadam DM (2017) Antimicrobial dependence of silver nanoparticles on surface plasmon resonance bands against *Escherichia coli*. Nanotechnology Sci Appl 10:1–5
19. Poletti A, Treville A (2016) Nano and micro-sensors: Real time monitoring for the smart and sustainable city. Chem Eng Trans 47:1–6
20. Amendola V, Pilot R, Frasconi M, Marago OM, Iati MA (2017) Surface plasmon resonance in gold nanoparticles: a review. J Phys: Condens Matter 29(20):203002
21. Stafford S, Serrano Garcia R, Gun'ko YK (2018) Multimodal magnetic-plasmonic nanoparticles for biomedical applications. Appl Sci 8(1):97
22. Blaber MG, Arnold MD, Ford MJ (2009) Search for the ideal plasmonic nanoshell: the effects of surface scattering and alternatives to gold and silver. J Phys Chem C 113(8):3041–3045
23. Yaremchuk I, Fitio V, Bobitski Y (2012) Silver nanoparticles under plasmon resonance conditions. In: Proceedings 28th international conference on microelectronics (MIEL'2012), 13–16 May, 2012, Nis, Serbia, pp 297–300

24. Shishodia MS, Fainberg BD, Nitzan A (2011) Theory of energy transfer interactions near sphere and nanoshell based plasmonic nanostructures. In: plasmonics: metallic nanostructures and their optical properties IX, vol 8096. 80961G-1–80961G-5
25. Kalele S, Gosavi SW, Urban J, Kulkarni SK (2006) Nanoshell particles: synthesis properties and applications. Curr Sci 1038–1052
26. Song HM, Wei Q, Ong QK, Wei A (2010) Plasmon-resonant nanoparticles and nanostars with magnetic cores: synthesis and magnetomotive imaging. ACS Nano 4(9):5163–5173
27. Khlebtsov NG (2013) T-matrix method in plasmonics: an overview. J Quant Spectrosc Radiat Transfer 123:184–217
28. Bohren CF, Huffman DR (2008) Absorption and scattering of light by small particles. John Wiley
29. Ahamed M, Alhadlaq HA, Khan MA, Karuppiah P, Al-Dhabi NA (2014) Synthesis, characterization, and antimicrobial activity of copper oxide nanoparticles. J Nanomater 17:4
30. Yaremchuk, I., Meškinis, S., Bulavinets, T., Vasiliauskas, A., Andrulevičius, M., Fitio, V., Bobitski, Y., Tamulevičius, S.: Effect of oxidation of copper nanoparticles on absorption spectra of DLC:Cu nanocomposites. Diamond Relat Mater 99:107538-1–107538-10 (2019)
31. Fitio V, Yaremchuk I, Vernyhor O, Ya Bobitski (2018) Resonance of surface localized plasmons in a system of periodically arranged gold and silver nanowires on a dielectric substrate. Appl Nanosci 8:1015–1024
32. Fitio V, Yaremchuk I, Vernyhor O, Bobitski Y (2019) Resonance of surface-localized plasmons in a system of periodically arranged copper and aluminum nanowires on a dielectric substrate. Appl Nanosci 1–8
33. Singh J, Kaur G, Rawat M (2016) A brief review on synthesis and characterization of copper oxide nanoparticles and its applications. J Bioelectron Nanotechnol 1(1):1–9
34. Tamayo L, Azócar M, Kogan M, Riveros A, Páez M (2016) Copper-polymer nanocomposites: an excellent and cost-effective biocide for use on antibacterial surfaces. Mater Sci Eng C 69:1391–1409
35. Bulavinets T, Varyshchuk V, Yaremchuk I, Bobitski Y (2018) Design and synthesis of silver nanoparticles with different shapes under the influence of photon flows. In: Nanooptics nanophotonics nanostructures and their applications. springer proceedings in physics. Springer, vol 210, pp 231–241

Fluorescence Properties of Doxorubicin-Loaded Iron Oxide Nanoparticles

V. Orel, M. Zabolotny, O. Rykhalskyi, A. Shevchenko, V. Yashchuck, M. Losytskyi, and V. B. Orel

1 Introduction

The incidence of cancer is linked with substantial increases in life expectancy, lifestyle risk factors, and commercial interests. Cancer has become the leading cause of death in high-income countries, while cardiovascular disease is the largest contributor to mortality in low- and middle-income countries. Recent estimates predict that 13 million people will die from cancer annually by 2030. Furthermore, cancer is responsible for the highest premature mortality rate and poses the rising burden in every country. In light of these observations, there are some serious obstacles to meeting the goal of a 30% decrease in the death rate from non-communicable diseases by 2030. In fact, reaching this goal demands improvements in cancer treatment and control [1].

A growing body of novel treatment technologies, including targeted nanomagnetic therapy, has been introduced to fight cancer over the past few decades. The technology of the targeted nanomagnetic therapy utilizes iron oxide magnetic nanoparticles (NP) and antitumor drugs to initiate cancer cells death via ferroptotic mechanisms. Ferroptosis is an iron-dependent cell death associated with lipid peroxidation [2]. Metal NP

V. Orel · O. Rykhalskyi
National Cancer Institute, Kiev, Ukraine

V. Orel
Biomedical Engineering Department, NTUU Igor Sikorsky KPI, Kiev, Ukraine

M. Zabolotny · V. Yashchuck · M. Losytskyi
Taras Shevchenko National University of Kyiv, Kiev, Ukraine

A. Shevchenko (✉)
G.V. Kurdyumov Institute for Metal Physics, Kiev, Ukraine
e-mail: admit@imp.kiev.ua

V. B. Orel
Medical Faculty, Bogomolets National Medical University, Kiev, Ukraine

O. Fesenko and L. Yatsenko (eds.), *Nanooptics and Photonics, Nanochemistry and Nanobiotechnology, and Their Applications*, Springer Proceedings in Physics 247, https://doi.org/10.1007/978-3-030-52268-1_30

exhibit localized electromagnetic spin resonances on their surface. Since electrons oscillating on a NP surface behave collectively, there is a practical way to control and manipulate the surface electrons at the nanoscale level. NP (e.g., iron oxide NP) can also produce reactive oxygen species (ROS) (hydroxyl radicals and superoxide) in the presence of H_2O_2 due to leaching of active metal ions (Fe^{2+} and Fe^{3+}) from the particle surface and triggering the Fenton reaction [3].

Anisotropic metal NP with complex shape have received considerable attention because of their unique spectroscopic properties, which depend on the NP geometry and their three-dimensional structures. Our previous studies showed that subtle modifications of the NP surface properties induced dramatic changes in NP interactions with serum proteins. The observed difference was attributed to conformational changes of a drug loaded onto the NP surface [4]. Conformational isomerism plays a key role in the activity of drug molecules [5] and takes place in almost all commercially available pharmaceuticals as well as compounds in clinical and pre-clinical trials.

The anthracycline antibiotic doxorubicin (DOXO) is widely used in cancer treatment. It is believed that the inhibitory effect of this compound on both normal and tumor cell growth is caused by interference with RNA synthesis through direct binding to the double-stranded DNA template. DOXO exhibits conformational diversity, i.e., conformational changes in the amino sugar ring and ring A of the aglycone. The relative orientation of the aglycone moiety and amino sugar determines the molecular geometry of anthracyclines [6]. Recent research has tended to focus on the fluorescence (FL) properties of DOXO loaded onto the metal NP. Distinctive FL properties indicate evidence for conformational changes in DOXO molecules around the NP surface [7].

The ratio between the quantity of the surface and bulk atoms comprising Fe_3O_4 NP also contributes to the conformational changes of DOXO interaction with ferromagnetic NP. Earlier FL studies have shown that the multi-domain NP cause more significant changes in conformational heterogeneity of DOXO molecules and a less pronounced antitumor effect than the single-domain NP [8].

This paper seeks to investigate FL properties of the antitumor anthracycline antibiotic DOXO as a part of iron oxide NP-based complex to advance the understanding of its pharmacological effects in cancer nanotherapy.

2 Materials and Methods

2.1 Magneto-Mechano-Cchemical Synthesis

Ferromagnetic iron oxide NP with diameters <50 nm (Sigma-Aldrich) and/or the antitumor anthracycline antibiotic DOXO (Pfizer, Italy) were loaded into the magneto-mechanical milling machine (NCI). Magneto-mechano-chemically synthesized (MMCS) nanocomplexes were obtained within 5 min. The compounds were

vibrated at a frequency of 36 Hz with an amplitude of 9 mm and energy of 20 W/g in the presence of electromagnetic fields (a frequency of 42 MHz, the initial power of 2 W, and the magnetic field strength of 8 mT). Mechano-chemically activated (MCA) DOXO were not subjected to electromagnetic fields (radio waves and constant magnetic field) during the activation. The magneto-mechano-chemical activation (MMA) DOXO were not subjected to radio waves only. The terms MMA and MCA refer to DOXO, while MMCS to DOXO + Fe_3O_4 NP complex. MNC were characterized by the hydrodynamic size (108 ± 19 nm) and zeta potential (+32 ± 2 mV). DOXO to Fe_3O_4 NP ratio was 1:2 with 33% loading efficiency. The zeta potential values were measured using a Malvern Zetasizer. The methodological approach and characteristics taken in this study were based on our previous investigation of MNC in physiological saline solutions [9].

2.2 Fluorescence Spectroscopy

Notable properties of DOXO fluorescence in the visible spectrum (500 nm) were used to identify the compound on the MNC surface. The excitation wavelength was adopted from previously recorded range (380–580 nm) for DOXO and MNC comprising DOXO and NP. FL spectra of both MNC and DOXO supernatants with concentrations similar to those administered to animals in previous investigations [9] were recorded at room temperature and then analyzed. A Cary Eclipse (Varian, Australia) fluorescence spectrophotometer was utilized to record fluorescence of the solutions poured into a quartz cell with the size of 1 × 1 cm.

2.3 Statistics

Pearson's r measured the linear correlation between FL spectra recorded from the investigated samples at 510–800 nm [10]. The degrees of freedom (the number of independent measurements) were 270. Kolmogorov–Smirnov's method was used to determine whether the datasets were normally distributed. The results were significant at the $p < 0.01$ level.

3 Results and Discussion

3.1 Fluorescence Spectra

Figures 1 and 2 compare the FL properties and Pearson's r of conventional DOXO with the same drug after MMA, MCA and with DOXO + Fe_3O_4 NP before and after

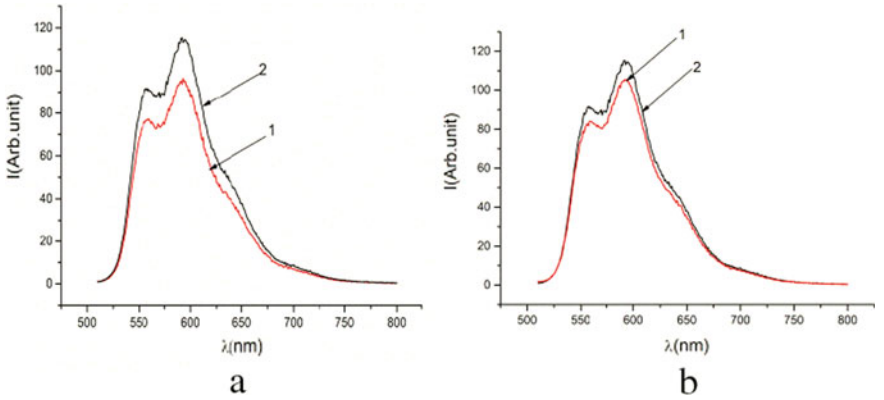

Fig. 1 Fluorescence spectra and the Pearson's correlation coefficient: **a**—1 conventional DOXO, (2) MCA DOXO (r = 0.99); **b** 1—conventional DOXO, 2—MMA DOXO ($r = 0.97$)

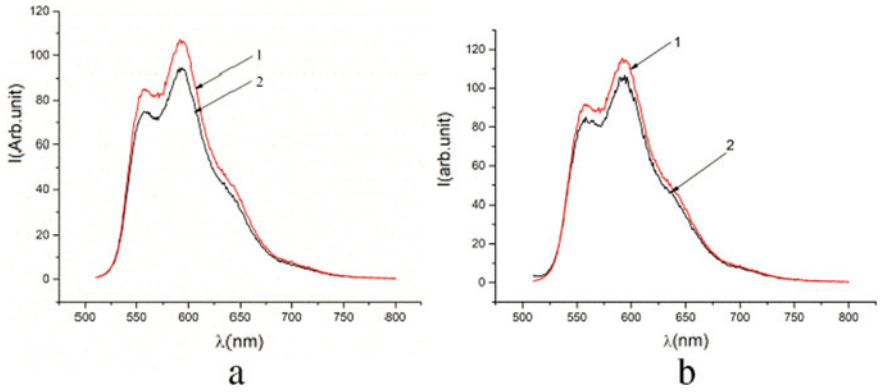

Fig. 2 Fluorescence spectra and the Pearson's correlation coefficient: **a** 1—conventional DOXO, 2—non-treatment DOXO + Fe_3O_4 ($r = 0.97$); **b** 1—conventional DOXO, 2—MMCS DOXO + Fe_3O_4 ($r = 0.94$)

MMCS (MNC). The main peaks of FL spectra are identical and located at 598 nm. The FL intensity of MMA and MCA DOXO was more than conventional DOXO. MNC on the contrary had less FL intensity than conventional DOXO.

The correlation analysis of the results has shown a positive correlation (from 0.94 to 0.99) between the investigated samples. The lowest values of the correlation coefficient $r = 0.94$ were found in MMCS MNC, while MCA and MMA DOXO solutions had a stronger correlation with $r = 0.99$ and $r = 0.97$.

3.2 Mathematical Modeling of Electron Transfer

The influence of mechano-chemical effects on contact interaction between rough surfaces of Fe_3O_4 NP and DOXO leads to free radical generation. Free radical reactions involve electron transfer and thus they give rise to positively and negatively charged fragments, depending on the electronegativity of compounds during MMCS, MMA, or MCA [11]. Non-ionizing electromagnetic irradiation is reported to regulate the electron transfer in MNC [9]. Therefore, a simple mathematical model explains the germinal transfers of an electron from a positively charged ion during MMCS, MMA, and MCA (Fig. 3).

The probability of electron transfer was considered as the main parameter in the current investigation. This probability depends on the MNC molecular composition and structure. The process of electron transfer in organic polymers depends on their structure directly in the charge localization center. The charge carrier becomes independent of the geminate positive ion at distances of several nanometers when its bond energy becomes ~k_BT (k_B—the Boltzmann constant; T—the thermodynamic temperature).

$n_0^-(t)n_0^+(t)$—the probability of electron (positive ion) being in a place of this localization at the time of the magneto-mechano-chemical effect termination (in centers 0^+ and 0^- ·.

$n_1^-(t)n_1^+(t)$—the probability of electron (positive ion) being in the electron trapping site 1^- (1^+) after the first transition.

$W_{ij}^-\left(W_{ij}^+\right)$—the probability of electron (positive ion) transition from state "i" to state "j" per time unit.

The charge carriers transition from the electron trapping site 1^- (1^+) is possible with probability W^- (W^+) per time unit.

$$\frac{\mathrm{d}n_0^+(t)}{\mathrm{d}t} = -\gamma \cdot n_0^+(t) \cdot n_0^-(t) - W_{01}^+ \cdot n_0^+(t) + W_{10}^+ \cdot n_1^+(t), \tag{1}$$

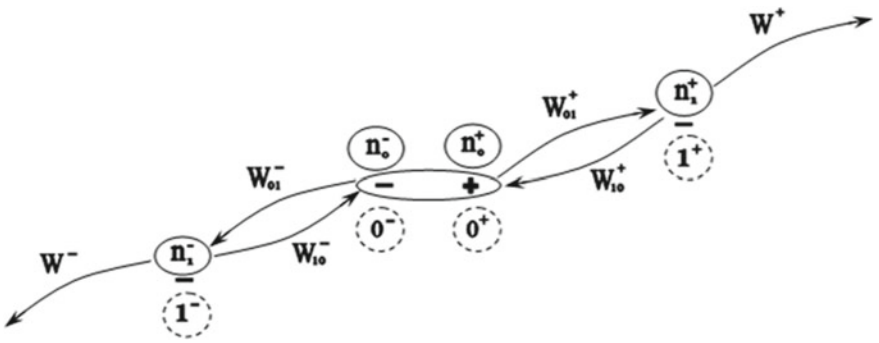

Fig. 3 Schematic representation of the germinal electron transfers from a positively charged ion during MMCS, MMA, and MCA

$$\frac{\mathrm{d}n_1^+(t)}{\mathrm{d}t} = W_{01}^+ \cdot n_0^+(t) - \left(W_{10}^+ + W^+\right) \cdot n_1^+(t), \tag{2}$$

$$\frac{\mathrm{d}n_0^-(t)}{\mathrm{d}t} = -\gamma \cdot n_0^+(t) \cdot n_0^-(t) - W_{01}^- \cdot n_0^-(t) + W_{10}^- \cdot n_1^-(t) \tag{3}$$

$$\frac{\mathrm{d}n_1^-(t)}{\mathrm{d}t} = W_{01}^- \cdot n_0^-(t) - \left(W_{10}^- + W^-\right) \cdot n_1^-(t) \tag{4}$$

γ–the electron-ion pair recombination ratio. Initial conditions:

$$n_0^-(0) = n_0^+(0) = 1$$

$$n_1^-(0) = n_1^+(0) = 0 \tag{5}$$

Namely, charged particles were in the localization centers 0^+ and $0^{-\,\cdot}$. Free charge carrier generation would be possible only in case when both particles came out from electron trapping sites. Otherwise, a stationary charge carrier might have captured a moving charge carrier of the opposite sign generated in another center. In that case, the centers 0^+ and $0^{-\,\cdot}$ neutrality would be disturbed after the pair dissociation or before the contact of the particles from two generation centers by MCA, MMA, or MMCS.

The following expressions can be derived from (1)–(5)

$$\frac{\mathrm{d}n_0^+(t)}{\mathrm{d}t} = -\gamma \cdot n_0^+(t) \cdot n_0^-(t) + \left\{ \frac{W_{10}^+ \cdot W_{01}^+}{W_{10}^+ \cdot W^+} \cdot \left[1 - \exp\left(-t \cdot \left(W_{10}^+ \cdot W^+\right)\right)\right] - W_{01}^+ \right\} \cdot n_0^+(t) \tag{6}$$

$$\frac{\mathrm{d}n_0^-(t)}{\mathrm{d}t} = -\gamma \cdot n_0^+(t) \cdot n_0^-(t) + \left\{ \frac{W_{10}^- \cdot W_{01}^-}{W_{10}^- \cdot W^-} \cdot \left[1 - \exp\left(-t \cdot \left(W_{10}^- \cdot W^-\right)\right)\right] - W_{01}^- \right\} \cdot n_0^-(t) \tag{7}$$

The system of nonlinear (6) and (7) can be solved by perturbation theory considering the values $n_1^+(t)$ and $n_1^-(t)$ are small. Then, we obtain:

$$n_0^+(t) = \exp\left[\frac{W_{01}^+ \cdot W_{10}^+}{W_{10}^+ \cdot W^+} \cdot (t-1) + \frac{W_{01}^+ \cdot W_{10}^+}{\left(W_{10}^+ \cdot W^+\right)^2} \cdot \exp(-t\cdot) - W_{01}^- \cdot t + \frac{\gamma}{C+R} \right.$$
$$\left. \left[-\exp\left[C \cdot t - \frac{W_{10}^- \cdot W_{01}^-}{\left(W_{10}^- \cdot W^-\right)^2} \right] \cdot \left(1 + \frac{R}{C}\right) - \frac{W_{10}^- \cdot W_{01}^-}{\left(W_{10}^- \cdot W^-\right)^2} \right.\right.$$

$$\cdot \exp\left(C \cdot t - \frac{W_{10}^{-} \cdot W_{01}^{-}}{\left(W_{10}^{-} \cdot W^{-}\right)^2} + R \cdot t\right) + \exp\left[-\frac{W_{10}^{-} \cdot W_{01}^{-}}{\left(W_{10}^{-} \cdot W^{-}\right)^2}\right] \cdot \left(1 + \frac{R}{C} + \frac{W_{10}^{-} \cdot W_{01}^{-}}{\left(W_{10}^{-} \cdot W^{-}\right)^2}\right)\Bigg] \tag{8}$$

where $C = \frac{W_{10}^{-} \cdot W_{01}^{-}}{W_{10}^{-} + W_{01}^{-}} - \left[W_{01}^{-} + \gamma\right]$ and $R = -\left(W_{10}^{-} + \gamma\right)$

The expression for $n_0^{-}(t)$ is similar to the (8). The obtained ratios for $n_0^{-}(t) n_0^{+}(t)$ along with (1), (3) fully determine the charge carriers kinetics in the system and allow to analyze the patterns and conditions of their exit beyond the complex.

The results obtained from the correlation analysis of conventional DOXO with non-treatment MNC from DOXO + Fe_3O_4 ($r = 0.97$) (Fig. 2A) pose a question of what factors could influence the change in the FL spectra recorded from non-treatment MNC.

It has conclusively been shown that FL spectroscopy of the antitumor anthracycline antibiotic DOXO in iron oxide NP depends on the physicochemical characteristics of NP (e.g., size, zeta potential, and magnetic properties) [8]. Several studies investigating methods for molecular dynamics have proved the dependence of the surface layer thickness on NP dimensions [12, 13]. For example, 5 nm NP have nearly 31% of atoms on the surface, whereas NP with a diameter of 50 nm have 3.4% of the surface atoms. Not only does the number of atoms which participate in a chemical reaction vary with a change in size, but also the chemistry of the surface atoms is different from the rest of atoms in NP due to changes in the lattice structure on the surface [14].

Iron oxide (Fe_3O_4) is a typical example of a material with cubic syngony (the lattice constant a ~ 0.84 nm) at room temperature [15]. We assumed that the surface structures were those of Fe_3O_4 NP, which were part of two layers (the layer thickness (d) ~ 1.6–2.5 nm) of crystalline cells located near the particle boundary. The remaining parts of NP volume were occupied by the bulk atoms. Here, the ratio between the number (X) of the surface atoms in cubic lattices of spherical NP with the length of an edge L and the total number of atoms in NP can be determined with the following expression:

$$X = \left(\frac{L - 2d}{L}\right)^3 \tag{9}$$

Figure 4 demonstrates the dependence of the ratio between the number (x) of the surface (curve 1), bulk atoms (curve 2), and their total number in a spherical NP with a cubic lattice of the volume (V) according to [15]. Similar calculations were performed for parallelepiped-shaped NP with the length three times greater than the baseline (curves 3 and 4).

Although the difference between Pearson's r did not exceed 0.05, the antitumor effects of the investigated drugs were significantly different. The most pronounced antitumor effect (minimal growth factor, maximal breaking ration of tumor growth,

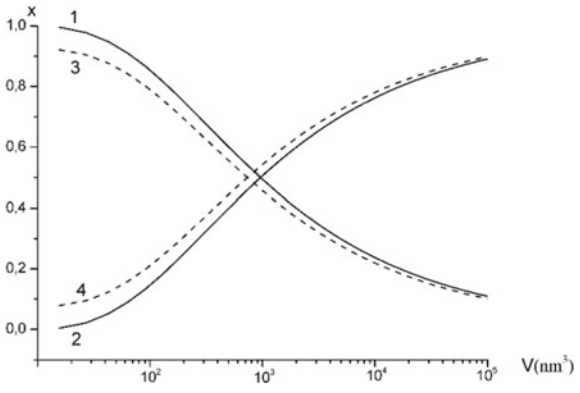

Fig. 4 Relation between the quantity of surface and bulk atoms comprising Fe_3O_4 NP and the particle volume

and index of metastasizing inhibition) was observed in animals treated with MMCS MNC and electromagnetic irradiation [9].

Collectively our findings further confirm that the antitumor effect (toxicity) of DOXO arises from the ability of the quinone ring in the drug to undergo electron transfer when the drug is loaded onto iron NP. Alterations of the quinone ring would change toxicity of the anthracycline. Iron bound to DOXO, on the other hand, can be reduced from Fe^{3+} to Fe^{2+} in a non-enzymatic manner by electron transfers from DOXO. MNC cycles can either reduce molecular oxygen or act as oxidants (perferryl ion) themselves and initiate lipid peroxidation since electrons transfer from DOXO to the iron NP surface and vice versa. On top of that, changes to the conformation of the amino sugar component of the anthracycline were shown to result in decreased reduction of bound iron, which correlated with decreased lipid peroxidation [16]. Therefore, it became apparent that the difference in the DOXO conformational changes was caused by electron transfers during MCA, MMA, MMCS or by the relationship between the quantity of surface and bulk atoms comprising Fe_3O_4 NP and the particle volume.

4 Conclusions and Futures Perspectives

The observed differences of FL spectra recorded from the antitumor anthracycline antibiotic DOXO in iron oxide NP and the proposed model for electron transfer can be used in pharmacy and medicine to predict and personalize the antitumor effect of MNC during its magneto-mechano-chemical synthesis.

References

1. Bray F, Ferlay J, Soerjomataram I et al (2018) Global cancer statistics 2018: GLOBOCAN estimates of incidence and mortality worldwide for 36 cancers in 185 countries. Cancer J Clin 68(6):394–424. https://doi.org/10.3322/caac.21492
2. Wang Shenghang, Luo Jie, Zhang Zhihao et al (2018) Iron and magnetic: new research direction of the ferroptosis-based cancer therapy. Am J Cancer Res 8(10):1933–1946
3. Singh N, Jenkins G, Asadi R, Doak SH (2010) Potential toxicity of superparamagnetic iron oxide nanoparticles (SPION). Nano Rev 1. https://doi.org/10.3402/nano.v1i0.53581
4. Alhareth K, Vauthier C, Bourasset F et al (2012) Conformation of surface-decorating dextran chains affects the pharmacokinetics and biodistribution of doxorubicin-loaded nanoparticles. Eur J Pharm Biopharm 81(2):453–457. https://doi.org/10.1016/j.ejpb.2012.03.009
5. Harrold MW (1996) The influence of conformational isomerism on drug action and design. Am J Pharm Educ 60:192–197. https://doi.org/aj6002192.pdf
6. Nakata Y, Hopfinger AJ (1980) An extended conformational analysis of doxorubicin. FEBS Lett 117:259–264. https://doi.org/10.1016/0014-5793(80)80957-4
7. Zhang T, Lu G, Shen H et al (2014) Photoluminescence of a single complex plasmonic nanoparticle. Sci Rep 4:3867. https://doi.org/10.1038/srep03867
8. Orel VE, Tselepi M, Mitrelias T et al (2019) The comparison between superparamagnetic and ferromagnetic iron oxide nanoparticles for cancer nanotherapy in the magnetic resonance system. Nanotechnology 30(41):415701. https://doi.org/10.1088/1361-6528/ab2ea7
9. Orel V, Shevchenko A, Romanov A et al (2015) Magnetic properties and antitumor effect of nanocomplexes of iron oxide and doxorubicin. Nanomedicine 11(1):47–55. https://doi.org/10.1016/j.nano.2014.07.007
10. Cohen J (2013) In: Statistical power analysis for the behavioral sciences, 2nd edn. Taylor and Francis, pp 567
11. da Silveira Beraldo, Balestrin L, Del Duque D, Soares da Silva D et al (2014) Triboelectricity in insulating polymers: evidence for a mechanochemical mechanism. Faraday Discuss 170:369–383. https://doi.org/10.1039/c3fd00118k
12. Albanese A, Tang PS, Chan WCW (2012) The effect of nanoparticle size, shape, and surface chemistry on biological systems. Annu Rev Biomed Eng 14:1–16. https://doi.org/10.1146/annurev-bioeng-071811-150124
13. Delogu F (2005) Structural and energetic properties of unsupported Cu nanoparticles from room temperature to the melting point: molecular dynamics simulations. Phys Rev B 72:205418. https://doi.org/10.1103/PhysRevB.72.205418
14. Christian P, Von der Kammer F, Baalousha M, Hofmann T (2008) Nanoparticles: structure, properties, preparation and behaviour in environmental media. Ecotoxicology 17:326–343. https://doi.org/10.1007/s10646-008-0213-1
15. Noh J, Osman OI, Aziz SG, Winget P, Brédas J-L (2014) A density functional theory investigation of the electronic structure and spin moments of magnetite. Sci Technol Adv Mater 15:044202. https://doi.org/10.1088/1468-6996/15/4/044202
16. Green M, Alderton P, Sobol M et al (1991) ICRF-187 (ADR-529) cardioprotection against anthracycline-induced cardiotoxicity: clinical and preclinical studies. In: Book new drugs, concepts and results in cancer chemotherapy. Springer Science + Bussines Media, New York, Muggia